Molecular Materials

Edited by

Duncan W. Bruce
University of York, UK

Dermot O'Hare
University of Oxford, UK

Richard I. Walton
University of Warwick, UK

WILEY
A John Wiley and Sons, Ltd, Publication

Molecular Materials

Inorganic Materials Series

Editors:

Series Titles

Functional Oxides
Molecular Materials
Porous Materials
Low-Dimensional Solids
Energy Materials

Molecular Materials

Edited by

Duncan W. Bruce
University of York, UK

Dermot O'Hare
University of Oxford, UK

Richard I. Walton
University of Warwick, UK

WILEY
A John Wiley and Sons, Ltd, Publication

This edition first published 2010

Registered office

John Wiley & Sons Ltd, The Atrium, Southern Gate, Chichester, West Sussex, PO19 8SQ, United Kingdom

Library of Congress Cataloging-in-Publication Data

Molecular materials / edited by Duncan W. Bruce, Dermot O'Hare, Richard I. Walton.
p. cm.
Includes bibliographical references and index.
ISBN 978-0-470-98677-6
1. Superconductors. 2. Organic conductors. 3. Magnetic materials—Optical properties.
4. Inorganic compounds—Optical peoperties. 5. Molecular dynamics.
6. Nonlinear optics. I. Bruce, Duncan W. II. O'Hare, Dermot. III. Walton, Richard I.
QC611.95.M65 2010
620.1′129—dc22

2009041767

A catalogue record for this book is available from the British Library.

ISBN: 978-0-470-98677-6 (Cloth)

Set in 10.5/13 Sabon by Integra Software Services Pvt. Ltd, Pondicherry, India.
Printed and bound by TJ International, Padstow, Cornwall

Contents

Inorganic Materials Series Preface

Back in 1992, two of us (DWB and DO'H) edited the first edition of *Inorganic Materials* in response to the growing emphasis and interest in materials chemistry. The second edition, which contained updated chapters, appeared in 1996 and was reprinted in paperback. The aim had always been to provide the reader with chapters that while not necessarily comprehensive, nonetheless gave a first-rate and well-referenced introduction to the subject for the first-time reader. As such, the target audience was from first-year postgraduate student upwards. Authors were carefully selected who were experts in their field and actively researching their topic, so were able to provide an up-to-date review of key aspects of a particular subject, whilst providing some historical perspective. In these two editions, we believe our authors achieved this admirably.

In the intervening years, materials chemistry has grown hugely and now finds itself central to many of the major challenges that face global society. We felt, therefore, that there was a need for more extensive coverage of the area and so Richard Walton joined the team and, with Wiley, we set about a new and larger project. The *Inorganic Materials Series* is the result and our aim is to provide chapters with a similar pedagogical flavour but now with much wider subject coverage. As such, the work will be contained in several themed volumes. Many of the early volumes concentrate on materials derived from continuous inorganic solids, but later volumes will also emphasise molecular and soft matter systems as we aim for a much more comprehensive coverage of the area than was possible with *Inorganic Materials*.

We approached a completely new set of authors for the new project with the same philiosophy in choosing actively researching experts, but also with the aim of providing an international perspective, so to reflect

the diversity and interdisciplinarity of the now very broad area of inorganic materials chemistry. We are delighted with the calibre of authors who have agreed to write for us and we thank them all for their efforts and cooperation. We believe they have done a splendid job and that their work will make these volumes a valuable reference and teaching resource.

DWB, York
DO'H, Oxford
RIW, Warwick
January 2010

Preface

One of the great attractions of working with molecular materials is the way in which the bulk macroscopic response of a material that can be held in the hand can be influenced by changes at the Ångström level. Thus molecular materials represent a class of substances where seemingly small, delicate changes in molecular structure can change totally the properties of the material in bulk.

Many molecular materials have been studied for a long period of time, but in the years since the 1980s there has been increasing emphasis on functional metal complexes able to demonstrate a wide range of physical phenomena. The scope is vast and it is simply not possible to encapsulate all in a single volume, hence we have chosen subjects that represent something of the diversity of the area, encapsulating magnetic, optical and electrical properties.

Once more, we have sought out active and expert practitioners from across the globe to distill the essence of their subject, providing well-referenced chapters with suitably pedagogical introductions and conveying the excitement of work in that field. We believe that they have done an excellent job and trust that you will agree.

DWB, York
DO'H, Oxford
RIW, Warwick
January 2010

List of Contributors

Koen Binnemans Department of Chemistry, Katholieke Universiteit Leuven, Leuven, Belgium

Hubert Le Bozec Laboratoire de Sciences Chimiques de Rennes, Université de Rennes, Rennes, France

Olivier Maury Laboratoire de Chimie, CNRS – Ecole Normale Supérieure de Lyon, Université de Lyon, Lyon, France

Eric J. L. McInnes School of Chemistry, The University of Manchester, Manchester, UK

Neil Robertson School of Chemistry, University of Edinburgh, Edinburgh, UK

Hisashi Tanaka Molecular Nanophysics Group, AIST, NRI, Tsukuba, Japan

Lydie Valade Laboratoire de Chimie de Coordination, CNRS, Toulouse, France

Richard E. P. Winpenny School of Chemistry, The University of Manchester, Manchester, UK

Gordon T. Yee Department of Chemistry, Virginia Polytechnic Institute and State University, Blacksburg, Virginia, USA

1

Metal-Based Quadratic Nonlinear Optical Materials

Olivier Maury[a] and Hubert Le Bozec[b]
[a]*Laboratoire de Chimie, CNRS - Ecole Normale Supérieure de Lyon,Université de Lyon, France*
[b]*Laboratoire de Sciences Chimiques de Rennes, Université de Rennes, France*

1.1 INTRODUCTION

Nonlinear optical (NLO) materials have been the focus of intensive investigations for several decades from both the fundamental and practical points of view for their possible applications in the domain of optoelectronics and photonics.[1–4] NLO materials can be used to manipulate optical signals, and when light interacts with such materials the incident light can be changed and new electromagnetic field components generated. NLO materials have potential applications in optical signal processing, frequency generation such as second and third harmonic generation (SHG and THG, respectively), and can also contribute to optical data storage and image processing. NLO activity can be found in inorganic crystals, such as $LiNbO_3$, and also in organic materials. The latter have attracted great interest owing to their fast and large nonlinearities, their inherent tailorability, which allows fine tuning of the NLO properties, and to their compatibility with polymer matrices. About twenty years ago, the field of NLO was extended to molecular materials featuring organometallic and coordination complexes.[5–11]

Molecular Materials Edited by Duncan W. Bruce, Dermot O'Hare and Richard I. Walton

Compared with organics, metal-based chromophores offer additional advantages due to their structural, electronic and optical properties. Greater design flexibility can be achieved by varying the metal, its oxidation state, the ligand environment and the geometry.

The subject of this chapter is to review some developments, made in the last fifteen years, in quadratic NLO materials based on organometallic and coordination compounds. After a brief introduction about the principles of nonlinear optics, the two main classes of second-order metal-based NLO chromophores are described, *i.e.* the dipoles and octupoles: the most widely investigated NLO metal complexes belong to the class of dipolar molecules constituted by a D-π-A system, in which the donor (D) and/or the acceptor (A), or the bridge (π) moieties are constituted by an organometallic or coordination group. Octupoles are nondipolar two-dimensional (2D) or three-dimensional (3D) chromophores, and coordination chemistry is particularly useful to design original octupolar architectures of octahedral or tetrahedral geometry. Recent advances in metal complexes as NLO switches and as precursors of supramolecular organised NLO materials are presented in the last two parts of the chapter.

1.2 BASIC CONCEPTS OF SECOND-ORDER NONLINEAR OPTICS

1.2.1 Introduction to Nonlinear Molecular Materials

NLO phenomena result from the interaction between light and matter and, more precisely, between the polarisable electron density and the strong electric field associated with a very intense laser beam. They were experimentally observed firstly in 1961 just after the development of intense laser sources in particular by Kaiser and Garett for two-photon absorption[12] and by Franken for SHG.[13] They can be divided in two main classes depending on the incident laser wavelength (Figure 1.1):

(i) the *nonresonant* NLO phenomena, such as SHG or THG, but also Pockel or Kerr effects, can be described as resulting from an electronic perturbation of the molecular ground state;
(ii) the *resonant* NLO phenomena, like two(multi)-photon absorption, are due to the quantic nature of molecule and occur only when

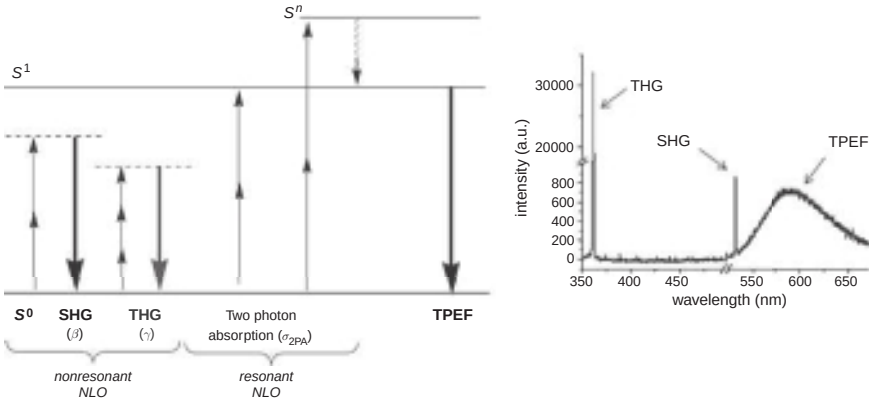

Figure 1.1 Jablonski diagram and spectral representations of NLO phenomena

the laser energy is a multiple of the energy gap between the ground and excited states. In this latter case, an electron is promoted from the fundamental to the excited state by nonlinear absorption, which is in marked contrast with nonresonant phenomena.

All these phenomena can occur simultaneously within the same material, as illustrated by the spectral response of an oriented polymer doped with DCM dye (4-dicyanomethylene-2-methyl-6-*p*-dimethylaminostyryl-4*H*-pyran) under 1.06 μm laser irradiation (Figure 1.1). The two sharp signals at 532 and 354 nm are coherent emission induced by SHG and THG, whereas the broad band is incoherent emission of two-photon excited fluorescence (TPEF).

The principles of nonlinear optics and the main techniques used to evaluate the second-order NLO properties are briefly presented here. Major details can be found in more specialised reviews and books.[1–11] At the molecular level, the interaction between polarisable electron density and the alternating electric field of the laser light beam (E) induces a polarisation response ($\Delta\mu$) that can be expressed following Equation 1.1:

$$\Delta\mu = \alpha \cdot E + \beta \cdot E^2 + \gamma \cdot E^3 + \ldots \tag{1.1}$$

where α, β and γ represent the first, second and third hyperpolarisability tensors, respectively. With normal values of E, the quadratic and cubic terms in Equation 1.1 can be neglected and only linear optical behaviour is observed. However, when E approaches the magnitude of atomic field

strengths (like a laser beam), the quadratic $\beta \cdot E^2$ and cubic $\gamma \cdot E^3$ terms become important. The equivalent form of Equation 1.1 at the macroscopic level is given in Equation 1.2, where ΔP is the induced macroscopic polarisation, and $\chi^{(1)}$, $\chi^{(2)}$ and $\chi^{(3)}$ are the first, second and third susceptibility tensors, respectively. For molecular systems, β and χ^2 are related if it is understood that polarisation is dipole moment/unit volume.

$$\Delta P = \chi^{(1)} \cdot E + \chi^{(2)} \cdot E^2 + \chi^{(3)} \cdot E^3 + \ldots \tag{1.2}$$

$\chi^{(2)}$ quantifies all second-order NLO effects such as SHG, electro-optic effect (Pockel) and frequency mixing. $\chi^{(3)}$ is representative of third-order NLO effects such as THG, optical Kerr effect and two-photon absorption (TPA). The real part of γ describes the nonlinear refractive index and its imaginary part the two-photon cross section (σ_2).

Due to parity considerations, nonzero β are restricted to noncentrosymmetric molecules and materials, while no symmetry restrictions are required for third-order NLO activity. Molecular engineering rules for the optimisation of second (β)- or third (γ, σ_2)- order NLO properties have been carefully established in the case of organic molecules or conjugated polymers; basically NLO chromophores possessing quadratic or cubic NLO activities can be divided into three main classes depending on the molecular symmetry (Figure 1.2): (i) the dipoles (D-π-A), (ii) the quadrupoles (D-π-D, A-π-A, D-π-A-π-D, -A-π-D-π-A...) or (iii) the octupoles of D_3 (A_3–D or D_3–A) or T_d/D_{2d} (A_4–D or D_4–A) symmetry (where D and A represent electron-donating and-withdrawing groups respectively, and π a conjugated skeleton). It is worth noting that only dipoles and octupoles are noncentrosymmetric; therefore, only these two approaches are discussed in this review.

1.2.2 Molecular Engineering of Quadratic NLO Chromophores

1.2.2.1 The Dipolar Approach

The vast majority of molecular compounds that possess large β values contain conjugated π-systems end-capped with donor (D) and acceptor (A) moieties. The linear optical properties of such dipolar, polarisable molecules are characterised by low energy, intramolecular charge transfer (ICT) transitions. Over the past twenty years, much effort has been directed towards the optimisation of β values, and several strategies have

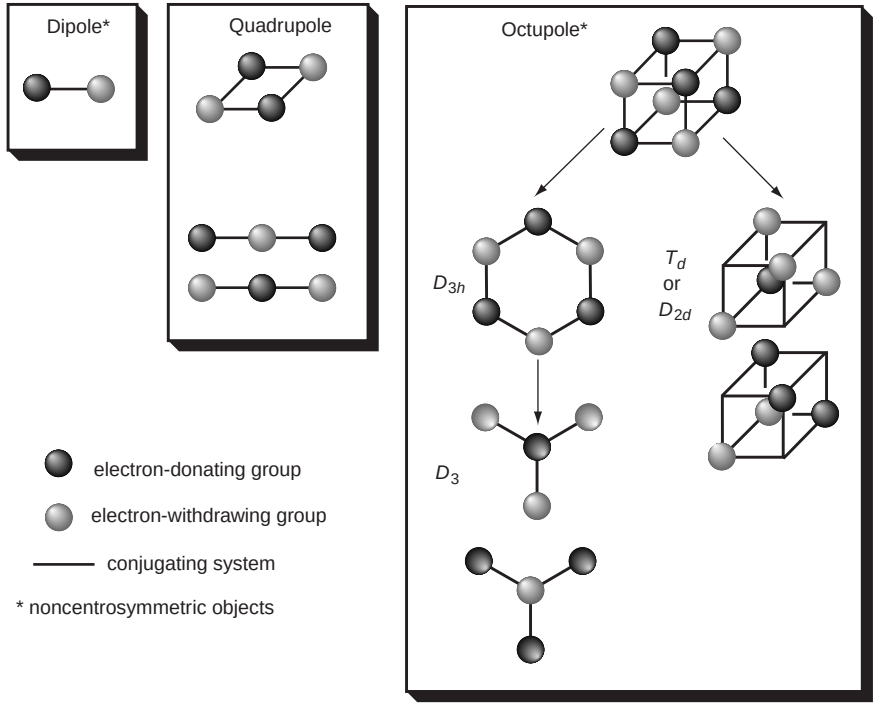

Figure 1.2 Schematic representation of the three main classes of NLO chromophores

emerged based on the classical 'two-state model'. This model invokes a polar ground state and charge separated first excited state, and β is correlated to the energy of the transition (E_{max}), the transition dipole moment (μ_{ge}) between the two states and the difference in dipole moment between the two states ($\Delta\mu_{ge} = \mu_e - \mu_g$) (Equation 1.3).

$$\beta \propto \Delta\mu_{eg} \times (\mu_{ge})^2/(E_{max})^2 \tag{1.3}$$

Representative examples of dipolar molecules that exhibit pronounced second-order NLO activities are shown in Figure 1.3; they are based on

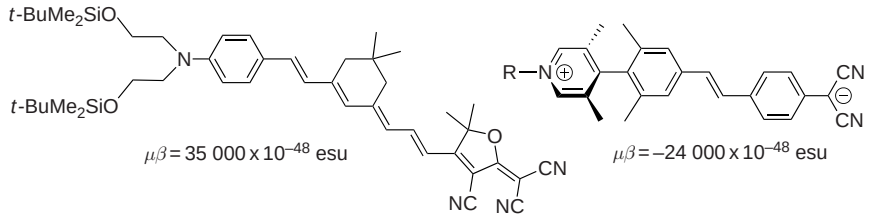

Figure 1.3 Representative examples of organic dipolar chromophores

polyenes connecting powerful electron donor and electron acceptor groups, such as dialkylamino and thiobarbituric acid or tricyanofuranyl, respectively.[14, 15] Unconventional zwitterionic molecules with twisted π-electron systems have also recently revealed exceptional molecular hyperpolarisabilities.[16, 17]

1.2.2.2 The Octupolar Approach

The archetype of the octupolar structure is a cube featuring donor and acceptor moieties at its edges or its derivatives obtained either by projection along a C_3 axis giving rise to the D_{3h} or D_3 symmetry ('TATB route') or by fusion of one type of charge in the barycenter leading to the D_{3h}, D_3, T_d or D_{2d} symmetry ('guanidinium route') (Figure 1.2).[18] Therefore, the molecular engineering of octupoles consists of a spatially controlled organisation of charge transfers within a molecule in order to reach the desired symmetry. This symmetry control can be achieved by taking advantage of the directionality of covalent bonds related to the hybridisation of the central core. For example: (i) D_{3h} symmetric octupoles are obtained by 1,3,5-functionalisation of a central aromatic core such as phenyl[19, 20], triazine[21] or boroxine[22]; (ii) D_{3h} or slightly twisted D_3 propeller like molecules exhibit a sp^2 hybridised carbon core (carbocation, carbanion or radical),[23] or a nitrogen atom;[24] whereas (iii) tetrahedral (T_d) octupoles comes from tetrasubstituted sp^3 hybridised carbon,[25] phosphonium[26] or tin[27] atoms. Some representative examples are shown in Figure 1.4.

1.2.2.3 Metal-Based NLO Chromophores

Like organic molecules, organometallic and coordination compounds can be used to design NLO molecular materials with large quadratic nonlinear responses.[5–11] One reason is that they offer a wide range of metals with different oxidation states and ligands which can give rise to tunable electronic properties. In addition, many complexes are known to possess low-lying charge-transfer transitions, such as intraligand (ILCT), metal-to-ligand (MLCT) and ligand-to-metal (LMCT), which can be associated with large second-order nonlinearities. Thus, in the case of dipolar as well as of octupolar NLO chromophores, the metal centre may act as the donor, the acceptor or even as the bridging moieties of a D-π-A network. Moreover, the metal centre can be used as template to build-up original octupolar architectures with D_{2d} or D_3 symmetry, thanks to the

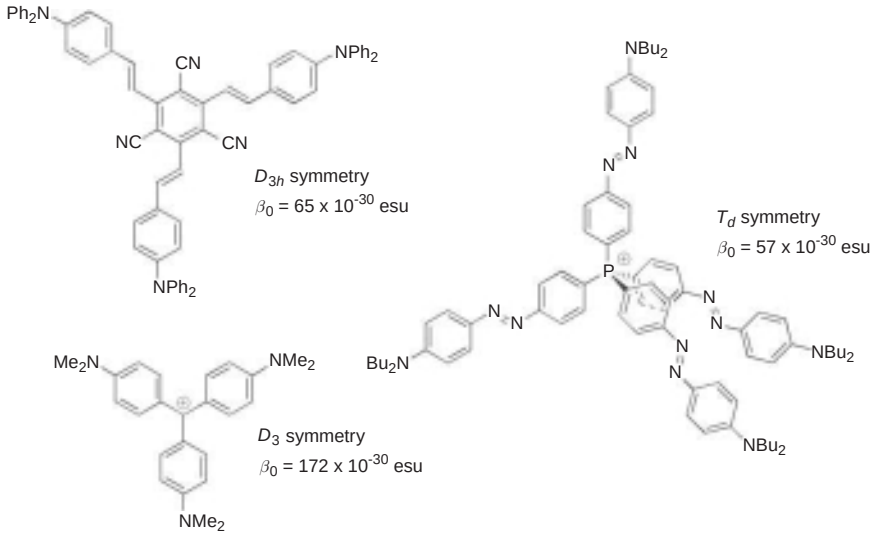

Figure 1.4 Representative examples of organic octupolar chromophores

large versatility offered by coordination chemistry. A nonexhaustive overview on both classes of metal-based NLO chromophores, that is dipoles and octupoles, is presented in Sections 1.3–1.6.

1.2.3 Experimental Measurements of Second-Order NLO Activities

Experimentally, molecular hyperpolarisabilities are generally determined in solution using two mains techniques: the Electric Field-Induced Second Harmonic Generation (EFISH) and Hyper-Rayleigh Scattering (HRS) [also termed Harmonic Light Scattering (HLS)] techniques. The EFISH method, suitable for neutral dipolar compounds, measures the second harmonic signal generated by a solution in which the chromophores are partially aligned by application of a strong, pulsed external electric field, synchronised with the incident laser beam. This technique allows the experimental determination of the product $\mu\beta_{zzz}$, where μ is the ground state dipole moment and β_{zzz} the vectorial projection of β along the molecular dipolar axis (z according to classical conventions). An independent experimental or theoretical determination of μ is necessary for the estimation of the quadratic hyperpolarisability. This experimental

method is not useful for charge dipolar molecules because it is not possible to apply a high voltage potential to an electrolyte-containing solution. In addition, it is also precluded for octupolar derivatives featuring zero ground state dipole moment. Therefore the HRS technique was developed in the beginning of the 1990s.[28, 29] This technique involves the detection of the incoherently scattering second harmonic light generated by each molecule in an isotropic solution and allows the determination of the $\beta \times \beta$ tensor product. Furthermore, selecting the polarisation of the incident laser beam and analysing the induced polarisation of the second harmonic signal makes possible the determination of each β tensor component that is directly related to the molecular symmetry.[18]

HRS presents several advantages over EFISH: it does not require any solution orientation and, consequently, can be used for neutral and also charged dipolar molecules as well as for octupolar derivatives. However, HRS signals are generally less intense and measurements are very sensitive to external noise or to parasitic signals such as TPEF. These drawbacks can be circumvented by the use of incident laser beam wavelengths located in the near-infrared spectral range (1500–1900 nm) or thanks to the frequency demodulation technique.[30] In this chapter, quadratic hyperpolarisability measured by EFISH or HRS with an incident laser beam wavelength (λ) are noted β_λ(EFISH) and β_λ(HRS), respectively. Whatever the measurement technique, the hyperpolarisability depends on the fundamental laser beam wavelength, which complicates rigorous comparison of data obtained by different laboratories using different experimental conditions. Therefore, a resonance enhancement correction is generally applied to provide the 'intrinsic' molecular hyperpolarisability (β_0), called static or zero-frequency hyperpolarisability on the basis of the simple two-levels model (Equation 1.4):

$$\beta_0 = \beta_\lambda \left[1 - \left(\frac{\lambda_{max}}{\lambda}\right)^2\right]\left[1 - \left(\frac{2\lambda_{max}}{\lambda}\right)^2\right] \tag{1.4}$$

where λ_{max} is the maximal absorption wavelength of the compound. Finally, the static hyperpolarisability (β_0), can be estimated by an indirect method according to the two-levels model (Equation 1.3) using Stark (or electroabsorption) spectroscopy that enables the determination of the $\Delta\mu_{ge}$ value. In the case of bulk materials like thin films or powders, the second-order susceptibility ($\chi^{(2)}$) is determined using the pseudo-quantitative Kurtz and Perry technique. This method allows the comparison of the intensity of the second harmonic signal with that of a reference compound, generally α-quartz or urea.

1.3 DIPOLAR METAL COMPLEXES

In this section, selected examples are described of dipolar second-order NLO chromophores in which an organometallic or coordination moiety may act as the donor (D), the acceptor (A) or even as the π-bridge connecting D to A. Representative examples of noncentrosymmetric bimetallic complexes containing metal-based fragments used as electron-donating and electron-accepting moieties, are also discussed.

1.3.1 Metal Complexes as Donor Groups

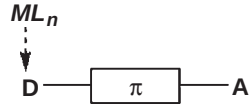

1.3.1.1 Metallocenyl Derivatives

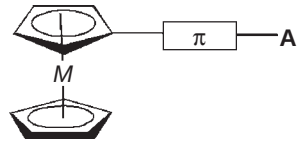

Since the pioneering work of Green *et al.* who, in 1987,[31] reported a powder SHG efficiency 62 times that of urea for *cis*-1-ferrocenyl-2-(4-nitrophenyl)ethylene, there has been considerable interest in using metallocenes as donor groups, and ferrocenyl compounds are amongst the most studied organometallic complexes for NLO.[32] The ferrocenyl group behaves as a moderate donor group and the nonlinearities are comparable with those of analogous methoxyphenyl organic chromophores (see, for example, compounds **1** and **2**, Figure 1.5).[33, 34] The β values are smaller than expected, based upon donor strength estimated from binding energy and redox potential. This behaviour is attributed to a poor electronic coupling between the metal *d*-orbitals and the π-network of the substituent. The low-energy spectra of ferrocenyl-based push–pull compounds are dominated by two bands, one between 300 and 400 nm assigned to π–π* transitions, and the second at about 450–600 nm assigned to a MLCT transition. These two transitions can both contribute to optical nonlinearity, so the two-level model, which

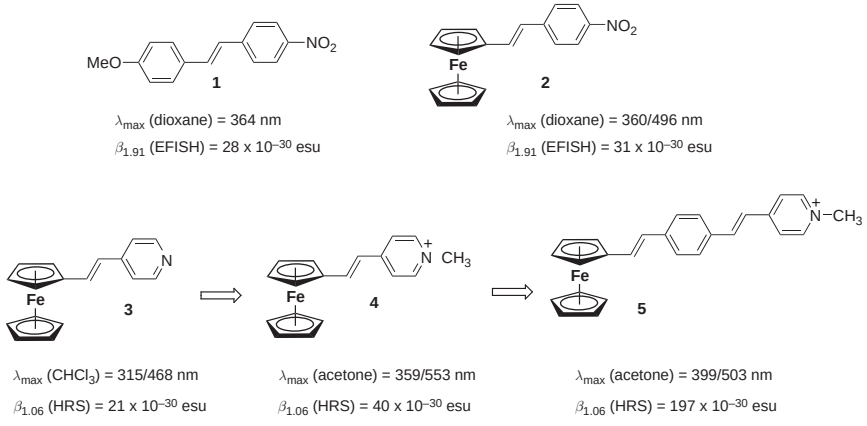

Figure 1.5 Selected ferrocenyl complexes

is employed to calculate the frequency-independent hyperpolarisability (β_0), is not appropriate for metallocenyl derivatives.[35] Some representative examples of push–pull derivatives where the ferrocenyl unit is connected to nitro, pyridine and pyridinium acceptor terminal groups through a conjugated π-linker are shown in Figure 1.5.[36] Similarly to push–pull organic chromophores, an increase of the nonlinearity is observed upon increasing the acceptor strength (*e.g.* **4** *vs* **3**) and upon conjugated π-linker lengthening (*e.g.* proceeding from **4** to **5**). (Note, however, that the second-order NLO activities of **3–5** have been measured by the EFISH technique with an incident wavelength of 1.06 μm, so the β values must be resonance enhanced.)

One advantage of organometallic complexes over organic compounds is the possibility of tuning NLO response by varying the metal centre. For example, the NLO properties of some ruthenocenyl species have been investigated and compared with those of related ferrocenyl complexes (Figure 1.6)[33, 37]: replacing iron by ruthenium results in a blue shift of the absorption bands and in a decrease of β (and $\mu\beta$) values, which can be understood by the higher ionisation energy of ruthenium *vs* iron.

Another interest in this type of organometallic NLO chromophore concerns their ability to afford noncentrosymmetric crystals displaying high bulk quadratic NLO efficiencies.[31] Several successful strategies have been developed recently (Figure 1.7), such as the use of enantiomerically pure analogues of chiral (*E*)-2-(4-nitrostyryl)ferrocene substituted by different R groups in the 2-position of the cyclopentadienyl ring (*e.g.* **8**), or the use of 1,1′-disubstituted ferrocenes (*e.g.* **9**); this give rise to favourable noncentrosymmetrical packing in which all molecules

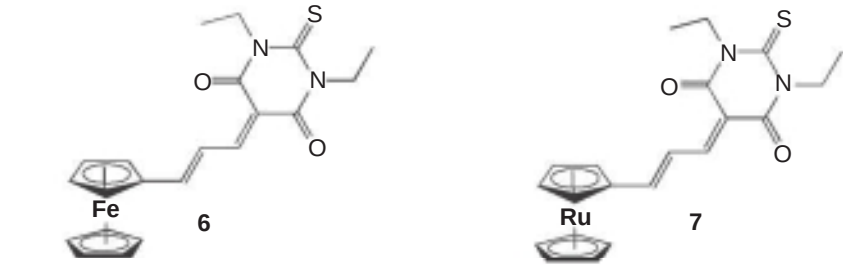

Figure 1.6 Selected ferrocenyl and ruthenocenyl complexes

are perfectly aligned and, thus, to large SHG efficiency in the solid state.[38, 39]

1.3.1.2 Cyclopentadienyl Metal Acetylide Derivatives

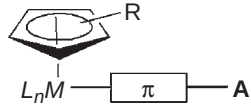

The NLO properties of cyclopentadienyl metal alkynyl complexes have also proven an especially popular research topic, particularly those containing Group 8 metals.[40, 41] Most of the studies have involved σ-acetylide ruthenium complexes with the $[Ru^{II}(\eta^5\text{–}C_5R_5)L_2]$ fragment (C_5R_5 = cyclopentadienyl, indenyl; L_2 = mono- or bisphosphines) as the electron donor group. These complexes display in the visible intense MLCT absorptions, which dominate the β responses, and, compared with

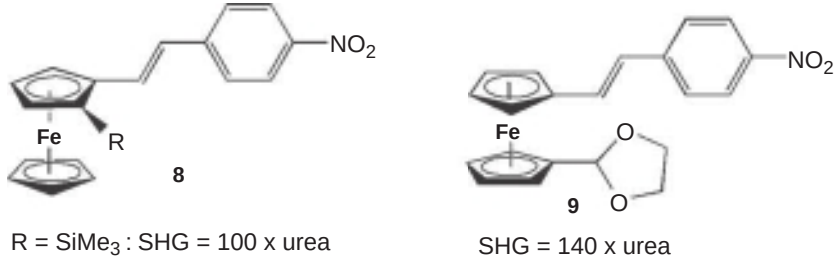

Figure 1.7 Selected examples of ferrocenyl chromophores with high SHG

metallocenyl-based chromophores, they give rise to a better coupling between the *d*-orbitals of the metal and the π*-orbitals of the alkynyl bridge and, hence, to larger quadratic nonlinearity. Selected examples of cyclopentadienyl ruthenium alkynyl NLO chromphores with their resonantly enhanced $\beta_{1.06}$ and two-level corrected β_0 values are represented in Figure 1.8. As expected, the nonlinearities can be enhanced by increasing the strength of the donor groups. For instance, replacement of two CO ligands by two PPh_3 ligands results in a significant bathochromic shift of the MLCT band along with a large increase in β_0 by a factor of 3.5 (*e.g.* **10** *vs* **12**).[42] In contrast, replacing PPh_3 by the stronger base PMe_3 results in a decrease in nonlinearity (*e.g.* **10** *vs* **11**), suggesting that the greater π-delocalisation through the phenyl group of PPh_3 is more important for quadratic NLO merit.[43] Substituting cyclopentadienyl by the more electron-rich indenyl ligand also results in a substantial enhancement of β_0 (*e.g.* **13** *vs* **10**).[44, 45] Similarly, lengthening the π-bridge results in a large increase in nonlinearity, as shown by the high β_0 value of complex **14** in comparison with that of **10**.[43]

Modulation of the NLO properties of cyclopentadienyl metal acetylide chromophores can also be achieved by varying the metal centre (Figure 1.9). An investigation on the quadratic NLO activity of Group 8 metals **15–17** has shown that the iron complex **15** has a lower β_0 value than ruthenium-containing analogue **16**, in contrast to the trend reported for donor–acceptor metallocenyl[33, 37] and nitrile complexes.[46] The molecular hyperpolarisabilities of Group 10 Ni^{II} complexes **18** and **19** are also smaller than those of the ruthenium analogues **10** and **14**, suggesting that the greater ease of oxidation of Ru^{II} *vs* Ni^{II} is important in determining NLO merit.[47]

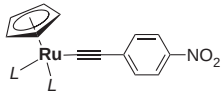

PPh_3 (**10**)	PMe_3(**11**)	CO (**12**)
λ_{max} (THF) = 460 nm	λ_{max} (THF) = 477 nm	λ_{max} (THF) = 364 nm
$\beta_{1.06}$ (HRS) = 468 x 10^{-30} esu	$\beta_{1.06}$ (HRS) = 248 x 10^{-30} esu	$\beta_{1.06}$ (HRS) = 58 x 10^{-30} esu
β_0 = 96 x 10^{-30} esu	β_0 = 39 x 10^{-30} esu	β_0 = 27 x 10^{-30} esu

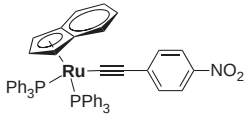

13

λ_{max} (CH_2Cl_2) = 476 nm
$\beta_{1.06}$ (HRS) = 746 x 10^{-30} esu
β_0 = 119 x 10^{-30} esu

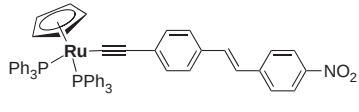

14

λ_{max} (THF) = 476 nm
$\beta_{1.06}$ (HRS) = 1455 x 10^{-30} esu
β_0 = 232 x 10^{-30} esu

Figure 1.8 Selected cyclopentadienyl ruthenium alkynyl complexes

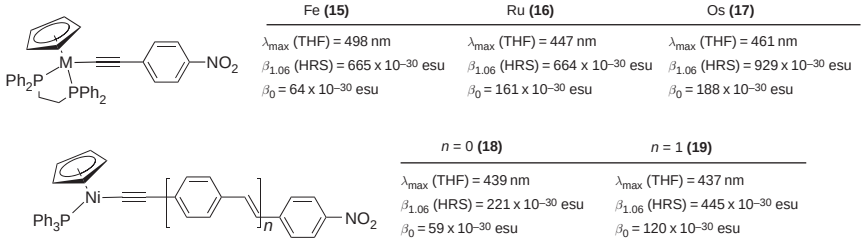

Figure 1.9 The effect of varying the metal centre on quadratic nonlinearity

1.3.1.3 Phosphine Metal Acetylide Derivatives

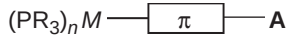

Chloro*bis*(diphosphine)metal fragments (M = iron, ruthenium, osmium) also behave as efficient donor groups in push–pull metal alkynyl complexes.[40, 41] Most of the NLO studies have focused on ruthenium complexes containing diphenylphosphinoethane (dppe) and diphenylphosphinomethane (dppm) as co-ligands (Figure 1.10).[48, 49] Other diphosphines, such as the chiral 1,2-*bis*(methylphenylphosphino) benzene ligand (*e.g.* **21**), have been used in order to ensure noncentrosymmetric crystal packing and bulk quadratic NLO activity.[50] These complexes display in the visible intense MLCT absorptions which dominate the β responses, and possess higher quadratic hyperpolarisability values than those of cyclopentadienyl ruthenium analogues (*e.g.* **20** *vs* **14**).

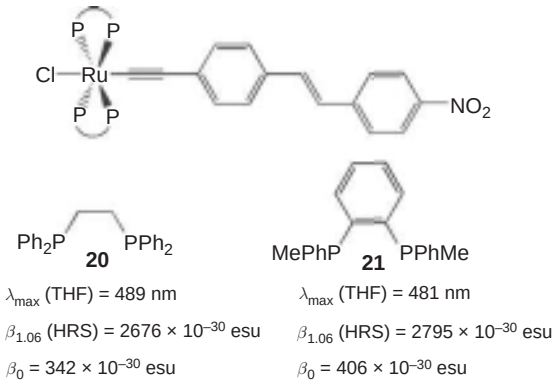

Figure 1.10 Selected examples of chloro*bis*(diphosphine)ruthenium alkynyl chromophores

	$n = 0$ **(22)**	$n = 1$ **(23)**
	λ_{max} (THF) = 338 nm	λ_{max} (THF) = 386 nm
	$\beta_{1.06}$ (HRS) = 22×10^{-30} esu	$\beta_{1.06}$ (HRS) = 120×10^{-30} esu
	$\beta_0 = 12 \times 10^{-30}$ esu	$\beta_0 = 49 \times 10^{-30}$ esu

Figure 1.11 Selected examples of linear gold(I) alkynyl chromophores

Linear triphenylphosphine gold(I) alkynyl compounds represent another class of dipolar chromophores in which the $(PPh_3)Au^I$ moiety behaves as a moderate donor group. They contain MLCT bands with absorption maxima at substantially higher energy than their ruthenium analogues ($\lambda_{max} = 340$–390 nm) and, thus, are optically transparent at both the fundamental and second harmonic wavelengths (Figure 1.11).[51] They have weaker quadratic NLO activity (*e.g.* **23** *vs* **14** and **20**), which is consistent with the 14 valence electrons, less oxidisable, gold(I) being a weaker donor than the 18-valence-electron, more oxidisable, ruthenium(II).

1.3.1.4 Metal Ammine Complexes

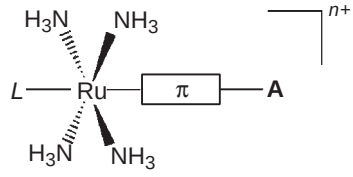

Ruthenium(II) ammine complexes are very interesting NLO chromophores because they combine well understood redox and charge-transfer absorption properties with synthetic versatility.[52] In such complexes, the Ru^{II} d^6 centre behaves as a powerful π donor and NLO properties can be tuned *via* ligand L^D (electron-rich ligand) and L^A (electron-accepting ligand) modification. They display intense solvatochromic visible $Ru^{II} \rightarrow L^A$ MLCT transitions, which dominate the β values. Some representatives examples are shown in Figure 1.12 with $L^A = N$-methyl-4,4′-bipyridinium (MeQ^+).[53] The NLO data obtained by HRS experiments with 1.064 μm incident wavelength in acetonitrile show that these metallochromophores display relatively large static β_0 values, in the range 10–130×10^{-30} esu. Moreover, Coe *et al.* have demonstrated that *N*-arylation of pyridinium L^A ligand increases λ_{max} and considerably increases β_0 (*e.g.* **26**: $\beta_0 = 410 \times 10^{-30}$ esu, Figure 1.12).[54]

An interesting peculiarity of these Ru^{II} ammine chromophores concerns the unusual effects of π-conjugation extension on the linear and

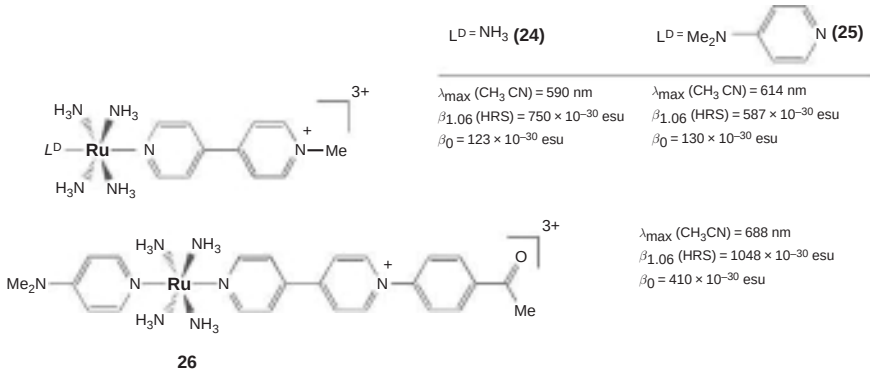

Figure 1.12 Selected examples of dipolar chromophores with ruthenium(II) ammine donor groups

NLO properties. For different polyene series (Figure 1.13), the MLCT bands unexpectedly blue-shift as the number of ethylene units increases from one to three, and β_0 maximises at $n = 2$.[55, 56] This behaviour is in marked contrast with known push–pull polyene organic chromophores, in which the π–π* intramolecular charge transfer (ICT) bands red-shift as the number of ethylene units increases and the β_0 values increase steadily with n.[57, 58] Time-dependent (TD)-DFT calculations corroborate the experimentally observed trends, and electrochemical, ^{1}H NMR and Stark spectroscopic data all show that the D–A electronic coupling is more effective in the polyene organic chromophores than in their Ru^{II} counterparts.[56–58] Furthermore, the D–A communication in the complexes falls off with distance, so that β_0 decreases above $n = 2$.

Ruthenium(II) ammines can also give rise to C_{2v} symmetric 2D dipolar chromophores featuring two *cis* pyridyl–pyridinium ligands L^A (*e.g.* **30**, Figure 1.14).[59] Such V-shaped complexes are interesting and unusual because they have a significant 'off-diagonal' tensor component β_{zyy} in addition to the classical β_{zzz} component. They display two MLCT bands in the visible, and TD-DFT calculations have shown that the lowest

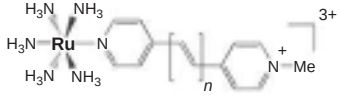

		λ_{max} (nm)	$\beta_{1.06}$ (10^{-30} esu)	β_0 (10^{-30} esu)
24	$n = 0$	590	750	123
27	$n = 1$	595	828	142
28	$n = 2$	584	2593	372
29	$n = 3$	568	1308	131

Figure 1.13 Selected examples of extended dipolar ruthenium(II) complexes

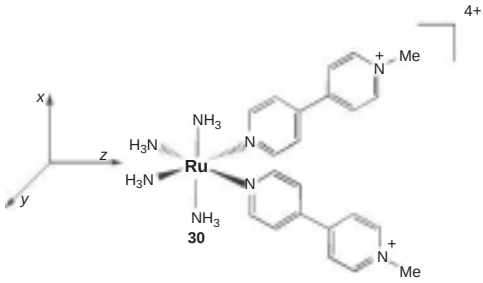

λ_{max} (nm)	β_0(HRS)	β_0 (calc) (10^{-30} esu)
570	139	β_{zyy} = 70
502		β_{zzz} = 18

Figure 1.14 An example of 2D dipolar ruthenium(II) complexes

energy MLCT transition is associated with β_{zyy} and the higher energy transition with β_{zzz}.[59]

1.3.1.5 Cyclometallated Complexes

Cationic complexes of cyclometallated $Ir^{III}(ppy)_2$ (ppy = 2-phenylpyridine) with chelated diimine ligands, such as bipyridines (bipy) and phenanthrolines (phen), have interesting phosphorescent properties with potential applications in electroluminescent devices. Such compounds show at rather high energy MLCT transitions ($\lambda_{max} = 340–380$ nm) from the $[Ir^{III}(ppy)_2]$-based HOMOs to the LUMOs based on the π^* -orbitals of the phen (or bipy) ligands. Thus, these complexes can be considered as push–pull molecules in which the $Ir^{III}(ppy)_2$ moiety acts as the donor and the diimine as the acceptor part.

Recent quadratic NLO studies have been investigated on a series of cationic iridium complexes bearing different substituents on the phenanthroline ligand (*e.g.* **31**: R = $N(CH_3)_2$, **32**: R = NO_2).[60] The $\mu\beta$ values were obtained by the EFISH technique working at 1.91 μm in dichloromethane, which allows by ion pairing the use of this technique with ionic chromophores. These complexes show quite large negative $\mu\beta$ values, from -1270 to -2230×10^{-48} esu (Figure 1.15). A theoretical sum-over-states (SOS)-TDDFT study has confirmed that the NLO response is mainly controlled by the MLCT transition and, as expected, the largest $\mu\beta$ value is that of the complex featuring the strong electron-withdrawing group NO_2. These new kinds of tunable chromophores are interesting as they show higher quadratic NLO responses than those of stilbazolium salts with no significant cost of transparency with respect to the SHG.

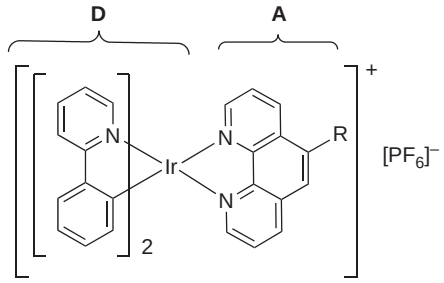

31 (R = NMe_2): λ_{max} (CH_2Cl_2) = 264/334 nm $\mu\beta_{1.91}$ (EFISH) = -1330×10^{-48} esu

32 (R = NO_2): λ_{max} (CH_2Cl_2) = 264/378 nm $\mu\beta_{1.91}$ (EFISH) = -2230×10^{-48} esu

Figure 1.15 Push–pull cyclometallated iridium(III) complexes

1.3.2 Metal Complexes as Acceptor Groups

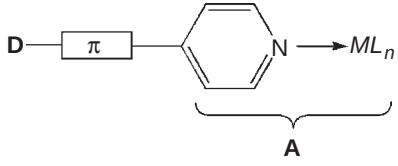

1.3.2.1 Pyridine and Bipyridine Metal Complexes

Metal complexes of nitrogen heterocyclic ligands, such as pyridines and oligopyridines, represent an important class of NLO chromophores which have received much attention during the last fifteen years.[61, 62] In particular, the molecular quadratic hyperpolarisabilities of donor-substituted pyridine[63, 64] and stilbazole[63–67] metal complexes have been studied by several groups. Some representative examples of donor-substituted stilbazole rhodium(I) and iridium(I) complexes **33** and **34** are shown in Figure 1.16.[64, 67] These compounds display intense positive solvatochromic intraligand charge transfer (ILCT) transitions, which dominate the β values. Upon coordination of the pyridine ligand to [MCl(CO)$_2$], which behaves as an electron acceptor, a bathochromic shift of the ILCT occurs, and therefore a significant enhancement of the EFISH β values can be observed. Note that the β values of **33** and **34** are similar to that of **35** ($M = BF_3$), suggesting an acceptor strength of [MCl(CO)$_2$] comparable with that of the Lewis acid BF_3.

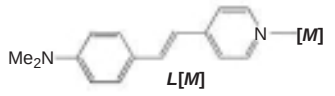

33: *L*[Rh(CO)$_2$Cl]; **34:** *L*[Ir(CO)$_2$Cl]; **35:** *L*[BF$_3$]

L[*M*]	λ_{max} (nm)	$\beta_{1.34}$ (10^{-30} esu)	β_0 (10^{-30} esu)
L	374	55	35
33	421	111	61
34	431	128	67
35	438	129	66

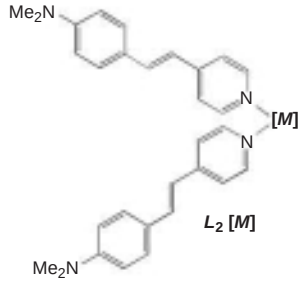

36: *cis*-*L*$_2$[PtCl$_2$]; **37:** *L*$_2$[Zn(CH$_3$CO$_2$)$_2$];
38: *L*$_2$[ZnCl$_2$]; **39:** *L*$_2$[Zn(CF$_3$CO$_2$)$_2$]

L$_2$[*M*]	λ_{max} (nm)	$\beta_{1.34}$ (10^{-30} esu)	β_0 (10^{-30} esu)
36	375	41	26
37	376	48	30
38	410	84	48
39	420	97	53

Figure 1.16 Stilbazole and bis(stilbazole) metal complexes

Quadratic NLO studies have been investigated on *cis*-bis(stilbazole) metal complexes such as the square-planar platinum(II) complex **36** and tetrahedral zinc(II) complexes **37–39** (Figure 1.16).[67] The EFISH $\beta_{1.34}$ value of the stilbazole ligand is almost not affected by coordination to the soft *cis*-$PtCl_2$ moiety and, strangely enough, to the weak Lewis acid $Zn(CH_3CO_2)_2$, in agreement with the irrelevant red-shift of the ILCT transition upon coordination ($\Delta\lambda = 1$–2 nm). However, an increase in the $\beta_{1.34}$ value and a significant red-shift ($\Delta\lambda = 36$–46 nm) is observed upon coordination to the stronger Lewis acids $ZnCl_2$ and $Zn(CF_3CO_2)_2$, respectively. Recently, a much larger bathochromic shift of the ILCT transition ($\Delta\lambda = 116$ nm) has been observed upon coordination of dimethylaminostilbazole ligand to the strong Lewis acid $Zn(CF_3SO_3)_2$ (*e.g.* **40**, Figure 1.17).[68] Consistent with such a large red-shift, the $\beta_{1.91}$ (EFISH) value measured in chloroform is much higher than those of related Zn^{II} complexes **37–39**. Surprisingly, the β value of **40** has been found to be dependent on the concentration, an effect that is not observed with for compounds **37–39**: below 10^{-4} M, β increases abruptly with decreasing concentration. Such large enhancement has been attributed to an increase concentration of the cation $[L_2Zn(CF_3SO_3)]^+$ produced by the facile solvolysis of the triflato ligand.

As in the case of donor-substituted stilbazoles, the second-order NLO responses of donor-substituted styryl bipyridines[69–71] and phenanthrolines [67] are significantly enhanced upon coordination to a metal centre.

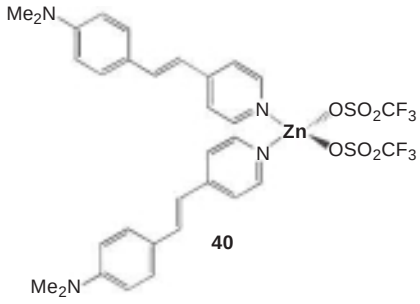

40

conc (mol dm^{-3})	λ_{max} (nm)	$\beta_{1.91}$ (10^{-30} esu)
5 x 10^{-4}	490	163
1 x 10^{-4}	–	220
0.5 x 10^{-4}	–	404

Figure 1.17 Bis(dimethylaminostilbazole)Zn(CF_3CO_2)$_2$ complex with large quadratic NLO response

For example, in the series **41–44**, the red-shift of the ILCT transition ($\Delta\lambda_{max} = 54$–87 nm) increases with the acceptor strength of the metal centre and follows the order $Re(CO)_3Br > ZnCl_2 > Zn(CH_3CO_2)_2 > HgCl_2$ (Figure 1.18). The ordering of the β values follows that found for the relative energies of the ILCT transitions, with the exception of the d^6 Re^I complex **41**, which is less efficient than those of the corresponding Zn^{II} complexes **42** and **44** due to the presence of the vectorially opposed MLCT transition, which can contribute to a lowering of the $\beta_{1.34}$ value. The NLO properties of bis(dialkylaminostyryl)bipyridinedichlorozinc(II) complexes (*e.g.* **45**) have also been studied.[70, 71] Interestingly, the NLO activity of **45** is significantly larger than that of the related Zn^{II} complex **38** of non-chelating dimethylaminostilbazole ligand (Figure 1.16), in agreement with the red-shift of the ILCT transition (**45** *vs* **38**, $\Delta\lambda_{max} = 50$ nm). This can be due to the more planar arrangement of the bipyridine ligand and, therefore,

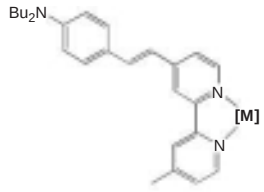

[M] **41**: $Re(CO)_3Br$; **42**: $Zn(CH_3CO_2)_2$; **43**: $HgCl_2$; **44**: $ZnCl_2$

	λ_{max} (nm)	$\beta_{1.34}$ (10^{-30} esu)	β_0 (10^{-30} esu)
L	388	14	8
41	475	71	35
42	447	116	57
43	442	65	32
44	460	152	71

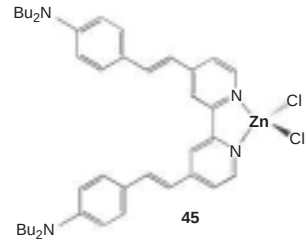

45

λ_{max} (CH_2Cl_2) = 459 nm

$\mu\beta_{1.34}$ (EFISH) = 1830 × 10^{-48} esu; $\mu\beta_0$ = 850 × 10^{-48} esu

β_0 (HRS) = 123 × 10^{-30} esu

Figure 1.18 Examples of donor-substituted styrylbipyridine metal complexes

to a stronger perturbation of the π*-orbitals and consequently to a shift of the ILCT at lower energy.[72]

1.3.2.2 Terpyridine Metal Complexes

The second-order NLO responses of various terdentate ligands, such donor-substituted terpyridines (terpy) and their corresponding metal complexes, have been investigated recently.[72, 73] An interesting EFISH study on 4′-dibutylaminophenyl-2,2′:6′,2″-terpyridine coordinated to different Lewis acids ($ZnCl_2$, $IrCl_3$, $Ru(CF_3CO_2)_3$) **46–48** has shown that different metal centres can influence not only the absolute value, but also the sign of the quadratic hyperpolarisability (Figure 1.19). All complexes display an ILCT transition that is red-shifted ($\Delta\lambda_{max} = 56$–105 nm) with respect to that of the free ligand ($\lambda_{max} = 360$ nm). The UV-visible spectrum of the Ir^{III} complex shows another band at lower energy corresponding to an MLCT transition, whereas that of the Ru^{III} complex displays two additional bands at 508 nm and 911 nm, which have been assigned by TD-DFT calculations to ILCT (with some MLCT character) and LMCT transitions, respectively. The enhanced positive molecular hyperpolarisability value of the terpyridine ($\beta_{1.34} = 22 \times 10^{-30}$ esu, $\beta_0 = 15 \times 10^{-30}$ esu) upon coordination to zinc chloride is similar to that found with other donor-substituted pyridine or bipyridine Zn^{II} complexes. However, upon coordination of the terpy ligand to an Ir^{III} and Ru^{III} centre, the absolute value of $\beta_{1.34}$ enhances significantly in agreement with the Lewis acidity of these metal centres and red-shift of ILCT, but the sign becomes negative. The negative values of β

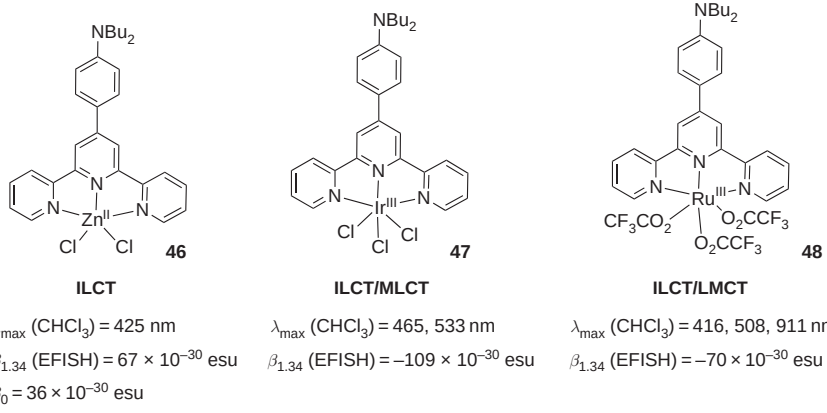

Figure 1.19 Examples of push–pull terpyridine metal complexes

have been confirmed by the negative solvatochromism of these two complexes ($\Delta\mu < 0$). For these complexes, the NLO response is not only influenced by the ILCT transition, but also by the other MLCT and/or LMCT transitions.

Lanthanide-containing NLO chromophores are very rare, and this is quite surprising because of their strong Lewis acidity and their ability to accept large coordinance (8–12), resulting in unusual geometries. A series of dipolar Ln^{III} **49** (lanthanum, gadolinium, dysprosium, ytterbium and yttrium) complexes containing an annelated dibutylaminophenyl functionalised terpyridyl ligand has been recently prepared and their NLO properties have been investigated by HRS at a nonresonant incident light of 1.91 μm (Figure 1.20).[74, 75] All lanthanide ions behave similarly in terms of their UV-visible spectra with the ILCT transition of the terpy ligand, which is red-shifted by *ca* 75 nm ($\lambda_{max} = 450$ nm) upon complexation, confirming the known similar ionochromic effect along the 4*f* elements. On the other hand, the β coefficient is clearly dependent on the nature of the metal ion: a significant increase of $\beta_{1.91}$ is observed on going from lanthanum to ytterbium, whereas for yttrium, which, like lanthanum, has no *f*-electrons there is no significant increase

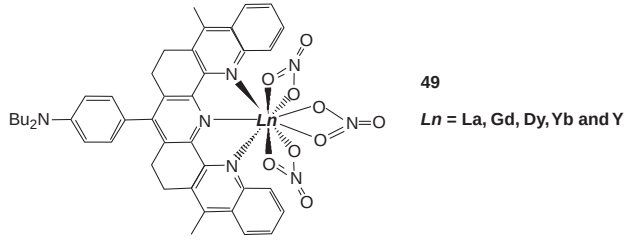

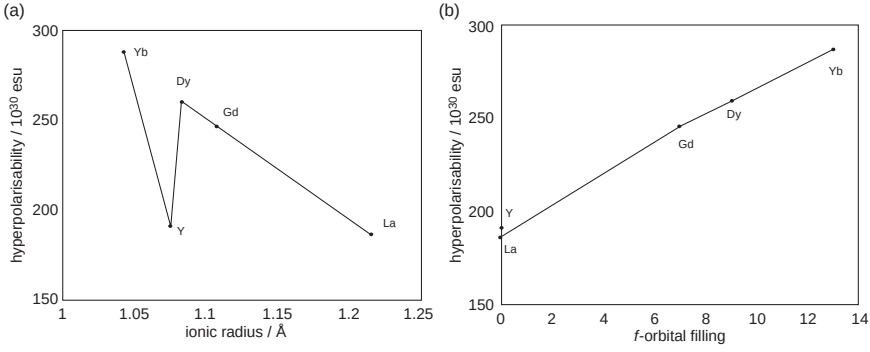

Figure 1.20 Annelated terpyridine lanthanide complexes and plots of the hyperpolarisability coefficient *vs* ionic radius (a) and *f*-orbital filling (b)

in β. This enhancement is supposed to be correlated with the *f*-electron configuration rather than to the ionic radius (Figure 1.20). This intrinsic property of rare earth metals is highly attractive in terms of transparency/nonlinearity trade-off, because improved NLO responses can be reached without any cost in transparency.

1.3.3 Bimetallic Push–Pull Complexes

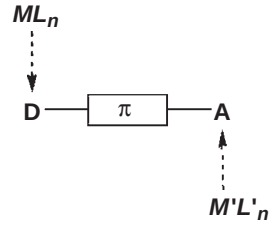

Metal-based fragments can be used as electron donating and electron accepting moieties, so the introduction of two metal atoms for the building of dipolar chromophores is a logical step, and this has been an area of interest in the past ten years. The majority of asymmetric bimetallic complexes for which second-order NLO properties have been reported contains one metallocenyl group as the donor part of the molecule. The sesquifulvalene iron–chromium complex **50** is a typical example in which the cationic cycloheptatrienyl chromium tricarbonyl is used as the acceptor moiety (Figure 1.21).[76] A pronounced negative solvatochromism is observed for the charge transfer absorption band about 600 nm, and a rather large quadratic hyperpolarisability has been measured by HRS at 1.06 μm.

The *ambivalent donor or acceptor role* of low-valent metal carbonyl species, such as $M(CO)_5$ [M = chromium, molybdenum, tungsten], in monometallic *p*-substituted pyridine (or stilbazole) complexes was investigated in detail by Kanis *et al.* in the early 1990s,[63] and later by Roberto *et al.* (Figure 1.22).[64] As already seen before, when the substituent is an

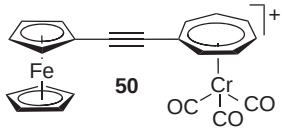

λ_{max} (CH_2Cl_2) = 600 nm
$\beta_{1.06}$ (HRS) = 570 × 10^{-30} esu
β_0 = 105 × 10^{-30} esu

Figure 1.21 A typical example of bimetallic NLO complex

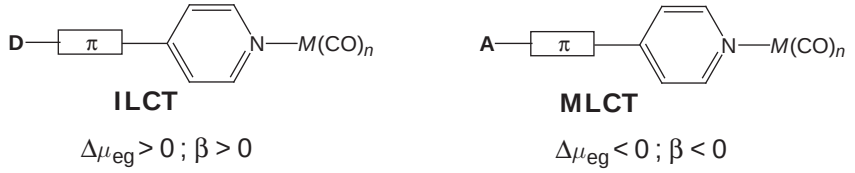

Figure 1.22 The ambivalent role of metal carbonyl complexes

electron-donating group D such as NR_2, β is dominated by an ILCT transition, with the metal centre functioning primarily as an inductive electron acceptor. By contrast, when the substituent is an electron-accepting group A such as NO_2, CHO or $COCH_3$, β is mainly dominated by a MLCT transition. In this case the sign of β(EFISH) is negative, due to the reduction of the dipole moment in the excited state ($\Delta\mu_{eg} < 0$).

The same situation can occur in heterobimetallic complexes featuring bridging nitrogen-based heterocyclic ligands and low-valent metal carbonyl complexes. In bimetallic complexes with ferrocene as donor (*e.g.* **52**), the tungsten pentacarbonyl fragment behaves as a good acceptor, as shown by the large enhancement of the β value upon coordination of the pyridyl ligand to $W(CO)_5$ (Figure 1.23).[77] A further large increase in β (by a factor of five) can be observed on replacing ferrocene by the much more efficient donor indenyl ruthenium alkynyl moiety (*e.g.* **53**).[78]

By contrast, the $W(CO)_5$ fragment acts as donor group in bimetallic complexes having π-acceptor linkers such as pyrazine (pyz) or 1,2-bis(4-pyridyl)ethylene (bpe). Coordination of $(CO)_5W(L)$ [L = pyz, bpe] to *cis*-[$RhCl(CO)_2$] (*e.g.* **54** and **55**) leads to an increase in the absolute quadratic hyperpolarisability values $\beta_{1.91}$ (by a factor of 5–6) determined by EFISH (Figure 1.24).[79, 80] The NLO response is dominated by the MLCT [$d(W) \rightarrow \pi^*(L)$] transition, and the negative values are in agreement with the negative $\Delta\mu_{eg}$ values as confirmed by a negative solvatochromism. In these heteronuclear bimetallic chromophores, the increase in β

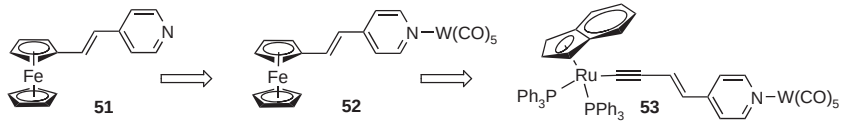

λ_{max} ($CHCl_3$) = 315/468 nm
$\beta_{1.06}$ (HRS) = 21 x 10^{-30} esu

λ_{max} ($CHCl_3$) = 362/491 nm
$\beta_{1.06}$ (HRS) = 101 x 10^{-30} esu

λ_{max} (CH_2Cl_2) = 462 nm
$\beta_{1.06}$ (HRS) = 535 x 10^{-30} esu
β_0 = 71 x 10^{-30} esu

Figure 1.23 Heterobimetallic complexes containing bridging pyridine ligands

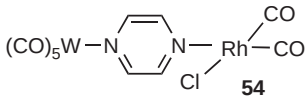

54

λ_{max} ($CHCl_3$) = 499 nm

$\beta_{1.91}$ (HRS) = –28 x 10^{-30} esu

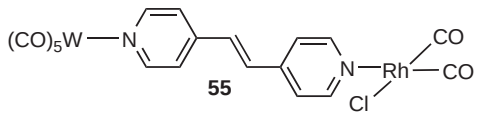

55

λ_{max} ($CHCl_3$) = 435 nm

$\beta_{1.91}$ (HRS) = –41 x 10^{-30} esu

Figure 1.24 Selected examples of bimetallic complexes with $W(CO)_5$ acting as donor

is due to the enhancement of the acceptor strength of the bridging ligands pyz and bpe upon coordination to the $RhCl(CO)_2$ fragment.

The same type of bridging ligands has also been used to prepare heteronuclear bimetallic NLO complexes (*e.g.* **56**) in which the electron-donating and electron-accepting units are *trans*-$[RuCl(pdma)_2]^+$ (pdma = 1,2-phenylenebis(dimethylarsine) and $[fac\text{-}Re(CO)_3(biq)]^+$ (biq = 2,2′-biquinoline), respectively (Figure 1.25).[81] The absorption spectra of these species are dominated by intense visible $d(Ru^{II}) \rightarrow \pi^*$(4,4′-bipy/bpe) MLCT bands in the region 440–462 nm and other absorptions at higher energy (360–380 nm), which are assigned to $d(Re^{I}) \rightarrow \pi^*$ (biq) MLCT transitions. The energies of the former are higher than those of the related species **57** with the electron-withdrawing *N*-methylpyridinium group. No clear evidence for intermetallic electronic communication is provided by cyclic voltammetry. Stark (electroabsorption) spectroscopic studies in butyronitrile glasses at 77 K showed that extending the conjugation affords increased first β_0 values, and comparisons with the monometallic species reveal that alkylation of the free pyridine nitrogen leads to larger β_0 responses than does the coordination of the rhenium(I) centre. This outcome can be attributed to the ambivalent electronic behaviour of the

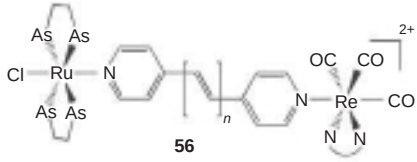

56

	λ_{max} (nm)	β_0 (10^{-30} esu)
n = 0	440	47
n = 1	462	114

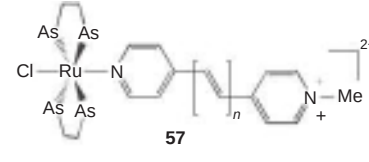

57

	λ_{max} (nm)	β_0 (10^{-30} esu)
n = 0	486	113
n = 1	492	123

Figure 1.25 Selected examples of dipolar complexes with Ru^{II} bis(diarsine) as donor group

rhenium(I) centre: although being a strong Lewis acid, it behaves as a π-donor, and this offsets its net electron-withdrawing effect.

1.3.4 Metal Complexes as π-Conjugated Bridges

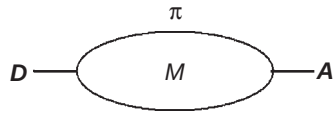

1.3.4.1 Metal Schiff Base Complexes

A number of NLO studies of bis(salicylaldiminato)metal complexes have been carried out over the past ten years.[82] For example, the quadratic hyperpolarisability of complexes **58–60** featuring different metal ions has been measured by the EFISH technique: these complexes exhibit enlarged NLO responses when compared with that of the free ligand, and the negative β responses are dominated by MLCT excitations, the metal acting as the donor (Figure 1.26).[83, 84] Interestingly, in passing from closed-shell Ni^{II} (d^8) to open-shell Co^{II} (d^7) and Cu^{II} (d^9) analogues, a substantial increase in the absolute value of β is observed due to the contribution of other low-lying MLCT states.

However, when the Schiff base ligand is substituted by donor and acceptor substituents such in **61** ($A = NO_2$), the situation is different and the β response is now dominated by intraligand charge transfer transitions, with the metal ion mainly acting as a bridging centre (Figure 1.26).[85, 86]

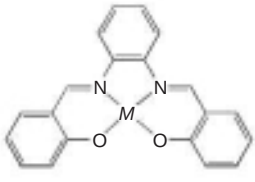

58 (M = Ni): $\beta_{1.34}$(EFISH) = –20 x 10^{-30} esu
59 (M = Co): $\beta_{1.34}$(EFISH) = –170 x 10^{-30} esu
60 (M = Cu): $\beta_{1.34}$(EFISH) = –50 x 10^{-30} esu

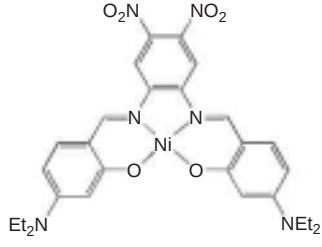

61 (A = NO_2): $\mu\beta_{1.91}$(EFISH) = + 1530 x 10^{-48} esu

Figure 1.26 Selected examples of Schiff base metal complexes

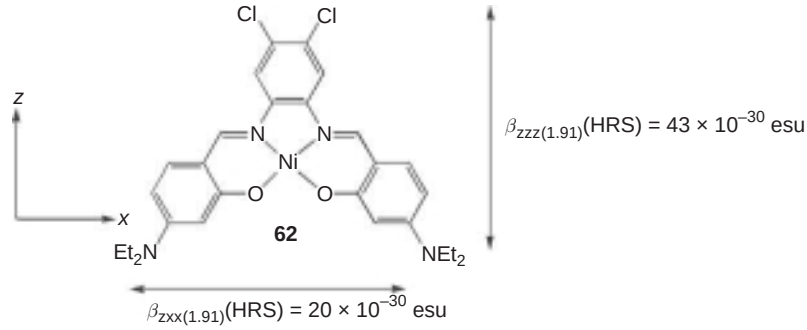

Figure 1.27 A donor–acceptor Schiff base metal complex

Such a type of donor–acceptor complex represents an original class of 2D dipolar NLO chromophore, and EFISH and HRS experiments in combination with INDO/singles configuration interaction(SCI)-SOS theoretical calculations have been used to investigate the 2D character of the β response in **62** ($A = \mathrm{Cl}$): the 2D optical nonlinearity is related to the existence of various low-energy charge transfer states, and while z-polarised electronic transitions contribute to the diagonal β_{zzz} tensor, perpendicular x-polarised transitions contribute to the off-diagonal β_{zxx} and β_{xzx} tensors (Figure 1.27).[87]

1.3.4.2 Phthalocyanine Metal Complexes

Due to their extensive delocalised π-electron systems, phthalocyanines and related metallophthalocyanines have been intensively investigated as NLO materials, mainly for their high cubic hyperpolarisabilities and good optical limiting properties.[88, 89] Phthalocyanines present intense π–π* bands in the visible (Q band) and the near UV region (B band) which mostly determine the NLO response. Their chemical versatility has also allowed the introduction of different donor and acceptor substituents at peripheral positions and, thus, push–pull molecules displaying second-order nonlinear responses to be obtained. Moreover, the possibility of incorporating many central metals offers the opportunity to tune the NLO activity. For example, the second-order NLO response of metallophthalocyanines **63–65** bearing the nitrostyryl electron-accepting substituent has been measured by means of the EFISH technique working with the nonresonant incident wavelength of 1.91 μm (Figure 1.28).[90] These complexes show moderate NLO activity, from 28 to 44 $\times$ 10^{-30} esu, depending on the nature of the metal centre.

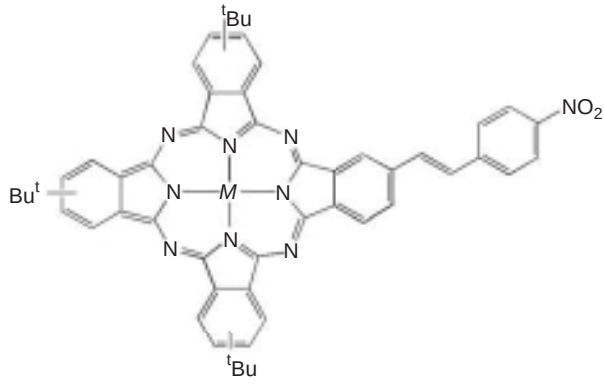

63 (*M* = Co): λ_{max} ($CHCl_3$) = 688 nm; β_0(EFISH) = 28 × 10^{-30} esu
64 (*M* = Ni): λ_{max} ($CHCl_3$) = 688 nm; β_0(EFISH) = 40 × 10^{-30} esu
65 (*M* = Cu): λ_{max} ($CHCl_3$) = 697 nm; β_0(EFISH) = 44 × 10^{-30} esu

Figure 1.28 Selected examples of dipolar phthalocyanine metal complexes

Later, much larger quadratic hyperpolarisability values have been reported for a family of push–pull zinc phthalocyanine complexes, such as **66a,b** containing either one or two nitrophenylethynyl substituents as acceptors and butoxy groups as donors, and **67** bearing one dimethylaminoethynyl donor substituent and propylsulfonyl acceptor groups (Figure 1.29).[91] The largest β value was obtained for **66b** containing two strong acceptor groups ($\beta = 520–530 \times 10^{-30}$ esu) by both HRS (working at 1.06 μm) and EFISH (working at 1.91 μm) experiments.

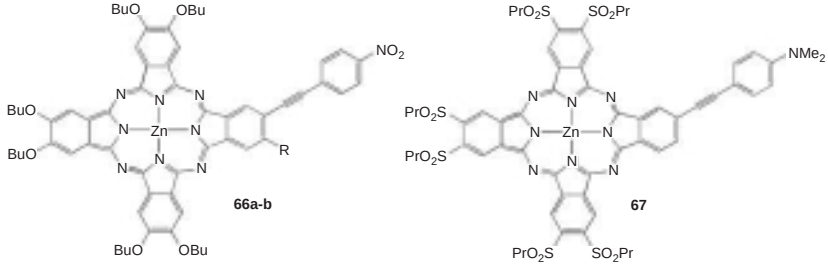

66a (R = H): λ_{max} ($CHCl_3$) = 696 nm; $\beta_{1.06}$(HRS) = 220 x 10^{-30} esu
66b (R =  NO_2): λ_{max} ($CHCl_3$) = 713 nm; $\beta_{1.06}$(HRS) = 530 x 10^{-30} esu
67: λ_{max} ($CHCl_3$) = 711 nm; $\beta_{1.06}$(HRS) = 114 x 10^{-30} esu

Figure 1.29 Dipolar phthalocyanine metal complexes with large β values

1.3.4.3 Porphyrin Metal Complexes

Porphyrins present similar electronic characteristics to those of phthalocyanines, and their absorption spectra show two, well-separated B (400–500 nm) and Q (600–700 nm) bands. Their optical properties can be tailored by changing the metal centre, its oxidation state and nature of the substituents at the peripheral sites of the macrocycle. Thus, an increasing number of metalloporphyrins have been used as efficient π-conjugated systems in push–pull NLO molecules.[62, 88] A prototypical example is 10,20-diphenylporphyrin and its Zn^{II}, Cu^{II} and Ni^{II} complexes **68–70** bearing an arylethynyl electron-donating and arylethynyl electron-withdrawing substituent in the 5- and 15-positions, respectively (Figure 1.30). Exceptionally high quadratic hypolarisability values have been reported for the Cu^{II} **68** ($\beta_{1.06} = 1501 \times 10^{-30}$ esu) and Zn^{II} **69** ($\beta_{1.06} = 4933 \times 10^{-30}$ esu) complexes, measured by HRS in chloroform with a resonant incident wavelength of 1.06 μm.[92] Later, the $\beta_{1.06}$ value for **69**, deduced from electroabsorption (Stark) data, was reported to be lower, although still high ($\beta_{1.06} = 1710 \times 10^{-30}$ esu).[93] By working with a nonresonant wavelength of 1.91 μm, the $\beta_{1.91}$ value was found to be again much lower ($\beta_{1.91} = 540 \times 10^{-30}$ esu). Finally, a similar lower value of quadratic hyperpolarisability $\beta_{1.91}$(EFISH) has been reported for the Ni^{II} compound **70** ($\beta_{1.91} = 80\text{–}100 \times 10^{-30}$ esu).[94]

The NLO properties of structurally related nickel(II) porphyrin chromophores bearing other electron-accepting substituents such as dicyanoethenyl **71** have also been studied by EFISH working at 1.91 μm (Figure 1.31).[95] This study has revealed a much lower $\beta_{1.91}$ value

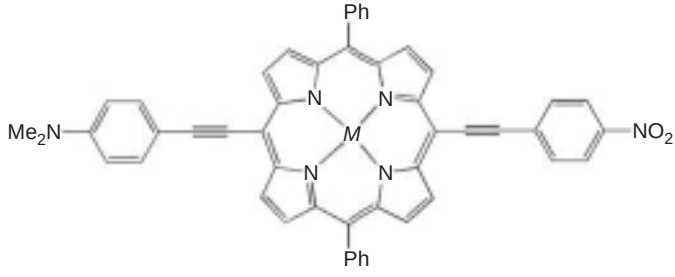

68 (*M* = Cu): $\beta_{1.06}$(HRS) = 1501 x 10^{-30} esu

69 (*M* = Zn): $\beta_{1.06}$(HRS) = 4933 x 10^{-30} esu;
$\beta_{1.06}$(Stark) = 1710 x 10^{-30} esu; $\beta_{1.91}$(Stark) = 540 x 10^{-30} esu

70 (*M* = Ni): $\beta_{1.91}$(EFISH) = 80–100 x 10^{-30} esu

Figure 1.30 Dipolar porphyrin metal complexes with large β values

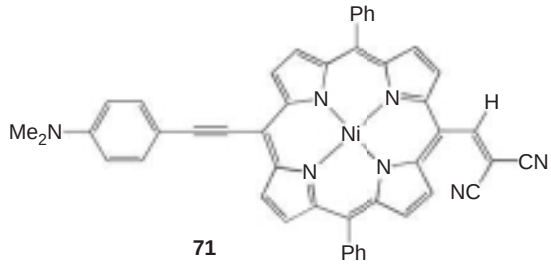

71

λ_{max} ($CHCl_3$) = 667 nm; $\beta_{1.91}$(EFISH) = 124 x 10^{-30} esu

Figure 1.31 A nickel(II) porphyrin chromophore

(124×10^{-30} esu); this can be in part explained by a deviation from coplanarity between the dicyanoethenyl fragment and the plane of the porphyrin, which decreases the electronic coupling across the donor–porphyrin–acceptor. Thus, direct comparison of the experimental hyperpolarisability for such a family of porphyrin chromophores is difficult because of differing experimental conditions at different incident wavelengths. Nevertheless, these studies show that metalloporphyrins behave as efficient π-linkers in push–pull systems.

With the aim of engineering larger second-order nonlinearities without shifting significantly the chromophore absorption to the red (the classical concept of nonlinearity/transparency trade-off), an extensive series of conjugated (porphyrinato)zinc(II) complexes featuring nitrooligothiophenyl electron accepting moieties has been synthesised (Figure 1.32).[96] All these chromophores absorb in the same range [λ_{max} (Q band) = 640–680 nm] and the second-order responses determined from HRS experiments gave $\beta_{1.30}$(HRS) values from 650 to 4350 $\times$ 10^{-30} esu,

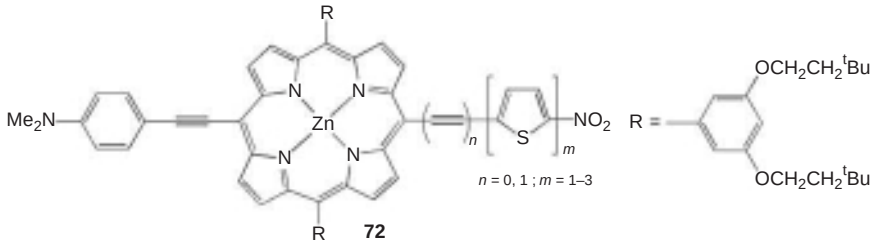

72

λ_{max} (THF) = 640–683 nm; ($\beta_{1.30}$(HRS) = 650–4350 x 10^{-30} esu

Figure 1.32 (Porphyrinato)zinc(II) complexes featuring nitrooligothiophenyl electron accepting moieties

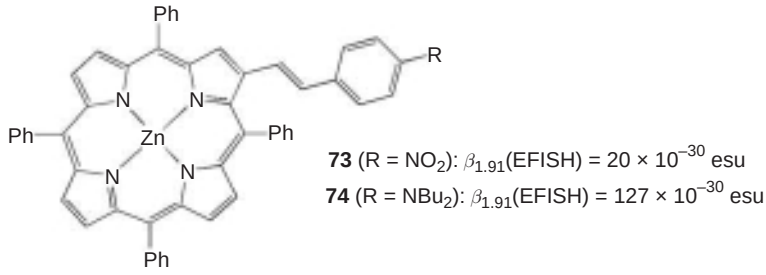

Figure 1.33 β-pyrrolic-substituted metalloporphyrins chromophores

the highest value was observed for compound **72** ($n = 0$, $m = 3$). However, it should pointed out again that these quadratic hyperpolarisabilities could be affected by a significant resonance enhancement, as the second harmonic (650 nm) is in the region of the Q band absorptions.

Interestingly, when the metalloporphyrin is substituted at the β-pyrrolic by conjugated electron-donating or electron-accepting substituents, the porphyrin ring plays the role of acceptor and donor group, respectively, in addition to the role of highly polarisable π-linker.[97] This ambivalent behaviour has been demonstrated, for example, for push–pull zinc complexes **73** and **74** featuring substituted styryl moieties:[98] when the substituent is the electron-withdrawing nitro group the porphyrin ring behaves as a moderate donor group comparable with ferrocene; on the contrary, when the substituent is the strong electron-donating dimethylamino group, the porphyrin chromophore acts as acceptor (Figure 1.33).

The structure of donor–acceptor porphyrin complexes such as **68** has very recently been modified to make a new family of amphiphilic porphyrin dyes with polar pyridinium acceptor head groups and hydrophobic dialkyl-aniline donors (Figure 1.34). The free porphyrins and

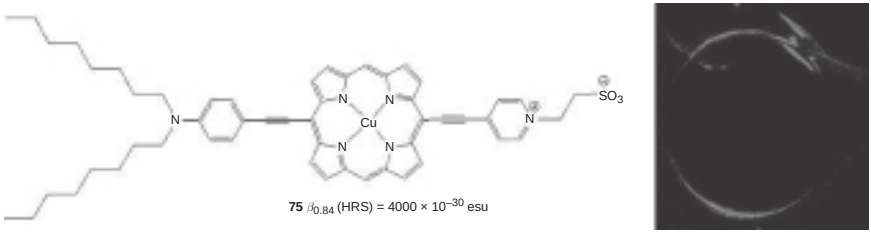

Figure 1.34 An example of amphiphilic metalloporphyrin for SHG imaging. Reprinted with permission from Reeve *et al.*, 2009 [99]. Copyright (2009) American Chemical Society

corresponding Cu^{II} and Ni^{II} compounds (*e.g.* **75**: M = Cu) have strong NLO activity and high affinities for biological membranes, making them promising probes for SHG imaging microscopy.[99]

1.4 OCTUPOLAR METAL COMPLEXES

As mentioned in the introduction, the archetype of the octupolar structure is a cube featuring donor and acceptor moieties at its edges or its projection featuring D_{3h}, D_3, T_d or D_{2d} symmetry (Figure 1.2). According to this strategy, several organometallic fragments have been used as electron-donating groups to build D_{3h} symmetric octupoles. On the other hand, original octupolar architectures have been designed taking advantage of the large versatility offered by coordination chemistry. In this review the focus is on the NLO activity of polypyridyl transition metal complexes (iron, ruthenium, nickel, copper, silver, zinc...) and *tris*(dipicolinato)lanthanide(III) series (lanthanum–lutetium) and special attention will be devoted to the role of the metal centre in the quadratic hyperpolarisability. Finally, other examples of octupolar structures are derived from particular molecular global symmetry or conformational restriction; this case is illustrated with the study of a conformational equilibrium of polymetallic complexes.

1.4.1 Metal as Peripheral Donor (or Acceptor) Substituent

As largely illustrated in the former section dealing with dipolar compounds, transition-metal-containing fragments can be used as electron-donating, -withdrawing or -transmitting moieties. In this context, the design of D_{3h} symmetric octupoles **77** and **79** by 1,3,5-substitution of a central benzene core with three sub-units containing $Ph-C\equiv C-Ru(dppe)_2-$ or Cp*Fe(dppe)-acetylide fragment (Figure 1.35) was achieved by the groups of Humphrey[100] and Lapinte[101], respectively. The comparison between these octupolar derivatives and their corresponding dipolar sub-units **76** and **78**, has been carried out: dipolar and octupolar compounds present almost the same maximal absorption wavelength, but a threefold enhancement of the oscillator strength is observed for the octupolar derivatives as expected for noninteracting, *meta*-substituted sub-units.[20] As a consequence, a threefold enhancement in the quadratic

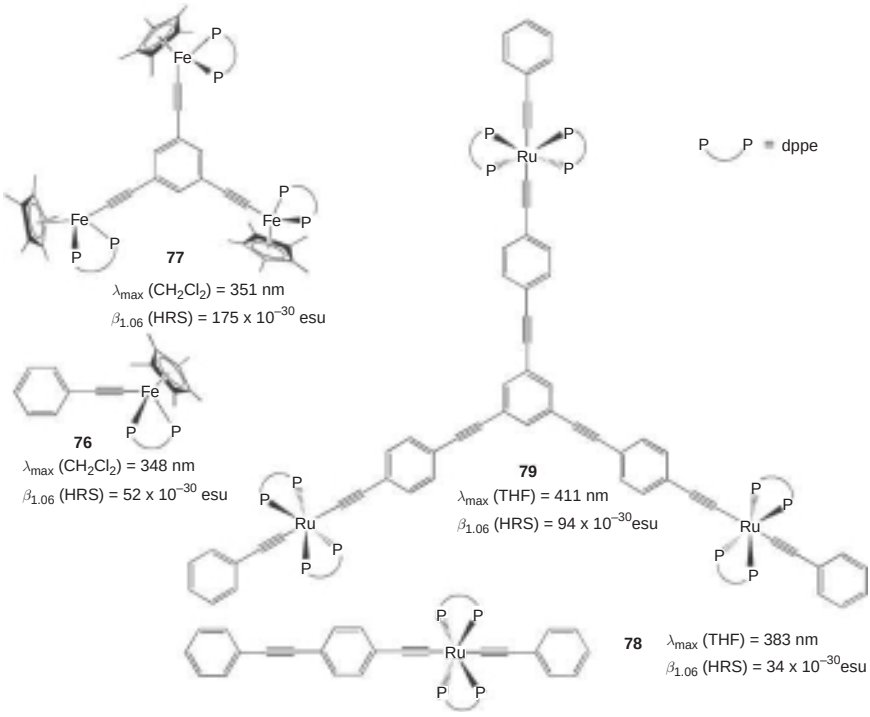

Figure 1.35 D_{3h} symmetric metal-containing octupolar derivatives

hyperpolarisability is also obtained and it is important to note that this NLO activity enhancement is achieved without any cost in terms of optical transparency. In addition these organometallic fragments present reversible redox behaviour and modulation of the NLO activity by successive one-, two- or three-electron oxidation is also described, which contributes to expand the concept of NLO-switch described in the case of dipolar compounds to octupolar derivatives.

1.4.2 Metal as Template

Beneath this classical use of metal-containing fragments as electron donating or withdrawing moieties, it is also possible to benefit from the octahedral or tetrahedral geometry frequently encountered in coordination chemistry to design original octupolar architectures. On one hand, the metal ion central core will gather ligands in a predetermined octupolar

symmetry, while the functionalisation of the ligand by polarisable π-conjugated moieties will enhance the NLO activity.

1.4.2.1 The Versatile Zinc(II) Ion

The case of zinc(II) is particularly interesting: this metal ion has a d^{10} electronic configuration and, therefore, does not present any ligand field stabilisation effect. As a consequence Zn^{II} is a unique transition metal ion able to expand its coordination sphere, giving either tetrahedral and/or octahedral complexes with diimine ligands. This characteristic was successfully used to design dipolar (D_{2d}) or octupolar (D_3) molecules by simple coordination of one, two or three donor π-conjugated functionalised bipyridine ligands (Figure 1.36).[71] The absorption spectra of these three complexes exhibits an intense intra-ligand charge transfer (ILCT) centred in the visible region. In all cases, complexation is accompanied by a strong bathochromic shift of the transition that is sensitive to the structure of the Zn^{II} complexes. This spectroscopic effect clearly illustrates the double role of the central metal ion: (i) powerful template controlling the overall complex symmetry and (ii) strong Lewis acid enforcing the accepting character of the bipyridine moieties. Moreover, complexes **45, 80** and **81** are good chromophores featuring high molecular extinction coefficients and the oscillator strengths of the ILCT transition follow a 1:1:2:3 ratio for free ligand and complexes **45, 80**

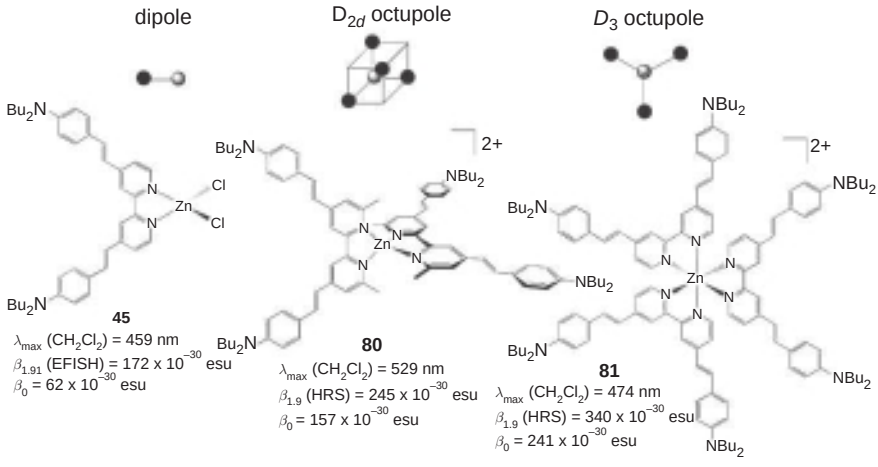

Figure 1.36 Dipolar or octupolar D_{2d} and D_3 bipyridine zinc(II) complexes

and **81**, respectively, as expected for noninteracting subchromophores. This is in agreement with the absence of an extended delocalisation through Zn^{II} between the bipyridine subchromophoric units in **80** and **81**. As a consequence, the off-resonant β_0 values increase with respect to the number of sub-chromophoric bipyridine ligands organised around the Zn^{II} centre, illustrating again the superiority of octupoles *vs* dipoles in terms of nonlinearity/transparency trade-off.

1.4.2.2 Pseudo-Tetrahedral D_{2d} Symmetric Complexes

Contrarily to the versatile zinc(II) ion, copper(I) and silver(I) are well known to stabilise preferentially D_{2d} *bis*(bipyridine)metal complexes provided the 6,6′-positions of the ligand are functionalised by an alkyl or aryl substituent to protect the central metal ion from the oxidation (*e.g.* 6,6′-dimethylbipyridine). Such type of pseudo-tetrahedral coordination sphere is frequently encountered in the design of catenane, rotaxane or knot architectures. Using donor π-conjugated functionalised 6,6′-dimethylbipyridine ligand, violet zinc(II) **80** and red-orange copper(I) **82** and silver(I) **83** complexes have been obtained, the stronger Lewis acidity of the dicationic zinc(II) ion inducing a larger bathochromic shift of the ILCT transition (Figure 1.37).[102] It is worth noting that in the case of copper(I) complexes a less intense $d\pi(Cu^{I}) \rightarrow \pi^{*}$(bpy) metal-to-ligand charge transfer transition (MLCT) is observed around 480 nm. The static quadratic hyperpolarisability coefficients β_0 are roughly the same for the

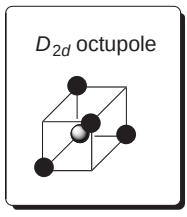

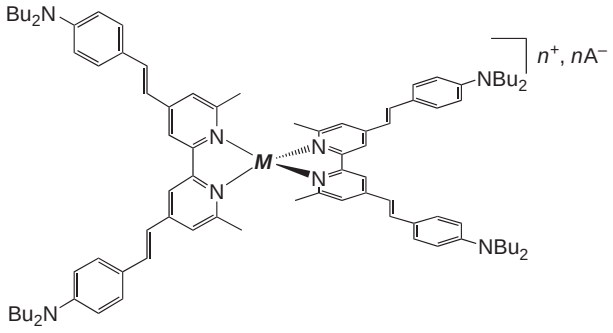

	λ_{max} (nm)	$\beta_{1.9}$ (HRS) (10^{-30} esu)	β_0 (10^{-30} esu)
80: *M* = Zn, *n* = 2, A = OTf	529	245	157
82: *M* = Cu, *n* = 1, A = PF_6	436/480	113	86
83: *M* = Ag, *n* = 1, A = OTf	431	90	70

Figure 1.37 Chemical structure of D_{2d} zinc(II), copper(I) and silver(I) complexes

copper(I) **82** and silver(I) **83** complexes but a twofold enhancement is observed for zinc(II) **80**. Theses variations of λ_{max} as well as of β_0 are clearly related to the nature of the metal ions. For a given geometry, the Lewis acidity of the central metal ions controls the strength of the ILCT bathochromic shift and, consequently, the stronger Lewis acid induces a more red-shifted ILCT transition, hence a larger NLO activity.

1.4.2.3 Octahedral D_3 Symmetric Complexes

Role of the geometry: Octupolar D_3 symmetric metal *tris*(bipyridine) complexes are known with a large variety of transition metals. Due to ligand field effect, d^6 ions like Fe^{II}, Ru^{II}, Os^{II}, Co^{III} give particularly stable *tris*(bipyridine) complexes but Ni^{II}, Cu^{II} and Zn^{II} have also been widely studied. This large choice gives the opportunity to investigate deeply the influence of the metal centre on the quadratic nonlinearities with complexes **81–87** (Figure 1.38).[103] Interestingly, all the complexes studied are

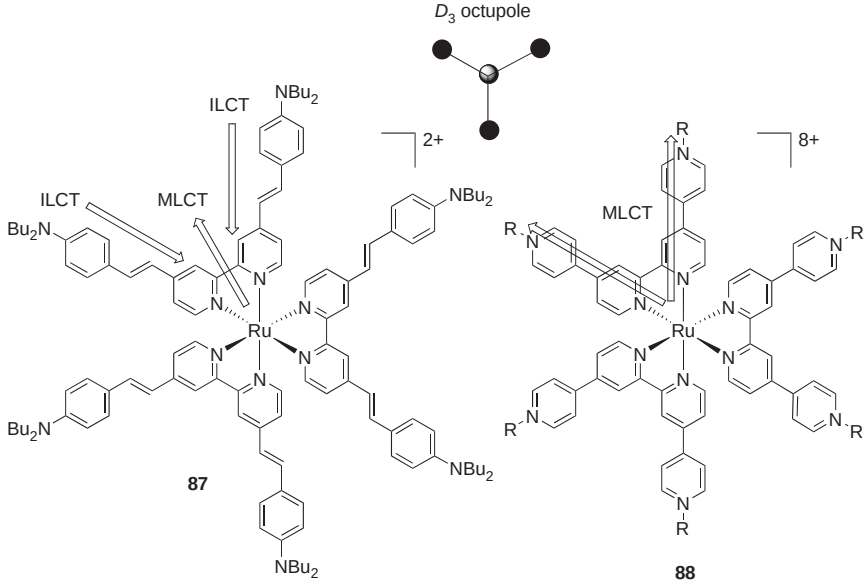

	λ_{max} (nm)	$\beta_{1.9}$ (HRS) (10^{-30} esu)	β_0 (10^{-30} esu)
81: *M* = Zn	474	340	241
84: *M* = Ni	476	211	149
85: *M* = Cu	474	229	161
86: *M* = Fe	470/573	235	–
87: *M* = Ru	442/513	340	–

λ_{max} (CH_3CN) = 498 nm/416 nm

$\beta_{0.8}$ (HRS) = 281 x 10^{-30} esu

Figure 1.38 Directionality of the ILCT and MLCT transitions within *tris*(bipyridine)ruthenium(II) complexes

dications and, therefore, present roughly the same Lewis acidity; as a consequence, little variation has been observed in the ILCT transition (Figure 1.38) centred around 470 nm. Thus, the series Zn^{II} (**81**), Ni^{II} (**84**), Cu^{II} (**85**) seem appropriate to compare the effect of the metal centre on the NLO activity. Surprisingly, significant variations occur replacing Zn^{II} by Cu^{II} or Ni^{II} with a substantial decrease of β_0 by a factor 1.5. Such variation cannot be ascribed to electronic effect, since ILCT transitions occurs at the same energy with similar oscillator strength, but should be related to a geometrical factor. In particular, d^9 copper(II) complexes are known to present important distortions from the ideal octahedral geometry due to the Jahn-Teller effect[104] and, recently, extension on the VB–CT model (valence bond–charge transfer) to coordination compounds has shown that distortions (even minor) from the ideal D_3 octupolar symmetry are able to induce profound perturbations in the octupolar nonlinearity.[105]

Role of the MLCT transition: The cases of Fe^{II} **86** and Ru^{II} **87** are different: these d^6 *tris*(bipyridine)metal complexes stabilise octahedral D_3 symmetric coordination but, owing to their low oxidation potential, show an additional MLCT $d\pi(Fe^{II}$ or $Ru^{II}) \rightarrow \pi^*$(bpy) band at 590 and 510 nm, respectively. These low energy transitions should also contribute to the NLO activity and preclude rigorous comparison of the static hyperpolarisability (β_0). The dipole moments of these two charge-transfer transitions (ILCT and MLCT) are parallel but with an opposite direction (Figure 1.38).[106] Vance and Hupp[107] proposed, on the basis of electroabsorption spectroscopy (Stark effect), that both transitions negatively interfere in the global NLO activity according to $\beta_{TOT} = |\beta_{ILCT}| - |\beta_{MLCT}|$. However, this simple model does not fully explain the NLO variations on the complete series of Zn^{II}, Ru^{II} and Fe^{II} complexes. Indeed, as the λ_{ILCT} values of the three complexes are almost the same, it can be anticipated that the ILCT contribution (β_{ILCT}) on the global NLO activity will be similar for the three complexes and equal to that of a Zn^{II} complex that does not feature any MLCT transition. As a consequence, if the two transitions negatively interfere according to the aforementioned model, the global NLO efficiency of ruthenium and iron complexes should be lower than that of zinc. This is the case for iron, where experimental measurements clearly show that $\beta(Zn) > \beta(Fe)$, but is not the case for ruthenium where $\beta(Ru) > \beta(Zn)$. Therefore, the model based on an antagonist contribution of both ILCT and MLCT does not allow all the experimental results to be rationalised; a more complex model involving extended delocalisation through the metal centre should perhaps be envisaged.

To take advantage of MLCT transition directionality, Coe *et al.* have designed new bipyridine ligands functionalised by electron-withdrawing moieties (Figure 1.38).[108] Due to the absence of electron-donating groups, the corresponding ruthenium complexes (*e.g.* **88**) do not exhibit any ILCT transition, rather extended MLCT transitions sensitive to the nature of the electron-acceptor moieties. Theoretical calculations clearly indicate that the MLCT transition occurs between HOMOs centred on the metals and LUMOs delocalised over the entire ligand. As a result the quadratic nonlinearities are rather large.

In conclusion, transition metal ions are powerful and versatile templates to gather NLO-active ligands in a predetermined stereochemical environment and various symmetries can be achieved: d^6 metal ions such as Fe^{II}, Ru^{II}, Os^{II} and Co^{III} lead to the formation of octahedral D_3 *tris*(bipyridine)metal complexes whereas Cu^{I} or Ag^{I} prefer pseudo-tetrahedral D_{2d} *bis*(bipyridine) complexes. Finally d^{10} Zn^{II} can present various dipolar or octupolar geometry/symmetry depending on the metal/ligand ratio. The metal is not only a keystone controlling the orientation of the entire architecture but, as a Lewis acid, it is also able to enhance the ILCT transition, and in some cases (Ru^{II}, Fe^{II}, Cu^{I}) the low-energy MLCT transitions contribute to the global NLO activity. Therefore, it is difficult to rationalise quantitatively the influence of the metal ion on the NLO activity due to geometric and electronic modifications occurring through a complex series.

1.4.2.4 The Case of Lanthanide Complexes

f-Block elements are particularly well suited for the study of the role of the central metal ion on the NLO properties. Indeed lanthanide(III) ions (lanthanum–lutetium) offer the unique opportunity to design an isostructural series without any MLCT transition (except for Ce^{III} compounds). The octupolar D_3 symmetric *tris*(dipicolinato)lanthanide(III) series **89** (Figure 1.39) is the benchmark for such a study. These complexes, known since the beginning of the 1970s, form a perfect isostructural family in the solid state[109] and in solution.[110] Collected X-ray diffraction data from the Cambridge crystallographic database unambiguously demonstrate that all complexes keep the D_3 symmetry whereas the Ln–N and Ln–O distances regularly decrease from lanthanum to lutetium in agreement with the lanthanide contraction (Figure 1.39a). As expected for an isostructural series, all the complexes exhibit rigorously the same UV-visible spectrum[111] (Figure 1.39b) with two bands in the UV be assigned to $\pi-\pi^*$ transitions of the coordinated pyridyl ring. It is worth noting that

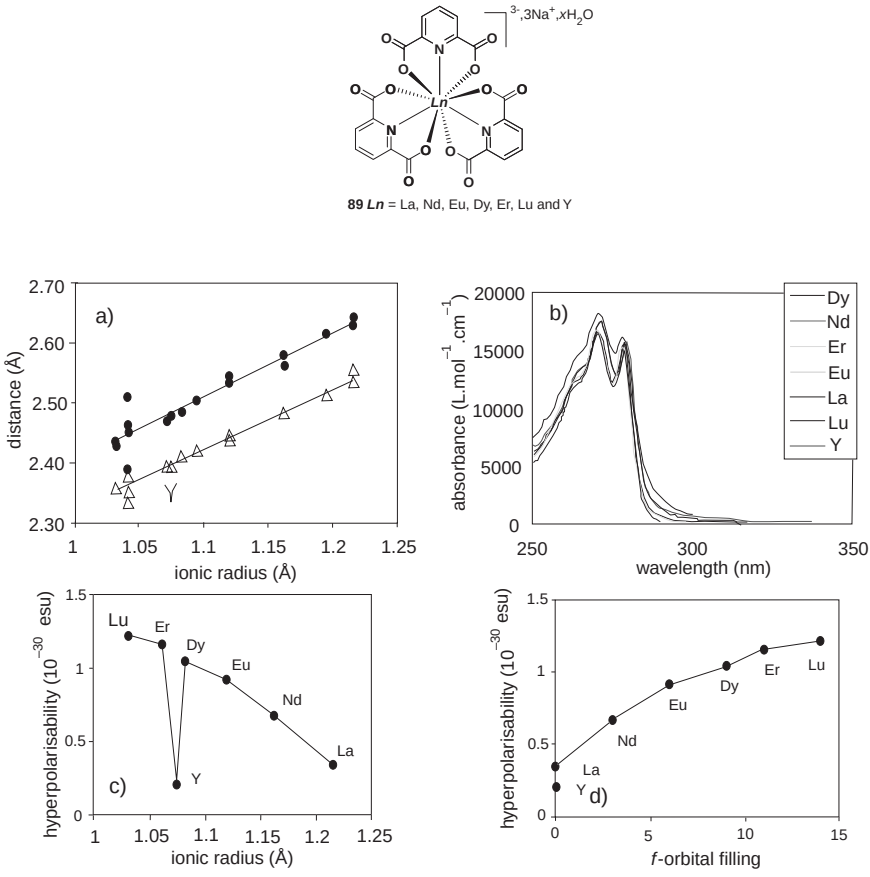

Figure 1.39 Generic structure of *tris*(dipicolinato)lanthanide complexes (top); (a) plot of the *L*n–N (circle) and *L*n–O (triangle) distances *vs* lanthanide ionic radius; (b) absorption spectra in water; plot of the hyperpolarisability coefficient β *vs* ionic radius (c) or *f*-orbital filling (d)

the absence of any ligand functionalisation suppresses the ILCT transition. The NLO activity measured in water solution is rather small, as expected for a nonfunctionalised ligand, but regularly increases along the series from lanthanum to lutetium. The 'metal-induced' NLO activity enhancement already observed for the dipolar series,[74, 75] is, therefore, clearly confirmed and appears to be a new intrinsic property of *f*-block elements.

The particular case of yttrium is very useful to gain a deeper insight into this effect. Yttrium presents strong chemical similarities with lanthanides and its ionic radius (1.075 Å) make it close to dysprosium (1.083 Å) or erbium (1.062 Å); on the other hand its electronic configuration ($4f^0$) is identical to that of lanthanum. Plotting the variation of β *vs* the

ionic radius as generally done for lanthanide properties clearly shows a discontinuity for yttrium whereas a very regular variation of β *vs* an electronic parameter like the *f*-electronic configuration is obtained (Figure 1.39c,d). This result clearly indicates that the metal contribution to the NLO activity is not due to geometrical considerations but to its electronic configuration. This contribution of the *f*-electron to the quadratic hyperpolarisability is the signature that *f*-electrons are sensitive to an external electric field, hence that they are polarisable, which is in marked contrast with the generally admitted inertness of *f*-electrons due to their shielding by $5s^2$ and $5p^6$ shells. In conclusion, the NLO study of lanthanide complexes allows the electronic contribution of the central metal ion to the quadratic hyperpolarisability to be established. The discovery of the polarisable character of *f*-electrons, further confirmed by theoretical calculations,[112] shows that quadratic NLO measurements can be a very sensitive tool to probe the intimate nature of the matter.

1.4.3 Conformational Studies Using Second-Order NLO Activity Measurements

Recently, polymetallic arrangements of Zn^{II} porphyrin and bis(terpyridine) Ru^{II} or Os^{II} complexes have been reported in the literature, and the sensitivity of the HRS signal to the molecular symmetry has been used to determine the supramolecular conformation in solution.[113] Both complexes *M*Zn*M* (*M* = ruthenium, osmium) (Figure 1.40) exhibit a non-zero hyperpolarisability in solution, clearly indicating that at least a fraction of the molecules must have a noncentrosymmetric structure. Depolarisation ratio measurements indicate that these molecules clearly belong to an octupolar D_2 or D_{2d} symmetry and, therefore, suggest that conformers in which $\Theta = -\Phi = 45°$ are present in solution. To check this hypothesis, ZnRuZn and ZnOsZn were designed in which the orthogonal configuration of the two terpyridyl units imposes a D_{2d} pseudosymmetry. HRS and depolarisation measurements clearly confirm the expected symmetry. Finally, such conformational analysis in solution has been extended to ZnEZn or ZnE_2Zn compounds in which two zinc porphyrin complexes are linked by an ethynyl or bis(ethynyl) fragment. Once again HRS hyperpolarisability and depolarisation ratio measurements unambiguously indicate the presence of D_{2d} symmetric conformers in solution and importantly the β value for ZnE_2Zn is extremely large ($\beta_{1.3} = 830 \pm 100 \times 10^{-30}$ esu). In the present case the sensitivity of HRS

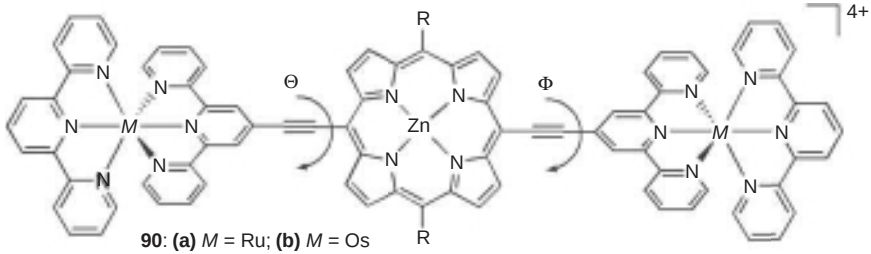

90: **(a)** *M* = Ru; **(b)** *M* = Os

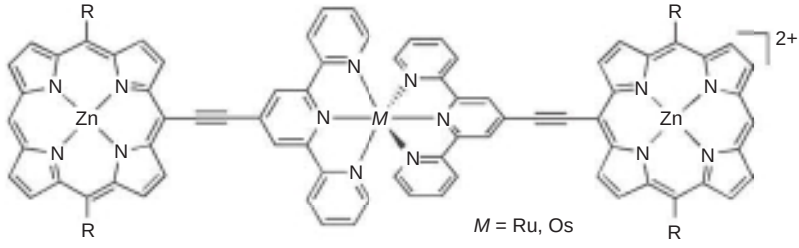

91: **(a)** *M* = Ru; **(b)** *M* = Os

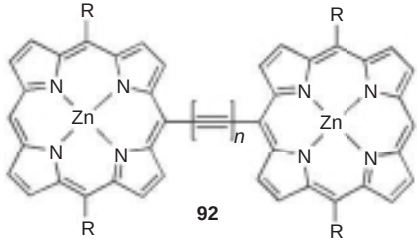

92

Figure 1.40 Octupolar arrangements of polymetallic Zn^{II} porphyrin and bis(terpyridine) Ru^{II} or Os^{II} complexes

measurements to the molecular symmetry is used as a powerful probe to investigate a conformational equilibrium in solution.

1.5 SWITCHING OPTICAL NONLINEARITIES OF METAL COMPLEXES

A current challenge is the development of efficient strategies for the design of switchable nonlinear optical (NLO) materials. The ability to switch the NLO activity of a molecule on and off is of relevance for the development of molecular photonic devices, as those properties can be

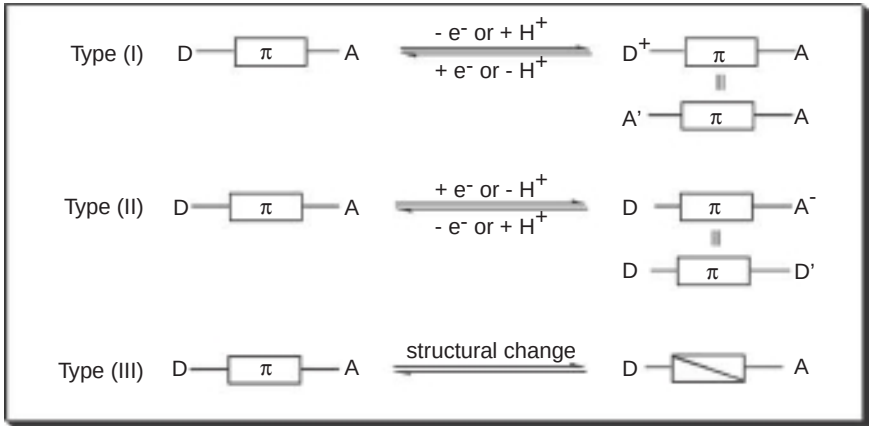

Figure 1.41 Schematic representations of strategies for switching NLO responses

switched by modifying one of the component parts.[114, 115] To achieve an efficient switching effect, the molecule must be stable in both the ON and OFF states and the response time must be relatively fast. As most molecules with large quadratic hyperpolarisability values comprise π-systems end-capped with donor and acceptor moieties, various strategies have been proposed and categorised into three types (Figure 1.41).[114] Types (I) and (II) include the alteration of either the electron donor or the electron acceptor capacity of the end groups by using external stimuli such as redox and protonation/deprotonation. Type (III) includes the alteration of the π-bridge using an external trigger such as light, and in this category photochromic compounds seem to be promising candidates for the design of photoswitchable NLO materials.[116]

Because of their rich redox properties, NLO chromophores featuring transition metal complexes are among the best candidates for the role of NLO molecular switches, and the majority of examples reported up to now concerns metal-based chromophores in which the NLO response is modified by a chemical (or electrochemical) oxidation/reduction sequence. Several examples of reversible proton- or photon-driven switching of β will also be discussed in the following.

1.5.1 Redox Switching of Quadratic Nonlinearities

The first demonstration of redox switching of NLO responses was reported in 1999 by Coe *et al.* on ruthenium ammine complexes of

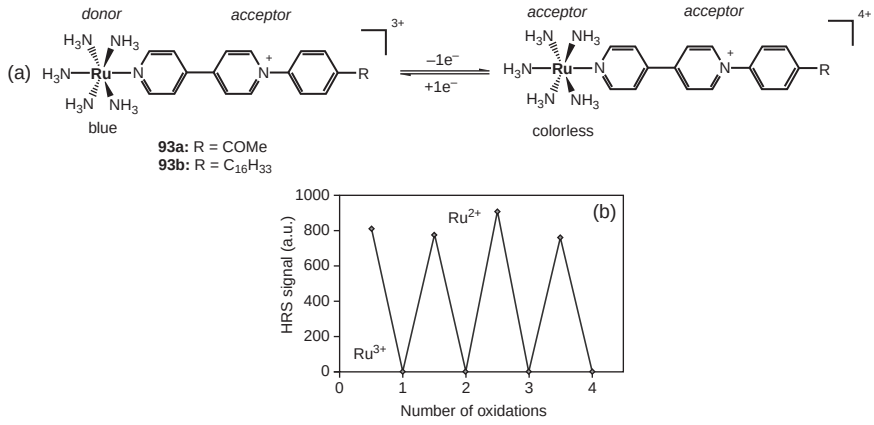

Figure 1.42 (a) Redox switching of HRS response between **93** and its oxidised form and (b) upon several chemical oxidations and reductions

4,4′-bipyridinium ligands (*e.g.* **93**).[117] In such dipolar chromophores, the d^6 Ru^{II} centre behaves as strong π-donor and can be readily oxidised either electrochemically or chemically to its electron deficient d^5 Ru^{III} analogue. For example, chemical oxidation of **93a** with 1:1 30% aqueous H_2O_2/2 M HCl results in a complete bleaching of the colour, and a dramatic decrease of β_{HRS} is observed (Figure 1.42a). After reduction with 62% $N_2H_4{\cdot}H_2O$, the original HRS signal is retrieved. The process is fully reversible and the difference in β between the two forms is approximately 10–20-fold (Figure 1.42b). Very recently, the redox switching of the NLO response of Langmuir–Blodgett thin films containing the ruthenium ammine complex **93b** has been reported.[118] Oxidation to Ru^{III} causes a *ca* 50% decrease in the SHG intensity, and the signal is almost restored on reduction.

Dipolar compounds containing ferrocene units as the electron donor have been very popular in nonlinear optics (Section 1.3), and the reversible redox ferrocene/ferrocenium couple has logically been used to switch the hyperpolarisability β.[119, 120] Complex **94**, containing an octamethylferrrocene donor linked to a nitrothiophene acceptor *via* an ethenyl bridge, shows a static hyperpolarisability much larger than that of the corresponding Fe^{III} complex (Figure 1.43). The switching effect has been demonstrated upon using Bu_4NBr_3 as oxidant and hydrazine as reducing agent.

An interesting redox switching of quadratic nonlinearities has been achieved on the open-shell donor–acceptor dyad **95**.[121] Such a compound is composed of two electroactive units linked by an CH=CH bridge, the acceptor unit being the polychlorinated triphenyl (PTM) radical and the

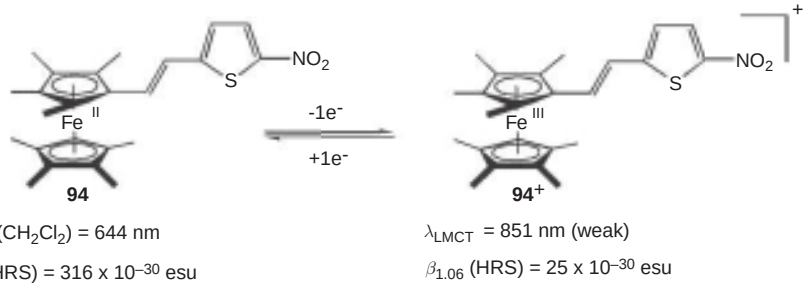

Figure 1.43 Redox switching of the quadratic NLO response of ferrocenyl complex **94**

donor unit the nonamethylferrocene group (Figure 1.44). The oxidation of **95** into the ferrocenium radical derivative $\mathbf{95}^{+}$ (Type I) or the reduction into its diamagnetic anionic form $\mathbf{95}^{-}$ (Type II), gives rise to three stable oxidation states exhibiting different linear and NLO responses as well as distinct magnetic properties. The dynamic hyperpolarisabilities measured by HRS at 0.800 μm incident wavelength give a large $\beta_{0.800}$ value for **95**. This value is reduced almost ninefold for $\mathbf{95}^{+}$, and even more for the reduced species $\mathbf{95}^{-}$.

Redox-switchable quadratic hyperpolarisabilities have also been demonstrated with electron-rich cyclopentadienyl metal alkynyl complexes.[122] A series of Fe^{II} and Fe^{III} complexes featuring acceptor groups such as NO_2 or CN have been prepared and their $\mu\beta$ values measured by EFISH at 1.91 μm (*e.g.* **96**). As expected, the Fe^{III} complexes show considerably depressed $\mu\beta$ values, relative to those of the Fe^{II} congeners (Figure 1.45).

The same organometallic fragment has been used to prepare the bimetallic Fe^{II}–Fe^{II} **97**, and the resulting Fe^{III}–Fe^{II} $\mathbf{97}^{+}$ and Fe^{III}–Fe^{III} $\mathbf{97}^{2+}$ complexes readily obtained by step-wise, one-electron oxidation

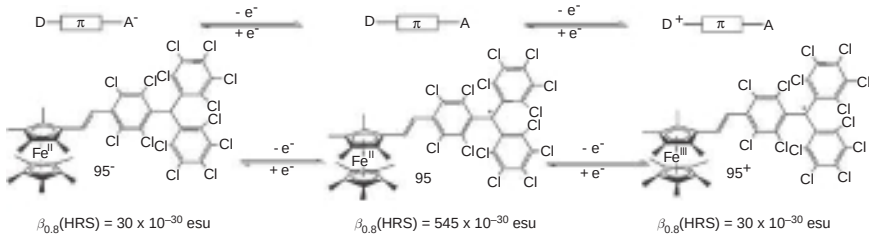

Figure 1.44 Three states redox switching of the quadratic NLO response of ferrocenyl complex **95**

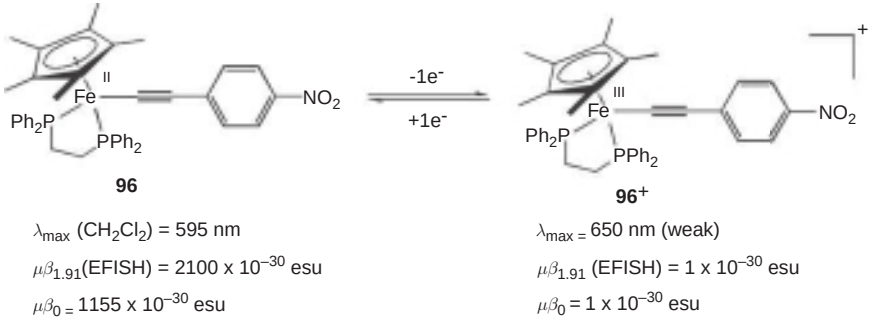

96

λ_{max} (CH_2Cl_2) = 595 nm

$\mu\beta_{1.91}$(EFISH) = 2100 x 10^{-30} esu

$\mu\beta_0$ = 1155 x 10^{-30} esu

96$^+$

λ_{max} = 650 nm (weak)

$\mu\beta_{1.91}$ (EFISH) = 1 x 10^{-30} esu

$\mu\beta_0$ = 1 x 10^{-30} esu

Figure 1.45 Redox switching of the quadratic NLO response of cyclopentadienyl iron complex **96**

(Figure 1.46).[101] The monocation **97**$^+$ can be considered as a push–pull chromophore and exhibits a $\beta_{1.06}$ (HRS) value twice that of its neutral precursor **97** and the fully oxidised compound **97**$^{2+}$. Complex **97**$^+$ is a class II mixed-valence complex, retaining charge localisation, but with enough electronic coupling between the redox centres to permit intervalence charge transfer transitions. As the redox couples **97**/**97**$^+$ and **97**$^+$/**97**$^{2+}$ are fully reversible, this system constitutes, like compound **95**, an interesting three-states NLO switch.

1.5.2 Acid/Base Switching of Quadratic Nonlinearities

Like ruthenium(II) ammine complexes of pyridinium-substituted ligands, pentacyanoiron(II) coordinated to 4,4′-bipyridinium ligands represent very interesting push–pull NLO chromophores, in which $[Fe^{II}(CN)_5]^{3-}$ behaves as an electron-rich metal centre (*e.g.* **98**, Figure 1.47).[123] They display intense visible $d(Fe^{II}) \rightarrow \pi^*(L)$ (L = pyridyl ligand) MLCT bands which are strongly solvatochromic: on moving from water to methanol a large red-shift of *ca* 0.50 eV is observed. The difference between the two solvents may be attributed at least in part to the greater hydrogen bond donating ability of water acting to reduce the basicity and enhance the π-accepting ability of the cyanide ligands. Their NLO properties have been investigated by HRS at an incident wavelength of 1.06 μm and 0.800 μm, and by Stark spectroscopic studies. In accordance with the large red-shifts in the MLCT transitions, the β_0 values also increase markedly on moving from water to methanol. In addition, acidification of aqueous solutions allows reversible switching of the NLO properties: the acidified samples show large blue-shifts of the MLCT bands that are

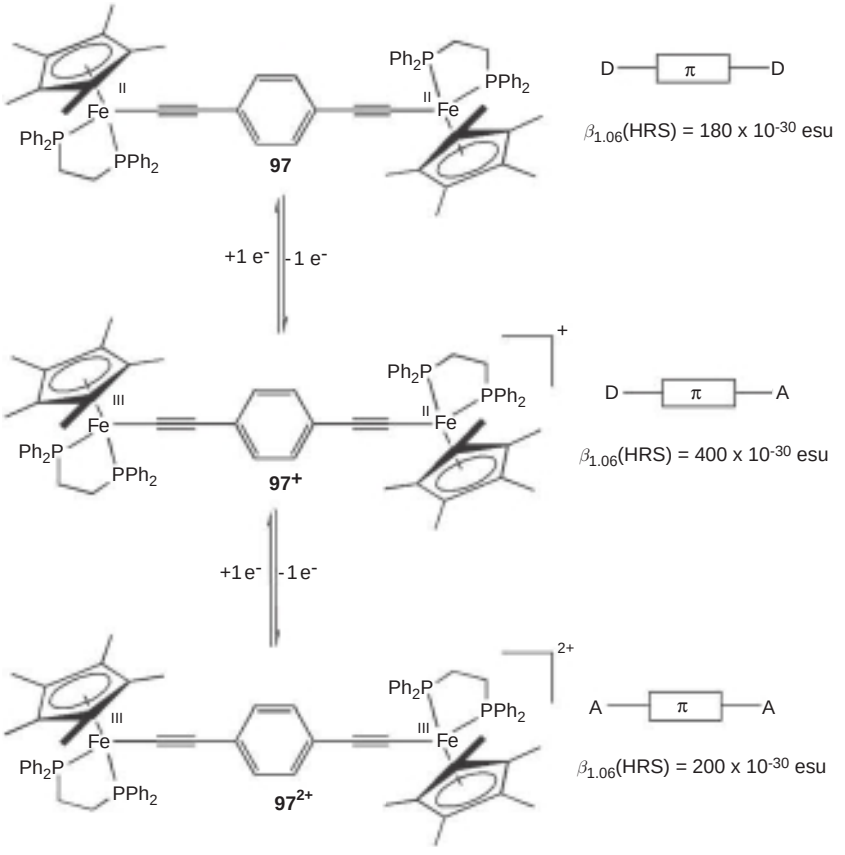

Figure 1.46 Three-state redox switching of the quadratic NLO response of bimetallic complex **97**

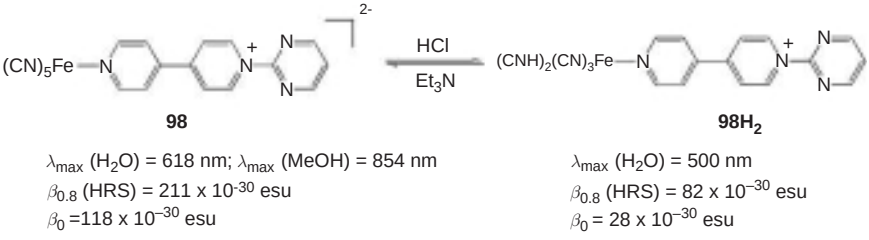

Figure 1.47 Proton switching of the quadratic NLO response of pentacyanoiron(II) complexes

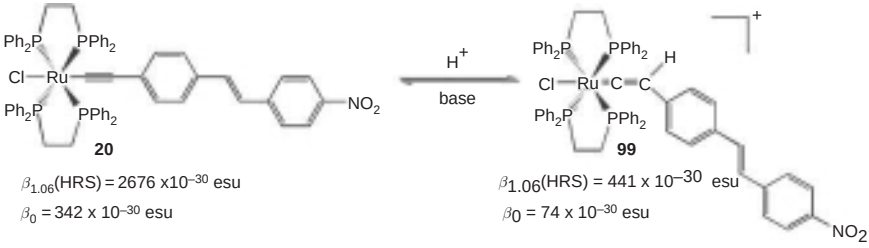

Figure 1.48 Proton switching of the quadratic NLO response of alkynyl ruthenium(II) complexes

accompanied by several-fold decreases in the β_0 responses due to the protonation of the cyanide ligands. Reversibility of the switching effect was demonstrated by adding alternatively HCl and Et_3N, showing a novel approach to proton switching of molecular NLO properties.

Protonation of metal-acetylide complexes affords the corresponding vinylidene complexes (*e.g.* **20** and **99**, Figure 1.48). Proceeding from **20** to **99** leads to a lowering of β values, by a factor of five.[48] As the vinylidene complexes can be easily deprotonated to give back to the alkynyl precursors, and this sequence can be repeated, these complex pairs can provide an interesting protically switchable NLO system.

1.5.3 Photoswitching of Quadratic Nonlinearities

The first demonstration of photoswitching of NLO responses was reported in 1992 by Sakaguchi *et al.* on a derivative of $[Ru^{II}(bpy)]_3^{2+}$ featuring a bipyridyl ligand substituted by two electron-withdrawing amide groups (*e.g.* **100**, Figure 1.49) in Langmuir–Blodgett films.[124–126] Upon irradiation at 378 nm, the SHG signal from a 590 nm dye laser decreased by 30% in less than 2 ps. The initial value returned to almost its initial value within several hundred picoseconds. The same effect was observed with 355 nm excitation and an incident 1.064 μm probe beam. The β value at 1.064 μm

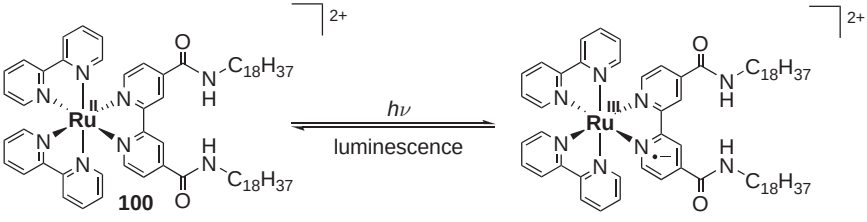

Figure 1.49 Photoswitching of the quadratic NLO response of a *tris*(bipyridine)-ruthenium(II) complex

has been estimated to be 70×10^{-30} esu. A correlation between the SHG time profile and the luminescence decay of the MLCT excited state indicates that the SHG switching is due to the change in β upon MLCT excitation. In this complex, the amide substituent will encourage MLCT into the substituted bipyridyl ligand, leading to simultaneous oxidation of the Ru^{II} centre to Ru^{III} and reduction of the bpy ligand to $bpy^{-\cdot}$, thereby giving a $\mathbf{D^{+}–A^{-}}$ structure, which corresponds to a combination of Type (I) and Type (II) strategies.

Another elegant way for the reversible photoswitching of NLO properties is the use of photochromic compounds.[127–129] Among them, dithienylethene (DTE) derivatives are the most promising because of their good fatigue resistance, the remarkable thermal stability of both isomers and the rapid response time, which are prerequisite conditions for practical applications.[130] Typically, DTE undergoes reversible interconversion between a nonconjugated open form and a π-conjugated closed form when irradiated in the UV and visible spectral ranges, respectively. Donor-substituted styryl bipyridine metal complexes[69–71] are push–pull NLO chromophores, and modulation of the NLO properties has been achieved by varying the donor terminal group as well as metal centre (Figure 1.18).[131] To carry out the photoswitching of the NLO properties, a new type of 4,4′-bis(ethenyl)-2,2′-bipyridine ligand functionalised by a dimethylaminophenyl-dithienylethene group and the corresponding zinc(II) complex **101** has recently been designed. This molecule undergoes an efficient reversible interconversion between a nonconjugated open form and a π-conjugated closed form when irradiated at 365 and 588 nm, respectively (Figure 1.50). The NLO properties of **101** have been evaluated by EFISH measurement for the open and

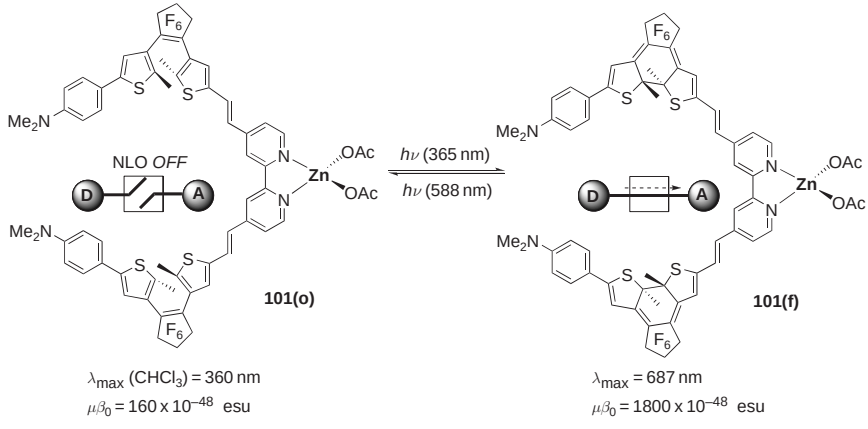

Figure 1.50 Photoswitching of the quadratic NLO response by using a photochromic metal complex

PSS closed forms: the $\mu\beta_0$ value for the open form is very small, in agreement with the absence of π-conjugation between the two thiophene rings of the DTE fragment. Upon conversion to the closed form in the photostationary state, the NLO activity dramatically increased, from 160 to 1800×10^{-48} esu. Thus, the huge enhancement of $\mu\beta_0$ clearly reflects the efficient delocalisation of the π-electron system in the closed forms and demonstrates an efficient ON/OFF switching of the NLO responses.

1.6 TOWARDS THE DESIGN OF PRE-ORGANISED MATERIALS

The greatest challenge in the field of second-order NLO materials is to transfer the molecular hyperpolarisability at the macroscopic level. To that end, several strategies have been developed to induce acentric arrangements of chromophores in the bulk materials. Three main approaches have been envisaged: (i) the orientation of an initially disordered material (polymer or sol-gel) by external stimulus like electrical poling of dipoles[132] or all-optical poling of octupoles;[133] (ii) the predetermined acentric orientation of NLO phores by taking advantage of physical interfaces like for Langmuir–Blodgett films,[118, 134] multilayer assemblies on surfaces[135] or orientation in a lipidic membrane;[136] (iii) the pre-organisation of NLO phores in materials or nanomaterials using intermolecular interactions pre-determined within crystals[137] or occurring spontaneously in nanoparticle.[138]

Metal-containing NLO chromophores were involved in these different approaches but generally the metal does not play any role in the orientation/organisation process. In this chapter the focus is on only two examples where the metallic centre is clearly responsible for the macroscopic orientation: the supramolecular octupolar self-ordering within metallodendrimers and crystal engineering using a metal/organic framework (MOF).

1.6.1 Supramolecular Octupolar Self-Ordering Within Metallodendrimers

Noncentrosymmetric pre-organisation of NLO chromophore was mainly achieved using organic dipolar compounds, and supermolecules

like calixarenes, cyclodextrins or dendrimers containing up to 64 dipolar chromophoric sub-units were reported in the literature.[139] Giant nonlinearities have been achieved, such as, for instance, in the case of a dendrimer containing 15 azobenzene NLO chromophore ($\lambda_{max} = 475$ nm, $\beta_0 = 3857 \times 10^{-30}$ esu).[139c] In the early 2000s, the design of poly-octupolar architectures containing up to 14 functionalised *tris*(bipyridine)-ruthenium(II) NLO-active species analogous to that described in Section 1.3.2 were reported.[140] The design of such polymetallic architectures is based of the ability of Ru^{II} to stabilise heteroleptic complexes upon sequential coordination of different bipyridine ligands. Therefore, polypyridyl ruthenium complexes are ideal building blocks for the construction of metallo-dendrimers, and for that purpose the group of Balzani has developed an elegant strategy named 'complex as metal/complex as ligand'.[141] According to this strategy, dimer **102** ($N = 2$) and trimer **103** ($N = 3$) were prepared as well as a polymeric species **104** ($N = 14$). The second generation dendritic species **105** containing seven octupolar sub-units was also reported (Figure 1.51).

The molecular NLO activity of these polymetallic species was rigorously compared with that of the parent monomeric sub-unit ($N = 1$) since all complexes present the same absorption spectrum. The NLO activity was found to increase from monomer ($N = 1$) to dimer ($N = 2$), trimer ($N = 3$) and heptamer ($N = 7$), but decrease from heptamer to polymer ($N = 14$) (Figure 1.51). According to the HRS principle, when the supramolecule is made of N fully disordered monomers, the number N of individual monomers can be inferred from the $\beta_{supra}(N)/\beta(N = 1) = \sqrt{N}$ relationship, where $\beta(N = 1)$ refers to the ruthenium monomer. For the polymer **104** the experimental hyperpolarisability ratio was about 4.0, very close to the theoretical value $\sqrt{14} = 3.7$. Such agreement accounts for the fully disordered assembly of monomeric ruthenium building blocks in the linear polymeric chain, the increase of β simply resulting of a concentration effect. A totally different behaviour was observed for the heptamer **105**, which exhibited a giant first hyperpolarisability of $\beta = 1900 \times 10^{-30}$ esu. In that case, the first hyperpolarisability satisfactorily fits with the linear relationship $\beta_{supra}(N)/\beta(1) = N$ (Figure 1.51). Such quasi-linear dependence is the signature of a quasi-optimised ordering of the individual building blocks in the heptamer. The heptamer can be described as a octupolar arrangement of seven octupolar sub-units, and in such highly ordered dendritic architecture each monomeric sub-unit coherently contributes to the NLO response.

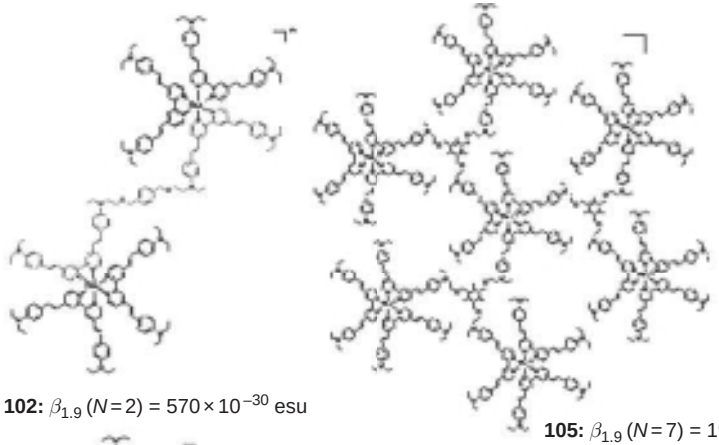

102: $\beta_{1.9}$ ($N = 2$) = 570×10^{-30} esu

105: $\beta_{1.9}$ ($N = 7$) = 1900×10^{-30} esu

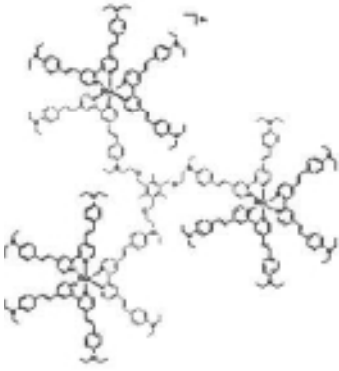

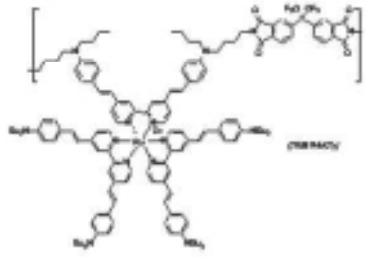

103: $\beta_{1.9}$ ($N = 3$) = 700×10^{-30} esu

104: $\beta_{1.9}$ ($N = 14$) = 1300×10^{-30} esu

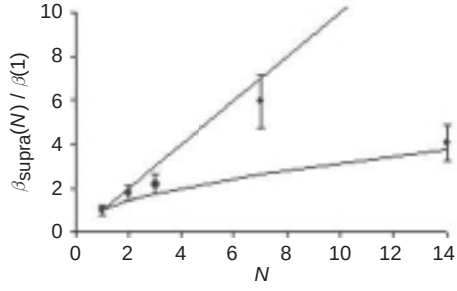

Figure 1.51 Structure of the poly-octupolar species and plot of the ratio $\beta(N)/\beta(1)$ *vs* N

1.6.2 Engineering of NLO-Active Crystals

Crystal engineering is an elegant way for the design of noncentrosymmetric dipolar or octupolar materials featuring high macroscopic nonlinearities. The acentric organisation in the crystal can be oriented by

taking advantages of chirality or of weak supramolecular interaction like hydrogen bonds. An alternative strategy is to exploit the strong and highly directional metal–ligand coordination bond for the construction of a so called metal–organic framework (MOF). In this context, a wide range of novel topologies can be obtained depending of the nature of the bi(multi)-dentate bridging ligand, the spacer and the metallic centre used as node. In addition, if the spacer presents an unsymmetrical π-conjugated backbone, the resulting noncentrosymmetric MOF will exhibit macroscopic NLO properties. This original strategy was explored by Lin[142] and more recently revisited by Liu *et al.*;[143] depending on the organic spacer, on the metallic node and on the hydrosolvothermal synthetic conditions, various (Figure 1.52) 2D or 3D networks were obtained with NLO activity up to 1000 times that of α-quartz or *ca* 100 times higher than the technologically important potassium dihydrogen phosphate. The global symmetry of the crystal is correlated to the packing and, in one case, the use of a D_{3h} symmetric spacer led to the formation of a purely octupolar trigonal network (Figure 1.53).[143]

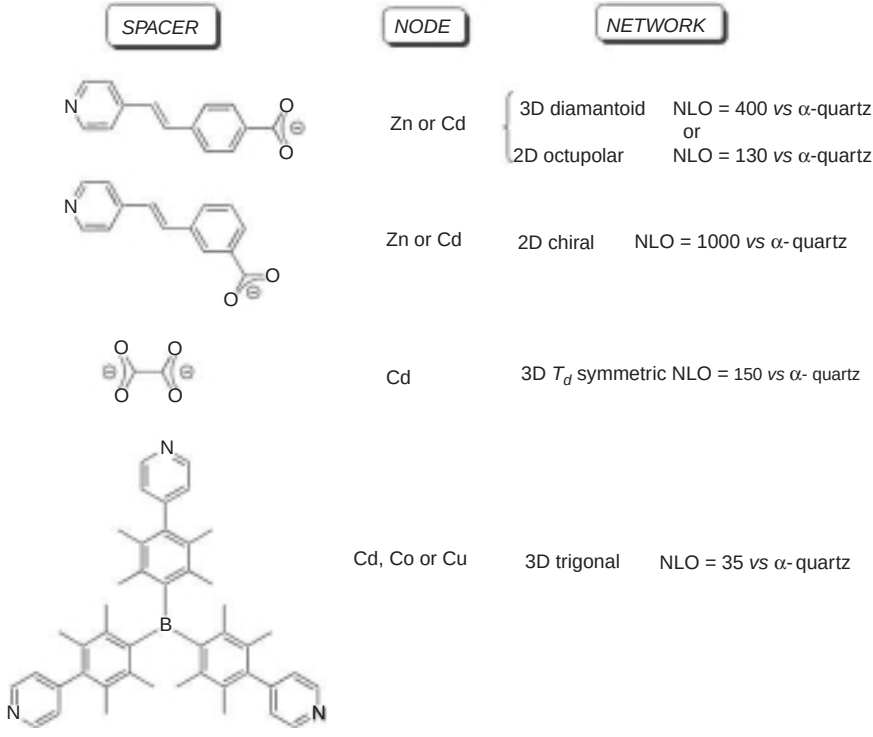

Figure 1.52 Examples of NLO-active MOFs

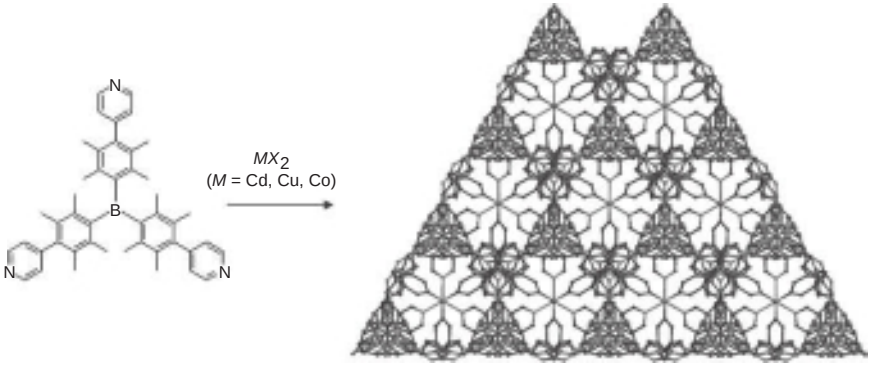

Figure 1.53 Octupolar MOF based on trigonal spacer. Reprinted with permission from Liu *et al.*, 2008 [143]. Copyright (2008) Wiley-VCH

1.7 CONCLUSIONS

The use of transition metals for NLO materials started in 1987, over twenty years ago. During the first decade (1987–1997), metal-containing NLO chromophores were mainly considered as an academic curiosity, interesting from a fundamental point of view but whose low NLO activity prohibited any applications. The second decade (1998–2009) showed an explosion of the research devoted to transition metal- or *f*-block element-containing chromophores. As illustrated in this chapter, the metals can play several roles in chromophore engineering: from an electronic point of view, they can act as electron-donating or electron-accepting groups, or can play an ambivalent role depending on the global chromophore architecture. They have also been used as transmitting units *via* the rigidification or perturbation of an existing π-skeleton or *via* the direct participation of *d*-orbitals into the conjugated backbone. Concerning geometry, metals are useful templates to gather ligands in a controlled symmetry giving rise to a large variety of octupolar architectures. But it must be underlined that metals are complex building blocks for NLO phore engineering and that their influence on the NLO efficiency is not fully rationalised for the moment. In this context, recent studies clearly indicated the direct contribution of *f*-electrons to the quadratic hyperpolarisability for dipolar and octupolar lanthanides containing chromophores. All these studies have allowed the design of optimised dipolar and octupolar dyes with NLO efficiency comparable with that of the best organic derivatives.

Furthermore, metals present additional intrinsic properties, such as redox reversibility, magnetism and luminescence. It is, therefore, possible to take benefit from these peculiarities for the design of redox-controlled NLO switches as illustrated in this chapter or for the elaboration of materials combining two or more properties. This latter field of research is in its infancy but it is possible to anticipate many improvements in the future for the elaboration of multifunctional molecular material optimising simultaneously all the wonderful capacities of metals.

REFERENCES

[1] D. S. Chemla and J. Zyss (eds) *Nonlinear Optical Properties of Organic Molecules and Crystals*, Academic Press, Orlando, FL, 1987.
[2] N. P. Prasad and D. J. Williams, *Introduction to Nonlinear Optical Effects in Molecules and Polymers*, John Wiley & Sons, Ltd, New York, NY, 1991.
[3] J. Zyss, *Molecular Nonlinear Optics: Materials, Physics and Devices*, Academic Press, Boston, MA, 1994.
[4] H. S. Nalwa and S. Miyata (eds), *Nonlinear Optics of Organic Molecules and Polymers*, CRC Press, Boca Raton, FL, 1997.
[5] H. S. Nalwa, *Appl. Organomet. Chem.*, **5**, 349–377 (1991).
[6] S. R. Marder, in *Inorganic Materials* (eds D. W. Bruce and D. O'Hare), John Wiley & Sons Ltd, Chichester, 1992.
[7] N. J. Long, *Angew. Chem. Int. Ed. Engl.*, **34**, 21–38 (1995).
[8] I. R. Whittall, A. M. McDonagh, M. G. Humphrey and M. Samoc, *Adv. Organomet. Chem.*, **42**, 291–362 (1998).
[9] J. Heck, S. Dabek, T. Meyer-Friedrichsen and H. Wong, *Coord. Chem. Rev.*, **190–192**, 1217–1254 (1999).
[10] (a) S. Di Bella, *Chem. Soc. Rev.*, **30**, 355–366 (2001); (b) H. Le Bozec and T. Renouard, *Eur. J. Inorg. Chem.*, 229–239 (2000).
[11] B. J. Coe, in *Comprehensive Coordination Chemistry II* (eds J. A. McCleverty and T. J. Meyer), Elsevier Pergamon, Oxford, 2004, pp. 621–687.
[12] W. Kaiser and C. G. B. Garrett, *Phys. Rev. Lett.*, **7**, 229–231 (1961).
[13] P. A. Franken, A. E. Hill and C. W. Peters, *Phys. Rev. Lett.*, **7**, 118–119 (1961).
[14] S. R. Marder, L. T. Cheng, B. G. Tiemann, A. C. Friedli, M. Blanchard-Desce, J. W. Perry and J. Skindhoej, *Science*, **263**, 511–514 (1997)
[15] Y. Shi, C. Zhang, H. Zhang, J. H. Bechtel, L. R. Dalton, B.H. Robinson and W. H. Steier, *Science*, **288**, 119–122 (2000)
[16] H. Kang, A. Facchetti, P. Zhu, H. Jiang, Y. Yang, E. Cariati, S. Righetto, R. Ugo, C. Zuccaccia, A. Macchioni, C. L. Stern, Z. Liu, S.-T. Ho and T. J. Marks, *Angew. Chem. Int. Ed.*, **44**, 7922–7925 (2005).
[17] H. Kang, A. Facchetti, H. Jiang, E. Cariati, S. Righetto, R. Ugo, C. Zuccaccia, A. Macchioni, C. L. Stern, Z. Liu, S.-T. Ho, E. C. Brown, M. A. Ratner and T. J. Marks, *J. Am. Chem. Soc.*, **129**, 3267–3286 (2007).
[18] J. Zyss and I. Ledoux, *Chem. Rev.*, **94**, 77–105 (1994).

[19] (a) I. Ledoux, J. Zyss, J. S. Siegel, J. Brienne and J. M. Lehn, *Chem. Phys. Lett.*, **172**, 440–444 (1990); (b) T. Verbiest, K. Clays, C. Semyr, J. Wolff, D. Reihoudt and A. Persoons, *J. Am. Chem. Soc.* **116**, 9320–9323, (1994); (c) J. L. Bredas, F. Meyers, B. M. Pierce and J. Zyss, *J. Am. Chem. Soc.*, **114**, 4928–4929 (1992).

[20] (a) J. J. Wolff, D. Längle, D. Hillenbrand, R. Wortmann, R. Matschiner, C. Glania and P. Krämer, *Adv. Mater.*, **9**, 138–143 (1997); (b) R. Wortmann, C. Glania, P. Krämer, R. Matschiner, J. J. Wolff, S. Kraft, B. Treptow, E. Barbu, D. Längle and G. Görlitz, *Chem. Eur. J.*, **3**, 1765–1773 (1997); (c) C. Lambert, G. Nöll, E. Schmälzlin, K. Meerholz and C. Bräuchle, *Chem. Eur. J.*, **4**, 2129–2135 (1998); (d) B. R. Cho, S. K. Lee, K. A. Kim, K. N. Son, T. I. Kang and S. J. Jeon, *Tetrahedron Lett.*, **39**, 9205–9208 (1998); (e) C. Andraud, T. Zabulon, A. Collet and J. Zyss, *Chem. Phys.*, **245**, 243–261 (1999); (f) A. Omenat, J. Barbera, J. L. Serrano, S. Houbrechts and A. Persoons, *Adv. Mater.*, **11**, 1292–1295 (1999); (g) B. R. Cho, S. J. Lee, S. H. Lee, K. H. Son, Y. H. Kim, I.-Y. Doo, G. J. Lee, T. I. Kang, Y. K. Lee, M. Cho and S.-J. Jeon, *Chem. Mater.*, **13**, 1438–1440 (2001); (h) J. Brunel, I. Ledoux, J. Zyss and M. Blanchard-Desce, *Chem. Commun.*, 923–924 (2001); (i) B. R. Cho, S. B. Park, S. J. Lee, K. H. Son, S. H. Lee, M.-J. Lee, J. Yoo, Y. K. Lee, G. J. Lee, T. I. Kang, M. Cho and S.-J. Jeon, *J. Am. Chem. Soc.*, **123**, 6421–6422 (2001).

[21] (a) S. Brasselet, F. Cherioux, P. Audebert and J. Zyss, *Chem. Mater.*, **11**, 1915–1920 (1999); (b) V. R. Thalladi, R. Boese, S. Brasselet, I. Ledoux, J. Zyss, R. K. R. Jetti and G. R. Desiraju, *Chem. Commun.*, 1639–1640 (1999); (c) F. Cherioux, H. Maillotte, P. Audebert and J. Zyss, *Chem. Commun.*, 2083–2084 (1999); (d) J. J. Wolff, F. Siegler, R. Matschiner and R. Wortmann, *Angew. Chem. Int. Ed.*, **39**, 1436–1439 (2000).

[22] G. Alcaraz, L. Euzenat, O. Mongin, C. Katan, I. Ledoux, J. Zyss, M. Blanchard-Desce and M. Vaultier, *Chem. Commun.*, 2766–2767 (2003).

[23] *For carbocations see*: (a) J. Zyss, T. Chauvan, C. Dhenaut and I. Ledoux, *Chem. Phys.*, **177**, 281–296 (1993); (b) A. Verbiest, K. Clays, C. Samyn, J. Wolff, D. Reinhoudt and A. Persoons, *J. Am. Chem. Soc.*, **116**, 9320–9323 (1994); (c) Y.-K. Lee, S.-J. Jeon and M. Cho, *J. Am. Chem. Soc.*, **120**, 10921–10927 (1998). *For carbanions see*: T. Verbiest, K. Clays, A. Persoons, F. Meyers and J.-L Brédas, *Opt. Lett.*, **18**, 525–527 (1993). *For carbon radicals see*: I. Ratera, S. Marcen, S. Montant, D. Molina-Ruiz, C. Rovira, J. Veciana, J.-F. Letard and E. Freysz, *Chem. Phys. Lett.*, **363**, 245–251 (2002).

[24] (a) S. Stadler, C. Braüchle, S. Brandl and R. Gompper, *Chem. Mater.*, **8**, 414–417 (1996); (b) C. Lambert, W. Gaschler, E. Schmälzlin, K. Meerholz and C. Bräuchle, *J. Chem. Soc. Perkin Trans.*, **2**, 577–587 (1999).

[25] P. D. Maker, *Phys. Rev. A*, **1**, 923 (1970).

[26] (a) C. Bourgogne, Y. Le Fur, P. Juen, P. Masson, J.-F. Nicoud and R. Masse, *Chem. Mater.*, **12**, 1025–1033 (2000); (b) C. Lambert, E. Schmälzlin, K. Meerholz and C. Bräuchle, *Chem. Eur. J.*, **4**, 512–521 (1998).

[27] M. Lequan, C. Branger, J. Simon, T. Thami, E. Chauchard and A. Persoons, *Adv. Mater.*, 1994, **6**, 851–853.

[28] P. D. Maker, *Phys. Rev. A*, **1**, 923–951 (1970).

[29] K. Clays and A. Persoons, *Phys. Rev. Lett.*, **66**, 2980–2983 (1991).

[30] E. Hendrickx, K. Clays and A. Persoons, *Acc. Chem. Res.*, **31**, 675–683 (1998).

[31] M. L. H. Green, S. R. Marder, M. E. Thompson, J. A. Bandy, D. Bloor, P. V. Kolinsky and R. J. Jones, *Nature*, **330**, 360–362 (1987).

[32] J. P. Morall, G. T. Dalton, M. G. Humphrey and M. Samoc, *Adv. Organomet. Chem.*, **55**, 61–136 (2008).
[33] J. C. Calabrese, L. T. Chen, J. C. Green, S. R. Marder and W. Tam, *J. Am. Chem. Soc.*, **113**, 7227–7232 (1991).
[34] L. T. Chen, W. Tam, S. H. Stevenson, G. R. Meredith, G. Riken and S. R. Marder, *J. Phys. Chem.*, **95**, 10631–10643 (1991).
[35] S. Barlow, H. E. Bunting, C. Ringham, J. C. Green, G. U. Bublitz, S. G. Boxer, J. W. Perry and S. R. Marder, *J. Am. Chem. Soc.*, **121**, 3715–3723 (1999).
[36] J. A. Mata, E. Peris, I. Asselberghs, J. A. Mata, E. Peris, I. Asselberghs, R. Van Boxel and A. Persoons, *New J. Chem.*, **25**, 1043–1046 (2001).
[37] V. Alain, M. Blanchard-Desce, C.-T. Chen, S. R. Marder, A. Fort and M. Barzoukas, *Synth. Met.*, **81**, 133–136 (1996).
[38] G. G. A. Balavoine, J. C. Daran, G. Iftime, P. G. Lacroix, E. Manaury, J. A. Delaire, I. Maltey-Fanton, K. Nakatani and S. Di Bella, *Organometallics*, **18**, 21–29 (1999).
[39] J. Chiffre, F. Averseng, G. G. A. Balavoine, J.-C. Daran, G. Iftime, P. G. Lacroix, E. Manoury and K. Nakatani, *Eur. J. Inorg. Chem.*, 2221–2226 (2001).
[40] M. P. Cifuentes and M. G. Humphrey, *J. Organomet. Chem.*, **689**, 3968–3981 (2004).
[41] C. E. Powel and M. G. Humphrey, *Coord. Chem. Rev.*, **248**, 725–756 (2004).
[42] C. E. Powell, M. P. Cifuentes, A. M. McDonagh, S. K. Hurst, N. T. Lucas, C. D. Delfs, R. Stranger, M. G. Humphrey, S. Houbrechts, I. Asselberghs, A. Persoons and D. C. R. Hockless, *Inorg. Chim. Acta.*, **352**, 9–18 (2003).
[43] I. R. Whittall, M. G. Humphrey, A. Persoons and S. Houbrechts, *Organometallics*, **15**, 1935–1941 (1996).
[44] V. Cadierno, S. Conejero, M. P. Gamasa, J. Gimeno, I. Asselberghs, S. Houbrechts, K. Clays, A. Persoons, J. Borge and S. Garcia-Granda, *Organometallics*, **18**, 582–597 (1999).
[45] S. Houbrechts, K. Clays, A. Persoons, V. Cadierno, M. P. Gamasa and J. Gimeno, *Organometallics*, **15**, 5266–5268 (1996).
[46] W. Wenseleers, A. W. Gerbrandij, E. Goovaerts, M. H. Garcia, M. P. Robalo, P. J. Mendes, J. C. Rodrigues and A. R. Dias, *J. Mater. Chem.*, **8**, 925–930 (1998).
[47] I. R. Whittall, M. P. Cifuentes, M. G. Humphrey, B. Luther-Davies, M. Samoc, S. Houbrechts, A. Persoons, G. A. Heath and D. Bogsanyi, *Organometallics*, **16**, 2631–2637 (1997).
[48] S. K. Hurst, M. P. Cifuentes, J. P. L. Morall, N. T. Lucas, I. R. Whittall, M. G. Humphrey, I. Asselberghs, A. Persoons, M. Samoc, B. Luther-Davies and A. C. Willis, *Organometallics*, **20**, 4664–4675 (2001).
[49] R. H. Naulty, A. M. McDonagh, I. R. Whittall, M. P. Cifuentes, M. G. Humphrey, S. Houbrechts, J. Maes, A. Persoons, G. A. Heath and D. C. R. Hockless, *J. Organomet. Chem.*, **563**, 137–146 (1998).
[50] A. M. McDonagh, M. P. Cifuentes, M. G. Humphrey, S. Houbrechts, J. Maes, A. Persoons, M. Samoc and B. Luther-Davies, *J. Organomet. Chem.*, **610**, 71–79 (2000).
[51] R. Whittall, M. G. Humphrey, S. Houbrechts, A. Persoons and D. C. R. Hockless, *Organometallics*, **15**, 5738–5745 (1996).
[52] B. J. Coe, *Acc. Chem. Res.*, **39**, 383–393 (2006)
[53] B. J. Coe, M. C. Chamberlain, J. P. Essex-Lopresti, S. Gaines, J. C. Jeffery, S. Houbrechts and A. Persoons, *Inorg. Chem.*, **36**, 3284–3292 (1997).

[54] B. J. Coe, J. A. Harris, L. J. Harrington, J. C. Jeffery, L. Rees, S. Houbrechts and A. Persoons, *Inorg. Chem.*, **37**, 3391–3399 (1998).
[55] B. J. Coe, L. A. Jones, J. A. Harris, B. S. Brunschwig, I. Asselberghs, K. Clays and A. Persoons, *J. Am. Chem. Soc*, **125**, 862–863 (2003).
[56] B. J. Coe, L. A. Jones, J. A. Harris, B. S. Brunschwig, I. Asselberghs, K. Clays, A. Persoons, J. Garin and J. Orduna, *J. Am. Chem. Soc.*, **126**, 3880–3391 (2004).
[57] B. J. Coe, J. A. Harris, K. Clays, A. Persoons, K. Wostyn and B. S. Brunschwig, *Chem. Commun.*, 1548–1549 (2001).
[58] B. J. Coe, J. A. Harris, B. S. Brunschwig, J. Garin, J. Orduna, S. J. Coles and M. B. Hursthouse, *J. Am. Chem. Soc.*, **126**, 10418–10427 (2004).
[59] B. J. Coe, J. A. Harris, L. A. Jones, B. S. Brunschwig, K. Song, K. Clays, J. Garin, J. Orduna, S. J. Coles and M. B. Hursthouse, *J. Am. Chem. Soc.*, **127**, 4845–4859 (2004).
[60] C. Dragonetti, S. Righetto, D. Roberto, R. Ugo, A. Valore, S. Fantacci, A. Sgamelotti and F. De Angelis, *Chem. Commun.*, 4116–4118 (2007).
[61] H. Le Bozec and T. Renouard, *Eur. J. Inorg. Chem.*, 229–239 (2000).
[62] E. Cariati, M. Pizzoti, D. Roberto, F. Tessore and R. Hugo, *Coord. Chem. Rev.*, **250**, 1210–1233 (2006).
[63] D. R. Kanis, P. G. Lacroix, M. A. Ratner and T. J. Marks, *J. Am. Chem. Soc.*, **116**, 10089–10102 (1994).
[64] D. Roberto, R. Ugo, S. Bruni, E. Cariati, F. Cariati, P. C. Fantucci, I. Invernizzi, S. Quici, I. Ledoux and J. Zyss, *Organometallics*, **19**, 1775–1788 (2000)
[65] D. W. Bruce and A. Thornton, *Mol. Cryst. Liq. Cryst.*, **231**, 253–256 (1993)
[66] M. J. G. Lesley, A. Woodward, N. J. Taylor, T. B. Marder, I. Cazenobe, I. Ledoux, J. Zyss, A. Thornton, D. W. Bruce and A. K. Kakkar, *Chem. Mater.*, **10**, 1355–1365 (1998)
[67] D. Roberto, R. Ugo, F. Tessore, E. Lucenti, S. Quici, S. Vezza, P. C. Fantucci, I. Invernizzi, S. Bruni, I. Ledoux and J. Zyss, *Organometallics*, **21**, 161–170 (2002).
[68] F. Tessore, D. Roberto, R. Ugo, P. Mussini, S. Quici, I. Ledoux and J. Zyss, *Angew. Chem. Int. Ed.*, **42**, 456–459 (2003).
[69] M. Bourgault, K. Baum, H. Le Bozec, I. Ledoux, G. Pucetti and J. Zyss, *New J. Chem.*, 517–522 (1998)
[70] A. Hilton, T. Renouard, O. Maury, I. Ledoux and J. Zyss, *Chem. Commun.*, 2521–2522 (1999).
[71] K. Sénéchal, O. Maury, H. Le Bozec, I. Ledoux and J. Zyss, *J. Am. Chem. Soc.*, **124**, 4561–4562 (2002).
[72] D. Roberto, F. Tessore, R. Ugo, D. Roberto, F. Tessore, R. Ugo, S. Bruni, A. Manfredi and S. Quici, *Chem. Commun.*, 846–847 (2002).
[73] F. De Angelis, S. Fantacci, A. Sgamelotti, F. Cariati, D. Roberto, F. Tessore and R. Ugo, *Dalton. Trans.*, 852–859 (2006).
[74] K. Sénéchal, L. Toupet, I. Ledoux, J. Zyss, H. Le Bozec and O. Maury, *Chem Commun.*, 2180–2181 (2004).
[75] K. Sénéchal-David, A. Hemeryck, N. Tancrez, L. Toupet, J. A. G. Williams, I. Ledoux, J. Zyss, A. Boucekkine, J.-P. Guégan, H. Le Bozec and O. Maury, *J. Am. Chem. Soc.*, **128**, 12243–12255 (2006).
[76] U. Behrens, H. Brussaard, U. Hagenau, J. Heck, E. Hendrickx, J. Kärnich, J. G. M. van der Linden, A. Perrsoons, N. Spek, A. L. Veldman, B. Voss and H. Wong, *Chem. Eur. J.*, **2**, 98–103 (1996).

[77] J. A. Mata, S. Uriel, E. Peris, R. Llusar, S. Houbrechts and A. Persoons, *J. Organomet. Chem.*, **562**, 197–202 (1998)
[78] S. Houbrechts, K. Clays, A. Persoons, V. Cadierno, M. Pilar Gamasa and J. Gimeno, *Organometallics*, **15**, 5266–5268 (1996)
[79] M. Pizzotti, R. Ugo, D. Roberto, S. Bruni, P. C. Fantucci and C. Rovizzi, *Organometallics*, **21**, 5830–5840 (2002)
[80] M. Bruschi, P. C. Fantucci and M. Pizzotti, *J. Phys. Chem. A*, **109**, 9637–9645 (2005)
[81] B. J. Coe, E. C. Fitzgerald, M. Helliwell, B. S. Brunschwig, A. G. Fitch, J. A. Harris, C. J. Coles, P. N. Horton and M. B. Hursthouse, *Organometallics*, **27**, 2730–2742 (2008)
[82] P. G. Lacroix, *Eur. J. Inorg. Chem.*, 339–348 (2001).
[83] S. Di Bella, I. Fragalà, I. Ledoux and T. J. Marks, *J. Am. Chem. Soc.*, **117**, 9481–9485 (1995)
[84] S. Di Bella, I. Fragalà, T. J. Marks and M. A. Ratner, *J. Am. Chem. Soc.*, **118**, 12747–12751 (1996)
[85] P. G. Lacroix, S. Di Bella and I. Ledoux, *Chem. Mater.*, **8**, 541–545 (1996)
[86] F. Averseng, P. G. Lacroix, I. Malfant, G. Lenoble, P. Cassoux, K. Nakatani, I. Maltey-Fanton, J. A. Delaire and A. Aukauloo, *Chem. Mater.*, **11**, 995–1002 (1999)
[87] S. Di Bella, I. Fragalà, I. Ledoux and J. Zyss, *Chem. Eur. J.*, **7**, 3738–3743 (2001)
[88] G. de la Torre, P. Vazquez, F. Agullo-Lopez and T. Torres, *Chem. Rev.*, **104**, 3723–3750 (2004)
[89] G. de la Torre, T. Torres and Agullo-Lopez, *Adv. Mater.*, **9**, 265–269 (1997)
[90] G. Rojo, G. de la Torre, J. Garcia-Ruiz, I. Ledoux, T. Torres, J. Zyss and F. Agullo-Lopez, *Chem. Phys.*, **245**, 27–34 (1999)
[91] E. M. Maya, E. M. Garcia-Frutos, P. Vazquez, T. Torres, G. Martin, G. Rojo, F. Agullo-Lopez, R. H. Gonzales-Jonte, V. R. Ferro, J. M. Garcie de la Vega, I. Ledoux and J. Zyss, *J. Phys. Chem. A*, **107**, 2110–2117 (2003).
[92] S. M. LeCours, H.-W. Guan, S. G. DiMagno, C. H. Wang and M. J. Therien, *J. Am. Chem. Soc.*, **118**, 1497–1503 (1996)
[93] L. Karki, F. W. Vance, J. T. Hupp, S. M. LeCours and M. J. Therien, *J. Am. Chem. Soc.*, **120**, 2606–2611 (1998)
[94] M. Pizzotti, E. Annoni, R. Ugo, S. Bruni, S. Quici, P. C. Fantucci, M. Bruschi, G. Zerbi and M. Del Zoppo, *J. Porph. Phthal.*, **8**, 1311–1324 (2004)
[95] M. Yeung, A. C. H. Ng, M. G. B. Drew, E. Vorpagel, E. M. Breitung, R. J. McMahon and D. K. P. Ng, *J. Org. Chem.*, **63**, 7143–7150 (1998)
[96] T-G. Zhang, Y. Zhao, I. Asselberghs, A. Persoons, K. Clays and M. Therien, *J. Am. Chem. Soc.*, **127**, 9710–9720 (2005)
[97] I. D. L. Albert, T. J. Marks and M. A. Ratner, *Chem. Mater.*, **10**, 753–762 (1998)
[98] E. Annoni, M. Pizzotti, R. Ugo, S. Quici, T. Morotti, M. Bruschi and P. Mussini, *Eur. J. Inorg. Chem.*, 3857–3874 (2005).
[99] J. E. Reeve, H. A. Collins, K. De Mey, M. M. Kohl, K. J. Thorley, O. Paulsen, K. Clays and H. Anderson, *J. Am. Chem. Soc.*, **131**, 2758–2759 (2009).
[100] A. M. McDonagh, M. G. Humphrey, M. Samoc, B. Luther-Davies, S. Houbrechts, T. Wada, H. Sasabe and A. Persoons, *J. Am. Chem. Soc*,. **121**, 1405–1406 (1999).
[101] T. Weyland, I. Ledoux, S. Brasselet, J. Zyss and C. Lapinte, *Organometallics* **19**, 5235–5237 (2000).
[102] T. Renouard, H. Le Bozec, I. Ledoux and J. Zyss, *Chem. Commun.*, 871–872 (1999).

[103] C. Feuvrie, O. Maury, H. Le Bozec, I. Ledoux, J. P. Morral, G. T. Dalton, M. Samoc and M. G. Humphrey, *J. Phys. Chem. A*, **111**, 8980–8985 (2007).
[104] O. P. Andreson, *J. Chem. Soc. Dalton Trans*., 2597–2601 (1972); B. Murphy, M. Aljabri, A. M. Ahmed, G. Murphy, B. J. Hataway, M. E. Light, T. Geilbrich and M. B. Hurthouse, *Dalton Trans*., 357–367 (2006).
[105] S. Bidault, S. Brasselet, J. Zyss, O. Maury and H. Le Bozec, *J. Chem. Phys*., **126**, 034312 (2007).
[106] O. Maury, L. Viau, K. Sénéchal, B. Corre, J.-P. Guégan, T. Renouard, I. Ledoux, J. Zyss and H. Le Bozec, *Chem. Eur. J*., **10**, 4454–4466 (2004).
[107] F. W. Vance and J. T. Hupp, *J. Am. Chem. Soc*., **121**, 4047–4053 (1999).
[108] B. J. Coe, J. A. Harris, B. S. Brunschwig, I. Asselberghs, K. Clays, J. Garıin and J. Orduna, *J. Am. Chem. Soc*., **127**, 13399–13410 (2005).
[109] (a) P. A. Brayshaw, J.-C.G. Bünzli, P. Froidevaux, J. M. Harrowfield, Y. Kim, A. N. Sobolev, *Inorg. Chem*., **34**, 2068–2076 (1995); (b) J. M. Harrowfield, Y. Kim, B. W. Skelton and A. H. White, *Aust. J. Chem*., **48**, 807–823 (1995).
[110] N. Ouali, B. Bocquet, S. Rigault, P.-Y. Morgantini, J. Weber and C. Piguet, *Inorg. Chem*., **41**, 1436–1445 (2002).
[111] N. Tancrez, C. Feuvrie, I. Ledoux, J. Zyss, L. Toupet, H. Le Bozec and O. Maury, *J. Am. Chem. Soc*., **127**, 13474–13475 (2005).
[112] E. Furet, K. Costuas, P. Rabiller and O. Maury, *J. Am. Chem. Soc*., **130**, 2180–2183 (2008).
[113] T. V. Duncan, K. Song, S.-T. Hung, T. Verbiest, M. Therien and K. Clays, *Angew. Chem. Int. Ed*., **47**, 2978–2981 (2008).
[114] B. J. Coe, *Chem. Eur. J*., **5**, 2464–2471 (1999).
[115] I. Asselberghs, K. Clays, A. Persoons, M. D. Ward and J. McCleverty, *J. Mater. Chem*., **14**, 2831–2839 (2003).
[116] J. A. Delaire and K. Nakatani, *Chem. Rev*., **100**, 1817–1845 (2000).
[117] B. J. Coe, S. Houbrechts, I. Asselberghs and A. Persoons, *Angew Chem. Int. Ed*., **38**, 366–369 (1999).
[118] L. Boubekeur-Lecaque, B. J. Coe, K. Clays, S. Foerier, T. Verbiest and I. Asselberghs, *J. Am. Chem. Soc*., **130**, 3286–3287 (2008).
[119] M. Malaun, Z. R. Reeves, R. L. Paul, J. C. Jeffery, J. McCleverty, M. D. Ward, I. Asselberghs, K. Clays and A. Persoons, *Chem. Commun*., 49–50 (2001).
[120] I. Asselberghs, K. Clays, A. Persoons, A. McDonagh, M. D. Ward and J. McCleverty, *Chem Phys. Lett*., **368**, 408–411 (2003).
[121] C. Sporer, I. Ratera, D. Ruiz-Molina, Y. Zhao, J. Vidal-Gancedo, K. Wurst, P. Jaitner, K. Clays, A. Persoons, C. Rovira and J. Veciana, *Angew. Chem. Int. Ed*., **43**, 5266–5268 (2004).
[122] F. Paul, K. Costuas, I. Ledoux, S. Deveau, J. Zyss, J.-F. Halet and C. Lapinte, *Organometallics*, **21**, 5229–5235 (2002)
[123] B. J. Coe, J. L. Harries, M. Helliwell, L. A. Jones, I. Asselberghs, K. Clays, B. S. Brunschwig, J. A. Harris, J. Garıin and J. Orduna, *J. Am. Chem. Soc*., **128**, 12192–12204 (2006).
[124] T. Nagamura, H. Sakaguchi and T. Matsuo, *Thin Solid Films*, **210**, 160–162 (1992).
[125] H. Sakaguchi, L. A. Gomez-Jahn, M. Pritchard, T. L. Penner, D. G. Whitten and T. Nagamura, *J. Phys. Chem*., **97**, 1474–1476 (1993).

[126] H. Sakaguchi, T. Nagamura, T. L. Penner and D. G. Whitten, *Thin Solid Films*, **244**, 947–950 (1994).
[127] S. L. Gilat, S. H. Kawai and J.-M. Lehn, *Chem. Eur. J.*, **1**, 275–284 (1995).
[128] K. Nakatani and J. A. Delaire, *Chem. Mater.*, **9**, 2682–2684 (1997).
[129] L. Sanguinet, J.-L. Pozzo, V. Rodriguez, F. Adamietz, F. Castet, L. Ducasse and B. Champagne, *J. Phys. Chem. B*, **109**, 11139–11150 (2005).
[130] M. Irie, *Chem. Rev.*, **100**, 1685–1716 (2000).
[131] V. Aubert, V. Guerchais, E. Ishow, K. Hoang-Thi, I. Ledoux, K. Nakatani and H. Le Bozec, *Angew. Chem. Int. Ed.*, **47**, 577–580 (2008).
[132] M. Eich, G. C. Bjorlddund and D. Y. Yoon, *Polym. Adv. Technol.*, **1**, 189 (1990).
[133] S. Bidault, L. Viau, O. Maury, S. Brasselet, J. Zyss, E. Ishow, K. Nakatani and H. Le Bozec, *Adv. Funct. Mater.*, **16**, 2252–2262 (2006).
[134] G. J. Ashwell, *J. Mater. Chem.*, **9**, 1991–2003 (1999).
[135] (a) S. Yitzchaik and T. J. Marks, *Acc. Chem. Res.*, **29**, 197–202 (1996); (b) H. E. Katz, G. Scheller, T. M. Putvinski, M. L. Schilling, W. L. Wilson and C. E. D. Chidsey, *Science*, **254**, 1485–1487 (1991); (c) A. Fachetti, A. Abbotto, L. Beverina, M. E. van der Boom, P. Dutta, G. Evmenenko, G. A. Pagani and T. J. Marks, *Chem. Mater.*, **15**, 1064–1072 (2003).
[136] (a) P. Yan, A. C. Millard, M. Wei and L. M. Loew, *J. Am. Chem. Soc.*, **128**, 11030–11031 (2006); (b) W. R. Zipfel, R. M. Williams and W. W. Webb, *Nat. Biotechnol.*, **21**, 1369–1377 (2003).
[137] (a) V. R. Thalladi, S. Brasselet, H.-C. Weiss, D. Blaser, A. K. Katz, H. L. Carrell, R. Boese, J. Zyss, A. Nangia and G. R. Desiraju, *J. Am. Chem. Soc.*, **120**, 2563–2577 (1998); (b) V. Le Floc'h, S. Brasselet, J. Zyss, B. R. Cho, S. H. Lee, S.-J. Jeon, M. Cho, K.S. Min and M. P. Suh, *Adv. Mater.*, **17**, 196–200 (2005).
[138] T. Yi, R. Clément, C. Haut, L. Catala, T. Gacoin, N. Tancrez, I. Ledoux and J. Zyss, *Adv. Mater.*, **17**, 335–338 (2005).
[139] (a) E. D. Rekaï, J.-B. Baudin, L. Jullien, I. Ledoux, J. Zyss and M. Blanchard-Desce, *Chem. Eur. J.*, **7**, 4395–4402 (2001); (b) E. J. H. Put, K. Clays, A. Persoons, H. A. M. Biemans, C. P. M. Luijkx and E. W. Meijer, *Chem. Phys. Lett.*, **260**, 136–141 (1996); (c) S. Yokoyama, T. Nakahama, A. Otomo and S. Mashiko, *J. Am. Chem. Soc.*, **122**, 3174–3181 (2000).
[140] (a) H. Le Bozec, T. Le Bouder, O. Maury, A. Bondon, J. Zyss and I. Ledoux, *Adv. Mater.*, **13**, 1677–1681 (2001); (b) T. Le Bouder, O. Maury, H. Le Bozec, A. Bondon, K. Costuas, E. Amouyal, J. Zyss and I. Ledoux, *J. Am. Chem. Soc.*, **125**, 12884–12899 (2003).
[141] V. Balzani, S. Campagna, G. Denti, A. Juris, S. Serroni and M. Venturi, *Acc. Chem. Res.*, **31**, 26–34 (1998).
[142] (a) W. Lin, O. R. Evans, R.-G. Xiong and Z. Wang, *J. Am. Chem. Soc.*, **120**, 13272–13273 (1998); (b) W. Lin, Z. Wang and L. Ma, *J. Am. Chem. Soc.*, **121**, 11249–11250 (1999); (c) W. Lin, L. Ma and O. R. Evans, *Chem. Commun.*, 2263–2264 (2000); (d) O. R. Evans and W. Lin, *Chem. Mater.*, **13**, 2705–2712 (1998); (e) O. R. Evans and W. Lin, *Acc. Chem. Res.*, **35**, 511–522 (2002).
[143] (a) Y. Liu, G. Li, X. Li and Y. Cui, *Angew. Chem. Int. Ed.*, **46**, 6301–6304 (2007); (b) Y. Liu, X. Xu, F. Zheng and Y. Cui, *Angew. Chem. Int. Ed.*, **47**, 4538–4541 (2008).

2

Physical Properties of Metallomesogens

Koen Binnemans
Department of Chemistry, Katholieke Universiteit Leuven, Belgium

2.1 INTRODUCTION

A metal centre can add unique magnetic, spectroscopic or redox properties to a liquid crystal.[1] Whereas the first examples of metal-containing liquid crystals (*metallomesogens*) mimicked the rod-like or disc-like shape of conventional organic liquid crystals, it gradually became clear that mesomorphism can also be observed for coordination geometries other than linear or square-planar.[2] For most of the metallic elements, at least one example of a liquid-crystalline metal complex has been described in the literature. Unfortunately, metallomesogens often have quite high transition temperatures, with melting points well above 100 °C. These high transition temperatures and the low thermal stability of the mesogens at these elevated temperatures were major drawbacks that hampered the study of the physical properties of these materials. However, careful design of metallomesogens on the basis of previously gained experience enables metal complexes to be obtained at present that are liquid-crystalline at very moderate temperatures or even at room temperature. As a consequence of these developments, more and more authors have started to study the magnetic and luminescence properties

Molecular Materials Edited by Duncan W. Bruce, Dermot O'Hare and Richard I. Walton

of metallomesogens in detail. These developments are of importance, because an often heard criticism of metallomesogens is that only very few applications have resulted from these research efforts.[3]

Metallomesogens have been the subject of several reviews, not only general reviews[4–12] but also reviews on more specialised items like lanthanide-containing metallomesogens (*lanthanidomesogens*),[13,14] silver-containing metallomesogens,[15] ferrocene-containing metallomesogens,[16,17] Schiff base complexes,[18] carboxylates,[19] metallomesogens with helical supramolecular organisation,[20] ionic metallomesogens,[21,22] polymeric metallomesogens,[23,24] lyotropic metallomesogens[25] or mineral liquid crystals.[26–31] However, most of these reviews focus on the relationship between the molecular structure and the mesophase behaviour. An exception is the book *Metallomesogens* edited by Serrano, in which considerable attention is paid to the physical properties of metallomesogens, and especially to their magnetic properties.[32] In this chapter, the physical properties of metallomesogens are described, with emphasis on the developments in this field after 1995. First, an overview of the most important liquid-crystal phases and of general properties of liquid crystals will be given, which will be helpful to those who are not very familiar with liquid crystals. Then, separate sections are devoted to the optical, electrical and magnetic properties of metallomesogens. Because the most exciting recent developments are about the magnetic properties (magnetic alignment, spin-crossover behaviour) and the optical properties (photoluminescence, polarised emission), these properties are discussed in more detail.

2.2 OVERVIEW OF MESOPHASES

The difference between crystals and liquids, the two most common types of condensed matter, is that the molecules in a crystal are well ordered in a three-dimensional lattice, whereas the molecules in a liquid are totally disordered. A molecular crystal consists of a more or less rigid arrangement of molecules, which possess both positional and orientational order; the molecules are constrained to occupy specific positions in the crystal lattice. At low temperatures, the attractive intermolecular forces in a crystal are strong enough to hold the molecules firmly in place, even though they all exhibit a random motion due to thermal vibrations. When a crystalline compound is heated, the thermal motions of the molecules increase and eventually become so strong that the intermolecular forces cannot keep the molecules in their position, so that the solid melts (Figure 2.1). The regular

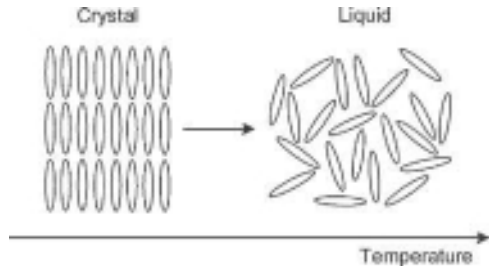

Figure 2.1 Schematic representation of the melting process of a nonmesomorphic molecular compound

arrangement of molecules is broken down with loss of long-range orientational and positional order to give a disordered isotropic liquid.

However, this melting process, which transforms a compound in one step from a highly ordered to a totally disordered phase, is a very destructive one and is not universal for all types of compounds. There exist phases that are called *orientationally ordered liquids* or *positionally disordered crystals*. In other words, phases that have more order than present in liquids, but less order than typical for molecular crystals. Compounds that exhibit such phases are called *liquid crystals*, since they share properties generally associated with both liquids and crystals. A more proper name for a liquid crystal molecule is *mesogen* and the phases it forms are known as *mesophases*. The terms *mesogenic* and *mesomorphic* are often used as synonyms, but they are not. A *mesogenic compound* has all the structural characteristics that are required to form a mesophase, but when a mesogenic compound is heated it does not necessarily form a mesophase. The term *mesogenic* tells something about the shape of the molecule, but nothing about the thermal behaviour. *Mesomorphic compounds* are compounds that have the shape necessary for the formation of a mesophase and that do exhibit such a mesophase. The expression *mesomorphic* tells something about both the shape and the thermal behaviour of a compound.

The motion of the molecules in liquid-crystalline phases is comparable with that of the molecules in a liquid, but the molecules maintain some degree of orientational order and sometimes some positional order as well (Figure 2.2). A vector, called the *director* (**n**) of the liquid crystal, represents the preferred orientation of the molecules.

A number of different types of molecules form liquid-crystalline phases. What most of them have in common is that their physical properties are anisotropic. Either the molecular shape is such that the length of

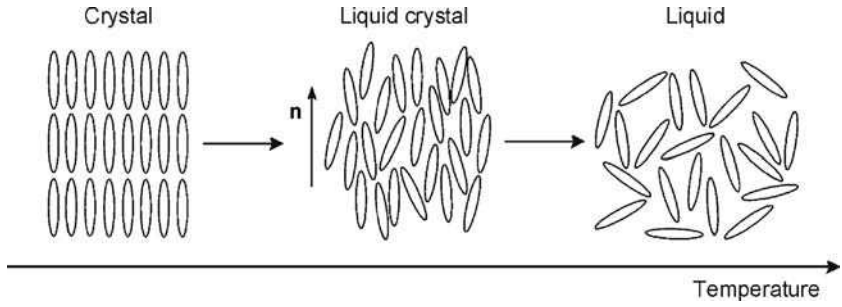

Figure 2.2 Schematic representation of the melting behaviour of a liquid crystal

one molecular axis is very different from the other two, or different parts of the molecules have very different solubility properties (amphiphilic compounds with a hydrophobic tail and a hydrophilic head group). In the former case, a mesophase can be formed by heating and/or cooling the compounds, and these compounds are called *thermotropic liquid crystals*. In the latter case, a solvent (in general, water) causes the formation of a mesophase. A mesophase formed in the presence of a solvent is a *lyotropic mesophase* and the compounds that form these mesophases are called *lyotropic liquid crystals*.

When a thermotropic liquid crystal is heated, it passes from the crystalline state into the liquid-crystalline state at a point called the *melting point*. By further heating, the birefringent (anisotropic) liquid crystal is transformed at the *clearing point* into an isotropic fluid: the birefringent fluid becomes clear and all molecular order is lost.

Thermotropic liquid crystals are generally divided into two main groups, depending on their structural features: *calamitic* mesogens (formed by rod-like molecules) and *discotic* mesogens (formed by disc-like molecules). In both cases, the molecules can be described as cylinders with a high degree of structural anisotropy. Calamitic compounds have a structure in which the axial part is more extended than the radial parts (Figure 2.3). On the other hand, in discotic compounds the radial parts are more extended than the axial part (Figure 2.4).

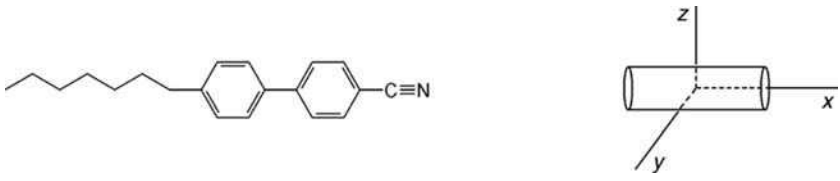

Figure 2.3 Typical example of a calamitic liquid crystal and schematic representation of its rod-like molecular shape

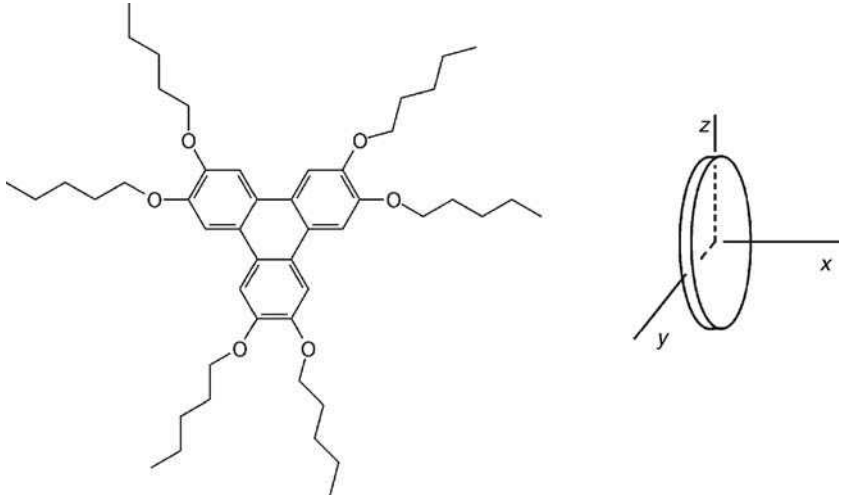

Figure 2.4 Typical example of a discotic liquid crystal and schematic representation of its disc-like molecular shape

Rod-like molecules can form a nematic phase or one of the different types of smectic phases. The least ordered mesophase is the *nematic phase* (N). The molecules in the nematic phase possess long-range orientational order, but are lacking positional order. The molecules have their long molecular axis on average parallel to a preferred direction indicated by the *director* (**n**) (Figure 2.5). They can move freely within the nematic phase and they are able to rotate around the long molecular axis. The nematic phase is technologically the most important of the many different types of mesophases. It is used in most of the commercially available liquid crystal displays (LCDs).

Smectic phases show a higher degree of order than the nematic phase. The molecules are not only oriented with their long molecular axis in one direction, but they also have some positional order in the sense that the

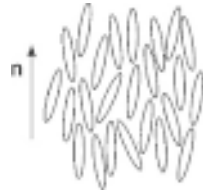

Figure 2.5 Molecular order in the nematic phase

molecules are organised into a layered structure. Within the layers there can be additional positional order. A number of smectic phases exist, and these phases differ from one another in the degree of order present both within and between the layers. In the *smectic A* phase (SmA), the molecules are aligned with their long molecular axis parallel to the layer normal (*i.e.* the director is perpendicular to the layer planes), but there is no positional order within the layers. In the *smectic C* phase (SmC), the long molecular axis is tilted with respect to the normal to the layer planes. There is no positional order within the layers. The arrangements of the molecules in the SmA and SmC phases are schematically represented in Figure 2.6. SmA and SmC phases are the least ordered smectic phases and are also the most commonly observed ones. Due to the molecular mobility inherent in these phases and their relative low viscosities, they are called *true smectic phases*.

Over the years, many smectic phases with ordering within the layers have been discovered. For example, in the *smectic B* (SmB) phase the molecules are arranged with their long molecular axis normal to the layer planes, but they are, within the planes, additionally ordered according to a two-dimensional hexagonal lattice. SmF and SmI phases are tilted analogues of the SmB phase.

While all of the previously described phases are genuine liquid-crystalline phases, there are other phases in which there is long-range positional order. They differ from true crystal phases in one important aspect: the molecules in them have the freedom of (at least) rotation around their long axis; their thermal motion is not completely frozen out. These phases are labelled *crystal smectic phases* (denoted by the letters B, E, G, H, J, K).

When the molecules that form a liquid-crystalline phase are chiral, the structure of these mesophases can have an additional property. In the *chiral nematic phase* (N^*) the director precesses about an axis perpendicular to the director and describes in this way a helix (Figure 2.7). The pitch of a chiral nematic phase is the distance along the helix over which the director rotates over 360°. The chiral nematic phase is sometimes

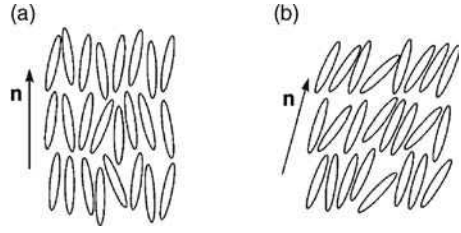

Figure 2.6 Molecular order in the SmA phase (a) and in the SmC phase (b)

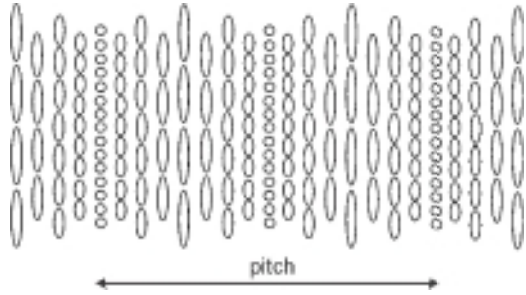

Figure 2.7 Schematic representation of a chiral nematic phase

called the *cholesteric phase*. There are also chiral versions of all the tilted smectic phases, for example SmC^*. In this phase the director maintains a constant tilt angle with respect to the layer normal and rotates around this normal in going from one layer to the next.

Molecules of a disc-like shape form either nematic or columnar phases. Structurally the most simple mesophase is the *discotic nematic phase* (N_D). Just as in the case of the nematic phase formed by calamitic molecules, the molecules possess orientational order, but no positional order (Figure 2.8). The *columnar nematic phase* (N_C) consists of short columns of a few molecules that act like the rod-like molecules in the nematic calamitic phase (Figure 2.9). There is no organisation of the columns in a two-dimensional lattice.

Most of the mesogenic molecules with a disc-like shape tend to be stacked one on top of the other into columns, and these columns are arranged side-to-side according to a two-dimensional lattice. There are several types of columnar mesophases, depending on the symmetry of the two-dimensional lattice (hexagonal, tetragonal or rectangular) and depending on the order or disorder of the molecular stacking within the columns (ordered and disordered columnar mesophases). The molecular arrangement in the *hexagonal columnar phase* (Col_h) is shown in Figure 2.10.

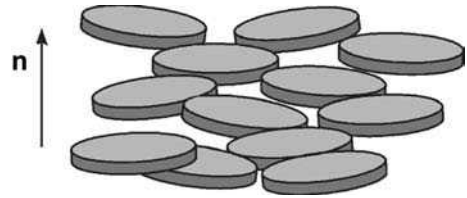

Figure 2.8 Schematic representation of a discotic nematic phase (N_D)

Figure 2.9 Schematic representation of a nematic columnar phase (N_C)

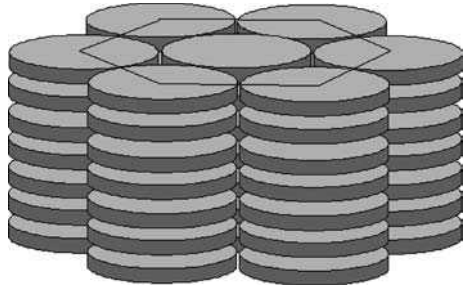

Figure 2.10 Schematic representation of a hexagonal columnar mesophase (Col_h)

2.3 OPTICAL PROPERTIES

2.3.1 Birefringence

Because liquid crystals are optically anisotropic materials, their optical properties are reminiscent of those of uniaxial crystals. For instance, liquid crystals show *birefringence* or *double refraction*. A light beam travelling through a liquid crystal is split into two linearly polarised light beams. The polarisation direction of one of these light beams is parallel to the optical axis (*i.e.* parallel to the director), whereas the polarisation direction of the second beam is perpendicular to that of the first. These light beams travel with different velocities through the liquid crystal, because the liquid crystal possess two principal refractive indices. The refractive index for the light beam polarised perpendicular to the optical axis is denoted n_e (or $n_{\parallel}$) and the refractive index for the light beam polarised perpendicular to the optical axis is n_o (or $n_{\perp}$). The

birefringence (Δn) is the difference between the two principal refractive indices: $\Delta n = n_e - n_o$. The birefringence is positive if $n_e > n_o$, and negative if $n_e < n_o$. The majority of the organic calamitic liquid crystals have a positive birefringence with Δn values between 0.1 and 0.2. However, negative birefringence values are observed for discotic liquid crystals and for liquid crystals forming a chiral nematic phase.

There are only very few studies on the birefringence of metallomesogens available. Measurements on calamitic metallomesogens in the nematic phase showed that birefringence was positive and that the birefringence values varied between 0.16 and 0.20 at a reduced temperature of 0.985 (*i.e.* $T/T_{NI} = 0.985$, were T_{NI} denotes the nematic-to-isotropic transition and T is the temperature of measurement).[33] However, the values of the birefringence increased with decreasing temperatures and Δn values up to 0.4 were found at room temperature. The effect of the introduction of a metal centre in the liquid crystal on the birefringence depends on the structure of the complex. The birefringence of a metallomesogen cannot only be very similar[34] or higher than that of the parent ligand,[33] but even lower. For instance, lower values were found by Versace *et al.* for a palladium(II) complex with azoxybenzene and β-diketonate ligands.[35]

Refractive index studies allow measurements of the birefringence, but also of the *polarisability*. The *mean polarisability* ($\overline{\alpha}$) can be determined using an isotropic liquid solution, whereas the *polarisability anisotropy* ($\Delta\alpha$) is measured in the mesophase. Polarisability studies have been made on palladium, platinum, iridium and silver metallomesogens, and show a higher polarisability for the metal complexes than for their parent ligands.[33]

2.3.2 Light Absorption and Colour

Transition metals are often associated with very colourful complexes. These colours can be due to light absorption in the visible spectral region by *d–d* transitions, but the most intense transitions are charge transfer transitions (metal-to-ligand charge transfer or ligand-to-metal charge transfer). Vividly coloured complexes can find applications as pigments or dyes, typical examples of which are the blue cobalt(II) compounds, the green copper(II) compounds or the yellow cadmium pigments. The introductions to several papers on metallomesogens state that an attractive feature of incorporating a metal ion in a liquid crystals is the possibility to

create coloured liquid crystals. Although metallomesogens often show intense colours, these colours are in many cases caused by ligand transitions. The prime function of the metal is not to provide an intrinsic colour, but rather to shift the positions of the ligand-centred absorption bands. Just like other physical properties of liquid crystals, light absorption by liquid crystals is also anisotropic. Aligned liquid crystals will show differences in light absorption when the incident light beam is linearly polarised along the long axis of the molecule than when it is polarised along the short axis. This difference in light absorption is called *dichroism*. Dichroic materials can find applications in polarisers, displays and in other optical devices. Dichroic materials in LCDs are often mixtures of a liquid crystal and an organic dye. The dye molecules are oriented by the liquid crystal matrix. In order to be useful for dichroic applications, the dyes need to fulfil certain requirements: (i) a good solubility in the liquid crystal host matrix, (ii) a good long-term chemical, photochemical and thermal stability, (iii) minor influence on the liquid crystal order parameter, (iv) a large molar absorption coefficient, (v) a low electrical conductivity, (vi) a large dichroic ratio and (vii) an absorption maximum located in the spectral region of interest and somewhat tunable by chemical modifications of the dye molecule.[36] The dichroic properties of dyes are described by two parameters: the optical order parameter and the dichroic contrast ratio. The *optical order parameter* (S_{opt}) is defined as:[32]

$$S_{opt} = \frac{A_{||} - A_{\perp}}{A_{||} + 2A_{\perp}} \tag{2.1}$$

where $A_{||}$ and $A_{\perp}$ are the absorbance values when the polarisation direction of the incident light beam is parallel and perpendicular to the alignment direction, respectively. The *dichroic contrast ratio* (R_D) is defined as the ratio of these absorbance values:

$$R_D = \frac{A_{||}}{A_{\perp}} \tag{2.2}$$

It has been proposed that highly coloured metallomesogens could be of interest as dichroic materials.

The colour of metallomesogens was a property that attracted the attention of the earliest workers in this field. Giroud and Mueller-Westerhoff reported that mesogenic nickel(II) dithiolene complexes formed dark, highly reflective crystals and were green in solution.[19] The corresponding

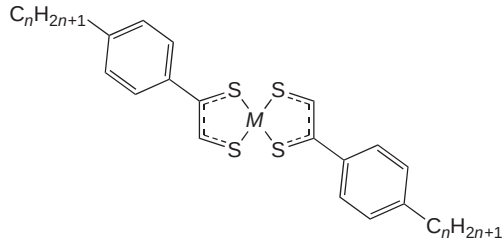

Figure 2.11 Mesogenic dithiolene complexes ($M = $ Ni, Pd, Pt)

palladium(II) complexes were bronze-coloured crystals, which dissolved with wine-red colour, while the platinum(II) analogues were purple in solution as well as in the solid. The nickel(II) and platinum(II) complexes showed smectic and nematic phases, while the palladium(II) compounds were unexpectedly not mesomorphic (Figure 2.11).[37–39] However, the absorption band of transition metal dithiolene complexes are found from 600 nm in the visible region up to 1600 nm in the near-infrared region. Therefore, these compounds can be valuable as near-infrared dyes in liquid crystal electro-optical devices.[36,40,41] For instance, a mesomorphic nickel(II) complex with C_4H_9 chains could be dissolved in the nematic host matrix 4-pentyl-4′-cyanobiphenyl (5CB) up to a concentration of 10% w/w and the optical order parameter (S_{opt}) measured at the absorption maximum at 869 nm was 0.57, while the contrast ratio (R_D) was 4.97 at 20 °C.[41] The molar absorption coefficient (ε) was 28 000 $dm^3\ mol^{-1}\ cm^{-1}$ for a solution in hexane.

The linear dichroism of nickel(II), palladium(II) and zinc(II) complexes of mesomorphic 4-alkoxydithiobenzoic acids has been investigated in the commercial eutectic mixture of cyanobiphenyls and cyanoterphenyls, E7 (from Merck) for the palladium(II) complexes and in the commercial mixture of cyanobicyclohexanes, ZLI2830 (from Merck) for the nickel(II) and zinc(II) complexes (Figure 2.12).[42] For the nickel(II) and palladium(II) complexes both a ligand-based transition and a charge-transfer band (MLCT) were observed, whereas only a ligand-based transition was present for the zinc(II) complexes. These complexes had a much lower solubility in the liquid crystal host matrix than the dithiolene

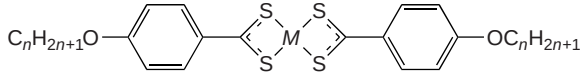

Figure 2.12 Mesogenic 4-alkoxydithiobenzoate complexes

complexes, so that concentrations used for the measurements were in general lower than 0.5% w/w. Also, the stability of the solutions was low and the compounds precipitated out overnight. Nevertheless, an optical parameter (S_{op}) up to 0.8 was observed for the palladium(II) complex with hexyloxy chains at 30 °C. This is indicative of a very good alignment of the metal complexes in the liquid crystal host. The palladium(II) complexes gave dichroic contrast ratios (R_D) between 8.7 and 12.8 for the charge transfer band at 30 °C. The nickel(II) and zinc(II) complexes gave lower values for S_{op} and R_D.

The colour of dinuclear cyclopalladated azobenzene complexes depends on the bridging group connecting the two cyclometallated moieties, so that colour-tuning could be achieved by a proper choice of the bridging group.[43] The colour of the investigated compound ranged from yellow (chloride bridge) to orange-yellow (oxalate bridge), orange (azide bridge), dark red (thiocyanate bridge) and violet (acetate bridge) (Figure 2.13).

An interesting property of some liquid crystals is *thermochromism*, that is a change of colour with temperature. Whereas thermochromism of organic liquid crystals is mainly restricted to chiral compounds exhibiting a cholesteric mesophase, for metallomesogens thermochromism is also observed for achiral compounds. Pioneering work in the field of thermochromism of metallomesogens has been done by Ohta *et al.*, who reported on the observation of this effect in discotic nickel(II),[44,45] palladium(II)[46] and platinum(II)[47] complexes of di-(3,4-dialkoxyphenyl)ethane-1,2-dioximes (Figure 2.14). With increasing temperature, the colour of the nickel(II) complexes gradually changed from red to yellow, the colour of the palladium(II) complexes from orange to yellow, whereas that of platinum(II) compounds rapidly changed from green at room temperature to red, orange and yellow with increasing temperatures.

Temperature-dependent electronic absorption spectra of the palladium(II) complexes showed that two characteristic absorption bands shift to higher energy (blue shift) with increasing temperature. The band that is located at a longer wavelength was assigned to the $4d_{z^2}$–$5p_z$ transition (d–p band), and that located at a shorter wavelength to a metal-to-ligand charge transfer transition (MLCT band).[48] The absorbance values of both bands were found to increase with increasing temperatures. The thermochromic properties are attributed to the metal–metal interactions in the one-dimensional columnar structure of the complexes. The blue shift can be explained by an increase of the intermolecular distance within the columns. With increasing temperatures, the increase in metal–metal distance leads to a larger band gap between

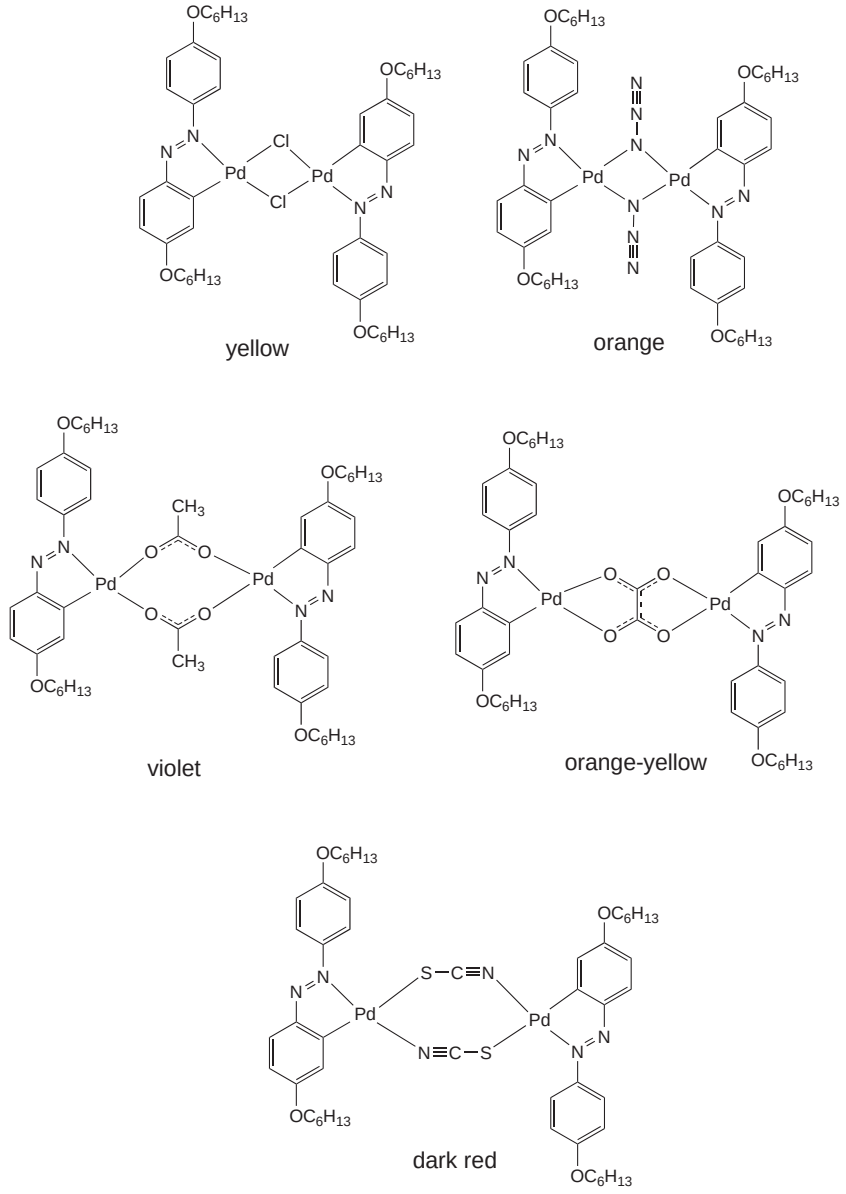

Figure 2.13 Deeply coloured dinuclear cyclopalladated azobenzene complexes. The colour depends on the bridging group

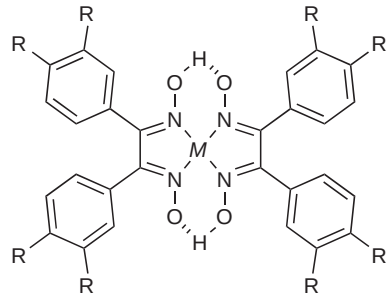

Figure 2.14 Thermochromic complexes of di-(3,4-dialkoxyphenyl)ethane-1,2-dioximes (M = Ni, Pd, Pt)

the filled nd_{z^2} valence band and the empty $(n+1)p_z$ conduction band of the metal. This enlargement of the band gap results in a blue shift of the absorption band in the electronic spectrum which is directly connected with *d–p* interactions between the upper and lower metals in the one-dimensional metal chains. Also, the length and nature (alkyl *vs* alkoxy) of the long chains was found to have an effect on the thermochromism.

Besides the above described mesomorphic 1,2-dioximes, Ohta *et al.* observed thermochromism for bis[1,2-bis(4-*n*-alkoxyphenyl)ethane-1,2-dithiolene]nickel(II) complexes (Figure 2.15).[49] The complexes with a decyloxy chain or longer showed two differently coloured discotic lamellar mesophases, a brown phase at lower temperatures and a green phase at higher temperatures. The colour of the isotropic liquid was green. The complexes, also those with shorter chains, exhibited a brown to green thermochromism, which was attributed to a slow transformation of the Ni–Ni bonded dimers to the Ni–S bonded dimers (Figure 2.16). Although metallomesogens with cholesteric mesophases are expected to exhibit thermochromism due to the

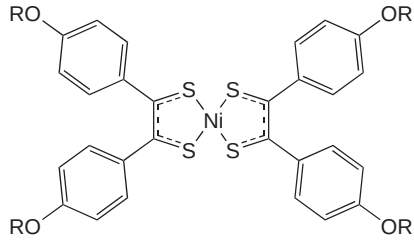

Figure 2.15 Thermochromic bis[1,2-bis(4-*n*-alkoxyphenyl)ethane-1,2-dithiolene]-nickel(II) complexes

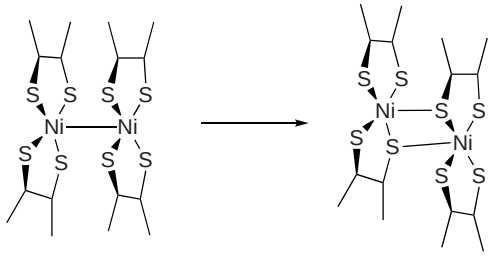

Figure 2.16 Transformation of N–Ni bonded dimers to Ni–S bonded dimers in bis[1,2-bis(4-*n*-alkoxyphenyl)ethane-1,2-dithiolene]nickel(II) complexes

temperature dependence of the cholesteric pitch, this type of metallomesogens has not been widely explored yet. Baena *et al.* observed temperature-dependent pitch changes and accompanying colour changes for chiral liquid-crystalline *ortho*-palladated Schiff base complexes with a combination of thiolato and carboxylato bridges, in mixtures with a nematic host liquid crystal.[50]

The colour of solution of metallomesogens in organic solvents often strongly depends on the choice of the solvent (*solvatochromism*). This solvatochromic effect is related to the dependence of the absorption spectra on the solvent polarity.[51] Ionic σ-alkynyl platinum(II) terpyridine complexes with methyl, dodecyl or phytol-like substituents exhibit a strong solvatochromism (Figure 2.17).[52] Addition of methanol (7% v/v) to the deep-red solution of a complex in dichloromethane ($\lambda_{max} = 487$ nm) resulted in a colour change of the solution to yellow, reflected in a λ_{max} shift of 17 nm to shorter wavelengths. In dodecane, a deep-green solution was formed with the appearance of a new, strong

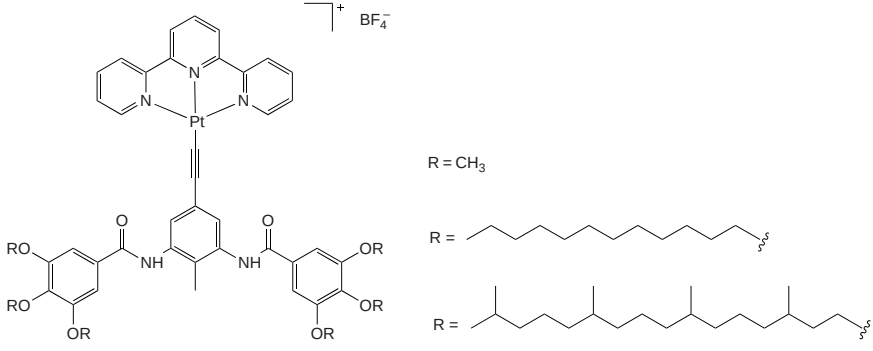

Figure 2.17 Solvatochromic ionic σ-alkynyl platinum(II) terpyridine complexes

absorption band at 644 nm, while the original intense metal-to-ligand charge transfer (MLCT) band was shifted by 11 nm to longer wavelengths. Several of the thermochromic metal complexes of the di-(3,4-dialkoxyphenyl)ethane-1,2-dioximes described by Ohta *et al.* also show solvatochromism.[44,45,47,48] The colour change was sensitive to the polarity of the solvents (yellow in polar solvents and red in nonpolar solvents) and could be attributed to the aggregation behaviour of the complexes in these solvents.

2.3.3 Luminescence

The study of the luminescent properties of metallomesogens is a recent development. Because the transition temperatures of the first generations of metallomesogens with spectroscopically active metal centres were very high (the melting points were often well above 100 °C), it was in the past difficult or even impossible to observe photoluminescence spectra of metallomesogens in the liquid crystal state. Therefore, luminescence studies of metallomesogens had to be restricted to solid or solution samples, although in some cases the mesophase order could be preserved at room temperature by supercooling the mesophase to a glassy state. Careful design of metallomesogens on the basis of previously gained experience leads to metal complexes that are liquid-crystalline at very moderate temperatures or even at room temperature to be obtained at present. Thanks to this recent progress, luminescence studies of metallomesogens in the liquid crystal state are starting to appear in the scientific literature.

The lanthanide-containing metallomesogens (*lanthanidomesogens*) are a well known class of luminescent metallomesogens.[13,14,53] Several studies report on the solid state or solution luminescence spectra of lanthanidomesogens.[54–61] The emission observed for these materials is metal-centred between energy levels within the 4*f*-shell of the trivalent lanthanide ion, thus the emission is due to intraconfigurational *f–f* transitions. An advantage of luminescence by trivalent lanthanide ions is that their luminescence spectra consist of narrow emission lines of a high colouric purity.[62–64] The relative intensities of the emission lines and their fine structure are only marginally influenced by the nature of the ligands in the first coordination sphere. The excited states have a long lifetime at room temperature, in the order of microseconds or even milliseconds.

The colour of the emitted light depends on the lanthanide ion. For instance, Eu^{3+} emits red light, Tb^{3+} green light, Sm^{3+} orange light and Tm^{3+} blue light. Yb^{3+}, Nd^{3+} and Er^{3+} are well known for their near-infrared luminescence, but other lanthanide ions (Pr^{3+}, Sm^{3+}, Dy^{3+}, Ho^{3+}, Tm^{3+}) also show transitions in the near-infrared region. Gd^{3+} emits in the ultraviolet region, but its luminescence can only be observed in the absence of organic ligands with low-lying singlet and triplet levels. Unfortunately, the light absorption by lanthanide(III) ions is weak. The molar absorption coefficient values of the forbidden intraconfigurational *f–f* transitions are typically less than 10 $dm^3\ mol^{-1}\ cm^{-1}$. Because the photoluminescence intensity is proportional to the amount of absorbed light energy, this weak light absorption by the metal centre is a major disadvantage of luminescent lanthanide compounds. The problem of weak light absorption can be overcome by the so-called *antenna effect*. Weissman discovered that intense metal-centred luminescence can be observed for lanthanide complexes with organic ligands upon excitation in an absorption band of the organic ligand.[65] Because of the intense absorption bands of organic chromophores, much more light can be absorbed by the organic ligands than by the lanthanide ion itself. Subsequently, the excitation energy is transferred from the organic ligands to the lanthanide ion by intramolecular energy transfer.

The commonly accepted mechanism of energy transfer from the organic ligands to the lanthanide ion is that proposed by Crosby and Whan (Figure 2.18).[66–68] Upon irradiation with ultraviolet radiation, the organic ligands of the lanthanide complex are excited to a vibrational level of the first excited singlet state ($S_1 \leftarrow S_0$). The molecule undergoes fast *internal conversion* to lower vibrational levels of the S_1 state, for instance through interaction with surrounding molecules. The excited singlet state can be deactived radiatively to the ground state (*molecular fluorescence*, $S_1 \rightarrow S_0$), or can undergo nonradiative *intersystem crossing* from the singlet state S_1 to the triplet state T_1. The triplet state T_1 can be deactivated radiatively to the ground state S_0, by the spin-forbidden transition $T_1 \rightarrow S_0$. This results in *molecular phosphorescence*. Alternatively, the complex may undergo a nonradiative transition from the triplet state to an excited state of the lanthanide ion. After this indirect excitation by energy transfer, the lanthanide ion may undergo a radiative transition to a lower 4*f*-state by characteristic line-like photoluminescence, or it may be deactivated by nonradiative processes. According to Whan and Crosby the main cause of nonradiative deactivation of the lanthanide ion is vibronic coupling with the ligands and with other molecules in the neighbourhood of the lanthanide ion.[66]

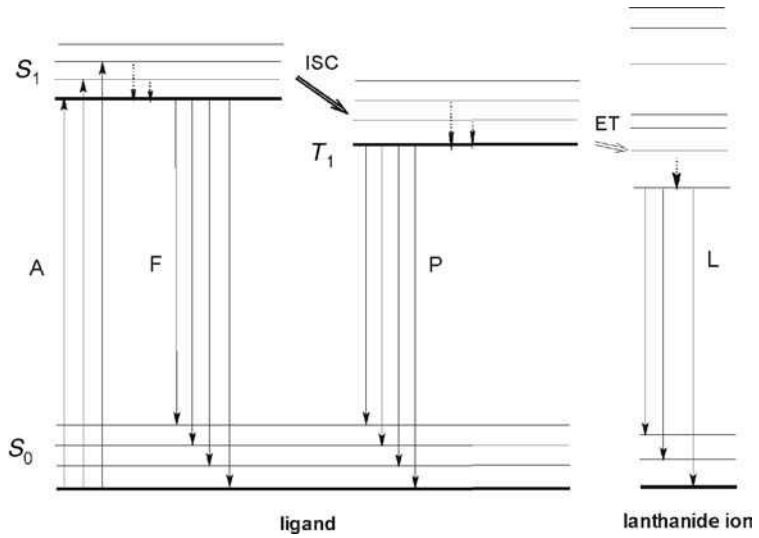

Figure 2.18 Schematic representation of photophysical processes in lanthanide(III) complexes (antenna effect). A = absorption, F = fluorescence, P = phosphorescence, L = lanthanide-centred luminescence, ISC = intersystem crossing, ET = energy transfer; S = singlet, T = triplet. Full vertical lines: radiative transitions; dotted vertical lines: nonradiative transitions

Luminescent transitions of lanthanide ions are only possible from certain levels, which are termed *resonance levels*. The main resonance levels are $^4G_{5/2}$ for Sm^{3+} (17 800 cm^{-1}), $^5D_0$ for Eu^{3+} (17 250 cm^{-1}), $^5D_4$ for Tb^{3+} (20 430 cm^{-1}) and $^4F_{9/2}$ for Dy^{3+} (20 960 cm^{-1}). If the lanthanide ion is excited to a nonemitting level, either directly by excitation in the 4*f*-levels or indirectly by energy transfer, the excitation energy is dissipated *via* nonradiative processes until a resonance level is reached. Radiative transitions then become competitive with the nonradiative processes and metal-centred emission can be observed. Line emission by a lanthanide ion is only possible if the nonradiative deactivation, the molecular fluorescence and phosphorescence can be minimised. In order to populate a resonance level of a lanthanide ion, it is necessary that the lowest triplet state of the complex is located at an energy nearly equal or above the resonance level of the lanthanide ion, not below. When the energy levels of the organic ligands are below that of the resonance level of the lanthanide ion, molecular fluorescence or phosphorescence of the ligand is observed, or no light emission at all. The luminescence observed for a specific lanthanide complex is, therefore, a sensitive function of the lowest triplet level of the complex relative to a resonance level of the

lanthanide ion. Because the position of the triplet level depends on the type of ligand, it is, therefore, possible to control the luminescence intensity observed for a given lanthanide ion by variation of the ligand.[69] The position of the triplet level is also temperature dependent, so that the luminescence caused by indirect excitation through the organic ligands is much more temperature sensitive than luminescence caused by direct excitation of the 4*f*-levels. The triplet levels are always located at a lower energy than the singlet levels. Although energy transfer to the lanthanide ion takes place from the lowest triplet level T_1, it is sometimes possible to observe in the phosphorescence higher lying triplet states, such as T_2, as well. The efficiency of the energy transfer is proportional to the overlap between the phosphorescence spectrum of the ligand and the absorption spectrum of the lanthanide ion. The overlap decreases as the triplet state energy increases. A close match between the energy of the triplet state and the energy of the receiving 4*f*-level of the lanthanide ion is not desirable either, because energy back transfer of the lanthanide ion to the triplet state can occur.

Pioneering work in the field of luminescence by lanthanidomesogens in the liquid crystal state has been done by Suarez *et al.* In a seminal paper, they monitored the luminescence intensity and the excited state lifetime of a solvated $Eu(NO_3)_3$ complex of a 1,7-diaza-18-crown ether with mesogenic pendant arms (Figure 2.19) as a function of the temperature to detect phase transitions.[70] The integrated intensity of the $^5D_0 \rightarrow {}^7F_2$ transition (I_{obs}) and the Eu($^5D_0$) lifetime (τ_{obs}) were found to decrease with increasing temperatures due to more efficient nonradiative relaxation of the excited state at higher temperatures. The $\ln(\tau_{obs}/\tau_{295K})$ *vs* $1/T$ and $\ln(I_{obs}/I_{295K})$ *vs* $1/T$ curves showed a sigmoidal shape, with a marked variation at the melting point, upon heating. Therefore, the luminescence measurements allowed the transition of the crystalline state to the hexagonal columnar phase during the first heating process to

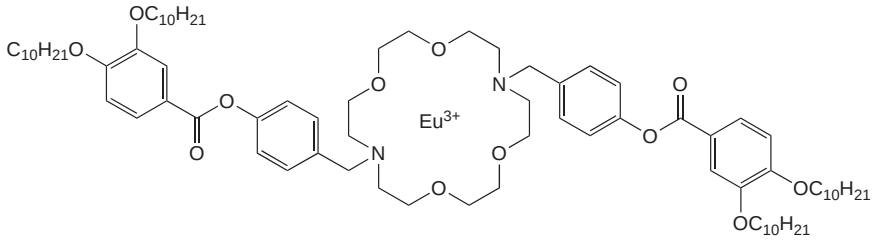

Figure 2.19 Europium(III) complex of a 1,7-diaza-18-crown ether with mesogenic pendant arms. The three nitrate counter ions are not shown

be accurately detected. The corresponding $\ln(I_{obs}/I_{295K})$ *vs* $1/T$ curve cooling curve was quite monotonic, whereas the $\ln(\tau_{obs}/\tau_{295K})$ *vs* $1/T$ cooling curve closely followed the variation observed during heating. By monitoring the integrated intensity of the $^5D_4 \rightarrow {}^7F_5$ transition of Tb^{3+}, it was possible to determine the crystal-to-mesophase transition in a terbium-containing metallomesogen.[71,72]

Further luminescence studies on $Ln(NO_3)_3$ complexes of 2,6-bis(1-ethylbenzimidazol-2-yl)pyridine derivatives synthesised by Terazzi *et al.* showed that the transition of a crystalline phase to a cubic mesophase could be detected by measurement of the luminescence properties during the first heating process.[53] However, the vitrification of the cubic mesophase upon cooling could not be observed. This shows that this luminescence technique cannot be applied to the detection of glass transitions. By rational design of the mesogenic ligand, it was possible to obtain liquid-crystalline lanthanide complexes with melting points between –43 °C and –25 °C, and with a mesophase stability range of more than 250 °C (Figure 2.20).[73]

Yang *et al.* reported on low melting lanthanidomesogens consisting of Lewis base adducts of a nonmesomorphic salicylaldimine Schiff base ligand *L* and tris(2-2-thenoyltrifluoroacetonato)lanthanide(III) or tris-(benzoyltrifluoroacetonate) lanthanide(III) complexes, $[Ln(tta)_3L_2]$ or $[Ln(bta)_3L_2]$ (Figure 2.21).[74] These compounds form a smectic A phase at room temperature. The luminescence spectra of the europium(III), samarium(III), neodymium(III) and erbium(III) complexes have been measured in the mesophase (Figure 2.22). Of interest is the fact

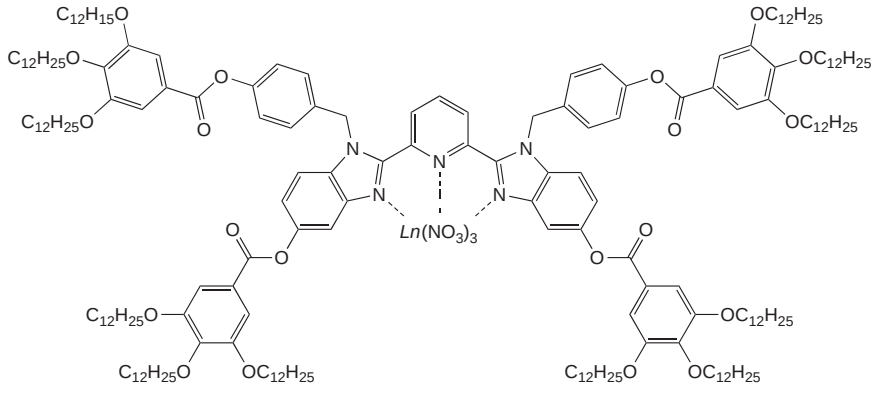

Figure 2.20 Luminescent room temperature lanthanidomesogens, designed by Piguet and co-workers

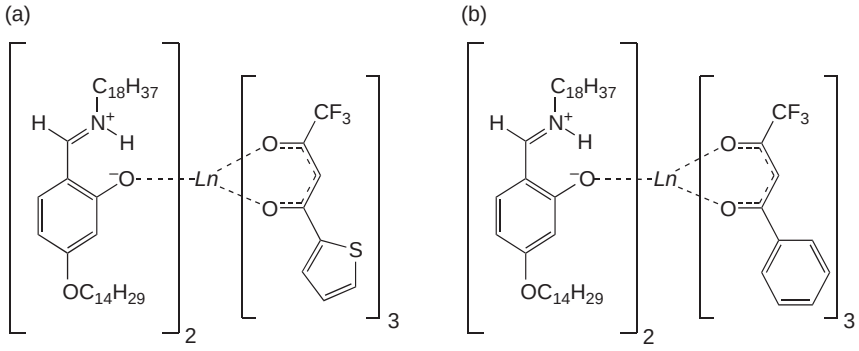

Figure 2.21 Structure of the lanthanide complexes $[Ln(\text{tta})_3L_2]$ (a) and $[Ln(\text{bta})_3L_2]$ (b). *Ln* represents a trivalent lanthanide ion, tta is 2-thenoyltrifluoroacetonate, bta is benzoyltrifluoroacetonate, and *L* is a Schiff base

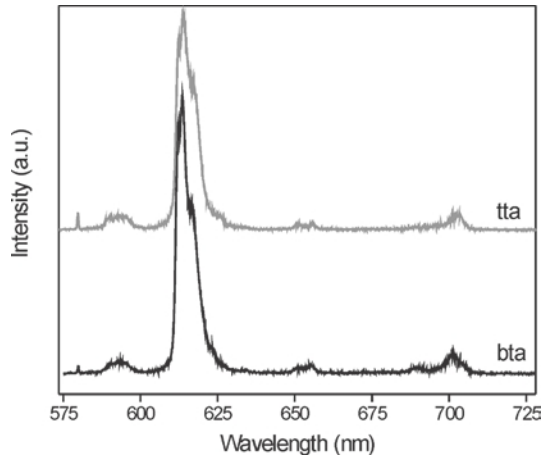

Figure 2.22 Luminescence spectra of $[Eu(\text{tta})_3L_2]$ (grey curve) and $[Eu(\text{bta})_3L_2]$ (black curve) as a thin film in the mesophase at 25 °C. The excitation wavelength was 370 nm. All transitions start from the $^5D_0$ level and end at the different *J* levels of the ^7F term ($J = 0$–4 in this spectrum). Reprinted with permission from Yang *et al.*, 2006 [74]. Copyright (2006) American Chemical Society

near-infrared emission by neodymium(III) and erbium(III) could be observed. Plots of the luminescence decay time of the $^5D_0$ level of $[Eu(\text{tta})_3L_2]$ or the $^4G_{5/2}$ level of $[Sm(\text{tta})_3L_2]$ as a function of the temperature show a gradual decrease of the luminescence lifetime with increasing temperatures. A marked fall was visible in these curves at the SmA → I transition (Figure 2.23). The intrinsic quantum yield of the complexes

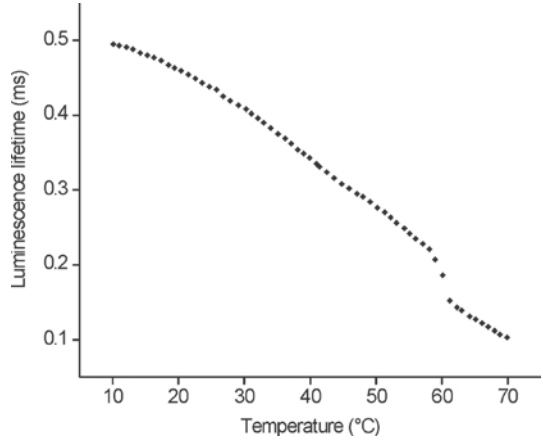

Figure 2.23 Luminescence decay time of the $^5D_0$ level of the [Eu(tta)$_3L_2$]complex as a function of the temperature. The luminescence was monitored at 613 nm ($^5D_0 \rightarrow {}^7F_2$ line) and the excitation wavelength was 370 nm. The measurements were made during cooling of the sample. The SmA $\leftrightarrow$ I transition (clearing point) can be observed as a jump in the curve at about 60 °C. Reprinted with permission from Yang *et al.*, 2006 [74]. Copyright (2006) American Chemical Society

[Eu(tta)$_3L_2$] and [Eu(bta)$_3L_2$] have been determined by photoacoustic methods.[75] Although glass transitions of the vitrified mesophase could not be detected by luminescence measurements, photoacoustic spectra clearly showed this transition.

Galyametdinov, Binnemans and co-workers prepared lanthanidomesogens that exhibit smectic A and nematic phases. The ligand was a rather unusual β-diketone with a cyclohexyl ring (Figure 2.24). When a thin film of the corresponding europium(III) complex in the nematic phase was supercooled to a glass phase in a liquid crystal cell with alignment layers for planar alignment, polarised luminescence could be observed for the aligned samples (Figure 2.25).[76] The lanthanide complexes were also well soluble in nematic liquid crystal mixtures. The polarisation effects were observable as differences in the intensities of crystal field transitions for the two mutually perpendicular polarisation directions.

Another approach to obtain luminescent lanthanide-containing liquid crystals is by dissolving a luminescent lanthanide complex in a suitable liquid crystal host matrix. The advantage of this method is that the luminescence and mesomorphic properties can independently be optimised. This allows easier access to nematic lanthanide-containing liquid

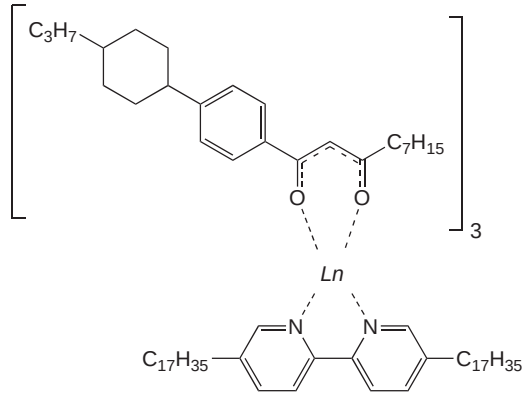

Figure 2.24 Nematogenic lanthanide complexes

crystal mixtures. However, what is often faced is the poor solubility of the molecular lanthanide complexes in the liquid-crystalline host matrix. The guest–host concept involving luminescent lanthanide complexes was first applied by Yu and Labes who doped the nematic liquid crystal 4-*n*-pentyl-4′-cyanobiphenyl (5CB) with europium(III) 2-thenoyltrifluoroacetonate trihydrate $[Eu(tta)_3 \cdot 3H_2O]$.[77] Binnemans and Moors showed by high resolution luminescence spectroscopy that well-resolved crystal field fine structures could be observed for $[Eu(tta)_3(phen)]$-doped

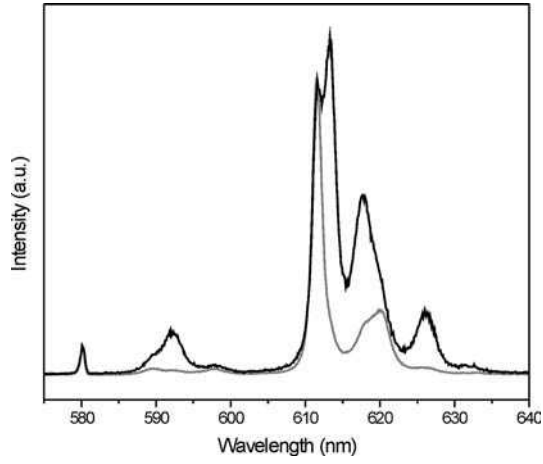

Figure 2.25 Polarisation effects in the room temperature luminescence spectra of an aligned supercooled thin film of the europium(III) complex of the type shown in Figure 2.24.[76] The polariser is either parallel (grey line) or perpendicular (black line) to the alignment layers in the liquid crystal cell

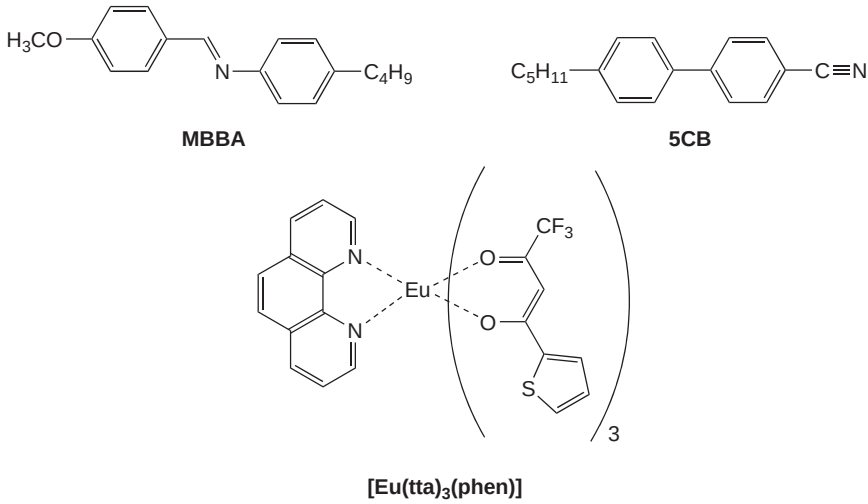

Figure 2.26 Structures of the nematic liquid crystal host matrices MBBA and 5CB, and the structure of the europium(III) complex $[Eu(tta)_3(phen)]$

in the liquid crystal hosts *N*-(4-methyloxybenzylidene)-4-butylaniline (MBBA) and 5CB (Figure 2.26).[78] The spectra are more reminiscent of what is observed for europium(III) ions doped in crystalline hosts rather than europium(III) complexes dissolved in organic solvents (Figure 2.27).

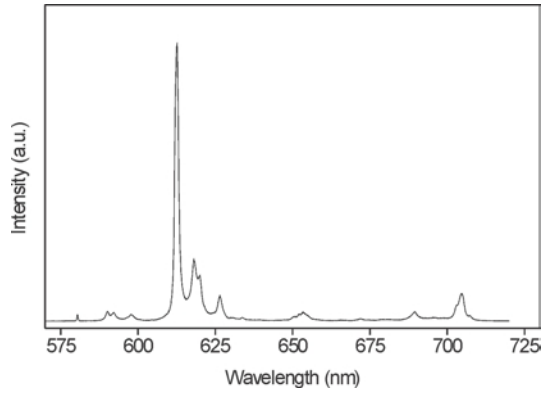

Figure 2.27 Room temperature luminescence spectrum of $[Eu(TTA)_3(phen)]$ in the nematic liquid crystal host MBBA. The doping concentration was 4% w/w. The excitation wavelength is 396 nm.[78] Reprinted with permission from Binnemans and Moors, **12,** 3374–3376 Copyright (2002) Royal Society of Chemistry

Van Deun *et al.* were the first to observe near-infrared luminescence from lanthanide-doped liquid crystal mixtures.[79] They studied the spectroscopic properties of the lanthanide(III) β-diketonate complexes [*Ln*(dbm)$_3$(phen)], where *Ln* = neodymium, erbium, ytterbium, and dbm is dibenzoylmethane, in the liquid crystal MBBA. By incorporation of an erbium(III)-doped nematic liquid crystal ($ErCl_3$ dissolved in E7) in the pores of microporous silicon, narrowing of the erbium(III) emission band in the near-infrared was observed.[80] Luminescent optically active liquid crystals were obtained by doping [Eu(tta)$_3$·3H_2O] into a mixture of cholesteryl nonanoate, cholesteryl tetradecanoate and the ternary liquid crystal mixture ZLI 1083 from Merck.[81,82]

Driesen *et al.* constructed a switchable near-infrared emitting liquid crystal cell.[83] The authors doped the lanthanide complexes [Nd(tta)$_3$(phen)] and [Yb(tta)$_3$(phen)] into the chiral nematic liquid crystal mixture of E7 and cholesteryl nonanoate. However, the contrast ratios were quite low. The photoluminescence intensity of europium(III) and terbium(III) complexes dissolved in nematic liquid crystal 4-(isothiocyanotophenyl)-1-(*trans*-4-hexyl)cyclohexane (6CHBT) strongly depends on the strength of the applied electric field.[84] This effect was tentatively assigned to a complex dipolar orientational mechanism in the liquid crystal matrix. Driesen and Binnemans prepared glass dispersed liquid crystal films doped with a europium(III) β-diketonate complex.[85] The luminescence intensity of the film was measured as a function of temperature. A sharp decrease in luminescence intensity was observed for the transition from the nematic phase to the isotropic phase. This decrease in luminescence intensity at the clearing point was attributed to weaker light scattering and thus less efficient use of the excitation light in the isotropic state.

The liquid crystal host matrix does not have to be limited to nematic liquid crystals. Bünzli and co-workers dissolved different europium(III) salts in the smectogenic ionic liquid crystal 1-dodecyl-3-methylimidazolium chloride, which exhibits a smectic A phase between –2.8 and 104.4 °C.[86] It was observed that concentrations of europium(III) salts as high as 10 mol% did not appreciably alter the liquid-crystalline behaviour of the host matrix. Interestingly, the emission colour of the europium(III)-containing liquid crystal mixture could be tuned from blue (emission colour of the host matrix) to red (emission colour of the trivalent europium ion), depending on the excitation wavelength and the counter ion of europium(III). Intense near-infrared emission could be obtained by doping the β-diketonate complexes [*Ln*(tta)$_3$(phen)] (*Ln* = neodymium, erbium, ytterbium) in the same ionic liquid crystal host.[87]

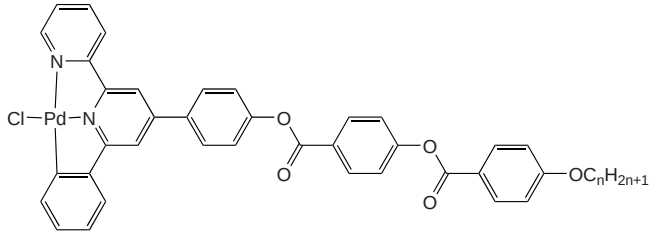

Figure 2.28 Palladium(II)-containing metallomesogen showing luminescence at 77 K

Several palladium(II)-containing metallomesogens show luminescence in the solid state. For instance, the palladium(II) complexes of the type shown in Figure 2.28 are photoluminescent at 77 K.[88] The dinuclear cyclopalladated azobenzene complexes described in the section on the light absorption of metallomesogens show, in general, weak photoluminescence in dichloromethane solution.[43] However, much more intense luminescence was observed for the complex with azide bridges. Some palladium(II) complexes based on heterocyclic 1,3,4-oxadiazole as core group are room temperature liquid crystals exhibiting columnar mesophases and their solutions in dichloromethane fluoresce in the ultraviolet or violet spectral region (Figure 2.29).[89] Dialkyl 2,2′-bipyridine-4,4′-dicarboxylates have been used for the design of luminescent palladium(II) and platinum(II) complexes (Figure 2.30).[90] For the palladium(II) complexes luminescence was detected for the *cis*-dichloro complex in dichloromethane solution and in the solid state, but not for the *cis*-dibromo, *cis*-diiodo or *cis*-diazido complexes. Interestingly, the *cis*-dichloroplatinum(II) compound is a blue emitter in solution, but a red emitter in the solid state. The corresponding *cis*-diazidoplatinum(II)

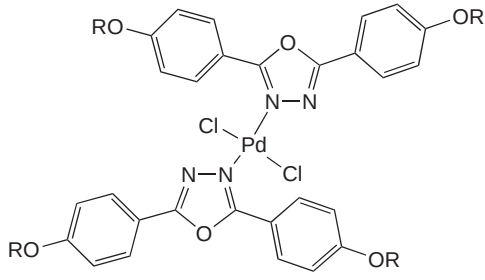

Figure 2.29 Luminescent palladium(II)-containing metallomesogens based on the heterocyclic 1,3,4-oxadiazole core

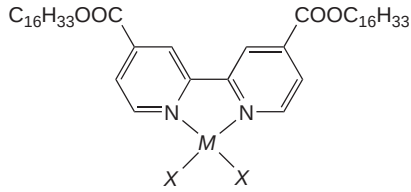

Figure 2.30 Dialkyl-2,2′-bipyridine-4,4′-dicarboxylate metallomesogens ($M = Pd$, Pt; $X = Cl$, Br, I, N_3)

complex is a red emitter in solution, but does not show luminescence in the solid state. A photophysical study of mononuclear *ortho*-platinated and -palladated metallomesogens with phenylpyrimidine and phenylpyridine ligands (Figure 2.31) revealed photoluminescence for the platinum(II) complexes, but not for the corresponding palladium(II) compounds.[91] Photoluminescence was reported for half-discoid metallomesogens based upon mononuclear *ortho*-platinated rod-like 2-phenylpyridine or 2-thienylpyridine heteroaromatics and 1,3-diketonate ligands.[92]

Kozhevnikov *et al.* observed that the luminescence colour of vitrified mesophase of liquid-crystalline *N*,*C*,*N*-coordinated platinum(II) complexes (Figure 2.32) is different from that observed for a film of the same compound obtained by fast cooling from the isotropic phase.[93] The samples that were fast cooled from the liquid crystal phase displayed monomer emission, whereas the samples fast cooled from the isotropic state showed excimer-like emission. Spin-coated thin films exhibited excimer-like emission, whereas heat treatment of the sample to 110 °C followed by cooling to room temperature resulted in a drastic change of the luminescence colour from the red of the excimer to the yellow of a mixture of the monomer and the excimer. However, rubbing of the heat treated film resulted in a return of the red excimer emission.

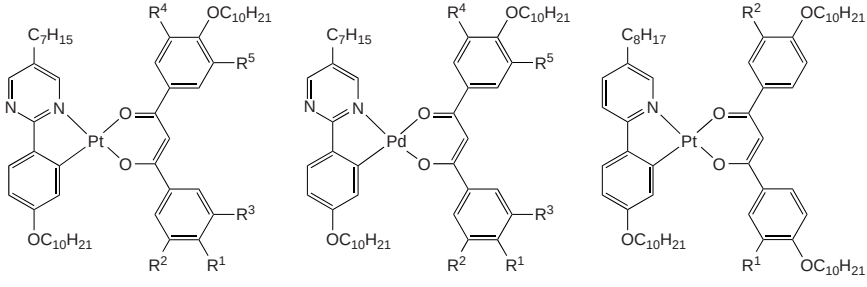

Figure 2.31 Luminescent mononuclear *ortho*-platinated and -palladated metallomesogens with phenylpyrimidine and phenylpyridine ligands

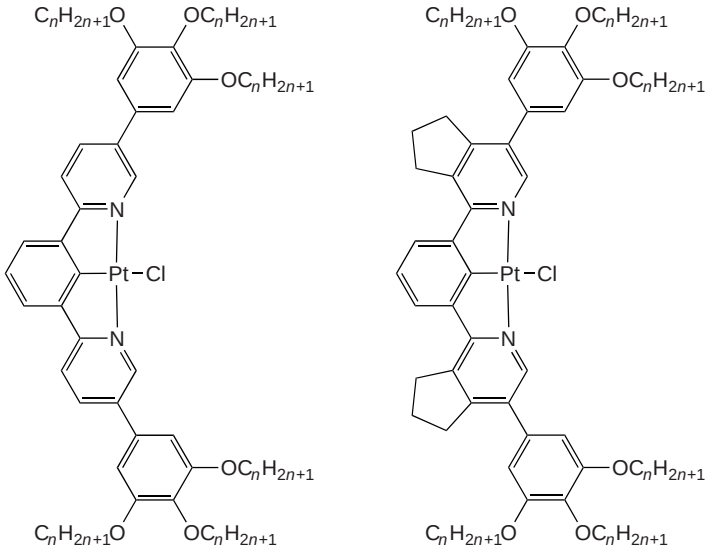

Figure 2.32 Luminescent *N*,*C*,*N*-coordinated platinum(II) metallomesogens

2-Aryl-substituted imidazo[4,5-*f*]-1,10-phenanthrolines were used as building blocks for rhenium(I)-containing metallomesogens (Figure 2.33).[94] The bromotricarbonyl rhenium(I) complexes emitted yellowish light. The broad emission band had a maximum around 590 nm. Mesomorphic tetraalkyltetrabenzoporphyrin nickel(II) complexes (Figure 2.34) dissolved in chloroform solution show fluorescence at room temperature and phosphorescence at 77 K.[95] Pucci *et al.* obtained a gallium(III)-based liquid crystal by grafting around the metal centre two chelating 2-methylquinolin-8-olate anions and one monodentate 3,4,5-tris(hexadecyloxy)benzoyloxy ligand (Figure 2.35).[96] The coordination polyhedron of the pentacoordinate gallium(III) ion can be described as a trigonal bipyramid. The complex exhibits a lamellocolumnar mesophase between 66 and 145 °C. Intense green photoluminescence could be observed for a solution of the complex in dichloromethane ($\lambda_{max} = 515$ nm) and for spin-coated films on quartz plate ($\lambda_{max} = 495$ nm). The quantum yield was 40% in solution. Dinuclear tetrafluorophenyl gold(I) complexes of type [μ-(4,4′-CN-RNC) $\{Au(C_6F_4OC_nH_{2n+1})\}_2$], containing a diisocyanide ligand bringing group two gold atoms (Figure 2.36) exhibited nematic mesomorphism and are luminescent at room temperature, both in solution and in the solid state.[97] The solid state emission colour was yellow-green.

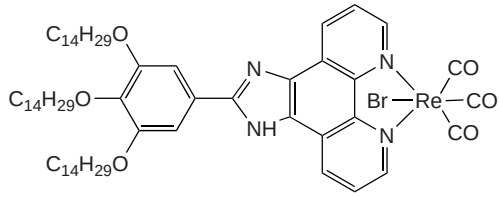

Figure 2.33 Luminescent rhenium(I)-containing metallomesogen

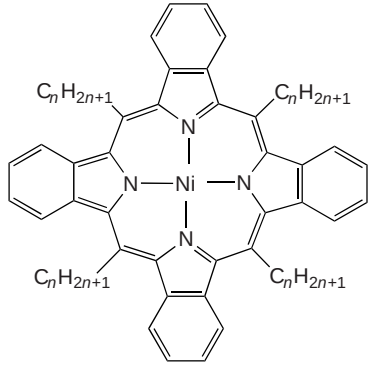

Figure 2.34 Tetraalkyltetrabenzoporphyrin nickel(II) metallomesogens

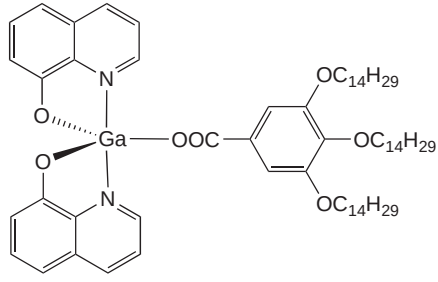

Figure 2.35 Luminescent gallium(III)-containing metallomesogen

The first examples of *d*-block metallomesogens emitting in the liquid crystal phase were the smectogenic rod-like gold(I) isocyanide complexes described by Bayón *et al.* (Figure 2.37).[98] The compounds in the solid state show three intense broad emission bands. For instance, one compound displayed emission bands at 384, 490 and 524 nm. The band at 384 nm was assigned to a fluorescent transition involving intraligand

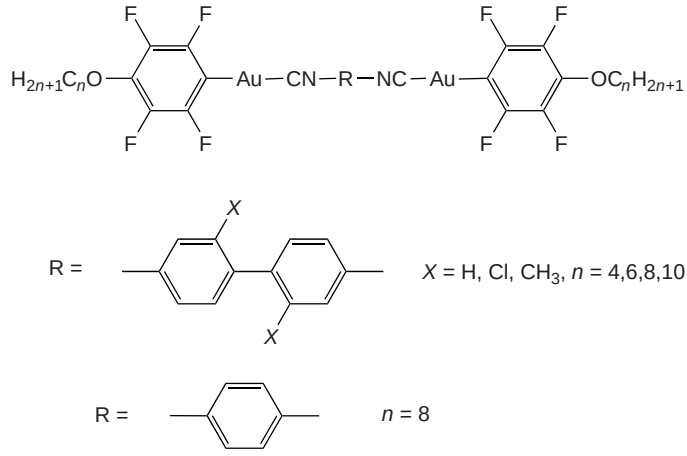

Figure 2.36 Luminescent dinuclear tetrafluorophenyl gold(I) metallomesogens

localised π- and π*-orbitals, whereas the phosphorescent transitions were mainly resulting from intramolecular intraligand transitions. When the samples were heated, a strong decrease in luminescence intensity was observed upon melting from the crystalline to the smectic phase, and the luminescence intensity continued to decrease until it totally vanished around 130 °C before reaching the isotropic state. However upon cooling, the luminescence transitions re-appeared. The emission bands associated with phosphorescence were found to weaken more rapidly with increasing temperature than the bands associated with fluorescence. The luminescence spectra of $[Au(C_6F_4OC_{10}H_{21})(CNC_6H_4C_6H_4OC_6H_{13})]$ in solution and in the solid state are shown in Figure 2.38, whereas in Figure 2.39 the temperature-dependent luminescence spectra are displayed. Fluoroalkyl derivatives of crown-ether-isocyanide gold(I) complexes are luminescent in the solid state, in the mesophase and in the isotropic liquid (Figure 2.40).[99] In fact, these are rare examples of metallomesogens emitting in the isotropic state.

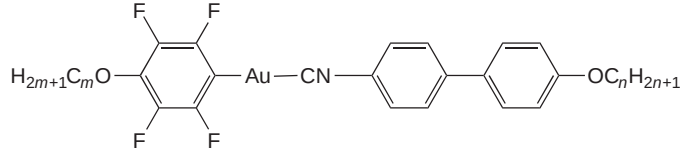

Figure 2.37 Luminescent liquid-crystalline gold(I) isocyanide complexes

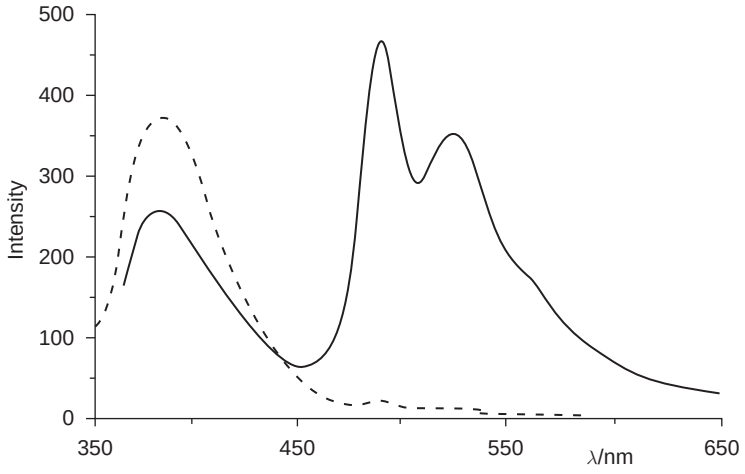

Figure 2.38 Emission spectra at 298 K of [Au($C_6F_4OC_{10}H_{21}$)($CNC_6H_4C_6H_4OC_6H_{13}$)] ($\lambda_{exc} = 344$ nm) in the solid state (solid line) and in CH_2Cl_2 (dashed line). Reprinted with permission from Bayón *et al.*, 2005 [98]. Copyright (2005) Wiley-VCH

The thermal behaviour of ionic silver(I) complexes with a 2,2′-bipyridine ligand containing the chiral *S*-(–)-β-citronellyl group was found to depend strongly on the counter ion (Figure 2.41).[100] Whereas the tetrafluoroborate and hexafluorophosphate derivatives are not liquid-crystalline, a room temperature columnar hexagonal phase with a columnar helical supramolecular structure was displayed by the triflate and dodecylsulfate derivatives. An interesting observation was that the non-mesomorphic tetrafluoroborate and hexafluorophosphate samples were not luminescent at room temperature in the solid phase, whereas the mesomorphic triflate and dodecylsulfate compounds showed blue luminescence in the mesophase at room temperature. The luminescence spectra exhibited a large Stokes shift (120–146 nm) and one structureless emission band. The lifetime of the excited state was determined to be less than 30 μs. These observations indicate that the luminescence is due to excimer emission. Excimers are formed when a monomeric molecule is excited to a higher electronic state by light absorption and when it subsequently reacts with an unexcited monomeric molecule. The excimers of these silver(I)-containing metallomesogens are only formed in the mesophase and not in concentrated solutions in organic solvents. Probably the excimers arise from the argentophilic interactions between the silver(I) ions within the columns of the mesophase.

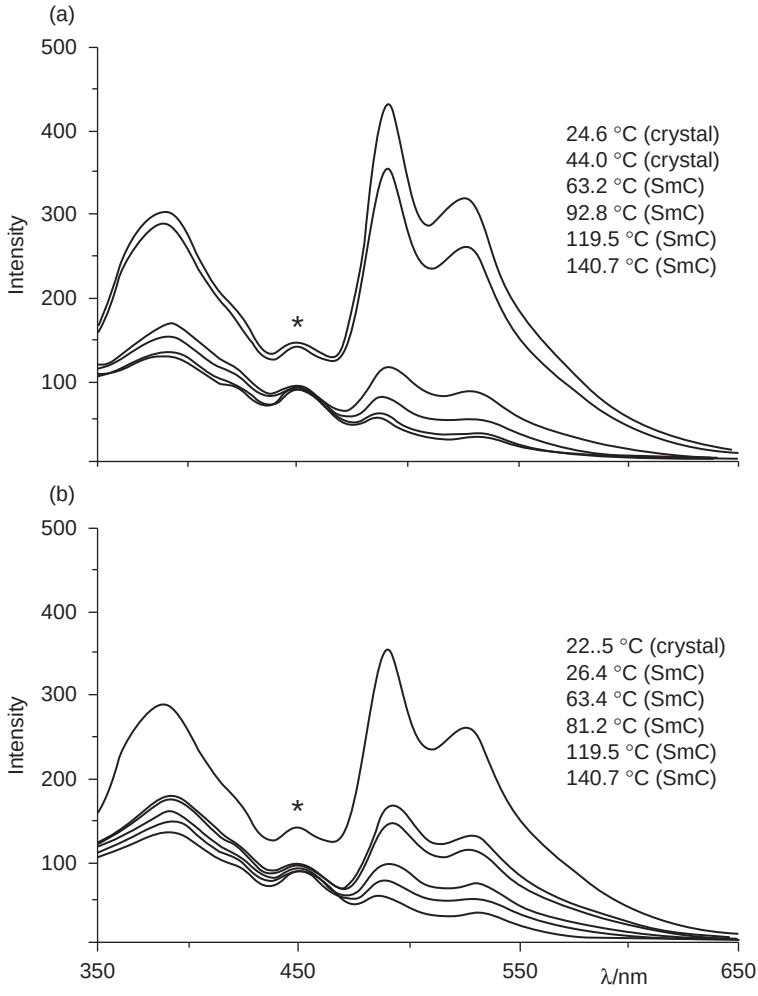

Figure 2.39 Emission spectra at 298 K of $[Au(C_6F_4OC_{10}H_{21})(CNC_6H_4C_6H_4OC_6H_{13})]$ ($\lambda_{exc} = 344$ nm) at different temperatures. The spectra and the temperature list follow the same top to bottom order. The corresponding phase is given in parentheses. (a) Heating from the crystal. (b) Cooling from the SmC mesophase. Peaks marked with * are due to scattering. Reprinted with permission from Bayón *et al.*, 2005 [98]. Copyright (2005) Wiley-VCH

Room-temperature tetrahedral zinc(II) complexes with polycatenar pyrazole or bis(pyrazolyl)methane ligands show luminescence in the near ultraviolet and blue spectral regions (Figure 2.42).[101] A broad, structureless emission band with a large Stokes shift was observed. The emission bands were found to red-shift with an increase in the number of

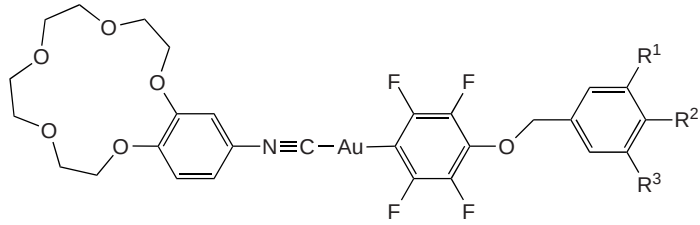

Figure 2.40 Luminescent fluorinated crown-ether-isocyanide gold(I) metallomesogens

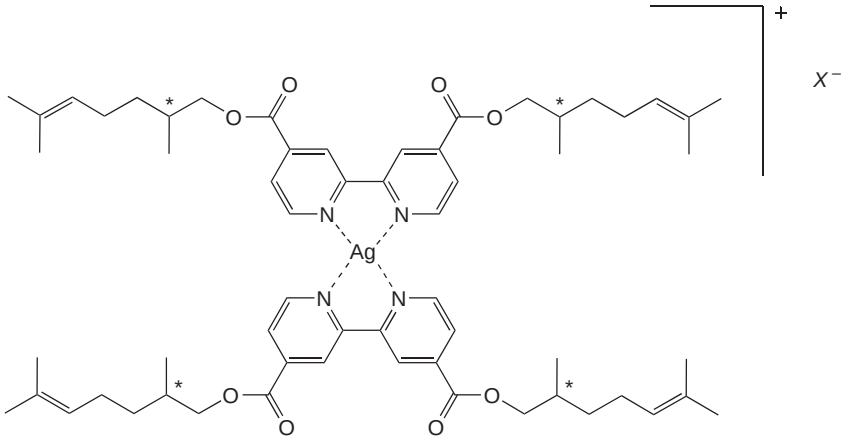

Figure 2.41 Room, temperature chiral silver(I)-containing metallomesogens (X = TfO, DOS)

alkoxy chains. The similarity between the absorption and excitation spectra excludes that the emission is caused by excimer formation, notwithstanding the large Stokes shift. The nonplanar shape of the zinc(II) compounds prevents the formation of excimers.

Liquid-crystalline copper(I) metallacrown complexes of pyrazolate ligands exhibit hexagonal columnar mesophases (Figure 2.43).[102] The luminescence colour of the mesomorphic complexes at room temperature depended on the cooling rate of the sample from the molten state. Red emission was observed upon rapid cooling and yellow emission upon slow cooling. This indicates that kinetic processes (rapid cooling) and thermodynamic processes (slow cooling) compete with one another in the self-assembly of the luminescent liquid crystals. The compounds also

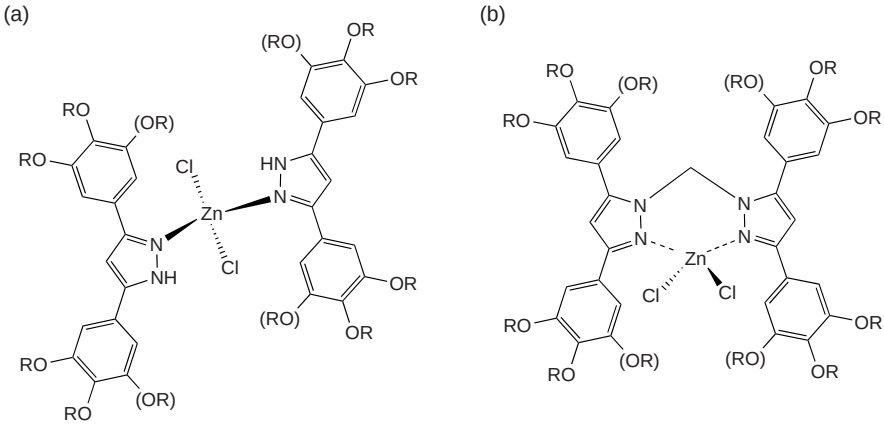

Figure 2.42 Luminescent mesomorphic tetrahedral zinc(II) complexes with polycatenar pyrazole ligands (a) or bis(pyrazolyl)methane ligands (b)

show luminescence in the mesophase. The luminescence has been attributed to copper(I)–copper(I) interactions. It has been proposed that a rewriteable phosphorescent paper for security applications is prepared on the basis of this type of metallomesogens. Light-emitting metallomesogens can also be obtained by incorporating an organic fluorophores in the metal complex. This was illustrated by Ghedini *et al.* who designed a liquid-crystalline palladium complex with the fluorescent Nile Red group (Figure 2.44).[103] The compound exhibited a rectangular columnar phase between 35.3 and 173.0 °C. The complex dissolved in organic solvents showed a red photoluminescence, but the emission maximum (λ_{max}) and luminescence quantum yield (Φ) strongly depended on the solvent: in cyclohexane, $\lambda_{max} = 640$ nm and $\Phi = 0.6\%$, whereas in dichloromethane $\lambda_{max} = 640$ nm and $\Phi = 23\%$. The palladium(II) complex showed also red emission in the solid state and in the liquid-crystal state ($\lambda_{max} = 610$ nm), although the luminescence intensity was low.

The number of studies on luminescence of metallomesogens in the liquid crystal state is still limited, but considerable progress is to be expected in the near future. New strategies for the design of room-temperature mesophases exhibited by metal complexes will make more types of metallomesogens available for photophysical studies. The possibility to obtain polarised emission *via* these systems and the use of these compounds in luminescent devices can be an additional drive for further exploration of this research field.[104] The most promising metal ions to be included in luminescent metallomesogens are Eu^{III}, Tb^{III}, Sm^{III}, Ru^{II},

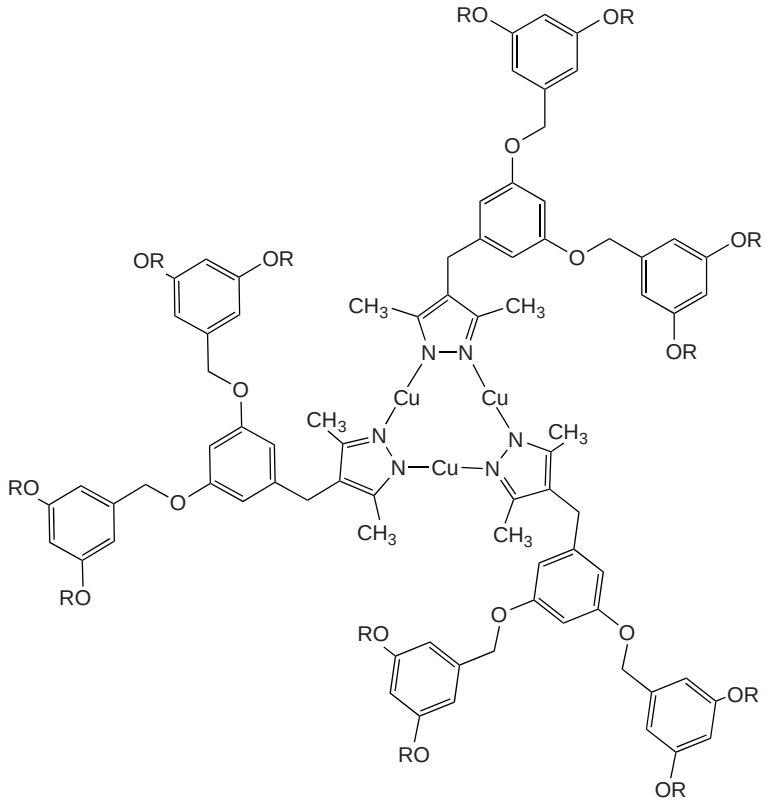

Figure 2.43 Liquid-crystalline copper(I) metallacrown complexes used for the preparation of phosphorescent paper ($R = C_nH_{2n+1}$; $n = 12, 18$)

Pd^{II}, Pt^{II}, Ir^{III}, Ga^{III} and the nonplatinum group d^{10} systems Cu^{I}, Ag^{I}, Au^{I}, Zn^{II}, and Cd^{II}.[105] It should be noted that most of the emissive excited states in metallomesogens are not metal-centred, with exception of the luminescence by the trivalent lanthanide ions. As a consequence, the luminescence properties of the metallomesogens containing *d*-block elements are more strongly affected by the intramolecular interactions in the mesophase than those of the lanthanidomesogens. The study of the luminescence of metallomesogens in the liquid crystal state can give valuable fundamental insight in the photophysics of ordered metal-containing systems. However, the host–guest approach (doping luminescent metal complexes in a liquid crystal matrix) should not be neglected, because this will be probably more useful for the development of new light-emitting devices.

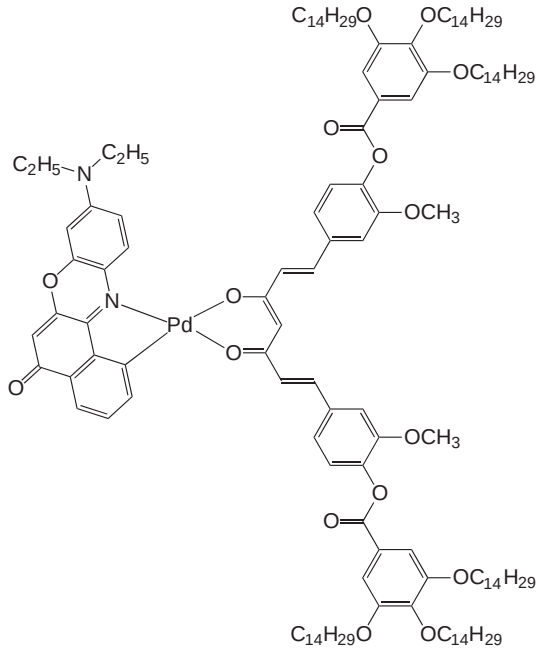

Figure 2.44 Liquid-crystalline palladium(II) complexes with the Nile Red fluorophores

2.3.4 Nonlinear Optical Properties

Metallomesogens have been studied for their potential as *nonlinear optical (NLO) materials*. Such materials could find applications in the domains of opto-electronics and photonics.[106] Nonlinearity of the optical properties means that when a molecule is placed in an intense light beam, there is no linear relationship between the induced electric dipole moment and the applied electric field, the induced dipole moment is given by Equation 2.3.

$$\mu_i = \sum_{j,k,l} \left(\alpha_{ij} E_j + \beta_{ijk} E_j E_k + \gamma_{ijkl} E_j E_k E_l + \ldots \right) \tag{2.3}$$

The summation runs over repeated indices. μ_i is the ith component of the induced electric dipole moment and E_i are components of the applied electromagnetic field. The coefficients α_{ij}, β_{ijk} and γ_{ijkl} are

components of the *linear polarisability*, the *first hyperpolarisability* and the *second hyperpolarisability tensor*, respectively. The first term on the right hand side of Equation 2.3 describes the linear response of the incident electric field, whereas the other terms describe the nonlinear response. The β tensor is responsible for second-order NLO effects such as *second harmonic generation* (SHG, frequency doubling), *frequency mixing*, *optical rectification* and the *electro-optic effect*. The β tensor vanishes in a centrosymmetric environment, so that most second-order NLO materials that have been studied so far consists of noncentrosymmetric, one-dimensional-charge-transfer molecules. At the macroscopic level, observation of the NLO susceptibility requires that the molecular nonsymmetry is preserved over the physical dimensions of the bulk structure. Whereas α, β and γ describe the NLO properties on a microscopic level, the NLO response on a macroscopic level (bulk sample) is described by the susceptibility coefficients $\chi^{(1)}$, $\chi^{(2)}$ and $\chi^{(3)}$, being the linear, the *quadratic (first order)* and *cubic (second order) susceptibilities*, respectively.

Bruce and Thornton reported the first hyperpolarisability (β) of chiral rhodium(I) and iridium(I) 4-alkoxystilbazole complexes *via* the technique of *electric-field induced second harmonic generation* (EFISH), and found values of about 24×10^{-30} esu.[107] Barbera *et al.* determined β values of square-planar rhodium(I) or iridium(I) β-diketonate complexes and rhodium(I) pyrazolate complexes *via* EFISH (Figures 2.45 and 2.46).[108] The rhodium(I) pyrazole complexes show slightly higher β values than the corresponding ligands. However, in the case of the β-diketonate complexes, the presence of a metal decreases the hyperpolarisability. Cipparone *et al.* reported on NLO effect in mesomorphic palladium(II) azoxybenzene complexes (Figure 2.47).[109] Espinet, Ortega and co-workers observed second harmonic generation in imine β-diketonate complexes of palladium(II) and platinum(II) (Figure 2.48).[110,111] These ferroelectric metallomesogens exhibit a chiral smectic C phase.

Third-order NLO properties have been described for liquid-crystalline phthalocyanine and porphyrin complexes. The $\chi^{(3)}$ values for the mesogenic cobalt(II), nickel(II), copper(II), zinc(II) and vanadyl complexes of 5,10,15,20-tetrakis(4-*n*-pentadecylphenyl)porphyrin have been measured in benzene solution by the technique of degenerate four-wave mixing (DFWM) at 532 nm. The $\chi^{(3)}$ values varied between 1.5 and 6.0×10^{11} esu for solutions with a concentration of 10^{-5} mol l^{-1}.[112] The molecular hyperpolarisability values γ of cobalt(II), nickel(II)

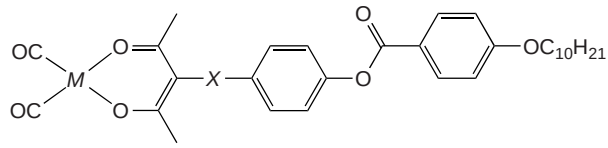

Figure 2.45 Square-planar rhodium(I) and iridium(I) β-diketonate metallomesogens ($M = \mathrm{Rh}$, Ir; $X = \mathrm{COO}$, OOC, $\mathrm{CH_2}$)

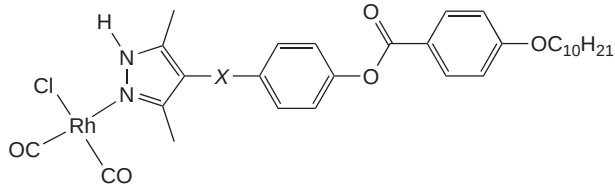

Figure 2.46 Rhodium(I) pyrazolonate metallomesogens ($X = \mathrm{COO}$, OOC, $\mathrm{CH_2}$)

and copper(II) complexes of octakis[(dioctylaminocarbonyl)methoxy]-phthalocyanine were determined in chloroform solution by third harmonic generation (THG) at 1340 nm and EFISH at 1064 nm (Figure 2.49).[113] The EFISH measurements show that the presence of a metal ion enhances γ in comparison with the metal-free macrocycle by one order of magnitude. Third-order nonlinear effects have been observed for these complexes in Langmuir–Blodgett films.[114] The nonlinear absorption and refraction of the metal-free compound and of the copper(II) complex have been measured by the *Z*-scan technique at 1064 nm.[115]

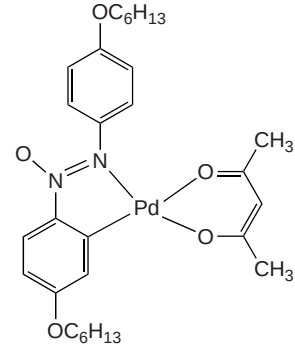

Figure 2.47 Mesomorphic palladium(II) azoxybenzene complex

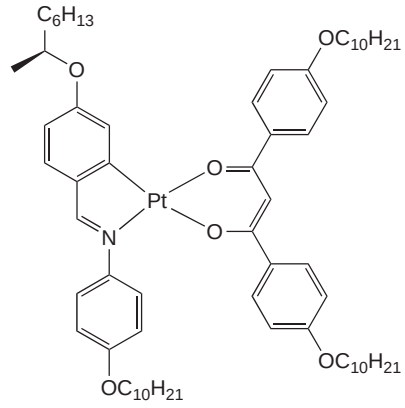

Figure 2.48 Mesomorphic platinum(II) imine β-diketonate complex

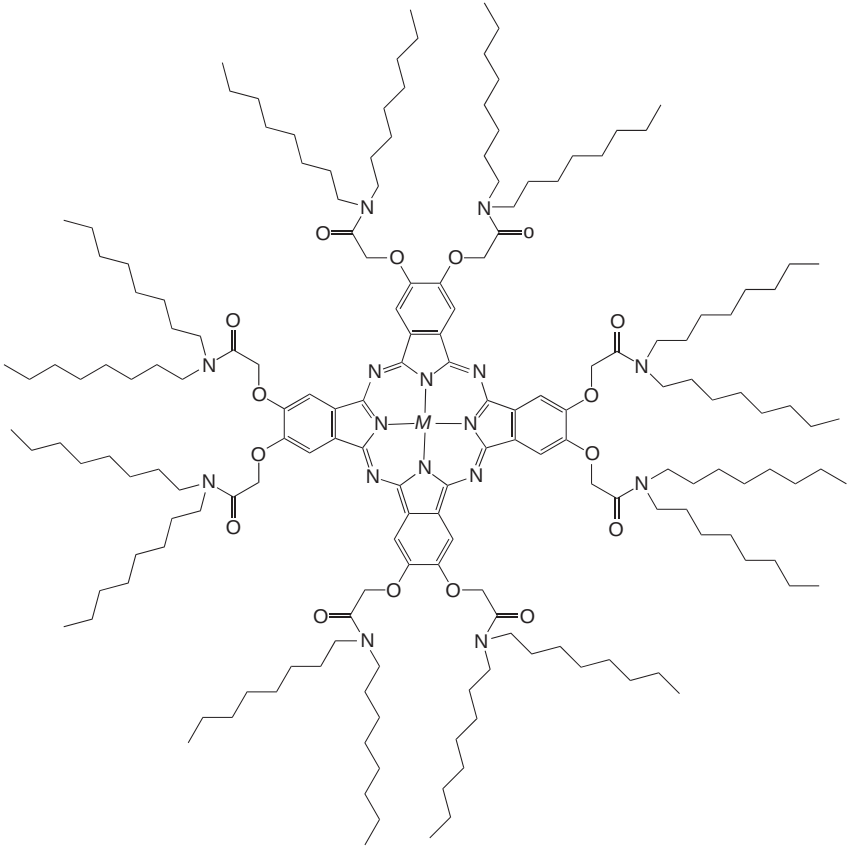

Figure 2.49 Octakis[(dioctylaminocarbonyl)methoxy]phthalocyanine complexes ($M = 2$H, Cu, Co, Ni)

2.4 ELECTRICAL PROPERTIES

2.4.1 Electrical Conductivity

A class of metallomesogens for which the electrical properties have been studied in detail are the substituted bis(phthalocyaninato)lanthanide(III) complexes and, especially, the bis(phthalocyaninato)lutetium(III) complexes, which were first described by Piechocki *et al.* in 1985.[116] In these compounds, the lanthanide(III) ion is sandwiched between two macrocycles. These authors were trying to obtain one-dimensional molecular semiconductors. The conductivity behaviour of the bis(phthalocyaninato)lutetium(III) sandwich complexes was known previously, but only at that time was it realised that aligned columnar mesophases formed by such metallophthalocyanines can be considered as electrical wires at a molecular level.[117] The molten alkyl chains are acting as insulating layers. The phthalocyanine ring is one of the most stable macrocycles. Although different substitution patterns are possible on the macrocycle ring, the easiest compounds to obtain are the octakis-substituted phthalocyanines. Different substitution patterns found in bis(phthalocyaninato)lanthanide(III) complexes are: alkoxy substitution, alkoxymethyl substitution, alkyl substitution, alkylthio substitution and poly(oxyethylene) substitution. A structure of an octakis-alkoxysubstituted *bis*(phthalocyaninato)lanthanide(III) sandwich complex is shown in Figure 2.50.

The free electron in both the unsubstituted and substituted bis(phthalocyaninato)lutetium(III) complexes is associated with the extensive π-system of the phthalocyanine macrocycles. The individual [Pc_2Lu] units can be considered nominally as [$Lu^{3+}Pc_2^{\bullet 3-}$]. There remains

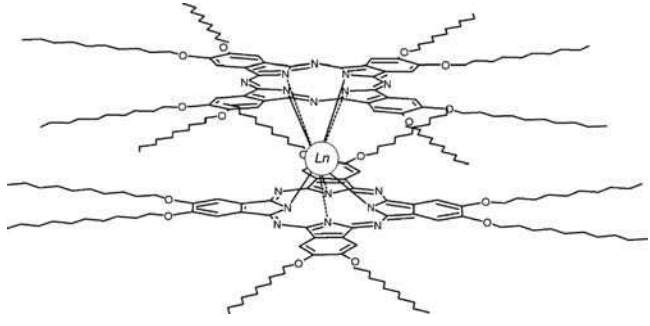

Figure 2.50 Structure of an octakis-alkoxysubstituted *bis*(phthalocyaninato)-lanthanide(III) sandwich complex

some discussion whether the unpaired electron is localised on a single phthalocyanine macrocycle at a given time, thus with formula $[Pc^{2-}Lu^{3+}Pc^{\bullet-}]$,[118] or can be considered to be completely delocalised between the two macrocycles.[119] It has been suggested that one phthalocyanine macrocycle is slightly more distorted than the other.[120] In any case, the lutetium ion is in its trivalent state (Lu^{3+}), and not in the tetravalent state.

The substituted bis(phthalocyaninato)lutetium(III) complexes are intrinsic molecular semiconductors. In such materials, the generation of charge carriers can be represented by the reaction $AAA \rightleftarrows A^+A^-A \rightleftarrows$ *free carriers*, where A is the molecular unit. The ionised pair A^+A^- is photochemically or thermally activated. The self-organisation of the discotic phthalocyanine compounds into columnar stacks provides a one-dimensional pathway for charge transport. The AC electric properties of $[\{(C_{18}H_{37}OCH_2)_8Pc\}_2Lu]$ were studied by Belarbi *et al.* over a large frequency range (10^{-3}–10^5 Hz), both in the solid state, in the mesophase and in the isotropic liquid.[121] In the solid state and in the mesophase, a $\omega^{0.8}$ frequency dependence was observed, with a very low activation energy of conduction (0.05 eV). The conductivities at 10^4 Hz were 8.2×10^{-10} S cm^{-1} in the solid state at room temperature and 1.8×10^{-9} S cm^{-1} in the mesophase at 52 °C. A capacitance increase associated with ionic conductivity was detected below 10 Hz. The very low activation energy was attributed to intercolumnar electron hopping of trapped charge carriers. Because of the limited size of the homogenous solid or liquid-crystalline domains, the conductivity at low frequencies was restricted by intercrystallite or intercolumnar hopping processes. In the isotropic liquid, the electric conduction was found to be frequency independent. At 60 °C and below 10^4 Hz, the electrical conductivity was 4×10^{-11} S cm^{-1}. At higher frequencies, a dipolar relaxation mechanism characterised by a ω^2 frequency dependence was observed. The thermal activation energy of the conduction (0.4 eV) corresponds to the energy required for energy hopping between the $[\{(C_{18}H_{37}OCH_2)_8Pc\}_2Lu]$ molecular subunits through the quasi-liquid paraffinic continuum. The electrical conductivity in the solid state, in the mesophase and in the isotropic liquid could be increased by partial oxidation of the compound with phenoxathiin hexachloroantimonate. Increase of the amount of oxidised species made the ionic conductivity occur at higher frequencies.

The electric studies were later extended by the same authors to $[\{(C_{12}H_{25}O)_8Pc\}_2Lu]$, and the oxidised species $[\{(C_{12}H_{25}O)_8Pc\}_2Lu]^+$-$[BF_4]^-$, obtained by oxidation of the parent compound with nitrosyl tetrafluoroborate.[122] The electrical properties were determined in the

frequency range between 10^{-3} and 10^{5} Hz. The macroscopic conductivities were very low: $< 10^{-10}$–10^{-12} S cm^{-1}. It was shown that the frequency dependence of the electrical conductivity is determined by the intercolumnar order: $\omega^{0.8}$ for the disordered columnar mesophase and $\omega^{0.5}$ for the ordered columnar mesophase. Because the ionisation potentials and electron affinities of paraffinic and aromatic moieties are very different, it was concluded that the charge carriers are entirely localised on the aromatic subunits and that, therefore, the electronic charge processes involve the aromatic cores of the columns. It was estimated that for the same activation energy, the intracolumnar hopping probability is 10^{7} times greater than the intercolumnar one. For [{$(C_{12}H_{25}O)_8$Pc}$_2$Lu], the intracolumnar mobility of the charge carriers is in the range 10^{-4}–10^{-2} cm^2 V^{-1} s^{-1}, with the number of charge carriers being about 10^{11} carriers cm^{-3}. At 10 GHz, the charge migration occurs over less than 1 Å and involves a hopping between only two localised sites, whereas multiple sites were postulated in the low frequency range.

The electrical conductivity of the liquid-crystalline [Pc$_2$Lu] is much lower than that of thin films and single crystals of unsubstituted [Pc$_2$Lu] complexes, due to the fact that the conductions occur only inside the columns along the columnar axis and that the layer of molten alkyl chains is insulating. Belarbi has studied the AC conductivity of [{$(C_{12}H_{25}O)_8$Pc}$_2$Lu] samples that have partially been aligned in a magnetic field.[123] He found an anisotropy of conduction of approximately 10, which means that the conductivity is 10 times higher when the columns are parallel to the magnetic field than when they are perpendicular to the magnetic field. The conductivity of the unaligned mesophase was in between these two limiting values. Most of the electric studies have been done on lutetium(III) complexes. However, studies on unsubstituted [Pc$_2$Ln] complexes have revealed major differences between the bisphthalocyanine complexes of lutetium ([Pc$_2$Lu]) and thulium ([Pc$_2$Tm]).[124,125] Whereas [Pc$_2$Lu] is an intrinsic molecular semiconductor (as discussed above), [Pc$_2$Tm] is an extrinsic molecular semiconductor. The low hole mobility of [{$(C_{12}H_{25}S)_8$Pc}$_2$Ce] in the hexagonal columnar phase (7×10^{-3} cm^2 V^{-1} s^{-1}) in comparison with that of the lutetium analogues was attributed to the absence of free radicals in the cerium complex.[126] Notice that cerium is tetravalent in this complex. Basova *et al.* reported on the conductivity of [{$(C_6H_{13}S)_8$Pc}$_2$Dy] film in the liquid crystal state.[127]

Van de Craats *et al.* used the *pulse-radiolysis time resolved microwave conductivity* (PR-TRMC) *technique* to study the charge-transport properties of [{$(C_{12}H_{25}O)_8$Pc}$_2$Lu].[128] Their results showed an increase in charge carrier mobility at the crystalline solid to Col$_x$ mesophase

transition and another strong increase by a factor of three at the transition to the higher temperature mesophase Col_h. In the mesophase above 90 °C, the charge carrier mobility gradually decreased and an abrupt decrease by a factor of about two was observed at the Col_h to isotropic liquid transition. In the solid state, the charge carrier mobility was more than one order of magnitude lower than in the solid state of other alkoxy-substituted phthalocyanines. This is possibly due to the sandwich structure of the individual molecules. The increase at the crystal-to-mesophase transition was attributed to a change from a tilted to an orthogonal stacking. The increase at the Col_x to Col_h transition was attributed to the equivalence of the phthalocyanine macrocycles within the columns, which leads to delocalisation of the radical site between neighbouring molecular units and which results in additional intracore binding over and above the electrostatic and π–π interactions normally responsible for columnar self-aggregation. The intracolumnar mobility determined just above the Col_x to Col_h transition at 90 °C was 0.17×10^{-4} m^2 V^{-1} s^{-1} and was at that time the highest yet determined using the PR-TRMC technique for a liquid crystal forming a columnar mesophase. The increase in charge mobility at the crystal-to-mesophase transition is in contrast to what is observed for other discotic molecules, such as porphyrins, perylenes, triphenylenes and even other alkoxy-substituted phthalocyanines. Because of the fast time response and ultra-high frequency involved in the PR-TRMC technique, the mobilities obtained were thought to be intrinsic, trap-free values associated with organised domains within the material.[129] Therefore, these mobilities can be considered to be close to the maximum value that can be obtained with well-organised monodomain layers.

Replacement of the oxygen atoms of alkoxy-substituted [Pc_2Lu] phthalocyanine complexes by sulfur atoms (giving alkylthio substituted phthalocyanines) resulted in an increase of more than an order of magnitude in the intramolecular charge mobility to values in the range of 0.15–0.3 cm^2 V^{-1} s^{-1}.[129] The pronounced positive effect on the charge-transport properties of sulfur compared with oxygen as chain-to-core coupling group was attributed to the larger size of the sulfur atom, which hinders rotational and translational displacements of the phthalocyanine macrocycles within the cores of the columns. The resulting decrease in structural disorder within the stacks of the alkylthio-substituted compounds is favourable for fast charge transport. The higher charge mobility can also be explained by the differences in electronegativity between the oxygen and sulfur atoms. Whereas the alkoxy group is electron donating to the phthalocyanine ring, the alkylthio group is in a first approximation

neither electron donating nor electron withdrawing. Therefore, the HOMO–LUMO gap is smaller in the alkylthio-substituted compounds, and hence the charge mobility is higher. The one-dimensional intracolumnar charge-carrier mobilities exhibit only a weak temperature dependence, except for an abrupt decrease by a factor of about three at the crystal-to-mesophase transition. This decrease can be attributed to the melting of the alkylthio chains, with a resulting increase in the disorder within the columns. The mobility remains high in the isotropic state, which indicates that a high degree of columnar order still exists and allows charge transport to occur *via* intermolecular charge transfer rather than by molecular ion diffusion. Because of the high charge mobility in the isotropic state, these compounds were considered as the first liquid phase organic semiconducting materials. As an example of conductivity measurements on liquid-crystalline metallophthalocyanines other than those containing lutetium, it can be mentioned that Belarbi *et al.* measured the conductivity of octakis(dodecyloxy)lithium phthalocyanine.[122]

Only very few conductivity measurements have been performed on metallomesogens other than metallophthalocyanine complexes. Godquin-Giroud *et al.* demonstrated a conductivity of the order of 10^{-8} S cm^{-1} for the copper(II) complex of the β-diketone bis(3,4-nonyloxybenzoyl)methane in a hexagonal columnar phase.[130]

The discotic liquid crystal 2,3,6,7,10,11-hexakis(hexyloxy)triphenylene (HAT6) (Figure 2.51) forms a hexagonal columnar mesophase and can be converted into a *p*-type semiconductor with the preferred direction of conduction being along the axes of the columns by doping with 1 mol% of the Lewis acid $AlCl_3$.[131] $AlCl_3$ attracts an electron from the triphenylene ring of HAT6 producing an electron hole in the π-bands of the triphenylene stacks. The electrical conductivity σ increased from less than 10^{-11} S cm^{-1} for the undoped sample to about 10^{-5} S cm^{-1} for the $AlCl_3$-doped sample. In macroscopically aligned samples, the

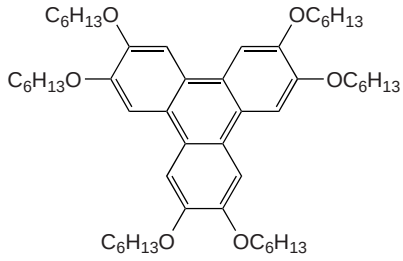

Figure 2.51 Structure of 2,3,6,7,10,11-hexakis(hexyloxy)triphenylene (HAT6)

conductivity along the column axis is about three orders of magnitude larger than in a direction perpendicular to the column axis.[132] A liquid-crystalline n-type semiconductor could be obtained by doping the π-deficient liquid crystal 2,3,7,8,12,13-hexakis(hexylthio)tricycloquinazoline (HHTQ) with 6 mol% of potassium metal as electron donor.[133] The conductivity in the direction of the column axis in the hexagonal columnar mesopase was 2.9×10^{-5} S cm^{-1}. The electrical conductivity of the discotic liquid crystals 2,3,6,7,10,11-hexakis(hexyloxy)triphenylene (HAT6) and 2,3,6,7,10,11-hexakis(hexylthio)triphenylene (HHTT) increased by several orders of magnitude by doping with ferrocenium ions, for aligned and unaligned liquid crystal samples.[134] Doping concentrations in the form of ferrocenium as the ferrocenium tetrafluoroborate salt up to 10% w/w were used. It was proposed that the electrical conductivity occurred by the hopping mechanism where the electron-rich triphenylene core donates an electron to the electron deficient ferrocenium ion, resulting in the formation of an electron-hole pair. The hopping conductivity of the electron-hole pair under the action of an applied DC electric field gives the electrical conductivity. The optical absorption spectra show that a charge-transfer complex is formed between the electron-rich discotic molecules and the electron-deficient ferrocenium ions.

Gold nanoparticles have been incorporated into organic liquid crystals with the aim to modify the electrical conductivity of these liquid crystals. Inclusion of dodecanethiol-gold nanoparticles in the liquid crystal 5CB increased the electrical conductivity.[135] The conductivity increased with increasing concentrations of gold nanoparticles and was more than two orders of magnitude higher for the sample doped with 5% (w/w) of gold nanoparticles than for the undoped sample. However, the presence of nanoparticles reduced the conduction anisotropy. Kumar *et al.* found an increase of the DC conductivity by a factor of 250 by doping the discotic liquid crystal 2,3,6,7,10,11-hexakis(hexyloxy)triphenylene (HAT6) with hexanethiol-capped gold nanoparticles.[136,137] Holt *et al.* noticed that the presence of 1% (w/w) of methylbenzenethiol-coated gold nanoparticles increased the electrical conductivity of HAT6 by about two orders of magnitude in the crystal, in the hexagonal columnar and in the isotropic liquid phase.[138] However, when an electric field (above a certain critical value) was applied to the isotropic phase, the electrical conductivity rapidly increased by another three or four orders of magnitude, after which the higher conductivity was maintained regardless of phase, field or temperature. This increase in conductivity was attributed to the formation of chains of gold nanoparticles. The high conductivity was maintained in

the liquid-crystalline and in the crystalline phase of the liquid crystal/nanoparticles composite. Kumar *et al.* found an increase in the electrical conductivity by a factor of more than 10^6 upon doping of the discotic liquid crystal 2,3,6,7,10,11-hexakis(heptyloxy)triphenylene (HAT7) with 1% w/w of triphenylene-capped gold nanoparticles.[139]

2.4.2 Photoconductivity

Photoconductivity is the light-induced enhancement of the electrical conductivity. In photoconductive materials, electron-hole pairs are generated by photon absorption, the increase in the number of free electrons and holes raises the electrical conductivity. The excited states generated in photoconductive materials and other semiconductors are described by the exciton formalism. An exciton can be considered as an electron-hole pair that can travel as a quasi-particle through the material and it provides a means to transport energy without transporting net charge. Simon and co-workers used time-resolved absorption spectroscopy to study laser-induced triplet excitons of the octakis(alkoxymethyl) metal-free and zinc(II) phthalocyanines in the crystalline phase and in the columnar mesophase.[140] The authors found that the photoconductivity is higher in the liquid-crystalline state than in the crystalline state and that the photoconductivity is improved by the presence of a metal ion. The columnar arrangement of molecules enhances the unidirectional character of the photonic energy migration. On the other hand, Gregg observed a sudden decrease in photocurrent and photovoltage at the crystal to liquid crystal phase transition for a mesogenic zinc(II) porphyrin complex.[141] This decrease was attributed to the greater disorder in the mesophase. The photoconductivity of the $[\{(C_{16}H_{37}S)_8Pc\}_2Ln]$ (Ln = europium, terbium, lutetium) complexes is very weak.[142] Nonradiative relaxation of the photoexcitations is dominating. A significant enhancement of the photoconductivity was observed after doping with C_{60}. In the case of the lutetium(III) complex, the photoconductivity parallel with the columns was two orders of magnitude larger than in the case of the undoped sample.

2.4.3 Electrochromism

The bis(phthalocyaninato)lanthanide(III) complexes show electrochromism: in solution or deposited as thin films they exhibit different colours

according to the applied potential.[143,144] For this reason, the potential of these materials for display applications has been investigated. The electrochromic behaviour of the octaalkoxymethyl-substituted [Pc_2Lu] has been investigated and it has been shown that they have similar properties in solution as the unsubstituted [Pc_2Lu] complexes.[145,146] It is even so that the substituted compounds are far more stable under electrochemical cycling (cyclic voltammetry) than the unsubstituted ones.[147] The green neutral form can be transformed *via* a one-electron oxidation step into an orange form and *via* a one-electron reduction step into a blue form:

$$[\{(C_nH_{2n+1}OCH_2)_8Pc\}_2Lu]^- \overset{-e^-}{\rightleftarrows} [\{(C_nH_{2n+1}OCH_2)_8Pc\}_2Lu] \overset{-e^-}{\rightleftarrows} [\{(C_nH_{2n+1}OCH_2)_8Pc\}_2Lu]^+$$

blue green orange

The redox processes are reversible. In the blue complex the *Q* band is at about 631 nm, in the green complex it is at about 671 nm and in the orange complex it is at about 704 nm. The total oxidation of [$\{(C_8H_{17}OCH_2)_8Pc\}_2Lu$] or [$\{(C_{12}H_{25}OCH_2)_8Pc\}_2Lu$] films to form an orange cation or reduction to form a blue anion could be achieved when the electrode potential was held for several minutes at +0.6 V or –0.1 V, respectively. It was shown that the potential of the oxidation step depends on the anion of the aqueous electrolyte in contact with the film. The oxidised and reduced compounds are stable in solution. In the presence of an external potential, the orange and blue species remain unchanged over at least 2 days. Without external potential, the colours remain for several hours or days, depending on the impurity concentration. An increase in the chain length makes both the reduction and the oxidation process more difficult.[147] For [$\{(C_{18}H_{37}OCH_2)_8Pc\}_2Lu$] films, it was necessary to heat the film at 55 °C and to increase the potential to overcome the Ohmic drop (typical potential values were +1.4 V and –1.0 V). Komatsu *et al.* pointed to the fact that substituents on the phthalocyanine ring have hardly any influence on the colours of the neutral green complex and the reduced blue species.[148] However, the colours of the oxidised species showed remarkable differences (in dichloromethane solution). The oxidised form of the unsubstituted [Pc_2Lu] was yellowish green, [$\{(C_{12}H_{25}OCH_2)_8Pc\}_2Lu]^+$ and [$\{(C_{12}H_{25}O)_8Pc\}_2Lu]^+$ were orange, whereas [$\{(C_{12}H_{25})_8Pc\}_2Lu]^+$ solution was red. With respect to the

alkoxy- and alkoxymethyl-substituted [Pc_2Lu], the *Q* band of the alkyl-substituted [Pc_2Lu] is shifted more than 8 nm to longer wavelengths (and is found at 712 nm). The oxidation potential of [{$(C_nH_{2n+1})_8Pc$}$_2Lu$] is at –0.17 V and the reduction potential is at +0.28 or +0.29 V. The electrochromism of these alkyl-substituted [Pc_2Lu] exhibits the three primary colours (blue, green, red) so that it is possible to construct a full-colour display using one single compound. The drawback of this type of display is the long response time: colour changes require several hundreds of seconds. On the other hand, once an image is formed by an electrochromic process, no further energy input is required to preserve it.

By incorporating electron-donating groups on the phthalocyanine ring, the complexes become more reducing and less oxidising.[149] This was illustrated by attaching pentyloxy or *n*-heptyl groups to the macrocycle ring. However, the difference between the oxidation and reduction potentials, which are a good estimate of the thermal activation energy in the [Pc_2Ln] complexes, remained relatively constant at *ca* 0.40 V. It should be mentioned that the theoretical explanation of the electrochromic behaviour of [Pc_2Lu] compounds is not without controversy. Some authors claim that the colour changes are acid–base in nature and not due to redox processes involving the phthalocyanine rings. Daniels *et al*. reported that in acetonitrile solution and in the absence of an applied potential, the colour change from blue over green to red could be obtained by the addition of acid and then quantitatively reversed by the addition of base.[150,151] The blue species is [Pc_2Ln]$^-$, the green [Pc_2LnH] and the red species [Pc_2LnH_2].

2.4.4 Ferroelectricity

Calamitic metallomesogens forming a chiral smectic C phase (SmC*) are *ferroelectric materials*. Due to the low symmetry of this phase when the helix is unwound (C_2) the molecular dipoles are aligned within the layers of the SmC* phase, giving rise to ferroelectric order in the layers. Because the SmC* phase has a helical structure, there is no net macroscopic dipole moment for the bulk phase. However, it is possible to unwind the helix by application of an external electric field or by surface anchoring in thin cells. Under such conditions, a well-aligned film of the ferroelectric liquid crystal can exhibit a net polarisation, called the *spontaneous polarisation* (P_s). Ferroelectric liquid crystals are of interest for display applications because the macroscopic polarisation can be switched very fast by an

electric field (in microseconds). The sign and magnitude of the spontaneous polarisation of metallomesogens is dominated by the structural characteristics of the organic ligand. It is difficult to predict the influence of the metal ions on the ferroelectric properties. In comparison with the spontaneous polarisation of the ligand, the spontaneous polarisation of the metal complex can be larger, smaller or virtually the same. The determining factor is the structure of the metallomesogen as a whole. Because ferroelectric metallomesogens have in general a higher viscosity than organic ferroelectric liquid crystals, their response times are slower, in the millisecond range. Measurements on ferroelectric mesogenic palladium(II) complexes showed that spontaneous polarisation values up to 200 nC cm^{-2} can be obtained.[152–155] Much smaller values (about 25 nC cm^{-2}) were measured for Schiff base copper(II) complexes.[156,152]

Spontaneous polarisation can also be observed for chiral discotic metallomesogens forming columnar mesophases, when the chiral molecules are tilted with respect to the column axis. The tilt induces a dipole moment within the plane of the molecule. A net macroscopic polarisation can be obtained for rectangular columnar phases with C_2 or $P2_1$ symmetry. Serrano and Sierra reported on ferroelectric switching in the columnar mesophase for chiral β-diketonate complexes (Figure 2.52).[157]

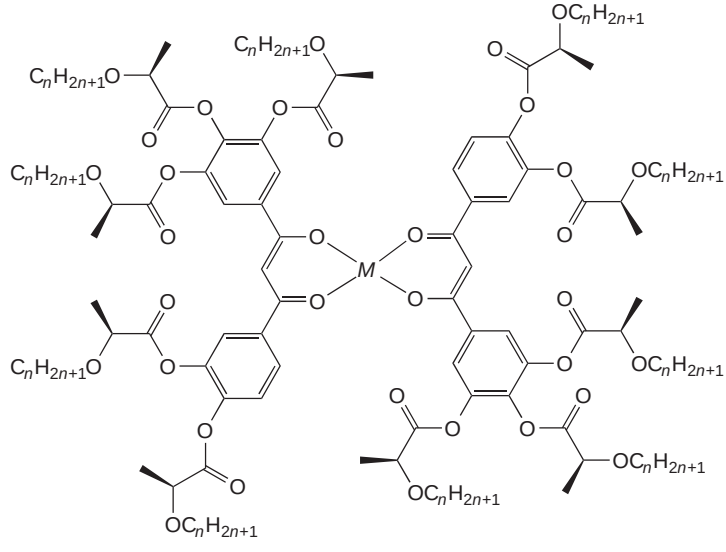

Figure 2.52 Ferroelectric liquid-crystalline chiral β-diketonate complexes (M = VO, Cu, Pd)

2.5 MAGNETIC PROPERTIES

2.5.1 Magnetic Anisotropy and Alignment in External Magnetic Fields

A liquid crystal can be aligned macroscopically by applying an external magnetic field. The magnetic alignment arises from the anisotropic magnetic energy of the liquid crystals.[158] Because of this anisotropy, there is a coupling between the magnetic field and the director of the mesophase, and the liquid crystal experiences a torque in the magnetic field, causing it to orient into a direction where its magnetic energy is at a minimum. It should be noted that isolated small molecules or ions do not undergo alignment in a magnetic field because the coupling energy between a molecule and the applied magnetic field is small compared with the thermal energy (k_BT) at room temperature. Thermal agitation will, therefore, destroy the alignment effects. Aggregates or assemblies having ordered structures like liquid crystal phases can undergo magnetic alignment, since their anisotropic magnetic energy exceeds the thermal agitation at room temperature. The molecular orientation in a mesophase by a magnetic field is a cooperative effect between 10^8 or more molecules in a liquid crystal microdomain.[159,160] The molecules in a mesophase microdomain have orientational order as a consequence of the anisotropic intramolecular interactions between the molecules. Alignment of mesophases by means of a magnetic field is of importance for the study of mesophases by X-ray diffraction, because the information content of an X-ray diffractogram of an aligned mesophase is much higher than the corresponding diagram of an unaligned mesophase. Also, for the measurements of anisotropy of physical properties such as the dielectric permittivity, electrical conductivity or viscosity, aligned mesophases are required. An advantage of magnetic alignment over mechanical alignment by rubbing or by alignment layers is that because the magnetic field can penetrate into the materials, alignment of the bulk sample rather than of the surface layers can be achieved. The direction along which the magnetic field is applied can easily be controlled, so that alignment inclined to a surface is possible. In contrast, with alignment layers or with alignment by means of an electric field, only parallel or perpendicular alignment can be achieved.

For easy alignment of the mesogens in a magnetic field a pronounced magnetic anisotropy is required. The *magnetic anisotropy* $\Delta\chi$ is the difference between the magnetic susceptibility parallel ($\chi_{\parallel}$) and

perpendicular ($\chi_\perp$) to the director **n**: $\Delta\chi = \chi_{\parallel} - \chi_\perp$. The free energy for alignment of liquid crystals in a magnetic field can be expressed as:

$$\Delta G_{\text{align}} = -(1/2)\Delta\chi(\boldsymbol{H}\cdot\mathbf{n})^2 \tag{2.4}$$

where **H** is the applied magnetic field and **n** is the director. In general, the molar magnetic anisotropy of organic liquid crystals is less than 100×10^{-6} cm^{-3} mol^{-1}. This value can be increased by introducing paramagnetic metal atoms in liquid-crystalline compounds. Lanthanide-containing metallomesogens are especially attractive for these purposes as they can exhibit a very high magnetic anisotropy, often one or two orders of magnitude larger than that of organic liquid crystals.

The orientation of liquid crystals in a magnetic field depends not only on the magnitude of the magnetic anisotropy ($\Delta\chi$), but also on its sign. Depending on the sign of $\Delta\chi$, the director $\tilde{\mathbf{n}}$ of the liquid crystal is oriented either parallel or perpendicular to the external magnetic field. If $\Delta\chi$ is positive, the molecules will be oriented with their molecular long axis parallel to the magnetic field. If $\Delta\chi$ is negative, the molecules will be aligned with their molecular long axis perpendicular to the magnetic field. Whereas it is in principle possible to obtain a monodomain liquid crystal when the director aligns parallel to the applied magnetic field ($\Delta\chi > 0$), this is not the case when the director aligns perpendicular to the magnetic field ($\Delta\chi < 0$); there is only one direction parallel to the magnetic field, but if $\Delta\chi < 0$ the director can taken any orientation in a plane perpendicular to the magnetic field. A polydomain is obtained where the different microdomains are randomly oriented, with the only restriction that the director is situated within a plane. A monodomain can be obtained by applying a second magnetic field perpendicular to the first magnetic field. If $\Delta\chi < 0$, the director will be oriented perpendicular to both magnetic field directions. Finally, it should be mentioned that a low viscous mesophase is desirable for good alignment of the sample in a magnetic field.

Diamagnetic calamitic liquid crystals have, in general, a positive magnetic anisotropy ($\Delta\chi > 0$) and diamagnetic discotic liquid crystals a negative magnetic anisotropy ($\Delta\chi < 0$). Therefore, calamitic molecules will align with the director parallel to the external magnetic field, while discotic molecules will align with the director perpendicular to the magnetic field. It is sometimes difficult to predict the direction of alignment of paramagnetic *d*-block metallomesogens, because there is a competition between the diamagnetic ($\Delta\chi_{\text{dia}}$) and the paramagnetic contributions

($\Delta\chi_{para}$) to the overall magnetic anisotropy ($\Delta\chi$). The diamagnetic contribution ($\Delta\chi_{dia}$) is nearly always positive (for calamitic molecules), but $\Delta\chi_{para}$ can be either positive or negative. In the case of oxovanadium (V=O) complexes $\Delta\chi_{para}$ is positive so that $\Delta\chi$ is always positive. Therefore, all calamitic oxovanadium complexes align with the director parallel to the magnetic field.[161–166] In the case of copper(II) complexes the situation is more complicated because $\Delta\chi_{para}$ is negative. It was found for liquid-crystalline copper(II) complexes with Schiff base ligands that the sign of $\Delta\chi$ depends on the number of aromatic rings present in the molecule.[161–168] If four aromatic rings are present in the complex, in general $\Delta\chi_{para} > \Delta\chi_{dia}$ and $\Delta\chi < 0$ (perpendicular orientation to the magnetic field), although the opposite situation can be observed due to steric effects. In copper(II) complexes with six or more aromatic rings $\Delta\chi_{para} < \Delta\chi_{dia}$ and $\Delta\chi > 0$ (parallel orientation to the magnetic field). In the latter type of complexes, the diamagnetic contribution to the magnetic anisotropy is large in comparison with the paramagnetic contribution. The diamagnetic contribution to the magnetic anisotropy can be calculated using an additive scheme (Pascal's scheme)[169,170] and the paramagnetic contribution can be found by subtracting the calculated $\Delta\chi_{dia}$ value from the experimental measured $\Delta\chi$ value. In the case where $\Delta\chi_{para} \approx \Delta\chi_{dia}$ and with the two contributions of opposite sign, the resulting $\Delta\chi$ value will be very small and, as a consequence, it will be very difficult to obtain an aligned monodomain by means of a magnetic field.

The situation is quite different in the case of lanthanide-containing liquid crystals (lanthanidomesogens), because the trivalent ions of the lanthanides (especially Tb^{3+}, Dy^{3+}, Ho^{3+}, Er^{3+},Tm^{3+}) have a very large magnetic anisotropy in comparison with other paramagnetic ions (*e.g.* Cu^{2+} or vanadyl). In the case of the paramagnetic lanthanide ions (all the ions of the lanthanide series except La^{3+}, Lu^{3+} and the rare earths Y^{3+} and Sc^{3+}), the diamagnetic contributions to $\Delta\chi$ can be neglected in comparison with the paramagnetic contribution. An exception is the Gd^{3+} ion, which is almost magnetically isotropic due to the *S* ground state $^8S_{7/2}$. In Table 2.1, an overview of the most important electronic and magnetic properties of the trivalent lanthanide ions is summarised.[171] The large magnetic anisotropy of liquid-crystalline lanthanide complexes was discovered soon after the first calamitic lanthanide-containing metallomesogens had been prepared.[13,172,173] The magnetic anisotropy and magnetic alignment of lanthanidomesogens has especially been studied for lanthanide complexes of Schiff base complexes of the type $[Ln(L\mathrm{H})_3X_3]$, where *Ln* is a trivalent lanthanide ion, *L*H is a salicylaldimine Schiff base and *X* is the counter anion.[174] Typical anions are

Table 2.1 Electronic and magnetic properties of the trivalent lanthanide ions Ln^{3+}

Ln^{3+}	Electronic configuration	Ground state	μ_{eff} calculated (Bohr magnetons)	μ_{eff} observed (Bohr magnetons)
Ce^{3+}	$[Xe]4f^1$	$^2F_{5/2}$	2.56	2.3–2.5
Pr^{3+}	$[Xe]4f^2$	$^3H_4$	3.58	3.4–3.6
Nd^{3+}	$[Xe]4f^3$	$^4I_{9/2}$	3.62	3.5–3.6
Pm^{3+}	$[Xe]4f^4$	$^4I_4$	2.68	—
Sm^{3+}	$[Xe]4f^5$	$^6H_{5/2}$	1.55–1.65	1.4–1.7
Eu^{3+}	$[Xe]4f^6$	$^7F_0$	3.40–3.51	3.3–3.5
Gd^{3+}	$[Xe]4f^7$	$^8S_{7/2}$	7.94	7.9–8.0
Tb^{3+}	$[Xe]4f^8$	$^7F_6$	9.72	9.5–9.8
Dy^{3+}	$[Xe]4f^9$	$^6H_{15/2}$	10.65	10.4–10.6
Ho^{3+}	$[Xe]4f^{10}$	$^5I_8$	10.60	10.4–10.7
Er^{3+}	$[Xe]4f^{11}$	$^4H_{15/2}$	9.58	9.4–9.6
Tm^{3+}	$[Xe]4f^{12}$	$^3H_6$	7.56	7.1–7.5
Yb^{3+}	$[Xe]4f^{13}$	$^2F_{7/2}$	4.54	4.3–4.9
Lu^{3+}	$[Xe]4f^{14}$	$^1S_0$	0	0

NO_3^-, Cl^- and DOS (dodecylsulfate). In Figure 2.53, the structure of the *L*H ligand *N*-octadecyl-4-tetradecyloxysalicylaldimine is shown. In the complex, three monodentate Schiff base ligands bind in a zwitterionic form to the lanthanide ion. The coordination sphere of the lanthanide ion is completed by coordination to the counter anions. All the complexes $[Ln(LH)_3X_3]$ form a smectic A phase.[13] The lowest transition temperatures are observed for the dodecylsulfate complexes.[175,176] Although the studies of the magnetic anisotropy have been largely been focused on Schiff base complexes, a few data for β-enaminoketone complexes are available.[177]

Because the sign of the magnetic anisotropy depends on the lanthanide ion, it is possible to obtain (with the same kind of ligand and with the proper choice of the lanthanide ion) compounds that can either be aligned perpendicular or parallel to the magnetic field. Analysis of the experimental magnetic susceptibility data shows that these compounds can be classified into two distinct groups, depending on the sign of $\Delta\chi$.[174,178]

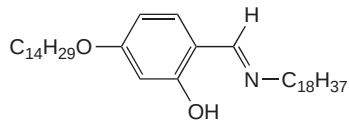

Figure 2.53 Salicylaldimine Schiff base ligand

The first group contains Ce^{3+}, Pr^{3+}, Nd^{3+}, Sm^{3+}, Tb^{3+}, Dy^{3+} and Ho^{3+} compounds, while the second group contains Eu^{3+}, Er^{3+}, Tm^{3+} and Yb^{3+} compounds. Two compounds not belonging to the same group always have opposite sign of $\Delta\chi$. For instance, if $\Delta\chi$ is negative for the first group of lanthanide compounds, $\Delta\chi$ is positive for the second group and *vice versa*. All experimental results obtained so far for lanthanide-containing liquid crystals are in agreement with a negative $\Delta\chi$ value for the first group and a positive $\Delta\chi$ value for the second group.[174,179] But theoretical work shows that the reverse situation can be expected too.[178,180,181]

The highest values of the magnetic anisotropy are observed for the heavy lanthanides Tb^{3+}, Dy^{3+}, Ho^{3+}, $Er^{3+}$and Tm^{3+} because these ions have a high magnetic moment. For metallomesogens containing these ions the absolute value of the magnetic anisotropy in the mesophase can be 5000×10^{-6} cm^{-3} mol^{-1} or even more. As shown below, the magnetic moment is related to the magnetic susceptibility and thus to the magnetic anisotropy. There is no one-to-one relationship between a high magnetic moment and a large magnetic anisotropy, but if the magnetic moment is small it is impossible to have a large magnetic anisotropy.

Another requirement for a high magnetic anisotropy besides a large magnetic moment is that the crystal field perturbation is strong. The ${}^{2S+1}L_J$ ground state splits under the influence of the crystal field potential in a number of crystal field levels, at maximum $2J+1$ for integer J (even number of f electrons), and $J + 1/2$ for half-integer J (odd number of f electrons). The magnetic anisotropy arises from the fact that when the crystal field splitting is large, not all the crystal field levels are statistically populated at a given temperature. The magnetic anisotropy increases when the temperature is lowered. At temperatures above room temperature, the magnetic behaviour becomes more and more isotropic and approaches the predictions in the free ion approximation. However, when the crystal field perturbation is large it is possible to have a large magnetic anisotropy, even at temperatures at which the mesophase of lanthanide-containing liquid crystals is stable. The magnitude of the magnetic anisotropy for a series of isostructural lanthanide-containing metallomesogens can be estimated on the basis of the crystal field splitting of the ${}^7F_1$ multiplet in the corresponding europium(III) compound.[182] This splitting is accessible *via* photoluminescence measurements. Model calculations have been used to relate the magnetic anisotropy to the type of coordination polyhedron around the central lanthanide ion.[180,181] Another approach for explaining the magnetic

anisotropy is based on the Bleaney theory, which is used to predict the lanthanide-induced shift in ^{1}H NMR spectra.[183] This theory was later generalised by Golding and Pyykkö.[184]

The main problem to cope with is the high viscosity of the mesophase, which prevents fast switching. Cooling rates in the order of 1°C min^{-1} are necessary to achieve good alignment in a magnetic field when going from the isotropic liquid to the mesophase. All the Schiff base complexes reported to date display a smectic A phase. The smectic A phase has an intrinsic higher viscosity than the nematic phase. By a proper choice of the counter ion the viscosity of the mesophase can be reduced considerably. For instance, a smectic A phase with a low viscosity is found for Schiff base complexes with perfluorinated alkylsulfates as counter ions.[185]

The sign of $\Delta\chi$ cannot be determined by magnetic susceptibility measurements and has to be obtained by an independent measurement, for instance *via* EPR (angle dependence of the EPR signal)[174] or *via* X-ray diffraction in a magnetic field (distribution of the diffraction maxima with respect to the external magnetic field).[179,185] In Figure 2.54 the determination of the sign of the magnetic anisotropy by X-ray diffraction is illustrated for a smectic A phase. It should be realised that the maximum value for the magnetic anisotropy ($\Delta\chi$) can only be measured on completely aligned samples. For real samples, alignment is never complete, so the measured value of $\Delta\chi$ is smaller than the value which can be theoretically expected.

$\chi_{\parallel}$ and $\chi_{\perp}$ can be measured directly by orientation of an aligned liquid crystal with the director parallel or perpendicular to the magnetic field. This implies that the measurements are carried out in a magnetic field that is not strong enough to reorient the liquid crystal. Alternatively, the aligned mesophase can be frozen into the glassy state. The $\chi_{\parallel}$ and $\chi_{\perp}$

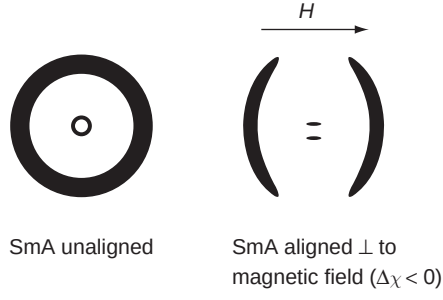

Figure 2.54 Determination of the sign of the magnetic anisotropy by X-ray diffraction

values of a glassy (aligned) mesophase can be measured as if measuring on a single crystal (orienting the sample with its long molecular axis parallel or perpendicular to the magnetic field lines). The situation is quite different for a mesophase in a magnetic field above a certain threshold strength H_0 because, in this case, the mesophase will be aligned by the magnetic field. A nematic phase can be oriented at any temperature within the mesophase because of the low viscosity of this phase. Due to the intrinsic higher viscosity, the smectic A phase can only be oriented at a temperature close to the clearing point. The orientation at this point will be preserved when the mesophase is cooled further. The magnetic anisotropy $\Delta\chi$ cannot be obtained *via* the relation $\Delta\chi = \chi_{||} - \chi_{\perp}$, because only one of the two components $\chi_{||}$ or $\chi_{\perp}$ can be determined. This problem can be overcome by measuring the magnetic susceptibility in the isotropic phase and in the mesophase. In the isotropic phase, χ_{iso} will be measured. It is assumed that χ_{iso} is equal to the average magnetic susceptibility ($\overline{\chi}$), which is defined as $\overline{\chi} = \left(\chi_{||} + 2\chi_{\perp}\right)/3$. In the mesophase the molecules will be oriented in such a way that the axis of maximal magnetic susceptibility will be parallel to the magnetic field. Because of alignment of the paramagnetic molecules, an increase in magnetic susceptibility will be observed (in comparison with $\overline{\chi}$) and the measured value is denoted as χ_{max}. If $\Delta\chi > 0$, χ_{max} corresponds to $\chi_{||}$ and $\Delta\chi = 3/2(\chi_{max} - \overline{\chi})$. If $\Delta\chi < 0$, χ_{max} corresponds to $\chi_{\perp}$ and $\Delta\chi = 3(\overline{\chi} - \chi_{max})$.

Although many experimental techniques are available for the measurements of the magnetic susceptibility, measurement by the Faraday method is convenient in the case of liquid crystals. A small amount of the sample is suspended in an homogeneous magnetic field such that the magnetic field gradient is constant over the whole volume of the sample (Figure 2.55).

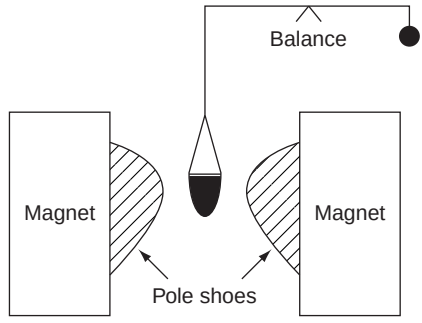

Figure 2.55 Faraday magnetometer

The magnetic susceptibility can be calculated by the use of Equation 2.5, after measurement of the weight of the sample in the presence and in the absence of the magnetic field:

$$\chi_{\text{exp}} = \frac{\Delta m.g.M}{m.H(\frac{\mathrm{d}H}{\mathrm{d}z})} - \chi_{\text{dia}} \tag{2.5}$$

where χ_{exp} is the experimental molar susceptibility (in $\text{cm}^3\ \text{mol}^{-1}$), m is the change in mass of the sample (in g), m is the mass of the sample (in g), M is the molar mass of the compound (in g mol^{-1}) and g is the gravity constant (981 cm s^{-2}). H is the strength of the magnetic field (typically between 0.9 and 1.5 T) and $\mathrm{d}H/\mathrm{d}z$ is the field gradient. χ_{dia} is the correction for the underlying diamagnetism. This correction factor can be calculated applying Pascal's scheme.[169,170] In fact, the experimental magnetic susceptibilities are temperature dependent, that is they decrease with increasing temperature according to the Curie–Weiss law. In calculating the effective magnetic moment, this bare temperature dependence is removed:

$$\mu_{\text{eff}} = \sqrt{\frac{3k}{N_{\text{A}}}} \cdot \sqrt{\chi T} = 2.828\sqrt{\chi T} \tag{2.6}$$

where μ_{eff} is the effective magnetic moment (in Bohr magneton, μ_{B}), k is the Boltzmann constant, N_{A} Avogadro's number, χ the magnetic susceptibility and T the absolute temperature. With this effective magnetic moment it is possible to evaluate changes to the magnetic susceptibility other than those induced by temperature, for example as a result of molecular alignment. The temperature dependence of the effective magnetic moment of the Schiff base complex $[\text{Tb}(LH)_3(\text{DOS})_3]$ during heating and subsequent cooling is shown in Figure 2.56.[179] LH represents the Schiff base *N*-octadecyl-4-tetradecyloxysalicylaldimine. The temperature-independent, constant value during heating the initial, polycrystalline sample points to a pure Curie–Weiss behaviour for the solid state, the following (unoriented $\sim$ magnetically isotropic) smectic A phase and the isotropic phase. On the other hand, when the sample is cooled down from the isotropic phase to the mesophase (in the presence of a magnetic field) a sharp increase in the magnetic moment (μ_{eff}) occurs in the vicinity of the clearing point. Upon further cooling, the magnetic properties varied according to the Curie–Weiss law, but with a

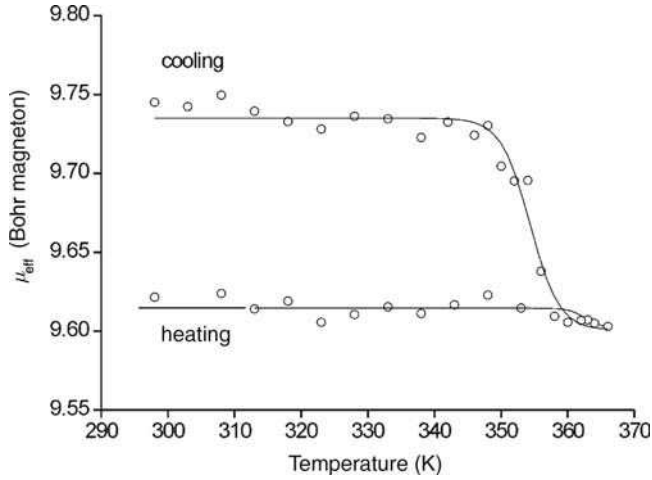

Figure 2.56 Effective magnetic moment μ_{eff} (in Bohr magneton units) of the liquid-crystalline complex $[Tb(LH)_3(DOS)_3]_3$ as a function of the temperature. Reprinted with permission from Galyametdinov *et al.*, 2007 [179]. Copyright (2007) American Chemical Society

higher μ_{eff} than in the heating run. This behaviour can be considered as a magnetic-field-induced orientation in the liquid-crystalline phase of magnetically anisotropic molecules with their axis of maximum magnetic susceptibility parallel to the magnetic field. Alignment of the smectic A phase was not observed during heating of the sample, because of the high viscosity of the mesophase at temperatures close to the melting point. The transitions temperatures of selected $[Ln(LH)_3(DOS)_3]$ complexes are given in Table 2.2,[175] and the results of the magnetic

Table 2.2 Mesophase behaviour of the $[Ln(LH)_3(DOS)_3]$ complexes, where *Ln* stands for a trivalent lanthanide ion, *L*H for the Schiff base *N*-octadecyl-4-tetradecyloxysalicylaldimine and DOS for dodecylsulfate[175]

Lanthanide	Transition temperatures (°C)[a]
Tb	Cr · 61 · SmA · 80 · I
Dy	Cr · 61 · SmA · 82 · I
Ho	Cr · 62 · SmA · 84 · I
Er	Cr · 61 · SmA · 85 · I
Tm	Cr · 60 · SmA · 86 · I
Yb	Cr · 60 · SmA · 87 · I

[a]Cr = crystalline phase, SmA = smectic A phase, I = isotropic liquid.

Table 2.3 Magnetic properties of the $[Ln(LH)_3(DOS)_3]$ complexes, where *Ln* stands for a trivalent lanthanide ion, *L*H for the Schiff base *N*-octadecyl-4-tetradecyloxysalicylaldimine and DOS for dodecylsulfate[179]a

Lanthanide	χ_{iso}	χ_{or}	$\lvert\chi_{or}\,\chi_{iso}\rvert$	$\Delta\chi_{exp}$
Tb	38 470	39 650	1180	−3540
Dy	48 790	44 850	3940	−11 820
Ho	41 820	43 480	1160	−4980
Er	35 820	35 185	635	+952
Tm	24 240	22 550	1690	+2535
Yb	7790	8200	410	+615

[a]All the magnetic susceptibility values (χ) are expressed in 10^{-6} cm^3 mol^{-1}. The calculation of the experimental magnetic anisotropy $\Delta\chi_{exp}$from ($\chi_{or} - \chi_{iso}$) is described in the text. The $\Delta\chi_{exp}$ value was determined at 40 °C.

anisotropy measurements on these complexes are shown in Table 2.3.[179] The $\Delta\chi$ values depend on the counter ion. The highest $\Delta\chi$ have been observed for complexes with perfluorinated counter ions.[185]

Pate *et al*. were the first to investigate the alignment of mesophases of discotic metallomesogens in an external magnetic field.[186] These authors studied metal complexes ($M = Co^{2+}$, Ni^{2+}, Cu^{2+}, Zn^{2+}) of 2,4,7,8,12,13,17,18-octakis(*n*-decylthio)porphyrazine. The compounds were heated to the isotropic state in the absence of an applied magnetic field. Magnetic alignment was induced by cooling in an applied magnetic field. The liquid crystal domains were aligned in such a way that the columns aligned with their director perpendicular to the magnetic field lines. Once the mesophase was aligned, removal of the magnetic field has hardly any effect on the alignment of the domains. This points to a very long relaxation time of the aligned liquid crystal domains. The molecular order in the aligned domains could be frozen into the solid state. The threshold magnetic field for alignment of the diamagnetic nickel(II) and zinc(II) complexes was about 1.2 T. The threshold aligning field was defined by the authors as that magnetic field strength at which a maximum alignment could be obtained and beyond which stronger magnetic field did not result in an increased alignment. The minimum magnetic field strength at which alignment of the nickel(II) and zinc(II) samples could be observed was 0.5 T.

The threshold magnetic field for alignment of the paramagnetic cobalt(II) complex was only half that of the diamagnetic nickel(II) and zinc(II) complexes. The paramagnetic moment of the cobalt(II) complex is within the *xy* plane of the ring. This enhances the tendency of the ring planes to align parallel to the magnetic field lines. Therefore, the

alignment of the columnar directors perpendicular to the magnetic field is easier. However, no well-aligned domains could be obtained for the copper(II) complex at an applied field of 1 T. This can be attributed to the fact that the paramagnetic moment is directed along the molecular z axis, whereas the diamagnetic moment is within the xy plane of the macrocycle ring. Because the diamagnetic and paramagnetic moments are of comparable magnitude, there is not preferential direction for domain alignment.

The alignment of the mesophase of the cobalt(II) complex was investigated in more detail in a follow-up study.[187] Upon cooling from the isotropic phase to the columnar mesophase in the presence of a static magnetic field (between 0.4 and 1.1 T), the cobalt(II) complex formed oriented columnar domains with the columnar directors being isotropically distributed in the plane normal to the external magnetic field. When the samples were continuously spun during cooling in a static applied magnetic field of 1.0 T, the cobalt(II) complex was observed to form uniaxially aligned columnar superstructures with the columnar domain directors being parallel to the rotation axis, which was normal to the external magnetic field. The optimal rotation speed for the alignment was found to be as low as 5–10 rpm. Aligned domains of a macroscopic size (*ca* 1 cm) could be obtained. A study of the influence of the alkyl side-chain length on the magnetic alignment process revealed that with the longer chains the magnetic alignment can occur at lower temperatures (due to the reduced clearing point), which facilitates the alignment process and reduces the problems with thermal decomposition of the samples, but the magnetic field strength required for alignment becomes higher.[188] The latter observation can be explained by an increase in entropy due to longer alkyl chains. The authors suggested that for a proper alignment of discotic metallomesogens, a proper selection of the alkyl side-chain length should be made.

Aligned domains of discotic liquid crystals forming columnar mesophases are of importance for the fabrication of electronic devices based on these materials. Such aligned domains can be obtained by magnetic alignment of the liquid crystals on a substrate by solvent evaporation in the presence of an external magnetic field. Solutions of discotic liquid crystals form randomly oriented columnar structures on substrates during drop-casting or spin-coating processes. Choi *et al*. drop-cast a solution of the 2,4,7,8,12,13,17,18-octakis(*n*-decylthio)porphyrazine cobalt(II) complex in hexane (4% w/w) on a quartz plate in the presence of an applied magnetic field ($\mathbf{H} = 0.7$ T) with the magnetic field lines being parallel to

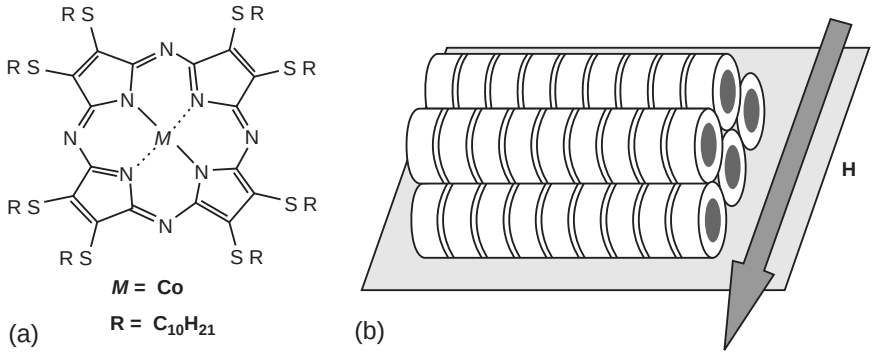

Figure 2.57 Mesogenic 2,4,7,8,12,13,17,18-octakis(*n*-decylthio)porphyrazine cobalt(II) complex and its alignment on a quartz substrate in an external magnetic field. Reprinted with permission from Lee *et al.*, 2006 [189]. Copyright (2006) Elsevier

the substrate plane (Figure 2.57).[189] It was shown by small angle neutron scattering (SANS) that structures with well-aligned columnar domains were obtained. Even better alignment could be obtained by replacing the quartz plate by an octadecyltrichlorosilane-functionalised silicon wafer.[190]

The *magnetoelectric effect* of metallomesogens has been studied by Domracheva *et al.*[191] This effect describes the influence of an external magnetic field on the magnetic properties of materials and consists of the creation of an additional magnetisation by the externally applied electric field. The effect can be observed for complexes of paramagnetic ions lacking an inversion centre. In mesophases, there can be an internal electric field present due to ferroelectric ordering of the molecules in smectic phases, and this internal electric field can have the same effect on the magnetic properties as an external electric field, that is the internal magnetic field can induce an additional magnetisation in the mesogen. For their investigations Domracheva *et al.* selected iron(III) complexes which were first described by Galyametdinov *et al.* (Figure 2.58).[192] These complexes exhibit a smectic phase. It was observed by EPR spectroscopy that the chelate plane of the complex is oriented perpendicular to the magnetic field. This means that the molecules have a maximum magnetic susceptibility along the *z*-axis, that is along the Fe–Cl bond. This is an unusual orientation, because model calculations have shown that in these calamitic molecules the diamagnetic anisotropy is larger than the paramagnetic anisotropy, so that the molecules are expected to align parallel to the magnetic field (positive

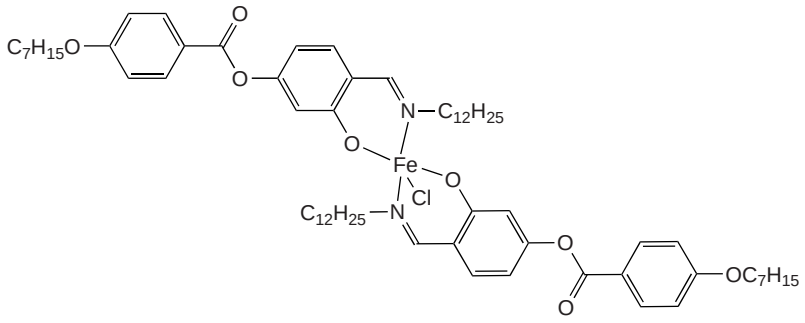

Figure 2.58 Mesogenic iron(III)-containing metallomesogen

diamagnetic anisotropy). It is assumed that the extra paramagnetic anisotropy necessary to get this orientation comes from the action of the local electric field present in the mesophase. The local ordering of the Fe–Cl electric dipoles along the chains in the smectic layers induces an additional magnetic susceptibility *via* the magnetoelectric effect, resulting in an increase of the total paramagnetic anisotropy of the mesophase.

Paramagnetic metal complexes have been doped into liquid crystals to achieve easier alignment. The critical magnetic field required for reorientation of 5CB doped with the iron(III) complex 5,10,15,20-tetraphenylporphyrinatoiron(III) chloride, FeTPPCl, was found to be one fourth of that needed for alignment of pure 5CB.[193] The concentration of the paramagnetic dopand was about 1% v/v. A similar effect was observed for the 5,10,15,20-tetraphenylporphyrinatomanganese(III) chloride, MnTPPCl.[194] It is assumed that there is an axial coordination between the cyano group of 5CB and the metal ion in the macrocyclic ring, resulting in a coupling between the paramagnetic complexes and the 5CB molecules. On the other hand, no reduction in the critical magnetic field was observed doping 5CB with the diamagnetic zinc(II) complex 5,10,15,20-tetraphenylporphyrinatozinc(II), ZnTPP. However, for unsymmetrically substituted 5,10,15,20-tetraphenylporphyrinatozinc(II) complexes the critical magnetic field could be decreased.[195] This was explained by the much larger diamagnetic anisotropies for the substituted complexes in comparison with ZnTPP. To show that the presence of a paramagnetic centre is not a sufficient condition, it should be noticed that a decrease in the critical magnetic field was also measured for 5CB doped with a five-coordinate copper(II) complex, but not for a structurally

rather similar six-coordinate copper(II) complex.[196] Even among the iron(III) complexes differences were observed. Although easier alignment of 5CB was observed upon doping with 5,10,15,20-tetraphenylporphyrinatoiron(III) chloride, this was not the case for doping with 5-(4-(3-pyridyloxyl)butoxy)phenyl-10,15,20-triphenylporphyrinatoiron(III) chloride.[197]

Another approach towards liquid crystals that can easily be aligned in an external magnetic field is the use of magnetic nano- or microparticles to dope liquid crystals.[198] Brochard and de Gennes proposed, in a theoretical paper, to disperse anisotropic magnetic particles (with a length-to-width ratio of at least 10) into a liquid-crystalline matrix.[199] The applied magnetic field would change the orientation of the magnetic nanoparticles and the nanoparticles would drag the liquid crystal molecules to change orientation. Such magnetic suspensions in nematic liquid crystals were called *ferronematics*. Experimentally, the dispersion of magnetic nanoparticles into a thermotropic liquid crystal was first done by Rault *et al*.[200] These authors mixed the liquid crystal MBBA (*p*-methoxybenzilidene-*p*-*n*-butylaniline) with γ-Fe_2O_3 (maghemite) magnetic needle-like particles, coated with surfactants. In the isotropic phase, no remanent magnetisation was observed, while in the nematic phase, large remanent magnetisations were observed which disappeared at the nematic–isotropic transition. Chen and Amer doped the MBBA with similar particles coated with dimethyloctadecylaminopropyltrimethoxysilyl chloride (DMOAP).[201] Ferronematic lyotropic liquid crystals were first prepared by Liebert and Martinet by doping Fe_3O_4 (magnetite) nanoparticles with an average diameter of 15.4 nm into a lyotropic phase formed by 35.9% of sodium decylsulfate, 7.2% of decanol and 56.9% of D_2O.[202] The ferronematic phase could be aligned by a magnetic field with a strength of only a few Gauss, which is about a factor 10^3 weaker than the magnetic field required for the alignment of the nematic phase. Addition of the chiral compound brucine led to the formation of a cholesteric phase, which could be transformed into a cholesteric lyotropic phase upon addition of Fe_3O_4 nanoparticles. Fabre *et al*. obtained lyotropic *ferrosmectics* by doping γ-Fe_2O_3 particles, stabilised by organophosphor surfactants, into a lamellar phase formed by water, sodium dodecylsulfate and 1-pentanol.[203] The layer thickness of the lamellar phases can be changed by addition of cyclohexane. A unique feature of the ferrosmectics is that the lamellae orientate in the direction of the magnetic field.[204]

2.5.2 Spin-Crossover Phenomena

Spin-crossover metallomesogens are multifunctional materials that combine spin-crossover properties and liquid-crystalline properties in one compound.[205] The spin-crossover effect is a reversible magnetic effect in inorganic materials where the spin state and the magnetic moment of a central *d*-block metal ion can be changed or controlled by external stimuli such as a change in temperature, pressure or by irradiation with light.[206] Spin-crossover occurs in octahedral complexes with a d^4 to d^7 electronic configuration. The best known example of an ion showing the spin-crossover effect is Fe(II) where the electronic configuration is $3d^6$, and the electrons can occupy all the lower t_{2g} level (low-spin, strong field) or they can occupy both t_{2g} and e_g levels (high-spin, weak field). In Figure 2.59, the low-spin to high-spin transition is shown for a $3d^6$ system. The spin state on the Fe^{II} ion changes from diamagnetic ($S = 0$) in the low-spin state, to paramagnetic ($S = 2$) in the high-spin state. The changes in the electronic structure (low-spin $\leftrightarrow$ high-spin transition) lead to structural changes and to changes in physical properties like magnetic moment, dielectric constant and colour.

The spin-crossover effect in iron(II) compounds is often accompanied by a striking colour change, which is the result of the increase in intensity of the metal-to-ligand charge transfer (MLCT) band around 550 nm, associated with the electron delocalisation from the t_{2g}-orbitals of the Fe^{II} ion to the π^*-orbitals of the ligands, which is facilitated by the high-spin to low-spin change. Typically low-spin Fe^{II} complexes that are white turn into pink high-spin Fe^{II} complexes upon heating above the spin transition temperature. Cooling of the pink complexes below the spin transition temperature give the white complexes again, showing that the effect is reversible. For some Fe^{II} complexes a light-induced low-spin $\rightarrow$ high-spin transition can be induced by irradiation with green light into a

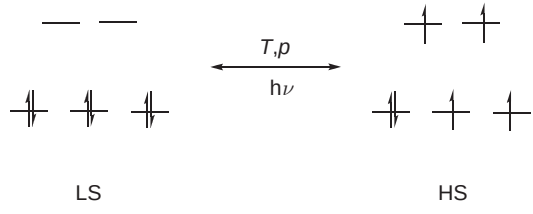

Figure 2.59 Low-spin (LS) to high-spin (HS) transition in a d^6 complex by external stimuli

d–d or metal-to-ligand charge transfer (MLCT) absorption band at temperatures well below the thermal spin transition temperature. This phenomenon is the *light-induced excited spin-state trapping* (LIESST) effect.[207,208]

As well as for Fe^{II} complexes ($3d^6$), spin-crossover effects are observed for Fe^{III} complexes ($3d^5$), Co^{II} complexes ($3d^7$) and, to a lesser extent, for Cr^{II} complexes ($3d^4$) and for Mn^{III} complexes ($3d^4$). Spin-crossover materials could find applications for the fabrication of rewritable optical, thermal or pressure memories at a nanometre scale.

A first step in the direction of the design of spin-crossover metallomesogens was achieved by Galyametdinov *et al.* who reported an iron(III) complex that combined both liquid-crystalline and spin-crossover properties.[209] Unfortunately, the two properties were not synchronous in the complex, inthe sense that the spin-crossover transition occurred at temperatures far below the temperature region in which the mesophase was stable. Their metallomesogen was a pseudo-octahedral cationic iron(III) complex $[Fe(L)_2][PF_6]$ with *N*-alkoxysalicylidenyl-*N*′-ethyl-*N*-ethylenediamine Schiff base ligands and hexafluorophosphate counter ions (Figure 2.60). The complex exhibits a smectic A phase between 388 and 419 K. It was observed that the molecules in the smectic A phase could be aligned by an external magnetic field, due to the pronounced magnetic anisotropy of the paramagnetic iron(III) complex. Measurement of the magnetic moment as a function of temperature revealed that the spin-crossover transition was not sharp, but gradually occurred (Figure 2.61). At 4 K about 88% of Fe^{3+} was in the low-spin state ($S = 1/2$), whereas Fe^{3+} in the high-spin state ($S = 5/2$) occurred at room temperature. These results were confirmed by ^{57}Fe Mössbauer spectroscopy. The spin transition

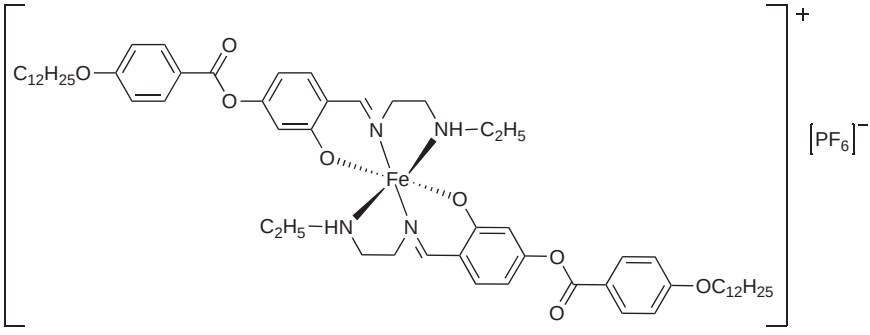

Figure 2.60 Pseudo-octahedral cationic iron(III) complex $[Fe(L)_2][PF_6]$ with *N*-alkoxysalicylidenyl-*N*′-ethyl-*N*-ethylenediamine Schiff base ligands, showing spin-crossover behaviour

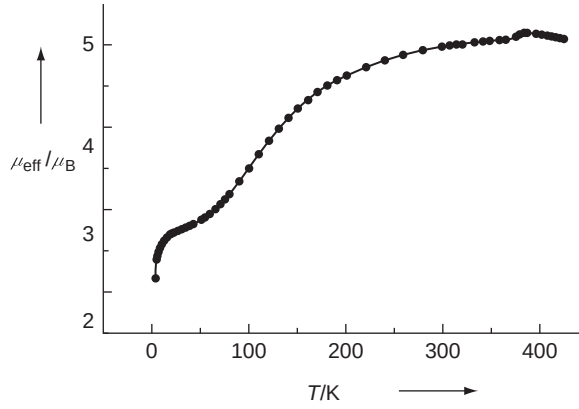

Figure 2.61 Temperature dependence of the effective moment of the iron(III) complex $[Fe(L)_2][PF_6]$ shown in Figure 2.60. Reprinted with permission from Galyametdinov *et al.*, 2001 [209]. Copyright (2001) Wiley-VCH

temperature $T_{½}$, the temperature at which 50% of each spin state is present in the complex, was found to be around 125 K.

Fujiyaga *et al.* have claimed the coexistence of the spin-crossover and liquid crystal properties in the same temperature region for one-dimensional iron(II) complexes with functionalised triazole ligands.[210] Unfortunately, the authors do not give sufficient evidence for the occurrence of a mesophase above the melting point and it seems that the described phase transitions corresponded to a simple melting of the alkyl chains. However, the interesting features of these compounds are the high-spin transition temperatures (up to 310 K). Hyami *et al.* succeeded in synthesising a liquid-crystalline iron(II) complex with Schiff base ligands (Figure 2.62) that exhibits a thermal and a light-induced spin transition.[211] The complex shows a smectic A phase between 345 and 400 K. The thermal spin transition temperature is 217 K, while the light-induced spin transition temperature is 60 K. Further work showed that the presence of the three hexadecyloxy chains in the Schiff base ligands is critical for the observation for the light-induced spin transition.[212] Corresponding complexes of ligands with one or two hexadecyloxy chains exhibit liquid-crystalline behaviour, but not the light-induced spin-crossover effect. The complex of the ligand with two hexadecyloxy chains still shows a thermal spin transition, but not a light-induced one.

The transition temperature for the thermal spin-crossover has a more pronounced dependence on the alkyl chain length of the ligands than the transition temperature for the light-induced spin transition (LIESST).[213]

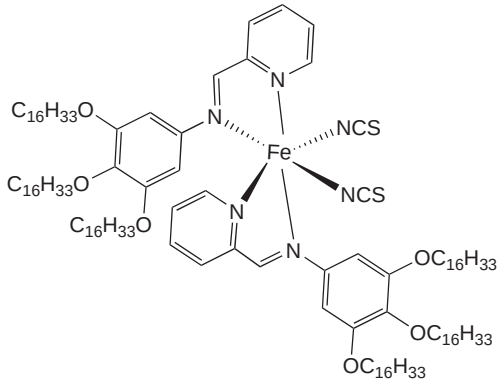

Figure 2.62 Liquid-crystalline iron(II) complex with Schiff base ligands that exhibits a thermal and a light-induced spin transition

For ionic iron(II) complexes of 2-(2-*n*-alkyl-tetrazol-5-yl)-1,10-phenanthroline (Figure 2.63) with perchlorate or tetrafluoroborate counter anions an influence of the alkyl chain length on the thermal spin-transition temperatures was observed also.[214] The complexes with long alkyl chains exhibit an unidentified mesophase. The iron(II) complexes of 2,6-bis(benzimidazol-2′-yl)-4-hexadecyloxypyridine and 2,6-bis(*N*-hexadecylbenzimidazol-2′-yl)pyridine with tetrafluoroborate counter ions (Figure 2.64) exhibit an unidentified mesophase.[215] The compound with the 2,6-bis(benzimidazol-2′-yl)-4-hexadecyloxypyridine showed a thermal and light-induced spin transition, whereas the compound with the 2,6-bis(*N*-hexadecylbenzimidazol-2′-yl)pyridine ligand was in the low-spin state.

Seredyuk *et al.* used a two-step procedure to obtain metallomesogens with a synchronous spin transition and a solid-to-mesophase transition.[216] They started with the selection of an iron(II) complex with triazole ligands

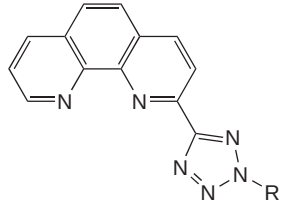

Figure 2.63 2-(2-*n*-Alkyl-tetrazol-5-yl)-1,10-phenanthroline ligand used for the synthesis of iron(II) metallomesogens showing spin-crossover effects

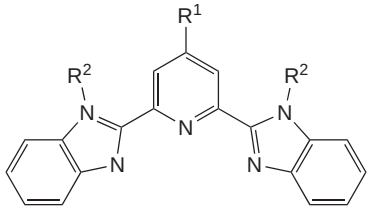

Figure 2.64 2,6-*bis*(Benzimidazol-2′-yl)-4-hexadecyloxypyridine ($R^1 = OC_{16}H_{33}$, $R^2 = H$) and 2,6-*bis*(*N*-hexadecylbenzimidazol-2′-yl)pyridine ($R^1 = H$, $R^2 = C_{16}H_{33}$)

that exhibits an abrupt spin transition near or above room temperature and in a second step they attached long alkyl chains to the aromatic ring of the triazole ligand (Figure 2.65). Reaction of 3,5-dialkoxy-*N*-4*H*-1,2,4-triazol-4-ylbenzamide (*L*) and iron(II) tosylate gave complexes with the general formula $[Fe(L)_2](4\text{-}MeC_6H_4SO_3)_2{\cdot}H_2O$. The corresponding zinc(II) complexes were obtained also. The complexes exhibited a hexagonal columnar phase. The spin transition occurred upon dehydration in the temperature range where the compound shows the hexagonal columnar mesophase. The anhydrous complexes show a spin state transition between 280 and 325 K. The authors concluded that the spin-transition behaviour in these metallomesogens is not driven by a phase transition from the crystalline to the liquid-crystalline state, but rather by subtle structural and electronic modifications tuned by the crystal packing, which determines the ligand field strength and the spin-crossover behaviour.

An interesting property of thin films of the iron(II) complexes in the mesophase is their thermochromism. A reversible colour change from purple (low-spin state) to whitish (high-spin state) was observed by heating or cooling the compound around 60 °C. This work was extended to complexes in which the tosylate counter ions were replaced by tetrafluoroborate and triflate ions.[217] The resulting compounds were polymeric with a one-dimensional structure. Several of the complexes were liquid-crystalline at room temperature and their mesophase was either hexagonal

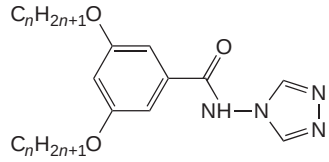

Figure 2.65 Mesogenic triazole ligand forming complexes of the type $[Fe(L)_2](4\text{-}MeC_6H_4SO_3)_2{\cdot}H_2O$

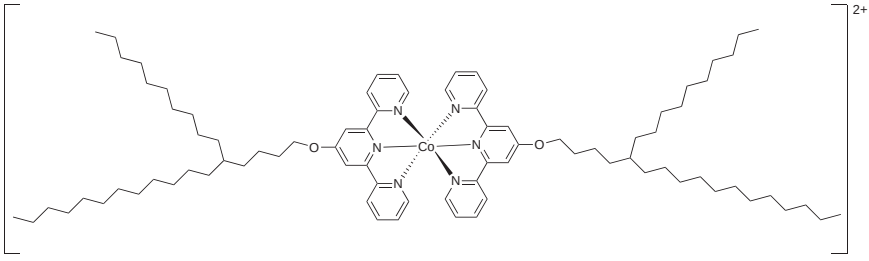

Figure 2.66 Mesogenic cobalt(II) complex with functionalised terpyridine ligands. The two tetrafluoroborate counter ions are not shown

columnar phase or a lamellar columnar phase. The low-spin ↔ high-spin transition occurred at temperatures close to room temperature.

An example of a spin-crossover metallomesogen in which the spin transition coincides with the solid-to-mesophase transition temperature is a cobalt(II) complex of a functionalised terpyridine ligand with a branched long alkyl chain and tetrafluoroborate counter anions, which was reported by Hayami *et al.* (Figure 2.66).[218] The coincidence of the two transition temperatures was achieved by subtle changes in the length and type (linear *vs* branched) of the alkyl chains. Three different polymorphic forms with melting points at 278, 288 and 296 K were observed for the complex. The melting point of the virgin sample was 288 K. The complex exhibited a smectic A mesophase up to 523 K. The spin transition upon heating occurred at 288 K, whereas upon cooling the transition was observed at 284 K. The transition from the crystalline to the liquid-crystalline state drives the spin-crossover effect.

Seredyuk *et al.* also showed that for one type of metallomesogen, subtle changes in the ligand (alkyl chain length) or counter ion can results in three classes of systems with different interplay or synergism between the spin-crossover and solid-to-mesophase phase transition: (i) systems with coupled phase transitions, where the structural changes associated with the phase transition from the crystalline to liquid-crystalline drives the spin state transition; (ii) systems where both transitions coexist in the same temperature region, but are not coupled; and (iii) systems with uncoupled phase transitions where the phase transitions take place in very different temperature regions.[219] Iron(II) metallomesogens derived of the ligand tris[3-aza-4-((5-C_n)(6-R)-(2-pyridyl))but-3-enyl]amine with C_n = hexyloxy, dodecyloxy, hexadecyloxy, octadecyloxy, eicosyloxy, R = hydrogen or methyl (C6,16,18,20-trenH or C6,12,18-trenMe) give examples of complexes belonging to each of the above mentioned three classes. The complexes

have the general formula $[Fe(C_n\text{-trenR})](A)_2 \cdot sH_2O$ ($s \geq 0$), with $A = ClO_4^-$, F^-, Cl^-, Br^- and I^-. In these compounds the iron atoms adopt a pseudo-octahedral symmetry and are surrounded by six nitrogen atoms belonging to imino groups and pyridines of the ligands C_n-trenH and C_n-trenMe. The complexes exhibit either a smectic A phase (SmA) or an unidentified smectic phase (SmX). It was found that, in general, the spin state depends mainly on the degree of hydration of the compound and not on the state of matter, being solid or liquid.

The compounds $\{[Fe(C_n\text{-trenH})](X)_2 \cdot 0.5H_2O\}$, where $n = 16$, 18, 20 and $X = Cl$ are examples of systems of type (i), where the change of aggregate of matter (Cr $\rightarrow$ SmX) drives the spin state transition. The compounds are dark purple in the low-spin state (crystalline state) and become light purple-brown when the iron(II) atoms are in the high-spin state (smectic A phase). The authors conclude that it is very difficult to predict the effect of hydration or counter ion on the spin-crossover behaviour, but they realize that control of the hydration and an appropriate choice of the anion are important tools to modify the transition temperatures or the nature of the transition. For compounds of class (i) it is also possible that the phase transition from the crystalline to liquid-crystalline state interferes with the spin state transition, but it is not the driving force of the spin-crossover process. It only affects the spin transition process by modifying slightly its completeness and cooperativity. Gütlich and co-workers observed this behaviour for iron(II)-containing metallomesogens based on the ligand 2,2,2-tris(2-aza-3-((5-alkoxy)(6-methyl)(2-pyridyl))prop-2-enyl)ethane (C_n-tameMe).[220] The complexes have the formulae $[Fe(C_n\text{-trenR})](A)_2 \cdot sH_2O$ ($s \geq 0$), with $A = ClO_4^-$ or BF_4^-, and $n = 6$, 10, 12, 14, 16, 17, 18, or 20. The complexes exhibit a smectic mesophase (SmX). In this mesophase the alkyl chains are in a molten state, but there is restricted movement through the ionic layer consisting of cationic spin-cross over complexes and counter anions. The complexes with tetrafluoroborate counter ions showed thermochromic behaviour. They were dark violet in the low-spin state ($T <$ 275 K, crystalline state), but became red in the high-spin state ($T > 275$ K, crystalline and liquid-crystalline state).

2.5.3 Single Molecule Magnets

A *single molecule magnet* (SMM) is a molecule that can be magnetised in a magnetic field and that will remain magnetised even after switching off

the magnetic field.[221] In contrast to traditional bulk magnets, the magnetic properties of single molecular magnets are not due to cooperative effects within magnetic domains, but are due to the molecule itself. At low temperatures, below the blocking temperature (typically a few degrees above the absolute zero temperature) the system can be trapped in one of the high-spin energy wells. This hysteresis of purely molecular origin allows a single molecule to be considered as the ultimate limit for information storage, because one bit is represented by one molecule. Because single molecule magnets show quantum mechanical properties like the quantum tunnelling of the magnetisation, these compounds are of interest for quantum computing. In order that single molecule magnetism to be observed, a certain number of requirements needs to be fulfilled: (i) a high-spin ground state; (ii) a high zero-splitting (due to a high magnetic anisotropy); and (iii) a negligible magnetic interaction between the molecules.

Most single molecular magnets belong to a class of compounds called *exchange coupled clusters*, where a small number (up to about 30) paramagnetic transition metal ions are linked together by bridging ligands like chloride, hydroxide, methoxide or acetate groups. A typical example is the mixed valence polymetallic compound 'Mn12', $[Mn_{12}O_{12}(OAc)_{16}(H_2O)_4]$, which contains twelve manganese centres linked by bridging acetate groups.[222–224] Eight of the manganese ions form a ring, each having a charge of +3 and a spin $S = 2$. The other four manganese ions form a tetrahedron, each having a charge of +4 and a spin $S = 3/2$. The exchange interactions within the molecule are such that the spins of the ring align themselves in opposition to the spins of the tetrahedron, giving the molecule a total net spin $S = 10$.

Terrazzi *et al*. succeeded in functionalising the Mn12 complex by mesogenic ligands in order to favour the self-organisation into liquid-crystalline phases, while preserving the magnetic properties of the original core.[225] They replaced the acetate groups in the original cluster with derivatives of gallic acid with methoxy, dodecyloxy or cyanobiphenyloxyundecyloxy groups *via* a ligand exchange reaction (Figure 2.67). The complex with the methoxy groups was not liquid-crystalline. The complex with the dodecyloxy chains exhibited a cubic mesophase (three-dimensional positional order) between –11.5 and 150.0 °C, whereas the complex with the cyanobiphenyloxyundecyloxy groups exhibited a smectic mesophase (one-dimensional positional order) between 40.5 and 150.0 °C. The smectic phase was of a special type, namely a *filled random mesh smectic phase*. The molecular arrangement in this smectic phase can be described as two incompatible segments (mesogens and aliphatic

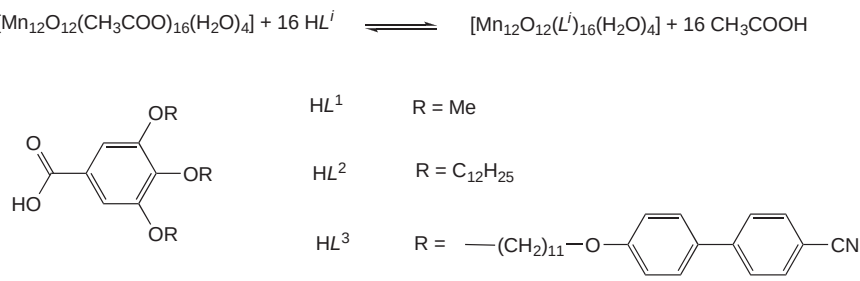

Figure 2.67 Synthesis of liquid-crystalline analogues of the manganese cluster 'Mn12', $[Mn_{12}O_{12}(OAc)_{16}(H_2O)_4]$, and structure of the gallic acid derivatives HL^1, HL^2 and HL^3

spacers) forming alternating layers, with tilt and interdigitation of the mesogens between successive periods, and the Mn12 cores being located in the aliphatic sublayers and arranged into a square-like planar array. There is no long range correlation between the layers. The complexes were not thermally stable above 150.0 °C. The magnetic properties were preserved upon functionalisation and the molecules. The blocking temperature of the complex with the cyanobiphenyloxyundecyloxy groups is 2.4 K.

2.6 CONCLUSIONS

The incorporation of metal ions into liquid crystals gives access to soft molecular materials with interesting magnetic, optical and electronic properties. Although the unique physical properties of metallomesogens and the opportunities created by these materials have been recognised by the earliest workers in this field, in-depth exploration of their properties has for a long time been hampered by the high transition temperatures and limited thermal stability of metallomesogens. However, a better understanding of the relationship between chemical structure and thermal behaviour of metallomesogens presently allows metal-containing liquid crystals with a stable mesophase to be prepared at moderate temperatures or even at room temperature. The availability of these new classes of metallomesogens facilitates the exploration of their physical properties. The magnetic and luminescent properties, especially, have been investigated during recent studies and have shed new light on potential applications of metallomesogens.

REFERENCES

[1] D.W. Bruce, *J. Chem. Soc., Dalton Trans.*, 2983–2989 (1993).
[2] D. W. Bruce, *Adv. Mater.*, **6**, 699–701 (1994).
[3] R. Gimenez, D. R. Lydon and J. L. Serrano, *Curr. Opin. Solid State Mater. Sci.*, **6**, 527–535 (2002).
[4] A. M. Giroud-Godquin and P. M. Maitlis, *Angew. Chem. Int. Ed. Engl.*, **30**, 375–402 (1991).
[5] S. A. Hudson and P. M. Maitlis, *Chem. Rev.*, **93**, 861–885 (1993).
[6] A. P. Polishchuk and T. V. Timofeeva, *Russ. Chem. Rev.*, **62**, 291–321 (1993).
[7] P. Espinet, M. A. Esteruelas, L. A. Oro, J. L. Serrano and E. Sola, *Coord. Chem. Rev.*, **117**, 215–274 (1992).
[8] B. Porta, J. Khamsi and J. C. Noveron, *Curr. Org. Chem.*, **12**, 1298–1321 (2008).
[9] B. Donnio and D. W. Bruce, *Struct. Bond*, **95**, 193–247 (1999).
[10] D. W. Bruce in *Inorganic Materials*, 2nd edn (eds D. W. Bruce and D. O'Hare), John Wiley & Sons, Ltd, Chichester, Chapter 8, 1996, pp. 429–522.
[11] S. R. Collinson and D. W. Bruce Metallomesogens – Supramolecular Organisation of Metal Complexes in Fluid Phases, in *Perspectives in Supramolecular Chemistry: Transition Metals in Supramolecular Chemistry*, vol. **5** (ed. J. P. Sauvage), Wiley, Inc., New York, 1999, pp. 285–369.
[12] B. Donnio, D. Guillon, R. Deschenaux and D. W. Bruce, Metallomesogens, in *Comprehensive Coordination Chemistry II*, vol. **7** (eds J. A. McCleverty and T. J. Meyer), Elsevier, Oxford, 2003, pp. 357–627.
[13] K. Binnemans and C. Görller-Walrand, *Chem. Rev.*, **10**, 2303–2345 (2002).
[14] C. Piguet, J.-C.G. Bünzli, B. Donnio and D. Guillon, *Chem. Commun.*, 3755–3768 (2006).
[15] D. W. Bruce, *Acc. Chem. Res.*, **33**, 831–840 (2000).
[16] C. Imrie, P. Engelbrecht, C. Loubser and C. W. Cleland, *Appl. Organomet. Chem.*, **15**, 1–15 (2001).
[17] R. Deschenaux and J. W. Goodby, Ferrocene-Containing Thermotropic Liquid Crystals, in *Ferrocenes: Homogeneous Catalysis, Organic Synthesis, Materials. Science* (eds A. Togni, and T. Hayashi), Wiley-VCH Verlag GmbH, Weinheim, 1995, pp. 471–495.
[18] N. Hoshino, *Coord. Chem. Rev.*, **174**, 77–108 (1998).
[19] A. M. Giroud-Godquin, *Coord. Chem. Rev.*, **178**, 1485–1499 (1998).
[20] J. L. Serrano and T. Sierra, *Coord. Chem. Rev.*, **242**, 73–85 (2003).
[21] K. Binnemans, *Chem. Rev.*, **105**, 4148–4204 (2005).
[22] F. Neve, *Adv. Mater.*, **8**, 277–289 (1996).
[23] L. Oriol, M. Pinol and J. L. Serrano, *Progr. Polym. Sci.*, **22**, 873–911 (1997).
[24] L. Oriol and J. L. Serrano, *Adv. Mater.*, **7**, 348–369 (1995).
[25] B. Donnio, Lyotropic metallomesogens, *Curr. Opin. Coll. Interface Sci.*, **7**, 371–394 (2002).
[26] P. Davidson and J. C. P. Gabriel, *Curr. Opin. Coll. Surf. Sci.*, **9**, 377–383 (2005).
[27] J. C. P. Gabriel and P. Davidson, *Top. Curr. Chem.*, **226**, 119–172 (2003).
[28] P. Davidson, P. Batail, J. C. P. Gabriel, J. Livage, C. Sanchez and C. Bourgaux, *Progr. Polym. Sci.*, **22**, 913–936 (1997).
[29] J. C. P. Gabriel and P. Davidson, *Adv. Mater.*, **12**, 9–20 (2000).

[30] A. S. Sonin, *Colloid J*., **60**, 129–151 (1998).
[31] A. S. Sonin, *J. Mater. Chem*., **8**, 2557–2574 (1998).
[32] J. L. Serrano, (ed.), *Metallomesogens: Synthesis, Properties and Applications*, Wiley-VCH Verlag GmbH, Weinheim, 1996.
[33] D. W. Bruce, D. A. Dunmur, P. M. Maitlis, M. M. Manterfield and R. Orr, *J. Mater. Chem*., **1**, 255–258 (1991).
[34] W. Pyzuk, E. Gorecka, A. Krowczynski, and J. Przedmojski, *Liq. Cryst*., **14**, 773–784 (1993).
[35] C. Versace, G. Cipparrone, D. Luchetaa, D. Pucci and M. Ghedini, *Mol. Cryst. Liq. Cryst*., **212**, 313–318 (1992).
[36] K. L. Marshall, G. Painter, K. Lotito, A. G. Noto and P. Chang, *Mol. Cryst. Liq. Cryst*., **454**, 47–79 (2006).
[37] A. M. Giroud and U. T. Mueller-Westerhoff, *Mol. Cryst. Liq. Cryst*., **41**, 11–13 (1977).
[38] A. M. Giroud, A. Nazzal and U. T. Mueller-Westerhoff, *Mol. Cryst. Liq. Cryst*., **56**, 225–228 (1980).
[39] U. T. Mueller-Westerhoff, A. Nazzal, R. J. Cox and A. M. Giroud, *Mol. Cryst. Liq. Cryst*., **56**, 249–255 (1980).
[40] K. L. Marshall, B. Schudel and I. A. Lippa, *SPIE*, **5213**, 201–212 (2003).
[41] K. L. Marshall and S. D. Jacobs, *Mol. Cryst. Liq. Cryst*., **159**, 181–196 (1988).
[42] D. W. Bruce, D. A. Dunmur, S. E. Hunt, P. M. Maitlis and R. Orr, *J. Mater. Chem*., **1**, 857–861 (1991).
[43] M. Ghedini, D. Pucci, A. Crispini, M. Ghedini, D. Pucci, A. Crispini, I. Aiello, F. Barigelletti, A. Gessi and O. Francescangeli, *Appl. Organomet. Chem*., **13**, 565–581 (1999).
[44] K. Ohta, H. Hasebe, M. Moriya, T. Fujimoto and I. Yamamoto, *J. Mater. Chem*., **1**, 831–834 (1991).
[45] K. Ohta, H. Hasebe, M. Moriya, T. Fujimoto and I. Yamamoto *Mol. Cryst. Liq. Cryst*., **208**, 43–54 (1991).
[46] K. Ohta, M. Moriya, M. Ikejima, H. Hasebe, T. Fujimoto and I. Yamamoto, *Bull. Chem. Soc. Jpn*., **66**, 3553–3558 (1993).
[47] K. Ohta, M. Ikejima, M. Moriya, H. Hasebe and I. Yamamoto, *J. Mater. Chem*., **8**, 1971–1977 (1998).
[48] K. Ohta, M. Moriya, M. Ikejima, H. Hasebe, T. Fujimoto and I. Yamamoto, *Bull. Chem. Soc. Jpn*., **66**, 3559–3564 (1993).
[49] H. Horie, A. Takagi, H. Hasebe, T. Ozawa and K. Ohta, *J. Mater. Chem*., **11**, 1063–1071 (2001).
[50] M. J. Baena, J. Buey, P. Espinet, H. S. Kitzerow and G. Heppke, *Angew. Chem. Int. Ed. Engl*., **32**, 1201–1203 (1993).
[51] C. Reichardt, Solvatochromic dyes as solvent polarity indicators, *Chem. Rev*., **94**, 2319–2358 (1994).
[52] F. Camerel, R. Ziessel, B. Donnio, C. Bourgogne, D. Guillon, M. Schmutz, C. Iacovita and J. P. Bucher, *Angew. Chem. Int. Ed*., **46**, 2659–2662 (2007).
[53] E. Terazzi, S. Suarez, S. Torelli, H. Nozary, D. Imbert, O. Mamula, J. P. Rivera, E. Guillet, J. M. Benech, G. Bernardinelli, R. Scopelliti, B. Donnio, D. Guillon, J.-C.G. Bünzli and C. Piguet, *Adv. Funct. Mater*., **16**, 157–168 (2006).
[54] R. W. Corkery and J. P. D. Martin, *J. Lumin*., **82**, 1–8 (1999).

[55] H. Nozary, C. Piguet, P. Tissot, G. Bernardinelli, J.-C.G. Bünzli, R. Deschenaux and D. Guillon, *J. Am. Chem. Soc.*, **120**, 12274–12288 (1998).
[56] K. Binnemans, L. Malykhina, V. S. Mironov, W. Haase, K. Driesen, R. Van Deun, L. Fluyt, C. Görller-Walrand and Y. G. Galyametdinov, *Chem. Phys. Chem.*, **2**, 680–683 (2001).
[57] Y. G. Galyametdinov, L. V. Malykhina, W. Haase, K. Driesen and K. Binnemans, *Liq. Cryst.*, **29**, 1581–1584 (2002).
[58] T. Cardinaels, K. Driesen, T. N. Parac-Vogt, B. Heinrich, C. Bourgogne, D. Guillon, B. Donnio and K. Binnemans, *Chem. Mater.*, **17**, 6589–6598 (2006).
[59] A. A. Knyazev, Y. G. Galyametdinov, B. Goderis, K. Driesen, K. Goossens, C. Görller-Walrand, K. Binnemans and T. Cardinaels, *Eur. J. Inorg. Chem.*, 756–761 (2008).
[60] T. Zhang, C. Spitz, M. Antonietti and C. F. J. Faul, *Chem. Eur. J.* **11**, 1001–1009 (2005).
[61] H. L. Li, W. F. Bu, W. Qi and L. X. Wu, *J. Phys. Chem. B*, **109**, 21669–21676 (2005).
[62] J.-C.G. Bünzli and C. Piguet, *Chem. Soc. Rev.*, **34**, 1048–1077 (2005).
[63] J.-C.G. Bünzli, *Acc. Chem. Res.*, **39**, 53–61 (2006).
[64] S. Faulkner, S. J. Pope and B. P. Burton-Pye, *Appl. Spectrosc. Rev.*, **40**, 1–31 (2005).
[65] S. I. Weissman, *J. Chem. Phys.*, **10**, 214–217 (1942).
[66] R. E. Whan and G. A. Crosby, *J. Mol. Spectrosc.*, **8**, 315–327 (1962).
[67] G. A. Crosby, R. E. Whan and R. M. Alire, *J. Chem. Phys.*, **34**, 743–748 (1961).
[68] G. A. Crosby, R. E. Whan and J. J. Freeman, *J. Phys. Chem.*, **66**, 2493–2499 (1962).
[69] N. Filipescu, W. F. Sager and F. A. Serafin, *J. Phys. Chem.*, **68**, 3324–3346 (1964).
[70] S. Suarez, O. Mamula, D. Imbert, C. Piguet and J.-C.G. Bünzli, *Chem. Commun.*, 1226–1227 (2003).
[71] E. Terazzi, S. Torelli, G. Bernardinelli, E. Terazzi, S. Torelli, G. Bernardinelli, J. P. Rivera, J. M. Benech, C. Bourgogne, B. Donnio, D. Guillon, D. Imbert, J.-C.G. Bünzli, A. Pinto, D. Jeannerat and C. Piguet, *J. Am. Chem. Soc.*, **127**, 888–903 (2005).
[72] S. Suarez, D. Imbert, F. Gumy, C. Piguet and J.-C.G. Bünzli, *Chem. Mater.*, **16**, 3257–3266 (2004).
[73] A. Escande, L. Guénée, H. Nozary, G. Bernardinelli, F. Gumy, A. Aebischer, J.-C.G. Bünzli, B. Donnio, D. Guillon and C. Piguet, *Chem. Eur. J.*, **13**, 8696–8713 (2007).
[74] Y. T. Yang, K. Driesen, P. Nockemann, K. Van Hecke, L. Van Meervelt and K. Binnemans, *Chem. Mater.*, **18**, 3698–3704 (2006).
[75] Y. T. Yang, J. J. Li, X. Liu, S. Y. Zhang, K. Driesen, P. Nockemann and K. Binnemans, *Chem. Phys. Chem.*, **9**, 600–606 (2008).
[76] Y. Galyametdinov, A. A. Knyazev, V. I. Dzhabarov, T. Cardinaels, K. Driesen, C. Görller-Walrand and K. Binnemans, *Adv. Mater.*, **20**, 252–257 (2008).
[77] L. J. Yu, and M. M. Labes, *Appl. Phys. Lett.*, **31**, 719–720 (1977).
[78] K. Binnemans and D. Moors, *J. Mater. Chem.*, **12**, 3374–3376 (2002).
[79] R. an Deun, D. Moors, B. De Fré and K. Binnemans, *J. Mater. Chem.* **13**, 1520–1522 (2003).
[80] S. M. Weiss, J. Zhang, P. M. Fauchet, V. V. Seregin and J. L. Coffer, *Appl. Phys. Lett.*, **90**, 031112 (2007).
[81] J. Boyaval, F. Hapiot, C. Li, N. Isaert, M. Warenghem and P. Carette, *Mol. Cryst. Liq. Cryst.*, **330**, 1387–1394 (1999).
[82] J. Boyaval, C. Li, F. Hapiot, M. Warenghem, N. Isaert, Y. Guyot, G. Boulon and P. Carette, *Mol. Cryst. Liq. Cryst.*, **359**, 337–350 (2001).

[83] K. Driesen, D. Moors, J. Beeckman, K. Neyts, C. Görller-Walrand and K. Binnemans, *J. Lumin.*, **127**, 611–615 (2007).
[84] K. Palewska, A. Miniewicz, S. Bartkieuwicz, J. Legendziewicz and W. Strek, *J. Lumin.*, **124**, 265–272 (2007).
[85] K. Driesen and K. Binnemans, *Liq. Cryst.* **31**, 601–605 (2004).
[86] E. Guillet, D. Imbert, R. Scopelliti and J.-C.G. Bünzli, *Chem. Mater.*, **16**, 4063–4070 (2004).
[87] L. N. Puntus, K. J. Schenk and J.-C.G. Bünzli, *Eur. J. Inorg. Chem.*, 4739–4744 (2005).
[88] F. Neve, M. Ghedini and A. Crispini, *Chem. Commun.*, 2463–2464 (1996).
[89] C. R. Wen, Y. J. Wang, H. C. Wang, H. S. Sheu, G. H. Lee and C. K. Lai, *Chem. Mater.*, **17**, 1646–1654 (2005).
[90] D. Pucci, G. Barberio, A. Crispini, O. Francescangeli, M. Ghedini and M. La Deda, *Eur. J. Inorg. Chem.*, 3649–3661 (2003).
[91] C. Damm, G. Israel, T. Hegmann and C. Tschierske, *J. Mater. Chem.*, **16**, 1808–1816 (2006).
[92] K. Venkatesan, P. H. J. Kouwer, S. Yagi, P. Mueller and T. M. Swager, *J. Mater. Chem.*, **18**, 400–407 (2008).
[93] V. N. Kozhevnikov, B. Donnio and D. W. Bruce, *Angew. Chem. Int. Ed.*, **47**, 6286–6289 (2008).
[94] T. Cardinaels, J. Ramaekers, P. Nockemann, K. Driesen, K. Van Hecke, L. Van Meervelt, S. B. Lei, S. De Feyter, D. Guillon, B. Donnio and K. Binnemans, *Chem. Mater.*, **20**, 1278–1291 (2008).
[95] M. H. Qi and G. F. Liu, *J. Mater. Chem.*, **13**, 2479–2484 (2003).
[96] D. Pucci, I. Aiello, A. Bellusci, A. Crispini, I. De Franco, M. Ghedini and M. La Deda, *Chem. Commun.*, 2254–2256 (2008).
[97] S. Coco, C. Cordovilla, P. Espinet, J. Martin-Álvarez and P. Muñoz, *Inorg. Chem.*, **45**, 10180–10187 (2006).
[98] R. Bayón, S. Coco and P. Espinet, *Chem. Eur. J.*, **11**, 1079–1085 (2005).
[99] J. Arias, M. Bardaji and P. Espinet, *Inorg. Chem.*, **47**, 3559–3567 (2008).
[100] D. Pucci, G. Barberio, A. Bellusci, A. Crispini, B. Donnio, L. Giorgini, M. Ghedini, M. La Deda and E. I. Szerb, *Chem. Eur. J.*, **12**, 6738–6747 (2006).
[101] E. Cavero, S. Uriel, P. Romero, J. L. Serrano and R. Gimenez, *J. Am. Chem. Soc*, **129**, 11608–11618 (2007).
[102] A. Kishimura, T. Yamashita, K. Yamaguchi and T. Aida, *Nature Mater.*, **4**, 546–549 (2005).
[103] M. Ghedini, D. Pucci, A. Crispini, A. Bellusci, M. La Deda, I. Aiello and T. Pugliese, *Inorg. Chem. Commun.*, **10**, 243–246 (2007).
[104] M. Grell and D. D. C. Bradley, *Adv. Mater.*, **11**, 895–905 (1999).
[105] A. Barbieri, G. Accorsi and N. Armaroli, *Chem. Commun.*, 2185–2193 (2008).
[106] T. Verbiest, S. Houbrechts, M. Kauranen, K. Clays and A. Persoons, *J. Mater. Chem.*, **7**, 2175–2189 (1997).
[107] D. W. Bruce and A. Thornton, *Mol. Cryst. Liq. Cryst.*, **231**, 253–256 (1993).
[108] J. Barbera, A. Elduque, R. Gimenez, F. J. Lahoz, J. A. Lopez, L. A. Oro, J. L. Serrano, B. Villacampa and J. Villalba, *Inorg. Chem.*, **38**, 3085–3092 (1999).
[109] G. Cipparone, C. Versace, D. Duca, D. Pucci, M. Ghedini and C. Umeton, *Mol. Cryst. Liq. Cryst.*, **212**, 217–224 (1992).
[110] P. Espinet, J. Etxebarria, C. L. Folcia, J. Ortega, M. B. Ros and J. L. Serrano, *Adv. Mater.*, **8**, 745–748 (1996).

[111] J. Ortega, C. L. Folcia, J. Etxebarria, M. B. Ros and J. A. Miguet, *Liq. Cryst.*, **23**, 285–291 (1997).
[112] T. Sakaguchi, Y. Shimizu, M. Miya, T. Fukumi, K. Ohta and A. Nagata, *Chem. Lett.*, 281–284 (1992).
[113] M. A. Diaz-Garcia, I. Ledoux, J. A. Duro, T. Torres, F. Agullo-Lopez and J. Zyss, *J. Phys. Chem.*, **98**, 8761–8764 (1994).
[114] M. A. Diaz-Garcia, F. Fernandez-Lazaro, G. de la Torre, E. M. Maya, P. Vasquez, Agullo-Lopez, F. and T. Torres, *Synth. Met.*, **84**, 923–924 (1997).
[115] M. A. Diaz-Garcia, A. Dogariu, D. J. Hagan and E. W. Van Stryland, *Chem. Phys. Lett.*, **266**, 86–90 (1997).
[116] C. Piechocki, J. Simon, J. J. André, D. Guillon, P. Petit, A. Skoulios and P. Weber, *Chem. Phys. Lett.*, **122**, 124–138 (1985).
[117] J. Simon and P. Bassoul, *Design of Molecular Materials: Supramolecular Engineering*, John Wiley & Sons, Ltd, New York, 2000.
[118] T. H. Tran-Thi, D. Markovitsi, R. Even and J. Simon, *Chem. Phys. Lett.*, **139**, 207–211 (1987).
[119] E. Orti, J. L. Brédas and C. Clarisse, *J. Phys. Chem.*, **92**, 1228–1235 (1990).
[120] A. De Cian, M. Moussavi, J. Fischer and R. Weiss, *Inorg. Chem.*, **24**, 3162–3167 (1985).
[121] Z. Belarbi, M. Maitrot, K. Ohta, J. Simon, J. J. André and P. Petit, *Chem. Phys. Lett.*, **143**, 400–403 (1988).
[122] Z. Belarbi, C. Sirlin, J. Simon and J. J. André, *J. Phys. Chem.*, **93**, 8105–8110 (1989).
[123] Z. Berlarbi, *J. Phys. Chem.*, **94**, 7334–7336 (1990).
[124] M. Bouvet and J. Simon, *Chem. Phys. Lett.* **172**, 299–302 (1990).
[125] G. Guillaud, M. Al Sadoun, M. Maitrot, J. Simon and M. Bouvet, *Chem. Phys. Lett.*, **167**, 503–506 (1990).
[126] F. Nekelson, H. Monobe, M. Shiro and Y. Shimizu, *J. Mater. Chem.*, **17**, 2607–2615 (2007).
[127] T. Basova, A. G. Gürek, V. Ahsen and A. K. Ray, *Org. Electron.* **8**, 784–790 (2007).
[128] A. M. van de Craats, J. M. Warman, H. Hasebe, R. Naito and K. Ohta, *J. Phys. Chem. B*, **101**, 9224–9232 (1997).
[129] K. Ban, K. Nishizawa, K. Ohta, A. M. V. van de Craats, J. M. Warman, I. Yamamoto and H. Shirai, *J. Mater. Chem.*, **11**, 321–331 (2001).
[130] A. M. Godquin-Giroud, G. Sigaud, M. F. Achard and F. Hardouin, *J. Phys. Lett.*, **45**, L387–L392 (1984).
[131] N. Boden, R. J. Bushby, J. Clements, M. V. Jesudason, P. F. Knowles and G. Williams, *Chem. Phys. Lett.*, **152**, 94–99 (1988).
[132] N. Boden, R. J. Bushby and J. Clements, *J. Mater. Sci. Mater. Electron.*, **5**, 83–88 (1994).
[133] N. Boden, R. C. Borner, R. J. Bushby and J. Clements, *J. Am. Chem. Soc.*, **116**, 10807–10808 (1994).
[134] P. S. Kumar, S. Kumar and V. Lakshminarayanan, *J. Phys. Chem. B*, **112**, 4865–4869 (2008).
[135] S. K. Prasad, K. L. Sandhya, G. G. Nair, U. S. Hiremath, C. V. Lamaggad and S. Sampath, *Liq. Cryst.*, **33**, 1121–1125 (2006).
[136] S. Kumar and V. Lakshminarayanan, *Chem. Commun.*, 1600–1601 (2004).
[137] S. Kumar, S. K. Pal and V. Lakshminarayanan, *Mol. Cryst. Liq. Cryst.*, **434**, 579–586 (2005).

[138] L. A. Holt, R. J. Bushby, S. D. Evans, A. Burgess and G. Seeley, *J. Appl. Phys.*, **103**, 063712-1-6 (2008).
[139] S. Kumar, S. K. Pal, P. S. Kumar and V. Lakshminarayanan, *Soft Matter*, **3**, 896–900 (2007).
[140] D. Markovitsi, I. Lecuyer and J. Simon, *J. Phys. Chem.*, **95**, 3620–3626 (1991).
[141] B. A. Gregg, *Mol. Cryst. Liq. Cryst.*, **257**, 219 (1994).
[142] K. Yoshino, S. B. Lee, T. Sonoda, H. Kawagishi, R. Hidayat, K. Nakayama, M. Ozaki, K. Ban, K. Nishizawa, K. Ohta and H. Shirai, *J. Appl. Phys.*, **88**, 7137–7143 (2000).
[143] P. M. S. Monk, R. J. Mortimer and D. R. Rosseinsky, *Electrochromism*, Wiley-VCH Verlag GmbH, Weinheim, 1995.
[144] C. Harnoode, K. Takamura, H. Kubota, K. Sho, K. Fujisawa, F. Kitamura, T. Ohsaka and K. Tokuda, *Electrochemistry*, **67**, 832–838 (1999).
[145] F. Castaneda, C. Piechocki, V. Plichon, J. Simon and J. Vaxiviere, *Electrochim. Acta*, **31**, 131–133 (1986).
[146] S. Besbes, V. Plichon, J. Simon and J. Vaxiviere, *J. Electroanal. Chem.*, **237**, 61–68 (1987).
[147] T. Toupance, V. Plichon and J. Simon, *New. J. Chem.*, **23**, 1001–1006 (1999).
[148] T. Komatsu, K. Ohta, T. Fujimoto and I. Yamamoto, *J. Mater. Chem.*, **4**, 533–536 (1994).
[149] J. Z. Jiang, R.C.W. Liu, T. C. W. Mak, J. Z. Jiang , R. C. W. Liu, T. C. W. Mak, T. W. C. Chan and D. K. P. Ng, *Polyhedron*, **16**, 515–520 (1997).
[150] R. B. Daniels, G. L. Payne and J. Peterson, *J. Coord. Chem.*, **28**, 23–31 (1993).
[151] R. B. Daniels, J. Peterson, W. C. Porter and Q. D. Wilson, *J. Coord. Chem.*, **30**, 357–366 (1993).
[152] M. Marcos, J. L. Serrano, T. Sierra and M. J. Gimenez, *Angew. Chem. Int. Ed. Engl.*, **31**, 1471–1472 (1992).
[153] M. Marcos, J. L. Serrano, T. Sierra and M. J. Gimenez, *Chem. Mater.*, **5**, 1332–1337 (1993).
[154] M. J. Baena, J. Barbera, P. Espinet, A. Ezcurra, M. B. Ros and J. L. Serrano, *J. Am. Chem. Soc.*, **116**, 1899–1906 (1994).
[155] N. J. Thompson, J. L. Serrano, M. J. Baena and P. Espinet, *Chem. Eur. J.*, **2**, 214–220 (1996).
[156] M. A. Athanassopoulou, S. Hiller, L. A. Beresnev, M. A. Athanassopoulou, S. Hiller, L. A. Beresnev, Y. G. Galyametdinov, M. Schweissguth and W. Haase *Mol. Cryst. Liq. Cryst.*, **261**, 29–39 (1995).
[157] J. L. Serrano and T. Sierra, *Chem. Eur. J.*, **6**, 759–766 (2000).
[158] M. Yamaguchi and Y. Tanimoto (eds), *Magneto-Science, Magnetic Field Effects on Materials: Fundamentals and Applications*, Springer, Berlin, 2006.
[159] P. G. de Gennes, *The Physics of Liquid Crystals*, Clarendon, Oxford, 1974.
[160] P. J. Alonso, Magnetic Properties of Metallomesogens, in *Metallomesogens, Synthesis, Properties and Applications* (ed. J. L. Serrano), Wiley-VCH Verlag GmbH, Weinheim, 1996, pp. 387–418.
[161] J. Barberá, X-Ray Studies of Metallomesogens, in *Metallomesogens, Synthesis, Properties and Applications* (ed. J. L. Serrano), Wiley-VCH Verlag GmbH, Weinheim, 1996, pp. 336–338.
[162] E. Campillos, M. Marcos, J. L. Serrano, J. Barberá, P. J. Alonso and J. I. Martìnez, *Chem. Mater.*, **5**, 1518–1525 (1993).

[163] M. Marcos and J. L. Serrano, *Adv. Mater.*, **3**, 256–257 (1991).
[164] P. J. Alonso, M. L. Sanjuán, P. Romero, M. Marcos, and J.L. Serrano, *J. Phys.: Condens. Matter*, **2**, 9173–9182 (1990).
[165] J. L. Serrano, P. Romero, M. Marcos and P. J. Alonso, *J. Chem. Soc., Chem. Commun.*, 859–861 (1990).
[166] I. Bikchantaev, Y. G. Galyametdinov, A. Prosvirin, K. Griesar, *Liq. Cryst*, **18**, 231–237 (1995).
[167] J. Barberá, A. M. Levelut, M. Marcos, J. Barberá, A. M. Levelut, M. Marcos, P. Romero and J. L. Serrano, *Liq. Cryst.*, **10**, 119–126 (1991).
[168] P. J. Alonso and J. I. Martìnez, *Liq. Cryst.*, **21**, 597–601 (1996).
[169] I. H. Ibrahim and W. Haase, *J. Phys. Coll. C3 (France)*, **40**, 164–168 (1979).
[170] E. A. Boudreaux and L. N. Mulay, (eds), *Theory and Applications of Molecular Paramagnetism*, Wiley, New York, 1976.
[171] J. H. Van Vleck, *The Theory of Electric and Magnetic Susceptibilities*, Oxford University Press, Oxford, 1966.
[172] Y. G. Galyametdinov, M. Athanassopoulou, W. Haase and I. V. Ovchinnikov, *Russ. J. Coord. Chem.*, **21**, 718–719 (1995).
[173] Y. G. Galyametdinov, M. A. Athanassopolou, K. Griesar, O. Kharitonova, E. A. Soto Bustamante, L. Tinchurina, I. Ovchinnikov and W. Haase, *Chem. Mater.*, **8**, 922–926 (1996).
[174] K. Binnemans, Y. G. Galyametdinov, R. Van Deun, D. W. Bruce, S. R. Collinson, A. P. Polishuk, I. Bikchantaev, W. Haase, A. V. Prosvirin, L. Tinchurina, I. Litvinov, A. Gubajdullin, A. Rakhmatullin, K. Uytterhoeven and K. Van Meervelt, *J. Am. Chem. Soc.*, **122**, 4335–4344 (2000).
[175] R. Van Deun and K. Binnemans, *Liq. Cryst.*, **28**, 621–627 (2001).
[176] K. Binnemans, Y. G. Galyametdinov, S. R. Collinson and D. W. Bruce, *J. Mater. Chem.*, **8**, 1551–1553 (1998).
[177] I. Bikchantaev, Y. G. Galyametdinov, O. Kharitonova, I. V. Ovchinnikov, D. W. Bruce, D. A. Dunmur, D. Guillon and B. Heinrich, *Liq. Cryst.*, **20**, 489–492 (1996).
[178] V. S. Mironov, Y. G. Galyametdinov, A. Ceulemans and K. Binnemans, *J. Chem. Phys.*, **113**, 10293–10303 (2000).
[179] Y. G. Galyametdinov, W. Haase, B. Goderis, D. Moors, K. Driesen, R. Van Deun, and K. Binnemans, *J. Phys. Chem. B*, **111**, 13881–13885 (2007).
[180] V. S. Mironov, Y. G. Galyametdinov, A. Ceulemans, C. Görller-Walrand and K. Binnemans, *Chem. Phys. Lett.*, **345**, 132–140 (2001).
[181] V. S. Mironov, Y. G. Galyametdinov, A. Ceulemans, C. Görller-Walrand and K. Binnemans, *J. Chem. Phys.*, **116**, 4673–4685 (2002).
[182] K. Binnemans, L. Malykhina, V. S. Mironov, K. Binnemans, L. Malykhina, V. S. Mironov, W. Haase, K. Driesen, R. Van Deun, L. Fluyt, C. Görller-Walrand and Y. G. Galyametdinov, *Chem. Phys. Chem.*, **2**, 680–683 (2001).
[183] B. Bleaney, *J. Magn. Reson.*, **8**, 91–100 (1972).
[184] R. M. Golding and P. Pyykkö, *Mol. Phys.*, **26**, 1389–1396 (1973).
[185] Y. G. Galyametdinov, W. Haase, L. Malykhina, A. Prosvirin, I. Bikchantaev, A. Rakhmatullin and K. Binnemans, *Chem. Eur. J.*, **7**, 99–105 (2001).
[186] B. D. Pate, S. M. Choi, U. Werner-Zwanziger, D. V. Baxter, J. M. Zaleski and M. H. Chisholm, *Chem. Mater.*, **14**, 1930–1936 (2002).
[187] J. H. Lee, S. M. Choi, B. D. Pate, M. H. Chisholm and Y. S. Han, *J. Mater. Chem.*, **16**, 2785–2791 (2006).

[188] J. H. Lee, H. S. Kim, B. D. Pate and S. M. Choi, *J. Appl. Cryst.*, **40**, S68–S72 (2007).
[189] J. H. Lee, H. S. Kim, B. D. Pate and S. M. Choi, *Physica B*, **385**, 798–800 (2006).
[190] H. S. Kim, S. M. Choi, J. H. Lee, P. Busch, S. J. Koza, E. A. Verploegen, and B. D. Pate, *Adv. Mater.*, **20**, 1105–1109 (2008).
[191] N. E. Domracheva, I. V. Ovchinnikov, A. Turanov and V. N. Konstantinov, *J. Magn. Magn. Mater.*, **269**, 385–392 (2004).
[192] Y. G. Galyametdinov, G. I. Ivanova and I. V. Ovchinnikov, *Bull. Russ. Acad. Sci., Div. Chem. Sci.*, **38**, 1776–1776 (1989).
[193] X. Ying, Z. Y. Lin, T. Li, J. Shi, J. W. Huang and L. N. Ji, *Mol. Cryst. Liq. Cryst.*, **339**, 139–143 (2000).
[194] X. Ying, S. Jue, Z. Y. Lin, L. Tao, J. W. Huang and L. N. Ji, *Liq. Cryst.*, **27**, 211–214 (2000).
[195] T. Li, X. Ying, L. P. Shi, J. W. Huang, Z. Y. Lin, J. Shi and L. N. Ji, *Liq. Cryst.*, **27**, 551–553 (2000).
[196] X. Ying, L. Tao, Z. Y. Lin and J. Lin, *J. Appl. Phys.*, **101**, 036109 (2007).
[197] H. D. Hu, X. P. Zou, Y. Xiang and T. Li, *Jpn. J. Appl. Phys.*, **42**, 3528–3530 (2003).
[198] C. Scherer and A. M. F. Neto, *Braz. J. Phys.*, **35**, 718–727 (2005).
[199] F. Brochard and P. G. de Gennes, *J. Phys.*, **31**, 691–708 (1970).
[200] J. Rault, P. E. Cladis and J. P. Burger, *Phys. Lett. A*, **32**, 199–200 (1970).
[201] S. H. Chen and N. M. Amer, *Phys. Rev. Lett.*, **51**, 2298–2301 (1983).
[202] L. Liébert and A. Martinet, *IEEE Trans. Magn.*, **16**, 266–269 (1980).
[203] P. Fabre, C. Casagrande, M. Veyssie, V. Cabuil and R. Massart, *Phys. Rev. Lett.*, **64**, 539–542 (1990).
[204] J. C. Dabadie, P. Fabre, M. Veyssie, V. Cabuil and R. Massart, *J. Phys.: Condens. Matter*, **2**, SA291–SA294 (1990).
[205] A. B. Gaspar, V. Ksenofontov, M. Seredyuk and P. Gütlich, *Coord. Chem. Rev.*, **249**, 2661–2676 (2005).
[206] P. Gütlich, *Struct. Bond.*, **44**, 83–195 (1981).
[207] P. Gütlich, A. Hauser and H. Spiering, *Angew. Chem. Int. Ed.*, **43**, 2024–2054 (2004).
[208] S. Decurtins, P. Gütlich, C. P. Kohler, H. Spiering and A. Hauser, *Chem. Phys. Lett.*, **105**, 1–4 (1984).
[209] Y. Galyametdinov, V. Ksenofontov, A. Prosvirin, I. Ovchinnikov, G. Ivanova, P. Gütlich and W. Haase, *Angew. Chem. Int. Ed.*, **40**, 4269–4271 (2001).
[210] T. Fujigaya, D. L. Jiang and T. Aida, *J. Am. Chem. Soc.*, **125**, 14690–14691 (2003).
[211] S. Hayami, K. Danjobara, K. Inoue, Y. Ogawa, N. Matsumoto and Y. Maeda, *Adv. Mater.*, **16**, 869–872 (2004).
[212] S. Hayami, K. Danjobara, S. Miyazaki, K. Inoue, Y. Ogawa and Y. Maeda, *Polyhedron*, **24**, 2821–2827 (2005).
[213] S. Hayami, N. Motokawa, A. Shuto, N. Masuhara, T. Someya, Y. Ogawa, K. Inoue and Y. Maeda, *Inorg. Chem.*, **46**, 1789–1794 (2007).
[214] W. Zhang, F. Zhao, T. Liu, M. Yuan, Z. M. Wang and S. Gao, *Inorg. Chem.*, **46**, 2541–2555 (2007).
[215] S. Hayami, N. Motokawa, A. Shuto, R. Moriyama, N. Masuhara, K. Inoue and Y. Maeda, *Polyhedron*, **26**, 2375–2380 (2007).
[216] M. Seredyuk, A. B. Gaspar, V. Ksenofontov, S. Reiman, Y. Galyametdinov, W. Haase, E. Rentschler and P. Gütlich, *Chem. Mater.*, **18**, 2513–2519 (2006).
[217] M. Seredyuk, A. B. Gaspar, V. Ksenofontov, Galyametdinov, Y., M. Verdaguer, F. Villain and P. Gütlich, *Inorg. Chem.*, **47**, 10232–10245 (2008).

[218] S. Hayami, R. Moriyama, A. Shuto, Y. Maeda, K. Ohta and K. Inoue, *Inorg. Chem.*, **46**, 7692–7694 (2007).
[219] M. Seredyuk, A. B. Gaspar, V. Ksenofontov, Y. Galyametdinov, J. Kusz and P. Gütlich, *J. Am. Chem. Soc.*, **130**, 1431–1439 (2008).
[220] M. Seredyuk, A. B. Gaspar, V. Ksenofontov, Y. Galyametdinov, J. Kusz and P. Gütlich, *Adv. Funct. Mater.*, **18**, 2089–2101 (2008).
[221] R. Seesoli, D. Gatteschi, A. Caneschi and M. A. Novak, *Nature*, **365**, 141–143 (1993).
[222] T. Lis, *Acta Cryst. B*, **26**, 2042–2046 (1980).
[223] D. Gatteschi and R. Sessoli, *Angew. Chem. Int. Ed.*, **42**, 268–297 (2003).
[224] R. Sessoli, H. L. Tsai, A. R. Schake, S. Y. Wang, J. B. Vincent, K. Folting, D. Gatteschi, G. Christou and D. N. Hendrickson, *J. Am. Chem. Soc.*, **115**, 1804–1816 (1993).
[225] E. Terrazzi, C. Bourgogne, R. Welter, J. L. Gallani, D. Guillon, G. Rogez and B. Donnio, *Angew. Chem. Int. Ed.*, **47**, 490–495 (2008).

3

Molecular Magnetic Materials

Neil Robertson[a] and Gordon T. Yee[b]
[a]*School of Chemistry, University of Edinburgh, UK*
[b]*Department of Chemistry, Virginia Poly.technic Institute and State University, Blacksburg, USA*

3.1 INTRODUCTION

The examination of the magnetic properties of molecules and molecule-based solids has emerged as an important area of research. Although originally focused on principally transition metal ions with unpaired electrons in *d*-orbitals, the building blocks in this field have grown to include elements with electrons in *f*-orbitals and, most importantly, organic molecules constructed from carbon, nitrogen, oxygen and sulfur with unpaired electrons in π-orbitals. Today, the definition is even broader. Here a molecule-based magnet is defined as any material in which a molecular orbital plays a central role: either one or more unpaired electrons reside in a molecular orbital or a molecular orbital mediates magnetic coupling between two or more spin centres.

Synthetic chemists studying molecule-based magnetic materials take advantage of the strength of organic chemistry to manipulate the electronic and steric properties of the constituent molecules in much the same way that medicinal chemists look for new drugs: the effect of a modification to the building block on the bulk magnetic properties can be studied in a systematic way. Combined with X-ray crystallography, this strategy

Molecular Materials Edited by Duncan W. Bruce, Dermot O'Hare and Richard I. Walton

has been used to uncover structure–property relationships and to study the underlying principles that govern magnetic coupling. These bottom-up molecular approaches are also particularly well suited for the construction of low-dimensional magnetic species designed to test the predictions of theoretical models that have been examined by physicists. The field thus represents an area that is intrinsically interdisciplinary and multifaceted, melding organic and inorganic synthesis with physical measurements and modelling.

Although essentially any species that has unpaired electrons will be 'magnetic', those compounds whose behaviour deviates from the Curie law, an expression analogous to the well-known ideal gas law, that relates magnetisation, applied field and temperature (*vide infra*), are those that are most interesting. Oftentimes, it is the interaction of one spin centre with others that imbues the solid with properties quite distinct from those of the single building block. One particular area that has emerged in the last 25 years is the study of molecule-based solids that exhibit long-range magnetic order, a characteristic of permanent magnets. An example of this is ferromagnetism, in which a macroscopic fraction of the unpaired electrons in a material are aligned in the same direction at a finite temperature. Starting with molecular building blocks allows the properties of the individual building blocks to be tuned to yield interesting properties in the bulk. For instance, an historically important example of tuning redox properties using organic synthesis to dramatically change magnetic properties: the starkly contrasting products of the reaction of ferrocene or decamethylferrocene with tetracyanoethylene (Figure 3.1a).[1] Combining solutions of ferrocene [$FeCp_2$] and tetracyanoethylene (TCNE) and removing the solvent gives rise to a solid consisting of an alternating stack of donors [$FeCp_2$] and acceptors (TCNE) in which each building block is still neutral and completely diamagnetic. Adding five methyl groups to the periphery of each cyclopentadienyl ring to give decamethylferrocene [$FeCp^*_2$] makes this molecule much more electron rich and, hence, a stronger reducing agent than [$FeCp_2$]. Combining solutions of [$FeCp^*_2$] and TCNE gives rise to an ionic solid in which an electron is completely transferred from the donor to the acceptor to give $[FeCp^*_2]^+[TCNE]^-$.[2] The structure of this compound is quite similar to that derived from the ferrocene analogue but, in the ionic compound, each anion and cation possesses an unpaired electron. Below 4.8 K, $[FeCp^*_2]^+[TCNE]^-$ is a ferromagnet exhibiting hysteresis (*vide infra*) illustrating that the presence or absence of methyl groups tunes the electrochemistry of one building block and changes the magnetic behaviour completely.

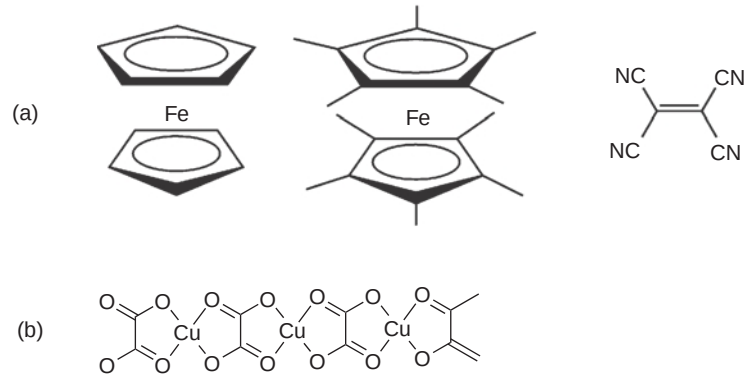

Figure 3.1 (a) Ferrocene, decamethylferrocene and TCNE; (b) oxalate-bridged Cu^{2+} chain

A second example where molecular building blocks excel is in control of structural anisotropy and dimensionality. Thus, it is relatively difficult to create a one-dimensional structure of a conventional magnetic material such as iron or nickel (a molecular wire), though it can, in principle, be achieved by lithography or by vapour phase deposition. In contrast, it is fairly simple to synthesise a coordination polymer, for instance, $[Cu(oxalate)]_n \bullet 1/3H_2O$ in which the ligand bridges square planar Cu^{2+} ions and the exchange coupling within the chain is well modelled by treating it as an ideal, infinite, one-dimensional chain.[3,4] Solutions to the Schrödinger equation for this and similar systems can, in certain cases, be solved numerically or analytically, yielding models of magnetic properties that can be fitted to the data. These types of compounds thus provide important test cases for solid-state theoretical calculations.

The target audience of this chapter is a new graduate student or advanced undergraduates, those who have already been exposed to advanced inorganic chemistry including some group theory as well as both quantum and statistical mechanics. The goal is to provide enough information to the student that he or she is prepared to read, critically, almost any journal article containing magnetic data. As such, a priority is placed on defining the vocabulary used in discussions of molecule-based magnetism. The explanations and examples below will guide the student through the experiment and data collection, the data analysis and modelling and will present many examples of how the information is used to further the understanding of the properties of the

isolated molecule or molecule-based solid. In the early parts of the chapter, a progressive consideration of different aspects of magnetochemistry from individual magnetic centres through to extended lattices of interacting spins is followed. By this approach, recent and important examples from the literature arise naturally to illustrate the concepts and points made. In the final section, a selection of additional topics is presented that illustrate how molecular magnetism has increasingly developed overlap with other areas including switchable, optical and conducting systems. This takes us to the very edge of 'molecular magnetic materials' and provides a taste of what may be important future developments in the field.

3.1.1 History of Measurements

The earliest methods for quantitative determination of magnetic properties date from the mid to late nineteenth century. The best known of these, the Faraday balance (1855) is still in use today for highly quantitative measurements at elevated temperatures. Information on this technique can be found in many textbooks, but it is essentially a force method: an inhomogeneous magnetic field exerts a force on the sample that can be quantified with an electronic balance as a change in mass. The Gouy balance, familiar from many undergraduate chemistry laboratories, is also based on a related force method. In the most general sense, *paramagnetic* materials are attracted to a magnetic field, and appear heavier, whereas *diamagnetic* materials are repelled by a magnetic field, and appear lighter.

Various adaptations that rely on force methods have been commercialised (the so-called Evans–Johnson–Matthey balance)[5] or designed from readily available parts and described in the literature.[6,7] The Evans method[8,9] uses NMR and can provide variable temperature data on molecules in solution, but the technique is limited to a window where solvents stay liquid and solutes stay in solution. The one development that has been crucial to the more recent rapid development of this research field is the availability of relatively inexpensive and easy-to-use, variable temperature, variable field instrumentation, specifically the Superconducting Quantum Interference Device (SQUID) magnetometer. With a SQUID, it is possible, even for relatively inexperienced users, to determine the magnetic properties of a sample (typically ~10–20 mg) as a function of temperature and applied field (down to 1.8 K and

up to 7 T) in less than a day. This ease of acquisition of data has fuelled the recent expansion in this field.

3.2 BASIC CONCEPTS

3.2.1 Magnetisation and Susceptibility

Magnetic properties are familiar at the macroscopic level, where it is recognised that a current going round a loop of wire gives rise to a magnetic moment with magnitude equal to the area of the loop times the magnitude of the current (Figure 3.2). This is the principle of an electromagnet.

However, we wish to relate such macroscopic observations to the quantum mechanical behaviour of individual molecules. By analogy it can be seen that electrons within an atom can be considered to produce a magnetic moment as the result of two types of motion, which give rise to orbital angular momentum and spin angular momentum (although the analogy should not be taken any further, as the spin and orbital properties of electrons cannot be pictured in any classical way). For an isolated atom, the combination of these will give rise to a magnetic moment that can be quantified in terms of the spin and orbital quantum numbers. For any closed subshell the total value of the orbital angular momentum and the spin angular momentum will be zero, since all positive and negative values for individual electrons will cancel. Thus magnetic measurements are primarily concerned with contributions from unpaired electrons in partially filled subshells.

When placed in a magnetic field, a substance will acquire a magnetisation (M), which may be thought of as the vector sum of the individual magnetic moments of the building blocks. The most typical experiments

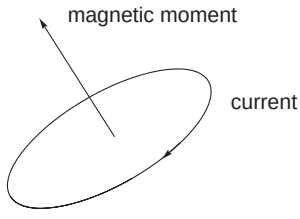

Figure 3.2 A current loop giving rise to a magnetic moment

in magnetochemistry involve measurement of the macroscopic magnetisation of a sample as a function of temperature (T) at fixed applied field and additionally as a function of applied magnetic field (H) at fixed temperature. From such measurements it is possible to derive detailed information on the electronic structure of the molecule that can often be related back to its geometry, oxidation state, bonding, and so on. To do this, it is convenient to determine a parameter that is independent of the magnitude of the applied field and so the volume magnetic susceptibility is defined:

$$\chi_V = \frac{M}{H} \tag{3.1}$$

where χ_V is the volume magnetic susceptibility. This equation is valid at low values of the applied magnetic field where a linear relationship between M and H exists. Typical SQUID measurements are performed in an applied field of 5000 G (0.5 T), which is generally in the linear regime, and provides both sufficient signal-to-noise and small relative error in H due to residual fields in the instrument.

It is very important to consider the units associated with these quantities. Units in magnetochemistry can be rather confusing due mainly to the existence of more than one system. The most commonly used system in the chemistry literature is the cgs emu system, rather than the SI system, and this is essentially an historical accident rather than having any more logical origin. This system of units is used in this chapter, as this is directly comparable with the literature; the reader is referred to other works for a comparison with SI units.[10,11] The volume susceptibility (χ_V) is dimensionless (though seldom reported) and in the cgs emu system has 'units' of emu cm^{-3}, such that the emu therefore has units of cm^3. Note that 'emu' is not really a unit, but a flag that indicates that the value is reported using this system of units. Nevertheless, it is possible to have a self-consistent system of units for the various quantities that arise. From this, the gram susceptibility ($cm^3\ g^{-1}$) can be determined through division of the volume susceptibility by the density (g cm^{-3}) which in turn can be converted to the most commonly reported quantity, the molar susceptibility (χ_m, in units of $cm^3\ mol^{-1}$) by multiplication by the molar mass in g mol^{-1}.

In practical experiments, the magnetometer is normally calibrated such that the experimentally determined magnetisation can be converted into the molar magnetic susceptibility (χ_m) through multiplication by the ratio of the molecular weight to the sample weight and dividing by the applied

magnetic field. The units of χ_m are also often expressed in the literature as emu mol^{-1} (because of the equivalence of emu and cm^3). If the applied magnetic field is measured in gauss (G), the units of molar magnetisation must be emu G mol^{-1} (or cm^3 G mol^{-1}).

Experimentally measured values of susceptibility are, in fact, a combination of two opposing factors: the paramagnetic susceptibility that normally arises primarily from unpaired electrons, which has a positive value, and also the diamagnetic susceptibility (χ_d.):

$$\chi_m = \chi_p + \chi_d \tag{3.2}$$

The latter is an induced response from the paired electrons that oppose the applied field, and the diamagnetic susceptibility therefore has the opposite sign (*i.e.* it is negative) from the paramagnetic susceptibility, (χ_p). Because χ_d largely arises from core electrons, it is approximately a constant for any given atom, and temperature-independent, although there can also be functional group effects where π-bonding occurs. This latter phenomenon is well known in the explanation for the significant downfield chemical shift of the protons in benzene. These corrective constants due to individual atoms are referred to as Pascal's constants and can be summed and subtracted from the total susceptibility to yield the paramagnetic susceptibility, which is the parameter of interest.[11] Note that since the diamagnetic correction is negative, this leads to a paramagnetic susceptibility that is larger than the experimental susceptibility. The diamagnetic correction is temperature independent and is generally much smaller than the paramagnetic susceptibility. A rough order of magnitude can be estimated as –(molecular weight/2) $\times$ 10^{-6} cm^3 mol^{-1} and this can be used as a check to make sure no gross error has been made in the application of Pascal's constants. For the rest of the chapter the term χ is taken to represent only the paramagnetic component of the molar susceptibility with the assumption that the experimental data have been corrected for diamagnetism.

3.2.2 The Curie and Curie–Weiss Laws

A bulk sample of a paramagnetic substance contains a multitude of individual magnetic moments arising from the individual molecules in the sample. The tendency of these to align with an applied magnetic field will be in competition with the randomisation of their orientations

through thermal effects at any finite temperature. This causes the paramagnetic susceptibility to be inversely proportional to temperature as expressed by the Curie law:

$$\chi = \frac{M}{H} = \frac{C}{T} \tag{3.3}$$

Note that this equation appears rather similar to the ideal gas law and serves a similar function. With the ideal gas law, plotting the compressibility factor, Z ($= PV/RT$), as a function of temperature at constant pressure reveals much about the behaviour of a real gas. Similarly, it will be shown that plots of χT as a function of T at constant applied magnetic field are very useful in revealing deviations from ideal behaviour. Just as Z is constant for an ideal gas, χT is constant for an ideal paramagnet.

From a practical standpoint, the way that the Curie law (and all subsequent expressions of temperature-dependent susceptibility) are used by experimentalists is to fit the data to the equation using a least squares fit with C as an adjustable parameter. If the data fit reasonably well, except perhaps at very low temperature, they are said to 'obey the Curie law' and the value of C is extracted.

As will be derived below, C is a function of the spin of the system:

$$C = \frac{Ng^2\beta^2}{3k} S(S+1) \tag{3.4}$$

where N is Avogadro's number, g is the Landé constant (which relates magnetic moment of an atom with the angular momentum vectors), β is the Bohr magneton (a collection of fundamental constants), S is the total spin on the ion and k is Boltzmann's constant. [Note that in Equation 3.4 and throughout Sections 3.2.2 and 3.2.3, only the spin of the ion (S) has been considered and not the orbital angular momentum (L). This is often a useful approximation that will be discussed in more detail shortly.] The units of C are thus emu K mol^{-1} or cm^3 K mol^{-1}. This expression is used to calculate the spin-only value of χT, which is applicable to many first row transition metal ions.

Deviations from Curie law behaviour occur most commonly for one of more of the following reasons:

(i) It has been assumed that the individual spins are not interacting with each other, only with the external magnetic field. In any

condensed phase, however, the individual magnetic moments will inevitably interact to a varying degree from extremely weakly to extremely strongly.

(ii) The presence of orbital angular momentum (L) can contribute to the magnetic moment and interactions between the spin and orbital degrees of freedom (spin-orbit coupling) can introduce anisotropy.

To accommodate these possibilities, experimental data can often be fitted using the Curie–Weiss law, which includes the additional parameter θ:

$$\chi = \frac{C}{T - \theta} \tag{3.5}$$

This equation acknowledges deviations from Curie law behaviour but it is important to note that it does not give direct information on the reasons for the deviation and great caution should be exercised in applying a physical interpretation to θ, which will be discussed later. However, one explanation for non-zero θ [case (i) above] is the parallel alignment of interacting moments (ferromagnetic coupling) or antiparallel alignment (antiferromagnetic coupling) due to an intermolecular coupling (Figure 3.3). Such interactions are of tremendous importance as it is these that give rise to interesting and important types of cooperative bulk magnetic behaviour dealt with later. Accordingly, it is often the goal of the magnetochemist to design systems where magnetic centres interact strongly with each other. In the absence of such deliberate design, however, many paramagnetic molecular solids show rather weak interactions between spins, due to the presence of closed shell ligands that intervene between the metals or other spin centres. In such cases, the Curie law, or Curie–Weiss law with small value of θ, is often followed rather well, particularly when case (ii) above does not apply. The absence of intermolecular interactions can be an advantage when the goal of the study is to investigate the magnetic properties of the individual molecules, for example to study the electronic properties of a biomimetic metal complex.[12] There are also some cases where weak intermolecular interactions are actually of benefit in the study of cooperative magnetic behaviour as it enables the system to be more easily perturbed through an applied magnetic field.[13]

Where ferromagnetic coupling of moments is dominant, the observed susceptibility will be higher at any given temperature than predicted by the Curie law and this will give a positive value of θ. Correspondingly,

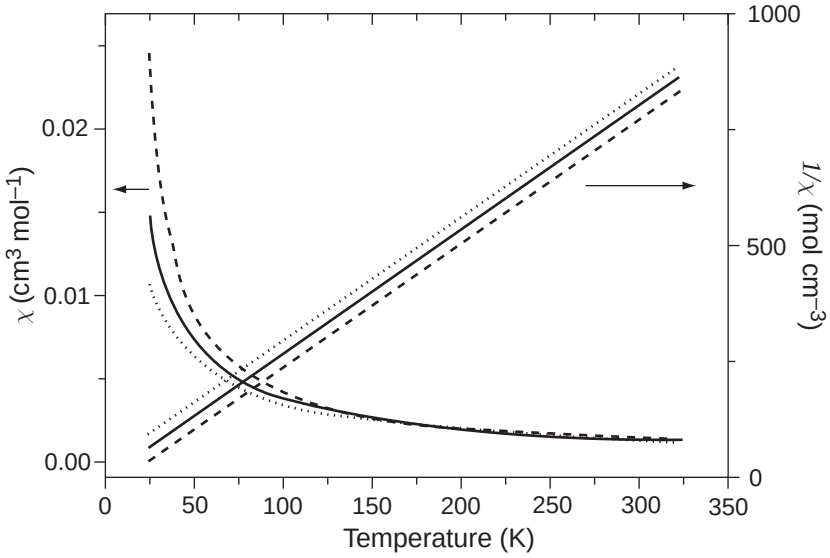

Figure 3.3 Plots of χ *vs* T and $1/\chi$ *vs* T from 25–325 K with $C = 0.375$ cm^3 K mol^{-1} for all cases, showing examples of ideal paramagnetism (solid line, $\theta = 0$ K), dominant ferromagnetic (dashed line, $\theta = +10$ K) and dominant antiferromagnetic (dotted line, $\theta = -10$ K) coupling

dominant antiferromagnetic interactions will lead to a negative value of θ. However, because qualitatively, in all of these cases, χ rises rapidly as T is lowered, it is quite often not obvious from this type of plot whether the data are indicative of ferro- or antiferromagnetic coupling (Figure 3.3). The sign and magnitude of θ are more readily revealed by a plot of $1/\chi$ *versus* T. For Curie–Weiss behaviour this should give a straight line plot with slope equal to $1/C$ and an extrapolated intercept onto the x-axis that equals θ (Figure 3.3). Note that the Curie–Weiss law can only apply when the temperature is significantly larger than the strength of the intermolecular interactions. It is important to note that ferromagnetic or antiferromagnetic *coupling* is not synonymous with ferromagnetic or antiferromagnetic *ordering*. Coupling can lead to ordering, much like intermolecular interactions can lead to condensation of a gas into a liquid or solid. It should also be borne in mind that even in cases where θ can confidently be attributed to interactions between magnetic moments rather than spin-orbit coupling (*vide infra*), it gives only average information and more detailed models are required to interpret the origins of the interactions at the molecular level. This is dealt with in subsequent sections.

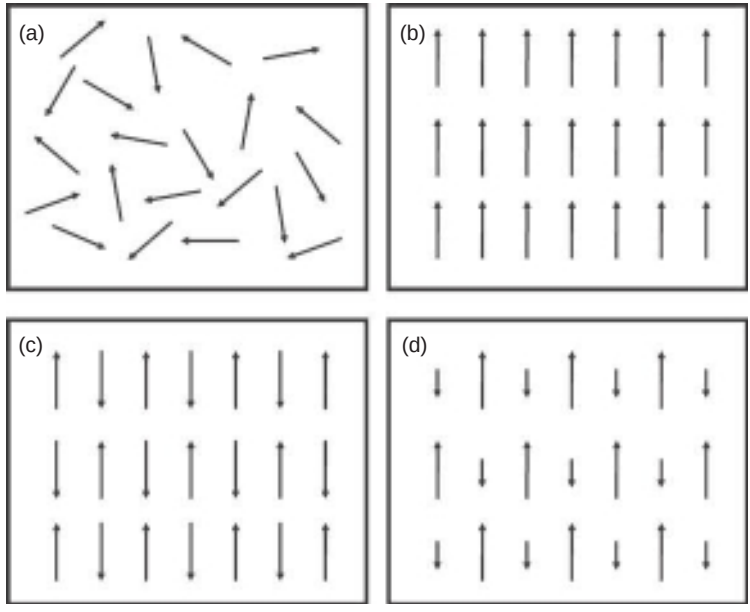

Figure 3.4 At high temperatures or if interactions are weak (a) paramagnetism is observed for all collections of spins, regardless of the sign of the interaction. At sufficiently low temperatures, interactions between neighbouring magnetic moments can give rise to (b) ferromagnetism, where moments are aligned parallel, (c) antiferromagnetism, where moments are aligned antiparallel, and (d) ferrimagnetism, where unequal moments are aligned antiparallel such that a net overall magnetisation results

At sufficiently low temperature, there is insufficient thermal energy available to overcome the tendency of the moments to align in a long-range fashion and the material will show bulk magnetic ordering into ferromagnetic, antiferromagnetic or more complex phases where the moments are aligned over macroscopic dimensions (Figure 3.4b, c, d). This behaviour is characterised by a phase transition from the higher-temperature paramagnetic phase to the lower-temperature phase, with the transition temperature labelled as T_C (Curie temperature) for the ferromagnetic case and T_N (Neél temperature) for the antiferromagnetic case.

As well as the simple ferro- and antiferromagnetic cases, another common situation involves ferrimagnetism. In this case, the dominant interactions between moments are antiferromagnetic; however, the existence in the sample of more than one type of magnetic moment means that these do not exactly cancel in the antiferromagnetic alignment. For

example, a lattice containing equal numbers of Cu^{2+} ions alternating with Mn^{2+} ions with antiferromagnetic interactions between neighbours will lead to an ordered state at low temperature (sometimes labelled T_C and sometimes T_N) with the Mn^{2+} moments aligned with each other but in the opposite sense to the Cu^{2+} moments (Figure 3.4d). These moments are of unequal size as Mn^{2+} has five unpaired electrons and Cu^{2+} has one, and there will, therefore, be a net magnetic moment over the bulk sample. Since it is much easier to engineer antiferromagnetic interactions rather than ferromagnetic interactions between neighbouring magnetic ions, the ferrimagnetic approach is an extremely useful and important strategy to prepare bulk molecule-based magnets (*vide infra*).

Besides these three important classes, there are a number of more exotic arrangements of spins that can occur; these are discussed in later sections.

For completeness of the discussion of relevant quantities and units, it should be noted that some authors still report the effective magnetic moment,(μ_{eff}), which is defined to be:

$$\mu_{eff} = \sqrt{8\chi T} = g\sqrt{S(S+1)} \text{ in units of Bohr magnetons (B.M. or } \beta) \quad (3.6)$$

The factor 8 arises due to a fortuitous combination of constants ($N\beta^2/3k \approx 0.125$ in cgs emu units). This definition of μ_{eff} is common in the older literature and found use because it scales linearly with g and nearly linearly with S. In an ideal Curie paramagnet, μ_{eff} is independent of temperature, since it contains the term χT, which equates with the Curie constant, C (Equation 3.3). It should be noted, however, that this definition of μ_{eff} is only really meaningfully related to the spin at high temperature. At lower temperatures, due to any finite value of θ and ultimately bulk magnetic ordering, it ceases to have any direct relationship with S. In older literature the experimental value of μ_{eff} was generally reported only at room or relatively high temperatures and could often be predicted well by Equation 3.6. In recent times, however, as variable-temperature measurements down to a few Kelvin have become commonplace, the product χT is more often employed instead. It carries the same information content as μ_{eff} but does not risk confusion by implying some additional significance as suggested by Equation 3.6. The product χT also has the attractive property of being additive, whereas μ_{eff} is not: if a molecule has two spin centres, the calculated value of χT is simply the sum of the χT contributions from each metal centre, whereas the value of μ_{eff} is not given by the sum of the individual μs because of the square root dependence on χ (which is itself additive). A plot of χT *vs* T is very useful;

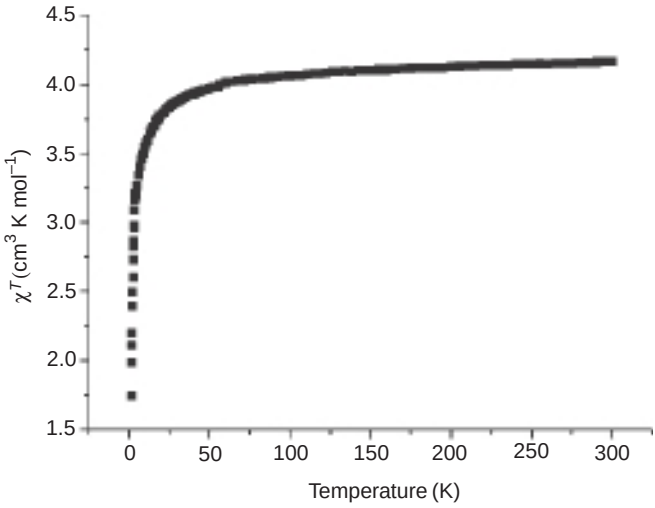

Figure 3.5 Plot of χT *vs* T for a Mn^{2+} complex of isonicotinic acid.[14] The complex is d^5, high spin and, for reasons discussed below, follows spin-only behaviour very well. This is confirmed by a value of χT = Curie constant = 4.17 $cm^3\,K\,mol^{-1}$ at higher temperatures, which compares well with the prediction of 4.375 $cm^3\,K\,mol^{-1}$ for an $S = 5/2$ ion. The decrease in χT at lower temperatures can be attributed to antiferromagnetic interactions between the Mn^{2+} ions

in the high-temperature, Curie–Weiss region it gives a temperature-independent straight line with a gradient C and a positive or negative value of θ is easily apparent as an upturn or downturn, respectively, at lower temperature (Figure 3.5).

3.2.3 Other Measurements

In addition to measurement of magnetisation *vs* temperature, measurement of magnetisation as a function of applied magnetic field is a very useful experiment. The normal form of this curve is for a linear increase in M with H which levels off at high values of field where the magnetisation begins to become saturated, that is all the spins are aligned and no further magnetisation can occur. The value at which this limit is attained is called the saturation magnetisation (M_{sat}) and can be related to the molecular properties by:

$$M_{sat} = NgS\beta \tag{3.7}$$

which for $S = 1/2$ and $g = 2$ has a value for 5585 emu G mol^{-1}. This formula, which considers only the contribution from the electron spin, can therefore be used to confirm the total spin of the complex, assuming there is some knowledge of the g value (*vide infra*). The plot of M *vs* H can also verify the values of field for which the M/H relationship is linear and, hence, the possible values of fixed field that could be chosen to measure M *vs* T and determine the susceptibility. Furthermore, the M *vs* H plot is a useful way to ensure that the sample does not contain a highly magnetic impurity, such as some iron oxides or fragments of nickel from a spatula, which would invalidate further analysis. Such strongly ferro- or ferrimagnetic materials, even if present in quantities undetectable through normal analysis, would give a rapid, nonlinear rise in M as H is increased and be immediately obvious. The use of M *vs* H plots is also of particular importance for the characterisation of ferro- or ferrimagnets as discussed in Section 3.4.5.

The measurements described so far involve a fixed (DC) magnetic field. Also increasingly common are measurements that use an alternating (AC) field, either on its own or superimposed upon a DC component. Such measurements give important information on the dynamics of ordering and fluctuations of the moments and can give detailed information in magnetically ordered materials. Methods that utilise AC measurements will not be discussed further in this chapter. More detailed accounts of general magnetic properties and characterisation can be found in specialised texts.[15,16]

3.2.4 Orbital Angular Momentum

As mentioned above, in addition to the contribution to the magnetic moment from the electron spin, there is another potential contribution to the observed magnetic properties due to the orbital motion of the electron about the nucleus. The total orbital angular momentum is the sum of the m_l values. In order for there to be a first-order orbital contribution to the magnetic moment, an orbital with non-zero angular momentum must be occupied with a different number of electrons from its partner corresponding to angular momentum of opposite sign. Although the model is completely wrong, it is useful to think of $m_l = +1$ or $+2$ as representing an electron orbiting the nucleus in one direction with one or two units or orbital angular momentum and –1 or –2 as an electron orbiting analogously in the opposite direction. The

requirement then for an orbital contribution is unequal numbers of electrons orbiting the nucleus in opposite directions. For example, if there is an electron in $m_l = +2$ and not in –2, there will be an orbital contribution. In the case of d^5, because each orbital is occupied with one electron, the net orbital angular momentum is zero. Thus, as can be seen in Figure 3.6, d^1 ions (and all other d^n except d^5) would be expected to exhibit an orbital contribution. Because of equal occupation of states of equal but opposite m_l, d^5 would be expected to exhibit a moment solely due to spin. Of course, d^{10} is nonmagnetic.

Both the spin and orbital angular momentum are vector quantities and are coupled together. In the limit of weak spin-orbit coupling the spin angular momentum, $S(=\Sigma m_s)$, and orbital angular momentum, $L(=\Sigma m_l)$, can be considered separately when analysing the magnetic properties of free atoms. The general expression for the susceptibility is given by:[17]

$$\chi = \frac{N\beta^2}{3kT}\left[g_e^2 S(S+1) + L(L+1)\right] \tag{3.8}$$

which expresses the additive nature of the susceptibility due to each contribution (g_e is the g-factor for the free electron = 2.0023 approximately). In practice, this expression has almost no predictive value because of two effects: ligand field quenching of orbital angular momentum and spin-orbit coupling, which becomes more important as the atomic number increases. However, this formula works perfectly for high-spin ions with half-filled subshells, such as Mn^{2+} or Fe^{3+}, because there is no first-order orbital angular momentum in the ground state ($L = 0$) and there are no low-lying excited states of the same spin multiplicity that do possess orbital angular momentum. For similar reasons, it would be predicted that Gd^{3+}, f^7, with an exactly half-filled f subshell, should also follow this expression and this is borne out.

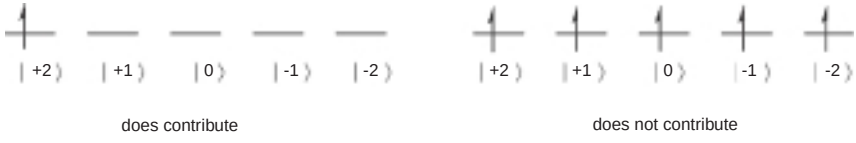

Figure 3.6 Determination of the orbital angular momentum from a set of degenerate d-orbitals

3.2.4.1 Ligand Field Quenching of Orbital Angular Momentum

Based on the above expression, for a complex ion containing Cr^{3+}, which is d^3, it might be expected that $\chi = \frac{N\beta^2}{3kT}\left[(2^2)\ \frac{3}{2}\left(\frac{5}{2}\right) + 2(3)\right]$, but this is not observed. Instead, what is usually observed is a value of the susceptibility that is consistent with nearly complete quenching of the orbital contribution, that is $L \sim 0$. This phenomenon is known as ligand-field quenching. This happens because the presence of the ligand field can mix states of equal but opposite angular momentum in many transition metal complexes; this is discussed in the following section. Because quenching of the orbital angular momentum often occurs, researchers, for convenience, define what is known as the spin-only formula and use this calculated quantity often to compare to the real data. By setting $L = 0$ in Equation 3.8, the so-called 'spin-only' values are given simply by:

$$\chi T = \frac{Ng^2\beta^2}{3k}[S(S+1)] \tag{3.9}$$

which was presented earlier in the form of Equation 3.4, and these are easily computed for various values of S (Table 3.1). For those ions whose properties are well explained by spin-only magnetism, the experimental value of χT or μ_{eff} will approach these calculated values asymptotically at room temperature, though it may deviate significantly at lower temperatures due to other effects (see, for example, Figure 3.5).

3.2.4.2 Explanation of Ligand Field Quenching

The canonical real *d*-orbital wave functions are linear combinations of the complex eigen functions (solutions) of the hydrogenic Schrödinger equation and the orbital angular momentum operator. Thus, instead of a set of five degenerate orbitals that may be indexed by values of orbital

Table 3.1 Computed spin-only values of χT and μ_{eff} for different numbers of unpaired electrons

Unpaired e	χT (emu K mol^{-1})	μ_{eff} (B.M.)
1	0.375	1.73
2	1.00	2.83
3	1.875	3.87
4	3.00	4.90
5	4.375	5.92

angular momentum ranging from $m_l = +2, +1, 0, -1$ and -2, we have quite equivalently five real d-orbitals d_{xz}, d_{yz}, d_{xy}, d_{z^2} and $d_{x^2-y^2}$ that are linear combinations of the previous set. In particular, d_{xz} and d_{yz} are linear combinations of equal parts $m_l = \pm 1$ and d_{xy} and $d_{x^2-y^2}$ are linear combinations of equal parts $m_l = \pm 2$ as shown below. The d_{z^2} orbital corresponds to $m_l = 0$ and contributes no orbital angular momentum. Of course, it is well known that in the presence of a ligand field, the d-orbitals are split. For the purposes of this discussion, octahedral symmetry will be considered, but all of the ideas are completely general.

The most convenient basis set in a ligand field consists of the real d-orbitals, though as will be seen, the choice is not unique. The real d-orbitals are linear combinations of complex wave functions. The braket notation below is used:

$$d_{z^2} = |0\rangle$$

$$d_{xz} = \left(\frac{1}{\sqrt{2}}\right)[|-1\rangle + |+1\rangle]$$

$$d_{yz} = \left(\frac{i}{\sqrt{2}}\right)[|-1\rangle - |+1\rangle]$$

$$d_{xy} = \left(\frac{i}{\sqrt{2}}\right)[|-2\rangle - |+2\rangle]$$

$$d_{x^2-y^2} = \left(\frac{1}{\sqrt{2}}\right)[|-2\rangle + |+2\rangle]$$

Note that the individual $|m_l\rangle$are eigen functions of the angular momentum operator, but linear combinations are not. In an octahedral field, the real d-orbitals are split into two sets: a triply degenerate t_{2g} (d_{xz}, d_{yz} and d_{xy}) and a doubly degenerate e_g (d_{z^2} and $d_{x^2-y^2}$), with the former lower in energy than the latter (Figure 3.7). Other ligand field geometries will yield different splitting patterns.

Notice that an unpaired electron in d_{xy} or $d_{x^2-y^2}$ in this geometry cannot contribute orbital angular momentum because each of the orbitals consists of equal parts of $m_l = \pm 2$. It might seem that this is true for the pair d_{xz} and d_{yz} as well, but because they are still degenerate in this geometry, it is possible to take linear combinations of these two wavefunctions and still have solutions to the Schrödinger equation.

Thus, the orbitals can just as correctly be labelled as shown in Figure 3.7b. So long as it is possible to occupy $+1$ and not -1 (or *vice versa*), in some arrangement of the electrons, there will be an orbital contribution, although this may still be less than would be shown for the equivalent free

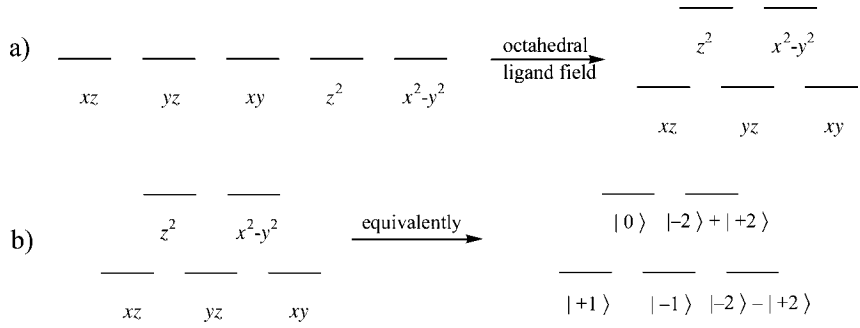

Figure 3.7 (a) Splitting of the real *d*-orbitals in an octahedral field (b) Relationship between real and complex *d*-orbitals in an octahedral field

ion due to the quenching of the ±2 contribution. In an octahedral field, the *d* electron counts that would all be expected to exhibit a first-order orbital contribution to the magnetic moment are d^1, d^2, low-spin d^4, d^5 and high-spin d^6, d^7. It is a simple matter to verify that all of these configurations correspond to a ground state *T* term (T_1 or T_2). By a similar argument, the reader could verify that in a tetrahedral field, which is always high spin, d^3, d^4, d^8 and d^9 electron configurations would exhibit an orbital contribution. It is relatively easy to understand that unless there is at least a C_n rotation axis where $n \geq 3$, all of the degeneracy among the *d*-orbitals is lifted and there can be no orbital contribution in first order.

3.2.4.3 Spin-Orbit Coupling

Based on the above explanation, for those ions with ground state *A* or *E* terms then, one might expect spin-only behaviour that follows the Curie or Curie–Weiss law. For example, nickel(II) has a $^3A_2$ ground state and exhibits a χT product that is largely temperature independent and close to the spin-only value. However, experimentally, the *g* value is usually slightly larger than 2.0 at around 2.2. For instance, $g = 2.24$ for $[Ni(OH)_6]^{2+}$ and 2.16 for $[Ni(NH_3)_6]^{2+}$. Referring to a Tanabe–Sugano diagram for this ion, the first excited state is $^3T_2$, which does have an orbital contribution and has the same spin multiplicity, so mixing of these two states can occur. The amount of mixing, not surprisingly, depends on the energy difference between the ground state and excited state (the energy gap between t_{2g} and e_g in an octahedral field) and this energy difference is called

$10Dq$ (Δ_o). The equation that governs the size of the g value for an octahedral complex is:

$$g = 2\left(1 - \alpha\frac{\lambda}{10Dq}\right) \tag{3.10}$$

where $\alpha = 2$ for an E term and 4 for an A_2 term and $10Dq$ is the energy gap between e_g and t_{2g}; λ is a constant that is related to the spin-orbit coupling constant (ζ). $\lambda = \pm\zeta/2S$ where ζ is always positive. The plus sign applies when shells are less than half full, whereas the minus sign applies when they are more than half full. Thus, the g value is expected to be less than two for the former and greater than two for the latter. Tables of the values of λ and ζ can be found in Earnshaw.[18] In practice, g is treated as a fitting parameter and its deviation from 2.0 is often not explained other than to note its similarity to related complexes.

So, in a fairly straightforward way, it is possible to predict the magnetic properties of many metal complexes based on symmetry and electron count. And, often, the orbital contribution is quenched by the ligand field. However, a very interesting example of a complex that behaves in the completely opposite way, that is in which there is almost no quenching of the orbital angular momentum is [Fe{C(SiMe$_3$)$_3$}$_2$]. The oxidation state of the iron is formally 2+, d^6.[19] In the free ion, the electron configuration would lead to two net units of orbital angular momentum and four unpaired electrons (Figure 3.8a).

The C–Fe–C backbone of the complex is rigorously linear and the overall symmetry is D_{3d}. The high symmetry preserves the important degeneracies (Figure 3.8b) and the small number of ligands produces a weak ligand field. As a result, the orbital contribution is almost completely unquenched consistent with $L = 2$ and $S = 2$. The saturation magnetisation is $\sim$32 500 emu G mol^{-1}, far exceeding the spin only value of $(N\beta g_e S) \sim$ 22 300 emu G mol^{-1} and close to the value expected for $N\beta(L+g_eS)$ $\sim$33 400 emu G mol^{-1}. Other high symmetry iron(II) complexes, for instance square-planar tetraazamacrocylic complexes, also show a strong orbital contribution.[20]

3.2.4.4 Rare Earth Ions

In contrast to early transition metals, the orbital contribution and spin-orbit coupling are very important for rare earth ions. The f-orbitals are relatively close to the nucleus and only weakly affected by ligand fields, leaving them essentially unsplit. Thus, when considering the magnetic

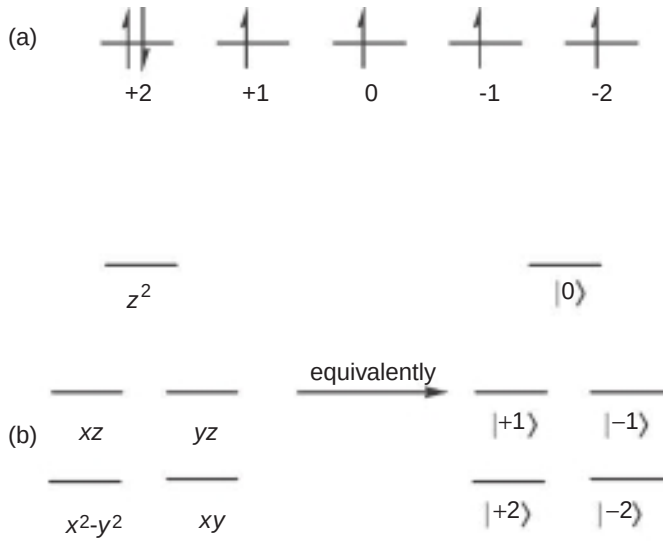

Figure 3.8 (a) Ground state *d*-orbital filling of a d^6 free ion; (b) *d*-orbital splitting for 'linear' $Fe[C(SiMe_3)_3]_2$

properties of rare earth ions, it is almost always necessary to consider the orbital contribution to the magnetic moment. As a consequence of the weak interaction between the *f*-electrons and the ligands, the magnetic properties of complexes containing rare earth ions can generally be described well by their single-ion behaviour in the dilute limit. Furthermore, with rare earth ions, spin-orbit coupling cannot be assumed to be small. The spin quantum number (S) and orbital quantum number (L) are no longer good quantum numbers and one must consider J, which can take on all values from $L + S$ to $L - S$ in integral steps, where L is the sum of the orbital angular momenta (m_l) of the occupied orbitals. The magnetic susceptibility is given by:

$$\chi = \frac{N\beta^2}{3kT} g_J^2 [J(J+1)] \tag{3.11}$$

where the g value is given by the equation:

$$g_J = \frac{3J(J+1) + S(S+1) - L(L+1)}{2J(J+1)} \tag{3.12}$$

It is left to the reader to verify that if $J = S$ (*i.e.* if $L = 0$ as for Gd^{3+}), this expression reduces to $g = 2$ and, therefore, Equation 3.11 becomes equivalent to the spin-only Equation 3.9.

Table 3.2 Expected values of χT for rare earth ions

	f electrons	*S*	*L*	*J*	*g*	χT
Ce^{3+}	1	0.5	3	2.5	0.86	0.80
Pr^{3+}	2	1	5	4	0.80	1.60
Nd^{3+}	3	1.5	6	4.5	0.73	1.64
Pm^{3+}	4	2	6	4	0.60	0.90
Sm^{3+}	5	2.5	5	2.5	0.29	0.09
Eu^{3+}	6	3	3	0	—	0.00
Gd^{3+}	7	3.5	0	3.5	2.00	7.88
Tb^{3+}	8	3	3	6	1.50	11.81
Dy^{3+}	9	2.5	5	7.5	1.33	14.17
Ho^{3+}	10	2	6	8	1.25	14.06
Er^{3+}	11	1.5	6	7.5	1.20	11.48
Tm^{3+}	12	1	5	6	1.17	7.15
Yb^{3+}	13	0.5	3	3.5	1.14	2.57
Lu^{3+}	14	0	0	0	—	0.00

For less than half-filled subshells, the ground state is given by $J = L - S$, whereas for more than half-filled subshells, $J = L + S$ is the ground state. This leads to predicted values of χT as given in Table 3.2. As a consequence of the coupling rules for J, the largest χT are associated with greater than half-filled shells.

Because of the significant orbital contribution, in general, rare earth ions will not obey the Curie law and analytical expressions for χ as a function of T are rare. Nevertheless, the limiting value of χT at room temperature should approach the values given in Table 3.2.

Although rare earth ions can possess many unpaired electrons, as a building block for preparing molecule-based magnets with high ordering temperatures, their utility has been relatively limited. Most of the work has focused on Gd^{3+} or Eu^{2+}, which are spin-only ions and, thus, their magnetic behaviour is relatively uncomplicated and described well by the Curie law at higher temperatures. The properties of spin-coupled molecules and extended structures containing rare earth ions are further discussed below.

3.3 THE VAN VLECK EQUATION

To derive expressions for the magnetic susceptibility as a function of temperature for a wide range of situations, including the interactions involved in exchange-coupled systems and zero field splitting, an expression

is needed that, using Boltzmann statistics, models the population of the various levels as a function of temperature and sums up the contribution of each level to the observed magnetic moment. This is achieved using the Van Vleck equation, a derivation for which is available in most specialist magnetochemistry texts.[21] By expressing the energy of each state as an expansion in powers of the applied magnetic field, without loss of generality, it is possible to derive an expression for the magnetic susceptibility:

$$E_n = E_n^{(0)} + E_n^{(1)}H + E_n^{(2)}H^2 + \text{higher order terms} \tag{3.13}$$

The Van Vleck equation then expresses the temperature-dependent magnetic susceptibility as a function of the various $E_n^{(i)}$ as:

$$\chi = \frac{N\sum_n \left[\frac{\left(E_n^{(1)}\right)^2}{kT} - 2E_n^{(2)}\right] \exp\left(\frac{-E_n^{(0)}}{kT}\right)}{\sum_n \exp\left(\frac{-E_n^{(0)}}{kT}\right)} \tag{3.14}$$

The terms $E_n^{(0)}$ are the energy of the each of the n spin levels of the system before application of a magnetic field. The terms $E_n^{(1)}$ and $E_n^{(2)}$, the first- and second-order Zeeman terms, respectively, quantify the response of the system to the applied magnetic field to the first and second orders. The exponential terms represent the relative population of each of these levels as a function of temperature according to Boltzmann statistics. The derivation of $E_n^{(1)}$ and $E_n^{(2)}$ for complex systems using perturbation theory[25] is beyond the scope of this introductory chapter; however, for illustration, the equation is applied to three cases to demonstrate its general use.

3.3.1 Application of the Van Vleck Formula to an Isolated, Spin-Only Metal Complex

Consider a metal centre with a ground state with no first-order angular momentum, well separated in energy from any excited states. Upon application of a magnetic field the degeneracy of the level will be split, with the energy of each state given by $E_n = m_s g\beta H$, where H is the applied field (Figure 3.9). If H/kT is small, the second-order terms $E_n^{(2)}$ can be neglected and all energies will be linear in H. We now have the terms required:

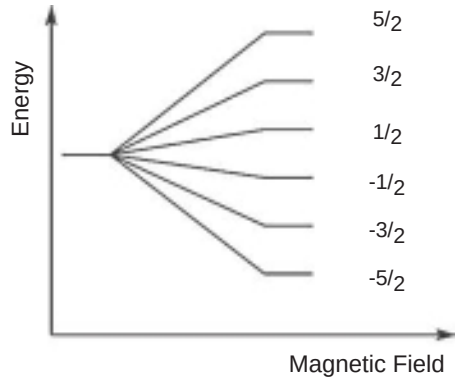

Figure 3.9 Energy splitting of an $S = 5/2$ ion in a magnetic field into individual m_s components ranging from –5/2 to +5/2

$E_n^{(0)} = 0$, since the zero energy position can be defined to be anything we like and for convenience choose that of the unsplit level;
$E_n^{(1)} = m_s g\beta$, where m_s can take on values from $-S, -S+1, \ldots$ to $+S$;
$E_n^{(2)} = 0$.

Substituting these values into Equation 3.14 and simplifying gives:

$$\chi = \frac{Ng^2\beta^2}{3kT}[S(S+1)]$$

which is the Curie law as expressed in Equation 3.9.

3.3.2 Deviations from the Curie Law: Zero-Field Splitting

For molecules of lower than cubic symmetry with more than one unpaired electron (*i.e.* $S > ½$), coupling to excited states through spin-orbit coupling can break the degeneracy of the m_s states even in the absence of an applied field. This phenomenon, known as zero-field splitting, in turn will lead to deviations from the Curie law. The behaviour of an $S = 1$ system will serve as an illustration. The form of the Hamiltonian is:

$$\mathbf{H}_{\mathrm{zfs}} = D\left[\hat{\mathbf{S}}_z^2 - \frac{1}{3}S(S+1)\right] + g_z\beta H_z\hat{S}_z + g_\perp\beta\left(H_x\hat{S}_x + H_y\hat{S}_y\right) \qquad (3.15)$$

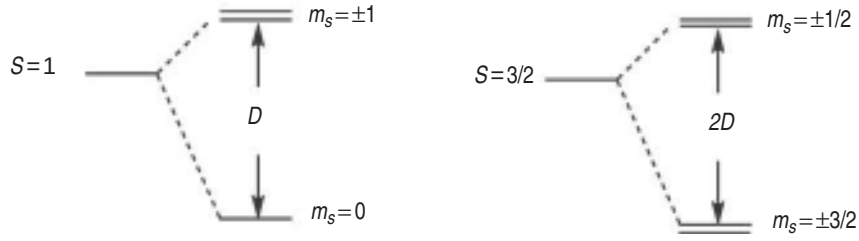

Figure 3.10 Zero-field splitting of $S = 1$ and $S = 3/2$ ions with positive and negative D, respectively

the first term of which results in breaking the degeneracy of states of different $|m_s|$, but retaining the degeneracy of states with the same $|m_s|$ in zero field. The value of D can be positive or negative (meaning that larger m_s could result in higher or lower energy) and, in general, it is impossible to determine this unequivocally based on powder or polycrystalline data. In Figure 3.10, by convention, D is positive and negative, respectively for $S = 1$ and 3/2. Subsequent application of a magnetic field results in Zeeman splitting of states of different m_s (second and third terms of Equation 3.15). However, m_s remains a good quantum number only for fields along the z direction. For fields perpendicular to z, mixing of the m_s states results in second-order Zeeman terms.

For the purposes of illustrating the Van Vleck equation, the effects of zero-field splitting for $S = 1$ can be examined as shown in Figure 3.10. In this case, it is no longer true that all of the $E_n^{(0)}$ terms are equal to 0 and so the Curie law will not be obeyed. With the applied field applied along the z direction, the $m_s = 0$ state will be unaffected, but the ±1 states will be Zeeman split and will vary linearly with applied field.

$$E_1^{(0)}=0 \text{ and } E_1^{(1)}=0;$$
$$E_2^{(0)}=\mathrm{D} \text{ and } E_2^{(1)}=-g\beta;$$
$$E_3^{(0)}=\mathrm{D} \text{ and } E_3^{(1)}=+g\beta.$$

$$\chi_z=\frac{2Ng_z^2\beta^2}{kT}\frac{\exp\left(-\frac{D}{kT}\right)}{1+2\exp\left(-\frac{D}{kT}\right)} \quad \chi_\perp=\frac{2Ng_\perp^2\beta^2}{D}\frac{1-\exp\left(-\frac{D}{kT}\right)}{1+2\exp\left(-\frac{D}{kT}\right)} \tag{3.16}$$

It is a relatively simple matter of plugging in these six values into the Van Vleck equation to obtain χ_z. Details of the derivation of the perpendicular susceptibility ($\chi_\perp$) may be found in Kahn[22] along with analogous derivations and expressions for the $S = 3/2$ and 5/2 cases. Since magnetic susceptibility data are most often collected on powdered or polycrystalline samples, it is useful to combine these expressions into one for the purposes of fitting. However, it must be noted that it is dangerous to overinterpret the least-squares fits, particularly with four or more fitting parameters. In particular, the sign on D is typically not uniquely determined from fits to powder data:

$$\chi_{\text{powder}} = \frac{\chi_z + 2\chi_\perp}{3} \tag{3.17}$$

To illustrate these general points, Figure 3.11 shows a plot of χT *vs* T for a tetrahedral Co^{2+} complex with a zero-field split $S = 3/2$ ground state.[23] The higher temperature data reach around 2.4 $cm^3\,K\,mol^{-1}$, slightly higher than the spin-only value of 1.875 $cm^3\,K\,mol^{-1}$ predicted in Table 3.1 due to mixing in of some orbital contribution as discussed above. Note also, the sharp drop in χT at low temperature due to decreasing population of the higher energy states. This appears qualitatively similar to Figure 3.5, where the drop in that case was attributed to intermolecular interactions rather than zero-field splitting. This emphasises again that a simplistic analysis of magnetic data using the Curie–Weiss law does not directly reveal the reason for any deviation from ideal Curie behaviour, and that some knowledge of the chemical system must be used to decide the model that should be applied.

3.3.3 Exchange Coupling

3.3.3.1 A Binuclear Complex of Interacting Cu^{II} Ions

For a binuclear complex with two interacting paramagnetic metals, the Hamiltonian should firstly be defined, which can be written as:

$$H = -J\left(\hat{S}_1 \bullet \hat{S}_2\right) \tag{3.18}$$

where $\hat{S}_1$ and $\hat{S}_2$ represent the spin operator for each of the two metal centres and J is the coupling constant that quantifies the magnitude of the interaction. As written, J is positive for ferromagnetic coupling and negative for antiferromagnetic coupling. Note that in some works the

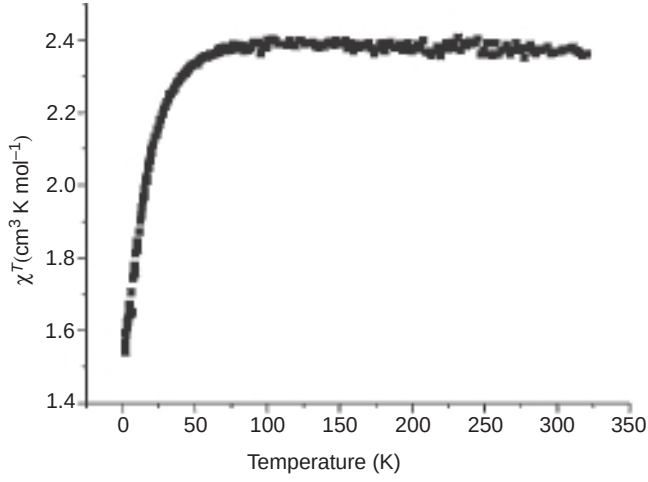

Figure 3.11 Plot of χT *vs* T for the tetrahedral $S = 3/2$ Co^{2+} complex $[Co(^{i}Pr_2P\{S\}NP\{S\}Ph_2)_2]$

negative sign before J is not included in the Hamiltonian and in some a factor of 2 before J is included. It is, therefore, essential to check the Hamiltonian that defines the parameters when comparing data. Equation 3.16 is an 'isotropic (Heisenberg) spin Hamiltonian', which means that any orbital angular momentum and its resulting anisotropy have artificially been ignored. This approximation is often sufficient to interpret magnetic data, provided J is sufficiently large to dominate the behaviour in the temperature range considered and other factors such as zero-field splitting only become significant at lower temperature. The term in the brackets is the dot-product of the two spin operators.

Taking the simple example of two equivalent Cu^{2+} centres, then $S_1 = S_2 = ½$ and the g values for each metal will be the same. The exchange coupling will give two energy levels with total spin $S_t = 0$ or 1. The large majority of dinuclear Cu^{2+} species are coupled antiferromagnetically and so the former is lower in energy (Figure 3.12).

Only the $S_t = 1$ state is split in the magnetic field (Figure 3.12). Substituting the values of $E^{(0)} = 0$ (where $S = 0$), $E^{(0)} = J$ (where $S = 1$); $E^{(1)} = 0$ (where $S_t = 0$) and $E^{(1)} = m_s g\beta$ (where $S_t = 1$ and where $m_s = -1$, 0, +1) into the Van Vleck equation gives Equation 3.19, which was first derived by Bleaney and Bowers.

$$\chi = \frac{2Ng^2\beta^2}{kT\left[3 + \exp\left(\frac{-J}{kT}\right)\right]} \tag{3.19}$$

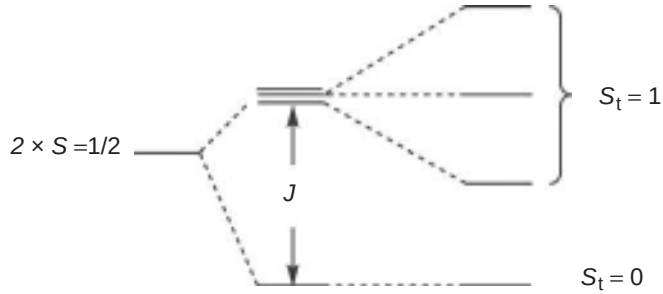

Figure 3.12 Antiferromagnetic coupling of two $S = 1/2$ metal ions and Zeeman splitting of the resulting energy levels due to an applied magnetic field

This is a special case of the expression for homonuclear dimers up to $S = 5/2$ on each centre.

$$\chi = \frac{2Ng^2\beta^2}{kT} \frac{e^x + 5e^{3x} + 14e^{6x} + 30e^{10x} + 55e^{15x}}{1 + 3e^x + 5e^{3x} + 7e^{6x} + 9e^{10x} + 11e^{15x}} \tag{3.20}$$

where $x = \frac{J}{kT}$.

For $S = 5/2$, the entire expression (Equation 3.20) is used, but for $S = 2$, the last exponential terms in the numerator and denominator are discarded. For $S = 3/2$, the last two terms are discarded, and so on. Details of the derivation can be found in Kahn.[24]

Examples of other polynuclear clusters that have more metals, dissimilar metals and/or higher spin metals will be of greater complexity than the simple example above, as they will have a larger number of energy levels to consider and it may be more laborious to specify the correct Van Vleck coefficients for each. The resulting expressions may then involve multiple g values, many exponential terms in the denominator and numerator and appear superficially complex; however, the principles for the derivation of such equations are the same as those presented here. Those interested in the methods required to treat the general case are referred to the literature.[25,26]

3.3.3.2 Mechanism of Magnetic Coupling

The occurrence of intermolecular interactions and resulting bulk ordering in magnetic materials was discussed in Section 3.2.2. However, it is important to consider the mechanisms by which such interactions occur as such understanding will enable the design and control of new

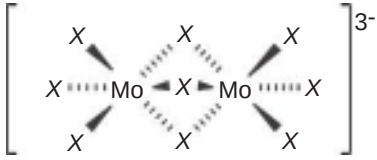

Figure 3.13 Schematic structure of bimetallic complexes $[X_3Mo(\mu\text{-}X)_3MoX_3]^{3-}$ (X = Cl, Br, I)[28]

materials. Magnetic dipole moments will always show an interaction through a classical, direct, through-space mechanism. However, this is too weak to account for the relatively strong interactions observed in materials where the magnetic centres are often far apart. Instead, the relatively strong coupling of magnetic moments in solids is explained by quantum mechanical exchange interactions. The simplest of these to consider is direct exchange, which involves the direct overlap of a partially occupied orbital on one magnetic centre with that on another. The structure of the bimetallic complexes $[X_3Mo(\mu\text{-}X)_3MoX_3]^{3-}$ is shown in Figure 3.13. The antiferromagnetic coupling between the metal ions was attributed largely to direct orbital overlap between *d*-orbitals of the different metals, which is facilitated by their close proximity in space.[27] The Pauli Exclusion Principle requires that the ground state be a spin singlet leading to the antiferromagnetic coupling between the metals. At higher temperatures, the spin triplet excited state can be partly populated leading to a gradual increase in magnetic susceptibility with increasing temperature. This basic concept is no different from that of the formation of a chemical bond through the overlap of orbitals. A distinction is made only because, in this case, the interaction is too weak to be considered as holding the molecule together and significant population of the excited state occurs at normal temperatures.

It is apparent, however, that in general metal ions are not sufficiently close in most solids for the magnetic properties to be explained by direct exchange, and thus superexchange is the most commonly encountered coupling mechanism in molecular magnetic materials. This involves coupling of the spins on two metal centres through the interaction of each with intervening ligand orbital(s) and is most readily pictured for a linear *M–L–M* arrangement (Figure 3.14a), where *L* is a closed shell ion such as oxide or halide. Considering for simplicity d^1 metals, if the first metal has its spin oriented up, the electron from the ligand delocalised onto the metal through orbital overlap must be spin down due to the exclusion principle. The other electron in the same ligand orbital must, therefore, be

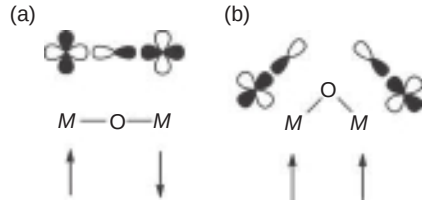

Figure 3.14 Illustration of superexchange in (a) a linear *M*–O–*M* fragment and (b) *M*–O–*M* with a 90° angle. In this case, the two sets of orbitals are shown separated for clarity

spin down and, as this can be delocalised onto the other metal, the other metal must be spin up. This corresponds to antiferromagnetic coupling between the metal ions. Alternatively, if the metal ions are arranged at 90° according to Figure 3.14b, the metals will interact with orthogonal orbitals on the ligand and the ground state will require spin density of the same sign to be transferred to each metal, which must now have the same spin orientation and be coupled ferromagnetically.

Furthermore, it can be seen that this simple analysis is reversed if the orbitals on the metals are of different symmetry to each other and interact differently with the bridging ligand. Thus, consideration of the geometry of the bridging interaction and *d*-orbital filling of the metals gives tremendous scope for designed magnetic properties in extended solids.[29]

The sign of the superexchange is generally well explained by what are known as the Goodenough–Kanamori rules.[30] Expanding on the rough indication given in Figure 13.4, these 'rules' consider the extent of overlap of the spin-containing molecular orbitals based on their local symmetry properties. In slightly over-simplified terms, if the active orbitals, those that are partially occupied, can overlap due to their appropriate local symmetry, antiferromagnetic coupling generally dominates, while if all of the active orbitals on each metal are orthogonal, ferromagnetic coupling results. This is illustrated by contrasting the expectation for two octahedral cyanide-bridged species: Cr^{3+} and V^{2+}, which couple antiferromagnetically,[31] and Ni^{2+} and Cr^{3+}, which couple ferromagnetically (Figure 3.15).[32] In the former, the active orbitals are all of t_{2g} symmetry (recall the octahedral coordination of the metals) and so overlap with the same orbitals on the ligand, while in the latter the active orbitals are e_g for Ni^{2+} and t_{2g} for Cr^{3+} and so overlap with orthogonal orbitals on the ligands.

These ideas for predicting the sign of the coupling do not work quite so well when the building blocks contain rare earth ions. Bellini and Gatteschi have reviewed this area of molecular magnetic materials recently.[33] Interest in these types of starting materials, of course, is the result of the

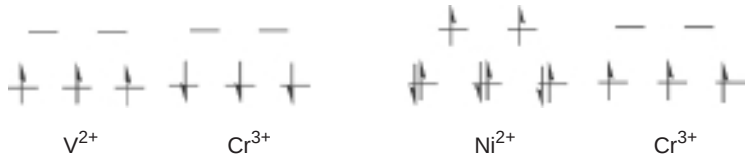

Figure 3.15 Illustration of antiferromagnetic coupling and ferromagnetic coupling of cyano-bridged metal ions depending on the symmetry of the metal singly occupied orbitals

greater number of possible unpaired electrons when *f*-orbitals are considered, as well as the orbital contribution to the magnetic moment. Because *f*-orbitals are relatively contracted, magnetic interactions that might result from direct overlap (exchange) between these orbitals on different ions are expected and observed to be small. Instead, researchers have focused on coupling between unpaired electrons in *f*-orbitals and either unpaired electrons in *d*-orbitals (on transition metal ions) or in π-orbitals (on organic radicals). For the most part, complexes of rare earth ions that have no orbital contribution (Gd^{3+} or Eu^{2+}) have dominated the effort because their spin-only behaviour makes analysis of the data much easier. For similar reasons, the use of Cu^{2+} and organic radicals permits the Heisenberg Hamiltonian, introduced above (Equation 3.18), to be used. Coupling between the spins on the f^7 rare earth ion and the Cu^{2+} or organic radical are typically quite weak, but have been observed to be both ferromagnetic and antiferromagnetic, even though by direct exchange only antiferromagnetic coupling might have been expected. An explanation of this involves mixing of charge-transfer excited states into the ground state.

Several synthetic strategies have been employed to prepare heteronuclear complexes. These have, for the most part, involved either creation of separate high coordination number environments (for the rare earth ion) and lower coordination number environments (for the transition metal) or secondary coordination, in which a rare earth complex is used as a ligand for a transition metal. Details may be found in Bellini and Gatteschi.[33]

3.4 DIMENSIONALITY OF MAGNETIC SYSTEMS

As indicated in Section 3.1, the molecular approach to magnetic materials offers particular advantages in the design of low-dimensional magnetic materials due to the ability to control the strength of magnetic exchange

in different directions and the possibility of placing metal ions in highly asymmetric coordination environments.[34,35] This section will address the key design and properties of such materials along with the models used to interpret their behaviour.

3.4.1 Lattice Dimensionality *vs* Single Ion Anisotropy

Before proceeding on a discussion of low-dimensional magnetic order, it is important to distinguish between anisotropy of the lattice and that of the magnetic moment of the individual building blocks. For a simple analogy, consider a one-dimensional chain of baseballs as an example of a highly anisotropic lattice consisting of isotropic building blocks. An isotropic ion is one in which the g values in each of the three mutually perpendicular directions are identical. High-spin Mn^{2+} or Fe^{3+} are good examples of this, but Ni^{2+} and Cu^{2+} are also typically well-behaved. This can be contrasted with a similar chain of American footballs or Frisbees, which can be taken to be analogues for ions with easy axis ($g_{\|} >> g_{\perp}$) and easy planes ($g_{\|} << g_{\perp}$) of magnetisation, respectively. Here, that the g value anisotropy reflects the anisotropy in the moment has been used without proof. Note that, in general, there need not be any restriction of the orientation of the American footballs or Frisbees relative to the chain axis and, similarly, there is no restriction on the orientation of the easy axis or easy plane relative to the chain axis. Likewise, a two-dimensional lattice (plane) could be constructed from isotropic or anisotropic building blocks, as could a three-dimensional structure. In all of the subsections below, the dimensionality in the subtitle refers to the physical structure of the lattice, not the magnetic anisotropy of the individual ions. Within each subsection, magnetic anisotropy will be discussed as appropriate.

3.4.2 Mean or Molecular Field Approximation in Any Dimension and Any Value of S

The most general treatment of intermolecular interactions gives rise to the Curie–Weiss law described above (Equation 3.5), allowing intermolecular interactions to be modelled by the parameter, θ. This is based on the mean or molecular field approximation, which can be generalised to

treat both the number of nearest neighbours and the magnitude of the spin (Equation 3.21):[17]

$$\chi = \frac{Ng^2\beta^2 S(S+1)}{3kT - zjS(S+1)} \tag{3.21}$$

where $\theta = \frac{zjS(S+1)}{3k}$.

Thus, in a refinement of the Curie–Weiss law, θ can be expressed as a function of zj, the product of the number of nearest neighbours and the coupling constant and the total spin (S). This expression has been generalised to take account of an intermolecular interaction as a perturbation on the single ion or single molecule magnetic behaviour of a general system. Again, though widely used, it is nevertheless still entirely phenomenological; it says nothing about the mechanism of magnetic coupling.

3.4.3 One-Dimensional Systems

3.4.3.1 Regular, One-Dimensional Chains

The simplest extended system, a one-dimensional chain, is intriguing because there are, for special cases, mathematical models that can be solved to adequately describe the temperature dependence of the magnetic susceptibility and because chemistry allows the synthesis of systems whose geometry approximates one-dimensional. Before a discussion of such systems, it is important to understand that a purely one-dimensional chain will never result in long-range magnetic order above 0 K. However, the chains in any actual material pack together in three dimensions and because of weak interchain interactions, long-range order may occur. So, in the present discussion of the temperature dependence of the magnetic properties, only the behaviour above the three-dimensional ordering temperature is being modelled. Magnetic order is treated in a later section.

The most basic form of a one-dimensional chain assumes an isotropic interaction, so-called Heisenberg behaviour (ferromagnetic or antiferromagnetic), between identical spin centres equally spaced. Perhaps, not surprisingly, the best experimental realisations of Heisenberg behaviour involve spin-only ions, such as Mn^{2+} and Fe^{3+} ($S = 5/2$) and Gd^{3+} ($S = 7/2$), but the high-spin value of these ions makes them more difficult to model. However, Cu^{2+} works quite well. Such systems can be described phenomenologically by a Heisenberg spin

Hamiltonian that takes into account only nearest neighbour interactions. In zero-field, this takes of the form of:

$$H = -J \sum_{i=1}^{n-1} \hat{S}_{A_i} \cdot \hat{S}_{A_{i=1}} \tag{3.22}$$

where the relationship of this operator to that for the simple two-body case described in Equation 3.18 should be clear: the single dot product is replaced by a sum over all nearest neighbour pairs. Again, caution must be exercised in comparing results from different researchers because the exact form of the Hamiltonian may differ. For an infinite chain, there is no analytical solution to finding the energy eigen values for this problem but, in 1964, Bonner and Fisher used a method of solving the problem exactly on small finite rings (up to 11), extrapolating to infinity and fitting these data to a numerical expression.[36]

For $J < 0$ (antiferromagnetic coupling):

$$\chi = \frac{Ng^2\beta^2}{kT}\left(\frac{0.25 + 0.074975x + 0.075235x^2}{1.0 + 0.9931x + 0.172135x^2 + 0.757825x^3}\right) \tag{3.23}$$

where $x = \frac{|J|}{kT}$.

It is interesting to note that depending on whether the ring has an even or odd number of spin centres, χ should either go to zero or infinity, respectively, as the temperature is lowered, corresponding to a diamagnetic or paramagnetic ground state, a seeming contradiction. In fact, Bonner and Fisher showed that the susceptibility for an infinite chain is neither infinite nor zero, but instead converges to a finite value because states of finite (nonzero) susceptibility lie infinitesimally in energy above the diamagnetic ground state.

For the case of ferromagnetic coupling, a high-temperature series expansion has been proposed:[37]

$$\chi = \frac{Ng^2\beta^2}{4kT}\left(\frac{A}{B}\right)^{2/3} \tag{3.24}$$

where

$$A = 1.0 + 5.7979916y + 16.902653y^2 + 29.376885y^3 + 29.832959y^4 + 14.036918y^5$$

$$B = 1.0 + 2.7979916y + 7.0086780y^2 + 8.6538644y^3 + 4.5743114y^4$$

The Bonner–Fisher method has been extended to an infinite chain of $S = 1$ centres by Weng, valid for $J < 0$ and applied by Kahn to the problem of modelling the behaviour of [Ni(NO_2)(en)]X, where X = ClO_4^- or I_3^-[38]:

$$\chi = \frac{Ng^2\beta^2}{kT}\left(\frac{2.00 + 0.0194x + 0.777x^2}{3.0 + 4.346x + 3.232x^2 + 5.834x^3}\right) \tag{3.25}$$

where $x = \frac{|J|}{kT}$.

Equation 3.25 makes the explicit assumption that it is reasonable to ignore anisotropy, that is that the zero-field splitting, $|D| << |J|$. It is possible to perform numerical calculations that take D into account, but these are probably of limited usefulness when trying to model real data. The Bonner and Fisher method becomes computationally difficult for $S > 1$ if the spin is treated as a quantum mechanical quantity. In the limit of large S, however, the spin can be treated as a classical quantity. Perhaps somewhat surprisingly, such a treatment works reasonably well for values of S as small as 5/2. Such a system can be synthetically realised with a chain of Mn^{2+}, which has an isotropic ^6A ground state. Fisher has derived an expression for an infinite chain of classical spins, scaled to a quantum spin, S[39]:

$$\chi = \frac{Ng^2\beta^2 S(S+1)}{3kT}\frac{1+u}{1-u} \tag{3.26}$$

where $u = \coth\left[\frac{JS(S+1)}{kT}\right] - \left[\frac{kT}{JS(S+1)}\right]$.

This equation was used to model the magnetic behaviour of $CsMnCl_3 \cdot 2H_2O$.[40]

Because it is significantly easier to achieve antiferrimagnetic, rather than ferromagnetic, coupling between nearest neighbours, there has been a great deal of effort made to synthesise ferrimagnetic one-dimensional chains and to model these systems. Although a general ferrimagnetic chain is rather difficult to model, the special case of alternating 5/2 and 1/2 has been treated. Again extending the Bonner and Fisher method, calculations have been performed on finite rings of the formula $(AB)_n$, where A and B possess different magnetic moments and are antiferromagnetically coupled ($J < 0$). The A site is taken to be well treated as a classical spin ($S \geq 5/2$) and the B site as a quantum spin ($S = 1/2$). This treatment yields the Seiden expression[41]:

$$\chi T = \frac{g^2}{4} \frac{4.75 - 1.62370x + 2.05042x^2 - 4.52588x^3 - 8.64256x^4}{1 + 0.77968x - 1.56527x^2 - 1.57333x^3 - 0.11666x^{4.5}} \quad (3.27)$$

where $x = \frac{|J|}{kT}$, which has been applied to, among other systems, alternating high-spin Mn^{2+} and organic radical chains.[42]

The Heisenberg Hamiltonian is a special case of the more general Hamiltonian:

$$H = -J \sum_{i=1}^{n-1} \alpha\left(\hat{S}^z_{\mathrm{A}} \cdot \hat{S}^z_{\mathrm{A}+1}\right) + \gamma\left(\hat{S}^x_{\mathrm{A}} \cdot \hat{S}^x_{\mathrm{A}+1} + \hat{S}^y_{\mathrm{A}} \cdot \hat{S}^y_{\mathrm{A}+1}\right) \quad (3.28)$$

with $\alpha = \gamma = 1$. For essentially isotropic ions such as Mn^{2+}, Ni^{2+} and Cu^{2+}, this model works reasonably well. However, if there is first-order angular momentum present, it is necessary to consider anisotropy in the Hamiltonian. Two limiting possibilities have been examined. The case where $\alpha = 1$ and $\gamma = 0$, is known as the Ising model and is applicable to systems that display uniaxial anisotropy. In this case, the magnetic moment prefers to be oriented in one of only two possible directions, though the orientation need not be along or perpendicular to the chain axis. If the easy axis of magnetisation is taken as the z axis, then the criterion for Ising behaviour is $g_z >> g_x$, g_y. Of course, to explore the magnetic properties, oriented single crystals are required.

Fisher has derived analytical expressions for the zero-field parallel and perpendicular susceptibility:

$$\begin{aligned} \chi_{||} &= \frac{Ng_{||}^2\beta^2}{2J}\left(\frac{J}{2kT}\right)\exp(J/kT) \\ \chi_{\perp} &= \frac{Ng_{\perp}^2\beta^2}{4J}\left[\tanh\left(\frac{J}{2kT}\right) + \left(\frac{J}{2kT}\right)\mathrm{sech}^2\left(\frac{J}{2kT}\right)\right] \end{aligned} \quad (3.29)$$

where parallel and perpendicular are relative to the unique z axis.[43] Related expressions for $\chi_{\perp}$ for two-dimensional Ising lattices are also contained in this paper, as well as references for $\chi_{||}$ for these geometries.

The case of $\alpha = 0, \gamma = 1$ is known as the XY model. Experimentally, this situation is less common than the Ising model and will not be discussed further. However, additional information may be found in Carlin.[44]

For many years, it was believed that the qualitative behaviour of one-dimensional chains with ions of differing spin would be the same. However, in 1983 Haldane made the prediction that one-dimensional antiferromagnetic chains with integer spin would behave differently from those with half-integer spin.[45–47] The former were predicted to show a

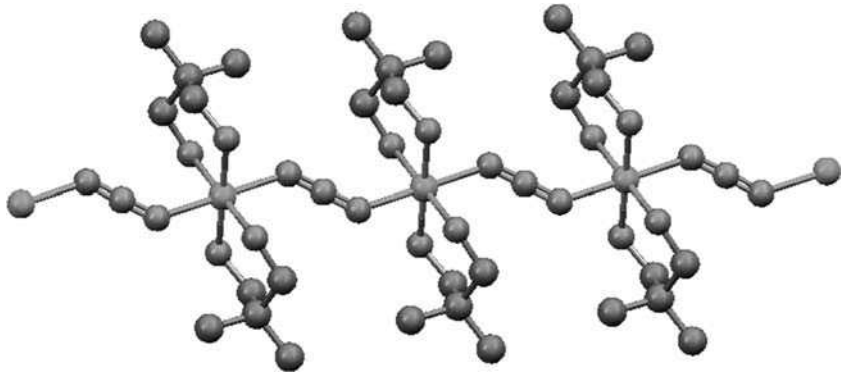

Figure 3.16 X-ray structure of NDMAP[51]

nonmagnetic, spin-singlet ground state with an energy gap between this and the first triplet excited state. This is of particular relevance to the field of superconductivity, where the relationship between a spin-gap phase and the superconducting phase is a subject of much interest.[48]

In order to test such a hypothesis, highly ideal model one-dimensional materials are required, since any interaction between chains must be minimised to enable Haldane Gap behaviour to be observed and studied. The molecular magnetic material $[Ni(\mu\text{-}N_3)(1,3\text{-diamino-}2,2\text{-dimethylpropane})_2]_n[PF_6]_n$ (NDMAP)[49] has emerged as an excellent model for such systems.[50] The X-ray structure (Figure 3.16) illustrates the chains of identical Ni^{II} centres, isolated by the relatively large 1,3-diamino-2,2-dimethylpropane ligand with Ni^{II}–Ni^{II} interaction through the bridging $[N_3]^-$ ligand.

The magnetic susceptibility of a single crystal[52] yielded the values $J/k_B = 30.0$, $D/J = 0.3$, $g_{\|} = 2.10$ and $g_{\perp} = 2.17$ (J is the intrachain exchange coupling constant, D is the single ion anisotropy and the g values are parallel and perpendicular to the chain, respectively). Studies showed that application of a magnetic field to the material led to a long-range ordered state at low temperature. This was explained by the splitting of the first triplet excited states in the magnetic field, which above a critical value led to crossing of the lowest energy component with the singlet ground state. The field-induced magnetic moments can then undergo long-range ordering due to the weak interchain coupling. The verification of the spin-gap behaviour of the $S = 1$ chain in this and other materials, and the observation of the magnetic field induced long-range order in the case of this material, have provided experimental realisation of the Haldane conjecture that would be difficult to obtain from less ideal, less crystalline and stronger coupling nonmolecular materials.

3.4.3.2 Spin Ladders

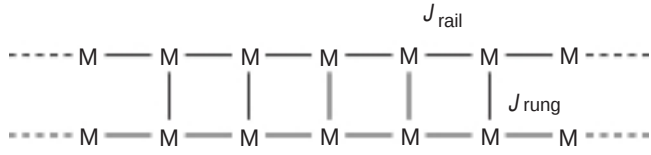

Figure 3.17 Schematic illustration of a two-legged spin ladder. Each 'M' represents a magnetic centre in the lattice

A related topic concerns that of spin ladders, which are structures intermediate between one- and two-dimensional spin lattices (Figure 3.17) characterised by coupling along the rail (J_{rail}) and across the rungs (J_{rung}) and in the ideal case isolated from interladder interactions. As additional legs are added to a ladder, it might be expected that a smooth transition from one-dimensional ($n = 1$) to two-dimensional ($n = \infty$) behaviour would occur. This is not the case, however, and a fluctuation in behaviour is shown between odd- and even-legged ladders, with the latter showing spin-gap behaviour with a singlet ground state analogous to a Haldane chain.[53] As well as the fundamental understanding that arises from the study of such low-dimensional quantum systems, spin ladders have been observed under some circumstances to undergo a transition to a superconducting phase.[54] Again, in the field of spin ladders, molecular materials can offer highly crystalline, structurally characterised materials that can be additionally probed through study of the magnetic excitation spectrum under high applied field facilitated by the typically weak exchange coupling in comparison with continuous-lattice systems.

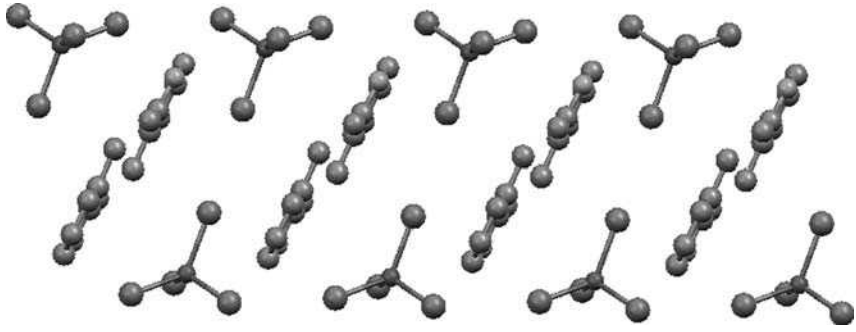

Figure 3.18 X-ray structure of [2,3-dimethylpyridinium]$_2$[$CuBr_4$] illustrating the spin ladder motif

The complex [2,3-dimethylpyridinium]$_2$[$CuBr_4$] displays the characteristics of a two-legged $S = ½$, spin ladder.[55] The structure consists of $[CuBr_4]^{2-}$ anions linked *via* intermolecular Br $\cdots$ Br contacts (Figure 3.18) and the susceptibility data were successfully fit to a ladder model with $J_{rung} = -3.10$ cm^{-1} and $J_{rail} = -6.02$ cm^{-1}, making this a rare example of a strong-rail spin ladder. Due to potential ambiguity in the magnetic analysis, the conclusions were supported by theoretical calculations suggesting this to be an excellent model system for further studies of the spin ladder phenomenon.

3.4.4 Two-Dimensional Magnetic Materials

One big difference between one- and two-dimensional systems is that whereas the former never order above 0 K (without interchain interactions), it is possible for a two-dimensional Ising system to order at finite temperature. Onsager has examined such a system for $S = 1/2$ and found theoretical evidence for ordering, on a square lattice and even if the coupling anisotropy in the two directions on a quadratic lattice (defined to be J/J') is 100.[56] An example that behaves as a two-dimensional Ising antiferromagnet is $Cs_3[CoBr_5]$.[34]

There have been several other efforts to design and synthesise examples of two-dimensional lattices composed of magnetic building blocks, although they do not truly realise this goal. Many of these efforts involve secondary coordination: using a metal complex as a ligand for a second metal ion. Talham *et al.* have exploited this idea and the Langmuir–Blodgett technique to produce two-dimensional square monolayers related to Prussian Blue analogues (Figure 3.19). They begin with substitutionally inert pentacyanoferrate anions possessing one alkyl chain-substituted pyridine ligand. These synthons self-assemble on an air–water interface with the alkyl chains above the water surface. Addition of a second labile ion to the water subphase (Mn^{2+}, Co^{2+} or Ni^{2+}) results in a two-dimensional network formation. Using repeated dipping cycles, it is possible to construct multilayers.[57]

The magnetic properties of these assemblies as multilayers are similar to their bulk counterparts, but with lower ordering temperatures. In particular, long-range magnetic order is observed for a 150 multilayer assembly of the Fe/Ni structure at ~8 K, which is lower than the bulk ordering temperature of the three-dimensional material (~23 K). The lower ordering temperature is presumably due to weaker interplane interactions due to the increased separation.

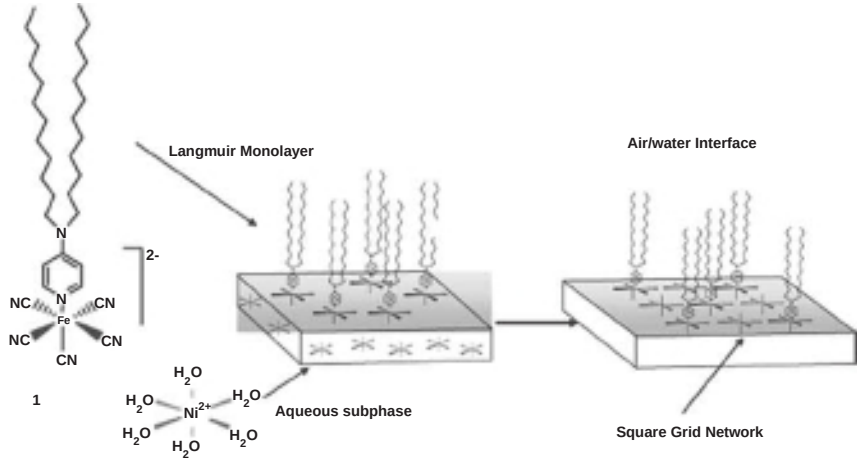

Figure 3.19 Formation of two-dimensional magnetic materials using the Langmuir–Blodgett technique. Reprinted with permission from Culp *et al.*, 2005 [57]. Copyright (2005) Elsevier

Okawa *et al.* first prepared the secondary coordination complex that results from the reaction in water of kinetically inert $Na_3[Cr(ox)_3]\bullet 3H_2O$, a metal(II) salt and NBu_4Br in a mole ratio of 1:1:1.5. It has subsequently been shown that this compound forms a two-dimensional sheet with alternating Λ and Δ stereochemistry at adjacent metal centres. The chirality at Cr and M are reversed in the next layer, such that the structure is overall achiral. These compounds are all ferromagnets with values of T_C that range from 6–14 K.[58] Kahn *et al.* extended this class of compounds to include the $S = 1/2$ building block $[Ru(ox)_3]^{3-}$ and published an expression for the susceptibility when M is sufficiently high spin enough to be treated as a classical spin.[59]

Another type of two-dimensional magnetic lattice that has received widespread attention is that of the layered perovskite materials. These are a general class of systems of formula $[A_2MX_4]$, whereby the MX_4 units form layers of corner-sharing (pseudo)octahedra, separated by layers of the A^+ counterions. These form a very extensive series of materials constructed from a vast range of different metals, bridging ligands and counterions, leading to varied and highly tunable magnetic, conducting and optical properties often linked with particular structural distortions of the lattice. These have been extensively reviewed[60,61] and will not be discussed again in detail here.

3.4.4.1 Magnetic Frustration in a Two-Dimensional Lattice

The vast majority of superexchange interactions lead to antiferromagnetic coupling; however, in certain lattice geometries it is impossible to satisfy this for all nearest neighbours. This leads to the phenomenon known as spin frustration (see, for example, Figure 3.20a and 3.20b), which can lead to a large number of nearly degenerate ground states and may lead to a variety of exotic spin states. The kagomé lattice is a two-dimensional topology of great theoretical interest due to the resulting spin frustration that arises from the interconnected triangular units.[62] Experimental realisations of a kagomé lattice generally suffer from deviations from ideality through interplane interactions or symmetry within the layer that is lower than the ideal case.[63] Using a molecular approach, a high symmetry kagomé lattice was self assembled using binuclear Cu^{2+} units interlinked by 1,3-benzenedicarboxylate ligands and capped with pyridine ligands at the apical positions to yield $[(Cu_2(py)_2(bdc)_2)_3]_n$ (Figure 3.20c).[64]

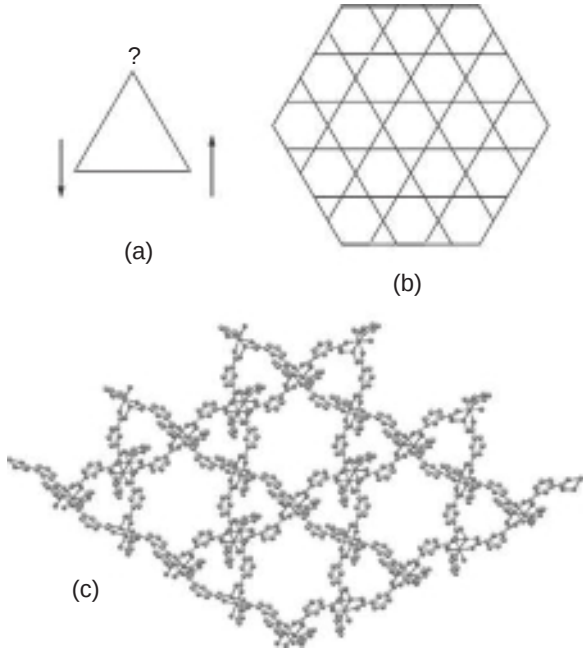

Figure 3.20 (a) Spin frustration in triangular geometry: the third spin cannot satisfy antiferromagnetic coupling simultaneously with both of the others. (b) The kagomé lattice leading to extended spin frustration in two dimensions. (c) X-ray structure of $[(Cu_2(py)_2(bdc)_2)_3]_n$ illustrating the kagomé lattice geometry[64]

Analysis of the magnetic data revealed antiferromagnetic coupling between the Cu_2 units. However, due to the inherent frustration this was not able to lead to a fully antiferromagnetically coupled ground state. Instead, spontaneous magnetisation was observed giving on hysteresis loop that was attributed to spin canting, the phenomenon whereby antiparallel moments are slightly tilted such that complete cancellation does not occur and a small uncompensated moment results (Section 3.4.5.1). This material has the added complication of strong antiferromagnetic exchange within each Cu^{2+} dimer. A related material with mononuclear Cu^{2+} centres was recently prepared of formula $[Cu(1,3\text{-bdc})]_n$. This material was shown to be a structurally perfect kagomé lattice with $S = 1/2$ Cu^{2+} ions at the vertices and was simply prepared by reaction of $Cu(OH)_2$ with 1,3-bdcH_2 under hydrothermal conditions.[65] The high-temperature susceptibility data yielded a Weiss constant of –33 K suggesting antiferromagnetic interaction between centres. Measurement of the magnetisation *vs* magnetic field at 2 K gave a hysteresis loop and heat capacity data also showed a feature at that temperature consistent with the onset of magnetic ordering. A convenient definition of the degree of spin frustration is given by the ratio of the absolute value of the Weiss constant to the ordering temperature. For this material $\theta/T_C = 33/2 = 16.5$, which falls in the range where frustration is considered to be strong. As in the previous example, the observation of an apparently ferromagnetic state despite the dominant antiferromagnetic interactions is only possible due to the strong spin frustration. It is suggested that weak ferromagnetic interactions occur between Cu^{2+} ions in different planes and, since antiferromagnetic order does not develop due to the frustration, these ferromagnetic interactions become apparent at very low temperatures.

3.4.5 Three-Dimensional Magnetic Materials

All known pseudo one- and two-dimensional magnetic solids order only at temperatures well below 200 K. Consequently, all of the molecule-based magnets that order above 200 K are three-dimensional coordination polymers and these can be separated into just two structural classes. Prussian Blue (PB) analogues, the better studied of these classes, consist of cubic arrays of alternating octahedral M and M' metal ions with ordered closed-shell cyanide bridges along the edges of the cubes, having the general formula $A_nM[M'(CN)_6]_m \bullet x$(solvent) (Figure 3.21). Prussian

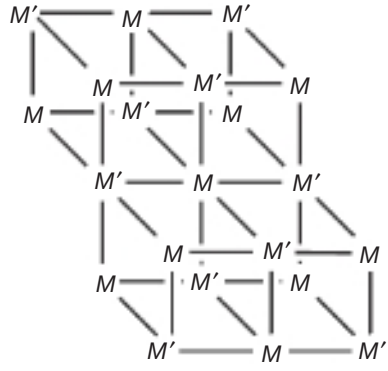

Figure 3.21 Illustration of the Prussian Blue lattice. Each M' represents a $[M'(CN)_6]^{n-}$ anion in which the carbon ends of the cyanide ligands are exclusively bound to the M' metal anion, leaving the nitrogen ends to bind to M. Each M and M' is six coordinate in the ideal structure

Blue itself has the formula $(Fe^{3+})_4[Fe^{2+}(CN)_6]_3 \bullet xH_2O$ and is a ferromagnet below 5.6 K. In this case, only the Fe^{3+} sites contribute to the spin; the Fe^{2+} cation in a strong ligand field is diamagnetic, but mediates the communication between the magnetic centres.

In the 1980s and 1990s, it was recognised that replacing the ferrous iron in Prussian Blue with a spin-containing ion caused the magnetic properties to improve. For example, Klenze *et al.* found $Mn^{2+}[Mn^{4+}(CN)_6]$, which orders at 49 K,[66] and Griebler *et al.* reported $CsMn^{2+}[Cr^{3+}(CN)_6]$, which orders at 90 K.[67] $Cs_2Mn^{2+}[V^{2+}(CN)_6]$ and $(Et_4N)_{0.5}Mn_{1.25}[V(CN)_5] \bullet 2H_2O$ were discovered by Entley and Girolami to order at 125 K and 230 K, respectively.[68] $[Cr_5(CN)_{12}] \bullet 10H_2O$ and $Cs_{0.75}[Cr_{2.125}(CN)_6] \bullet 5H_2O$ were made by Mallah *et al.* and observed to order at 240 K and 190 K, respectively.[69] The culmination of this effort, in terms of moving to the left in the periodic table, was the discovery by Dujardin *et al.* of air-sensitive $C^+_yV^{2+}[Cr^{3+}(CN)_6]_z \bullet xH_2O$,[70] (where C^+ is an alkali metal cation) which orders around 315 K.[31] Related compounds incorporating O^{2-} and $SO_4{}^{2-}$ ligands have similar values of T_C. Girolami *et al.* have reported that the synthesis can be optimised by using a sol-gel route to give $K(V^{2+})[Cr^{3+}(CN)_6] \bullet 2H_2O$,[71,72] which orders at 376 K. Recently, a different synthesis of this compound has been reported, which yields a phase with more stable properties.[73] Note that this compound, if perfect, would be an antiferromagnet because it nominally has the same number of unpaired electrons on the M and M' sites. The residual magnetism arises from the fact that it is nonstoichiometric and/or has

random defects. The general trend observed in this family is that as the metal ions become more electron rich by moving to the left in the periodic table, T_C rises. This was explained by noting that backbonding mediates superexchange between the metal centres and the CN^- ligand, which increases as the donor level of the metal rises in energy in moving to the left in the periodic table.[74] Numerous examples of discrete polynuclear model compounds have been constructed with CN bridges[75–77] and the magnetic coupling in these molecular species is consistent with what is presumed to be operative in the three-dimensional structure. Recently, the first cubic single crystal structure, $Na[MnCr(CN)_6]$, was reported.[78]

The second structural class consists of three-dimensional radical anion bridged coordination networks (RAB networks) of the general formula $M[\text{acceptor}]_x \bullet y(\text{solvent})$, where M is a spin-containing transition metal and 'acceptor' is an organic radical anionic bridging ligand.[79] (Figure 3.22) The first and best known example is $V[TCNE]_2 \bullet y(CH_2Cl_2)$, where TCNE = tetracyanoethylene, which was originally reported to decompose at approximately 350 K. Recently, improvements in the synthesis have led to values of T_C in the range 385–390 K, but the materials are still noncrystalline and air sensitive.

To prepare additional examples, the identity of the transition metal has been varied with modest success. Miller *et al.* have reported $M(TCNE)_2$ species based on replacing V^{2+} by Mn^{2+}, Fe^{2+}, Co^{2+} and Ni^{2+} that exhibit ordering, albeit at lower temperatures, though still above 100 K.[80] Casellas *et al.* have extended this list to include a vapour-phase

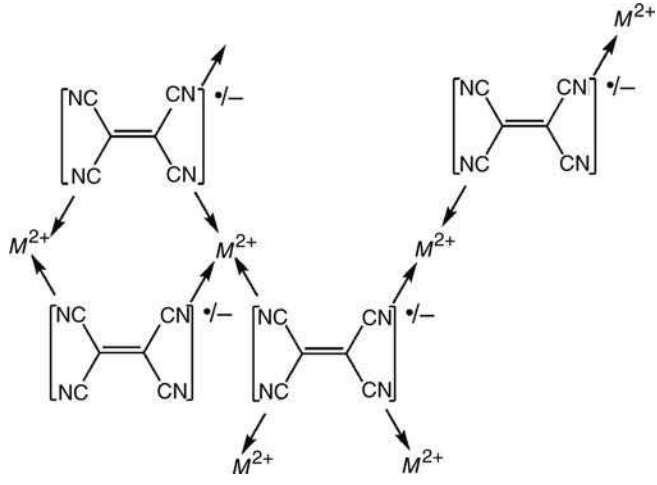

Figure 3.22 Schematic of the $M(TCNE)_2$ lattice

deposition method of preparing $Cr(TCNE)_2$, which orders around 5 K as a thin film.[81]

Miller *et al.* have also synthesised two rare earth analogues based on TCNE and Gd^{3+} and Dy^{3+}. The former is a spin-only ion and the latter has the highest possible value of J. These solids are ferrimagnets with T_Cs of 3.5 K and 8.5 K, respectively.[82]

The Miller group and Yee group have separately extended the list of organic radical anions that are capable of mediating exchange leading to magnetic order near or above room temperature. The former have published V[acceptor]$_2$ in which the acceptor is 1,2,4,5-tetracyanopyrazine (200 K)[83] and 1,2,4,5-tetracyanobenzene (T_C = 323 K).[84] The latter compound is believed to belong to a new compositional family. The Yee group has reported dicyanoperfluorostilbene (205 K)[85] and various fluoro-substituted phenyl tricyanoethylenes (Figure 3.23) with ordering temperatures up to 315 K (Table 3.3).[86–88]

The series of compounds in Table 3.3 is an example of the utility of synthetic organic chemistry for preparing systematically related building blocks that exhibit interesting trends in bulk magnetic properties. The compounds are all easily synthesised from the corresponding benzaldehydes in moderate yield. High T_C is favoured by substitution in the 2- and 6-positions and disfavoured by substitution in the 4-position. Explanations for this observation involve a combination of both steric and electronic effects.

Table 3.3 Magnetic ordering temperatures for a series of vanadium coordination polymer magnets using halogen-substituted phenyl tricyanoethylene acceptors. (Explanation of abbreviation: numbers indicate substitution position; PTCE = phenyl tricyanoethylene)

Acceptor	T_c (K)
H_5PTCE	215
2-FPTCE	259
3-FPTCE	238
4-FPTCE	159
2,3-F_2PTCE	278
2,4-F_2PTCE	244
2,5-F_2PTCE	276
2,6-F_2PTCE	298
3,5-F_2PTCE	267
2,3,5-F_3PTCE	279
2,3,6-F_3PTCE	310
2,3,5,6-F_4PTCE	315
F_5PTCE	307

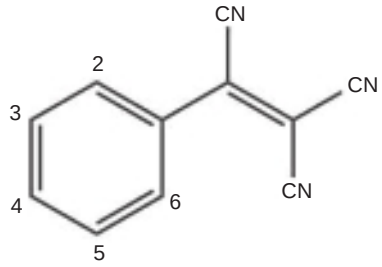

Figure 3.23 Phenyl tricyanoethylene showing the number scheme for substitution on the phenyl ring

It is not accidental that examples of PB analogues and RAB networks share several features. For one, they all have coordinate-covalent bonds that extend in three dimensions (*vide infra*). It is evident that in one- and two-dimensional magnetic solids, weak through-space coupling in the other dimension(s) severely limits the magnitude of T_C. For another, almost all of them are ferrimagnets, meaning that antiferromagnetic coupling exists between adjacent spin centres that possess different numbers of unpaired electrons.

Having identified some of the similarities, it is important to note that there is a fundamental difference between Figures 3.21 and 3.22: PB analogues rely on *superexchange*, mediated by the diamagnetic cyanide ligand to couple the spins on adjacent metals, whereas in the RAB networks, *direct exchange* between the metal centre and the radical on the organic ligand mediates the coupling. Direct exchange can be tuned by modifying the organic bridging ligand using conventional synthetic techniques in a way that is not possible with PB analogues.

Unfortunately, cyanide appears to be an indispensable bridging ligand, so more generally, any approach that involves other closed shell ligands appears unfavourable for synthesising room temperature magnets. Other pseudohalides and related compounds have been investigated including the thiocyanate anion (SCN^-),[89,90] azide anion (N_3^-),[91–93] dicyanamide anion ($N(CN)_2^-$, dca),[94] tricyanomethanide anion ($C(CN)_3^-$, tcm)[94], acetylide anion[95] and oxalate dianion.[96] While magnetic coupling and, in some instances, long-range magnetic order is observed, none of these ligands yield materials that order at high

temperatures. This seems to be an issue of both the difficulty in obtaining three-dimensional structures and weak coupling strengths that can be achieved in some of the common bonding modes for the bridging ligands. For instance, oxalate mostly gives one- and two-dimensional structures and dca and tcm couple rather weakly, so that none supports magnetic order above 50 K.[94,96]

3.4.5.1 Other Kinds of Three-Dimensional Order: Metamagnetism and Canted Antiferromagnetism

Application of a sufficiently large magnetic field to antiferromagnets typically results in transition to what is known as a spin-flop state. In this transition, the individual magnetic moments re-orient from being aligned antiparallel to each other to residing in a plane perpendicular to the applied magnetic field. However, with antiferromagnets with uniaxial magnetic anisotropy (an easy axis of magnetisation), a common occurrence with molecule-based systems, a transition to a ferromagnet-like state results instead. This phenomenon, called metamagnetism, results in alignment, or near alignment, of the spins with the applied magnetic field (rather than perpendicular to it). An example that displays this kind of behaviour is the charge-transfer salt that results from the reaction of decamethylferrocene and 2,3-dicyano-1,4-naphthoquinone (DCNQ).[97]

Ignoring for the moment the slightly open loop near zero applied field (Figure 3.24a), the sample appears to be antiferromagnetically ordered in zero applied field and to switch to a magnetic state at a critical field (H_c,) of around 3000 G. Because there are two unpaired electrons per formula unit (one on the iron and one on the organic acceptor), the saturation magnetisation is expected to be around $2 \times (5585$ emu G $mol^{-1})$.

A completely separate phenomenon that happens also to occur in this compound is canted antiferromagnetism (also known as weak ferromagnetism). In the nominally antiferromagnetic state (*i.e.* below the critical field), anisotropy creates a situation in which antiparallel alignment of the spins is imperfect. Because the spins are vector quantities, a small nonzero angle between them results in incomplete cancellation (Figure 3.24b). This gives rise to a net moment that, in the case of $[FeCp^*_2][DCNQ]$, is manifest as a tiny hysteresis loop centred about zero.

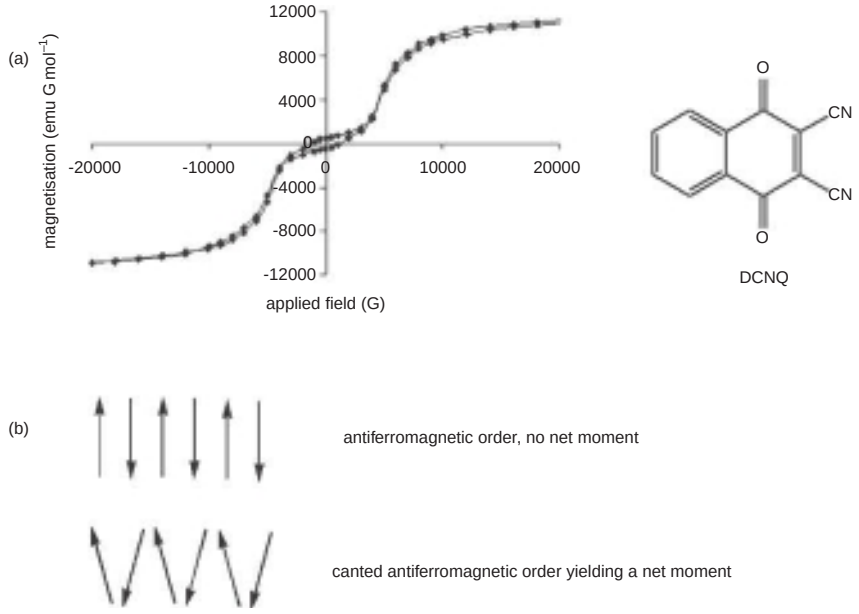

Figure 3.24 (a) Plot of magnetisation *vs* applied field for [FeCp*$_2$][DCNQ] showing metamagnetic behaviour and canted antiferromagnetic behaviour. (b) A schematic illustration of canted antiferromagnetism

3.5 SWITCHABLE AND HYBRID SYSTEMS AND FUTURE PERSPECTIVES

3.5.1 Bistable and Switchable Magnetic Materials

The possibility of reversibly switching the phase of a material between two states that differ in their optical or magnetic properties opens up opportunities in data recording and display applications. To be useful, the material should show hysteresis in the phase switching, meaning that the temperature at which the transition occurs upon cooling is lower than the corresponding temperature at which the transition occurs upon warming. Ideally, the hysteresis loop should be centred around room temperature, allowing the material to show long-term stability in either phase under ambient conditions. Progress in this area over the last decade has extended the known classes of systems in which such bistability is observed and demonstrated wide hysteresis loops at temperatures consistent with, or close to, the ideal of room temperature. Cobalt complexes

of noninnocent ligands can also display the related phenomenon of temperature-dependent valence tautomerism, whereby an electron is transferred from the semiquinonate ligand to the Co^{3+} centre upon raising the temperature, accompanied by transition of the cobalt centre from low-spin d^6 to high-spin d^7.[98] This will not be discussed further here, other than to draw attention to the analogy with the thermal and optical switching of Prussian Blue analogues described in Section 3.5.1.3. There is no doubt that switchable materials is an area where molecular magnetism has proven highly versatile and powerful in identifying new instances of bistability and in tuning the properties observed. The following examples illustrate some of the key material types where such behaviour has been studied.

3.5.1.1 Spin Crossover Compounds

For octahedral complexes with d^4–d^7 electron configurations, the ground spin state depends on the magnitude of Δ_o, the energy gap between the higher lying doubly degenerate e_g and the lower lying triply degenerate t_{2g}, relative to the electron–electron repulsion (ρ) that results from double occupation of the same orbital. With small Δ_o, high spin (HS) is favoured, whereas with large Δ_o, low spin (LS) is favoured (Figure 3.25). It is not exactly the case that crossover occurs when $\Delta_o = \rho$, because there are geometric changes that accompany the transition that affect the size of Δ_o, but when the difference in energy is of the order of kT, a spin state change can occur. If the transition is written as LS $\leftrightarrow$ HS, then $\Delta H > 0$ and $\Delta S > 0$ for this process. This can be rationalised by noting that the high-spin state has electrons in higher energy antibonding orbitals, weaker bonds and higher spin degeneracy. At low temperature, the low-spin state is favoured. This area has been reviewed many times and only a general overview will be presented here.[99,100]

Although the two phases should, in principle, be in equilibrium at all temperatures, there can be kinetic barriers to achieving this. The shape of

Figure 3.25 Spin crossover in an octahedral d^6 metal ion

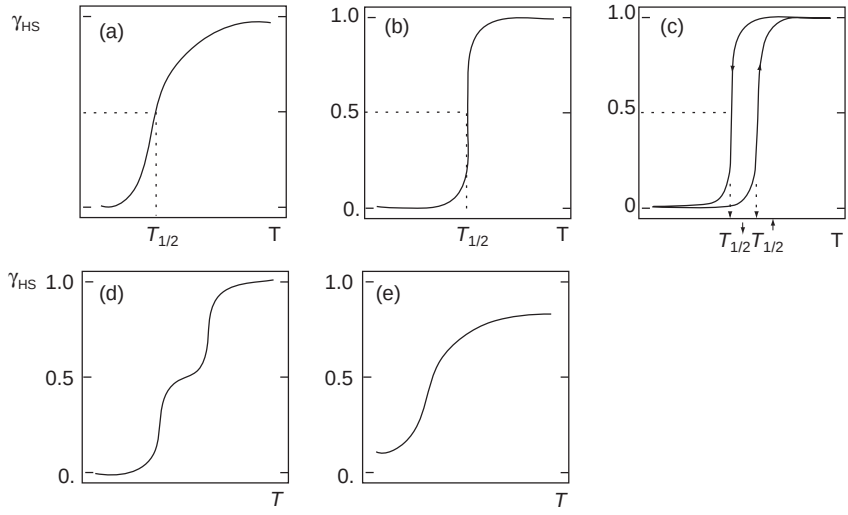

Figure 3.26 Possible crossover behaviour as a function of temperature.[101] Reprinted from Gütlich and Goodwin [101] with permission from Elsevier.

the transition depends on structural factors because the change from low spin to high spin is accompanied by a significant metal ligand bond length change and perhaps changes in symmetry due to Jahn–Teller distortions, and the solid must adjust to accommodate this, creating the barrier. Figure 3.26 illustrates the main types of spin crossover transition including: (a) gradual, (b) abrupt, (c) hysteretic, (d) two-step and (e) incomplete. The *y*-axis is γ_{HS}, the mole fraction of high-spin species.[101] Depending on the degree of cooperativity in the transition, *i.e.* how changing the structure of one molecule or in one part of the crystal depends on the structure of a different molecule or different part of the crystal, it may be hysteretic. Researchers have sought to introduce greater degrees of cooperativity by introducing intermolecular hydrogen bonding contacts, coordination polymers and and π stacking.

Thermal spin crossover has involved tuning the ligand field to position the spin transition in the vicinity of room temperature as this, together with substantial hysteresis, will enable both spin states to show long-term stability at ambient conditions.[102] The most thoroughly characterised spin crossover complexes contain d^6 Fe^{2+}, which conveniently switch from nonmagnetic $S = 0(t_{2g}{}^6)$ to highly magnetic $S = 2(t_{2g}{}^4 e_g{}^2)$ as the temperature is raised. Efforts led, several years ago, to a family of

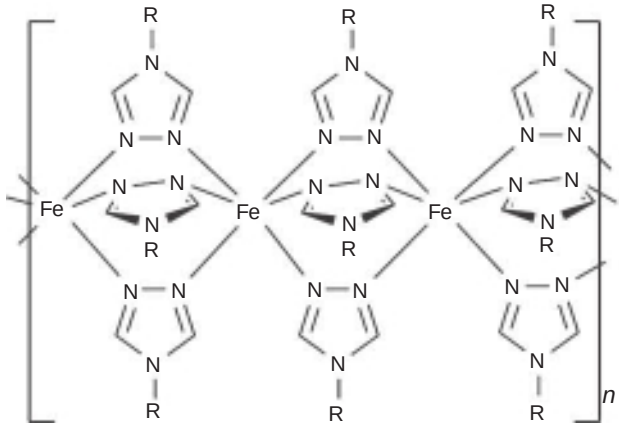

Figure 3.27 General structure of coordination polymer chains in the spin crossover species $[Fe(Rtrz)_3][X]_2$, R = NH_2, Rtrz = 4-R-1,2,4-triazole (X = various counterions or mixed counterions)

Fe^{2+} 1,2,4-triazole coordination polymers that differ in terms of the 4-substituent on the triazole (Figure 3.27), the counterion and the included solvent molecule, all of which play a role in adjusting the transition temperature. Alloys of different materials were shown to have predictable properties intermediate between those of the parent materials, and using this approach the material $[Fe(Htrz)_{3\text{-}3x}(NH_2trz)_{3x}][ClO_4]_2$ was prepared with $x = 0.15$ giving a hysteresis loop positioned exactly around room temperature. This material has been used in prototype device studies.[103]

Within the Fe^{2+} class of compounds, additional work has focused on switching such materials using both thermal switching and optical methods: the light-induced excited spin state trapping (LIESST) effect. The LIESST effect is highly attractive, enabling optical switching between the high and low spin states. The disadvantage to date has been the limitation to low temperature observation due to limited lifetime of the photomagnetic states. Systematic studies, however, have shown a simple relationship between the maximum observable temperature for the LIESST effect in a material and its thermal spin transition temperature. This insight may provide the opportunity to design materials with a LIESST temperature sufficiently high for applications.[104] The study of spin crossover is now attracting attention in the context of multifunctional materials. The objective is to couple the phenomenon with other material properties

such as conductivity, long-range magnetic exchange, liquid-crystalline properties, porous materials or optical properties.[105]

3.5.1.2 Phase Transitions in Thiazyl Radicals

A wide variety of stable radical compounds are known, based on delocalised rings containing sulfur and nitrogen atoms and known generally as thiazyls.[106] Earlier study of this class of materials centred on the preparation of magnetically ordered materials that show spontaneous magnetisation at temperatures up to 36 K (or 65 K under applied pressure), much higher than any other material that does not contain a metal.[107] More recently, these have attracted additional attention due to the observation of interesting phase transition phenomena, typically between dimerised and nondimerised structures.[108]

The thiazyl radical BDTA (Figure 3.28) shows complex behaviour upon heating and cooling. The X-ray structure at 293 K[109] shows a two-dimensional network of centrosymmetric diamagnetic dimers. On the first heating cycle, a fresh sample of BDTA displays melting at 360 K followed by immediate solidification to a new high-temperature (HT) phase which itself melts at 364 K, indicating that the original low-temperature (LT) phase had been superheated. Upon lowering the temperature, supercooling of the paramagnetic HT phase occurred eventually into an antiferromagnetically ordered phase at 11 K. After repeated thermal cycles, the superheating and supercooling behaviour was lost, with observation instead of LT–HT phase transition at 346 K when warming and HT–LT phase transition at 320 K when cooling, giving a significant hysteresis loop somewhat above room temperature (Figure 3.29). Although the structure of the HT phase is not known, its paramagnetic character suggests break-up of the diamagnetic BDTA dimers that exist in the LT phase.

The properties of TTTA (Figure 3.28) are even more attractive from the point of view of applications, as it shows a very wide hysteresis loop (around 75 K) that encompasses room temperature (Figure 3.30).[110,111]

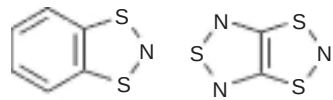

(a) (b)

Figure 3.28 Structures of (a) BDTA and (b) TTTA

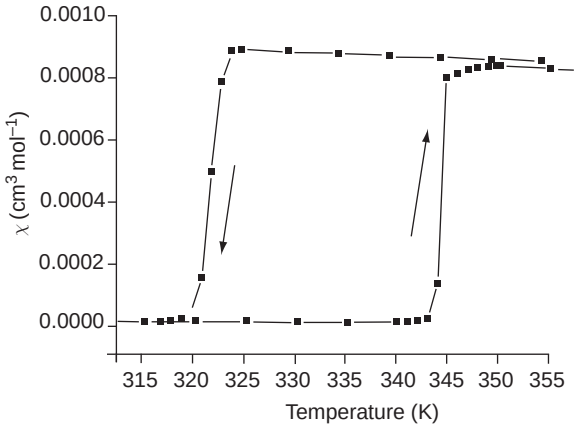

Figure 3.29 Hysteresis loop for BDTA. (Replotted from data kindly supplied by K. Awaga)

Variable temperature EPR and variable temperature susceptibility measurements showed that, analogous to BDTA, the LT phase is diamagnetic and the HT phase paramagnetic. In this case, however, both HT and LT X-ray structures have been determined (Figure 3.30), demonstrating clearly the dimerisation in the LT phase that leads to the diamagnetic behaviour. The HT phase, in contrast, consists of uniformly stacked

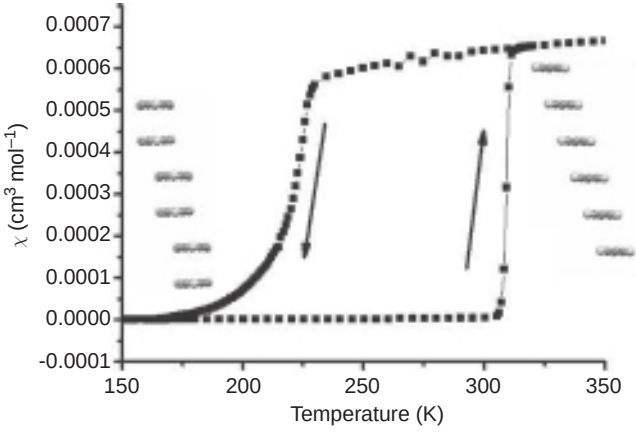

Figure 3.30 Hysteresis loop for TTTA. (Replotted from data kindly supplied by K. Awaga.) Also shown are the crystal structures of TTTA showing at low temperature stacked dimers and at high temperature uniform stacking. (Redrawn using original crystallographic data kindly supplied by W. Fujita)

molecules. The behaviour of the species has been discussed in terms of a competition between exchange coupling, which dominates at LT, and the electrostatic repulsion of the molecules, which dominates at HT,[108] although McManus *et al.*[111] separately emphasised the importance of interstack interactions in competition with a Peierls distortion. The conductivity of the HT phase was found to be very low, but increased by four or five orders of magnitude upon doping with I_2. This was interpreted as evidence of a Mott insulator state through strong on-site coulombic repulsion with one unpaired electron strongly localised on each site in the undoped form.

3.5.1.3 Switching Effects in Prussian Blue Analogues

Prussian Blue (PB) analogues (discussed in Section 3.4.5) have displayed a variety of switchable magnetic effects, based on light,[112] pressure[113,114] and temperature.[115] These switching effects arise due to spin crossover processes or charge transfer between the metal ions combined with spin crossover. This leads to large changes in both optical and magnetic properties of the materials between the different phases and the significant structural reorganisation involved can lead to sharp cooperative transitions that may have a wide hysteresis loop. This makes such materials of potential interest in devices such as displays and memories.

Certain PB analogues based on the $Co[Fe(CN)_6]$ motif have shown an optical electron transfer from low-spin Fe^{2+} to low-spin Co^{3+} associated with transition of the resulting Co^{2+} to high spin. This leads to a metastable photoinduced ferromagnetic state.[116] The related species $Na_{0.36}Co_{1.32}[Fe(CN)_6]\bullet 5.6H_2O$ has recently been shown to undergo reversible optical switching between states.[117] Figure 3.31 illustrates the optical and magnetic properties of the material.

The LT phase is dominated by low-spin d^6 ions, possesses a correspondingly low magnetic moment and displays a metal-to-metal charge transfer transition (MMCT) from Fe^{2+} to Co^{3+}. Above 230 K, transition to the HT phase takes place involving charge transfer from iron to cobalt and spin transition at the resulting Co^{2+} centre. Reversal of this process occurs on cooling at 197 K giving a wide hysteresis loop of 33 K. In comparison with previous work involving spin transitions (whether in PB analogues or molecular complexes), a reversible photoswitching process was observed within the temperature bounds of the hysteresis loop such that both optical switching processes occurred to stable states. Switching was achieved at a common wavelength and control of the switch direction achieved by

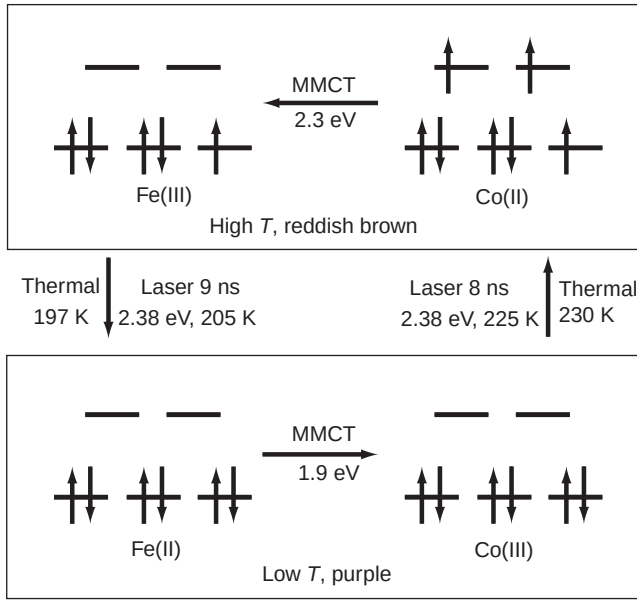

Figure 3.31 Optical and magnetic properties of $Na_{0.36}Co_{1.32}[Fe(CN)_6]\bullet 5.6H_2O$

temperature adjustment. Thus, in both directions, the switching was attributed to a domino effect requiring a threshold intensity of the radiation. The structural changes occurring at local excited states lead to a cooperative action giving a phase transition to the more stable state at the given temperature: the purple phase at 205 K and the reddish-brown phase at 225 K. It was also observed that the presence of various defects arising from the nonstoichiometry is essential to the mechanism since the 2.38 eV laser pulse is absorbed by $Co(NC)_4\bullet 2H_2O$ centres in the HT phase and by $Co(NC)_5\bullet H_2O$ centres in the LT phase. Thus, the phase transition propagates from different initiation points in each case. Although these processes occur below room temperature, they are in a sufficiently HT region to suggest that with further tailoring of materials, similar behaviour might be observed with hysteresis around room temperature and the possibility of applications.

3.5.2 Multifunctional Magnetic Materials

One of the most attractive features of a molecular approach to magnetism is the modular approach to synthesis, whereby more than one

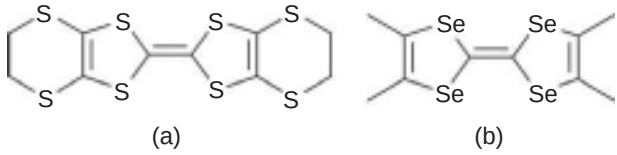

Figure 3.32 (a) BEDT-TTF and (b) TMTSF.

well-defined building block can be incorporated into a single crystalline lattice while retaining the complex functionality of each component. This is most simply achieved through the combination of anions and cations, where each brings a different type of property to the resulting solid. This can include examples of magnetic, conducting and optical properties.[118] The appealing concept is that the interaction between the functional components will lead to some completely new cooperative behaviour, not observed in any of the building blocks. In addition, manipulation of one property may lead to changes in the manifestation of another, leading to switchable properties. For illustration, the combination of magnetic and conducting properties, that is localised and delocalised unpaired electrons, will be considered, as this has been a very active field in recent times leading to some landmark materials.

3.5.2.1 Hybrid Magnetic-Conducting Systems

Conducting molecular salts generally comprise planar, π-delocalised organic molecules showing significant intermolecular interaction, often through π-stacking, such that a band electronic picture is appropriate. Also in the lattice are counterions in a ratio such that a fractional average charge is on the organic components. This leads to a partially filled conduction band and often metallic conductivity.[119] This is typified by families such as $[BEDT\text{-}TTF]_2X$ and $[TMTSF]_2X$ (Figure 3.32); $X =$ for example, $[BF_4]^-$, $[PF_6]^-$, $[ClO_4]^-$, and so on. Study of this class of material has been motivated by the high-crystallinity, flexibility of the synthetic strategy, observation of superconductivity in certain examples, low dimensionality and, more recently, through the relationship to small-molecule molecular semiconductors that are finding uses in devices.[120]

The motivations for synthesis of hybrid salts arise from different factors such as whether, and under what special circumstances, superconductivity can co-exist with magnetic order and in particular ferro- or ferrimagnetism. Superconductivity is destroyed by an externally applied

critical field above a certain critical field through destruction of the diamagnetic Cooper pairs, and the presence of an internal magnetic field may play a similar role. Additionally, the conduction electrons may provide a mechanism for coupling of the localised moments through the Ruderman–Kittel–Kasuya–Yosida [RKKY] mechanism, which involves spin polarisation of the sea of conduction electrons by the localised moment. Such a phenomenon in molecular materials would likely be very different in character from established cases in *f*-block metals, where the conduction electrons are much more 'free electron' like, than in the molecular species, where the tight binding band model is more appropriate. Thus the *s–f* coupling in the former may display different features from the π–*d* coupling of the latter.

The straightforward synthetic strategy for hybrid conducting-magnetic salts uses a paramagnetic ion for X^- rather than a simple closed-shell counterion. Many examples have been studied including tetrahalogenato, hexahalogenato, pseudohalogenato and oxalate complexes of paramagnetic metals, polyoxometallates, lanthanide complexes and metal dithiolene complexes.[118] A recurring difficulty, however, has been a lack of electronic interaction between the conducting and magnetic sublattices, which is perhaps not surprising given that the magnetic ion is generally surrounded by ligands that may greatly reduce the communication of spin information.

Two classes of materials have given rise to the most interesting systems. First, the salt λ-$[BETS]_2[FeCl_4]$ has displayed clear evidence of coupling between the π and *d*-electrons. This was demonstrated by the observation of magnetic-field-induced superconductivity for λ-$[BETS]_2FeCl_4$, which shows a metal–insulator transition at the point of antiferromagnetic ordering. The isostructural salt λ-$[BETS]_2[GaCl_4]$ displays a superconducting transition at 8.5 K, suggesting that the Fe^{3+} analogue is non-superconducting due to the presence and ordering of the paramagnetic iron atoms.[121] The related salt $[BETS]_2[FeBr_4]$ shows a complex pattern of behaviour involving a superconducting phase with antiferromagnetically ordered Fe^{3+} ions below 1.1 K, metamagnetic behaviour of the Fe^{3+} ions above 1.6 T to forced-ferromagnetic metal (and destruction of superconducting state), and a field-induced superconducting phase at around 1.6 T.[122] Much further detailed study and comparison of these materials, which is beyond the scope of this chapter, has been carried out,[123] but the main point is that where a significant interaction between the delocalised and localised electrons can be achieved, unusual and perhaps unique behaviour is likely to follow. Also of much recent interest is the salt β-$[BEDT\text{-}TTF]_3[MnCr(oxalate)_3]$ (Figure 3.33).[124] This material possesses two-dimensional ferromagnetic layers of Mn^{2+} and Cr^{3+}

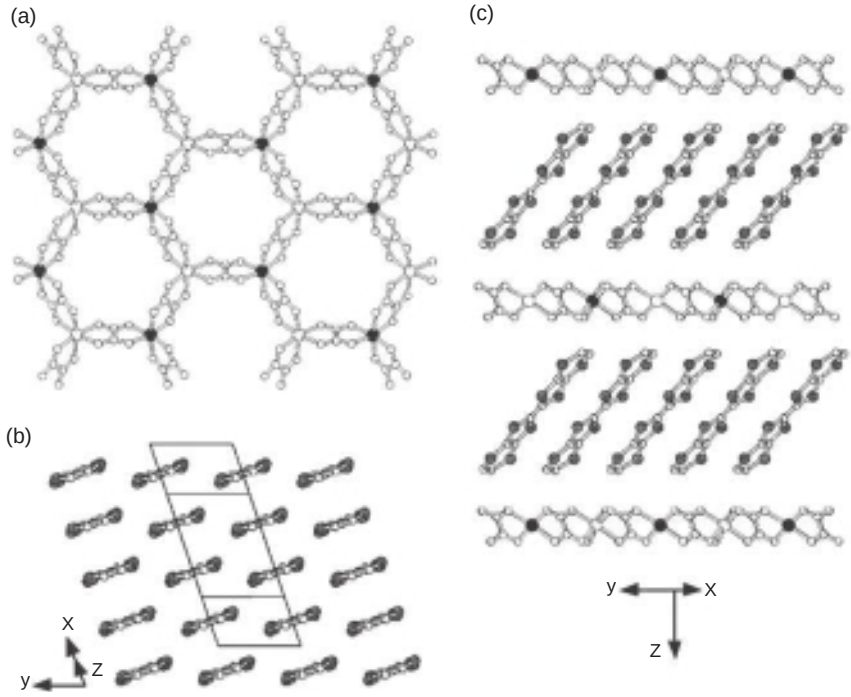

Figure 3.33 Structure of the hybrid material showing: (a) view of the $[M^{2+}M^{3+}(C_2O_4)_3]^-$ bimetallic layers; (b) the structure of the organic layer, showing the packing of the BEDT-TTF ions; and (c) the hybrid structure shown along the *c*-axis. Reprinted by permission from Coronado *et al.*, 2000 [124]. Copyright (2000) Macmillan Publishers Ltd

ions bridged by oxalate ligands discussed above with $T_c = 5.5$ K. These alternate with π-stacked layers of BEDT-TTF molecules that remain conducting down to 0.2 K. Subsequently, related salts with different metal combinations and different crystal phases have been prepared that display similar ferromagnetic-metal behaviour.

In summary, this is a field that has yielded a comparatively small number of key examples with unique properties despite the study of a very large combination of precursors. The difficult progress has been linked to the weak or negligible interaction between the different sublattices. However, the more recent emergence of very interesting examples may now provide the insight and guidance that will allow a targeted approach to the preparation of other π–*d* interacting materials. For example, magnetoresistance effects evidencing the π–*d* interaction in the metallic organic conductors [EDT-DSDTFVO] (ethylenedithiodiselenadithiafulualenoquinone-1,3-dithiolemethide)$[MX_4]$ have been

observed[125] and there is growing interest in molecules that combine a π-stacking component and a paramagnetic component in a single molecule to enhance communication between the components.[126]

3.5.2.2 Molecular Spintronics

The field of spintronics is recent, but extremely important, and derives from the observation in the late 1980s of giant magnetoresistance (GMR) in layered structures of ferromagnets and metals. The large change in conductivity through the device observed upon application of a magnetic field is now exploited in hard-drive read heads and led to the Nobel Prize in Physics in 2007 for the discoverers. The significance of this breakthrough was that the spin, as well as the electrical charge, of electrons could be exploited in electronic devices.[127] In the last few years, interest has grown in the possibility of molecular spintronics, which might be able to exploit additional effects through the unique properties of molecular species.[128–130] These opportunities to design new devices are coupled to the steady growth of applications for molecular or organic electronic materials, which enable low cost 'plastic' materials to be used for applications such as light emitting diodes and transistors.[131] Molecular electronic materials that additionally include spin degrees of freedom would offer exciting and unique new opportunities.

Two types of molecular device have been examined to date; a magnetic molecule coupled to nonmagnetic electrodes and a molecular spin valve. Experimentally, the former has been realised for the single molecule magnet Mn_{12}.[132] Single molecule magnets are discussed in Chapter 5 of this volume and this discussion focuses on the latter device and, in particular, on the molecular materials involved. This topic stretches right to the fringes of 'molecular magnetic materials', involving coupling of molecular materials to nonmolecular solids and alignment of unpaired electrons in molecular materials that can be either magnetic or nonmagnetic in the resting state.

A spin valve comprises two conducting ferromagnetic layers as electrodes (*e.g.* alloys of iron, cobalt or nickel) separated by a nonmagnetic layer. One of the magnetic layers will have a large coercive field and the other will be small, such that one can be easily switched to the opposite spin alignment without switching the other. The conductivity across the device will depend on the relative alignment of the magnetic layers, with higher conductivity generally for parallel alignment (Figure 3.34). This is directly analogous to the devices used in hard-drive read heads using established continuous-lattice materials. The magnetoresistance is

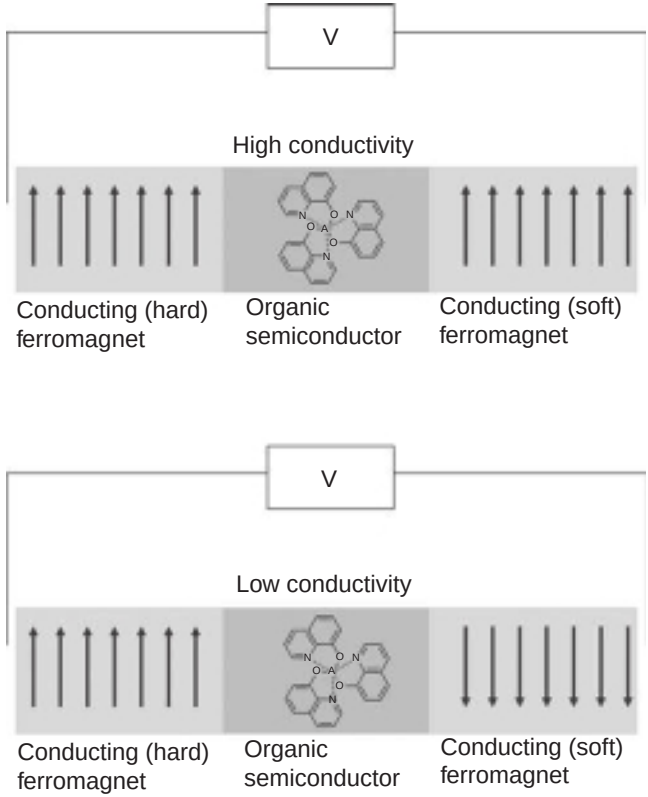

Figure 3.34 Different conductivity across a spin valve depending on the spin alignment of the ferromagnetic electrodes. An example conducting molecular material, Alq_3, is also shown[133]

explained through the spin-polarised density of states in the conducting ferromagnetic electrodes, which leads to majority- and minority-spin bands that may also have different orbital character. When both ferromagnetic electrodes are aligned parallel, this provides a lower resistance path for electron transport, since the band structures of the majority carriers in both terminals are matched.

A crucial parameter for the operation of a spin valve is the spin diffusion length (λ_s), as it is clearly essential for the spin to retain its orientation during passage through the middle layer. Both the spin-orbit coupling and the coupling with nuclear spins (hyperfine interaction) can lead to loss of spin coherence. A study of carbon nanotubes between cobalt electrodes[134] has reported λ_s as long as 130 nm and study of graphenes has given λ_s up to a phenomenal 1.5–2 μm,[135] explained by the very

low spin-orbit coupling and hyperfine coupling for carbon, which is a light atom with $I = 0$ for ^{12}C with around 99% abundance.

To date, a relatively small number of materials have been explored in a molecular spintronics device and much remains to be understood. For example, the coupling between the molecular layer and the magnetic electrodes is believed to play a very significant role due to the discrete nature of the molecule's HOMO and LUMO, in contrast to the band properties inherent in a continuous-lattice material. The energies of the frontier orbitals with respect to the Fermi level of the electrodes, the broadening of the frontier orbitals into (narrow) bands and the orientation-dependent orbital overlap between molecule and electrode will all contribute to the transport of spins across the interface.[127] Study of the magnetic properties of molecule surface systems is, therefore, highly important and may also lead to new types of spintronic devices.

In this context, paramagnetic molecules have been studied on non-magnetic substrates and shown to exhibit different properties upon structural variation. The deposition of copper and manganese phthalocyanines (MPc) on a polyimide substrate (Kapton) by molecular beam deposition has led to controllable polymorphism in the typically 60 nm thick molecular layer.[136] The initial deposit of α-CuPc can be converted through thermal annealing to β-CuPc. Both of these phases have the molecular plane perpendicular to the substrate and a different phase with the molecules parallel to the substrate could also be obtained through a templating effect with the polyaromatic perylenetetracarboxylic dianhydride. Significantly, the α phase showed antiferromagnetic correlations and a one-dimensional Heisenberg antiferromagnetic chain ground state, whereas the β phase, the polymorph normally stable under ambient conditions (Figure 3.35), was essentially paramagnetic. For the MnPc, antiferromagnetic and ferromagnetic phases were observed. The mechanism suggested for the spin coupling in α-CuPc is a molecular analogue of the RKKY mechanism for ferromagnetic conductors.

A striking example of specific interaction between molecular layer and substrate has been shown by monolayer and sub-monolayer films of iron(octaethylporphyrin)chloride [FeCl(OEP)], deposited by sublimation, on ferromagnetic films of nickel and cobalt (Figure 3.36).[137] It was shown by X-ray absorption spectroscopy and X-ray magnetic circular dichroism that the paramagnetic molecules order ferromagnetically on the substrate, and the orientation of the iron magnetic moment in the porphyrins can be controlled through magnetic reversal of the substrate. The coupling between the film and the underlying substrate is

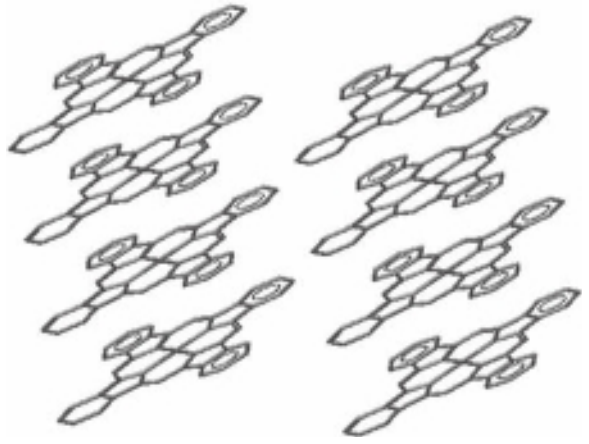

Figure 3.35 Molecular packing of the β phase of CuPc

ferromagnetic, as demonstrated by element-specific hysteresis loops at 300 K, and is attributed to a 90° superexchange mechanism between the iron and the cobalt or nickel atoms in the substrate. As discussed in Section 3.4.5, bulk ordering in molecular magnetic materials at room temperature is very rare and requires very specific three-dimensional arrangements of paramagnetic components combined with particularly strong interactions between spin centres. In this context, the generation and control of a ferromagnetically aligned molecular layer at ambient temperature is particularly significant and paves the way for spintronics applications that exploit the molecular alignment. In addition, the ferromagnetic monolayer could possibly play a role in tuning the crucial interface properties between the ferromagnetic electrode and a subsequent molecular spacer layer.

It is apparent that molecular spintronics is in its infancy, with only a limited number of demonstration experiments achieved, confined to a handful of molecular species. This is not surprising, given that spintronics itself originated only a couple of decades ago, yet already the molecular approach is showing distinct differences from continuous-lattice materials, arising from the specific and discrete nature of molecular components and the resulting molecule–molecule and molecule–substrate interactions. The established literature on molecular magnetism has generated a vast range of building blocks and structures of various dimensions that can now serve as a library of potential materials to expand and diversify the novel phenomena recently observed in thin-film structures on both inert and magnetic substrates.

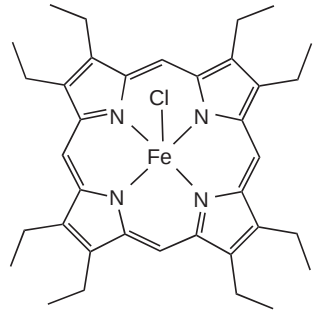

Figure 3.36 The chloro(octaethylporphyrin)iron(III) molecule. Calculations and experiment suggest that the chloride may be lost and Fe^{2+} is present upon surface binding to the nickel or cobalt film

3.6 CONCLUSIONS

In this chapter, some of the diversity of molecular magnetic materials has been illustrated and an account given of the concepts and techniques required to interpret their properties. Examples have been shown where a magnetic measurement is simply another aspect of a full electronic characterisation of a metal complex, through to the wealth of examples where development of novel magnetic properties was the objective of the study. Much of the early work in the area was concerned with using the unique aspects of molecular materials, such as low dimensionality, to aid the development of models of their behaviour. Later, much interest centred around new materials with spontaneous magnetisation, including examples where no metal atom was present. It has become clear, however, that magnetic ordering in molecular materials is generally limited to low temperatures, due to the inherently weaker interactions between spin centres compared with continuous-lattice materials such as iron oxides or metal alloys. Only two classes of molecular material have shown spontaneous magnetisation at room temperature and these are both in the coordination polymer category. Studies on these unusual materials continue but there is no indication of the emergence of any other class.

In more recent times, the field has increasingly focused on topics where molecular materials have an advantage over continuous-lattice solids. Such studies can exploit the modular synthesis of molecular materials, whereby different molecules with differing functions can be combined to form a hybrid material with interacting magnetic and/or conducting and/or optical properties. This is leading to new fields such as molecular spintronics, multifunctional and switchable materials where

understanding the magnetic properties of the system is just the beginning. There is no doubt that as our ability to exploit the unique features of molecules grows, a new age of molecular magnetic materials will develop into areas that may not be foreseeable at present.

REFERENCES

[1] G. T. Yee and J. S. Miller, in *Magnetism: Molecules to Materials V* (eds Miller, J. S. and Drillon, M.), Wiley-VCH Verlag GmbH, Mannheim, (2004).
[2] J. S. Miller, J. C. Calabrese, H. Rommelmann, S. R. Chittipeddi, J. H. Zhang, W. M. Reiff and A. J. Epstein, *J. Am. Chem. Soc.*, **109**, 769–781 (1987).
[3] R. W. Jotham, *J. Chem. Soc. Chem. Commun.*, 178–179 (1973).
[4] K. T. McGregor and Z. G. Soos, *Inorg. Chem.*, **15**, 2159–2165 (1976).
[5] http://pureguard.net/Library/data_sheets/MSB_Brochure.pdf (Johnson Matthey magnetic susceptibility balance). Date of access: 20.1.2010.
[6] Y. Itami and K. Sone, *J. Chem. Educ.*, **79**, 1002–1004 (2002).
[7] K. C. De Berg and K. J. Chapman, *J. Chem. Educ.*, **78**, 670–671 (2001).
[8] G. S. Girolami, T. B. Rauchfuss and R. J. Angelici, *Synthesis and Technique in Inorganic Chemistry*, 1999, pp. 125–126.
[9] S. K. Sur, *J. Mag. Reson.*, **82**, 169–173 (1989).
[10] T. I. Quickenden and R. C. Marshall, *J. Chem. Educ.*, **49**, 114–116 (1972).
[11] C. J. O'Connor, *Prog. Inorg. Chem.*, **29**, 203–283 (1982).
[12] S. Mukherjee, T. Weyhermueller, E. Bothe, K. Wieghardt and P. Chaudhuri, *Dalton Trans.*, **22**, 3842 (2004).
[13] S. S. Staniland, A. Harrison, N. Robertson, K. V. Kamenev and S. Parsons, *Inorg. Chem.*, **45**, 5767 (2006).
[14] N. Robertson and S. James, unpublished results
[15] A. F. Orchard, *Magnetochemistry*, Oxford University Press, Oxford, 2003.
[16] R. L. Carlin, *Magnetochemistry*, Springer-Verlag, Berlin, 1986; S. Blundell, *Magnetism in Condensed Matter*, Oxford University Press, Oxford, 2001.
[17] A. F. Orchard, *Magnetochemistry*, Oxford University Press, Oxford, 2003, p. 88.
[18] A. Earnshaw, *Introduction to Magnetochemistry*, Academic Press, New York, 1968, p. 59.
[19] W. M. Reiff, A. M. LaPointe and E. H. Witten, *J. Am. Chem. Soc.*, **126**, 10206–10207 (2004).
[20] W. M. Reiff, C. M. Frommen, G. T. Yee and S. P. Sellers, *Inorg. Chem.*, **39**, 2076–2079 (2000).
[21] O. Kahn, *Molecular Magnetism*, VCH, New York, 1993, p. 6.
[22] O. Kahn, *Molecular Magnetism*, VCH, New York, 1993, pp. 17–26.
[23] D. Maganas, S. S. Staniland, A. Grigoropoulos, F. White, S. Parsons, N. Robertson, P. Kyritsis and G. Pneumatikakis, *Dalton Trans.*, 2301–2315 (2006).
[24] O. Kahn, *Molecular Magnetism*, VCH, New York, 1993, pp. 112–114.
[25] F. E. Mabbs and D. J. Machin, *Magnetism and Transition Metal Complexes*, Dover Publications Inc., New York, 2008.
[26] E. Sinn, *Coord. Chem. Rev.*, **5**, 313–347 (1970).

[27] G. A. Medley and R. Stranger, *Inorg. Chem.*, **33**, 3976–3985 (1994).
[28] R. Stranger, I. E. Grey, I. C. Madsen and P. W. Smith, *J. Solid State Chem.*, **69**, 162–170 (1987).
[29] U. Bossek, D. Nuhlen, E. Bill, T. Glaser, G. Krebs, T. Weyhermuller, K. Wieghardt, M. Lengen and A. X. Trautwein, *Inorg. Chem.*, **36**, 2834–2843 (1997).
[30] O. Kahn, *Molecular Magnetism*, VCH, New York, 1993, pp. 190–191.
[31] E. Dujardin, S. Ferlay, X. Phan, C. Desplanches, C. Cartier dit Moulin, P. Sainctavit, F. Baudelet, E. Dartyge, P. Veillet and M. Verdaguer, *J. Am. Chem. Soc.*, **120**, 11347–11352 (1998).
[32] V. Gadet, T. Mallah, I. Castro, M. Verdaguer and P. Veillet, *J. Am. Chem. Soc.*, **114**, 9213–9214 (1992).
[33] C. Bellini and D. Gatteschi, *Chem. Rev.*, **102**, 2369–2387 (2002).
[34] L. J. de Jongh and A. R. Miedema, *Adv. Phys.*, **23**, 1–260 (1974).
[35] R. Georges, J. J. Borras-Almenar, E. Coronado, J. Curely and M. Drillon, One-dimensional magnetism: an overview of the models, in *Magnetism: Molecules to Materials, Models and Experiments* eds. J. S. Miller and M. Drillon, Wiley-VCH Verlag GmbH, New York, 2001, Chapter 1.
[36] J. C. Bonner and M. E. Fisher, *Phys. Rev.*, **135**, A640–A658 (1964).
[37] G. A. Jr Baker, G. S. Rushbrooke and H. E. Gilbert, *Phys. Rev.*, **135**, A1272–1277 (1964).
[38] A. Meyer, A. Gleizes, J. J. Girerd, M. Verdaguer and O. Kahn, *Inorg. Chem.*, **21**, 1729–1739 (1982) and references therein.
[39] M. E. Fisher, *Am. J. Phys.*, **32**, 343–346 (1964).
[40] T. Smith and S. A. Friedberg, *Phys. Rev.*, **176**, 660–665 (1968); H. Kobayashi, I. Tsujikawa and S. A. Friedberg, *J. Low Temp. Phys.*, **10**, 621–633 (1973).
[41] M. Verdaguer, A. Gleizes, J. P. Renard and J. Seiden, *J. Phys. Rev. B*, **29**, 5144–5155 (1984).
[42] A. Caneshi, D. Gatteschi, P. Rey and R. Sessoli, *Inorg. Chem.*, **27**, 1756–1761 (1988).
[43] M. E. Fisher, *J. Math. Phys.*, **4**, 124–135 (1963).
[44] R. Carlin, *Magnetochemistry*, Springer-Verlag, New York, 1986, p. 173.
[45] R. Carlin, *J. Chem. Educ.*, **68**, 361 (1991).
[46] F. D. M. Haldane, *Phys. Rev. Lett.*, **50**, 1153–1156 (1983).
[47] M. Yamashita, T. Ishii and H. Matsuzaka, *Coord. Chem. Rev.*, **198**, 347–366 (2000).
[48] E. Dagotto, *JOM*, **49**, 18–23 and 50 (1997).
[49] M. Monfort, J. Ribas, X. Solans and M. Font-Bardia, *Inorg. Chem.*, **35**, 7633–7638 (1996).
[50] K. Katsumata and Z. Honda, *J. Phys. Chem. Solids*, **65**, 51–54 (2004).
[51] X-ray structures in this chapter have been represented using 'Mercury': C. F. Macrae, I. J. Bruno, J. A. Chisholm, P. R. Edgington, P. Mccabe, E. Pidcock, L. Rodriguez–Monge, R. Taylor, J. van de Streek and P. A Wood, *J. Appl. Cryst.*, **41**, 466–470, (2008).
[52] Z. Honda, H. Asakawa and K. Katsumata, *Phys. Rev. Lett.*, **81**, 2566–2569 (1988).
[53] E. Dagotto and T. M. Rice, *Science*, **271**, 618–623 (1996).
[54] E. Dagotto, *J. Electron Spectrosc. Relat. Phenom.*, **117-118**, 223–236 (2001).
[55] A. Shapiro, C. P. Landee, M. M. Turnbull, J. Jornet, M. Deumal, J. J. Novoa, M. A. Robb and W. Lewis, *J. Am. Chem. Soc.*, **129**, 952–959 (2007).
[56] L. Onsager, *Phys. Rev.*, **65**, 117–149 (1944).

[57] J. T. Culp, J.-H. Park, F. Frye, Y.-D Huh., M. W. Meisel and D. R. Talham, *Coord. Chem. Rev*., **249**, 2642–2648 (2005).
[58] H. Tamaki, Z. J. Zhong, N. Matsumoto, S. Kida, M. Koikawa, N. Achiwa, Y. Hashimoto and H. Okawa, *J. Am. Chem. Soc*., **114** , 6974–6979 (1992).
[59] J. Larionova, B. Mombelli, J. Sanchiz and O. Kahn, *Inorg. Chem*., **37**, 679–684 (1998).
[60] D. B. Mitzi, *Prog. Inorg. Chem*., **48**, 1–121 (1999).
[61] P. Day, *J. Chem. Soc. Dalton Trans*, 701–705 (1997).
[62] J. L. Atwood, *Nature Mater*., **1**, 91–92 (2002).
[63] A. Harrison, *J. Phys.: Condens. Mater*., **16**, S553–S572 (2004).
[64] B. Moulton, J. Lu, R. Hajndl, S. Hariharan and M. J. Zaworotko, *Angew. Chem. Int. Ed*., **41**, 2821–2824 (2002).
[65] E. A. Nytko, J. S. Helton, P. Müller and D. G. Nocera, *J. Am. Chem. Soc*., **130**, 2922–2923 (2008).
[66] R. Klenze, B. Kanellakopulos, G. Trageser and H. H. Eysel, *J. Chem. Phys*., **72**, 5819–5828 (1980).
[67] W. D. Griebler and D. Babel, *Anorg. Chem. Org. Chem*., **37B**, 832–837 (1982).
[68] W. R. Entley and G. S. Girolami, *Science*, **268**, 397–400 (1995).
[69] T. Mallah, S. Thiebaut, M. Verdaguer and P. Veillet, *Science*, **262**, 1554–1557 (1993).
[70] E. Dujardin, S. Ferlay, X. Phan, C. Desplanches, C. P. Cartier dit Moulin, P. Sainctavit, F. Baudelet, E. Dartyge, P. Veillet and M. Verdaguer, *J. Am. Chem. Soc*., **120**, 11347–11352 (1998).
[71] S. D. Holmes and G. S. Girolami, *J. Am. Chem. Soc*., **121**, 5593–5594 (1999).
[72] Ø. Hatlevik, W. E. Buschmann, J. Zhang, J. L. Manson and J. S. Miller, *Adv. Mater*., **11**, 914–918 (1999).
[73] R. Garde, F. Villian and M. Verdaguer, *J. Am. Chem. Soc*., **124**, 10531–10538 (2002).
[74] W. R. Entley, C. R. Treadway and G. S. Girolami, *Mol. Cryst. Liq. Cryst*., **273**, 153–166 (1995).
[75] A. Marvilliers, C. Hortholary, G. Rogez, J.-P. Audière, E. Rivière, J. C. Boquera, C. Paulsen , V. Villar and T. Mallah, *J. Solid State Chem*., **159**, 302–307 (2001).
[76] C. P. Berlinguette, J. R. Galan-Mascaros and K. R. Dunbar, *Inorg. Chem*., **42**, 3416–3422 (2003).
[77] P. A. Berseth, J. J. Sokol, M. P. Shores, J. L. Heinrich and J. R. Long, *J. Am. Chem. Soc*., **122**, 9655–9662 (2000).
[78] W. Dong, L.-N. Zhu, H.-B. Song, D.-Z. Liao, Z.-H. Jiang, S.-P. Yan, P. Cheng and S. Gao, *Inorg. Chem*., **43**, 2465–2467 (2004).
[79] J. M. Manriquez, G. T. Yee, R. S. McLean, A. J. Epstein and J. S. Miller, *Science*, **252**, 1415–1417 (1991).
[80] J. Zhang, J. Ensling, V. Ksenofontov, P. Gütlich, A. J. Epstein and J. S. Miller, *Angew. Chem. Int. Ed*., **37**, 657–660 (1998).
[81] H. Casellas, D. de Caro, L. Valade and P. Cassoux, *Chem. Vap. Deposition*, **8**, 145–147 (2002).
[82] J. W. Raebiger and J. S. Miller, *Inorg. Chem*., **41**, 3308–3312 (2002).
[83] E. B. Vickers, T. D. Selby and J. S. Miller, *J. Am. Chem. Soc*., **126**, 3716–3717 (2004).
[84] M. L. Taliaferro, M. S. Thorum and J. S. Miller, *Angew. Chem. Int. Ed*., **45**, 5326–5331 (2006).

[85] B. B. Kaul, J. P. Fitzgerald and G. T. Yee, *Chem. Commun.*, 49–50 (2000).
[86] M. D. Harvey, J. T. Pace and G. T. Yee, *Polyhedron*, **26**, 2037–2041 (2007).
[87] M. D. Harvey, T. D. Crawford and G. T. Yee, *Inorg. Chem.*, **47**, 5649–5655 (2008).
[88] M. D. Harvey and G. T. Yee, unpublished results.
[89] L. L. Shen and Xu Y-Z., *J. Chem. Soc. Dalton Trans.*, 3413–3414 (2001).
[90] B. Zurowska, J. Mrozinski, M. Julve, F. Lloret, A. Maslejova and W. Sawka-Dobrowolska, *Inorg. Chem.*, **41**, 1771–1777 (2002).
[91] T.-F. Liu, D. Fu, S. Gao, Y.-Z. Zhang, H.-L. Sun, G. Su and Y.-J. Liu, *J. Am. Chem. Soc.*, **125**, 13976–13977 (2003).
[92] E.-Q. Gao, Z.-M. Wang and C.-H. Yan, *Chem. Commun.*, **14**, 1748–1749 (2003).
[93] A. Fu, X. Huang, J. Li, T. Yuen and C. L. Lin, *Chem. Eur. J.*, **8**, 2239–2247 (2002).
[94] S. R. Batten and K. S. Murray, *Coord. Chem. Rev.*, **246**, 103–130 (2003).
[95] L. A. Berben and J. R. Long, *J. Am. Chem. Soc.*, **124**, 11588–11589 (2002).
[96] R. Clement, S. Decurtins, M. Gruselle and C. Train, *Monatsh. Chem.*, **134**, 117–135 (2003).
[97] G. T. Yee, M. J. Whitton, R. D. Sommer, C. M. Frommen and W. M. Reiff, *Inorg. Chem.*, **39**, 1874–1877 (2000).
[98] D. M. Adams, A. Dei, A. L. Rheingold and D. N. Hendrickson, *J. Am. Chem. Soc.*, **115**, 8221–8229 (1993).
[99] P. Gütlich, A. Hauser and H. Spiering, *Angew. Chem. Int. Ed. Engl.*, **33**, 2024–2054 (1994).
[100] P. Gütlich, Y. Garcia and H. A. Goodwin, *Chem Soc. Rev.*, **29**, 419–427 (2000).
[101] P. Gütlich and H. A. Goodwin, Electronic spin crossover, in *Comprehensive Coordination Chemistry II from Biology to Nanotechnology* (eds J. A. McCleverty and T. J. Meyer), Elsevier, 2004, pp. 421–426.
[102] O. Kahn, *Curr. Opin. Solid State Mater. Sci.* **1**, 547–554 (1996).
[103] O. Kahn, J. Kröber and C. Jay, *Adv. Mater.*, **4**, 718–728 (1992).
[104] J.-F. Letard, *J. Mater. Chem.*, **16**, 2550–2559 (2006).
[105] A. B. Gaspar, V. Ksenofontov, M. Seredyuk and P. Gütlich, *Coord. Chem. Rev.*, **249**, 2661–2676 (2005).
[106] K. E. Preuss, *Dalton Trans.*, 2357–2369 (2007).
[107] J. Rawson, A. Alberola and A. Whalley, *J. Mater. Chem.*, **16**, 2560–2575 (2006).
[108] K. Awaga, T. Tanaka, T. Shirai, M. Fujimori , Y. Suzuki, H. Yoshikawa and W. Fujita, *Bull. Chem. Soc. Jpn.*, **79**, 25–34 (2006).
[109] E. G. Awere, N. Burford, R. C. Haddon, S. Parsons, J. Passmore, J. V. Waszczak and P. S. White, *Inorg. Chem.*, **29**, 4821–4830 (1990).
[110] W. Fujita and K. Awaga, *Science*, **286**, 261–262 (1999).
[111] G. D. McManus, J. M. Rawson, N. Feeder, vanDuijn, J. E. J. L. McInnes, J. J. Novoa, R. Burriel, F. Palacio and P. Oliete, *J. Mater. Chem.*, **11**, 1992–2003 (2001).
[112] F. Varret, M. Nogues and A. Ggoujon, in *Magnetism, Molecules to Materials*, vol. **1** (eds J. S. Miller and Drillon, M.), Wiley-VCH Verlag Gmbh, New York, 2001, pp. 257–295.
[113] D. Papanikolaou, W. Kosaka, S. Margadonna, H. Kagi, S.-I. Ohkoshi and K. Prassides, *J. Phys. Chem. C*, **111**, 8086–8091 (2007).
[114] L. Egan, K. Kamenev, D. Papanikolaou, Y. Takabayashi and S. Margadonna, *J. Am. Chem. Soc.*, **128**, 6034–6035 (2006).
[115] M. Castro, J. A. Rodriguez-Velamazan, K. Boukheddaden, F. Varret, H. Tokoro and S. Ohkoshi, *EPL*, **79**, 1–6 (2007).

[116] A. Bleuzen, C. Lomenech, V. Escax, F. Villain, F. Varret, C. Cartier and M. Verdaguez, *J. Am. Chem. Soc.*, **122**, 6648–6652 (2000).
[117] H. W. Liu, K. Matsuda, Z. Z. Gu, K. Takahashi, A. L. Cui, R. Nakajima, A. Fujishima and O. Sato, *Phys. Rev. Lett.*, **90**, 167403 (2003).
[118] E. Coronado and P. Day, *Chem. Rev.*, **104**, 5419–5448 (2004).
[119] P. Day, *Philos. Trans. R. Soc. London, Ser A*, **357**, 3163–3184 (1999).
[120] M. Aonuma, T. Oyamada, H. Sasabe, T. Miki and C. Adachi, *Appl. Phys. Lett.*, **90**, 183503, 1–3 (2007).
[121] S. Uji, H. Shinagawa, T. Terashima, T. Yakabe, Y. Terai, M. Tokumoto, A. Kobayashi, H. Tanaka and H. Kobayashi, *Nature*, **410**, 908–910 (2001).
[122] H. Fujiwara, H. Kobayashi, E. Fujiwara and A. Kobayashi, *J. Am. Chem. Soc.*, **124**, 6816–6817 (2002).
[123] H. Kobayashi, H. Cui and A. Kobayashi, *Chem. Rev.*, **104**, 5265–5288 (2004).
[124] E. Coronado, J. R. Galan-Mascaros, C. J. Gomez-Garcia and V. Laukhin, *Nature*, **408**, 447–449 (2000).
[125] H. Fujiwara, T. Hayashi, T. Sugimoto, H. Nakazumi, S. Noguchi, L. Li, K. Yokogawa, S. Yasuzuka, K. Murata and T. Mori, *Inorg. Chem.*, **45**, 5712–5714 (2006).
[126] B. Zhou, M. Shimamura, E. Fujiwara, A. Kobayashi, T. Higashi, E. Nishibori, M. Sakata, H. Cui, K. Takahashi and H. Kobayashi, *J. Am. Chem. Soc.*, **128**, 3872–3873 (2006).
[127] M. Johnson, *J. Phys. Chem. B*, **109**, 14278–14291 (2005).
[128] S. Sanvito and S. A. R. Rocha, *J. Comput. Theor. Nanosci.*, **3**, 624–642 (2006).
[129] S. Sanvito, *J. Mater. Chem.*, **17**, 4455–4459 (2007).
[130] S. Sanvito, *Nat. Mater.*, **6**, 803–804 (2007).
[131] Y. Shirota, *J. Mater. Chem.*, **10**, 1–25 (2000).
[132] L. Bogani and W. Wernsdorfer, *Nature Mater.*, **7**, 179–186 (2008).
[133] T. S. Santos, J. S. Lee, P. Migdal, I. C. Lekshmi, B. Satpati and J. S. Moodera, *Phys. Rev. Lett.*, **98**, 1–4 (2007).
[134] K. Tsukagoshi, B. W. Alphenaar and H. Ago, *Nature*, **401**, 572–574 (1999).
[135] N. Tombros, C. Jozsa, M. Popinciuc, H. T. Jonkman and B. J. vanWees, *Nature*, **448**, 571–574 (2007).
[136] S. Heutz, C. Mitra, W. Wu, A. J. Fisher, A. Kerridge, M. Stoneham, T. H. Harker, J. Gardener, H-.H. Tseng, T. S. Jones, C. Renner and G. Aeppli, *Adv. Mater.*, **19**, 3618–3622 (2007).
[137] H. Wende, M. Bernien, J. Luo, C. Sorg, N. Ponpandian, J. Kurde, J. Miguel, M. Piantek, X. Xu, Ph. Eckhold, W. Kuch, K. Baberschke, P. M. Panchmatia, B. Sanyal, P. M. Oppeneer and O. Eriksson, *Nat. Mater.*, **6**, 516–520 (2007).

4

Molecular Inorganic Conductors and Superconductors

Lydie Valade[1,2] and Hisashi Tanaka[3]
[1]*LCC (Laboratoire de Chimie de Coordination), CNRS, Toulouse, France*
[2]*UPS, INPT, LCC, Université de Toulouse, France*
[3]*Molecular Nanophysics Group, AIST (National Institute of Advanced Industrial Science and Technology), NRI (Nanotechnology Research Institute), Tsukuba, Japan*

4.1 INTRODUCTION

Since the beginning of the 1970s, several hundreds of conducting and superconducting molecular systems have been isolated.[1–8] A large majority of them arises from organic molecules combined together or associated with inorganic species, while a smaller number derive from coordination compounds being associated with organic or inorganic counter species (Figure 4.1). Since the publication in 1996 of 'Molecular Inorganic Superconductor' (P. Cassoux and L. Valade)[9] in the second edition of *Inorganic Materials* (edited by D.W. Bruce and D. O'Hare),[10] many new findings have appeared in this field. First of all, new superconducting phases based on [M(dmit)$_2$] complexes have been isolated,[7] and the first neutral metallic conductors based on nickel complexes of the TTF (tetrathiafulvalene)-extended dithiolene

Molecular Materials Edited by Duncan W. Bruce, Dermot O'Hare and Richard I. Walton

ligand were prepared at the beginning of 2000.[6] Secondly, more and more research groups have been concerned with the preparation of molecular conductors and superconductors as films or nanowires,[11,12] a more appropriate morphology to envisage their applications into devices.

This chapter first gives background on compounds that can be qualified as benchmarks in the field of molecular organic and inorganic conductors and superconductors. Focus is then further given to systems based on metal bis-dithiolene complexes. The last section considers the processing methods that can be applied to grow films of molecular conductors and superconductors.

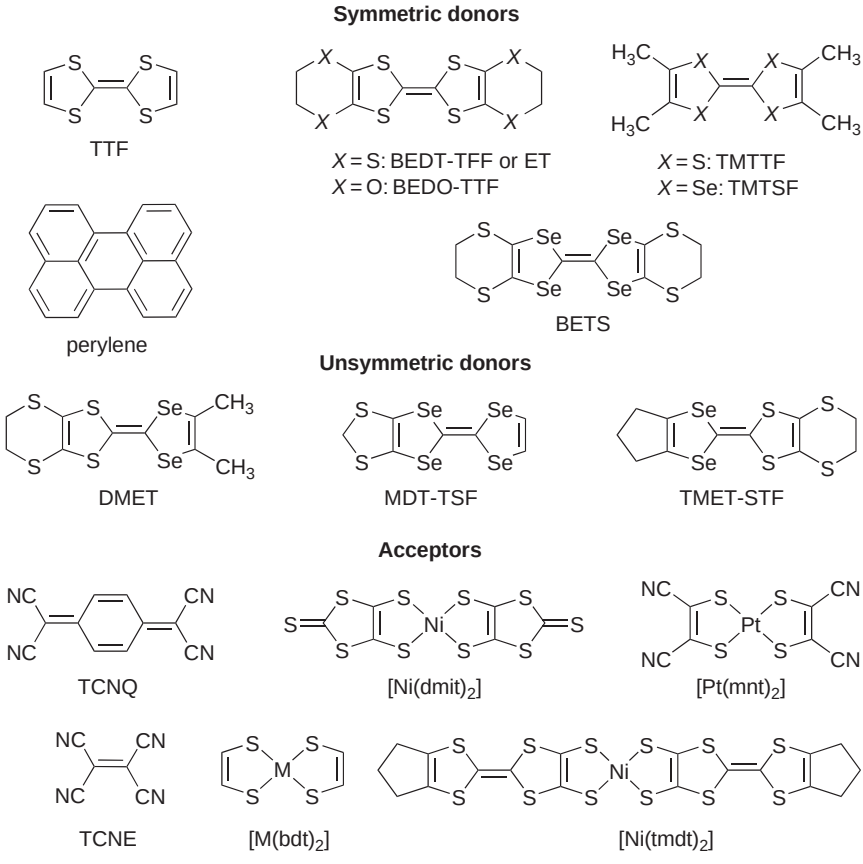

Figure 4.1 Examples of molecular conductor building blocks

4.2 FAMILIES OF MOLECULAR CONDUCTORS AND SUPERCONDUCTORS

4.2.1 From Molecules to Conductors and Superconductors

4.2.1.1 Molecular Assemblies

In conducting materials, the means of ensuring the flow of electrons is based on structural conditions. In the case of metals, each atom assembles and forms solids where each atomic orbital overlaps sufficiently to secure the conduction path. The situation is different in materials based on organic molecules, which have to fulfil specific conditions to secure conduction. In materials consisting of self-assembled organic molecules, the most part of the self-assembling force originates from intermolecular forces. Generally, since the atomic orbital expansion of every element of organic molecules is weak in contrast to their inorganic equivalents the overlap of molecular orbitals between organic molecules is consequently not large. Therefore, the organic molecules applied for building conductors have to be selected among those exhibiting good planarity to favour molecular stacking and containing larger atoms like chalcogens to enhance interactions between adjacent molecules.

4.2.1.2 Origin of Electrical Properties in Molecular Assemblies

In molecular assemblies, molecular stacking alone is not a sufficient criterion for the generation of electrical carriers. As shown in Figure 4.2, when planar molecules with π-conjugated orbitals pile up, two bands are generated: a HOMO-based valence band and a LUMO-based conduction band. The bandwidth depends on the degree of interaction between the molecular orbitals. However, no free carriers exist in the conduction and valence bands. To generate conductivity, it is necessary to inject electrons/holes by charge transfer or partial oxidation/reduction. Except for one family of neutral metal complexes, carrier generation requires at least the association of two molecular species. Thus, the so-called Charge-Transfer Salts result from partial charge transfer between a donor and an acceptor molecule, while Fractional-Oxidation-State Salts consist of partially oxidised donor molecules associated with counter anions for charge compensation. As mentioned above, single-component conductors have been obtained from neutral metal complexes.[6] In these

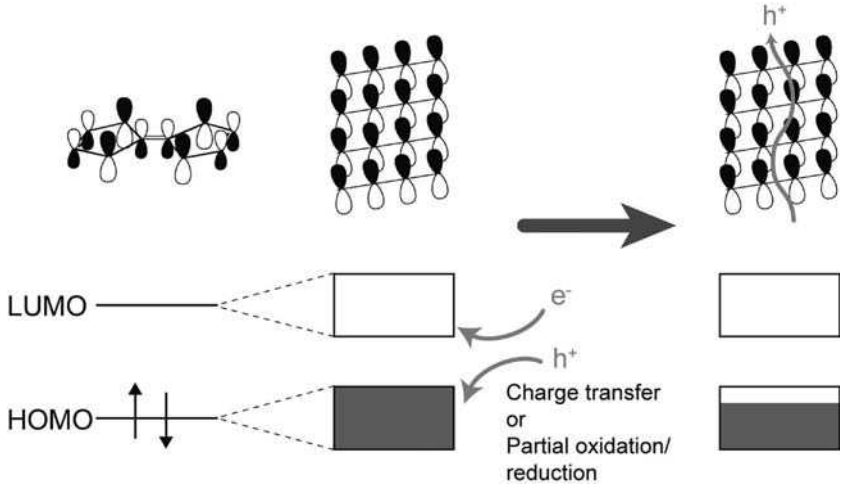

Figure 4.2 Schematic figure of band formation and generation of carriers. The planar organic molecules with π-conjugated orbitals pile up and form a conduction column

systems, further described in Section 4.3, partial filling of the conduction band originates from crossing HOMO and LUMO bands.

In two-component assemblies, the interaction, between donor and acceptor molecules or donor molecules and anions, affects their molecular arrangement and physical property as well. Polymeric anions may govern the donor packing, and magnetic anions often interact with the conduction π-electrons. This is one of the interesting aspects of the study of organic molecular conductors: not only the freedom of molecular design but also the combination of molecules.

4.2.1.3 On the Guidelines for Selecting Candidate Systems for Molecular Conductors

A number of structural, experimental and theoretical studies on organic molecular conductors have revealed the criteria required for the formation of stable metallic molecular conductors, while the following guidelines are quite fundamental; however, they are useful indicators for synthetic chemists.

(i) Planar molecules: as described above, molecular stacking is important for the formation of the conduction path, and planar molecules with π-conjugated orbitals afford advantage to secure

conduction columns. Additionally, the molecular stacking can be modified by introducing flexible terminal groups on the molecules.

(ii) Extended π-conjugated systems: molecules with extended π-conjugated orbitals are efficient for reducing the on-site coulombic repulsion between electrons on the same molecules. This is an important guideline for synthesising stable metallic conductors. Moreover, the control of electron correlation seems to be also important for the investigation of superconductors.

(iii) Chalcogen atom replacement: as shown in Figure 4.3 for typical molecules encountered in organic conductors as TTF (tetrathiafulvalene)-based donors, the replacement of sulfur atoms by selenium atoms is an effective strategy for designing molecules with enhanced intermolecular interactions. Tetraselenafulvalene (TSF), the selenium derivative of TTF, is more likely to produce metallic molecular conductors. Bis(ethylenedithio)tetrathiafulvalene (BEDT-TTF) is a well-known donor which produces two-dimensional electronic band structures and bis(ethylenedithio)-tetraselenafulvalene (BETS), where the four central chalcogen atoms are replaced by selenium atoms, is expected to have much interaction not only in the direction of molecular stacking but also through lateral molecular contacts. Multi-dimensional interactions increase the stability of the electronic array and prevent phase transitions towards lower-conducting structural arrangements, inherent in one-dimensional structures.[13]

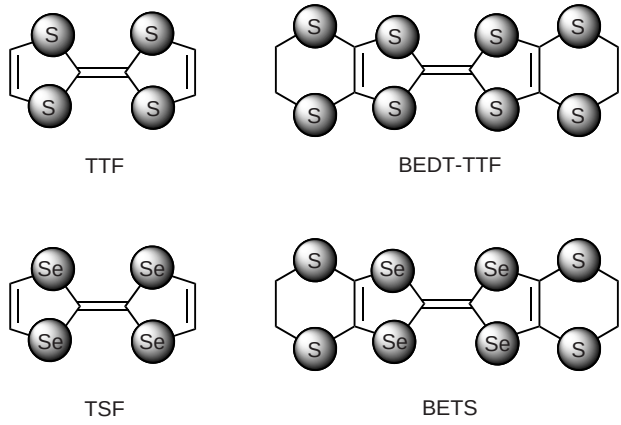

Figure 4.3 Chalcogen substitution in TTF-based donor molecules

(iv) Redox potentials criterion: partial filling of the conduction band is necessary to afford conducting materials. In fractional oxidation state salts, partial oxidation of the donor is performed by electrochemical/chemical methods. Donor ability is given by the redox potential of the donor. In charge-transfer salts, the amount of charge transfer also depends on the respective redox potentials of the donor and the acceptor. Coupling of a strong donor and a strong acceptor will lead to full charge transfer, while the coupling of a weak donor and a weak acceptor will result in little or no charge transfer. The donor and acceptor ability, that is the ionisation potential of the donor molecule, and the electron affinity of the acceptor molecule, can be estimated from their redox potential values in solution. The difference between the redox potentials of the donor (oxidation) and the acceptor (reduction) should preferably lie within the range 0–0.3 V to expect partial charge transfer.[8,14,15]

4.2.2 Organic Metals and Superconductors

In 1954, Akamatsu *et al.* reported the highly conductive organic compound based on perylene and bromine.[16] This discovery was the bursting buds of organic conductor study. Then, Little's suggestion in 1964 of the possibility to develop an organic superconductor with high critical temperature (T_c) accelerated the study of organic conductors.[17] Later on, while the study of the family of platinum chain compounds such as KCP complexes (KCP: $K_2[Pt(CN)_4]X_{0.3}{\cdot}nH_2O$, X = Br, Cl) was progressing,[18,19] the improvement of electronic dimensionality was regarded to be inevitable for the development of stable metals and superconductors.[13]

Due to the many degrees of freedom in molecular design, in molecular structural flexibility and in molecular arrangements, molecular conductors can adopt various patterns of molecular packing. Additionally, the variety of anions leads to a huge number of molecular conductors. The anion often takes an important role in molecular conductors; sometimes it governs the crystal symmetry or donor molecular arrangements, and sometimes it interacts with conduction electrons, as in the case of magnetic anions. In the past three decades, organic molecular conductors have been regarded as one of the remarkable materials affording novel physics. In this section a chronological presentation of the most

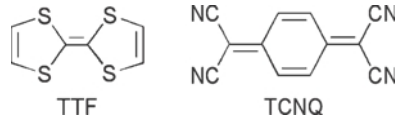

Figure 4.4 TTF and TCNQ molecules

representative families of organic molecular conductors and superconductors is given.

4.2.2.1 TTF-TCNQ

The planar acceptor molecule, 7,7,8,8-tetracyano-*p*-quinodimethane (TCNQ) (Figure 4.4), was synthesised in 1960 by Acker *et al.*,[20] and many of its salts were reported as electrically conducting.[21] Ten years later, the planar donor molecule, tetrathiafulvalene (TTF) (Figure 4.4), was synthesised by Coffen *et al.* and Wudl *et al.*,[22,23] and its salts with halides were reported to be conducting.[24,25]

The synthesis of the first 'organic metal' TTF·TCNQ was reported in 1973 by Coleman *et al.* [26] and Ferraris *et al.*[27] In this compound, TTF and TCNQ molecules are in 1:1 ratio and form separate stacked donor (TTF) columns and stacked acceptor (TCNQ) columns. A partial charge transfer between TTF and TCNQ transforms the molecular stacks into one-dimensional conductive paths *via* the formation of partially filled bands. Although TTF·TCNQ shows metallic conductivity down to around 60 K, it abruptly transfers to an insulator below 54 K, which was explained by a charge-density wave (CDW) phase-locking (Peierls transition[13]) due to its one dimensionality.[28,29]

4.2.2.2 TMTSF Superconductors

In spite of the tremendous effort in searching for organic conductors, none of the TTF·TCNQ-like organic metals retained their metallic characteristics down to low temperatures. At the beginning of the 1980s, Bechgaard *et al.* searched for compounds based on $[TMTSF]_2[X]$, so-called Bechgaard salts, where TMTSF is tetramethyltetraselenafulvalene, (Figure 4.5) and X^- is a monovalent anion (PF_6^-, AsF_6^-, SbF_6^-, BF_4^- or NO_3^-), and found that this series of salts showed high conductivity (10^4–10^6 S cm^{-1}) at low temperatures. Although these salts transferred into

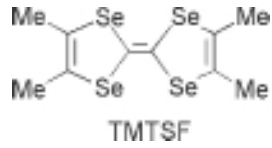

Figure 4.5 The TMTSF molecule

insulators at lower temperatures, some of their metal–insulator transition temperatures came down below 20 K.[30]

The first 'organic superconductor' $[TMTSF]_2[PF_6]$ was found by Jérome *et al*. in 1980. They studied the conductance of Bechgaard salts under high pressure and found that $[TMTSF]_2[PF_6]$ shows superconductivity at 0.9 K under a pressure of 12 kbar.[31] At ambient pressure, $[TMTSF]_2[PF_6]$ shows a metal–insulator transition at 15 K.[30] At the early stages of the study of $[TMTSF]_2[PF_6]$, it was guessed to be a Peierls transition following CDW formation, as in TTF·TCNQ. However, as the peculiar $2k_F$ diffraction patterns did not show up according to the X-ray measurements, this mechanism was denied.[32] From the NMR, ESR and anisotropic magnetic measurements, the insulating transition phase was concluded as being due to Spin Density Wave (SDW) phase.[33–36] In $[TMTSF]_2[PF_6]$, the transfer energy along the donor stacking direction is almost ten times larger than that in the lateral direction, which suggests a one-dimensional electronic structure for this salt.[37,38]

Subsequently, the superconductivity under pressure in $[AsF_6]^-$, $[SbF_6]^-$, $[TaF_6]^-$ and $[ReO_4]^-$ salts were observed.[39,40] The first discovered organic superconductor at ambient pressure was $[TMTSF]_2[ClO_4]$, for which T_c is 1.3 K.[41] One of the interesting features of the TMTSF family can be seen in the comparison with anion exchanged salts, which enables this system to be studied systematically and helps one of the important role of anions, 'chemical pressure', to be understood. It was summarised in the generalised phase diagram of pressure *vs* temperature including the TMTTF (tetramethyltetrathiafulvalene) family of compounds, the so-called Fabre salts.[42]

4.2.2.3 BEDT-TTF Superconductors

In the process towards stable organic metals and superconductors, increasing the dimensionality could be a way to avoid the ubiquitous metal–insulator transition, which inevitably occurs in one-dimensional electronic systems.[13] Compared with TTF and TMTSF, BEDT-TTF

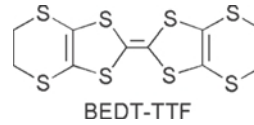

Figure 4.6 The BEDT-TTF molecule

[bis(ethylenedithio)tetrathiafulvalene; Figure 4.6] has more extended π-conjugated orbitals, promotes interactions between donor molecules and has less on-site coulombic repulsions. Additionally, the flexibility of the terminal ethylene groups causes the abundant variety of molecular arrangement observed in BEDT-TTF salts.[3,8] The first BEDT-TTF superconductor was [BEDT-TTF]$_2$[ReO_4] which shows T_c at 2 K under 4 kbar of pressure.[43]

The well-known superconducting modifications of BEDT-TTF salt are *β*-, *θ*- and κ-type crystals, where the donor molecular arrangements are shown in Figure 4.7. The superconductor [BEDT-TTF]$_2$[I_3] can adopt these three modifications. In spite of the difference in molecular arrangements, all of them have two-dimensional features, and show superconducting transitions at ambient pressure.[44] T_c of β-[BEDT-TTF]$_2$[I_3] is as high as 8 K under certain conditions.[45–47]

Based on the guideline that compounds exhibiting larger cell volume per BEDT-TTF molecule have a tendency to higher values of T_c, various kinds of BEDT-TTF salts with polymeric anions have been synthesised.

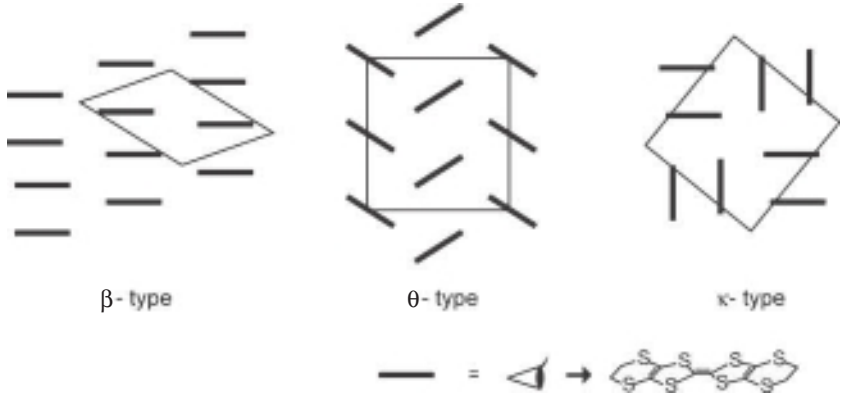

Figure 4.7 Schematic figures of donor molecular arrangements in β-, θ- and κ-type salts. The figures are the projections viewed from the molecular long axis

The first organic superconductor whose T_c was over 10 K was κ-[BEDT-TTF]$_2$[Cu(NCS)$_2$] ($T_c = 10.4$ K) in 1987.[48] Subsequently, T_c was raised to 11.6 K at ambient pressure [49] in κ-[BEDT-TTF]$_2$[Cu{N(CN)$_2$}][Br], and its isostructural salt, κ-(BEDT-TTF)$_2$Cu[N(CN)$_2$]Cl, showed superconductivity at 12.8 K under 0.3 kbar of pressure.[50,51] The correlation between T_c and the cell volume was systematically studied in the association of BEDT-TTF with polymeric anions: the donor–anion interaction, arising from the short atomic contacts between the terminal ethylene groups of donors and open sites of anions, plays a significant role in these systems.[8,52] In 2003, the highest T_c of organic superconductors was reported by Taniguchi *et al.* The Mott insulator, β′-(BEDT-TTF)$_2$ICl$_2$, shows superconducting transition at 14.2 K under extreme pressure, 82 kbar.[53]

After the 1990s, a number of BEDT-TTF salts with anions including magnetic metals have been synthesised. For example, [BEDT-TTF]$_2$[FeCl$_4$] and [BEDT-TTF]$_2$[FeBr$_4$] contain Fe^{3+} ions, and their electric properties are semiconducting and insulating, respectively. Both salts show a magnetic moment $S = 5/2$ (Fe^{3+}: d^5, high spin). However, interactions between donors and anions are not observed.[54] The BEDT-TTF salt with a polymeric manganate anion, [BEDT-TTF]$_2$[Mn$_2$Cl$_5$(EtOH)], shows metallic conductance down to 2 K. Magnetic measurements give $S = 5/2$ (Mn^{2+}: d^5, high spin) and temperature dependence shows antiferromagnetic interactions without ordering.[55] The paramagnetic organic superconductor, β″-[BEDT-TTF]$_4$(H$_3$O)[Fe(C$_2$O$_4$)$_3$]•C$_6$H$_5$CN, was reported by Kurmoo and Day *et al.* in 1995.[56] Its critical temperature T_c is 7.0 K, and superconductivity and paramagnetism coexist below T_c, which suggests that little interaction works between donors and anions. In 2000, Coronado *et al.* reported the ferromagnetic organic metal, [BEDT-TTF]$_3$[MnCr(C$_2$O$_4$)$_3$].[57] In this compound, the anion layer forms a two-dimensional honeycomb structure based only on a bimetal oxalate and gives ferromagnetic ordering below 5.5 K. The metallic behaviour is not disturbed by the ferromagnetic ordering and remains down to 2 K.

4.2.2.4 BETS Magnetic Superconductors

The design of molecular conductors with interactions between localised *d*-electrons and conducting π-electrons is one of the attractive topics in the study of molecular conductors. This study revealed outstanding physical properties such as metal-to-insulator transition with magnetic ordering, superconducting state induced by strong magnetic field, and so on.

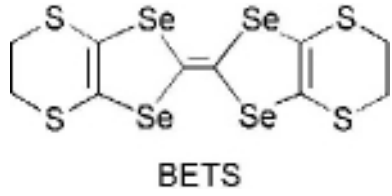

Figure 4.8 The BETS molecule

The organic molecule BETS [bis(ethylenedithio)tetraselenafulvalene, BEDT-TSeF, Figure 4.8] is one of the key molecules of this type.[58]

As mentioned above, since in common with BEDT-TTF, the BETS molecule has extended π-conjugated orbitals, and includes selenium atoms, which could increase the interactions not only between donor molecules but also between donors and anions.[59,60] As such, it forms stable conductors with various anions, such as linear, tetrahedral, octahedral anions [61,62] and magnetic anions.[63] A series of λ-type BETS salts with tetrahedral anions, λ-$[BETS]_2[MX_4]$ (M = Fe, Ga; X = Cl, Br) shows abundant conductive and magnetic properties. The anion size of non-magnetic $[GaCl_4]^-$ and magnetic $[FeCl_4]^-$ being almost equivalent, the $[GaCl_4]^-$ sites can be advantageously replaced by $[FeCl_4]^-$ at a desired ratio.[5] Therefore, it is possible to control the content of magnetic species in λ-$[BETS]_2[Fe_xGa_{1-x}Cl_4]$ between $x = 0$ (superconductor below 5.5 K (midpoint)) and $x = 1.0$ (antiferromagnetic insulator below 8.5 K). As shown, for example, in Figure 4.9, the λ-type BETS salt with $x = 0.45$ shows a metal–superconductor transition around 4 K and a superconductor–antiferromagnetic insulator transition around 3 K. In addition, the chloride in $[MCl_4]^-$ can be replaced by bromide (to give $[MBr_4]^-$), increasing the volume of the anion. The extra volume disturbs the solid-state arrangement and reduces the overlap between BETS units (a kind of 'pressure reduction'). This is shown in Figure 4.9 as the plot of P against the reversed y axis.

The suppression of the antiferromagnetic insulator state in λ-$[BETS]_2[FeCl_4]$ and the appearance of a metallic state above 11 T was reported by Brossard *et al.* in 1998.[64] The conductive properties under high magnetic field revealed more information about this system. In 2001, Uji *et al.* reported the superconducting state of λ-$[BETS]_2[FeCl_4]$ induced by high magnetic fields (>17 T).[65,66] The phase diagram of temperature *vs* magnetic field is shown in Figure 4.10. The field-induced superconducting (FISC) state was systematically studied in a series of λ-$[BETS]_2[Fe_xGa_{1-x}Cl_4]$ and

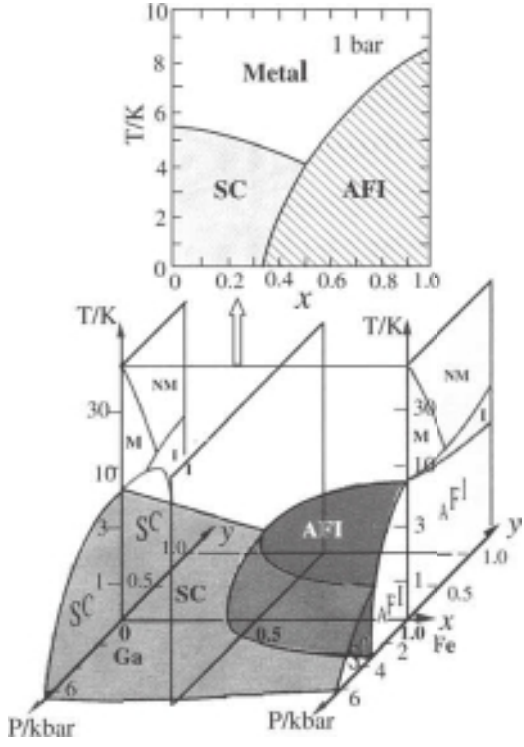

Figure 4.9 Phase diagram of λ-$[BETS]_2[Fe_xGa_{1-x}Cl_4]$. Reprinted with permission from Kobayashi *et al.*, 2004 [6]. Copyright (2004) American Chemical Society

λ-$[BETS]_2[FeBr_xCl_{4-x}]$ by Uji *et al.*, and the possibility of Jaccarino and Peter effect† has been proposed as the mechanism.[67–69]

The κ-type BETS salts with $[MX_4]^-$ anions show interesting phenomena at low temperatures. For example, κ-$[BETS]_2[FeBr_4]$ remains metallic down to 1.1 K. Although it shows an antiferromagnetic transition at 2.5 K, it retains metallic conductivity. Upon decreasing the temperature, it finally turns to a superconductor below 1.1 K, where antiferromagnetic ordering still coexists. Furthermore, the κ-$[BETS]_2[FeBr_4]$ salts also show FISC state under 12.5 T.[70–72] The detailed ^{77}Se NMR studies on the FISC state were carried out for λ-type BETS salts by Hiraki *et al.* [73] and for κ-type BETS salts by Fujiyama *et al.*[74]

† The Jaccarino and Peter effect is the production of superconductivity in certain ferromagnetic metals through the application of an external magnetic field that compensates for the polarisation of the conduction electrons. It is also known as the compensation effect.

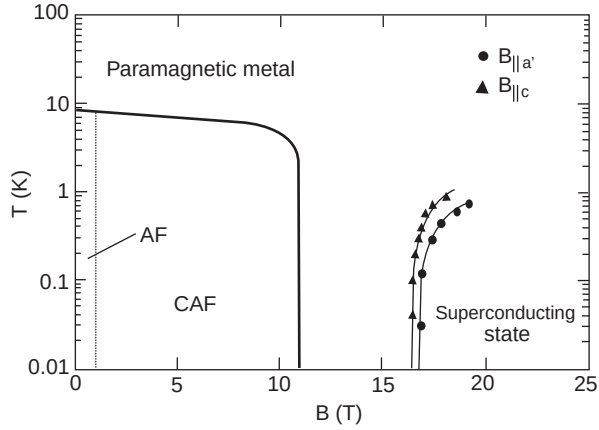

Figure 4.10 Temperature *vs* magnetic field phase diagram of λ-$[BETS]_2[FeCl_4]$. Reprinted by permission from Uji *et al.*, 2001 [65]. Copyright (2001) Macmillan Publishers Ltd

The estimation of π–*d* interactions in these organic conductors has been reported by Mori *et al.*[75] The interactions are estimated from intermolecular overlap integrals: overlaps between anions (J_{dd}) and between donors and anions ($J_{\pi d}$). The calculated contributions of *d*–*d* and π–*d* interactions become in reasonable agreement with the experiments. In λ-$[BETS]_2[FeCl_4]$, it becomes clear that the π–*d* interactions are relatively large compared with *d*–*d* interactions.

4.2.2.5 Other Families

Among the large number of organic conductors,[8] a selection of organic superconductors based on special donors will be described.

The asymmetric organic molecule, dimethyl(ethylenedithio)diselenadithiafulvalene (DMET, Figure 4.11), is a hybrid of TMTSF and BEDT-TTF molecules. DMET yielded eight superconductors with seven linear anions, $[DMET]_2[X]$ where X are $[I_3]^-$ (β), $[IBr_2]^-$ (β), $[AuI_2]^-$ (β), $[AuBr_2]^-$ (β, κ), $[AuCl_2]^-$ (β), $[Au(CN)_2]^-$ (β) and $[CuCl_2]^-$ (β).[76–78] DMET salts with other anions, such as octahedral or tetrahedral examples, do not form superconductors. Since β-$[DMET]_2[X]$ superconductors have quasi one-dimensional electronic structures, some of them show SDW instability and need pressure to exhibit superconductivity. T_c of these β-salts are lower than 1.6 K. Only κ-$[DMET]_2[AuBr_2]$ ($T_c = 1.9$ K) has a two-dimensional electronic structure, which is confirmed by the observation of dHvA (de Haas–van Alphen) oscillations.

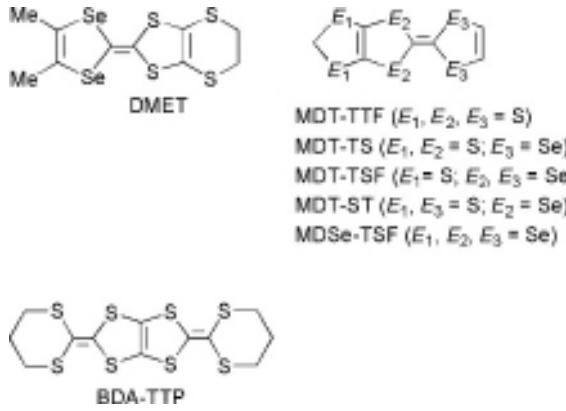

Figure 4.11 Structural formulae of DMET, MDT-TTF and its family, and BDA-TTP donors

Methyldithiotetrathiafulvalene (MDT-TTF, Figure 4.11) and its selenium-substituted family are also unsymmetric donors. MDT-TTF is a donor, being a hybrid of TTF and BMDT-TTF (bis(methylenedithio) tetrathiafulvalene) molecules. These donors yield superconductors with monohalogen anions or linear anions such as trihalogen or $[AuI_2]^-$ anions, and T_c are in the range 3.2–4.7 K.[79–86] In the salts of all sulfur-substituted (MDT-TTF) and all selenium-substituted donors (MDSe-TSF), the composition of donor:anion was reported to be 2:1. On the other hand, the other salts of sulfur–selenium donors show nonstoichiometric structures, the anion lattice being incommensurate with the donor lattice in these superconductors.[82,85,87]

The 2,5-bis(1,3-dithian-2-ylidene)-1,3,4,6-tetrathiapentalene (BDA-TTP, Figure 4.11) based organic superconductors, β-[BDA-TTP]$_2$[X], [88,89] do not have the TTF unit in the donor structure. Due to the molecular planarity, flexibility of terminal bonds and electrochemical stability, many BDA-TTP salts with various anions were reported.[90] The first β-[BDA-TTP]$_2$[X] superconductors at ambient pressure are the salts with octahedral anions ($X^- = [SbF_6]^-$, $[AsF_6]^-$ and $[PF_6]^-$). According to the magnetisation measurements, the onset of the diamagnetic transition of these salts was observed at 6.9 K for the SbF_6 salt and 5.9 K for both the AsF_6 and PF_6 salts, respectively. Subsequently, β-[BDA-TTP]$_2$[X] superconductors with tetrahedral anions (X = $GaCl_4$ and $FeCl_4$) were reported. These two salts exhibit superconducting transition under applied pressure. They have an isomorphous structure and show similar metal–insulator transition around 120 K. The insulating states are

suppressed by pressure and the superconducting transitions were observed at 3.1 K under 7.6 kbar for the $GaCl_4$ salt and ≈2 K under 9.7 kbar for the $FeCl_4$ salt. The latter salt including a magnetic anion also showed antiferromagnetic ordering below 8.5 K. The comparison with the magnetoresistance measurement suggests that the magnetic interaction (J) between the conduction electrons and the magnetic moments in the $FeCl_4$ salt is small.[89]

4.2.3 Transition Metal Complex-Based Conducting Systems

Certain kinds of metal complexes have been regarded as promising compounds for the study of molecular-based conductors, because their composition combines metals and organic moieties. Metal complexes consist of central metals surrounded by ligands including functionalised moieties. The electronic state of the central metals governs the ligand coordination mode (square planar, tetrahedral, octahedral, *etc.*). Furthermore, it governs the whole molecular structure, and the mixing of the metal and ligand orbitals causes the characteristic properties of molecular conductors based on metal complexes. The electric conductivity mainly results from the d_{z^2} orbitals overlap of metals in the case of linear-chain metal complexes. However, in macrocyclic metal complexes and metal dithiolene complexes, conductance is supported by the ligand part through the overlap of extended ligand orbitals. This section gives a presentation of the most representative families of transition metal complex-based conducting systems.

4.2.3.1 Linear Chain Systems

The first episode of linear chain type molecular conductors was written by Knop and Schnedermann in the middle of the nineteenth century.[91] Although the isolated crystals of $K_2[Pt(CN)_4]$ oxidised by chlorine or bromine were reported to show metallic luster, the character of conducting compounds was not clarified.

The first compound widely noticed as a 'molecular inorganic conductor' was KCP, $K_2[Pt(CN)_4]X_{0.3}\bullet nH_2O$ (X = Cl, Br), which was reported in 1968.[18] KCP is a partially oxidised platinum complex, later called the Krogmann salt, and was prepared by oxidising a platinum(II) complex with halogen, or by electrochemical oxidation, or by mixing platinum(II) and platinum(IV) complexes. The KCP structure is characterised by

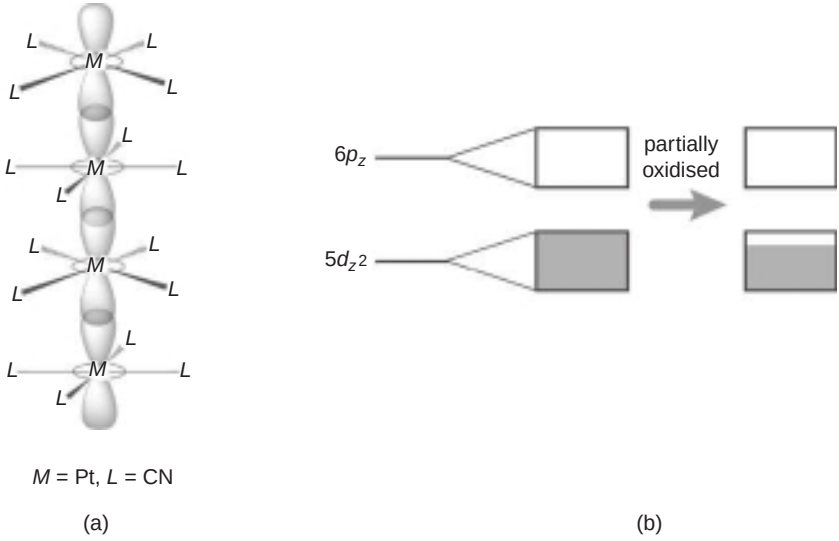

Figure 4.12 (a) Schematic figure of the linear chain structure of KCP and (b) band structure of partially oxidised KCP.

columns of $Pt(CN)_4$ anions, where planar $Pt(CN)_4$ are stacked along the direction perpendicular to the molecular plane allowing the overlap of platinum $5d_{z^2}$ orbitals (Figure 4.12). Since each CN–Pt–NC angle in adjacent $Pt(CN)_4$ moieties is rotated by almost 45°, interplane repulsion is minimised along the chains and the Pt–Pt distance in partially oxidised KCP is very short at 2.88 Å. This distance is much shorter than in non-oxidised KCP (3.48 Å in $K_2[Pt(CN)_4]\cdot n(H_2O)$) and slightly longer than in platinum metal (2.77 Å). On the other hand, the Pt–Pt distance between two nearest adjacent columns is 9.87 Å, which means that each linear platinum chain is well isolated. Thus, KCP is a one-dimensional linear chain system from a structural point of view.

The electrical transport of KCP was reported by Zeller *et al.*[19] The room-temperature conductivity along the molecular stacking direction is 300–400 S cm^{-1}, which is 10^5 greater than the conductivity perpendicular to the chain direction. The temperature dependence of conductivity along the chain direction shows metallic behaviour down to around 250 K and semiconducting behaviour below that temperature. The broad maximum of conductivity around 250 K is due to the one-dimensionality of the linear-chain system. The large anisotropy of conductivity in directions parallel and perpendicular to the chains confirms the one-dimensional character of KCP.

Following these findings, the KCP complex and its analogues have attracted the attention of theoretical, physical and chemical scientists, and have been discussed in several review articles.[92–94] Monovalent iridium, Ir^{I}, having the same d^8 electronic configuration as Pt^{II}, was regarded as a good candidate metal for linear chain conducting systems and a number of partially oxidised dihalogenodicarbonyliridium complexes, $C_x[IrX_2(CO)_2]$ ($C^+ = H^+$, K^+, Na^+, TTF^+ ; $0 < x < 1$; $X = Cl$, Br), have been reported.[95,96] Their structural arrangements are similar to that of KCP, showing linear chains with overlap of iridium $d_z{}^2$ orbitals, where the Ir–Ir distance is 2.86–2.78 Å. They show semiconducting temperature dependence, with room-temperature conductivity ranging from 0.01 to 5 S cm^{-1}. Structural and physical studies of dihalogenodicarbonyliridium complexes were difficult to conduct because of their instability. Nevertheless, the formal oxidation state of iridium was clearly established in the range of +1.39 to +1.44.[95]

The bis(oxalato)platinate(II) complexes based on $[Pt(C_2O_4)_2]^{2-}$, forms another family of linear chain systems, and the partially oxidised complex series, $C_x[Pt(C_2O_4)_2]\cdot n(H_2O)$ ($C^+ = K^+$, Rb^+, Mg^{2+}, Co^{2+}, Ni^{2+}, Zn^{2+}), was reported.[94] According to elemental analysis and X-ray diffuse scattering measurements, the formal oxidation state of platinum in this series is estimated in the range of +2.19 to +2.38. The average Pt–Pt distance is 2.84–2.89 Å and the conductivity at room temperature is 10^{-2}–10^{2} S cm^{-1}, depending on the associated cation.

These linear-chain metal complexes have been used as textbook examples to understand the basic nature of one-dimensional conductors, such as: the validity of tight-binding calculations, the effectiveness of chemical modifications of ligands, the phase control by ion doping, and so on.

4.2.3.2 Macrocyclic Metal Complexes

Numerous macrocyclic metal complexes have been considered as building blocks of one-dimensional conducting systems. This is due to their good planarity and, in some cases, to the extended delocalised π system of their ligands.

In this section, three representative examples are described (Figure 4.13): (i) metal complexes with soft macrocyclic ligands such as glyoximate; (ii) metal complexes with rigid and extended π-delocalised ligands as tetraazaannulene; and (iii) metal complexes with very rigid and much extended π-delocalised ligands such as phthalocyanines.

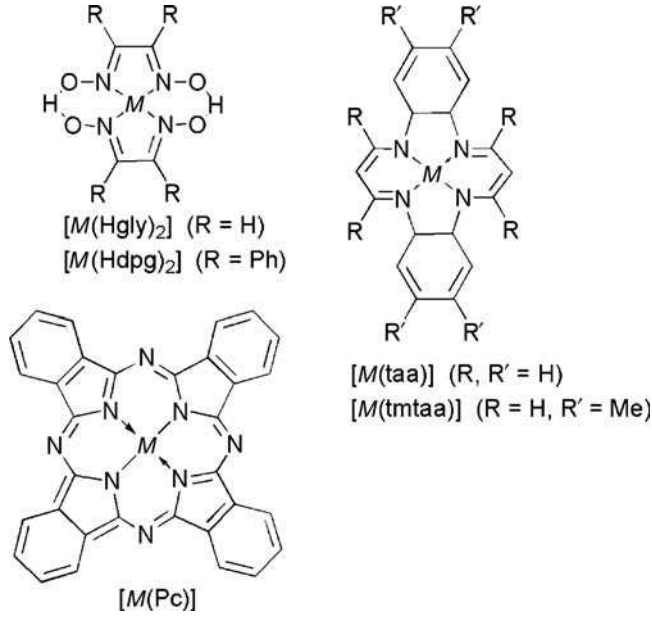

Figure 4.13 Molecular structures of macrocyclic metal complexes: metal bis(glyoximate), metal tetraazaanulene and metal phthalocyanine complexes

The palladium complex with glyoximato ligands, $[Pd(Hgly)_2]$ (Hgly = glyoximate), is easily oxidised by iodine to black needle-like crystals of $[Pd(Hgly)_2]I$. In the crystal, the palladium complexes form columns: the Pd–Pd distance is 3.558 Å before oxidation and 3.224 Å after oxidation.[97] Nickel complexes are similarly oxidised by iodine to $[Ni(Hdpg)_2]I$ (Hdpg = diphenylglyoximate), also exhibiting a one-dimensional molecular arrangement: the Ni–Ni distance of 3.271 Å is shorter than before oxidation (3.547 Å) and much longer than in nickel metal (2.49 Å).[98] According to the Raman and Mössbauer measurements, the iodine state is not I^- but $[I_3]^-$ and the formal oxidation state of nickel is +2.3. The conductivity at room temperature ranges from 10^{-2} to 10^{-4} S cm^{-1}, lower *vs* Krogmann salts, but consistent with the long distance between metal centres.

Macrocyclic ligands with extended π-delocalisation were studied in order to improve the conductivity of linear-chain complexes, because extended π delocalisation may reduce the on-site coulombic repulsion. The metal dibenzotetraazaannulene complexes, [*M*(taa)] (taa = dibenzotetraazaannulene; *M* = H_2, Ni, Pd, Co, Cu) and [*M*(tmtaa)] (tmtaa = tetramethyl dibenzotetraazaannulene; *M* = H_2, Ni, Pd) (Figure 4.13), are

also easily oxidised by iodine.[99,100] The conductivity at room temperature of both compounds improves 10^{14} times after oxidation: [Ni(taa)] $\sigma \approx 10^{-15}$ S cm^{-1}; [Ni(taa)]I_x $\sigma \approx 10^{-1}$ S cm^{-1}; [Ni(tmtaa)] $\sigma \approx 10^{-14}$ S cm^{-1}; [Ni(tmtaa)] I_x $\sigma \approx 10^{-2}$ S cm^{-1}.

A large, macrocyclic ligand such as phthalocyanine is a very stable ligand with extended π-delocalisation and rigid macrocyclic structure. It can form metal complexes, [*M*(Pc)] (Pc = phthalocyanine), with many metals (*M* = Ni, Pt, Co, Fe, Cu, *etc.*)[101] and the planarity of the molecule is retained in most cases. Additionally, metal phthalocyanate complexes exhibit reversible, multistep, redox changes and have strong absorption in the visible region. These complexes are also well known as synthetic dyes. The partial oxidation by iodine gives a black powder of [*M*(Pc)]I_x.[101–103] The iodine state is determined to be $[I_3]^-$ for $x < 3$, from Raman and Mössbauer measurements. The crystal structure of [Ni(Pc)]I, strictly $[Ni(Pc)]^{+0.33}(I_3)^-_{0.33}$, is shown in Figure 4.14. The [Ni(Pc)] molecules stack with almost a 40° rotation from complex to complex and form one-dimensional columns, where the Ni–Ni distance is 3.244 Å. The counter ion, $[I_3]^-$, occupies the one-dimensional narrow spaces along [Ni(Pc)] columns with disorder. The conductivity at room temperature of purified single [Ni(Pc)]I crystals is 6×10^2 S cm^{-1}. The temperature dependence shows metallic behaviour and the value is 30 times higher at low temperatures.[104] In spite of the one-dimensional structure of [Ni(Pc)]I, no phase transition such as the Peierls transition is observed on cooling. This rather rigid phthalocyanine complex molecule supports well electron excitation or charge transfer. ESR measurements show that the partial oxidation of [Ni(Pc)] occurs on the phthalocyanine ligand but not the nickel atoms.[103] A number of partial oxidised salts of $[M(Pc)]^{x+}$ with anions, such as Br^-, $[BF_4]^-$, $[ClO_4]^-$, $[PF_6]^-$, $[AsF_6]^-$, and so on, have also been synthesised.[103]

As the phthalocyanine is a rigid, macrocyclic ligand, it can coordinate to various metals, not only d^8 metals but others, and form planar and almost similar size molecules. Therefore, the crystal structures of [*M*(Pc)]*X* have a similar space group (*P4/mcc, Pn*2), similar lattice parameters and similar molecular overlaps, so that their interplanar distances lie in the range 3.12–3.25 Å in spite of large difference of metal sizes.[103] On the other hand, the phthalocyanine complexes with axial cyano ligands show interesting overlap. Figure 4.15 shows the crystal structure of $[PPh_4][M^{III}(Pc)(CN)_2]_2$ (*M* = Fe, Co). Since the $[M^{III}(Pc)(CN)_2]$ entity has additional two CN ligands in its axial positions, it cannot adopt an eclipsed stacking mode. Rather the molecules adopt the slipped stacking and the molecular overlap comes from the π–π stacking of the edge of phthalocyanine, as shown in Figure 4.15b.

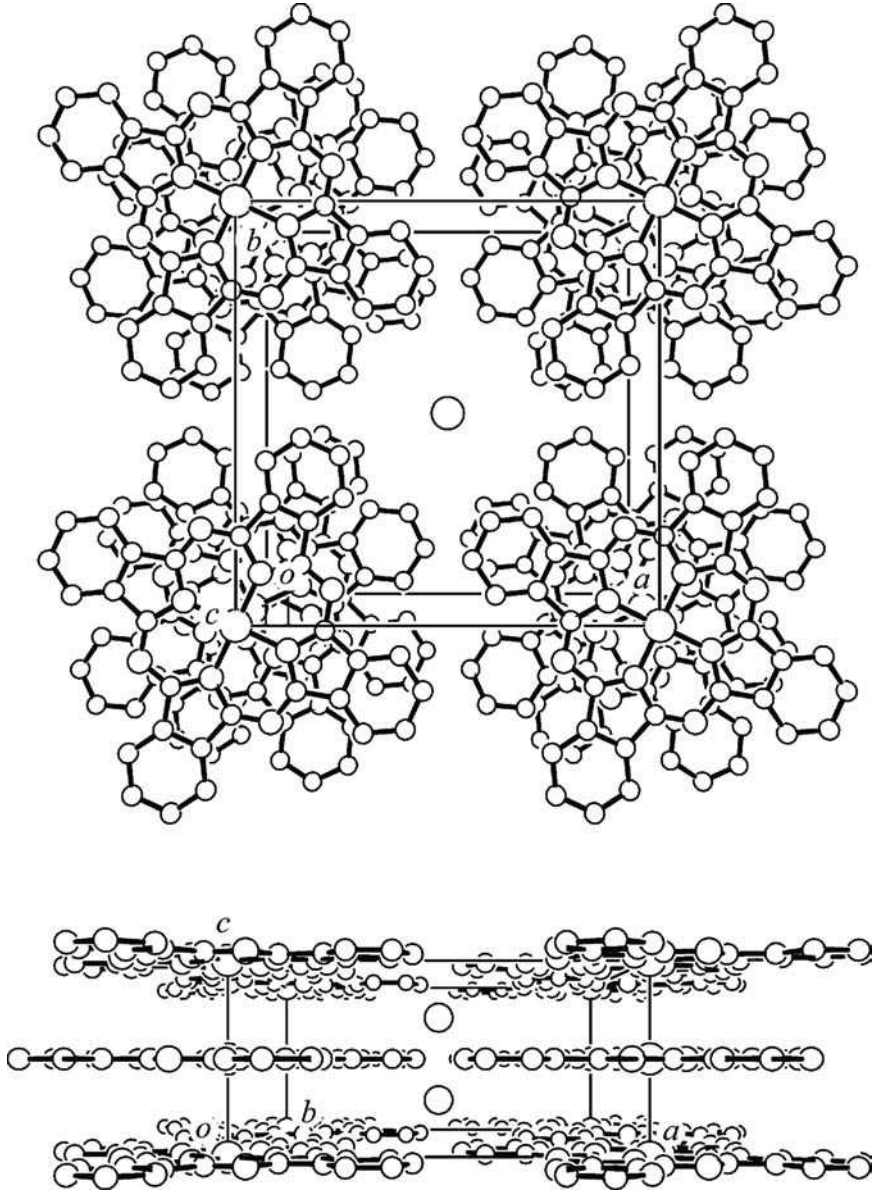

Figure 4.14 Crystal structure of [Ni(Pc)]I. The neighbouring [Ni(Pc)] molecules within a column are not eclipsed but rotated by almost 40° from one another. Reprinted with permission from Inabe and Tajima, 2004 [103]. Copyright (2004) American Chemical Society

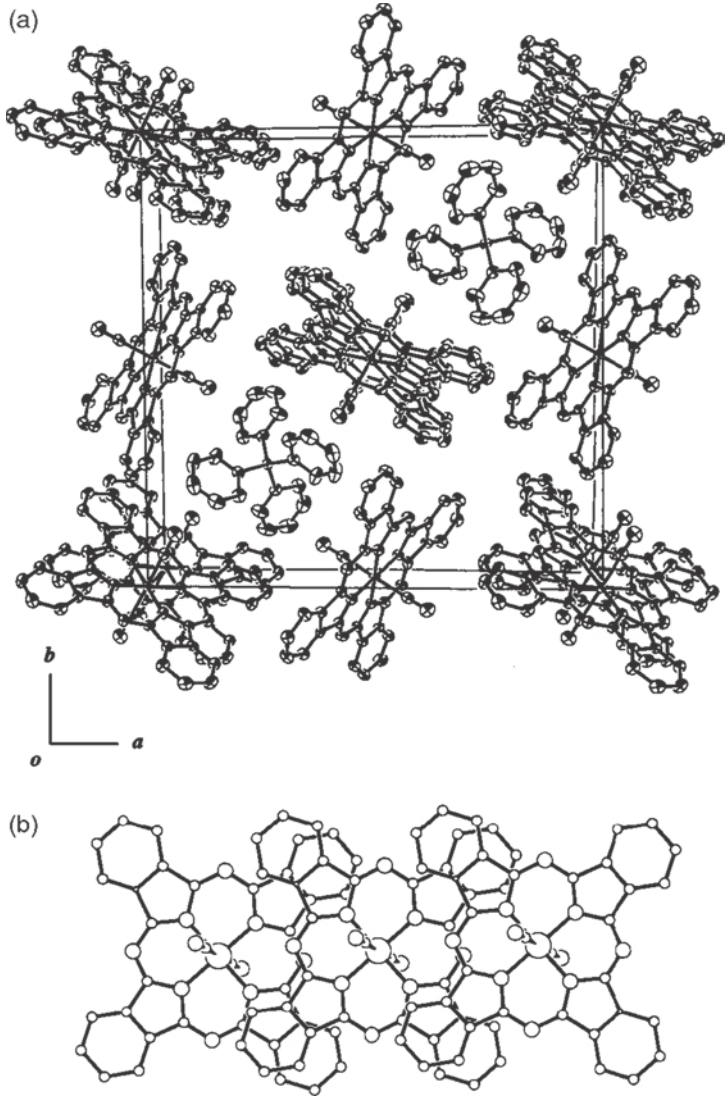

Figure 4.15 (a) Crystal structure of TPP[Fe^{III}(Pc)$(CN)_2$] and (b) overlap of [PPh_4] [Fe^{III}(Pc)$(CN)_2$] molecules. Reprinted with permission from Matsuda *et al.*, 2000 [105]. Copyright (2000) Royal Society of Chemistry

The metal ions are in low spin state, that is, $S = 0$ for Co^{3+} and $S = 1/2$ for Fe^{3+}, due to the coordination of CN ligands in the axial positions. Although the electrical transport is undertaken on a phthalocyanine site where the partial oxidation occurs, the conductivity of $[PPh_4][Fe^{III}(Pc)(CN)_2]_2$ and $[PPh_4][Co^{III}(Pc)(CN)_2]_2$ show differences. The Fe^{III} complex exhibits a conductivity of 5 S cm^{-1} at room temperature and semiconducting behaviour with an activation energy of 0.016–0.030 eV changing with temperature, while the Co^{III} complex exhibits 10^2 S cm^{-1} and simple semiconducting behaviour with an activation energy of 0.01 eV. Considering the complicated magnetic property of Fe^{III} and nonmagnetic property of Co^{III} complexes, the electrical transport of Fe^{III} complex is affected by π–d interaction between conduction electrons on phthalocyanine ligand and central metal.[105]

4.2.3.3 Metal Bis-Dithiolene Complexes

Before the 1960s, metal bis-dithiolene complexes were mainly encountered in analysis of metal ions. Due to their remarkable coordination chemistry, more intensive studies developed until the end of the 1970s. Besides primary interests in structure, bonding and reactivity, a wide range of new properties of these complexes arose later in the field of biology and, more importantly, in material science. The optical, magnetic, conducting and superconducting properties evidenced in these complexes have placed them among the most important families of precursors to new generations of electronic materials. The most comprehensive book describing all aspects from synthesis to properties and applications of metal bis-dithiolenes was edited by Stiefel in 2004.[106] Reviews and papers by Olk *et al.*,[107] Almeida and Henriques,[108] Cassoux,[109] Pullen and Olk,[110] Robertson and Cronin,[111] Kato,[7] Kobayashi *et al.*,[6] Almeida *et al.*[112,113] and Lopes *et al.*[113] are also worth consulting.

The metal complexes of the maleonitriledithiolene, $[M(mnt)_2]$ (mnt = maleonitriledithiolate, or 1,2-dicyanoethylene-1,2-dithiolene, see Figure 4.16), have been one of the most widely studied families of dithiolene complexes in the past three decades.[114] In 1981, a new one-dimensional metal $Li_{0.82}(H_3O^+)_{0.33}[Pt(mnt)_2]\cdot 1.67H_2O$ (α-LiPtmnt) was prepared, which shows a conductivity of 2×10^2 S cm^{-1} at room temperature and metallic behaviour above 220 K.[115] The metal–insulator transition around 220 K is explained by a Peierls distortion from X-ray diffraction measurement.[116] The Pt–Pt distance is 3.64 Å, too long to form a good conduction path by the overlap of Pt $5d_{z^2}$ orbitals, so the intermolecular contacts of sulfur

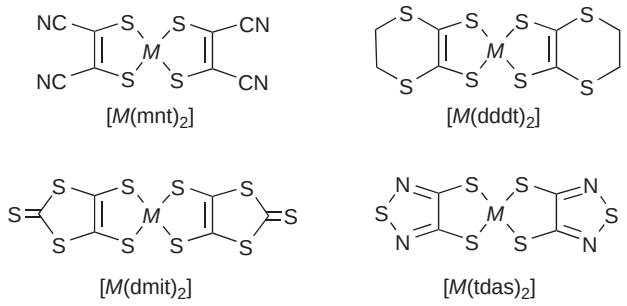

Figure 4.16 Structural formulas of metal dithiolene complexes

atoms play an important role for conductivity in this salt. Although α-LiPtmnt is a simple structural conductor including small cations and a small amount of water, $[M(\text{mnt})_2]$ complexes often give charge-transfer salts with various donors like perylene, BEDT-TTF, other TTF-derivatives, and so on, which have been discussed in several articles.[106,108,111,117]

The other most widely studied families of dithiolene complexes are metal complexes of dmit, $[M(\text{dmit})_2]$ (dmit = 1,3-dithiole-2-thione-4,5-dithiolate, see Figure 4.16). A large number of chemical modifications and physical and theoretical studies of these compounds have been reported.[7,107,110] The $[M(\text{dmit})_2]$ complexes are sulfur-rich molecules, interacting not only along the molecular stacking and side-by-side directions, but also along the direction of the molecular long axis. They are well known as the molecules generating many anion-based superconductors.[7] Since superconductors based on $[M(\text{dmit})_2]$ are described in Section 4.3.3, some other examples of $[M(\text{dmit})_2]$ exhibiting interesting physics are described here.

Besides the electrical conductivity, a number of other applications of $[M(\text{dmit})_2]$ have been investigated. For example, molecular-based magnets, such as the spin ladder compound [*p*-EPYNN][Ni(dmit)$_2$] [*p*-EPYNN]$^+$ = *p*-*N*-ethylpyridinium α-nitronyl nitroxide) was reported in 1996.[118] In the crystal, the radical cationic molecules, *p*-EPYNN, form one-dimensional chains with ferromagnetic interactions, while the chains of [Ni(dmit)$_2$]$^-$ monovalent anions, in a ladder formation, exhibit antiferromagnetic interactions. The magnetisation is explained by the sum of them.

In contrast to anionic $[M(\text{dmit})_2]$ acceptor molecules, the metal complexes with dddt ligands, $[M(\text{dddt})_2]$ (dddt = 5,6-dihydro-1,4-dithiin-2,3-dithiolate, Figure 4.16), belong to the electron-donor group, that is,

the $[M(\text{dddt})_2]$ forms partially oxidised salts with various anions.[7,111,119] The $[M(\text{dddt})_2]$ molecule is an analogue of the organic BEDT-TTF donor molecule, where the central C=C moiety is replaced by a metal. Although the symmetry of HOMO and LUMO are similar to those of $[M(\text{dmit})_2]$, the HOMO is more important for $[M(\text{dddt})_2]^{\delta+}$, and similar to that of BEDT-TTF. Additionally, since the HOMO–LUMO gap of $[M(\text{dddt})_2]$ is small, these levels are inverted in some cases. Therefore, the $[M(\text{dddt})_2]$ complex takes a position between an organic donor such as BEDT-TTF and a metal complex. For example, with the $[BF_4]^-$ anion, $[Ni(\text{dddt})_2]_3[BF_4]_2$, $[Pt(\text{dddt})_2]_3[BF_4]_2$ and $[Au(\text{dddt})_2]_x[BF_4]$ were reported.[120] The conductivity at room temperature is 1–2 S cm^{-1} for the nickel complex, 0.5–1 S cm^{-1} for the platinum complex and 50–90 S cm^{-1} for the gold complex. The X-ray structure analysis of $[Ni(\text{dddt})_2]_3(BF_4)_2$ crystal, shows that the $[Ni(\text{dddt})_2]$ molecules stack and form columns. The formal oxidation state of $[Ni(\text{dddt})_2]$ is +2/3 and three $[Ni(\text{dddt})_2]$ molecules trimerise slightly.

The first metal complexes of the tdas ligand, $[M(\text{tdas})_2]$ (tdas = 1,2,5-thiadiazole-3,4-dithiol, M = Ni, Pd, Pt, Cu or Fe, Figure 4.16), were reported in 1990.[121] The electrochemical oxidation of TTF and $[Ni(\text{tdas})_2]^{n-}$ gives a salt of $[TTF]_2[Ni(\text{tdas})_2]$ with a conductivity of 0.1 S cm^{-1} at room temperature, which evidenced the potential of tdas complexes as conducting materials.[122] Subsequently, the X-ray crystal structure analysis of $[Bu_4N][Fe(\text{tdas})_2]$ revealed that the iron atom takes a distorted five-coordinate geometry, four sulfur atoms from two tdas ligands and one sulfur atom from adjacent $[Fe(\text{tdas})_2]^-$ ions, that is, two $[Fe(\text{tdas})_2]^-$ are dimerised.[123] The $[Bu_4N][Fe(\text{tdas})_2]$ salt shows interesting magnetic behaviour. Upon decreasing temperature, the re-entrant transitions between low- to high-spin moment (10% increase) around 250 K and high to low (10% decrease, back to the original state) around 200 K are observed. The Mössbauer study of the iron state in this salt indicates that the iron has intermediate spin state of S = 3/2 and the increase/decrease of moment can not be explained by the change of spin state.[123]

As the investigation of molecular conductors based on metal dithiolene complexes was progressing, chemical scientists tried to synthesise new complexes able to yield more stable metals. One of the solutions is to extend the π-conjugated system on ligands, following a similar approach as for organic donor molecules. Several representative ligands of extended-TTF dithiolate are shown in Figure 4.17.[6,124–127] At the beginning of the study of extended-TTF dithiolate ligands, it was well known that the anionic metal complexes were difficult to handle because they

were easily oxidised in air. However, the considerably high conductivity at room temperature (10^{-3}–0.7 S cm^{-1}) of the oxidised neutral black powders increased interest to these molecules.[124–126]

The first molecular metal based on single component and electrically neutral metal complex, [Ni(tmdt)$_2$] (tmdt = trimethylenetetrathiafulvalenedithiolate, Figure 4.17) was reported in 2001.[128] Details of this compound and some other single component molecular conductors are given in Section 4.3.4 and in several review articles.[6,127,129]

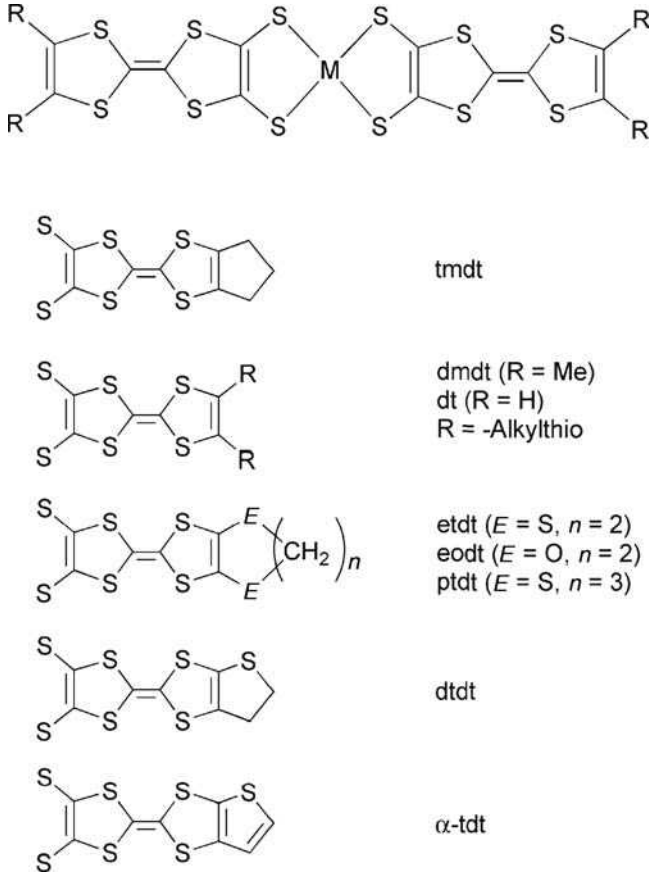

Figure 4.17 Structural formulas of extended-TTF-dithiolate ligands

4.3 SYSTEMS BASED ON METAL BIS-DITHIOLENE COMPLEXES

4.3.1 Synthesis of Metal Bis-Dithiolene Complexes

4.3.1.1 Review of Synthetic Methods

The first paper reporting on the quantitative synthesis of metal bis-dithiolene was published by Schrauzer *et al.* in 1962.[130] Many synthetic procedures for metal dithiolene complexes have been reported later. Rauchfuss recently reviewed the procedures leading to both ligands and complexes.[131] This review is a major basis for the synthesis of mono-, bis- or tris-dithiolene complexes including one or more metallic centres. Another review by Fourmigué[132] focuses on the synthetic procedures to mixed cyclopentadienyle/dithiolene complexes, an important class of precursor to magnetic molecular materials.[133] Other families of dithiolene complexes bearing hydrogen bond donor/acceptor groups or thiazole backbones were reported by Baudron *et al.* in 2005[134] and Eid *et al.* in 2007,[135] respectively.

4.3.1.2 Synthesis of $[M(\text{dmit})_2]$ Complexes

The $[\text{dmit}]^{2-}$ or $[C_3S_5]^{2-}$ ligand is probably the most popular dithiolene ligand. Indeed, it is the only dithiolene ligand that gives rise to superconducting compounds. The synthesis of the sodium dmit salt, $Na_2(C_3S_5)$, involves the reduction of carbon disulfide by sodium in dimethylformamide[136] (Figure 4.18), which also leads to the sodium trithiocarbonate salt, $Na_2(CS_3)$. The procedure was largely improved later. In 1979, in order to overcome the poor stability of the sodium dmit salt, Steimecke *et al.* isolated the air-stable zinc complex $[R_4N]_2[Zn(\text{dmit})_2]$ on a multigramme scale,[137] and in 1998, Wang *et al.* doubled the reaction yield by using an excess of carbon disulfide to convert the trithiocarbonate side product into dmit.[138] Another way to stabilise the dmit ligand consists of treating $[R_4N]_2[Zn(\text{dmit})_2]$ with benzoyl chloride to form the stable 4,5-bis(benzoylthio)-1,3-dithiol-2-thione $(\text{dmit}(\text{COPh})_2)$[137] (Figure 4.18). This thioester can be conveniently stored in multigramme amounts and further converted back to the $[\text{dmit}]^{2-}$ anion by treatment with sodium methoxide.[137]

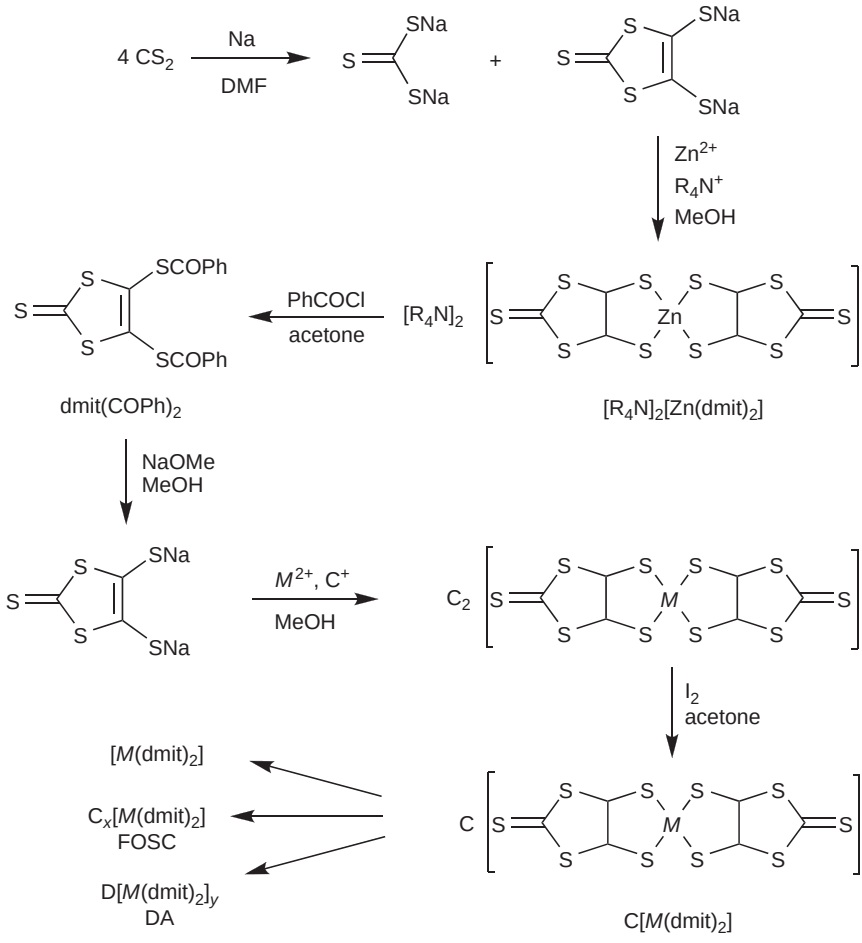

Figure 4.18 Synthesis of the $[dmit]^{2-}$ ligand, its storable derivatives and $[M(dmit)_2]$ compounds. (FOSC = fractional oxidation state compound; DA = donor–acceptor compound)

In some cases, the isolation of the highly reactive $[Na_2(dmit)]$ salt by precipitation from diethyl ether using standard Schlenk techniques [137] is more convenient. This method allows not only very clean further synthesis but also synthesis in which high pH values of the reaction mixture would prohibit the precipitation of the desired complex; for example, when mono-, di- or tri-alkylammonium salts are used as counter-cations. Alternatively, the $[dmit]^{2-}$ anion can be prepared by electrochemical reduction of carbon disulfide.[139–141] It should be noted that the dmit

ligand and dmit-based compounds are also major precursors to organic molecules,[142] in particular TTF derivatives.[143,144]

A large number of $C_n[M(\text{dmit})_2]$ complexes ($n = 2, 1, 0$) have been prepared.[131,145] The dianion salts $[R_4N]_2[M(\text{dmit})_2]$ can be obtained by treating a solution of Na_2dmit in methanol with the appropriate M^{2+} metal salt and the appropriate tetraalkylammonium bromide (Figure 4.18). The corresponding monoanionic salt $[R_4N][M(\text{dmit})_2]$ is obtained from the dianionic salt by iodine oxidation.[137] Further oxidation may lead to the neutral complex or to fractional oxidation state compounds (FOSCs) or donor–acceptor (DA) compounds. These oxidation steps are described in Section 4.3.2.

4.3.1.2 Synthesis of $[M(\text{tmdt})_2]$ Complexes

$[M(\text{tmdt})_2]$ complexes belong to the so-called extended TTF-dithiolate family. The synthesis applies the use of cyanoethyl protecting groups on the sulfur atoms of the dithiolene moiety of the ligand before coupling with the second moiety to form the TTF unit.[146] Since this TTF-dithiolate unit is unstable in air, all the synthetic procedure, including electrochemical oxidation, should be carried out under a strictly inert atmosphere and the synthesis of the precursors to the neutral species has to be performed at low temperature (–80 °C). Schemes for the preparation of the $[Ni(\text{tmdt})_2]^{n-}$ complex, one of the single component molecular conductors, are shown in Figure 4.19.[126] The other complexes can be obtained by the same procedures. Numerous other extended TTF-dithiolate complexes have been isolated. Their preparation and properties have been reviewed by Kobayashi *et al.*[6]

4.3.2 Synthesis of Conductors and Superconductors Based on Metal Bis-Dithiolene Complexes

4.3.2.1 Chemical Methods

Metal bis-dithiolene complexes exhibiting conducting or superconducting properties can be neutral or in a fractional oxidation state. In FOSCs, the associated cation is of the closed-shell type, while in DA compounds, the metal bis-dithiolene is an acceptor and the donor is an open-shell cation. As already mentioned in Section 4.2.2.3, the most encountered

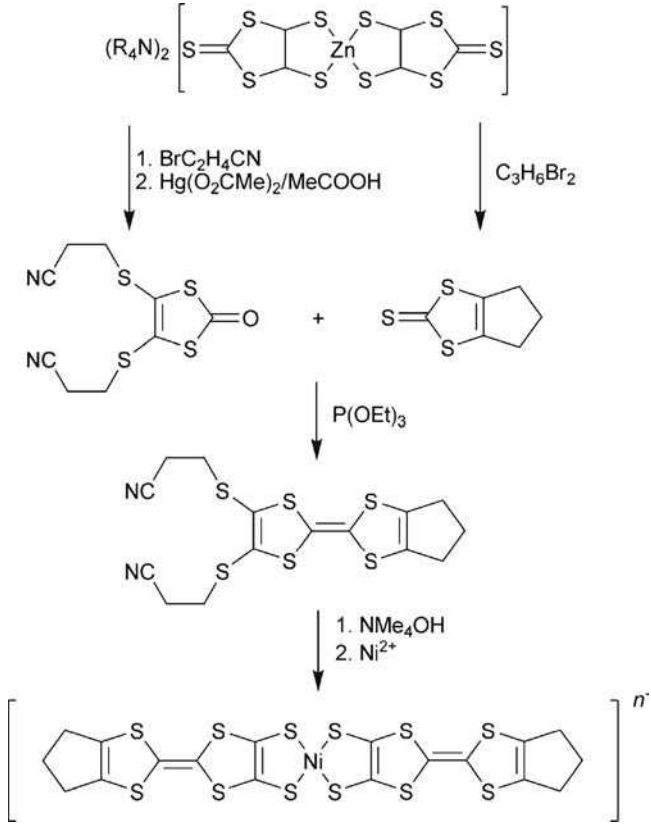

Figure 4.19 Synthesis of trimethylenetetrathiafulvalenedithiolate nickel complexes

donor molecules associated with metal bis-dithiolenes are TTF and its derivatives.[7]

FOSCs can be obtained by further chemical oxidation of the corresponding C[M(dmit)$_2$] precursor complex. However, in many cases direct aerial oxidation, or oxidation with an oxidising agent such as iodine or bromine, is not well controlled and a mixture of partially oxidised species with different stoichiometries is obtained; an example is given by the bromine oxidation of [Bu_4N][Ni(dmit)$_2$].[147] Moreover, direct chemical oxidation mostly yields poor quality crystals. As any molecular conductors are insoluble in common solvents, it is not possible to recrystallise them. Therefore, in order to isolate good quality crystals, convenient for structural and physical studies, specific crystal growth techniques have to be used.

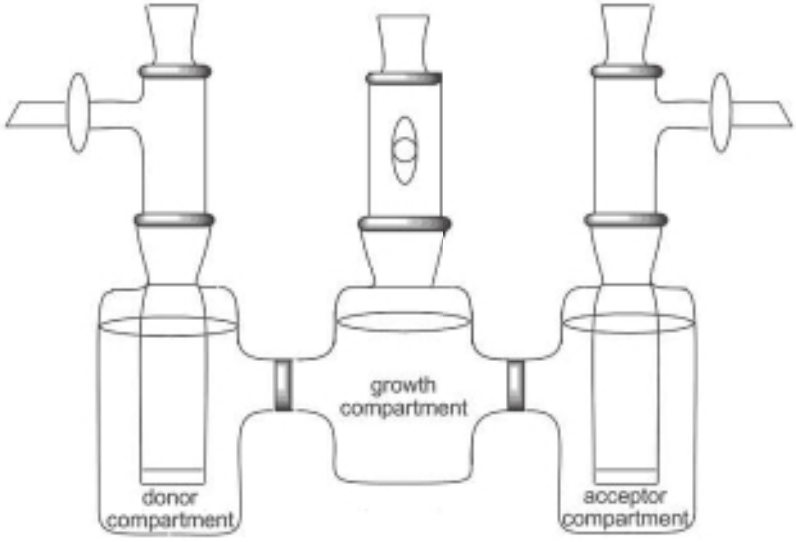

Figure 4.20 Three-compartment diffusion cell

Slow interdiffusion of solutions of a precursor complex and the appropriate oxidising agent can be applied for growing both FOSCs and DA compounds. A typical three-compartment diffusion cell, inspired by those described by several authors,[148–150] comprises a central solvent chamber and porous glass frits between compartments, as illustrated in Figure 4.20. The concentrations of the solutions can be kept close to saturation by means of additional containers filled with an excess of starting reagents, placed in the appropriate compartment and communicating with it through a glass frit. [TTF][Ni(dmit)$_2$]$_2$ crystals were isolated in such a cell placed in a dark chamber for 15 days at a temperature of 40 °C. A mixture of fine needles (majority product) and a few platelets was obtained: the needle-shaped phase was identified as [TTF][Ni(dmit)$_2$]$_2$[151] and the platelets as the neutral [Ni(dmit)$_2$].[147]

4.3.2.2 Electrochemical Methods

The electrochemical method is the most widely used technique to grow FOSC crystals. The technique also applies to grow crystals of DA compounds. The so-called electrocrystallisation of molecule-based materials has been reviewed elsewhere.[152–154]

During electrocrystallisation, compounds are intended to grow attached to the electrode surface. Typically, this technique is applied every time the electrochemically produced compound is insoluble in its final stage; the compound is formed and well crystallised in a single step. However, it is clear that only conductive species may be considered, as the covered electrode should retain a high enough conductivity at any time during the process. For these reasons, electrocrystallisation is the method of choice for growing crystals of molecular conductors or superconductors. It should be noted that an electrochemical synthesis may be conducted either under potentiostatic or galvanostatic conditions.[152] Whatever the crystallisation method, the growth rate is highly important to control the size and quality of the crystals. For this reason, galvanostatic conditions are preferentially applied for electrocrystallising molecular conductors. In this section, the focus is on electrocrystallisation of materials including dithiolene complexes. For a comprehensive review of the electrochemical reactivity of dithiolene complexes, the paper published by Wang can be consulted.[155]

Except for the family of neutral extended TTF-dithiolene complexes, the conducting properties of DA compounds or FOSCs originate from the partial oxidation state of the constitutive molecules or building blocks. Two synthetic routes allow this feature to be realised: (i) electrochemical oxidation of the complex, that is, change in its oxidation state, and (ii) concomitant formation of complex and material. FOSCs including metal bis-dithiolene species associated with closed-shell cations are grown following the first route.[7,109,111,145] The second route has mainly been encountered for the synthesis of organic donor based FOSCs including various cyano and thiocyano copper anionic complexes.[48,152,156–160]

The electrochemical reaction leading to a metal bis-dithiolene FOSC may be summarised as:

$$[M(\mathrm{dmit})_2]^- \rightarrow [M(\mathrm{dmit})_2]^{x-}(1-x)\mathrm{e}^-$$

High-speed cyclic voltammetry, using ultra-microelectrodes and performed on $[Ni(dmit)_2]$ complexes, showed that the formation of $[Ni(dmit)_2]^{x-}$ species follows an EC mechanism before the crystallisation of the compound occurs on the electrode [161]:

E-step $[\mathrm{Ni}(\mathrm{dmit})_2]^- \rightarrow [\mathrm{Ni}(\mathrm{dmit})_2]^0 + 1\mathrm{e}^-$

C-step $n[\mathrm{Ni}(\mathrm{dmit})_2]^0 + m[\mathrm{Ni}(\mathrm{dmit})_2]^- \rightarrow \{[\mathrm{Ni}(\mathrm{dmit})_2]^{x-}\}_{n+m}$

with $x = n/(n+m)$.

Either the associated cation is already part of the starting complex, or it is brought by the supporting electrolyte. In the latter, incorporation of the cation is governed by the respective solubility constants of the competing species. The cation-free neutral TTF-dithiolene complexes are also electrocrystallised. The starting complexes are generally the dianionic because the monoanionic are highly unstable [6]:

$$[M(\text{TTF-dithiolene})_2]^{2-} \rightarrow [M(\text{TTF-dithiolene})_2]^0 + 2e^-$$

The electrochemical reaction leading to DA compounds, including $[M(\text{dmit})_2]$ complexes, involves the oxidation of the donor in the presence of the $[M(\text{dmit})_2]^-$ salt which plays the role of both the acceptor and the supporting electrolyte as:

E-step $D^0 \rightarrow D^+ + 1e^-$
C-step $nD^+ + m[M(\text{dmit})_2]^- \rightarrow (D^{+\delta/m})_n\{[M(\text{dmit})_2]^{-\delta/n}\}_m$

Competing electrochemical reactions may occur in the case of such DA crystals because both the donor and the acceptor molecules may undergo oxidation. As their half wave potentials are often close, the growth of the DA compound may compete with that of the FOSC. This feature was observed in the case of [TTF][Ni(dmit)$_2$]. Single crystals of this phase were electrocrystallised using TTF and [Bu$_4$N][Ni(dmit)$_2$].[162] Cyclic voltammetry studies of each compound show that [Ni(dmit)$_2$]$^-$ is oxidised at a potential 120 mV lower than that of TTF. However, addition of TTF to a solution of [Bu$_4$N]$_{0.29}$[Ni(dmit)$_2$], inhibits the formation of the (nBu$_4$N)$_{0.29}$ [Ni(dmit)$_2$] FOSC in favour of the TTF[Ni(dmit)$_2$]$_2$ DA compound.[163]

The singular electrochemical behaviour of bis-dithiolenes complexes bearing the (dddt) ligand should be mentioned. These complexes may appear as anionic,[111,164,165] neutral and cationic species.[7,120,166–170] Therefore, they may act both as donor[167] or acceptor[171] systems. To our knowledge, they are the only 1,2-bis-dithiolenes complexes to undergo oxidation towards stable cationic species. One-electron oxidation of neutral $M(S_2C_2Ph_2)_2$ (M = Ni, Pd, Pt) complexes was reported,[172] but shown to be irreversible due to ligand de-coordination.

The quality of the crystals depends on multiple factors: nature and purity of the solvent, morphology of the electrode surface, current density and temperature.[152] Galvanostatic growth is generally conducted in two-compartment cells with an electrode configuration allowing homogeneous current lines (Figure 4.21). The electrolysis duration is likely to be in the range of 1–3 weeks.

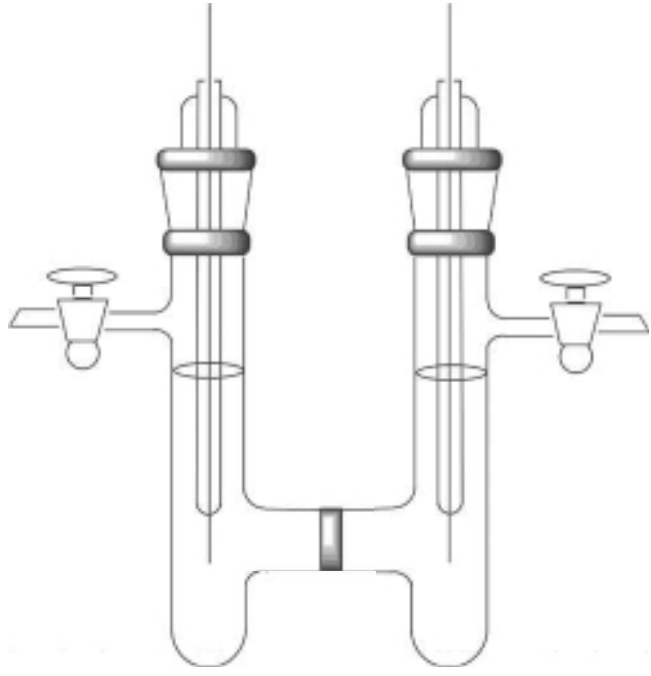

Figure 4.21 Electrocrystallisation cell

4.3.3 Superconductors Based on [M(dmit)$_2$] Complexes

[M(dmit)$_2$] complexes are the only metal bis-dithiolenes known to lead to superconductive phases. Twelve compounds have been isolated to date (Table 4.1).

4.3.3.1 [TTF][Ni(dmit)$_2$]

[TTF][Ni(dmit)$_2$] is a DA type compound and was first isolated by Ribas and Cassoux in 1981 [185] by direct metathesis in acetonitrile between the TTF salt [TTF]$_3$[BF$_4$]$_2$ and either [Bu$_4$N]$_2$[Ni(dmit)$_2$] or [Bu$_4$N][Ni(dmit)$_2$]. As described in Section 4.3.2, good quality single crystals suitable for conductivity measurements and X-ray diffraction studies were later isolated either by slow interdiffusion of saturated solutions of [TTF]$_3$[BF$_4$]$_2$ and [Bu$_4$N][Ni(dmit)$_2$],[151] or by galvanostatic electrolysis of an acetonitrile solution containing [Bu$_4$N][Ni(dmit)$_2$] and a large excess of neutral TTF.[162]

Table 4.1 Superconductors based on $[M(\text{dmit})_2]$ complexes

Compound	$\sigma_{RT/1\ bar}$ (S cm^{-1})	T_c (K)	P (kbar)	Ref.
$TTF[Ni(dmit)_2]_2$	300	1.62	7	[173,174]
α-$[TTF][Pd(dmit)_2]_2$	800	1.7	22	[175]
α'-$[TTF][Pd(dmit)_2]_2$	600	5.93	24	[176]
α-[EDT-TTF][$Ni(dmit)_2$]	100	1.3	Amb.	[177]
α-$[Et_2Me_2N][Pd(dmit)_2]_2$	10-80	4	2.4	[178]
β'-$[Et_2Me_2P][Pd(dmit)_2]_2$	10	4	6.9	[179]
$[EtMe_3P][Pd(dmit)_2]_2$	13	5	3.3	[180]
β'-$[EtMe_3As][Pd(dmit)_2]_2$	13	4.3	7	[180]
$[Me_4N][Ni(dmit)_2]_2$	60	5	7	[181,182]
β-$[Me_4N][Pd]dmit)_2]_2$	30	6.2	6.5	[183]
β'-$[Me_4As][Pd(dmit)_2]_2$	10	4	7 (uniaxial)	[184]
β'-$[Me_4Sb][Pd(dmit)_2]_2$	10	3	10	[179]

The structure of $[TTF][Ni(dmit)_2]_2$ can be described as segregated stacks along the (010) direction of the TTF and $[Ni(dmit)_2]$ molecules (Figure 4.22). The spacing between the stack sites, that is between the metal atoms, is constant at 3.73 Å.[151,162] From this viewpoint, this phase could be considered as strictly one-dimensional with uniform stacking.

On the other hand, an examination of the interatomic distances between molecules in adjacent stacks reveals a number of sulfur–sulfur contacts which are appreciably shorter than the van der Waals' separation of 3.70 Å (Figure 4.22). S···S contacts as short as 3.45 Å are observed between $[M(\text{dmit})_2]$ units in adjacent stacks (arranged along (001)) involving molecules at different levels along (001). Consequently, a two-dimensional array of closely-spaced $[Ni(dmit)_2]$ molecules is formed in the {100} plane. This high degree of molecular connectivity in this plane suggests the existence of substantial electronic coupling along both the *b* and *c* directions. Note that the rather large interplanar separation within the TTF and the $[Ni(dmit)_2]$ stacks results in *intrastack* S···S distances larger than the van der Waals' separation. Short S···S contacts are also found between the terminal sulfur atom of the $[Ni(dmit)_2]$ units and sulfur atoms of the TTF molecules, possibly extending the range of electronic interactions into the third direction. Thus, on the basis of these structural observations, an appreciable deviation from the usual '1D metal' description was anticipated, and indeed $[TTF][Ni(dmit)_2]_2$ appears to have a *quasi three-dimensional* network of intermolecular S···S interactions. It should be noted that α- and α'-$[TTF][Pd(dmit)_2]_2$ phases are isostructural with $[TTF][Ni(dmit)_2]_2$ and exhibit the same network of S···S interactions. In $[Me_4N]_{0.5}[Ni(dmit)_2]$, sheets containing

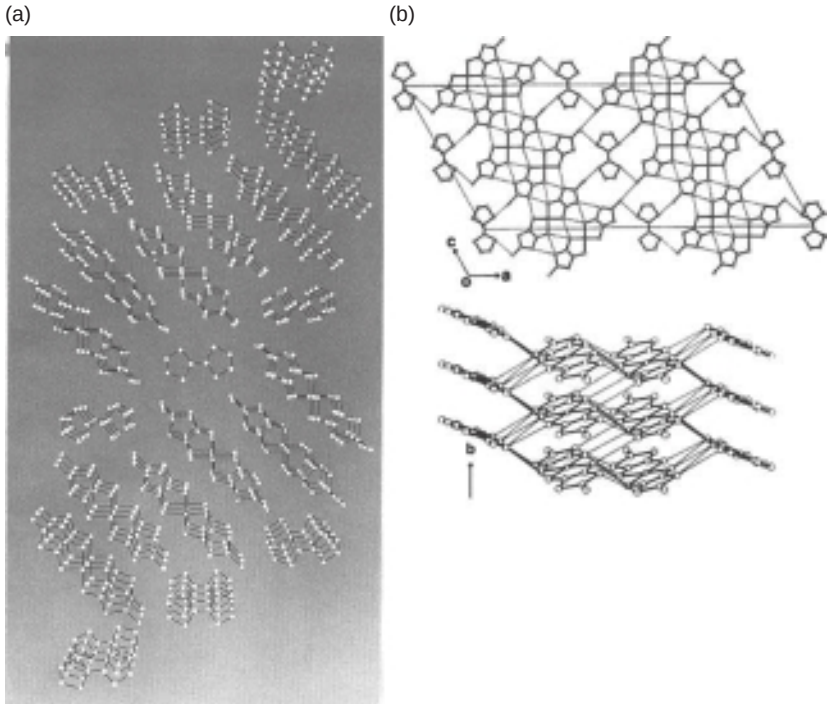

Figure 4.22 A three-dimensional view of the structure of [TTF][Ni(dmit)$_2$]$_2$ (a) and the S···S interactions network developing between Ni(dmit)$_2$ units and [Ni(dmit)$_2$] and TTF units (b)

stacks of [Ni(dmit)$_2$] pairs are separated by slabs of $[Me_4N]^+$ cations. S···S contacts as short as 3.49 Å develop within the [Ni(dmit)$_2$] sheets. The structure of this compound can be described as *two-dimensional*.[186]

The observation of a high degree of molecular connectivity, as reflected by short S···S distances, may not necessarily mean that these contacts correspond to effective electronic interactions (orbital symmetry should obviously be also taken into account), and that high conductivity is observed in several directions of the crystals. Tight-binding band calculations have been performed on [TTF][Ni(dmit)$_2$]$_2$ using the X-ray structural data obtained at room temperature. The calculation included both the LUMO bands of [Ni(dmit)$_2$] and the HOMO bands of TTF and [Ni(dmit)$_2$].[187] The most significant, and surprising, result is that the LUMO-based bands overlap appreciably with the HOMO-based ones; this is due to the weak HOMO–LUMO energy splitting (0.4 eV). Consequently, both the HOMO and LUMO series of bands are partially filled. Joint analysis of diffuse X-ray scattering results[188] and band

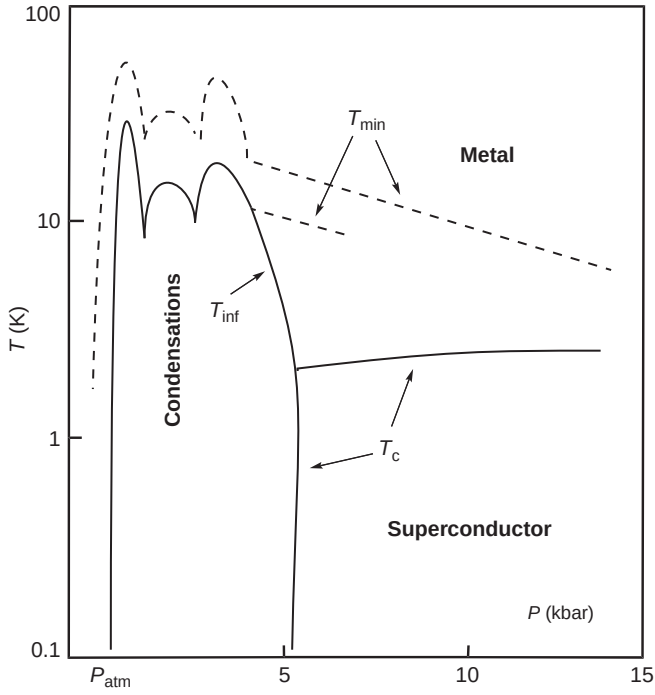

Figure 4.23 Temperature/pressure phase diagram of $[TTF][Ni(dmit)_2]_2$

structure calculations[187] give a change-transfer value of 0.8. This value is in agreement with thermopower measurements.[189] Raman spectroscopy studies performed on single crystals also confirm the fractional charge of the TTF units: the $\nu_{C=C}$ central bond of TTF appears at 1435 cm^{-1}. From the study performed by Bozio *et al.*,[190] this frequency value leads to a +0.81 charge for the TTF (linear variation of $\nu_{C=C}$ as a function of the charge, from 1518 cm^{-1} for TTF^0 to 1420 cm^{-1} for TTF^+).

$[TTF][Ni(dmit)_2]_2$ was the first isolated superconductive phase of the series, and superconductivity was found in 1986.[173,174] The superconducting transition occurs at 1.62 K under a hydrostatic pressure of 7 kbar. The pressure–temperature phase diagram of this phase was deeply studied by AC resistivity measurements up to 14 kbar.[191] Numerous electronic phase transitions occur upon increasing the applied pressure: from high temperature metal to, successively, metallic, semi-metallic, semiconducting and re-entrant superconducting ground states (Figure 4.23).

From this rather complicated phase diagram, two unique features have been observed: the transition temperature (T_c) increases with pressure [192]

and, at pressures around 5.3 kbar, the superconductive ground state is re-entrant into the low pressure insulating state. Also observed in the α′-[TTF][Pd(dmit)$_2$]$_2$ phase, this was explained by the occurrence of CDW instabilities connected to a unique multisheets Fermi surface based on both the HOMO and the LUMO bands of the building blocks already mentioned above.[193]

4.3.3.2 α-[EDT-TTF][Ni(dmit)$_2$]

Among the [*M*(dmit)$_2$]-based superconductors, α-[EDT-TTF][Ni(dmit)$_2$] is also of DA type and has two outstanding features; it is the only one to contain a 1:1 molar ratio of donor and acceptor units and to exhibit superconductivity at ambient pressure.[177] The phase is superconductive below 1.3 K under ambient pressure (Figure 4.24). α-[EDT-TTF][Ni(dmit)$_2$] exhibits a unique metallic behaviour with a characteristic resistivity peak at around 14 K. Magnetoresistance studies shown that the conduction mainly takes place along the Ni(dmit)$_2$ stacks below 10 K, while both [Ni(dmit)$_2$] and [EDT-TTF] stacks are involved above 20 K.[194,195]

4.3.3.3 [EtMe$_3$P][Ni(dmit)$_2$]$_2$

[Pd(dmit)$_2$] complexes afforded nine of the 12 superconductive [M(dmit)$_2$]-based phases, the majority with closed-shell cations.[7] This family also gathers the largest number of phases, including dimerised [Pd(dmit)$_2$] units.[7] Dimerisation is most of the time associated with poor electrical conduction, as it induces a discontinuity in the electronic path, due to irregular intermolecular distances along stacks. Nevertheless, all superconductive FOSCs based on [Pd(dmit)$_2$] show structures including dimers.[7]

The later isolated phase, [EtMe$_3$P][Pd(dmit)$_2$]$_2$, becomes superconducting at 5 K under 3.3 kbar.[180] This phase exhibits an interesting packing organisation showing uniformly stacked dimers (Figure 4.25). Intra- and inter-dimer HOMO–HOMO overlap integrals indicate that [Pd(dmit)$_2$] molecules are strongly dimerised. The crystal structure of the phase performed at 10 K, reveals pairing of dimers. Therefore, in order to explain the properties of the phase, it is necessary to consider each dimer as the building unit.

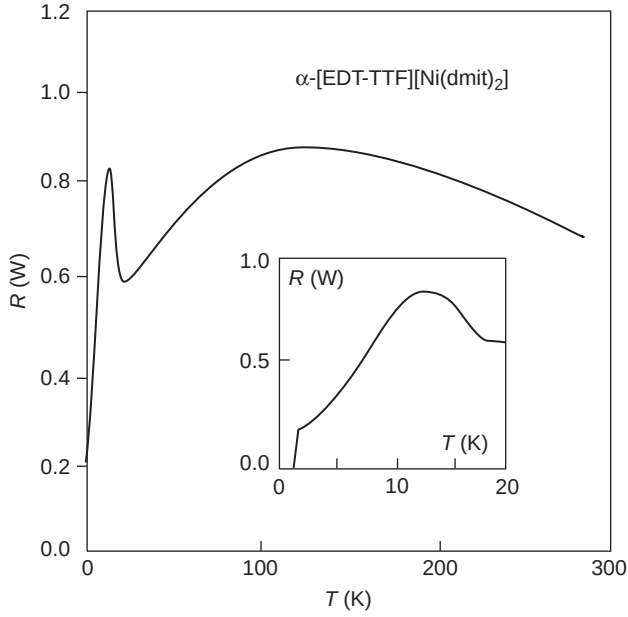

Figure 4.24 Ambient pressure superconductivity in α-[EDT-TTF][Ni(dmit)$_2$]. The inset shows the superconductive transition at 1.3 K. Reprinted with permission from Tajima *et al.*, 1995 [194]. Copyright (1995) Elsevier Ltd

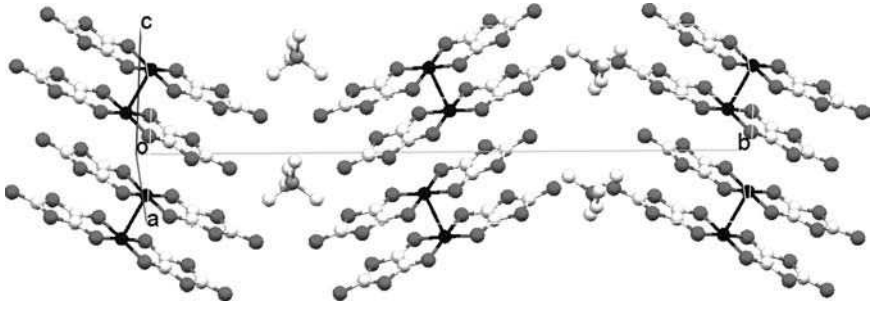

Figure 4.25 Crystal structure of [EtMe$_3$P][Pd(dmit)$_2$]$_2$ viewed from the a^* axis

4.3.4 Conductors Based on Neutral Metal Bis-Dithiolene Complexes

Neutral metal bis-dithiolene complexes were isolated from a very few ligands considering the number of existing bis-dithiolene ligands. A selection is shown in Figure 4.26. Most neutral metal bis-dithiolene complexes are not conductive. Only the TTF-dithiolene ones exhibit a metallic behaviour. Examples of conducting neutral complexes, that is $[Ni(dmit)_2]$, $[Ni(tmdt)_2]$, and $[Ni(dtdt)_2]$, are described in this section.

4.3.4.1 $[Ni(dmit)_2]$

During the synthesis of $[TTF][Ni(dmit)_2]$[151] by slow interdiffusion of acetonitrile solutions of $[TTF]_3[BF_4]_2$ and $[Bu_4N][Ni(dmit)_2]$, a few crystals whose morphology (platelet) was different from that (needle) of the majority of the species were recovered. The room temperature conductivity of these crystals (3.5×10^{-3} S cm^{-1}) was significantly different from the value obtained for $[TTF][Ni(dmit)_2]_2$ (300 S cm^{-1}). These crystals were finally characterised by crystal structure determination as the neutral complex $[Ni(dmit)_2]$.[147] In the neutral phase, the $[Ni(dmit)_2]$

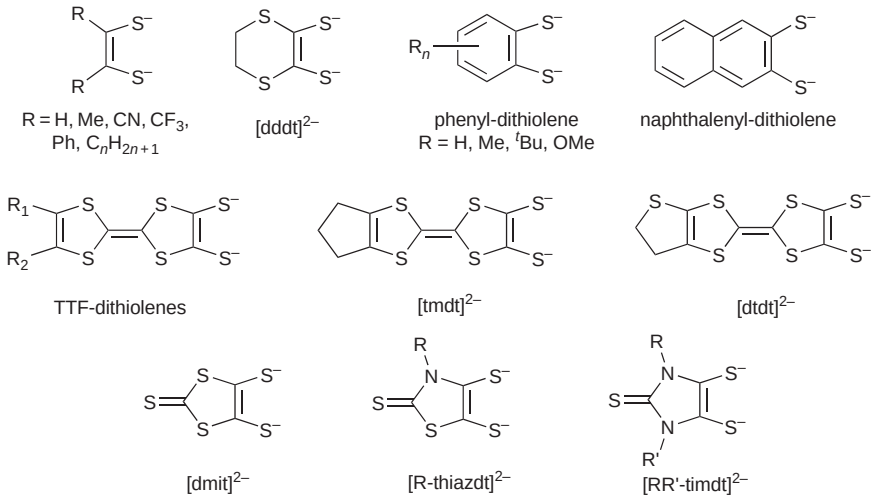

Figure 4.26 Dithiolenes ligands leading to neutral complexes[6,127,135,155,196–200]

molecules are centrosymmetric and close to planarity. Molecules stack regularly, and short S···S distances between [Ni(dmit)$_2$] entities are observed: one contact within a stack, and several between molecules of adjacent stacks. Note that [Ni(dmit)$_2$] meets most of the required structural criteria for obtaining highly conducting systems, that is, close regular stacking and short intermolecular contacts, but not the presence of a fractional oxidation state which accounts for the low conductivity of this material at room temperature. However, as will be seen in the next section, this criterion was later contradicted when the neutral extended TTF-dithiolene materials were isolated.

4.3.4.2 [Ni(tmdt)$_2$] and Other Neutral Extended TTF-dithiolate Complexes

The discovery of conducting neutral extended TTF-dithiolate complexes was major in the field of molecular conductors. Conductivity arises from the partial occupancy of electronic bands, known to be obtained through charge transfer between two independent molecules within DA compounds or through partial oxidation using either electrolysis or a chemical oxidant within FOSCs, that is, through an intermolecular mechanism. In 1997, Canadell examined the two band electronic structures often encountered in [M(tmdt)$_2$]-containing phases, and described the possibility of existence of 'internal electron transfer'[201] in such systems. The [Ni(tmdt)$_2$] phase was the first example of a single-component molecular conductor.

A mechanism to generate conduction carriers in single-component molecular conductors is illustrated in Figure 4.27. In general, since the HOMO–LUMO energy gap of organic donor molecules is large, the formed HOMO and LUMO bands also have a gap and no carrier is generated. Therefore, the design of molecules with a small HOMO–LUMO gap is the key point of development of single-component molecular conductors. The HOMO–LUMO gaps of single-component molecular conductors were evaluated to be unprecedentedly small by infrared absorption measurement.[202]

The molecular arrangement in the crystals of neutral [Ni(tmdt)$_2$] is illustrated in Figure 4.28; the [Ni(tmdt)$_2$] molecules are ideally flat and closely packed. Three-dimensional short S···S contacts develop within the structure. The conductivity at room temperature is 4×10^2 S cm^{-1} and it shows metallic behaviour (Figure 4.28).[128] The band calculations based on first principle calculations and extended Hückel tight-binding calculation

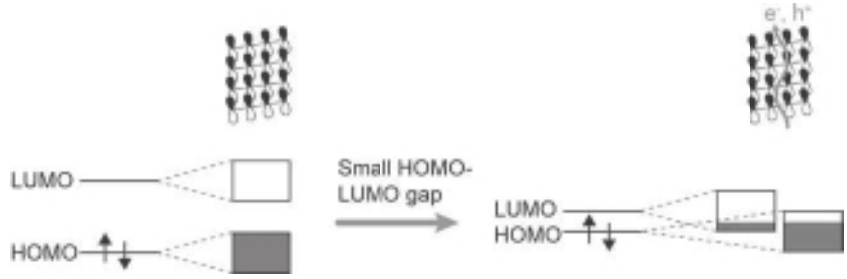

Figure 4.27 Schematic figures of the mechanism to generate conduction carriers in single-component molecular conductors

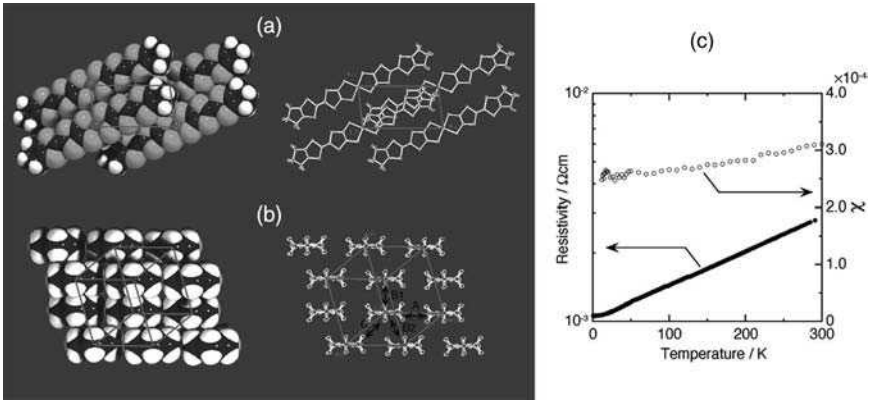

Figure 4.28 Crystal structure and physical property of $[Ni(tmdt)_2]$. Molecular arrangement view along the molecular stacking direction (a) and along the molecular long axis direction (b). Temperature dependence of resistivity and magnetic susceptibility (c). Reprinted with permission from Tanaka *et al.*, 2001 [128]. Copyright (2001) American Association for the Advancement of Science

both gave three-dimensional, semi-metallic Fermi surfaces.[25,136,203–205] Direct experimental evidence for the nature of the Fermi surface in $[Ni(tmdt)_2]$, and thus confirmation of the existence of a real single-component molecular metal, was obtained later by detecting the quantum oscillations in magnetisation at very high magnetic field, the so-called de Haas–van Alphen (dHvA) effect.[206] Torque magnetometry measurements of single crystals of $[Ni(tmdt)_2]$ using a sensitive micro-cantilever at low temperature revealed dHvA oscillatory signals for all directions of a magnetic field, showing the presence of three-dimensional electron and hole Fermi surfaces.

A number of single-component molecular conductors have been reported in this decade, including new compounds showing metallic behaviour such as [Ni(dmdt)$_2$] (dmdt = dimethyltetrathiafulvalenedithiolate) and [Au(tmdt)$_2$].[5,207] The copper and cobalt complexes also show closed molecular packing and comparatively high conductivity, but no magnetic ordering.[208,209] Recently, antiferromagnetic ordering around 110 K was observed in [Au(tmdt)$_2$] without conductivity anomaly. A series of complexes with the [dtdt]$^{2-}$ and [α-tdt]$^{2-}$ ligands (Figure 4.17) was isolated recently.[127] Gold and nickel complexes were studied. The polycrystalline samples of the nickel complexes exhibit high conductivities, 200 and 24 S cm^{-1} for [Ni(dtdt)$_2$] and [Ni(α-tdt)$_2$], respectively. A metallic behaviour is observed down to 80 K for the highly conducting Ni(dtdt)$_2$ compound. This family enlarges the number of single-component molecular metals.

4.4 TOWARDS THE APPLICATION OF MOLECULAR INORGANIC CONDUCTORS AND SUPERCONDUCTORS

Nowadays, the miniaturisation of components is an important challenge in electronic industry. Two approaches are being developed: the top-down one uses conventional inorganic materials while the bottom-up one develops the organisation of atoms or molecules on surfaces. By using single molecules, materials have been produced as nanoparticles, nanowires, thin films or monolayers.[11,210–216] For producing reliable components, chemists should afford materials showing electronic properties in the bulk, but also organise these materials on surfaces, the key step towards efficient devices. Many organic materials have already been proved to act as OLEDs (organic light-emitting diodes), TFTs (thin-film transistors) or been incorporated in flexible electronic paper.[217–221] To our knowledge, metalorganic materials in commercialised products are not well developed, although sensing, memory or photoactive properties have been evidenced in some cases.[222–224]

4.4.1 Processing Methods

Molecular materials are more commonly prepared and studied as single crystals. In such morphology, they cannot be easily applied to device

fabrication. The thin film morphology is more appropriate, but nanowires, organised on patterned surface, have also great potential for advanced devices. Processing techniques commonly used for electronic device fabrication may be applied to molecule-based materials. Depending on the material, various factors should be taken into account for choosing the appropriate technique.[11]

When gas-phase reactions are involved (dry techniques), such as chemical vapour deposition (CVD) and evaporation under ultra-high vacuum (UHVD), precursor molecules should fit specific physical and chemical criteria.[11] CVD is one of the typical techniques used to grow a solid material as a thin film on the surface of a substrate using gaseous starting compounds (precursors).[225] CVD allows the growing of a large variety of materials, such as metals, solid solutions, composite materials and ceramic materials, on a large set of substrates. In this process, the precursors are vaporised and further transported towards the substrate surface using a carrier gas. The most important characteristic that the precursor molecules should fulfil to be used in dry techniques is their ability to be vaporised (vapour pressure > 13 Pa at ≈ 373 K). It is understood from this criterion, that only molecular materials resulting from volatile precursors – that is, mostly neutral precursor molecules – may be grown as thin films using CVD. Examples of films of molecular conductors or magnets, produced by CVD and various other dry methods, are reported in the book of Fraxedas[154] and elsewhere.[11,226]

In solution-based techniques (wet techniques), such as dip coating (DC),[11] spin coating (SC), electrodeposition (ED), zone casting,[227,228] reticulate doping (RDP)[229] and the Langmuir–Blodgett (LB) technique,[230,231] the chemical characteristics of the precursor molecules are more familiar to synthetic chemists, solubility being of course one of the first. Orienting the growth towards either films or nanowires implies the control of other factors. Specific formation of nanowires will depend on the substrate's ability to induce such type of growth. Therefore, the substrate surface nature and morphology have a determinant influence on both the deposit nature (film or nanowires) and its adhesion.

Growth of molecular inorganic conductors and superconductors as films or nanowires is mainly conducted by electrodeposition due to the physico-chemical properties of the precursors and the necessary electrochemical activation to produce the conductive phase.

4.1.1.1 Electrodeposition

Electrocrystallisation is the usual method applied to grow single crystals of molecule-based conductive materials.[152–154] Confined electrocrystallisation has been applied to grow ultra-thin crystals of molecular conductors.[232] However, either confined electrodes or the commonly used wire shape platinum electrode are not appropriate to grow thin films. In electrodeposition the substrate has to be conducting as it acts as the electrode. Numerous types are cited and referenced elsewhere[12]: platinum foil, single-crystal Au(110), SnO_2, glassy carbon and highly oriented pyrolytic graphite, gold electrodes modified by an LB-film, copper and ITO (indium tin oxide) and anodic aluminum oxide (AAO).[233,234] More recently, the use of silicon (100) wafers as electrodes to grow the films has been considered,[235] as the electronic domain is largely based on silicon technology.

4.4.1.2 Silicon Electrodes

The conductivity of silicon covers a wide range of values whether the material is doped or not. Electrolyses can be conducted using either intrinsic silicon, that is a low conductive type ($\sigma = 5–3 \times 10^{-3}$ S cm^{-1}), or *p*-type one. The entire silicon wafer (diameter 2 in, thickness 275 μm) or strips of it (3×0.5 cm) can be used. The use of the entire wafer is interesting when a large amount of material is expected instead of film formation.[236] Cleaning procedures are applied before dipping the substrate in the electrolytic solution.[12,237] Cleaning has two main goals: removing impurities from the surface and etching the surface in order to improve the anchorage of the deposit. The cleaning treatment of silicon substrates can lead to a nanostructuring of the surface, an increase in its roughness and an improvement in the adherence of the coatings. Moreover, the nanostructuring equalises the charge distribution on the substrate surface and may avoid localised nucleation that leads to crystal growth instead of film growth. A platinum wire is typically used as counter electrode. Galvanostatic electrolysis is carried out using similar solutions of the precursors as in conventional electrocrystallisation.

4.4.1.3 Patterned Electrodes

The fabrication of organic transistors requires both patterned structures and thin continuous layers. Films can be produced by combining printing

and coating techniques as shown by Tobjörk *et al.*[220]: polymer-based organic transistors are built on a plastic substrate by a five-step method suitable for low-cost large-scale roll-to-roll manufacturing. Another recent work by Leufgen *et al.*[219] describes the formation of single crystals of TTF derivatives on top of micro-patterned silicon substrates by drop casting. In this case, single crystals were expected for investigating the intrinsic transport properties of the studied materials. Following this objective, patterned electrodes are valuable supports for growing nano-sized crystals and studying the influence of the size reduction on the properties of the grown material. The growth of nanocrystals on electrodes and direct measurement of conductance of the crystals have been reported recently.[238] Yamamoto *et al.* grew a fine needle crystal of Cu [(DMe-DCNQI-d_7)$_2$] on finely patterned electrodes with special configurations, and observed metallic conductivity on the nanocrystal down to helium temperature (4 K), while the bulk Cu [(DMe-DCNQI-d_7)$_2$] showed a metal–insulator transition at 80 K.[239]

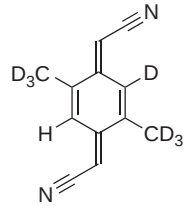

DMe-DCNQI-d_7

4.4.1.4 Modified Electrodes

Surface modifications of the deposition electrodes have various objectives. It has been seen above that the nanostructuring of silicon electrodes increases the surface coverage and the adherence of coatings. Hybrid organic–inorganic films have been produced by electropolymerisation of pyrrole or aniline in the presence of metal complexes or oxides[240–242] with the idea of combining the best chemical and physical properties of both components. These techniques afford smoother and more continuous films, although they do not lead to oriented growth. As most of the molecular materials show highly anisotropic physical properties, their preparation as fibre-like materials in which molecular units are well arranged is of great importance to reach the best physical performances. The LB [230,231] and zone casting [227,228] techniques may afford such an organisation through the use of a moving substrate in the

interface with the solution containing the material precursor. In both cases, oriented films are isolated. However, for isolating well-oriented micro- and nanofibre-like materials, template substrates offer more appropriate conditions. When aluminium is anodised, porous alumina containing well aligned nano-channels is formed.[243] Gold is evaporated to cover the channel surfaces and the so-called AAO templates may be used as depositing electrode. Nanofibres grow inside the channels and can be separated after dissolution of the template.[233] Another method to create channels on a substrate surface is to create a multilamellar layer as shown by Xing *et al.*[244] A phospholipidic membrane is formed on a silicon substrate and used as an electrode to grow nickel hydroxide within the interheadgroup spaces of the phospholipid bilayers. The deposit consists of inorganic sublayers into organic templates. The space between phospholipid bilayers controls the size of the electrocrystallised fibres towards the nanometre range. One limitation of this method is that the separation of the fibres from the membrane is difficult compared with inorganic templates as the AAO described above.

4.4.2 Films and Nanowires of Molecular Inorganic Conductors

Although preparation of films and nanowires of molecular materials is a young research domain, the literature is already very large and it is impossible to cover all systems in this chapter. It will therefore give – *hopefully* – the 'best taste of the field' by describing electrodeposited systems that have been selected according to the various factors which influence their growth as films, microcrystals or nanowires: cell configuration, growth conditions, substrate nature and morphology and chemical nature of components and additives. Two reviews can be consulted for further description of the electrodeposition of molecular conductors: one highlights metal complex containing materials [12] and the other the application of silicon wafers as electrodes.[235] Note that single-molecule deposition will not be covered: a recent review on unimolecular electronics published by Metzger can be consulted.[211]

4.4.2.1 Cell Configuration

Reduction of the size of the processed materials can be performed *via* the reduction of the size of the electrochemical cell. Thakur *et al.* described a

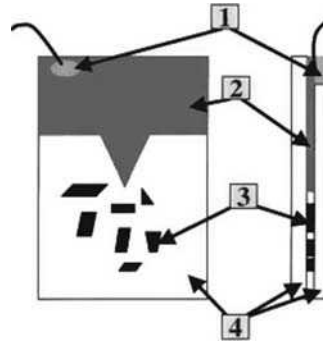

Figure 4.29 Drawing of a typical confined anode: typical size 1 cm × 3 cm × 4 m; 1 represents the connection with an external electric circuit, 2 the metal deposit, 3 the thin single crystals and 4 the glass substrates. Reprinted with permission from Deluzet *et al.*, 2002 [232]. Copyright (2002) Wiley-VCH

method for the preparation of thin single crystal films of organic superconductors on various substrates.[245] The method is based on a unique design of the electrochemical cell in which the anode structure imposes oriented crystallisation to occur within the interface of two opposing substrates. Micrometre single crystal films can be obtained. Deluzet *et al.* applied this so-called confined electrocrystallization (CEC) method to grow thin single crystals of various TTF derivatives: $[TMTTF]_2[ReO_4]$, $[TMTSF]_2[ReO_4]$ and $[TMTSF]_2[W_6O_{19}]$, κ-$[BEDT\text{-}TTF]_2[Cu_2(NCS)_2]$, $[BEDT\text{-}TTF][Cu_2(NCS)_3]$, β″-$[BEDT\text{-}TTF]_4[Re_6Se_6Cl_8]$ and β″-$[BEDT\text{-}TTF]_4[Mo_6Cl_{14}]$, and $[EDT\text{-}TTF]_3[Re_6Se_6Cl_8]\bullet(CH_3CN)(CH_2Cl\text{–}CHCl_2)$.[232] The electrode configuration in a CEC cell (Figure 4.29) limits the electron transfer rate because chemical species move more slowly to the electrodes than in a conventional cell.

For overcoming this problem, the authors enriched the electrode surface with the molecule precursor to the electrodeposited material. This step was performed by sublimation under vacuum, a method that the authors previously used to grow oriented films of neutral TMTSF and TTF derivatives.[246,247] The combination of sublimation and electrolysis methods significantly improves the crystal quality and reduces the growth time. The electrode configuration may induce the formation of a different phase of the material: $[TMTSF]_2[W_6O_{19}]$ is obtained by CEC while $[TMTSF]_2[W_6O_{19}]\bullet(DMF)$ grows in a conventional cell. To activate the crystal growth, the temperature was increased. This also favoured the growth of different phases: κ-$[BEDT\text{-}TTF]_2[Cu(NCS)_2]$ at 25 °C and $[BEDT\text{-}TTF][Cu_2(NCS)_3]$ at 60 °C. A thin crystal of the latter phase is shown in Figure 4.30.

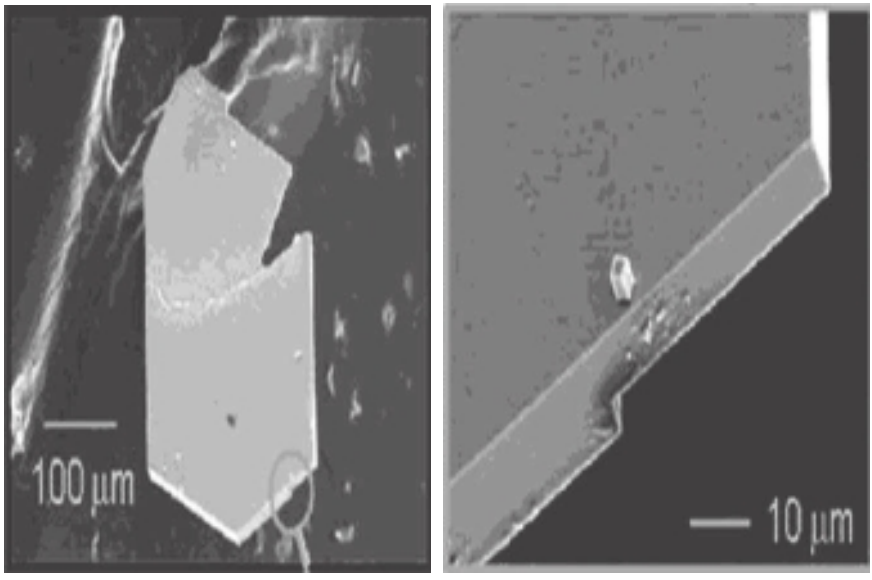

Figure 4.30 SEM images of a CEC grown thin crystal of [BEDT-TTF][$Cu_2(NCS)_3$]. Reprinted with permission from Deluzet *et al.*, 2002 [232].Copyright (2002) Wiley-VCH

The CEC method leads to micrometric thin crystals. Further reduction of the distance between electrodes is necessary to grow sub-micrometric crystals. This can be done by using sub-micropatterned electrodes. Such configuration of electrodes allows growing sub-microcrystals with

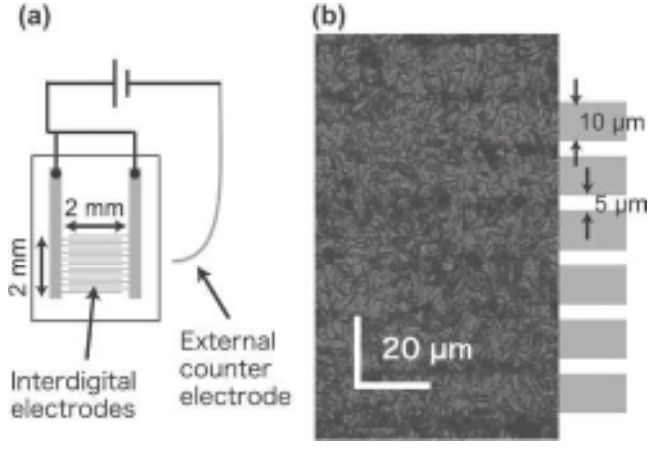

Figure 4.31 The schematic figure of interdigitated electrodes (a) and the picture of [$Ni(dmdt)_2$] microcrystals grown on the gold electrodes (b).[207] Reprinted with permission from the Chemical Society of Japan

properties that can be measured *in situ*. As shown in Figure 4.31, Tanaka *et al*. prepared sub-microcrystals of $[Ni(dmdt)_2]$ and $[Au(tmdt)_2]$ on finely patterned interdigitated electrodes by electrochemical deposition, and succeeded in observing metal-like conductance of these materials. The length of crystals growing on the electrodes is <5 μm and their thickness is <100 nm. It would not have been possible to measure their transport properties by conventional methods.[207]

4.4.2.2 Growth Conditions

It has been seen above that nanowires of conducting neutral TTF-dithiolenes derivatives can be isolated using patterned electrodes. Continuous thin films of $[Ni(tmdt)_2]$ were grown on silicon substrates.[248] The three SEM images of the films (Figure 4.32) clearly show that dense films have grown. Moreover, various morphologies, from rods to rose-like structures and microflowers, appear as a function of the growth rate, which is directly proportional to the current density.

An enlargement of the rose-like deposit shows substructures of nanometre size as the building units of the roses (Figure 4.33). Rose-like deposits showing substructures were also observed by Cui *et al*. when they electrodeposited films of $[Me_4N][Ni(dmit)_2]_2$ on nanostructured AAO substrates.[234] As for $[Ni(tmdt)_2]$ films, the shape and size of the $[Me_4N][Ni(dmit)_2]_2$ grown structures are strongly dependent on the current density and growth time. Rose-like formation results from instantaneous nucleation followed by a diffusion-limited growth.[233] The rose-like topography of $[Me_4N][Ni(dmit)_2]_2$ films exhibits superhydrophobic properties after treatment by a gold film covered by a *n*-dodecanethiol layer.[234] An extremely large contact angle ($152 \pm 1.7°$) is measured and the low tilt angle (4°) indicates that water droplets can roll off the surface

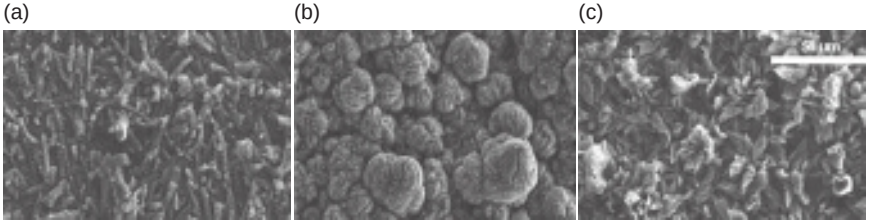

Figure 4.32 SEM images at same scale of $[Ni(tmdt)_2]$ films grown on silicon. (a) Rod-like structure, 1.1 μA cm^{-2}, 12 days. (b) Rose-like structure, 1.4 μA cm^{-2}, 19 days. (c) Microflowers, 2.5 μA cm^{-2}, 5 days

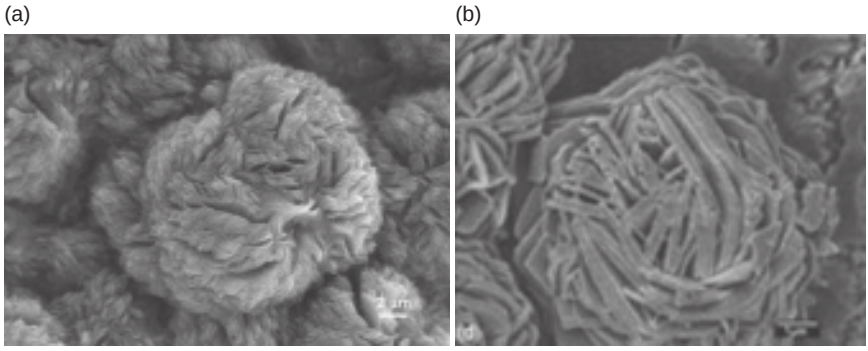

Figure 4.33 (a) Nanometre substructure of a 20 μm rose-like structure in $[Ni(tmdt)_2]$ film grown on silicon at 1.4 μA cm^{-2} during 19 days. (b) Rose-like microstructures in $(Me_4N)[Ni(dmit)_2]_2$ films grown on AAO substrate at 15 μA cm^{-2} after 7 h. Reprinted with permission from Cui *et al.*, 2006 [234]. Copyright (2006) Elsevier Ltd

very easily. Superhydrophobicity is very interesting for applications of conducting materials in terms of self-cleaning and interfacial properties.

The rod-like morphology of the $Ni(tmdt)_2$ film grown at the lower current density highly resembles the nanowires of $[Me_4N][Ni(dmit)_2]_2$ grown also at a lower current density than the rose-like deposits (Figure 4.34).[233] Note that both the rods and the nanowires are constructed (at a different scale) from linear assemblies of grains or pearls as named by Cui *et al.*[233] The well-organised structurisation of the $[Me_4N][Ni(dmit)_2]_2$ deposit comes from the use of a template substrate.

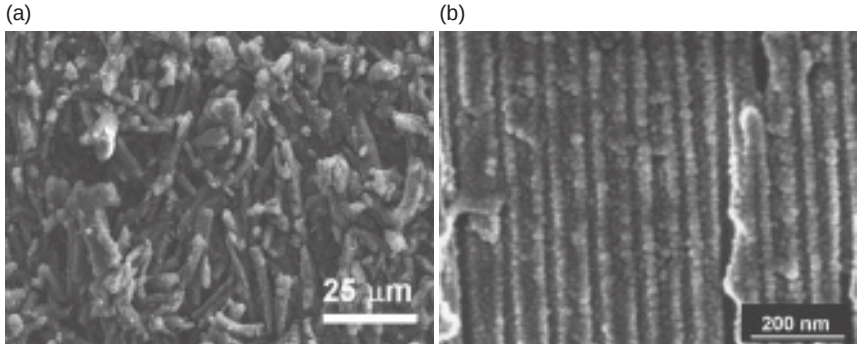

Figure 4.34 (a) Rod-like structures in $[Ni(tmdt)_2]$ film grown on silicon at 1.1 μA cm^{-2}. (b) Nanowire arrays in $[Me_4N][Ni(dmit)_2]_2$ films grown on AAO substrate at 5–10 μA cm^{-2}. Reprinted with permission from Cui *et al.*, 2004 [233]. Copyright (2004) American Chemical Society

This influence of the substrate nature will be discussed in the next section.

Whatever their morphology, the above described films are polycrystalline and their structures are identical to single crystals analogues. However, a significant difference between the films of these two materials appears in their electrical properties. Both nanopearl and rose-like structures of the $[Me_4N][Ni(dmit)_2]_2$ films are semiconductive while single crystals exhibit a metal-like behaviour down to 100 K.[186] Moreover, the room temperature conductivity of the films is $\approx 5 \times 10^{-3}$ S cm^{-1}, much lower than the value of 60 S cm^{-1} measured on single crystals. Loss in electronic transport efficiency is not surprising in polycrystalline films. This is explained by the significant contribution of resistive grain boundaries to the overall resistivity of the material. However, polycrystalline $[Ni(tmdt)_2]$ films exhibit metallic behaviour (Figure 4.35).[248]

Moreover, the room temperature conductivity of the films shows values as high as 135 S cm^{-1}, that is, very close to the single crystal value of 400 S cm^{-1}.[128] The high conductivity value and metallic behaviour of $[Ni(tmdt)_2]$ films can be explained by a chemical continuity between crystallites. Each crystallite being conducting plays the role of an electrode of same chemical nature as the growing material: such conditions favour epitaxial growth, therefore a real chemical continuity between grains. This is first supported by the comparison of conductivity behaviour of the film with that of compacted powder samples

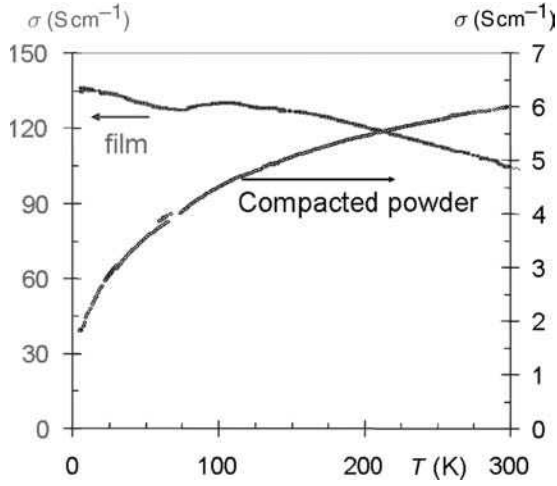

Figure 4.35 Thermal behaviour of the conductivity of $[Ni(tmdt)_2]$ films: comparison of film with compacted powder samples

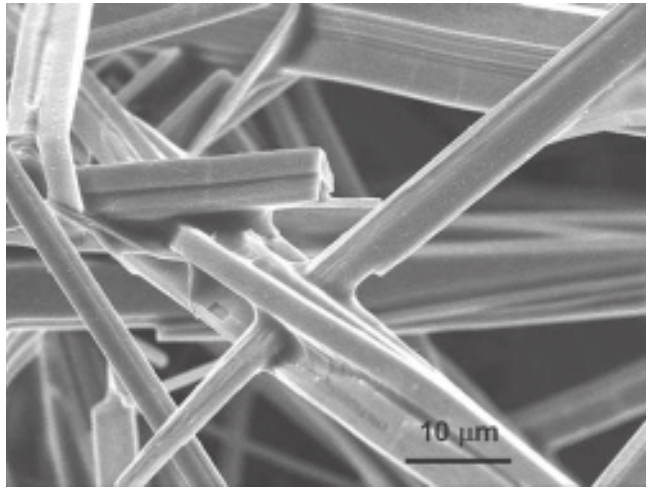

Figure 4.36 SEM of a $[TMTSF]_2[ClO_4]$ film electrodeposited on silicon

(Figure 4.16): the latter are semiconducting because of the resistive contribution of grain boundaries, suppressed in the case of the film by the chemical continuity described above. Another proof for this explanation is given by the image of an electrodeposited $[TMTSF]_2[ClO_4]$ film in which interconnected fibres are clearly evidenced (Figure 4.36). This film, less dense than the $[Ni(tmdt)_2]$ films, exhibits almost constant conductivity *vs* temperature ($E_a \approx 1$ meV).[249]

4.4.2.3 Substrate Nature and Morphology

Rose-like and nanopearl-structured $[Me_4N][Ni(dmit)_2]_2$ films have been grown on anodised aluminium oxide (AAO) template. The difference in morphology of the deposit is attributed to the size of the channels of each AAO template. The nanowires made of nanopearl chains grow inside the channels of the AAO template and accommodate their size to the channel diameter: 49 ± 2 and 32 ± 4 nm.[233] Rose-like structures are obtained on AAO template with smaller channel diameter: 15 ± 4 nm.

Figure 4.37 shows the morphology of two $[TTF][Ni(dmit)_2]_2$ films grown on silicon. The difference between the two deposits originates from both the applied current density and the surface morphology of the silicon substrate which induces different seeding conditions.[235,250] The grain-like film is obtained on a nonpolished silicon wafer exhibiting

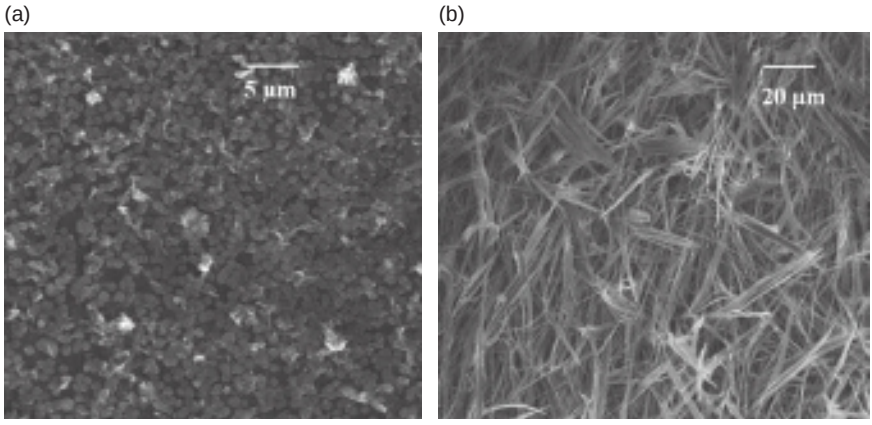

Figure 4.37 [TTF][Ni(dmit)$_2$]$_2$ films. (a) Grains on microrough silicon at 1.5 μA/cm^2. (b) Fibres on nano-structured silicon at 6.2 μA cm^{-2} [250][251]. Reprinted with permission from Wiley-VCH and the Institute of Physics

a microrough surface. On the other hand, the fibre-like film grows on a pre-treated silicon surface exhibiting nanopores.[251] When the substrate is placed inside the electrolytic solution, both micropores and nanopores are filled with the solution: micro- and nanopores act as independent flasks where the seeding process takes place. Three-dimensional growth of the nucleates is favoured in larger pores while fibres are favoured from nanoseeds. Moreover, crystals of molecular conductors classically grow along the best conductive pathway. When conventional electrocrystallisation is used, most of them appear as needles and their conductivity is the highest along the needle. Upon size reduction, the former needles grow as fibres.

The analyses of both deposits confirm that they contain the [TTF][Ni(dmit)$_2$]$_2$ phase; both exhibit a metallic behaviour. A deeper study of the transport properties of the fibre-like films showed that superconductivity manifests by a broad drop of the resistance below 0.8 K. Although the transition is incomplete because of inter-fibre resistance contributions, Figure 4.38 shows that superconductivity is confirmed by the application of a magnetic field perpendicular to the plane of the film.

Another example of fibre-like deposits is given by the electrodeposition of [Per][Au(mnt)$_2$] (Per = perylene, Figure 4.1) on a silicon anode which leads to a uniform black film.[252] Scanning electron micrographs reveal that the film is made of nanowires (Figure 4.39). The diameter of an individual nanowire is in the 35–55 nm range, smaller than the [TTF][Ni(dmit)$_2$]$_2$ fibres previously described. The conductivity of

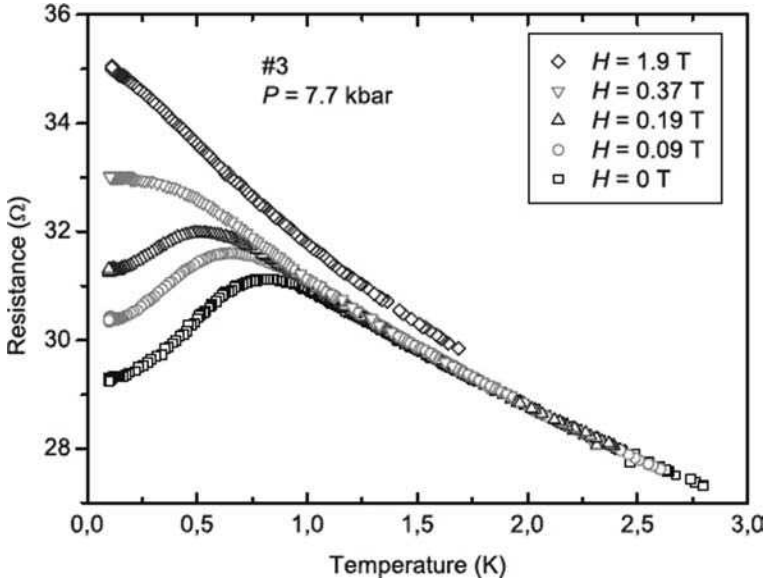

Figure 4.38 Temperature dependence of the resistance of $[TTF][Ni(dmit)_2]_2$ film at $P = 7.7$ kbar, in the superconducting temperature domain, for different applied magnetic fields ranging from 0 to 1.9 T. The critical field is $\approx$0.45 T [251]. Reprinted with permission of Institute of Physics

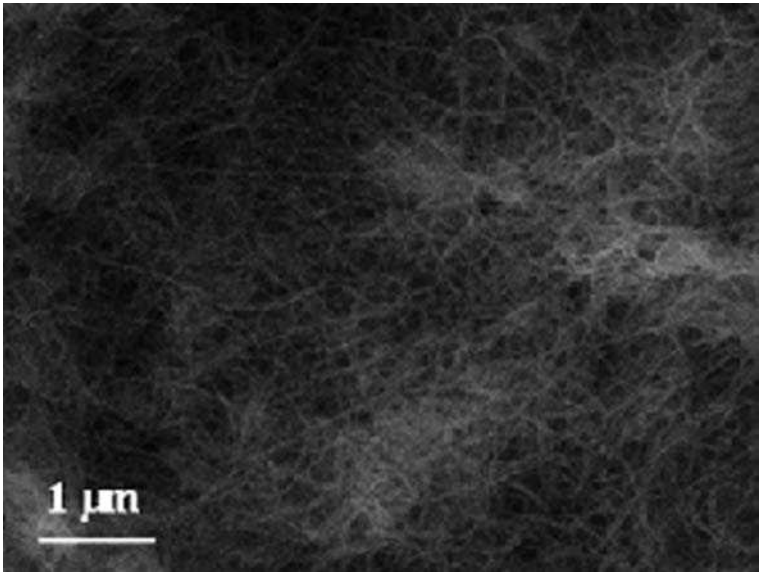

Figure 4.39 SEM image of $[Per][Au(mnt)_2]$ nanowire films [235]. Reprinted with permission of Institute of Physics

[Per][Au(mnt)$_2$] nanowire films is $\approx$0.02 S cm^{-1} at room temperature and follows a semiconducting behaviour ($E_a = 88$ meV).

4.4.2.4 Chemical Nature of Components and Additives

Various methods have been reported for improving the quality of the films and their nanostructuration. We will report on some examples using precursors, including long chain species, incorporated into polymers, or electrolysed into organic templates.

Recent accounts by Zang *et al.*[253] and by Palmer and Stupp[254] give interesting overviews on self-assembly methods leading to nanowires of organic materials. Most examples involve precursors containing long-chain substituents. Inclusion of long-chain substituents has also been studied for growing inorganic conductors.

The Langmuir–Blodgett (LB) technique implies the use of long-chain ions. For reviews on LB preparations of conductive or magnetic films, the reports by Nakamura *et al.*[255,256] and Talham *et al.*[257] are worth consulting. Miura has studied the growth of films of [Au(dmit)$_2$] by the LB technique for a long time. The starting complex contains an alkylammonium cation bearing one to three long chains.[12] The LB film is processed and further oxidised to obtain conducting films. Films of [2C$_{14}$–Au(dmit)$_2$] exhibit a room-temperature conductivity of 40 S cm^{-1} and metallic behaviour in the 58–300 K range.[258] A superconducting phase was suggested in this compound below 4 K.[259–261] LB films are not continuous; they consist of large domains whose size reduces upon electrochemical oxidation.[262] Among numerous other films, [2C$_8$–Au(dmit)$_2$] films show a relatively high room-temperature conductivity of up to 17 S cm^{-1} which increases up to 50 S cm^{-1} upon electrochemical oxidation.[263]

Inclusion in polymer matrices is another way to prepare continuous conducting films. The reticulate doping technique was applied by Laukhina *et al.*[264] and Mas-Torrent *et al.*[265] to produce organic conducting films. Two per cent w/w of BEDT-TTF and BET-TTF donors are cast inside a polycarbonate matrix, and the blend is exposed to iodine or bromine vapour, leading to films containing the [BEDT-TTF]$_2$[I$_3$] and θ-[BEDT-TTF]$_2$Br·3H$_2$O phases, respectively. Similarly, a hybrid material based on polyaniline including 50% w/w of Cs[In(dmit)$_2$] was recently isolated and shows a conductivity of 2.3×10^{-5} S cm^{-1}.[242] This hybrid material is formed as a flexible, self-supporting film. A different method was applied by da Cruz *et al.* to prepare such hybrid films. Pyrrole is electropolymerised in acetonitrile using the inorganic

anions as supporting electrolytes. Polypyrrole/$[M(\text{dmit})_2]^{n-}$ (with M = Ni, Pd, Pt, Bi) and polypyrrole/$[\text{Sn(dmit)}_3]^{2-}$ films are reported.[266,267] Polypyrrole/$[\text{Pd(dmit)}_2]^{2-}$ is the more conductive of the series (4.3×10^{-3} S cm^{-1}). Highest conductivities have been obtained with inclusion of other type of transition metals [268]: for example Ppy/$[\text{Fe(CN)}_4]^{3-}$ has a conductivity of 20 S cm^{-1}. Note that in these polymer/complex composites, the complex is not in a fractional oxidation state, that is, not in a conducting state. This explains the lower conductivity values of the composites *vs* those of the pure polymers.

Another method to include polymeric moieties within the films was reported by Shen *et al.*:[269] the polymeric PVOP cation is the counter-ion of the starting $[M(\text{dmit})_2]$ complex. The complex is further oxidised and films are grown on copper substrates. The quality of the films is improved by the presence of polyvinyloctylpyridinium bromide. Although $[M(\text{dmit})_2]$ species are partially oxidised in the films, their conductivities are low: 3.2×10^{-4} S cm^{-1} and 4.0×10^{-4} S cm^{-1} for the nickel and palladium derivatives, respectively.

Polymeric additives may also be used for modifying the electrode surface. Xing *et al.* recently reported on a novel approach for fabricating phospholipid/Ni(OH)_2 superlattices by electrochemical deposition of the inorganic component into solid-supported multilamellar templates.[244] The well-ordered multilamellar templates are produced by spreading a lipid solution on silicon surfaces. These templates are used as working electrodes and can preserve their lamellar structure in the electrolyte solution. The phospholipid ($DC_{8,9}PC$), precursor to the membrane, contains a zwitterion type headgroup and two long alkyl chains (Figure 4.40).

These silicon-supported multilamellar membranes were applied to grow $[\text{EDT-TTFVO}]_4[\text{FeCl}_4]_2$ films,[252] in order to avoid the formation

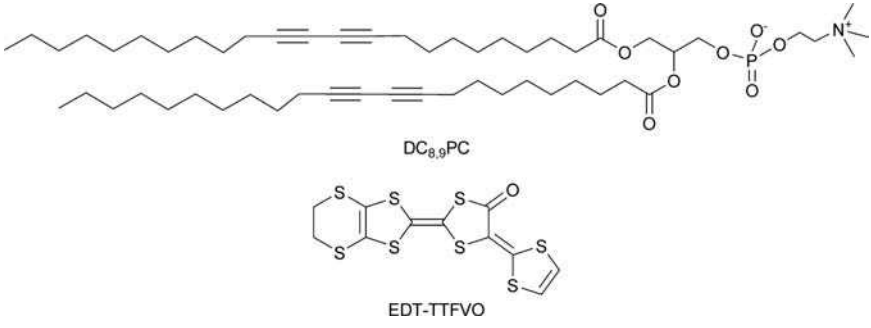

Figure 4.40 $DC_{8,9}PC$, precursor to the membrane described in Xing *et al.*[244] and the EDT-TTFVO molecule

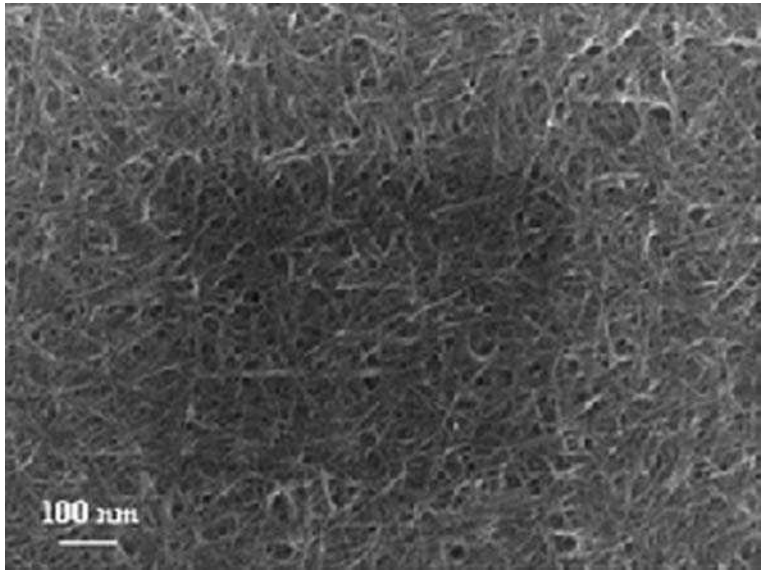

Figure 4.41 SEM image of $[EDT\text{-}TTFVO]_4[FeCl_4]_2$ nanofibres grown on silicon-supported multilamellar membranes at 0.15 μA cm^{-2} for 10 days

of randomly distributed single crystals as usually observed on non-treated silicon. Electron micrographs evidence that the film (Figure 4.22) is actually made of severely aggregated nanofibres (diameter ≤20 nm). A plausible growth mechanism is as follows: EDT-TTFVO molecules migrate from the solution/membrane interface to the substrate surface *via* long alkyl chains and are oxidised to produce the charge transfer salt with $[FeCl_4]^{2-}$ ions, which are largely present at the vicinity of the hydrophilic silicon surface. As the growing salt is in contact with $[FeCl_4]^{2-}$ ions in interheadgroup spaces, the growth continues by forming nanofibres along the channels between the long alkyl chains. Even when the growing salt reaches the membrane surface, the growth still continues towards the formation of long nanofibres perpendicular to the membrane surface, as evidenced by scanning electron microscopy (Figure 4.41).

4.5 CONCLUSIONS

Since the discovery of the first molecular inorganic superconductor $[TTF][Ni(dmit)_2]_2$ in 1986,[173,174] only eleven other phases (Section 4.3.3.1) have been isolated. Although many other dithiolene ligands

were explored, the dmit ligand is still the only one leading to superconducting complexes. Moreover, only nickel and palladium complexes appear in the superconductive phases. Apart from superconductivity, the most important discovery in the domain was the preparation of the first conductors based on neutral complexes.[128] It seems that electronic pathways are favoured in such dithiolene systems. If the chemical structures of TTF and $[Ni(dmit)_2]$ are looked at, it is observed that extended-TTF dithiolates can be described as combining a 'dmit-like' core and 'TTF-like' external moieties (Figure 4.42).

As mentioned earlier, bis-dithiolenes complexes are also studied for their optical or magnetic properties. They are also involved in multi-property systems. Combination of properties has been one of the most developed task of the past twenty years, magnetism and conductivity coupling being the more active field. Some examples were given in Section 4.2.2.4 with the family of BETS magnetic superconductors. Other examples involve $[M(mnt)_2]$ complexes,[119] or spin-crossover complexes.[270,271] Among the more recently discovered properties, a photo-induced phase transition was evidenced in $[Et_2Me_2Sb][Pd(dmit)_2]_2$.[272] The majority of bifunctional systems combine two different building blocks, each affording one property. Note that *unimolecular* bifunctional materials have been studied. These compounds are composed of a conductive moiety chemically bonded to a magnetic moiety. Examples are: $[Cu(hfac)_2(TTF\text{-}py)_2][X]_2{\cdot}2CH_2Cl_2$ ($X = PF_6$, BF_4)[273–275] and $[(ppy)Au(C_8H_4S_8)]_2[PF_6]$.[276]

During the past ten years, the major developments in molecular conductors have been observed in the field of their processing as films or nano-objects. This domain is very important to develop more molecular materials towards devices. The large variety of methods combined with

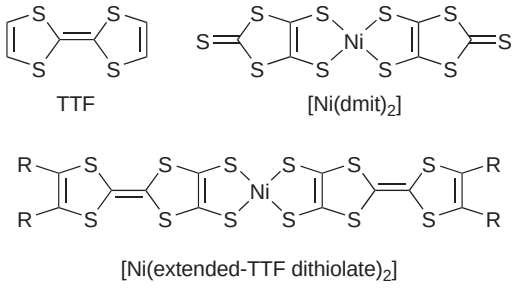

Figure 4.42 Molecular structures of TTF, $[Ni(dmit)_2]$ and [Ni(extended-TTF dithiolate)$_2$] complexes

the huge number of already known molecular materials makes the field wide open to new findings.

ACKNOWLEDGEMENTS

We wish to pay a special tribute to our favorite *quatuor* of distinguished chemists and physicists who have attracted us to the very exciting world of molecular materials, namely our Professors, Patrick Cassoux, Akiko Kobayashi, Hayao Kobayashi and Madoka Tokumoto.

We would like to thank our collaborators and all cited authors for their active contribution to the field of molecular conductors and superconductors.

REFERENCES

[1] J. M. Williams, J. R. Ferraro, R. J. Thorn, T. A. Carlson, U. Geiser, H. H. Wang, A. M. Kini and M. H. Whangbo, *Organic Superconductors*, Prentice Hall, Englewood Cliffs, 1992.
[2] J.-P. Farges, *Organic Conductors: Fundamentals and Applications*, Marcel Dekker, New York, 1994.
[3] T. Ishiguro, K. Yamaji and G. Saito, *Organic Superconductors*, Springer, Berlin, 1998.
[4] P. Cassoux and J. S. Miller, in *Chemistry of Advanced Materials: an Overview* (eds L. V. Interrante and M. J. Hampden-Smith), Wiley-VCH Verlag GmbH, New York, 1998, pp. 17–19.
[5] H. Kobayashi, H. B. Cui and A. Kobayashi, *Chem. Rev.*, **104**, 5265–5288 (2004).
[6] A. Kobayashi, E. Fujiwara and H. Kobayashi, *Chem. Rev.*, **104**, 5243–5264 (2004).
[7] R. Kato, *Chem. Rev.*, **104**, 5319–5346 (2004).
[8] G. Saito and Y. Yoshida, *Bull. Chem. Soc. Jpn.*, **80**, 1–137 (2007).
[9] P. Cassoux and L. Valade, in *Inorganic Materials* (eds D. W. Bruce and D. O'Hare), John Wiley & Sons Ltd, Chichester, 1996, pp. 1–64.
[10] D. W. Bruce and D. O'Hare, *Inorganic Materials*, John Wiley & Sons Ltd, Chichester, 1996.
[11] L. Valade, D. de Caro and I. Malfant, in *Organic Conductors, Superconductors and Magnets: From Synthesis to Molecular Electronics,* Vol. 139 (eds L. Ouahab and E. B. Yagubskii), Kluwer Academic & NATO Science Series II, 2004, pp. 241–268.
[12] L. Valade, D. de Caro, M. Basso-Bert, I. Malfant, C. Faulmann, B. Garreau de Bonneval and J.-P. Legros, *Coord. Chem. Rev.*, **249**, 1986–1996 (2005).
[13] R. E. Peierls, *Quantum Theory of Solids*, Oxford University Press, Oxford, 2001.
[14] J. B. Torrance, *Acc. Chem. Res.*, **12**, 79–86 (1979).
[15] G. Saito and J. P. Ferraris, *Bull. Chem. Soc. Jpn.*, **53**, 2141–2145 (1980).

[16] H. Akamatsu, H. Inokuchi and Y. Matsunaga, *Nature*, **173**, 168–169 (1954).
[17] W. A. Little, *Phys. Rev. J1 – PR*, **134**, A1416–A1424 (1964).
[18] K. Krogmann and H.-D. Hausen, *Z. Anorg. Allg. Chem.*, **358**, 67–81 (1968).
[19] H. R. Zeller and A. Beck, *J. Phys. Chem. Solids*, **35**, 77–80 (1974).
[20] D. S. Acker, R. J. Harder, W. R. Hertler, W. Mahler, L. R. Melby, R. E., Benson and W. E. Mochel, *J. Am. Chem. Soc.*, **82**, 6408–6409 (1960).
[21] B. A. Scott, S. J. LaPlaca, J. B. Torrance, B. D., Silverman and B. Welber, *Ann. NY Acad. Sci.*, **313**, 369–376 (1978).
[22] D. L. Coffen, *Tetrahedron Lett.*, **11**, 2633–2636 (1970).
[23] F. Wudl, G. M. Smith and E. J. Hufnagel, *J. Chem. Soc., Chem. Commun.*, 1453–1454 (1970).
[24] J. S. Miller, *Ann. NY Acad. Sci.*, **313**, 25–60 (1978).
[25] L. C. Isett and E.A. Perez-Albuerne, *Ann. NY Acad. Sci.*, **313**, 395–406 (1978).
[26] L. B. Coleman, M. J. Cohen, D. J. Sandman, F. G. Yamagishi, A. F., Garito and A. J. Heeger, *Solid State Commun.*, **12**, 1125–1132 (1973).
[27] J. Ferraris, D. O. Cowan, V. Walatka and J. H. Perlstein, *J. Am. Chem. Soc.*, **95**, 948–949 (1973).
[28] F. Denoyer, F. Comès, A. F. Garito and A. J. Heeger, *Phys. Rev. Lett.*, **35**, 445–449 (1975).
[29] S. Kagoshima, T. Ishiguro and H. Anzai, *J. Phys. Soc. Jpn.*, **41**, 2061–2071 (1976).
[30] K. Bechgaard, C. S. Jacobsen, K. Mortensen, H. J. Pedersen and N. Thorup, *Solid State Commun.*, **33**, 1119–1125 (1980).
[31] D. Jérome, A. Mazaud, M. Ribault and K. Bechgaard, *J. Phys. Lett.*, **41**, 95–98 (1980).
[32] J. P. Pouget, R. Moret and R. Comes, *Mol. Cryst. Liq. Cryst.*, **79**, 485–499 (1982).
[33] D. Jérome, *Mol. Cryst. Liq. Cryst.*, **79**, 511–538 (1982).
[34] D. Jérome, *Physica B and C*, **109–110**, 1447–1460 (1982).
[35] J. C. Scott, H. J. Pedersen and K. Bechgaard, *Phys. Rev. Lett.*, **45**, 2125–2128 (1980).
[36] K. Mortensen, Y. Tomkiewicz, T. D. Schultz and E. M. Engler, *Phys. Rev. Lett.*, **46**, 1234–1237 (1981).
[37] J. F. Kwak, *Phys. Rev. B*, **26**, 4789–4792 (1982).
[38] K. Yamaji, *J. Phys. Soc. Jpn.*, **52**, 1361–1372 (1983).
[39] S. S. P. Parkin, M. Ribault, D. Jerome and K. Bechgaard, *J. Phys. C: Solid State Phys.*, **14**, 5305–5326 (1981).
[40] S. S. P. Parkin., D. Jerome and K. Bechgaard, *Mol. Cryst. Liq. Cryst.*, **79**, 569–580 (1982).
[41] K. Bechgaard, K. Carneiro, F. B. Rasmussen, M. Olsen, G. Rindorf, C. S. Jacobsen, H. J., Pedersen and J. C. Scott, *J. Am. Chem. Soc.*, **103**, 2440–2442 (1981).
[42] D. Jérome, *Science*, **252**, 1509–1514 (1991).
[43] S. S. P. Parkin, E. M. Engler, R. R. Schumaker, R. Lagier, V. Y. Lee, J. C. Scott and R. L. Greene, *Phys. Rev. Lett.*, **50**, 270–273 (1983).
[44] E. B. Yagubskii, I. F. Shchegolev, V. N. Laukhin, P. A. Kononovich, M. V. Karatsovnik, A. V. Zvarykina and L. I. Buravov, *JETP Lett.*, **39**, 12–16 (1984).
[45] K. Murata, M. Tokumoto, H. Anzai, H. Bando, G. Saito, K. Kajimura and T. Ishiguro, *J. Phys. Soc. Jpn.*, **54**, 1236–1239 (1985).

[46] V. N. Laukhin, E. E. Kostyuchenko, Y. V. Sushko, I. F. Shchegolev and E. B. Yagubskii, *JETP Lett.*, **41**, 81–84 (1985).
[47] F. Creuzet, G. Creuzet, D. Jerome, D. Schweitzer and H. J. Keller, *J. Phys. Lett.*, **46**, 1079–1085 (1985).
[48] H. Urayama, H. Yamochi, G. Saito, K. Nozawa, T. Sugano, M. Kinoshita, S. Sato, K. Oshima, A. Kawamoto and J. Tanaka, *Chem. Lett.*, 55–58 (1988).
[49] A. M. Kini, U. Geiser, H. H. Wang, K. D. Carlson, J. M. Williams, W. K. Kwok, K. G. Vandervoort, J. E. Thompson and D. L. Stupka, *Inorg. Chem.*, **29**, 2555–2557 (1990).
[50] U. Geiser, A. J. Schultz, H. H. Wang, D. M. Watkins, D. L. Stupka, J. M. Williams, J. E. Schirber, D. L. Overmyer, D. Jung, J. J. Novoa and M. H. Whangbo, *Physica C*, **174**, 475–486 (1991).
[51] T. Ishiguro, H. Ito, Y. Yamauchi, E. Ohmichi, M. Kubota, H. Yamochi, G. Saito, M. V. Kartsovnik, M. A. Tanatar, Y. V. Sushko and G. Y. Logvenov, *Synth. Met.*, **85**, 1471–1478 (1997).
[52] H. Yamochi, T. Komatsu, N. Matsukawa, G. Saito, T. Mori, M. Kusunoki and K. Sakaguchi, *J. Am. Chem. Soc.*, **115**, 11319–11327 (1993).
[53] H. Taniguchi, M. Miyashita, K. Uchiyama, K. Satoh, N. Mori, H. Okamoto, K. Miyagawa, K. Kanoda, M. Hedo and Y. Uwatoko, *J. Phys. Soc. Jpn.*, **72**, 468–471 (2003).
[54] T. Mallah, C. Hollis, S. Bott, M. Kurmoo, P. Day, M. Allan and R. H. Friend, *J. Chem. Soc., Dalton Trans.*, 859–865 (1990).
[55] H. Miyasaka, Y. Yoshino, T. Ishii, R. Kanehama, T. Manabe, M. Yamashita, H. Nishikawa, I. Ikemoto, H. Kishida, H. Matsuzaki and H. Okamoto, *J. Solid State Chem.*, **168**, 418–426 (2002).
[56] M. Kurmoo, A. W. Graham, P. Day, S. J. Coles, M. B. Hursthouse, J. M. Caulfield, J. Singleton, L. Ducasse and P. Guionneau, *J. Am. Chem. Soc.*, **117**, 12209–12217 (1995).
[57] E. Coronado, J. R. Galan-Mascaros, C. J. Gomez-Garcia and V. Laukhin, *Nature*, **408**, 447–449 (2000).
[58] R. P. Schumaker, V. Y. Lee and E. M. Engler, *IBM Res. Rep.* (1983).
[59] R. Kato, H. Kobayashi, A. Kobayashi and Y. Sasaki, *Chem. Lett.*, 1231–1234 (1985).
[60] R. Kato, H. Kobayashi, A. Kobayashi and Y. Sasaki, *Chem. Lett.*, **14**, 1943–1946 (1985).
[61] R. Kato, H. Kobayashi and A. Kobayashi, *Synth. Met.*, **42**, 2093–2096 (1991).
[62] A. Kobayashi, R. Kato, T. Naito and H. Kobayashi, *Synthe. Met.*, **56**, 2078–2083 (1993).
[63] H. Kobayashi, H. Tomita, T. Naito, A. Kobayashi, F. Sakai, T. Watanabe and P. Cassoux, *J. Am. Chem. Soc.*, **118**, 368–377 (1996).
[64] L. Brossard, R. Clerac, C. Coulon, M. Tokumoto, T. Ziman, D. K. Petrov, V. N. Laukhin, M. J. Naughton, A. Audouard, F. Goze, A. Kobayashi, H. Kobayashi and P. Cassoux, *Eur. Phys. J. B*, **1**, 439–452 (1998).
[65] S. Uji, H. Shinagawa, T. Terashima, T. Yakabe, Y. Terai, M. Tokumoto, A. Kobayashi, H. Tanaka and H. Kobayashi, *Nature*, **410**, 908–910 (2001).
[66] S. Uji, H. Shinagawa, C. Terakura, T. Terashima, T. Yakabe, Y. Terai, M. Tokumoto and A. Kobayashi, *Phys. Rev. B*, **64**, 024531 (2001).
[67] S. Uji, C. Terakura, T. Terashima, T. Yakabe, Y. Terai, M. Tokumoto, A. Kobayashi, F. Sakai, H. Tanaka and H. Kobayashi, *Phys. Rev. B*, **65**, 113101 (2002).

[68] S. Uji, T. Terashima, C. Terakura, T. Yakabe, Y. Terai, S. Yasuzuka, Y. Imanaka, M. Tokumoto, A. Kobayash, F. Saka, H. Tanaka, H. Kobayashi, L. Balicas and J. S. Brooks, *J. Phys. Soc. Jpn.*, **72**, 369–373 (2003).
[69] S. Uji, S. Yasuzuka, M. Tokumoto, H. Tanaka, A. Kobayashi, B. Zhang, H. Kobayashi, E. S. Choi, D. Graf and J. S. Brooks, *Phys. Rev. B*, **72**, 184505 (2005).
[70] H. Fujiwara, H. Kobayashi, E. Fujiwara and A. Kobayashi, *J. Am. Chem. Soc.*, **124**, 6816–6817 (2002).
[71] H. Fujiwara and H. Kobayashi, *Bull. Chem. Soc. Jpn.*, **78**, 1181–1196 (2005).
[72] T. Konoike, S. Uji, T. Terashima, M. Nishimura, S. Yasuzuka, K. Enomoto, H. Fujiwara, B. Zhang and H. Kobayashi, *Phys. Rev. B*, **70**, 094514 (2004).
[73] K.-i. Hiraki, H. Mayaffre, M. Horvatic, C. Berthier, S. Uji, T. Yamaguchi, H. Tanaka, A. Kobayashi, H. Kobayashi and T. Takahashi, *J. Phys. Soc. Jpn.*, **76**, 124708 (2007).
[74] S. Fujiyama, M. Takigawa, J. Kikuchi, H. B. Cui, H. Fujiwara and H. Kobayashi, *Phys. Rev. Lett.*, **96**, 217001 (2006).
[75] T. Mori and M. Katsuhara, *J. Phys. Soc. Jpn.*, **71**, 826–844 (2002).
[76] K. Kikuchi, K. Murata, Y. Honda, T. Namiki, K. Saito, T. Ishiguro, K. Kobayashi and I. Ikemoto, *J. Phys. Soc. Jpn.*, **56**, 3436–3439 (1987).
[77] K. Kikuchi, K. Murata, Y. Honda, T. Namiki, K. Saito, H. Anzai, K. Kobayashi, T. Ishiguro and I. Ikemoto, *J. Phys. Soc. Jpn.*, **56**, 4241–4244 (1987).
[78] H. Ito, D. Suzuki, Y. Yokochi, S. Kuroda, M. Umemiya, H. Miyasaka, K.-I. Sugiura, M. Yamashita and H. Tajima, *Phys. Rev. B: Condens. Matter*, **71**, 212503 (2005).
[79] G. C. Papavassiliou, G. A. Mousdis, J. S. Zambounis, A. Terzis, A. Hountas, B. Hilti, C. W. Mayer and J. Pfeiffer, *Synth. Met.*, **27**, B379–B383 (1988).
[80] T. Takahashi, Y. Kobayashi, T. Nakamura, K. Kanoda, B. Hilti and J. S. Zambounis, *Physica C*, **235–240**, 2461–2462 (1994).
[81] K. Takimiya, Y. Kataoka, Y. Aso, T. Otsubo, H. Fukuoka and S. Yamanaka, *Angew. Chem. Int. Ed.*, **40**, 1122–1125 (2001).
[82] T. Kawamoto, T. Mori, K. Takimiya, Y. Kataoka, Y. Aso and T. Otsubo, *Phys. Rev. B*, **65**, 140508 (2002).
[83] K. Takimiya, M. Kodani, Y. Kataoka, Y. Aso, T. Otsubo, T. Kawamoto and T. Mori, *Chem. Mater.*, **15**, 3250–3255 (2003).
[84] K. Takimiya, A. Takamori, Y. Aso, T. Otsubo, T. Kawamoto and T. Mori, *Chem. Mater.*, **15**, 1225–1227 (2003).
[85] K. Takimiya, M. Kodani, N. Niihara, Y. Aso, T. Otsubo, Y. Bando, T. Kawamoto and T. Mori, *Chem. Mater.*, **16**, 5120–5123 (2004).
[86] M. Kodani, A. Takamori, K. Takimiya, Y. Aso and T. Otsubo, *J. Solid State Chem.*, **168**, 582–589 (2002).
[87] T. Kawamoto, T. Mori, K. Enomoto, T. Konoike, T. Terashima, S. Uji, A. Takamori, K. Takimiya and T. Otsubo, *Phys. Rev. B: Condens. Matter*, **73**, 024503 (2006).
[88] J.-I. Yamada, M. Watanabe, H. Akutsu, S. I. Nakatsuji, H. Nishikawa, I. Ikemoto and K. Kikuchi, *J. Am. Chem. Soc.*, **123**, 4174–4180 (2001).
[89] E. S. Choi, D. Graf, J. S. Brooks, J. Yamada, H. Akutsu, K. Kikuchi and M. Tokumoto, *Phys. Rev. B: Condens. Matter*, **70**, 024517 (2004).
[90] J. Yamada, H. Akutsu, H. Nishikawa and K. Kikuchi, *Chem. Rev.*, **104**, 5057–5083 (2004).

[91] W. Knop and G. Schnedermann, *J. Prakt. Chem.*, **37**, 461–475 (1846).
[92] J. M. Williams, A. J. Schultz, A. E. Underhill and K. Carneiro, in *Extended Linear Chain Compounds*, Vol. **1** (ed. J.S. Miller), Plenum Press, New York, 1982, pp. 73–118.
[93] J. R. Ferraro and J. M. Williams, *Introduction to Synthetic Electrical Conductors*, Academic Press, New York, 1987.
[94] A. E. Underhill, D. M. Watkins, J. M. Williams and K. Carneiro, in *Extended Linear Chain Compounds* (ed. J.S. Miller), Vol. **1**, Plenum Press, New York, pp. 119–156, 1982.
[95] A. P. Ginsberg, J. W. Koepke and J. J. Hauser, *Inorg. Chem.*, **15**, 514–519 (1976).
[96] A. H. Reis, Jr, in *Extended Linear Chain Compounds*, Vol. **1** (ed. J.S. Miller), Plenum Press, New York, 1982, pp. 157–196.
[97] H. Endres, H. J. Keller, R. Lehmann and J. Weiss, *Acta Crystallogr., Sect. B.*, **32**, 627–628 (1976).
[98] A. Gleizes, T. J. Marks and J. A. Ibers, *J. Am. Chem. Soc.*, **97**, 3545–3546 (1975).
[99] L.-S. Lin, T. J. Marks, C. R. Kannewurf, J. W. Lyding, M. S. McClure, M. T. Ratajack and T.-C. Whang, *J. Chem. Soc., Chem. Commun.*, 954–955 (1980).
[100] B. M. Hoffman, J. Martinsen, L. J. Pace and J. A. Ibers, in *Extended Linear Chain Compounds*, Vol. **3** (ed. J. S. Miller), Plenum Press, New York, 1982, pp. 459–549.
[101] J. L. Petersen, C. S. Schramm, D. R. Stojakovic, B. M. Hoffman and T. J. Marks, *J. Am. Chem. Soc.*, **99**, 286–288 (1977).
[102] C. J. Schramm, R. P. Scaringe, D. R. Stojakovic, B. M. Hoffman, J. A. Ibers and T. J. Marks, *J. Am. Chem. Soc.*, **102**, 6702–6713 (1980).
[103] T. Inabe and H. Tajima, *Chem. Rev.*, **104**, 5503–5534 (2004).
[104] J. A. Thompson, K. Murata, D. C. Miller, J. L. Stanton, W. E. Broderick, B. M. Hoffman and J. A. Ibers, *Inorg. Chem.*, **32**, 3546–3553 (1993).
[105] M. Matsuda, T. Naito, T. Inabe, N. Hanasaki, H. Tajima, T. Otsuka, K. Awaga, B. Narymbetov and H. Kobayashi, *J. Mater. Chem.*, **10**, 631–636 (2000).
[106] E. I. Stiefel, *Dithiolene Chemistry. Synthesis, Properties and Applications*, John Wiley & Sons, Inc., Hoboken, NJ, 2004.
[107] R. M. Olk, B. Olk, W. Dietzsch, R. Kirmse and E. Hoyer, *Coord. Chem. Rev*, **117**, 99–131 (1992).
[108] M. Almeida and R. T. Henriques, in *Handbook of Organic Conductive Molecules and Polymers*, Vol. **1** (ed. H. S. Nalwa), John Wiley & Sons, Inc., New York, 1997, pp. 87–149.
[109] P. Cassoux, *Coord. Chem. Rev.*, **185-186**, 213–232 (1999).
[110] A. E. Pullen and R. M. Olk, *Coord. Chem. Rev.,* **188**, 211–262 (1999).
[111] N. Robertson and L. Cronin, *Coord. Chem. Rev.*, **227**, 93–127 (2002).
[112] H. Alves, D. Simao, I. C. Santos, V. Gama, R. T. Henriques, H. Novais and M. Almeida, *Eur. J. Inorg. Chem.*, 1318–1329 (2004).
[113] E. B. Lopes, H. Alves, I. C. Santos, D. Graf, J. S. Brooks, E. Canadell and M. Almeida, *J. Mater. Chem.*, **18**, 2825–2832 (2008).
[114] P. I. Clemenson, *Coord. Chem. Rev*, **106**, 171–203 (1990).
[115] A. E. Underhill and M. M. Ahmad, *J. Chem. Soc., Chem. Commun.*, 67–68 (1981).
[116] A. Kobayashi, T. Mori, Y. Sasaki, H. Kobayashi, M. M. Ahmad and A. E. Underhill, *Bull. Chem. Soc. Jpn.*, **57**, 3262–3268 (1984).

[117] T. Devic, B. Domercq, P. Auban-Senzier, P. Molinié and M. Fourmigué, *Eur. J. Inorg. Chem.*, 2844–2849 (2002).
[118] H. Imai, T. Inabe, T. Otsuka, T. Okuno and K. Awaga, *Phys. Rev. B: Condens. Matter*, **54**, R6838–R6840 (1996).
[119] C. Faulmann and P. Cassoux, in *Dithiolene Chemistry. Synthesis, Properties, and Applications*, Vol. **52** (ed. E.I. Stiefel), John Wiley & Sons, Inc., Hoboken, NJ, 2004, pp. 399–489.
[120] E. B. Yagubskii, A. I. Kotov, E. E. Laukhina, A. A. Ignat'ev, L. I. Buravov, A. G. Khomenko, V. E. Shklover, S. S. Nagapetyan and Y. T. Struchkov, *Synth. Met.*, **42**, 2515–2522 (1991).
[121] I. Hawkins and A. E. Underhill, *J. Chem. Soc., Chem. Commun.*, 1593–1594 (1990).
[122] O. A. Dyachenko, S. V. Konovalikhin, A. I. Kotov, G. V. Shilov, E. B. Yagubskii, C. Faulmann and P. Cassoux, *J. Chem. Soc., Chem. Commun.*, 508–510 (1993).
[123] K. Awaga, T. Okuno, Y. Maruyama, A. Kobayashi, H. Kobayashi, S. Schenk and A. E. Underhill, *Inorg. Chem.*, **33**, 5598–5600 (1994).
[124] N. Le Narvor, N. Robertson, T. Weyland, J. D. Kilburn, A. E. Underhill, M. Webster, N. Svenstrup and J. Becher, *Chem. Commun.*, 1363–1364 (1996).
[125] M. Nakano, A. Kuroda, T. Maikawa and G.-E. Matsubayashi, *Mol. Cryst. Liq. Cryst.*, **284**, 301–305 (1996).
[126] M. Kumasaki, H. Tanaka and A. Kobayashi, *J. Mater. Chem.*, **8**, 301–307 (1998).
[127] J. P. M. Nunes, M. J. Figueira, D. Belo, I. C. Santos, B. Ribeiro, E. B. Lopes, R. J. Henriques J. Vidal-Gancedo, J. Veciana, C. Rovira and M. Almeida, *Chem. Eur. J.*, **13**, 9841–9849 (2007).
[128] H. Tanaka, Y. Okano, H. Kobayashi, W. Suzuki and A. Kobayashi, *Science*, **291**, 285–287 (2001).
[129] A. Kobayashi, H. Tanaka and H. Kobayashi, *J. Mater. Chem.*, **11**, 2078–2088 (2001).
[130] G. N. Schrauzer and V. Mayweg, *J. Am. Chem. Soc.*, **84**, 3221–3221 (1962).
[131] T. B. Rauchfuss, Synthesis of transition metal dithiolenes, in *Dithiolene Chemistry. Synthesis, Properties, and Applications*, Vol. **52** (ed. E.I. Stiefel), John Wiley & Sons, Inc., Hoboken, NJ, 2004, pp. 1–54.
[132] M. Fourmigué, *Coord. Chem. Rev.*, **178–180**, 823–864 (1998).
[133] M. Fourmigué, *Acc. Chem. Res.*, **37**, 179–186 (2004).
[134] S. A. Baudron, N. Avarvari and P. Batail, *Inorg. Chem.*, **44**, 3380–3382 (2005).
[135] S. Eid, M. Fourmigue, T. Roisnel and D. Lorcy, *Inorg. Chem.*, **46**, 10647–10654 (2007).
[136] G. Steimecke, R. Kirmse and H. Hoyer, *Z. Chem.*, **15**, 28–29 (1975).
[137] G. Steimecke, H.-J. Sieler, R. Kirmse and E. Hoyer, *Phosphorus and Sulfur*, **7**, 49–55 (1979).
[138] C. Wang, A. S. Batsanov, M. R. Bryce and J. A. K. Howard, *Synthesis*, **11**, 1615–1618 (1998).
[139] S. Wawzonek and S. M. Heilmann, *J. Org. Chem.*, **39**, 511–514 (1974).
[140] G. Bontempelli, F. Magno, G.-A. Mazzocchin and R. Seeber, *J. Electroanal. Chem.*, **63**, 231–237 (1975).
[141] M. F. Hurley and J. Q. Chambers, *J. Org. Chem.*, **46**, 775–778 (1981).
[142] N. Svenstrup and J. Becher, *Synthesis*, 215–234 (1995).
[143] K. S. Varma, A. Bury, N. J. Harris and A. E. Underhill, *Synthesis*, 837–838 (1987).
[144] O. Jeannin and M. Fourmigue, *C. R. Chim.*, **9**, 1287–1294 (2006).

[145] P. Cassoux, L. Valade, H. Kobayashi, A. Kobayashi, R. Clark and A. E. Underhill, *Coord. Chem. Rev.*, **110**, 115–160 (1991).
[146] L. Binet, J. M. Fabre, C. Montginoul, K. B. Simonsen and J. Becher, *J. Chem. Soc., Perkin Trans.*, **1**, 783–788 (1996).
[147] L. Valade, J.-P. Legros, M. Bousseau, P. Cassoux, M. Garbauskas and L. V. Interrante, *J. Chem. Soc. Dalton Trans.*, 783–794 (1985).
[148] M. L. Kaplan, *J. Cryst. Growth*, **33**, 161–164 (1976).
[149] H. Anzai, *J. Cryst. Growth*, **33**, 185–187 (1976).
[150] J. R. Andersen, E. M. Engler and K. Bechgaard, *Ann. NY Acad. Sci.*, **313**, 293–300 (1978).
[151] M. Bousseau, L. Valade, M.-F. Bruniquel, P. Cassoux, M. Garbauskas, L. V. Interrante and J. Kasper, *Nouv. J. Chim.*, **8**, 3–6 (1984).
[152] P. Cassoux, L. Valade and P.-L. Fabre, Electrochemical methods, electrocrystallisation, in *Comprehensive Coordination Chemistry II: From Biology to Nanotechnology, Fundamentals: ligands, Complexes, Synthesis, Purification and Structure*, Vol. **1** (ed. A.B.P. Lever), Elsevier, Amsterdam, 2003, pp. 761–773.
[153] P. Batail, K. Boubekeur, M. Fourmigué and J.-C.P. Gabriel, *Chem. Mater.*, **10**, 3005–3015 (1998).
[154] J. Fraxedas, *Molecular Organic Materials: Synthesis, Characterisation and Physical Properties. From Molecules to Crystalline Solids*, Cambridge University Press, Cambridge, 2006.
[155] K. Wang, in *Dithiolene Chemistry. Synthesis, Properties, and Applications*, Vol. **52** (ed. E.I. Stiefe), John Wiley & Sons, Inc., Hoboken, NJ, 2004, pp. 267–314.
[156] H. Urayama, H. Yamochi, G. Saito, S. Sato, A. Kawamoto, J. Tanaka, T. Mori, Y. Maruyama and H. Irokuchi, *Chem. Lett.*, 463–466 (1988).
[157] H. H. Wang, A. M. Kini, L. K. Montgomery, U. Geiser, K. D. Carlson, J. M. Williams, J. E. Thompson, D. M. Watkins and W. K. Kwok, *Chem. Mater.*, **2**, 482–484 (1990).
[158] H. Mori, *Intl. J. Mod. Phys. B*, **8**, 1–45 (1994).
[159] T. Komatsu, T. Nakamura, N. Matsukawa, H. Yamochi, G. Saito, H. Ito, T. Ishiguro, M. Kusunoki and K. Sakaguchi, *Solid State Commun.*, **80**, 843–847 (1991).
[160] T. Komatsu, N. Matsukawa, T. Inoue and G. Saito, *J. Phys. Soc. Jpn.*, **65**, 1340–1354 (1996).
[161] J. B. Tommasino, B. Pomarede, D. Medus, D. deMontauzon and P. Cassoux, *Mol. Cryst. Liq. Cryst.*, **237**, 445–456 (1993).
[162] M. Bousseau, L. Valade, J.-P. Legros, P. Cassoux, M. Garbauskas and L. V. Interrante, *J. Am. Chem. Soc.*, **108**, 1908–1916 (1986).
[163] L. Valade, J. P. Legros, D. De Montauzon, P. Cassoux and L. V. Interrante, *Isr. J. Chem.*, **27**, 353–362 (1986).
[164] J. H. Welch, R. D. Bereman, P. Singh and C. Moreland, *Inorg. Chim. Acta*, **158**, 17–25 (1989).
[165] J. H. Welch, R. D. Bereman and P. Singh, *Inorg. Chem.*, **29**, 68–73 (1990).
[166] C. Faulmann, A. Errami, J. P. Legros, P. Cassoux, E. B. Yagubskii and A. I. Kotov, *Synth. Met.*, **56**, 2057–2062 (1993).
[167] C. Faulmann, P. Cassoux, E. B. Yagubskii and L. V. Vetoshkina, *New J. Chem.*, **17**, 385–391 (1993).

[168] E. B. Yagubskii, A. I. Kotov, L. I. Buravov, A. G. Khomenko, V. E. Shklover, S. S. Nakhapetyan, Y. T. Struchkov, L. V. Vetoshkina and L. Y. Ukhin, *Synth. Met.*, **35**, 271–280 (1990).
[169] E. B. Yagubskii, A. I. Kotov, A. G. Khomenko, L. I. Buravov, A. I. Shchegolev and R. P. Shibaeva, *Synth. Met.*, **46**, 255–259 (1992).
[170] E. B. Yagubskii, L. A. Kushch, V. V. Gritsenko, O. A. Dyachenko, L. I. Buravov and A. G. Khomenko, *Synth. Met.*, **70**, 1039–1041 (1995).
[171] U. A. Geiser, J. Schultz, H. H. Wang, M. A. Beno and J. M. Williams, *Acta Crystallogr., Sect. C*, **C44**, 259–262 (1988).
[172] G. A. Bowmaker, P. D. W Boyd and G. K. Campbell, *Inorg. Chem.*, **22**, 1208–1213 (1983).
[173] L. Brossard, M. Ribault, M. Bousseau, L. Valade and P. Cassoux, *C. R. Acad. Sci.*, **302-II**, 205–210 (1986).
[174] L. Brossard, M. Ribault, L. Valade and P. Cassoux, *Physica B*, **143**, 378–380 (1986).
[175] L. Brossard, M. Ribault, L. Valade and P. Cassoux, *J. Phys.*, **50**, 1521–1534 (1989).
[176] L. Brossard, H. Hurdequint, M. Ribault, L. Valade, J. P. Legros and P. Cassoux, *Synth. Met.*, **27**, 157–162 (1988).
[177] H. Tajima, M. Inokuchi, A. Kobayashi, T. Ohta, R. Kato, H. Kobayashi and H. Kuroda, *Chem. Lett.*, 1235–1238 (1993).
[178] H. Kobayashi, K. Bun, T. Naito, R. Kato and A. Kobayashi, *Chem. Lett.*, **21**, 1909–1912 (1992).
[179] R. Kato, Y. Kashimura, S. Aonuma, N. Hanasaki and H. Tajima, *Solid State Commun.*, **105**, 561–565 (1998).
[180] R. Kato, A. Tajima, A. Nakao and M. Tamura, *J. Am. Chem. Soc.*, **128**, 10016–10017 (2006).
[181] A. Kobayashi, H. Kim, Y. Sasaki, R. Kato, H. Kobayashi, S. Moriyama, Y. Nishio, K. Kajita and W. Sasaki, *Chem. Lett.*, 1819–1822 (1987).
[182] A. Kobayashi, H. Kim, Y. Sasaki, S. Moriyama, Y. Nishio, K. Kajita, W. Sasaki, R. Kato and H. Kobayashi, *Synth. Met.*, **27 B**, 339–346 (1988).
[183] A. Kobayashi, H. Kobayashi, A. Miyamoto, R. Kato, R. A. Clark and A. E. Underhill, *Chem. Lett.*, **20**, 2163–2166 (1991).
[184] R. Kato, N. Tajima, M. Tamura and J.-I. Yamaura, *Phys. Rev. B*, **66**, 020508 (2002).
[185] J. Ribas and P. Cassoux, *C. R. Acad. Sci.*, **293**, 287–290 (1981).
[186] H. Kim, A. Kobayashi, Y. Sasaki, R. Kato and H. Kobayashi, *Chem. Lett.*, 1799–1802 (1987).
[187] E. Canadell, I. E. I Rachidi, S. Ravy, J. P. Pouget, L. Brossard and J. P. Legros, *J. Phys.*, **50**, 2967–2981 (1989).
[188] S. Ravy, E. Canadell and J. P. Pouget, in *ISSP International Symposium*, Vol. **51** (eds G. Saito and S. Kagoshima), Springer Verlag, Berlin, 1990, pp. 252–256.
[189] W. Kang, D. Jerome, L. Valade and P. Cassoux, *Synth. Met.*, **42**, 2343–2345 (1991).
[190] R. Bozio, I. Zanon, A. Girlando and C. Pecile, *J. Chem. Phys.*, **71**, 2282–2293 (1979).
[191] L. Brossard, M. Ribault, L. Valade and P. Cassoux, *Phys. Rev. B*, **42**, 3935–3943 (1990).
[192] J. E. Schirber, D. L. Overmyer, J. M. Williams, H. H. Wang, L. Valade and P. Cassoux, *Phys. Lett. A*, **120**, 87–88 (1987).

[193] E. Canadell, S. Ravy, J. P. Pouget and L. Brossard, *Solid State Commun.*, **75**, 633–638 (1990).
[194] H. Tajima, M. Inokuchi, S. Ikeda, M. Arifuku, T. Ohta, M. Tamura, A. Kobayashi, R. Kato, T. Naito, H. Kobayashi and H. Kuroda, *Synth. Met.*, **70**, 1035–1038 (1995).
[195] A. Kobayashi, A. Sato, K. Kawano, T. Naito, H. Kobayashi and T. Watanabe, *J. Mater. Chem.*, **5**, 1671–1679 (1995).
[196] E. Kogut, J. A. Tang, A. J. Lough, C. M. Widdifield, R. W. Schurko and U. Fekl, *Inorg. Chem.*, **45**, 8850–8852 (2006).
[197] M. C. Aragoni, M. Arca, F. A. Devillanova, F. Isaia, V. Lippolis, A. Mancini, L. Pala, Slawin, A. M. Z. and J. D. Woollins, *Inorg. Chem.*, **44**, 9610–9612 (2005).
[198] F. Bigoli, P. Cassoux, P. Deplano, M. L. Mercuri, M. A. Pellinghelli, G. Pintus, A. Serpe and E. F. Trogu, *J. Chem. Soc., Dalton Trans.*, 4639–4644 (2000).
[199] S. Curreli, P. Deplano, C. Faulmann, A. Ienco, C. Mealli, M. L. Mercuri, L. Pilia, G. Pintus, A. Serpe and E. F. Trogu, *Inorg. Chem.*, **43**, 5069–5079 (2004).
[200] A. Sournia-Saquet, B. Garreau-de Bonneval, K. I. Chane-Ching and L. Valade, *J. Electroanal. Chem.*, **624**, 84–90 (2008).
[201] E. Canadell, *New J. Chem.*, **21**, 1147–1159 (1997).
[202] A. Kobayashi, M. Sasa, W. Suzuki, E. Fujiwara, H. Tanaka, M. Tokumoto, Y. Okano, H. Fujiwara and H. Kobayashi, *J. Am. Chem. Soc.*, **126**, 426–427 (2004).
[203] C. Rovira, J. J. Novoa, J. L. Mozos, P. Ordejon and E. Canadell, *Phys. Rev. B*, **65**, 081104 (2002).
[204] H. Seo, S. Ishibashi, Y. Okano, H. Kobayashi, A. Kobayashi, H. Fukuyama and K. Terakura, *J. Phys. Soc. Jpn.*, **77**, 023714 (2008).
[205] S. Ishibashi, M. Terakura and A. Kobayashi, *J. Phys. Soc. Jpn.*, **77**, 024702 (2008).
[206] H. Tanaka, M. Tokumoto, S. Ishibashi, D. Graf, E. S. Choi, J. S. Brooks, S. Yasuzuka, Y. Okano, H. Kobayashi and A. Kobayashi, *J. Am. Chem. Soc.*, **126**, 10518–10519 (2004).
[207] H. Tanaka, S. Hara, M. Tokumoto, A. Kobayashi and H. Kobayashi, *Chem. Lett.*, **36**, 1006–1007 (2007).
[208] H. Tanaka, H. Kobayashi and A. Kobayashi, *J. Am. Chem. Soc.*, **124**, 10002–10003 (2002).
[209] E. Fujiwara, K. Hosoya, A. Kobayashi, H. Tanaka, M. Tokumoto, Y. Okano, H. Fujiwara, H. Kobayashi, Y. Fujishiro, E. Nishibori, M. Takata and M. Sakata, *Inorg. Chem.*, **47**, 863–874 (2008).
[210] R. M. Metzger, in *Organic Conductors, Superconductors and Magnets: From Synthesis to Molecular Electronics*, Vol. **139** (eds L. Ouahab and E. B. Yagubskii), Kluwer Academic and NATO Scientific Affairs Division, 2004, pp. 269–293.
[211] R. M. Metzger, *J. Mater. Chem.*, **18**, 4364–4396 (2008).
[212] D. L. Allara, C. McGuiness and R. M. Metzger, in *Organic Conductors, Superconductors and Magnets: From synthesis to Molecular Electronics*, Vol. **139** (eds L. Ouahab and E. B. Yagubskii), Kluwer Academic and NATO Scientific Affairs Division, 2004, pp. 295–315.
[213] P. Delhaes, in *Organic Conductors, Superconductors and Magnets: From synthesis to Molecular Electronics*, Vol. 139 (eds L. Ouahab and E. B. Yagubskii), Kluwer Academic and NATO Scientific Affairs Division, 2004, pp. 217–230.
[214] U. Geiser and J. A. Schlueter, *Chem. Rev.*, **104**, 5203–5242 (2004).
[215] N. L. Rosi and C. A. Mirkin, *Chem. Rev.*, **105**, 1547–1562 (2005).

[216] J. C. Love, L. A. Estroff, J. K. Kriebel, R. G. Nuzzo and G. M. Whitesides, *Chem. Rev.*, **105**, 1103–1170 (2005).
[217] T. W. Kelley, P. F. Baude, C. Gerlach, D. E. Ender, D. Muyres, M. A. Haase, D. E. Vogel and S. D. Theiss, *Chem. Mater.*, **16**, 4413–4422 (2004).
[218] S. Logothetidis, *Mater. Sci. Eng., B*, **152**, 96–104 (2008).
[219] M. Leufgen, O. Rost, C. Gould, G. Schmidt, J. Geuits, L. W. Molenkamp, N. S. Oxtoby, M. Mas-Torrent, N. Crivillers, J. Veciana and C. Rovira, *Organ. Electron.*, **9**, 1101–1106 (2008).
[220] D. Tobjörk, N. J. Kaihovirta, T. Mäkelä, F. S. Pettersson and R. Österbacka, *Organ. Electron.*, **9**, 931–935 (2008).
[221] H. Wada, K. Shibata, Y. Bando and T. Mori, *J. Mater. Chem.*, **18**, 4165–4171 (2008).
[222] J. R. Bates, P. Kathirgamanathan and R. W. Miles, *Electron. Lett.*, **31**, 1225–1227 (1995).
[223] S. A. Wang, Y. Q. Liu, X. B. Huang, G. Yu and D. B. Zhu, *J. Phys. Chem. B*, **107**, 12639–12642 (2003).
[224] A. Bousseksou, C. Vieu, J.-F. Létard, P. Demont, J. P. Tuchagues, L. Malaquin, J. Menegotto and L. Salmon, 2003, International extension 2004, FR2829293, PCT EP1430552.
[225] F. Teyssandier and A. Dollet, in *Non-equilibrium processing of materials* (ed. C. Suryanarayana), Pergamon Press, Amsterdam, 1999, pp. 257–285.
[226] D. de Caro, C. Faulmann and L. Valade, *Chem. Eur. J.*, **13**, 1650–1663 (2007).
[227] A. Tracz, J. Ulanski, T. Pakula and M. Kryszewski, *Pol. Pat.* PL116850 (1981).
[228] A. Tracz, T. Pakula and J. K. Jeszka, *Mater. Sci. Poland*, **22**, 415–421 (2004).
[229] E. Laukhina, J. Ulanski, A. Khomenko, S. Pesotskii, V. Tkatchev, L. Atovmyan, E. Yagubskii, C. Rovira, J. Veciana, J. Vidal-Gancedo and V. Laukhin, *J. Phys. I France*, **7**, 1665–1675 (1997).
[230] I. Langmuir, *J. Am. Chem. Soc.*, **39**, 1848–1906 (1917).
[231] K. B. Blodgett, *J. Am. Chem. Soc.*, **57**, 1007–1022 (1935).
[232] A. Deluzet, S. Perruchas, H. Bengel, P. Batail, S. Molas and J. Fraxedas, *Adv. Funct. Mater.*, **12**, 123–128 (2002).
[233] G. L. Cui, W. Xu, C. W. Guo, X. W. Xiao, H. Xu, D. Q. Zhang, L. Jiang and D. B. Zhu, *J. Phys. Chem. B*, **108**, 13638–13642 (2004).
[234] G. L. Cui, W. Xu, X. H. Zhou, X. W. Xiao, L. Jiang and D. B. Zhu, *Colloids Surf., A*, **272**, 63–67 (2006).
[235] D. de Caro, I. Malfant, J.-P. Savy and L. Valade, *J. Phys.: Condens. Matter*, **20**, 184012 (2008).
[236] L. Pilia, I. Malfant, D. de Caro, F. Senocq, A. Zwick and L. Valade, *New J. Chem.*, **28**, 52–55 (2004).
[237] G. Hodes, *Electrochemistry of Nanomaterials*, Wiley-VCH Verlag GmbH, 2001.
[238] H. Hasegawa, T. Kubota and S. Mashiko, *Synth. Met.*, **135**, 763–764 (2003).
[239] H. M. Yamamoto, H. Ito, K. Shigeto, K. Tsukagoshi and R. Kato, *J. Am. Chem. Soc.*, **128**, 700–701 (2006).
[240] B. R. Saunders, K. S. Murray, R. J. Fleming and Y. Korbatieh, *Chem. Mater.*, **5**, 809–819 (1993).
[241] G. Wang, H. Chen, H. Zhang, H. Zhang, Y. Shen, C. Yuan, Z. Lu, G. Wang and W. Yang, *Phys. Lett. A*, **237**, 165–168 (1998).

[242] P. H. S. Picciani, F. G. Souza, N. M. Comerlato and B. G. Soares, *Synth. Met.*, **157**, 1074–1079 (2007).
[243] A. L. Prieto, M. S. Sander, M. S. Martin-Gonzalez, R. Gronsky, T. Sands and A. M. Stacy, *J. Am. Chem. Soc.*, **123**, 7160–7161 (2001).
[244] L.-L. Xing, D.-P. Li, S.-X. Hu, H.-Y. Jing, H. Fu, Z.-H. Mai and M. Li, *J. Am. Chem. Soc.*, **128**, 1749–1754 (2006).
[245] M. Thakur, R. C. Haddon and S. H. Glarum, *J. Cryst. Growth*, **106**, 724–727 (1990).
[246] S. Molas, P. Batail, A. Figueras, M. A. Petruska, J. Santiso, D. R. Talham and J. Fraxedas, *J. Mater. Chem.*, **10**, 2662–2665 (2000).
[247] S. Molas, J. Caro, J. Santiso, A. Figueras, J. Fraxedas, C. Mézière, M. Fourmigué and P. Batail, *J. Cryst. Growth*, **218**, 399–409 (2000).
[248] I. Malfant, K. Rivasseau, J. Fraxedas, C. Faulmann, D. deCaro, L. Valade, L. Kaboub, J.-M. Fabre and F. Senocq, *J. Am. Chem. Soc.*, **128**, 5612–5613 (2006).
[249] L. Valade, D. de Caro, J.-P. Savy, I. Malfant, C. Faulmann, M. Almeida, J. Fraxedas and J. S. Brooks, *J. Low Temp. Phys.*, **142**, 393–396 (2006).
[250] D. de Caro, J. Fraxedas, C. Faulmann, I. Malfant, J. Milon, J.-F. Lamère, V. Collière and L. Valade, *Adv. Mater.*, **16**, 835–838 (2004).
[251] J.-P. Savy, D. de Caro, L. Valade and J.-P. Legros, *Europhys. Lett.*, **78**, 37005 (2007).
[252] J.-P. Savy, D. de Caro, C. Faulmann, L. Valade, M. Almeida, T. Koike, H. Fujiwara, T. Sugimoto, J. Fraxedas, T. Ondarçuhu and C. Pasquier, *New J. Chem.*, **31**, 519–527 (2007).
[253] L. Zang, Y. Che and J. S. Moore, *Acc. Chem. Res.*, **41**, 1596–1608 (2008).
[254] L. C. Palmer and S. I. Stupp, *Acc. Chem. Res.*, **41**, 1674–1684 (2008).
[255] T. Nakamura, in *Charge Transfer Salts, Fullerenes and Photoconductors*, Vol. **1** (ed. H. S. Nalwa), John Wiley & Sons Ltd, Chichester, 1997, pp. 727–780.
[256] T. Nakamura, Y. Miura, M. Matsumoto, H. Tashibana, M. Tanaka and Y. Kawabata, in *The Physics and Chemistry of Organic Superconductors*, Vol. **51** (eds G. Saito and S. Kagoshima), Springer-Verlag, Berlin/Heidelberg, 1990, pp. 424–427.
[257] D. R. Talham, *Chem. Rev.*, **104**, 5479–5502 (2004).
[258] M. Kitao, H. Matsui, S. I. Morita, Y. F. Miura, M. Sugi M. Hedo and Y. Uwatoko, LB films, *Trans. Mater. Res. Soc. Jpn.*, **31**, 621–624 (2006).
[259] Y. F. Miura, M. Horikiri, S. H. Saito and M. Sugi, *Solid State Commun.*, **113**, 603–605 (2000).
[260] Y. F. Miura, M. Horikiri, S. Tajima, T. Wakaita, S. Saito and M. Sugi, *Synth. Met.*, **120**, 727–728 (2001).
[261] Y. F. Miura, M. Horikiri, S. Tajima, T. Wakaita, S. H. Saito and M. Sugi, *Synth. Met.*, **133**, 663–664 (2003).
[262] Y. F. Miura, K. Hayashi, M. Kitao, M. Takagi, H. Matsui and M. Sugi, *Thin Solid Films*, **516**, 2518–2521 (2008).
[263] Y. Takigawa, R. Watanabe, S. Morita, Y. F. Miura and M. Sugi, *Jpn. J. Appl. Phys. 1*, **45**, 394–396 (2006).
[264] E. E. Laukhina, V. A. Merzhanov, S. I. Pesotskii, A. G. Khomenko, E. B. Yagnbskii, J. Ulanski, M. Kryszewski and J. K. Jeszka, *Synth. Met.*, **70**, 797–800 (1995).
[265] M. Mas-Torrent, E. Laukhina, C. Rovira, J. Veciana, V. Tkacheva, L. Zorina and S. Khasanov, *Adv. Funct. Mater.*, **11**, 299–303 (2001).

[266] A. G. B. da Cruz, J. L. Wardell, M. V. D. Rangel, R. A. Simao and A. M. Rocco, *Synth. Met.*, **157**, 80–90 (2007).
[267] A. G. B. da Cruz, J. L. Wardell and A. M. Rocco, *J. Mater. Sci.*, **43**, 5823–5836 (2008).
[268] B. R. Saunders, K. S. Murray, R. J. Fleming, R. Cervini and N. S. Allen, in *Handbook of Conductive Polymers: Spectroscopy and Physical Properties*, Vol. **3** (ed. H. S. Nalwa), John Wiley & Sons Ltd, 1997, p. 634.
[269] R. Shen, W. Xu, D. Zhang and D. Zhu, *Solid State Commun.*, **130**, 401–404 (2004).
[270] C. Faulmann, S. Dorbes, B. Garreau de Bonneval, G. Molnar, A. Bousseksou, C. J. Gomez-Garcia, E. Coronado and L. Valade, *Eur. J. Inorg. Chem.*, 3261–3270 (2005).
[271] S. Dorbes, L. Valade, J. Real and C. Faulmann, *Chem. Commun.*, 69–71 (2005).
[272] N. F. Tadahiko Ishikawa, Yoshitaka Matsubara, Ryohei Nakajima, Ken Onda, Yoichi Okimoto, Shin-ya Koshihara, Masafumi Tamura, Reizo Kato, Maciej Lorenc, Eric Collet, *Phys. Status Solidi c*, **6**, 112–115 (2009).
[273] F. Setifi, L. Ouahab, S. Golhen, Y. Yoshida and G. Saito, *Inorg. Chem.*, **42**, 1791–1793 (2003).
[274] K. Hervé, Y. L. Gal, L. Ouahab, S. Golhen and O. Cador, *Synth. Met.*, **153**, 461–464 (2005).
[275] L. Ouahab and T. Enoki, *Eur. J. Inorg. Chem.*, 933–941 (2004).
[276] K. Kubo, A. Nakao, Y. Ishii, T. Yamamoto, M. Tamura, R. Kato, K. Yakushi and G.-E. Matsubayashi, *Inorg. Chem.*, **47**, 5495–5502 (2008).

5

Molecular Nanomagnets

Richard E.P. Winpenny and Eric J.L. McInnes
School of Chemistry, The University of Manchester, Manchester, UK

5.1 INTRODUCTION

At a time when there is an increasing tendency of funding agencies worldwide to want to target research on specific challenges, it is always worth remembering that this is not how science works. Many advances occur by accident, by fortunate coincidence where research designed to solve one problem opens up a quite different area. Molecular nanomagnets are a very good example of where this principle applies.

The area of molecular magnetism grew slowly through the 1970s and 1980s, largely aiming for production of ferro- or ferrimagnetic materials but where the spin carriers were linked through organic groups rather than through oxides. There was also some effort in understanding how the superexchange interaction through organic ligands might depend on structural parameters. The study of zero-dimensional magnetic materials, that is *molecules* which have interesting magnetic behaviour, was a very minor component in these studies. Probably the most significant result was the report by Caneschi *et al.* of a cyclic hexametallic cage $[Mn_6(hfac)_{12}(NITPh)_6]$ (hfac = 1,1,1,6,6,6-hexafluoroacetylacetonate, NITPh is a nitronyl nitroxide),[1] where the metal centres are linked by nitronyl nitroxide radicals, leading to a molecule with a spin of $S = 12$ in

Molecular Materials Edited by Duncan W. Bruce, Dermot O'Hare and Richard I. Walton

the ground state due to antiferromagnetic exchange between the $S = 5/2$ Mn(II) ions and the $S = 1/2$ nitroxides.

The change in emphasis in molecular magnetism came about in a rather circuitous way, and arises from studies within Christou's group dedicated to the synthesis of model compounds for the oxygen-evolving complex in Photosystem II. This work resulted in a very large number of polymetallic mixed-valent manganese complexes being made; the magnetic properties of these compounds were studied in collaboration with David Hendrickson's group and involved reports of many high spin molecules through the 1980s. The work was very well reviewed at the time.[2]

In attempting to make a model for the highest oxidation state of the oxygen-evolving complex, the Christou group made a compound of formula $[Mn_{12}O_{12}(O_2CPh)_{16}(H_2O)_4]$.[3] This was a new compound, but rather surprisingly it had a very close precedent: in 1980 Lis had made $[Mn_{12}O_{12}(O_2CMe)_{16}(H_2O)_4]$ and published the crystal structure and preliminary variable temperature magnetic susceptibility measurements.[4] The magnetic data were not interpreted. Even this is not the first such proposal of a dodecanuclear manganese complex from this type of reaction; in 1921 Weinland and Fischer had proposed formation of a dodecanuclear manganese compound,[5] however no techniques were available at the time to allow them to arrive at the correct formula.

Both $\{Mn_{12}\}$ molecules have spin ground states of $S = 10$, so this is not as high as the hexanuclear manganese wheel reported by Gatteschi's group. However the physics of the $\{Mn_{12}\}$ cages is much more exciting because the spin ground state is very anisotropic, and this anisotropy of the spin introduces an energy barrier to reorientation of the magnetisation of the molecule. This, in turn, means that if a sample of $\{Mn_{12}\}$ is magnetised at low temperature the magnetisation is lost only slowly when the magnetic field is switched off.[6] The behaviour is analogous to that of superparamagnets; however, it takes place in a molecule much smaller than a paramagnetic nanoparticle, and in a species which is monodisperse and where an ordered crystallographic array of such species can be made. These two factors allow more precise studies of the physics of such objects than can be achieved on nanoparticles, and it is this aspect that has attracted so many physicists to studying these materials. As the compound retains magnetisation in a single molecule, this led to the name 'single molecule magnets' (SMMs); in many ways this is a contradiction in terms, but the phrase has stuck.

The other cause for excitement was that in $\{Mn_{12}\}$ cages magnetic information is being stored at a molecular level – in an object which is several orders of magnitude smaller than the magnetic grains used to store information in data storage devices. Therefore, potentially, the density of

information being stored could also rise by several orders of magnitude. The scale of the advance can be seen by considering a typical magnetic tape, which might store ninety minutes of music; if this could be made to work with $\{Mn_{12}\}$ the tape could store one hundred and fifty years of music. The drawback, and technically it remains unsurmounted, is that the temperature at which $\{Mn_{12}\}$ stores information for significant periods is less than 4 K. There is no significant advantage in data storage at such temperatures regardless of the density stored. Until the energy barrier to reorientation of magnetisation rises very significantly then use of SMMs in data storage remains a distant dream.

However, the inspiration caused by SMMs has led to physicists and chemists working together much more closely than before in studying the physics of molecular nanomagnets, and that will probably lead to new technology. There are already clear advantages in such systems in areas such as low temperature cooling, and proposals that molecular nanomagnets could be used in applications such as quantum information processing. None of this work would have resulted without the original papers on $\{Mn_{12}\}$.

Reviews of the physics and the quantum phenomena of SMMs have been published previously,[7,8] including an excellent book authored by Gatteschi *et al.*[9] Synthetic routes to SMMs, covering the literature exhaustively until May 2005, were reviewed by Aromì and Brechin in 2007.[10] Here we provide an introduction to the physics which should be comprehensible to an undergraduate chemist (deliberately avoiding mathematical descriptions), discuss the techniques used and what the results mean, and point out some recent trends which may come to dominate molecular magnetism beyond 2010, in the way that SMMs dominated the area for the last decade and a half.

Finally, a word on nomenclature: the use of the name 'single molecule magnet' is restricted to a molecule that exhibits slow magnetisation relaxation. The term 'molecular nanomagnet'[9] (MNM) is adopted as a generic term for large paramagnetic molecules; hence, SMMs are a subset of MNMs. (Some physicists refer to any large paramagnetic molecule as an SMM.)

5.2 A VERY BRIEF INTRODUCTION TO MAGNETOCHEMISTRY

Before describing the magnetic properties of complicated exchange coupled molecules, it is worth briefly summarising some basic

definitions and concepts. This discussion is kept as qualitative as possible but the reader should be aware that a full appreciation of these concepts and practical interpretation of magnetic data require an understanding of the spin Hamiltonian formalism that underlies it. This is covered in many good books on general quantum mechanics and/or spectroscopy.[9,11–13]

When a paramagnet is placed in a magnetic field (H), its energy is lowered as the magnetic moments tend to align with the field: this gives us a definition of 'magnetisation', $M = -dE/dH$. How quickly the sample magnetises with applied field is the magnetic susceptibility, $\chi = dM/dH$. Up to a certain field strength this relationship is linear, $M = \chi H$, and χ is independent of H (Figure 5.1).

The origin of this paramagnetism is unpaired electrons: the electron spin (S) is accompanied by a magnetic moment. Its orientation is quantised, described by the quantum number M_S (the projection of the spin on the axis of quantisation) taking values from $+S \ldots -S$ in integer steps; hence the state S is $2S+1$-fold degenerate.

In an applied magnetic field the energies of these states vary as $E(M_S) = M_S g\beta H$, where g is the electronic g value and β is the Bohr magneton (*e.g.* Figure 5.2). This is called Zeeman splitting. For an ensemble of paramagnets there is a Boltzmann population distribution among these states. The bulk magnetisation arises from their unequal population. As H is increased, or as the temperature is decreased, the population will tend towards $M_S = -S$ (*i.e.* the spins of all the molecules will tend to align with H), and the magnetisation increases. By considering the contribution of the population of each individual M_S state (varying in field as $M_S g\beta H$) to the total magnetisation ($M = -dE/dH$),

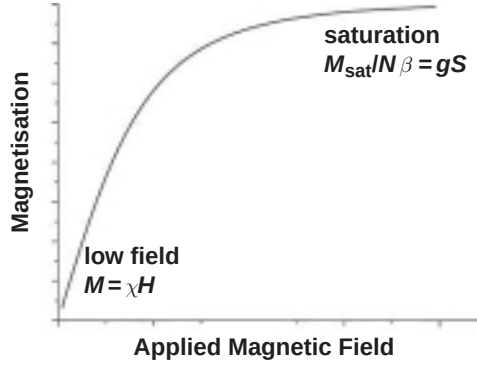

Figure 5.1 Typical magnetisation *vs* applied magnetic field curve for a paramagnet

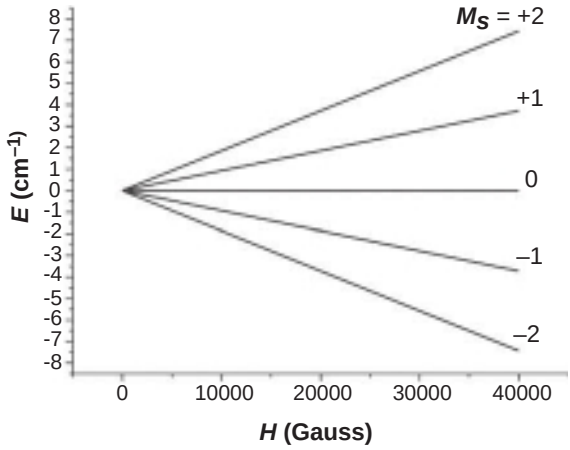

Figure 5.2 Zeeman splitting of an isotropic $S = 2$ paramagnet in an applied magnetic field

it is possible to show that when $M = \chi H$ the molar susceptibility is given by:

$$\chi = \frac{N\beta^2}{3kT} g^2 S(S+1) \tag{5.1}$$

where N is Avogadro's number, k is Boltzmann's constant and T is the temperature. Hence, χ is proportional to $1/T$ – this is Curie's law. At sufficiently high field and/or low temperature all the paramagnets will be in the state $M_S = -S$. Then all the spins in the ensemble are aligned and increasing H or decreasing T has no further effect on M – it is saturated, with $M_{sat} = g\beta S$ or simply gS per molecule if units of $N\beta$ are used. Hence, both χ (or rather χT) and M_{sat} can be used to determine the spin.

In the above we have assumed that the $2S+1$ different M_S states are degenerate in zero field. This is not generally true: the degeneracy can be lifted by the magnetic dipolar interaction between unpaired electrons and by interactions with excited states *via* spin-orbit coupling. This is called zero field splitting (ZFS). The form of the ZFS depends on the symmetry of the molecule. In molecules with cubic symmetry (*e.g.* O_h, T_d) the ZFS is nil (at least to second order, see later). In axially symmetric molecules (*e.g.* D_{4h}, C_{4v}) the M_S states split in zero field according to $E(M_S) = D[M_S^2 - S(S+1)/3]$ (in the usual definition) where D is called the axial ZFS parameter (Figure 5.3). Hence, states with the largest or smallest $|M_S|$ are at lowest energy for negative or positive D, respectively.

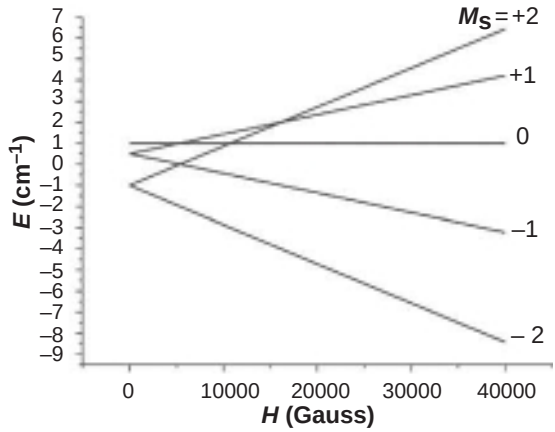

Figure 5.3 Zeeman splitting of an $S = 2$ paramagnet with $D = -0.5$ cm^{-1}, with the applied field along the molecular z axis

Note the ZFS introduces preferred orientations for the spin in zero applied field. For negative D, in axial symmetry, this is along the unique symmetry axis (z), for positive D it is in the plane (xy) perpendicular to this axis, leading to the terms 'easy axis' or 'easy plane' type magnetic anisotropy. Application of an applied field along z separates the states as $M_S g\beta H$ as before (*e.g.* Figure 5.3).

The anisotropy in the magnetic properties means that M and χ are dependent on the orientation of the molecule with respect to **H** (a vector). Mathematically χ is a 3×3 tensor (for isotropic systems it can be treated as a scalar). The ZFS is also described by a 3×3 tensor, with principal components $D_{xx,yy,zz}$, where x,y,z correspond to specific orientations of the molecule and $D_{xx}+D_{yy}+D_{zz} = 0$. From these, axial (see above) and rhombic ZFS parameters can be defined as $D = D_{zz} - (D_{xx} + D_{yy})/2$ and $E = (D_{xx}-D_{yy})/2$. The latter can be nonzero only in symmetry lower than axial (*i.e.* $x \neq y$). In this case there are now easy, intermediate and hard axes of magnetisation. For $S \geq 2$ other ZFS terms become allowed – these will be considered later.

When more than one paramagnetic centre is in the molecule the magnetic properties become dominated by the interactions between them – the exchange coupling. For two paramagnetic centres of spin S_A and S_B, respectively, it is possible to define a total spin quantum number for the pair which will take all values from S_A+S_B to $|S_A-S_B|$ in integer steps. For example, interaction of two spin 1/2 ions will generate total spin states $S = 0$ and 1 (Figure 5.4). Their separation in energy is quantified by the isotropic exchange constant (J). The interaction is described as

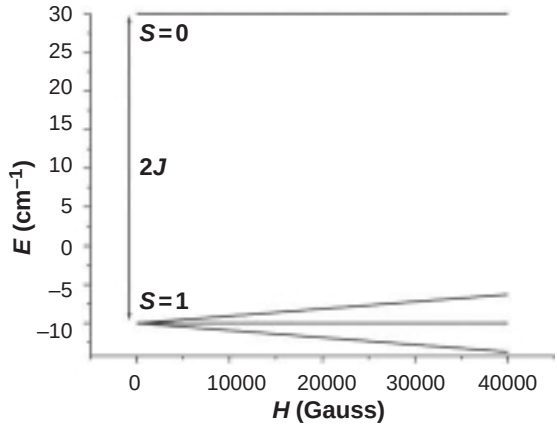

Figure 5.4 Zeeman diagram for a ferromagnetically coupled dimer of $S = 1/2$ centres, calculated with $2J = +40$ cm^{-1}

ferro- or antiferromagnetic depending on whether the $S = 1$ or 0 state, respectively, is lowest in energy. There is no universal agreement on the definition of J, and the singlet–triplet gap is variously defined as $\pm J$, $\pm 2J$. Here we take the most commonly used convention in the chemistry literature that the energy gap is $2J$, with a negative value implying an antiferromagnetic interaction ($H = -2J\hat{S}_A.\hat{S}_B$ in Hamiltonian form).

Unlike an isolated spin, the product χT will now be strongly temperature dependent as the relative populations of singlet (diamagnetic) and triplet (paramagnetic) states change with temperature, and modelling of this behaviour allows determination of J (Figure 5.5). This involves

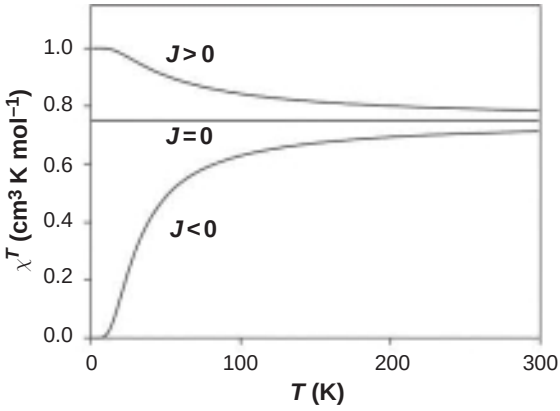

Figure 5.5 Calculated plots of χT *vs* T for a dimer of $S = 1/2$ ions with $2J = +40, -40$ and 0 cm^{-1} ($g = 2.0$)

summing over the weighted contributions from each individual state of the molecule. This is trivial for the above example, as there are only four states arising from the possible combinations of the M_S states of the individual ions. In general, for n coupled ions of spin S there will be $(2S+1)^n$ coupled states and the spin structures get complicated very rapidly with increasing size of cluster – $\{Mn_{12}\}$, for example, has 10^8 coupled states – and exact modelling to get J values may become impossible.

When all molecules are in the ground spin state the magnetic behaviour will be identical to that of an isolated paramagnet of that spin the low temperature limiting value of χT can be used to determine the ground state spin from Equation 5.1.

5.3 TECHNIQUES

Before describing the physics and chemistry of molecular nanomagnets in more detail, the experimental techniques that are most commonly used to probe their magnetic properties are surveyed briefly here. More technical detail on these and other techniques can be found in, for example, the recent text by Gatteschi *et al.*[9] and references therein.

5.3.1 Magnetometry

The determination of M and χ as a function of H and temperature (T) are usually performed using a SQUID (Superconducting QUantum Interference Device) magnetometer. This technique is an inductive method of measuring magnetic moments: the sample, magnetised by an external field, is moved through a set of sensing coils inducing a current which depends on the magnetic moment. In a SQUID magnetometer the sensing coils are superconducting and are inductively coupled to the SQUID itself, a superconducting ring containing one or more insulating barriers called Josephson junctions. The SQUID essentially acts as a very sensitive amplifier that can detect tiny induced fields, hence allowing measurement of very small magnetic moments.

However they are measured, the data are manipulated (with knowledge of the molar weight, and estimations of diamagnetic corrections for sample and holder) to give M, which is determined as a function of T and/or H.

Hence, the useful plots of χ (usually calculated as M/H), χT and χ^{-1} *vs* T at fixed H, and M *vs* H at fixed (usually low) T, can be constructed. These data can provide a wealth of information on exchange coupled clusters. An increase in χT as T decreases is a signature of low lying states with big spin S. If χT plateaus at low temperature, then the usual assumption is that only the ground state is populated and its value can be used to determine the value of S. An important early example of a high-spin ground state molecule is $[Mn_6(hfac)_{12}(NITPh)_6]$ (see above).[1] χT increases with decreasing temperature reaching a plateau at *ca* 75 $cm^3\,K\,mol^{-1}$ below 50 K (note the authors report the value per $\{Mn(hfac)_2(NITPh)\}$ unit; Figure 5.6). This gives a ground state spin of $S = 12$, consistent with antiferromagnetic coupling between Mn(II) and nitronyl nitroxide giving an alternating 'spin up' and 'spin down' structure. Note that an increase in χT with decreasing T is not a signature of ferromagnetic coupling, simply that there are low lying states of significant spin.

It is often the case that χT does not plateau at low temperature, even when only the ground state is populated. This can be a function of ZFS of the ground state, intermolecular interactions, or both. For samples with large magnetic anisotropy the crystallites may torque in the applied magnetic field and give readings different from those expected on the basis of Equation 5.1.

It is generally safer to take the ground state spin from the saturation value of M *vs* H at the lowest temperature available. Here the assumption

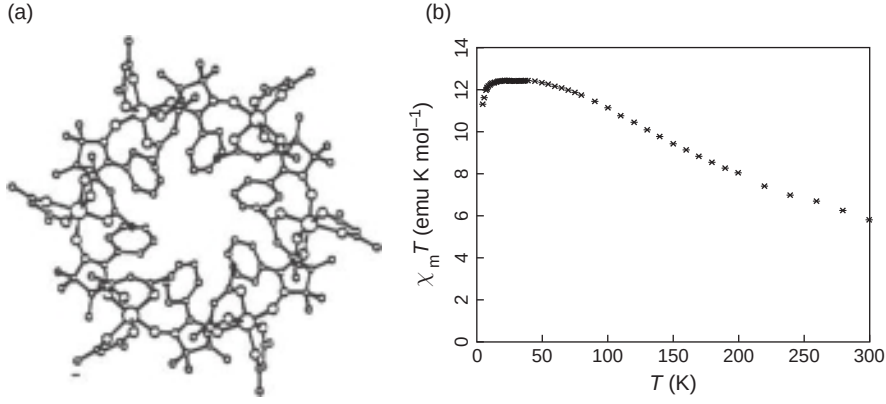

Figure 5.6 (a) Structure of $[Mn_6(hfac)_{12}(NITPh)_6]$. (b) $\chi T(T)$ per $\{Mn(Hfac)_2(NITPh)\}$ unit. Reprinted with permission from Caneschi *et al.*, 1988 [1]. Copyright (1988) American Chemical Society

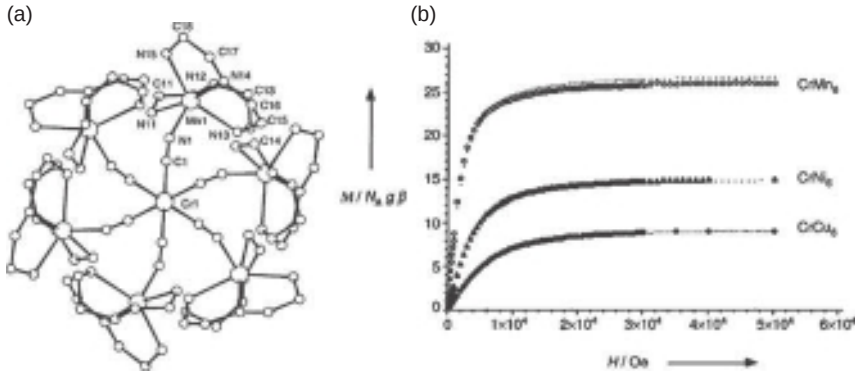

Figure 5.7 (a) Structure of $[Cr(CN–ML)_6]^{9+}$, where M^{II} = Mn, Ni, Cu. (b) Magnetisation as a function of applied magnetic field at 2 K. Reprinted with permission from Marmaud *et al.*, 2003 [14]. Copyright (2003) Wiley-VCH

is that if you can saturate the magnetisation then you are exclusively populating the ground state. For example, Figure 5.7 shows $M(H)$ data at 2 K for the heterometallic compounds $[Cr(CN–ML)_6]^{9+}$, where L is a penta-coordinating ligand that binds a divalent metal ion M and six $[ML]^{2+}$ fragments bind to a central $[Cr(CN)_6]^{3-}$ ion.[14] The M_{sat} values of 9 (M = Cu), 15 (Ni) and 27 $N\beta$ (Mn) imply ground states of $S = 9/2$, 15/2 and 27/2, respectively, which implies ferromagnetic Cr . . . M coupling for M = Cu and Ni and antiferromagnetic coupling for M = Mn. This agrees with $\chi T(T)$ data.

However, care needs to be taken. For example, if there are excited states of greater S than the ground state (this is the norm), then at some critical value of the applied field (H_c) the ground state will change, because the $M_S = -S$ levels decreases in energy more rapidly for larger S (*e.g.* Figure 5.8a). A recent example is the SMM $(Et_3NH)_2[Mn^{III}{}_{18}Mn^{II}{}_2O_{12}(OH)_2(O_3PCH_2Ph)_{12}(O_2CCMe_3)_{10}(py)_2]$.[15] Measured on a powder sample at 1.55 K the magnetisation saturates at 60 $N\beta$. However, a single crystal measurement shows a rapid saturation to a plateau at 40 $N\beta$, which then increases slowly to 60 $N\beta$. This indicates an $S = 20$ ground state with a low lying $S = 30$ excited state. It is proposed that the latter arises from flipping the spins of the two Mn^{II} ions.

If only the ground state is populated in the low temperature range, then M(H,T) data can in principle be modelled to determine the ZFS. However, excited state population can have similar effects and often there is not a unique fit to the data. ZFS parameters are more safely determined by spectroscopic methods (see below).

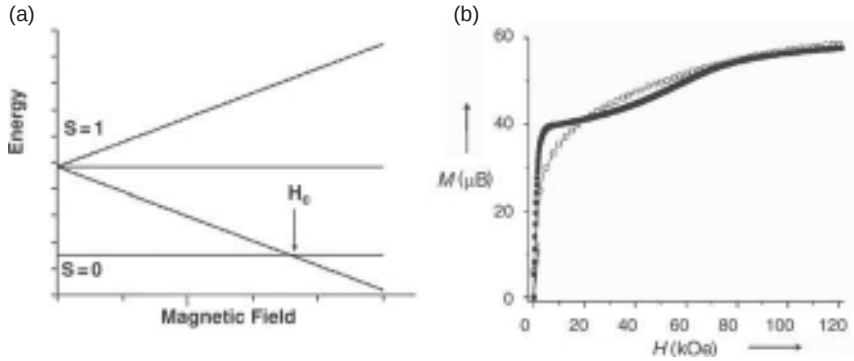

Figure 5.8 (a) Example of how ground spin state can change with applied magnetic field. (b) $M(H)$ for a $\{Mn_{20}\}$ SMM at 1.55 K, measured on a powder (open squares) and a single crystal (filled squares). Reprinted with permission from Maheswaran *et al.*, 2003 [15]. Copyright (2005) Wiley-VCH

Of course, magnetisation relaxation rate information can be obtained from monitoring M as a function of time (t), for example following saturation of M ($= M_0$) and then switching the field off. This often follows an exponential law, such that the relaxation time (or, more correctly, time constant) τ can be defined as:

$$M_t = M_0 \exp\left(\frac{-t}{\tau}\right) \tag{5.2}$$

If the relaxation is slow enough then magnetisation–applied field cycles can be performed to measure hysteresis loops (see later). In SMMs this slow relaxation is a result of the ZFS interactions in the ground spin state. Since magnetic anisotropy is being probed here, these measurements are ideally performed on single crystals.

5.3.2 AC Magnetometry

In AC susceptibility experiments a small alternating magnetic field is applied to the sample by means of an AC current in a surrounding coil. The alternating field induces an alternating magnetisation in the sample that is detected by a secondary coil. This can be performed in zero static field or with an additional static field. Since changes in the magnetisation with the alternating field are being measured (dM/dH) this gives the

susceptibility (χ_{AC}) directly with no assumptions about linearity of M *vs* H. Importantly, the frequency (ω) of the alternating field can be varied and this gives access to information on the dynamics of the magnetisation to much faster timescales than DC measurements. The susceptibility can be measured in-phase (χ_{AC}') and out-of-phase (χ_{AC}'') with the alternating field. If ω is small with respect to the magnetisation relaxation time (τ), then M oscillates in-phase with the AC field: χ_{AC}' should be equal to χ_{DC} and there is no out-of-phase signal. This, and the ability to measure in zero or very small static fields, can be exploited to determine ground state S (from $\chi_{AC}'T$) in the presence of low lying excited states. However, if the magnetic relaxation is slow then M cannot keep in phase with the oscillating field and a nonzero χ_{AC}'' will be observed, accompanied by a decrease in the in-phase signal, reaching a maximum when $\omega\tau = 1$. Measurements are typically performed at a series of fixed temperatures at several different ω. Thus, the temperature dependence of the relaxation time can be determined from the maxima in plots of $\chi_{AC}''(T)$ for each ω (Figure 5.9).

5.3.3 Micro-SQUIDs

Far greater sensitivity than a conventional SQUID magnetometer can be achieved with micro-SQUIDs.[17] Here the sample is placed directly on a SQUID loop of micrometre dimensions (actually an array of such loops) prepared by lithographic techniques. This technique can be used to study micro-metre sized single crystals, although it is not possible to determine the absolute magnetisation. The whole device can be placed in a dilution refrigerator allowing measurements down to mK temperatures. This has allowed the discovery of very important quantum physics in molecular nanomagnets (see below).

5.3.4 Specific Heat

The specific heat (C) is the amount of energy required, per unit mass or per mole, to raise the temperature of a substance by one degree. This is the derivative of its internal energy dU/dT, and since magnetic levels make a contribution to this their separations can in principle be measured from $C(T)$ measurements.[18] However, the magnetic contribution to the specific heat must be disentangled from that of lattice vibrational modes.

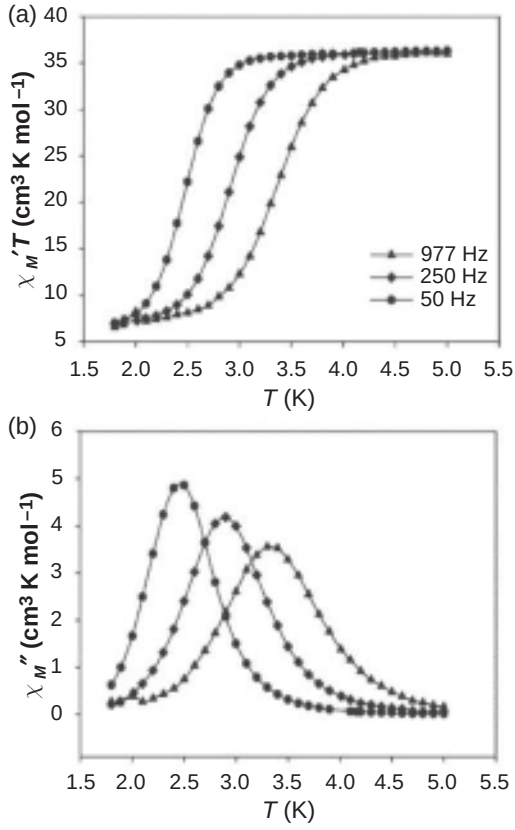

Figure 5.9 (a) Product of in-phase AC susceptibility and temperature ($\chi_M'T$) *vs* T for the $S = 17/2$ ground state SMM $[Mn_9O_7(O_2CMe)_{11}(thme)(py)_3(H_2O)_2]$. (b) Out-of-phase AC susceptibility (χ_M'') *vs* T measured at $\omega = 977$ (triangles), 250 (diamonds) and 50 Hz (circles). Reprinted with permission from the Piligkos *et al.*, 2005 [16]. Copyright (2005) ACS

Because the latter is utterly dominant above *ca* 10 K, the useful magnetic information (at least for molecules) is restricted to low temperatures. The level separations give rise to a so-called Schottky anomaly – a peak in the $C(T)$ curve. For a simple two-level system, when $kT << \Delta E$ there is insufficient thermal energy to promote population to the upper state; when $kT >> \Delta E$ the population of the states is approximately equal. In either case, increasing T has little effect on the internal energy, hence C is small. Between these extremes increasing T has a significant effect on the population distribution, hence $C(T)$ peaks and the energy gap can be determined. For example, $[Fe_{10}(O_2CCH_2Cl)_{10}(OMe)_{20}]$ has an $S = 0$ ground state with an $S = 1$ lowest lying excited state. The downward

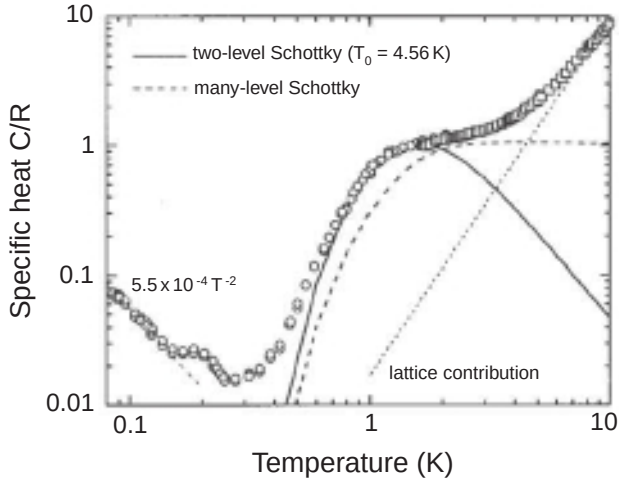

Figure 5.10 Specific heat of $[Fe_{10}(O_2CCH_2Cl)_{10}(OMe)_{20}]$ (open symbols), with modelled contributions from lattice (dotted line) and magnetic contributions considering only the two lowest total spin states (solid line). Reprinted with permission from Evangelisti *et al.*, 2006 [19]. Copyright (2006) Royal Society of Chemistry

trend in C with decreasing T (Figure 5.10) is due to the collapse of the lattice contribution, the pronounced shoulder at 1–3 K is due to the separation of the $S = 0$ and 1 states.[19] Modelling gives the splitting as 3.2 cm^{-1}. Hence, the level splitting can be determined in the absence of an applied magnetic field. Alternatively, a field can be applied to induce the splittings to be determined.

Magnetic (or structural) phase transitions (*e.g.* the onset of long-range ordering) are associated with 'λ-type' anomalies in $C(T)$ at the critical temperature – this can be an important test when assigning an observed magnetic phenomenon to molecular or cooperative behaviour. An excellent review on the use of specific heat measurements for molecular nanomagnets has been published by Evangelisti *et al.*[19]

5.3.5 Torque Magnetometry

Measurement of magnetic anisotropy can be performed by single crystal magnetometry methods. A particularly sensitive way to do this is by cantilever torque magnetometry where the crystal is mounted on an upper plate (the cantilever), fixed at one end, above a lower metallic plate. When a magnetic field is applied to an anisotropic substance it experiences a torque $\mathbf{T}$ given by the cross product $\mathbf{T} = \mathbf{M} \times \mathbf{H}$

(remembering that **M** and **H** are vector quantities). This is detected as a change in the capacitance between the two plates, since the torque changes the distance between them. The torque can be measured as a function of orientation and **H** and can give information on, for example, ZFSs or even exchange couplings. Nice examples illustrating both of these are provided by antiferromagnetic rings. For example, $[Cr_8F_8(O_2CCMe_3)_{16}]$ has $S = 0$ and $S = 1$ ground and first excited states, respectively.[20] The singlet state is, of course, isotropic and there is no torque signal if only this state is populated (*i.e.* at very low temperature). On increasing field a pronounced step appears at *ca* 7 T (Figure 5.11a) due to the anisotropy of the $S = 1$ state, which is now the ground state (as in Figure 5.8a). Because of the anisotropy of the triplet, the field at which this step is observed depends on the angle of the crystal (molecule) to the field (Figure 5.11b). Fitting these data gives the singlet–triplet gap (6.51 cm^{-1}) and the axial ZFS of the triplet ($D = 1.59$ cm^{-1}).[20]

With any magnetisation measurements on single crystals it has to be remembered that it is the property of the crystal that is being measured. If the molecules are not all magnetically equivalent (with respect to the applied field) then analysis of the data to determine molecular properties, for example ZFSs, is not straightforward. Spectroscopic methods, where transitions between the M_S states are observed, give this information more directly.

5.3.6 Electron Paramagnetic Resonance (EPR) Spectroscopy

In the EPR experiment, transitions are observed between the Zeeman split M_S components of a spin S in an applied field. Typical commercial

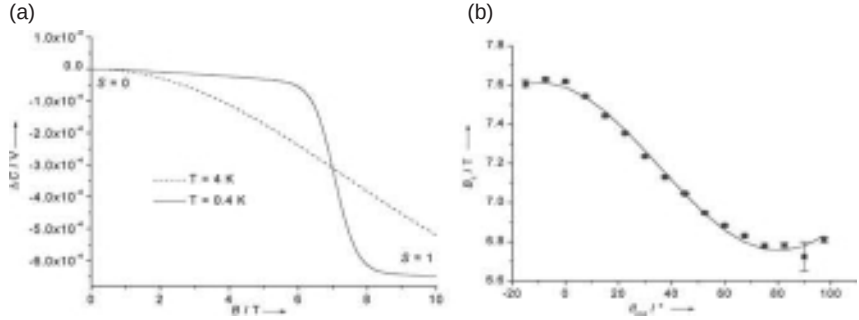

Figure 5.11 (a) Capacitance change of a single crystal of $[Cr_8F_8(O_2CCMe_3)_{16}]$ at $\theta = 45^o$ as a function of H. (b) Level crossing field as a function of orientation (θ) of crystal unique axis with respect to H, measured at 0.4 K. Reprinted with permission from van Slageren *et al.*, 2002 [20]. Copyright (2002) Wiley-VCH

spectrometers use electromagnets and the Zeeman splittings correspond to microwave energies. In the continuous wave (cw) experiment the frequency (ν) is kept constant and H is swept. The spectrum is usually detected as the first derivative of the absorption *via* a secondary small oscillating field. The selection rule is $\Delta M_S = \pm 1$ and hence for a spin S it is expected to see $2S$ allowed transitions, in the high field limit, for a given orientation of the field with respect to the molecule. Hence, the magnitude of S can be determined. For a simple $S = 1/2$ system the resonance condition $h\nu = g\beta H$ gives an accurate measure of the g value. In addition, for $S > 1/2$ the separations of the $2S$ lines are a function of the ZFS parameters. For an axially symmetric paramagnet in the high field limit the transitions are separated by $2|D|/g\beta$ or $|D|/g\beta$ (in field units) when H is oriented parallel or perpendicular, respectively, to the unique axis z (Figure 5.12).

By measuring EPR on a single crystal as a function of its orientation, it is possible to determine the orientation of the principal axes of the ZFS ($D_{xx,yy,zz}$) with respect to the crystal and, therefore, the molecular geometry. For powder samples the weighted sum of all orientations is measured.

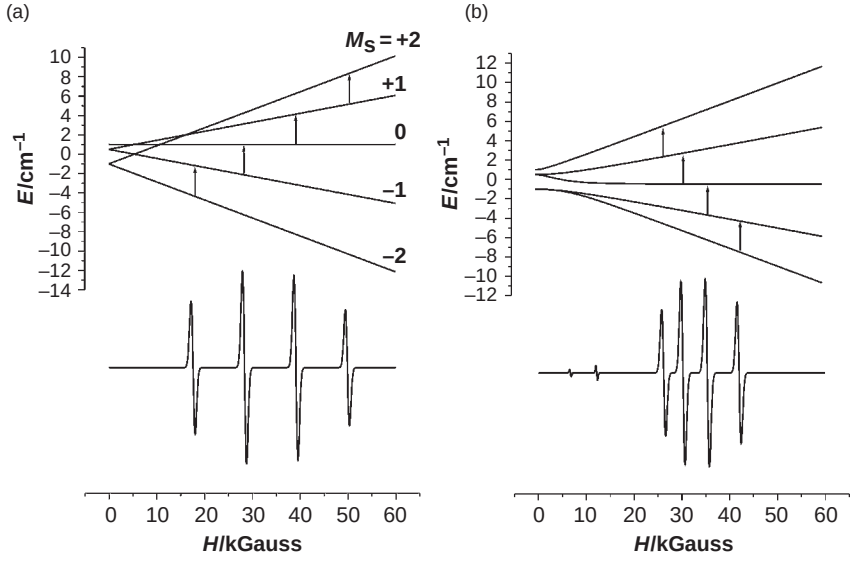

Figure 5.12 Calculated EPR spectra ($\nu = 93$ GHz; $T = 100$ K) for an axial $S = 2$ paramagnet with $g = 2.0$ and $D = -0.5\,\text{cm}^{-1}$. H oriented parallel (a) and perpendicular (b) to the unique axis (z). [Note that when H is not along z it induces mixing of the M_S states and the levels are nonlinear. This can also induce formally forbidden transitions (as seen at low field). At high field the states become linear and can be labelled as 'M_S' with the understanding that the quantisation is along H not z.]

However, measurement of the first derivative spectrum means that, in the high field limit, only features corresponding to x, y and z orientations will be observed, thus greatly simplifying matters. Unfortunately, measuring in the high field limit is not always possible. For very anisotropic samples it may be necessary to immobilise polycrystalline samples (*e.g.* in wax or as a pellet) in order to prevent torquing of the crystallites (see above).

For the example with negative D in Figure 5.12, it can be seen that with H parallel to z the transition originating from the lowest M_S state is at the lowest resonance field. Hence, at $kT << g\beta H$ (*i.e.* at low T and/or large H) this is the only transition observed. For H perpendicular to z only the highest field transition would be observed. The opposite would be true for positive D. Hence variable temperature behaviour (at high enough field/frequency) can be used to directly determine the sign of D.

Several of these features are illustrated for the SMM $[Fe_8O_2(OH)_{12}(tacn)_6]Br_8$ (Figure 5.13). This molecule has an $S = 10$ ground state with $D = -0.20$ cm^{-1}, hence the EPR spectrum is spread over a very wide field range and it is necessary to measure at high frequency with associated wide field sweeps.[21] Not all the $2S$ allowed transitions are observed because of the Boltzmann population distribution within the $2S+1$ multiplet. For example, when H is parallel to z the intensities decrease to higher field: this shows that D is negative. Analysis of powder and crystal data also show the rhombic nature of the ZFS, with $E = 0.038$ cm^{-1}. Other important (higher order) ZFS terms are also determined from the non-regular spacings of the transitions.

A comprehensive text on EPR of exchange coupled materials has been published by Bencini and Gatteschi[22] and an excellent tutorial on the benefits of high-frequency/field EPR as applied to high spin and anisotropic molecules by Barra *et al.*[23]

5.3.7 Inelastic Neutron Scattering (INS)

In INS a beam of monochromatic neutrons is fired at the sample under the study. The magnetic interaction between the neutrons (spin 1/2 particles) and the sample leads to scattering of the neutrons, with energy gain and loss, inducing transitions within the sample with the selection rules $\Delta S = 0, \pm 1$ and $\Delta M_S = 0, \pm 1$. Thus, INS can give direct information not only on ZFS interactions (as in EPR) but also inter-multiplet splittings,

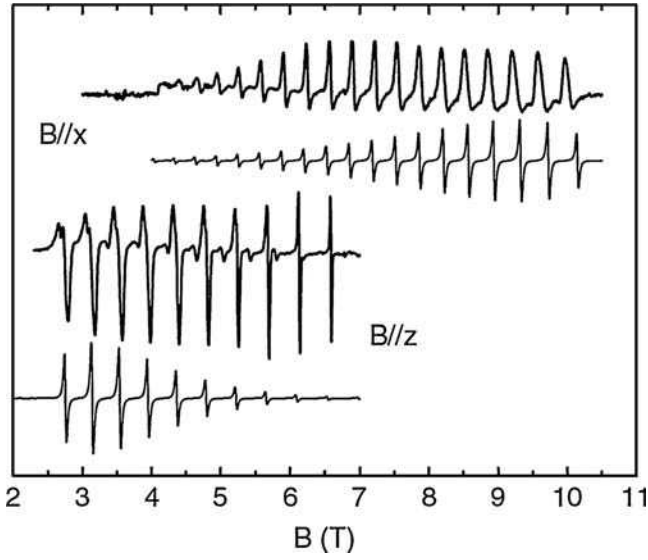

Figure 5.13 Experimental (upper) and calculated (lower) EPR spectra ($\nu = 190$ GHz) of a single crystal of $[Fe_8O_2(OH)_{12}(tacn)_6]Br_8$ oriented with applied field along the easy (z; $T = 20$ K) and hard (x; $T = 35$ K) axes of magnetisation. Reprinted with permission from Barra *et al.*, 2005 [21]. Copyright (2005) John Wiley & Sons, Ltd

hence exchange interactions (see later sections for examples). A further advantage is that the experiment can be performed in zero applied field (or finite static field). A disadvantage is the requirement for gramme-scale quantities of sample and that deuteration is often required due to the large cross-section of ^{1}H for incoherent neutron scattering.

As an example of the determination of ZFS parameters, Figure 5.14 shows the INS between 2 and 18 K of the SMM $[Mn_4O_3(O_2CMe)_4(dmb)_3]$, which has an $S = 9/2$ ground state, split by a near axial ZFS of $D = -0.46$ cm^{-1}.[24] The intense central peak arises from elastic scattering. The temperature-dependent peaks on either side arise from $\Delta M_S = +1$ and -1 transitions (energy loss and gain from the neutron) as illustrated in the level scheme. Similarly to EPR, modelling the peak positions gives the ZFS parameters very accurately (with the added advantage of being measured in zero field) and the temperature dependence gives the sign of D directly. An excellent review of INS as applied to molecular paramagnetic species has been published by Basler *et al.*[25]

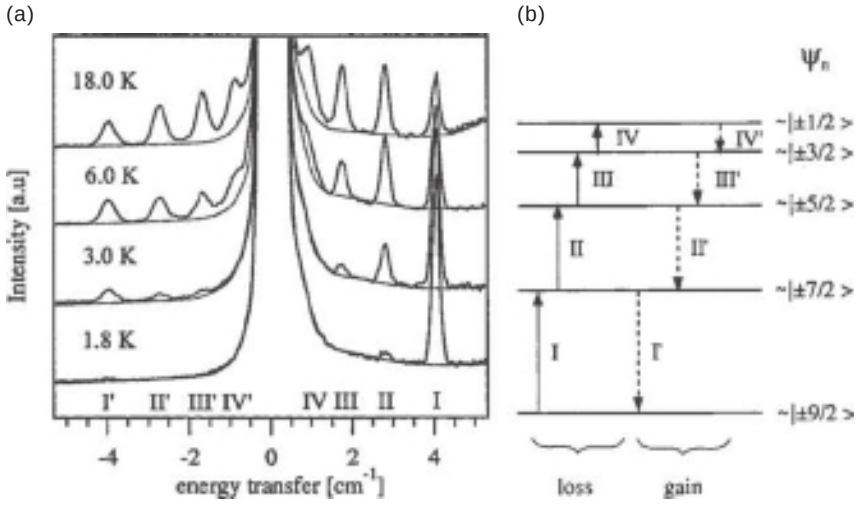

Figure 5.14 (a) INS spectra of $[Mn_4O_3(O_2CMe)_4(dmb)_3]$ recorded with incident neutron wavelength 7.5 Å. (b) Level scheme for $S = 9/2$ ground state and transition assignments for energy gain and loss. Reprinted with permission from Andres *et al.*, 2000 [24]. Copyright (2000) American Chemical Society

5.3.8 Nuclear Magnetic Resonance (NMR) Spectroscopy

'Standard' paramagnetic NMR is, of course, an important tool in the characterisation of paramagnetic molecules in solution, testing for example the cluster integrity. Over and above this, low temperature solid-state techniques can be used to probe the internal magnetic structure of clusters and to give information on local spin dynamics. The local fields experienced by the nuclei under study, and therefore their shifts in the NMR spectrum, are strongly affected by the electron spin density distribution (*via* the hyperfine interaction), and hence the latter can be determined. Electron spin dynamics can be probed *via* the NMR response at low temperature because the nuclear spin lattice relaxation rate ($1/T_1$) is strongly dependent on fluctuations in the molecular magnetisation (hence local hyperfine fields) which arise from thermally driven transitions between the M_S states for a given spin S (remembering that electron T_1 is much faster than nuclear T_1).[26]

For SMMs at temperatures below the blocking temperature, the magnetisation becomes frozen on the NMR timescale, that is, the local hyperfine fields become static. This is demonstrated spectacularly in $[Mn_{12}O_{12}(MeCO_2)_{16}(H_2O)_4]\cdot 2MeCO_2H.4H_2O$ by the observation of a ^{55}Mn (100% natural abundance, $I = 5/2$) NMR spectrum in *zero applied*

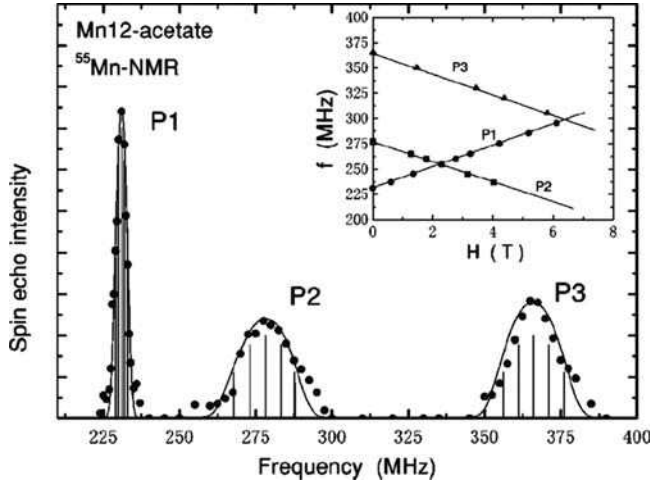

Figure 5.15 ^{55}Mn NMR spectrum in zero applied field of an oriented polycrystalline sample of $[Mn_{12}O_{12}(MeCO_2)_{16}(H_2O)_4]\cdot 2MeCO_2H\cdot 4H_2O$ at 1.5 K. P1 is from Mn^{IV}, P2,3 from Mn^{III}. Inset: Applied field dependence of the three resonances. Reprinted with permission from Furukawa *et al.*, 2001 [27]. Copyright (2001) American Physical Society

field (Figure 5.15), where a peak is observed for each magnetically unique ion [one Mn^{IV} and two Mn^{III} sites resulting from the tetragonal molecular symmetry].[27]

Magnetisation relaxation can be monitored by switching or reversing the external field and monitoring the NMR response as a function of time. Comprehensive reviews of NMR studies of molecular nanomagnets have been published recently by Borsa *et al.*[28,29]

5.4 SINGLE MOLECULE MAGNETS

5.4.1 Physics of Single Molecule Magnets

The physics of SMMs was quickly recognised as being important, since these materials combined some of the classical macroscale properties of a magnet (*e.g.* magnetisation hysteresis) with the quantum mechanical properties of a molecular species (*e.g.* tunnelling phenomena). Hence, they allowed the study of quantum size effects in magnets with huge advantages over, for example, magnetic nanoparticles, since they are essentially

perfectly monodisperse and also orientable in the form of single crystals. For example, this led to the first observations of quantum tunnelling of magnetisation[30,31] and quantum phase interference effects in magnets.[32]

5.4.1.1 Magnetic Hysteresis and Thermal Activation

The most obvious spectacular physical property of SMMs is such severe slowing of magnetisation relaxation at low temperature that hysteresis can be observed in magnetisation *vs* applied magnetic field response. This hysteresis is of an unambiguously *molecular* origin (*cf*. bulk magnets) and was first observed in $\{Mn_{12}\}$ (Figure 5.16a).[6] The magnetisation of the sample is saturated at a specific temperature. For a conventional paramagnet the $M(H)$ curve would retrace itself on decreasing H back towards zero. However, when the relaxation is slow (on the timescale of the experiment) then M will not decrease to nil at zero field but will have some remnant value. Applying the field in the opposite direction (negative H) will eventually force M back to nil (at the 'coercive field') and then ultimately saturate M in the opposite sense. Removing the field leaves an equal but opposite remnant magnetisation. This implies bistability – in zero applied field M can take one of two values. The molecule 'remembers' the sense of the field that was applied to it even after removal of the field. This immediately led to proposals that such molecules could be used to store information.

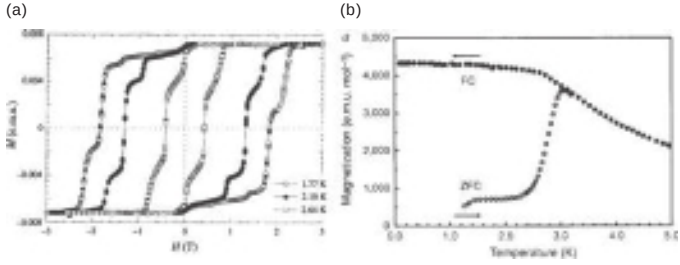

Figure 5.16 (a) Magnetisation *vs* applied magnetic field loops at 1.77, 2.10 and 2.64 K, measured on a single crystal of $[Mn_{12}O_{12}(MeCO_2)_{16}(H_2O)_4]\cdot 2MeCO_2H.$ $4H_2O$ with field oriented along the tetragonal axis (molecular z axis). The waiting time at each field is *ca* 10 min. (b) Magnetisation *vs* temperature measured in zero field cooled (ZFC) and field cooled (FC) regimes, see main text, for a 100 G field. Reprinted by permission from Sessoli *et al*., 1993 [6] and Thomas *et al*., 1996 [30]. Copyright (1993) and (1996) Macmillan Publishers Ltd

The magnetisation relaxation for $\{Mn_{12}\}$ is temperature dependent with the width of the loops becoming narrower at higher temperature (Figure 5.16a), and only being observed below a certain 'blocking' temperature (T_B). One measure of T_B is from the $M(H)$ behaviour in field cooled (FC) and zero field cooled (ZFC) regimes (Figure 5.16b). In the FC experiment the sample is cooled in an applied field and M is measured on decreasing T. In the ZFC experiment the sample is cooled in zero field (hence nil magnetisation) to base temperature, then the field is switched on and M measured as T is increased. These curves diverge when the relaxation is slow: for $\{Mn_{12}\}$ this occurs below *ca* 3 K (Figure 5.16b). With a faster experiment such as AC susceptibility measurements, slow relaxation is observed to higher temperatures: out-of-phase peaks are observed up to around 9 K for $\omega = 200$ kHz.[33] The temperature dependence of the relaxation time, from DC and AC measurements, shows that relaxation follows a thermally activated behaviour (Figure 5.17). The effective energy barrier to relaxation, U_{eff}, can then be determined from the Arrhenius equation:

$$\tau = \tau_0 \exp\left(\frac{U_{\text{eff}}}{T}\right) \tag{5.3}$$

Hence, fitting to a plot of $\ln(\tau)$ *vs* $1/T$ (or T, as in Figure 5.17) gives U_{eff}. For $\{Mn_{12}\}$ this was found to be $U_{\text{eff}} = 62$ K (43 cm^{-1}) with $\tau_0 = 2.1 \times 10^{-7}$ s.[6] This corresponds to relaxation times of *tens of years* below *ca* 2 K!

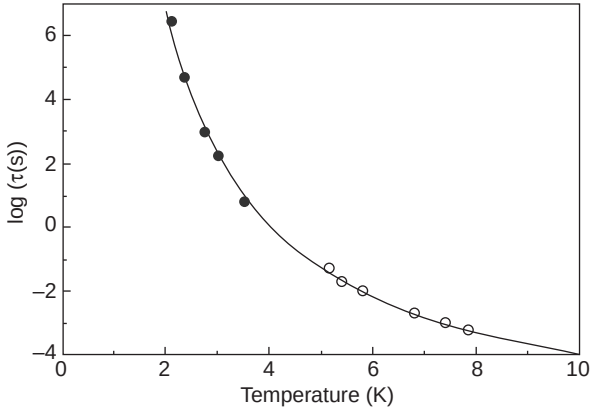

Figure 5.17 Temperature dependence of magnetisation relaxation time τ for $[Mn_{12}O_{12}(MeCO_2)_{16}(H_2O)_4]\cdot 2MeCO_2H\cdot 4H_2O$, from DC (solid circles) and AC (open circles) SQUID measurements, and fit to Arrhenius law (solid line). Reprinted by permission from Sessoli *et al.*, 1993 [6]. Copyright (1993) Macmillan Publishers Ltd

5.4.1.2 Summary of $[Mn_{12}O_{12}(MeCO_2)_{16}(H_2O)_4]$ Properties

These properties are most easily explained by example, and here we briefly survey the key points for the first discovered SMM,[6] $[Mn_{12}O_{12}(MeCO_2)_{16}(H_2O)_4]$ (Figure 5.18). This complex is a mixed valent $\{Mn^{III}{}_8Mn^{IV}{}_4\}$ cage. It crystallises as the $2MeCO_2H{\cdot}4H_2O$ solvate in a tetragonal space group, and the cluster lies on a special site imposing S_4 point symmetry and there are only three metal ions [one Mn^{IV} and two Mn(III)] in the asymmetric unit.[4] Thus, the cluster is axially symmetric and all molecules have their local z axes oriented along the crystal c axis. This is important when considering single crystal magnetic measurements (see later). The four Mn^{IV} ions form a heterocubane and are surrounded by a ring of eight Mn^{III} ions, with bridging *via* oxides and carboxylates.

Magnetisation experiments reveal an $S = 10$ ground state, with $M_{sat} \approx 20\ N\beta$ at low temperatures.[33] This results from strong antiferromagnetic interactions between the Mn^{IV} and Mn^{III} ions with much weaker antiferromagnetic $Mn^{IV}\ldots Mn^{IV}$ and $Mn^{III}\ldots Mn^{III}$ interactions. If $|J_{Mn^{IV}Mn^{III}}| >> |J_{Mn^{IV}Mn^{IV}}|, |J_{Mn^{III}Mn^{III}}|$ then all the Mn^{IV} spins might be expected to be antiparallel to all the Mn^{III} spins in the ground state (Figure 5.18b) giving total $S = (8 \times 2) - (4 \times 3/2) = 10$. However, it is far from obvious that this is the result. Calculations show that the ground state S depends subtly on the ratios of the exchange constants (as is the norm for molecules with competing antiferromagnetic interactions). Modelling susceptibility data to obtain these parameters is not straightforward given the size of the spin system and there are no definitive values. However, values of $2J_{Mn^{IV}Mn^{III}} \approx -45\ cm^{-1}$, $2J_{Mn^{IV}Mn^{IV}} \approx 2J_{Mn^{III}Mn^{III}} \approx -5\ cm^{-1}$ have been determined by restricting solutions to those with $S = 10$ ground states – as found from experiment – and fitting to INS data where $S = 10 \rightarrow 9$ and 11 excited state transitions have been observed.[34]

The simple 'spin up–spin down' picture of Figure 5.18 is confirmed by, for example, ^{55}Mn NMR studies (Figure 5.15). As noted above, below the blocking temperature an NMR spectrum can be observed even in zero field because the magnetisation is blocked giving large internal fields at the manganese nuclei, and a peak is observed for each magnetically unique ion. When a magnetic field is applied along the unique axis, the two Mn^{III} peaks shift to lower frequencies and the Mn^{IV} peak shifts to higher frequencies. This implies that the internal fields at the Mn^{III} and the Mn^{IV} sites are of opposite sign hence the local magnetic moments are oriented antiparallel.[27]

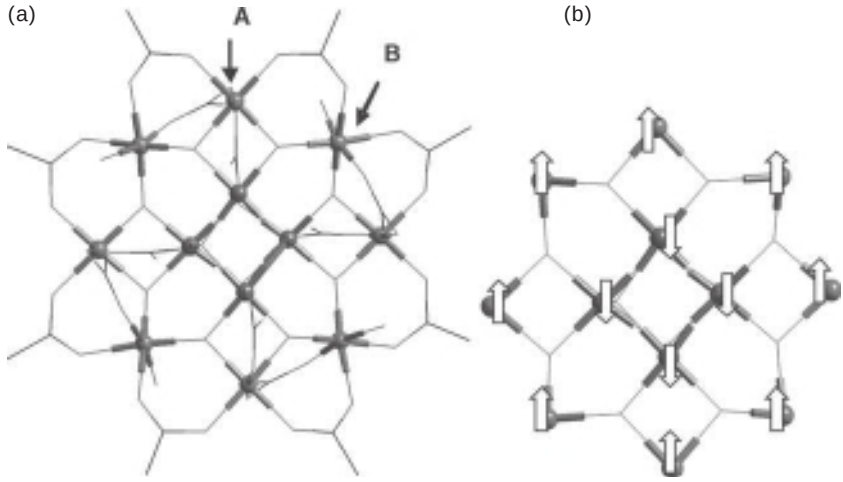

Figure 5.18 (a) Structure of $[Mn_{12}O_{12}(MeCO_2)_{16}(H_2O)_4]$ viewed down the tetragonal axis (z) with crystallographically distinct Mn^{III} sites (A and B) labelled; scheme: Mn (large spheres; the inner four icons are the Mn^{IV}), O and C (skeletal), H not shown. (b) Representation of relative orientations of Mn^{III} ($S = 2$) and Mn^{IV} ($S = 3/2$) spins in the ground state

The $S = 10$ state is confirmed by EPR[35] and INS[36] experiments (see also Figure 5.20). Furthermore, these experiments give direct measurements of the ground state ZFS parameters; the accepted value for D is -0.46 cm^{-1}, although there are minor differences depending on the technique used, with the sign coming from variable temperature behaviour. The physical origin of the ZFS of the *cluster* (D) lies largely in those of the *individual metal ions* (d).[35] The six-coordinate Mn^{III}, high-spin d^4 ion ($S = 2$) has a rather large ZFS resulting from its Jahn–Teller distortion; this single ion d is negative for the usual elongation. The more symmetrical d^3, Mn^{IV} ion is expected to have a much smaller d. Crucially, in $\{Mn_{12}\}$ the Jahn–Teller axes of the eight Mn^{III} ions (defining the orientations of d_{zz}) are all crudely aligned (either 11° or 37°) about the unique axis of the cluster (defining the orientation of D_{zz}) and they collectively 'project' a negative ZFS on the ground state. If they were misaligned they would tend to cancel each other out. There are relatively straightforward numerical relationships governing this under the conditions that the total spin states of the cluster are well separated (the 'strong exchange limit').[22]

In summary, experiments show that $\{Mn_{12}\}$ has an $S = 10$ ground state with $D = -0.46$ cm^{-1}. The negative sign means that within the

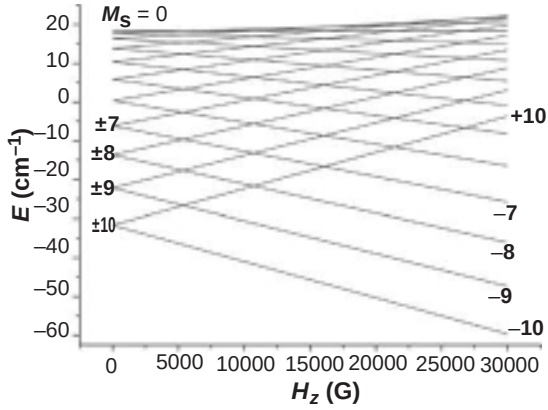

Figure 5.19 Zeeman diagram for $S = 10$ with $D = -0.5$ cm^{-1} and a magnetic field applied along the z axis

ground state the $M_S = \pm 10$ doublet is lowest in energy, then ±9, ±8, and so on, up to $M_S = 0$ at highest energy (Figure 5.19). The energy separation between the $M_S = \pm 10$ and ±9 doublets in zero field has been measured directly by INS[36] and frequency-swept EPR[37] spectroscopies and is 10 cm^{-1} (Figure 5.20), in agreement with the $M_S{}^2D$ energy dependence. Hence, at low temperature only the $M_S = \pm 10$ doublet is populated.

5.4.1.3 The Origin of Slow Magnetisation Relaxation in SMMs

An alternative representation of the energy distribution of the M_S states is given on the left-hand side of Figure 5.21 (this is often pictured as a double potential energy well in SMM literature). At low enough temperature only the $M_S = \pm 10$ components of the ground state are populated. If the sample has been cooled in zero field then there is an equal population of +10 and −10 (Figure 5.21, left). Application of a magnetic field along the molecular z axis (H_z; often referred to as a longitudinal field) will, of course, separate these states in energy according to $E(M_S) = M_S g\beta H_z$ (Figure 5.19). At high enough (positive) H_z all the population will be in $M_S = -10$ (and the magnetisation is saturated; Figure 5.21, middle). On removal of the field half of the molecules must return to $M_S = +10$ (*i.e.* flip the orientation of their spin), in order for the magnetisation to relax back to zero. In other words, an equilibrium Boltzmann distribution must be re-established. This occurs through transfer of energy with the environment – spin lattice relaxation. If there is sufficient thermal energy (kT) then the molecule

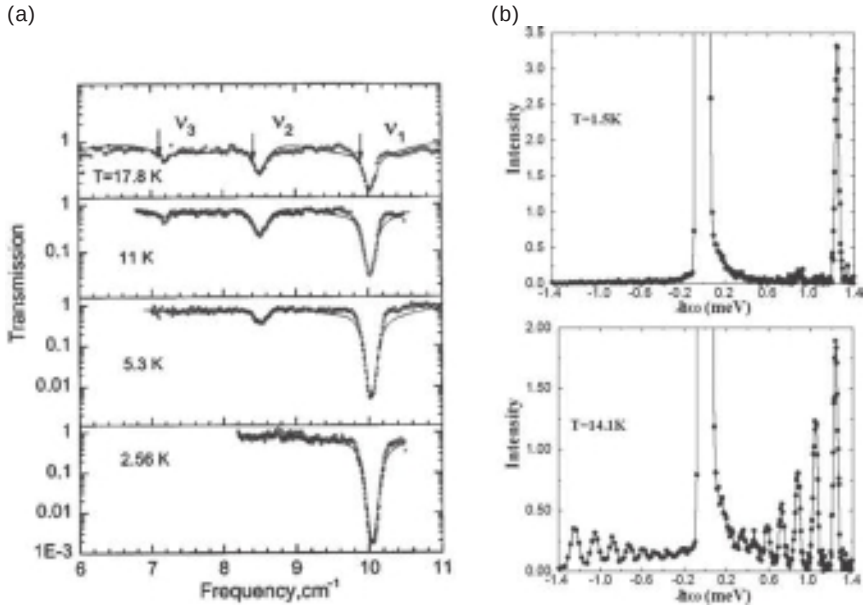

Figure 5.20 (a) Frequency-swept EPR spectra of $[Mn_{12}O_{12}(MeCO_2)_{16}(H_2O)_4]\cdot 2MeCO_2H\cdot 4H_2O$ at variable temperature and zero applied magnetic field. Reproduced with permission from Mukhin *et al.*, 1998 [37]. Copyright (1998) EDP Sciences. (b) INS spectrum (incident neutron wavelength 5.9 Å) at variable temperature and zero applied field. Reprinted with permission from Mirebeau *et al.*, 1999 [36]. Copyright (1999) APS and with permission from Mukhin *et al.*, 1998 [37]. Copyright (1998) EDP Sciences

can absorb heat from the vibrational system of the lattice. Physicists refer to lattice vibrational modes as phonons and often refer to absorption/emission of phonons to describe heat being transferred from/to the lattice. There are selection rules associated with the transitions between M_S states that can take place *via* spin phonon interactions; for our purposes the most important is $\Delta M_S = \pm 1$ (± 2 is also allowed). Thus, in order for a spin in the $M_S = -10$ state to flip to $M_S = +10$, it must successively absorb phonons until it reaches $M_S = 0$, the highest energy state, and then it can reach $M_S = -10$ through phonon emission (Figure 5.21, right).

This is the origin of the thermal energy barrier U_{eff} (Equation 5.3) to magnetisation relaxation in SMMs. For an integer spin the height of the barrier is simply the energy difference between the $M_S = \pm S$ and $M_S = 0$ states, $|D|S^2$. For an half-integer spin it is the energy difference between $M_S = \pm S$ and $M_S = \pm 1/2$ states, $|D|(S^2 - 1/4)$. S is determining the number of rungs in the ladder and D is determining the spacing between the rungs. It also becomes clear why D must be negative – if it were positive then

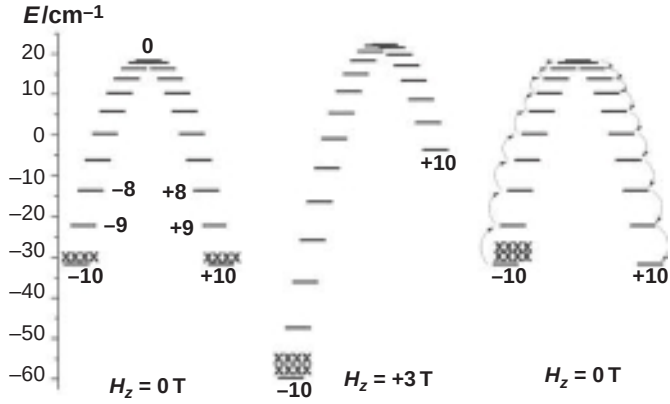

Figure 5.21 Energy distribution of the M_S states for S = 10 and D = −0.5 cm^{-1} in zero (left) and +3 T (middle) applied field along the molecular *z* axis, with illustration of equilibrium population distributions assuming only the lowest states are populated. (Right) Population distribution immediately after saturation at +3 T then removal of the field. The arrows indicate the path to relaxation *via* absorption then emission of thermal energy (phonons) from/to the lattice

Figure 5.21 would depict an energy well with $M_S = 0$ at the bottom and there is no barrier.

Hence, after magnetisation and at sufficiently low temperatures (Figure 5.21, right) there is insufficient thermal energy to promote a molecule from M_S = –10 to –9 and the spin is 'frozen' – the magnetisation cannot relax. Of course, on application of a magnetic field in the opposite sense (H_z negative), M_S = +10 will become energetically favoured over $M_S = -10$ (reversing Figure 5.21, middle), the barrier is destroyed and at some field value relaxation will occur. Ultimately, *M* will saturate in the opposite sense (exclusive population of M_S = +10), the field can be removed and the spin is frozen in the opposite orientation. This is the cause of the hysteresis in magnetisation *vs* applied field loops (Figure 5.16).

5.4.1.4 Quantum Tunnelling of Magnetisation (QTM)

The *M vs H* loops in Figure 5.16, measured on a single crystal of $\{Mn_{12}\}$ with applied field oriented along the unique axis (*z*), are not smooth. There are steps at regular field intervals: 0.44, 0.88, 1.32, . . . 2.64 T.[30,31] These are shown more clearly as peaks in a plot of *dM/dH* (Figure 5.22a), and correspond to rapid enhancement of the relaxation rate at these

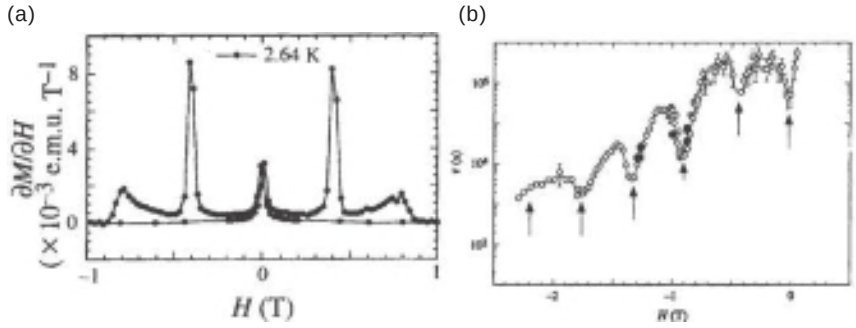

Figure 5.22 (a) Derivative of the 2.64 K magnetisation *vs* applied field loop in Figure 5.16, measured on a single crystal of $[Mn_{12}O_{12}(MeCO_2)_{16}(H_2O)_4]\cdot 2MeCO_2H\cdot 4H_2O$ with field oriented along the molecular z axis. (b) Longitudinal (z) field dependence of relaxation time at 2.1 K. Reprinted by permission from Thomas *et al.*, 1996 [30]. Copyright (1996) Macmillan Publishers Ltd

fields (Figure 5.22b). At these critical field values M_S states on either side of the barrier become degenerate (Figures 5.23 and 5.24). For example, at zero field $M_S = -10$ crosses with $+10$, -9 with $+9$, and so on. At $H_z = 0.44$ T $M_S = -10$ crosses with $+9$, -9 with $+8$, and so on. Given that the levels are at energy $DM_S^2 + M_S g\beta H_z$, it is easy to see that the separation between adjacent crossings is $\Delta H_z = D/g\beta$.

This provides an additional pathway to relaxation. Imagine the magnetisation has been saturated at very low temperature and positive field

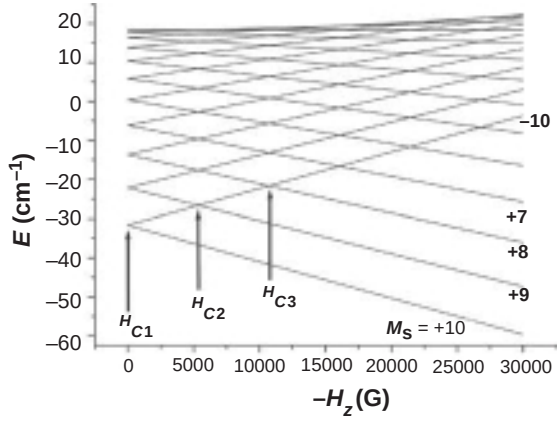

Figure 5.23 Zeeman diagram for $S = 10$ with $D = -0.5$ cm^{-1} and a magnetic field applied along the z axis. Critical fields where there is a crossing of M_S levels are shown

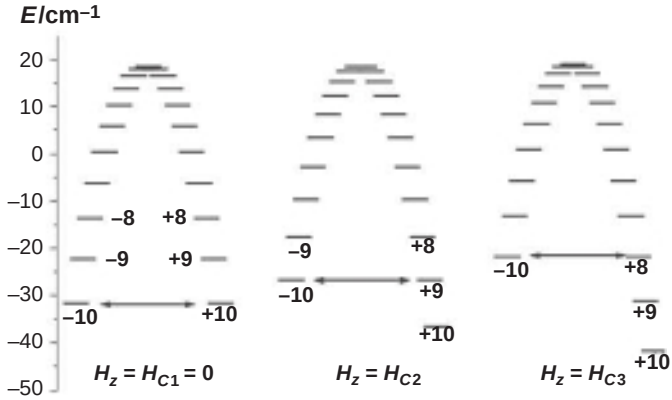

Figure 5.24 Resonance between M_S levels on opposite sides of the barrier at specific applied magnetic fields, H_z. The degeneracy of the states with $M_S = -10$ is highlighted but the excited states also come into resonance

and all the population is in $M_S = -10$ (Figure 5.21, middle). On decreasing field the $M_S = -10$ state first crosses with another state (+10) at zero field (Figures 5.23 and 5.24, left). If there is an appropriate connection between these two states (see later) then some of the spins can directly flip to $M_S = +10$ and the magnetisation suddenly decreases (Figure 5.24, left). On applying the field in the opposite (negative) sense these two levels separate again, the connection is lost and relaxation is slow again until $M_S = -10$ comes into resonance with $M_S = +9$ (Figure 5.24, middle). Some spins can flip to +9 and then relax to +10 *via* phonon emission. At higher negative field $M_S = -10$ meets +8 (Figure 5.24, right), and so on. Hence, the spins are finding a short-cut through the energy barrier – this is resonant quantum tunnelling of the magnetisation.

This effect can in principle be measured by any technique that is sensitive to the magnetisation dynamics and in addition to the SQUID measurements above quantum tunnelling of magnetisation (QTM) has been observed for $\{Mn_{12}\}$ by, for example, torque magnetometry,[38] ^{1}H and ^{55}Mn nuclear relaxation rates in NMR,[39,40] and specific heat.[41]

The quantum tunnelling relaxation pathway is expected to be dominant at very low temperatures (when there are very few phonons). At higher temperatures the thermally activated regime, up-and-over the barrier, is dominant. At intermediate temperatures both mechanisms are important. This is easily understood from Figure 5.24: at zero field $M_S = +9$ and –9, +8 and –8, and so on are in resonance in addition to $M_S = \pm 10$. Hence, the spin can be thermally promoted to, for example, –9

by phonon absorption and then tunnel to +9. This is thermally assisted QTM – it can occur at all the critical fields (Figure 5.24, right) and is important because the probability of tunnelling increases for smaller $|M_S|$ (see below), so that even in the thermally activated regime there is a short-cut through the barrier.

One implication is that the relaxation rate (and the width of the hysteresis loop) is temperature dependent only down to a certain temperature. Below this, when there are insufficient phonons to promote population to $M_S = -9$, the relaxation should become temperature independent being governed only by QTM. This has been observed for $\{Mn_{12}\}$ and derivatives below 0.6 K.[42,43] Although relaxation is so slow at these temperatures that it is difficult to measure it accurately, the onset of the pure quantum regime has been observed by the temperature independence of hysteresis loops and measurements where tunnelling *via* ground and *via* exited states are resolved and their temperature dependence can be determined separately.

QTM was a long-predicted quantum size effect for magnetic particles, but $\{Mn_{12}\}$ provided the first clear-cut experimental observation of this phenomenon, allowing quantitative tests for theories of quantum magnetic behaviour. The first obvious question to be asked is: how do the spins tunnel?

5.4.1.5 Mechanism for QTM

If there is no quantum mechanical connection between the two states on either side of the energy barrier then there is no mixing. As the applied field is changed they simply cross each other and there is no mechanism for transfer of population (QTM) between them. If there is a connection between them then they will mix, with this mixing being more efficient the closer they are in energy. Then, instead of crossing on changing magnetic field, there is an avoided crossing (*e.g.* see inset to Figure 5.25) with an energy gap known as the tunnel splitting. The wave functions of the system are linear combinations of the M_S states, with the mixing maximised at the avoided crossing: they are delocalised over the two sides of the barrier. It is this mixing that allows QTM to take place with the probability being related to the magnitude of the tunnel splitting.

The 'appropriate connection' between the states can arise from ZFS interactions and/or from an applied magnetic field in the *xy* plane of the molecule.

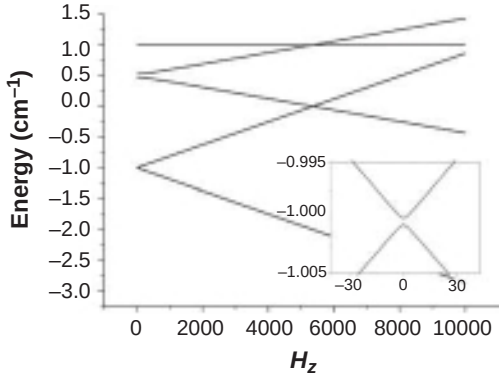

Figure 5.25 Zeeman splitting of an $S = 2$ paramagnet with $D = -0.5$ cm^{-1} and $E = 0.01$ cm^{-1} with the applied field along the molecular z axis. Inset: expansion of level anti-crossing between 'M_S' $= \pm 2$ at zero field

(i) *Zero field splitting*: The axial ZFS parameter D simply splits states differing in $|M_S|$ but does *not* mix these states. The rhombic term E *does* mix the states, specifically those differing in $|M_S|$ by ± 2. For example, for $S = 2$ a nonzero E will directly mix $M_S = +1$ and -1 with a large energy splitting ($2E$) between the resultant states in zero field. $M_S = \pm 2$ are not mixed directly, but because $M_S = +2$ is mixed with 0, and then 0 with -2, there is still a small splitting (Figure 5.25, using the same parameters as in Figure 5.3 but with a small nonzero E). In general, the splitting of states due to E gets smaller for larger $|M_S|$. Nevertheless, these tiny splittings are very important in allowing QTM.

D and E are 'second-order' ZFS terms, which means that the Hamiltonian contains terms that are squares of spin operators (this is why E mixes states differing by $|M_S| = \pm 2$). For a spin S, ZFS terms of order $\leq 2S$ are allowed, with their importance usually assumed to decrease with increasing order. Terms up to sixth order[44] have been determined for $\{Mn_{12}\}$ derivatives by single crystal EPR. The higher order rhombic and certain axial terms also result in mixing (between $|M_S| = \pm 4$ for fourth order, *etc.*).

(ii) *Transverse applied magnetic field*: a field applied in the xy plane, that is, perpendicular to the easy axis (z), is referred to as a transverse field. Such a field induces mixing of states differing in M_S by ± 1.

Some of the consequences of the above are that: (i) nonzero E should allow QTM between states on opposite sides of the energy barrier that differ in M_S by $2n$, where n is an integer; (ii) fourth-order ZFS terms will allow QTM between states differing by $4n$ and this becomes allowed even

for axial symmetry ($E = 0$); (iii) ZFS *cannot* split $\pm M_S$ states for half-integer spin and these must be degenerate in zero field (this is known as Kramers' degeneracy); (iv) a transverse field should induce QTM between any pair of states.

$[Mn_{12}O_{12}(MeCO_2)_{16}(H_2O)_4]\cdot 2MeCO_2H\cdot 4H_2O$ has tetragonal symmetry, and hence it is expected to have $E = 0$. Fourth-order ZFS terms have been detected from EPR and INS measurements.[45,46] Therefore, it is only expected to see QTM between states differing in M_S by $4n$. However, all possible steps are observed experimentally. A possible explanation for this came from a detailed analysis of the X-ray diffraction data:[47] solvent disorder breaks the global symmetry giving subsets of molecules with only twofold symmetry. Indeed, detailed single crystal EPR[45] and INS[46] studies detected nonzero E. This could give a mechanism for the 'even' ($2n$) QTM steps but not the 'odd' steps. Further EPR measurements provided evidence for tilting of the molecular easy (z) axes with respect to the tetragonal axis of the crystal for some subsets of the molecules, also as a result of disorder:[48] this would result in a transverse (x,y) field component for these molecules and could give rise to the odd QTM steps. However, both $2n$ even and odd steps are still observed for $\{Mn_{12}\}$ derivatives where there is no experimental evidence for these disorder effects.[42,49] Transverse field components due to nuclear hyperfine and/or intermolecular dipolar interactions[50] have been implicated, as have so-called antisymmetric components of the exchange interaction (as opposed to the isotropic exchange J),[42] but this problem remains unsolved.

An important example of an inherently rhombic symmetry SMM is $[Fe_8O_2(OH)_{12}(tacn)_6]Br_8$, which has an $S = 10$ ground state (like $\{Mn_{12}\}$) with $D = -0.20\ cm^{-1}$. The symmetry of the cation is only C_1 and $|E/D|$ is in the range 0.15–0.19 from EPR and INS.[51] The effect of this large rhombic ZFS is to thoroughly scramble the low $|M_S|$ states, destroying the simple picture of pairs of degenerate $\pm M_S$ (Figure 5.26a). However, the lowest states can still be loosely described as $M_S = \pm 10, \pm 9 \ldots$ and there is still a barrier to relaxation ($U_{eff} \approx 23\,K$ from AC susceptibility).[52]

The large rhombicity gives a tunnel splitting between $M_S = \pm 10$ that is circa three orders of magnitude greater than in $\{Mn_{12}\}$. Hence, relaxation *via* QTM is much more efficient. In fact, the relaxation dynamics are rapid enough that the pure quantum regime can be observed directly *via* magnetisation relaxation, becoming temperature independent below 0.4 K (Figure 5.26b). $\{Fe_8\}$ was the first molecule where this was possible and allowed direct measurement of the effect of external perturbations, for example applied fields, on tunnel splittings and

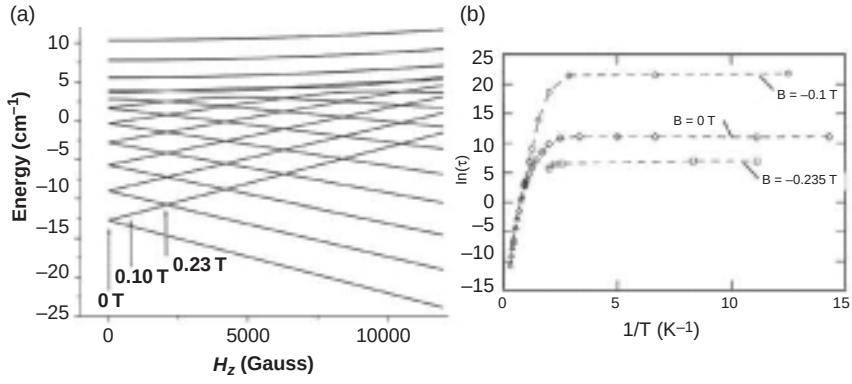

Figure 5.26 (a) Zeeman diagram for $[Fe_8O_2(OH)_{12}(tacn)_6]Br_8$ calculated with $D = -0.2$, $E/D = 0.19$ cm^{-1} and with applied field along the easy (z) axis. (b) Temperature dependence of relaxation time measured in different applied fields. Reprinted with permission from Sangregorio *et al.*, 1997 [52]. Copyright (1997) American Physical Society

relaxation times in the pure quantum regime. For example, Figure 5.26 shows that relaxation is several orders of magnitude slower at 0.1 T than at 0 or 0.235 T, because $M_S = -10$ is 'on' resonance with $M_S = +10$ and $+9$ at 0 and 0.235 T, respectively, but 'off' resonance at the intermediate field.

The tunnel splitting (Δ) between the bottom pair of states of $\{Fe_8\}$ has been measured in micro-SQUID experiments in the pure quantum regime.[32] The longitudinal field (H_z) is swept over the avoided crossing of a sample where the magnetisation has been saturated (*i.e.* over a step in the M *vs* H loop), and the fraction of molecules that relaxes is measured. This gives the tunnelling rate, which is directly related to Δ (*via* the Landau–Zener model). Using this method a fascinating effect was observed with an applied field along the hard axis (H_x, a second applied field is possible in the micro-SQUID apparatus): Δ oscillates with a characteristic period on increasing H_x (Figure 5.27), rather than simply increasing monotonically. This can be explained numerically: there are two Zeeman terms (in H_z and H_x), in addition to the ZFS terms, which can cancel to zero splitting at certain fields. It has also been interpreted as a quantum phase interference effect between different tunnelling pathways in a semi-classical model. Imagine the magnetisation vector (**M**) pointing along z. QTM can be envisaged as interference between rotation of M about the x axis clockwise (*via* y) and counter-clockwise (*via* $-y$) to reach $-z$. The phases of these two paths can interfere constructively or destructively to give maxima and minima in

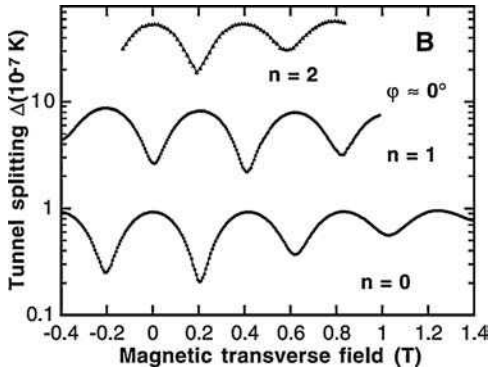

Figure 5.27 Measured variation of the tunnel splitting Δ between $M_S = -10$ and $M_S = S - n$ (in the pure quantum regime) with applied magnetic field along the hard axis (x). Reprinted with permission from Wernsdorfer and Sessoli, 1999 [32]. Copyright (1999) American Association for the Advancement of Science

Δ depending on the strength of H_x and with a period of oscillation $\Delta H_x = (2k/g\beta)[2E(E+D)]$. Hence, the effect is not be observed for the axially symmetric $\{Mn_{12}\}$ ($E = 0$) and Δ does increase monotonically with H_x for this molecule.[53]

The second important observation from these experiments was that if H_z is applied at an 'odd' level crossing (*e.g.* between –10 and +9; $n = 1$ in Figure 5.27) then similar oscillatory behaviour is found but with a 180° phase shift. This difference between 'odd' and 'even' steps can be considered a parity effect and is analogous to the differences expected between integer and half-integer spins (because of Kramers' degeneracy in zero field for the latter). Since these first observations, measurements on redox-related integer ($S = 10$) and half-integer ($S = 19/2$) $\{Mn_{12}\}^{2-/1-}$ derivatives (with rhombic symmetry) have shown this parity effect directly, with the tunnel splitting between $M_S = \pm S$ being at a maximum and minimum, respectively, in zero field.[53]

Such effects had long been predicted for quantum magnets but only became observable with the advent of SMMs. Wernsdorfer and Sessoli, the workers who first observed them in $\{Fe_8\}$, noted that because of these effects complete control of the molecular magnetisation can be gained – the system can be made to relax or not – by application of specific magnetic fields in two dimensions (H_z and H_x).[32] Other external effects on QTM in SMMs have also been investigated, including exchange coupling with another molecule[54] and pumping with electromagnetic radiation.[55]

5.4.2 Chemistry of Single Molecule Magnets

The range of single molecule magnets that have been made was thoroughly reviewed by Aromì and Brechin in 2006.[10] The review covers the period until 2005. Here, the general approaches are discussed without attempting to review all SMMs exhaustively.

The majority of SMMs contain manganese(III) and the choice of starting material was originally considered to be a problem because there are few simple salts of manganese(III) that are commercially available. The problem was solved by two distinct routes, with the original work done in the Christou group in both cases.

5.4.2.1 Reactions from Simple Salts Requiring Oxidation State Change

Comproportionation reactions involving a Mn^{II} substrate, typically manganese(II) carboxylate, oxidised with permanganate were the original route to the $\{Mn_{12}\}$ cages. This route has been developed further by the realisation that in air many Mn^{II} substrates will oxidise even in the absence of permanganate, and the further realisation that permanganate will be reduced by almost any organic ligand. Therefore, while comproportionation looks chemically elegant, all that is really required is that conditions are employed that will allow manganese to change oxidation state.

Two examples of the use of *in situ* oxidation of Mn^{II} salts illustrate the approach. The highest spin SMM, a $\{Mn_{25}\}$ cage reported by Murugesu *et al.*,[56] involves reaction of manganese^{II} chloride with two bridging ligands – azide and pyridine-2,6-dimethanol – using tetramethylammonium hydroxide as a base. This reaction, done in methanol/acetonitrile, produces a cage containing eighteen bridging oxides clearly illustrating that Mn^{II} will be oxidised with concomitant formation of oxide ligands when reactions are done in air. The azide and pyridine-2,6-dimethanol ligands coat the exterior of the cage, and prevent formation of an intractable polymeric material. The cage has an $S = 51/2$ ground state and shows hysteresis at below 1 K.

The second example is a family of $\{Mn_6\}$ cages reported by Milios *et al.*[57] Here the preparation is from manganese(II) perchlorate, which is reacted in air with a derivatised oxime and a carboxylic acid; one of the advantages of this particular chemistry is the ease with which different derivatives can be prepared simply by varying the oxime and carboxylic acid. These cages contain two oxide bridges, and are best described as

two $\{Mn^{III}_3O\}$ triangles linked *via* oxygen atoms derived from the derivatised oxime ligands. The oxidant is again atmospheric oxygen. The ability to make a family of these cages has allowed Brechin and his coworkers to correlate the energy barrier for loss of magnetisation with structural parameters;[57] this correlation again shows the vital importance of the relative orientations of the Jahn–Teller axes in Mn^{III} cage complexes as a controlling factor in deciding the magnetic behaviour. One of these $\{Mn_6\}$ cages has the highest energy barrier (86 K) for loss of magnetisation of any polymetallic complex.

Reduction of permanganate has also been used, for example in preparing a new family of mixed-valent manganese cages. With benzoic acid, a dodecanuclear manganese cage can be made – different to the $\{Mn_{12}\}$ family above, but related in that it contains an outer wheel of Mn^{III} ions containing a $\{Mn^{IV}_4\}$ inner cage, but with the inner cage forming a rhombus rather than a cubane.[58] With other carboxylates a $\{Mn_{16}\}$ cage results, where the outer wheel contains ten Mn^{III} centres and the inner cage contains a hexanuclear Mn^{IV} fragment.[59] This route has not been explored as exhaustively as the *in situ* oxidation of Mn^{II} compounds.

5.4.2.2 Reactions from Pre-formed Manganese Cages

This route is by far the most commonly adopted.[10] This literature includes the formation of the largest SMM – a $\{Mn_{84}\}$ cage made by the Christou group (Figure 5.28),[60] which is made from reaction of $\{Mn_{12}\}$ with permanganate in the presence of acetic acid and methanol.

More commonly, the pre-formed cage used is a derivative of the well known oxo-centred manganese carboxylate triangles. This approach was pioneered in the 1980s by Christou,[2] and in many ways there have been few advances on this work other than use of different ligands. Two recent examples illustrate what is possible; both involve tripodal ligands. Use of triol ligands allows the triangles to be linked into a variety of different cages;[61] the precise cage formed depends on the triol used, on reaction conditions and on the carboxylate present in the original triangle. Addition of further bridging ligands, such as azides, leads to even greater structural complexity. While it is impossible to predict the cage that will result – and the variation is dramatic, from dimers to $\{Mn_{32}\}$ cages – it is clear this route is very productive. Similarly, use of phosphonates has produced new manganese SMMs; some have both high spin and high coercivity in the magnetic hysteresis.[15] As with the work with triols,

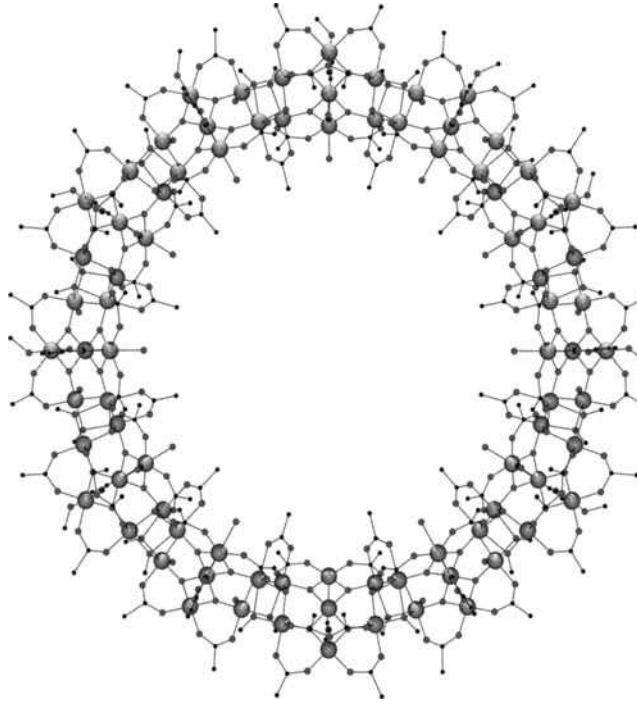

Figure 5.28 The structure of $[Mn_{84}O_{72}(O_2CMe)_{78}(OMe)_{24}(OH)_6(MeOH)_{12}(H_2O)_{42}]$. Reprinted with kind permission from Aromi and Brechin, 2006 [10]. Copyright (2006) Springer Science + Business Media

precise conditions and the substituents present on the phosphonate ligands control the structure found in an uncontrollable manner.

This work shows how much remains to be understood in the chemistry of polymetallic cage complexes. It is now comparatively easy to make large cage complexes of manganese, but designing syntheses to specific cages has not been achieved. Linking cages into larger clusters works, but has really only been studied in depth for the oxo-centred triangles with systematic studies of linking of larger cages lacking.

5.4.2.3 SMMs Involving Other Trivalent Metal Ions

There are three significant types of iron(III) SMMs. The first two were made by controlled hydrolysis reactions, with the control provided by a polydentate ligand. In the $\{Fe_8\}$ SMM the ligand used is 1,4,7-triazacyclononane[62]

while in an $\{Fe_{17}\}$ SMM the ligands used are derivatives of *N*-(1-hydroxyethyl)aminodiacetic acid.[63] The former cage is the second most studied SMM after $\{Mn_{12}\}$ having some advantages for studying the physics, for example it is possible to isotopically enrich the iron and thus study how nuclear hyperfine interactions influence QTM.[64] In both cases the synthetic procedure involves dissolving an Fe(III) compound in water and allowing hydrolysis to proceed. The third significant family of Fe(III) SMMs are tetranuclear cages of formula $[Fe_4(OR)_6(L)_3]$, where R = methyl, ethyl and L = a β-diketonate such as dipivaloylmethane (Hdpm) (Figure 5.29). These cages are made by dissolution of iron(III) chloride in methanol in the presence of the β-diketonate, followed by addition of a source of methoxide as base.[65] In many ways it is related to the other Fe(III) SMMs, but here it is a controlled oligomerisation involving alkoxide bridges, rather than a controlled hydrolysis involving hydroxide/oxide bridges. These tetranuclear iron(III) SMMs are important because they can be easily modified simply by changing the alkoxide or β-diketonate

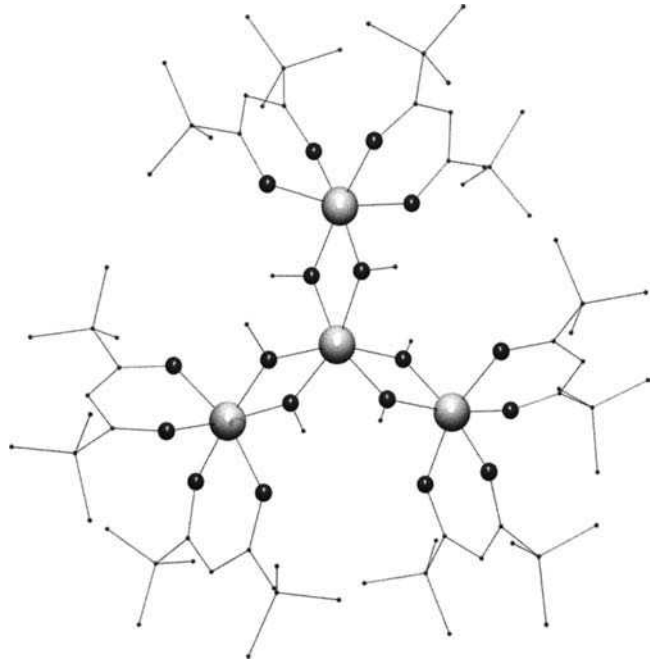

Figure 5.29 The structure of $[Fe_4(OMe)_6(dpm)_3]$. Reprinted with kind permission from Aromi and Brechin, 2006 [10]. Copyright (2006) Springer Science + Business Media

present in the reaction. This has led to the first report where the properties of an SMM are retained when the SMM is bound to a surface;[66] this work shows the flexibility of the system – while dipivaloylmethane is retained as the β-diketonate, methoxide is replaced by 11-(acetylthio)-2,2-bis(hydroxymethyl)undecan-1-ol, which allows a tris(alkoxide) to bind to the $\{Fe_4\}$ core – increasing stability by having a multi-nucleating ligand – while containing a long chain thiolate tether which allows the cage to be bound to a gold surface.

There has been little further development of SMMs based on this spin centre, probably because the d^5 electronic configuration is often isotropic and, hence, has small single ion ZFS in most complexes. The only other trivalent 3*d* ion found to produce SMMs is vanadium(III), and there is only one example with this metal. The compound – a tetranuclear V^{III} cage[67] – contains a butterfly core similar to cores known for Mn^{III} cages. It has an $S = 3$ ground state and a large D value of $-1.5\ cm^{-1}$. It is made by reaction of $[VCl_3(THF)_3]$ with a carboxylate in the present of a chelating ligand such as 2,2′-bipyridyl; two μ_3-oxides are found in the structure, which may come from the THF used in the reaction or adventitious oxygen. There is some thought that V^{III} should present advantages in design of SMMs, as the single ion ZFS is large and strong ferromagnetic exchange between V^{III} centres has been seen in dimeric complexes.

5.4.2.4 SMMs involving Divalent Metal Ions

The first SMMs found where the spin carrier is divalent are nickel cages; a $\{Ni_4\}$ cubane and a $\{Ni_{12}\}$ ring were reported to be SMMs at about the same time.[68,69] Further Ni^{II} SMMs have been reported, but probably fewer than might have been expected given that Ni^{II} frequently has large ZFS and when superexchange between nickel centres can be found to be ferromagnetic. The nickel cubanes can be made with a range of alkoxides and tris(alkoxides) and all show similar chemistry, with μ_3-alkoxides at the alternate corners of a cubane with Ni^{II} sites at the other corners. Such cubanes are remarkably easy to make, requiring little beyond a nickel(II) salt, an alcohol and some form of bridging or chelating ligand to prevent oligomerisation. Predicting the magnetic properties is much more difficult because whether an $S = 0$ or $S = 4$ ground state results is related to the Ni–O–Ni angles at the alkoxides;[70] synthetic control of inter-bond angles is currently beyond coordination chemists in most cases.

A series of nickel SMMs has been made using citrate to control nucleation; this includes the largest nickel SMM.[71] The synthesis – controlled hydrolysis blocked by a polydentate ligand – is related to the procedure developed for the iron(III) SMMs mentioned above.

Citrate is also used frequently in reports of cobalt(II) SMMs;[72] however, Co^{II} SMMs remain poorly understood. Several examples have been reported, but in most cases the behaviour is significantly different to SMMs involving Mn^{III} or Fe^{III}. The examples reported are difficult to assess. Sometimes there are significant intermolecular interactions, which suggest the magnetic behaviour could be due to extended structures rather than single molecules. In the physical data reported there are often low ratios of $\chi'':\chi'$ in AC susceptibility measurements, which suggest that only a small percentage of the sample is undergoing slow relaxation. Occasionally, fitting relaxation behaviour to an Arrhenius law can lead to very high energy barriers and physically meaningless pre-exponential factors. In most studies there is very limited coercivity in any hysteresis loop, and there is normally a collapse in magnetisation at zero external field, which is assigned to quantum tunnelling.

The major problem with understanding the magnetic behaviour of these compounds is that Co^{II} has an orbitally degenerate electronic ground state ($^4T_{1g}$) in octahedral and distorted octahedral geometries. The large spin-orbit coupling could contribute to a large energy barrier, which would be an advantage, but also favours rapid QTM at zero field (Section 5.4.1). In turn, this raises a semantic argument: the only point of the name 'single molecule magnet' is that it implies retention of magnetisation in the absence of a magnetic field; if an SMM loses all magnetisation due to quantum tunnelling at zero field, it has to be questionable whether the term means anything.

The synthetic procedures to make cobalt SMMs are often based on known nickel SMMs, for example the first example is a cobalt(II) cubane which is isostructural to a Ni^{II} SMM,[73] while the several reports[72] of polymetallic cobalt citrate cages showing slow relaxation are based on the nickel citrate syntheses. Other examples are based on tripodal ligands and use similar procedures to those developed for nickel(II) or iron(III).

There is a very small group of iron(II) SMMs; the first reported by Oshio *et al.*[74] These first examples are also cubanes, made using a Schiff base ligand with a pendant alcohol which, once deprotonated, provides the μ_3-oxygen for the alternate corners of the cubane. This work is extremely instructive, as Oshio's group analysed how the ZFS values (d) for the individual Fe^{II} centres project onto to the molecular D value of the SMM. Unfortunately, the S_4 symmetry of the molecule means that the axes

of the individual Fe^{II} ions are orthogonal to one another, and that *D* is only one-eighth the size of the ZFS of the constituent spin centres (*d*).

A second family of Fe^{II} cages has been reported to be SMMs by Boudalis *et al.*[75] This involves use of the dipyridylketone and is based on chemistry originally developed for Co^{II} and Ni^{II}. Again, this is instructive, as it suggests that similar cages should be possible for all three divalent ions, if the conditions can be optimised for the individual cages. As with the cobalt(II) cages, treatment of AC susceptibility data for these cages using the Arrhenius law leads to very small pre-exponential factors and it is not clear why this should be the case.

5.4.2.5 Cyanide-bridged SMMs

Cyanide is a ubiquitous ligand in molecular magnetism. However, the first SMM reported using cyanide only appeared in 2002, reported by Sokol *et al.*[76] This was a $\{MnMo_6\}$ cage, where the Mo^{III} centres are at the corners of an octahedron, bridged to a central Mn^{II} *via* the cyanides. Growth of the cage is controlled by the presence of tri-*N*-methyl-1,4,7-triazacyclononane ligands attached to each molybdenum site. Other cyanide-bridged SMMs have appeared since, all based on a similar approach: sites on one or more metal centres are blocked with polydentate ligands, and these complexes are then reacted with metallocyanates. The highest energy barrier found for a metallocyanate SMM is 33 cm^{-1} – again reported by the Long group.[77]

Cyanides have allowed the inclusion of 4*d* and 5*d* ions into SMMs, which should enhance anisotropy. Some of these metallocyanate SMMs are also redox switchable, for example the $\{ReMn_4\}$ cage with the high energy barrier can be switched to a simple paramagnet by a one-electron reduction.

5.4.2.6 Heterometallic 3*d*–4*f* SMMs

A further method to introduce anisotropy would be to include a lanthanide element, such as dysprosium or terbium, where there is a high orbital contribution to the magnetism of the single 4*f* ion. This approach to SMMs began, however, with a report of a $\{Mn_8Ce\}$ SMM from the Christou group.[78] Other Mn–*Ln* cages have been reported to be SMMs,[79] as have Cu–*Ln* cages.[80] The Mn–*Ln* cages are made from reaction of a pre-formed manganese cage with a source of lanthanide ions, relying on the extremely oxophilic nature of the lanthanide ions to

cause them to bind to oxygen atoms from carboxylates. The Cu–*Ln* cages are based on work originated by Benelli and Gatteschi, where 3*d*–4*f* cages were made using Schiff base ligands;[81] the more recent Cu–*Ln* SMMs involve linking these species into larger aggregates.

The energy barriers in these 3*d*–4*f* SMMs are not higher than those in the homometallic Mn^{III} SMMs.

5.4.2.7 Future Targets

The difficulty in targeting higher energy barriers for SMMs – and there seems little point in further studies unless higher energy barriers are found – is that control has to be achieved of delicate structural parameters. The synthetic chemist has to control the exchange interaction between metal centres, to control the ground state spin; correlations of exchange with structural parameters exist, but controlling parameters such as M–O–M angles at bridging hydroxides is not straightforward. The single ion anisotropy also has to be controlled and maximised; this is possible in mononuclear species, for example Mallah and co-workers have been showing remarkable ZFS for monometallic nickel(II) species,[82] but rarely possible in polymetallic complexes. Thirdly, the anisotropy axes of the individual centres must be correctly orientated; this has been clear for some time in $\{Mn_{12}\}$ and demonstrated beautifully by Oshio for divalent ions,[74] and recently Glaser *et al.*, have chosen to consider symmetry as a major design feature in their synthetic approach – deliberately making an SMM which has C_3 symmetry.[83] However, no-one has yet been able to combine all three considerations into a single molecule, for example in the Glaser *et al.* work synthetic control is achieved using $[Cr(CN)_6]^{3-}$, which is an isotropic spin centre. Synthetic processes to target control of individual anisotropy, exchange and cluster symmetry are needed.

5.5 EMERGING TRENDS

5.5.1 Monometallic SMMs

In 2003 a new class of SMMs was reported which contain only a single paramagnetic metal ion.[84] These were the *bis*-phthalocyanine (H_2Pc) lanthanide sandwich complexes $(Bu_4N)[Ln(Pc)_2]$, where the Ln^{3+} ion has

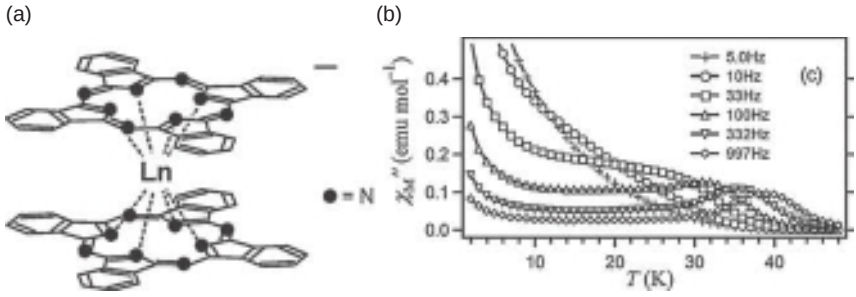

Figure 5.30 (a) Structure of $[Ln(Pc)_2]^-$ anion. (b) Out-of-phase AC susceptibility data for $(Bu_4N)[Tb(Pc)_2]$ (*ca* 2%) doped in $(Bu_4N)[Y(Pc)_2]$. Reprinted with permission from Ishikawa *et al.*, 2004 [85]. Copyright (2004) American Chemical Society

8-coordinate, square-antiprismatic geometry (Figure 5.30). Three of these complexes, with $Ln = Tb$, Dy and Ho, showed slow magnetisation relaxation as first observed by out-of-phase peaks in the AC susceptibility[84] and later by magnetisation hysteresis.[85,86] Remarkably, the Tb^{3+} complex showed $\chi''(T)$ peaks at temperatures up to 40 K (for $\omega = 1$ kHz), much higher than observed for any cluster-based SMM, and Arrhenius analysis of the frequency-dependent data gave a barrier height of 230 cm^{-1}. The Dy^{3+} and Ho^{3+} complexes have much lower barriers.

In all the examples of SMMs described so far (with the exception of the Co(II)-based species), it has been possible to discuss their magnetic properties in terms of their electron spin. However, if orbital angular momentum is not quenched, then this also gives rise to a magnetic moment. Hence, for the Tb^{3+} ($4f^8$), Dy^{3+} ($4f^9$) and Ho^{3+} ($4f^{10}$) ions, which have $^7F_6$, $^6H_{15/2}$ and $^5I_8$ ground states, respectively, the *total* angular momentum given by the quantum number $J = 6$, 15/2 and 8, respectively, must be considered. Just as the quantised orientation of S is described by M_S (the projection of S on z, the axis of quantisation), we have J and M_J quantum numbers and the $2J+1$ degeneracy can be split in zero applied field by crystal field effects. From NMR and susceptibility experiments on $(Bu_4N)[Tb(Pc)_2]$, the $M_J = \pm 6$ substates were found to be lowest lying followed by $M_J = \pm 5$ at 436 cm^{-1} above this; for $(Bu_4N)[Dy(Pc)_2]$, $M_J = \pm 13/2$ are lowest followed by $M_J = \pm 11/2$ at 35 cm^{-1}.[87] Hence, there is an easy-axis type magnetic anisotropy and a relaxation mechanism involving $M_J = \pm 1$ transitions can be envisioned in analogy to 'conventional' SMMs. Hence, the gaps to the first excited M_J levels are of the same order as the experimentally determined energy barriers.[84,85]

The simplicity of these small coordination compounds can be exploited to modify the structure and magnetic properties through simple methods. For example, it is possible to tune the sub-level spacing and energy barrier by redox.[88] Two-electron oxidation of $[Ln\{Pc(OEt)_8\}_2]^-$ to $[Ln\{Pc(OEt)_8\}_2]^+$ (where the ethoxide-derivatised ligand gives greater solubility to the redox products) leads to a contraction of the *Ln*–ligand distances and an increase in the ligand field strength. This results in an increased energy gap between ground and first excited M_J states and the energy barrier is increased. For $Ln = Tb^{3+}$ the $\chi''(T)$ peak for $\omega = 1$ kHz shifts from 40 to 52 K.

The simplicity of $(Bu_4N)[Ln(Pc)_2]$ also makes it easy to prepare isostructural diamagnetic analogues. Doping with the paramagnetic species of interest allows study of the SMM in the absence of inter-molecular effects (*e.g.* Figure 5.31b, right).[84,85] This has made it possible to observe weak interactions such as nuclear hyperfine effects (of the order of 10^{-2} cm^{-1}) and their influence on QTM. Micro-SQUID measurements on single crystals of *ca* 2% Tb-doped $(Bu_4N)[Y(Pc)_2]$ show large QTM steps around zero field where $M_J = \pm 6$ cross (Figure 5.31a).[6] In fact, this is a series of steps at low field (Figure 5.31b). These cannot be due to anti-crossings with excited M_J

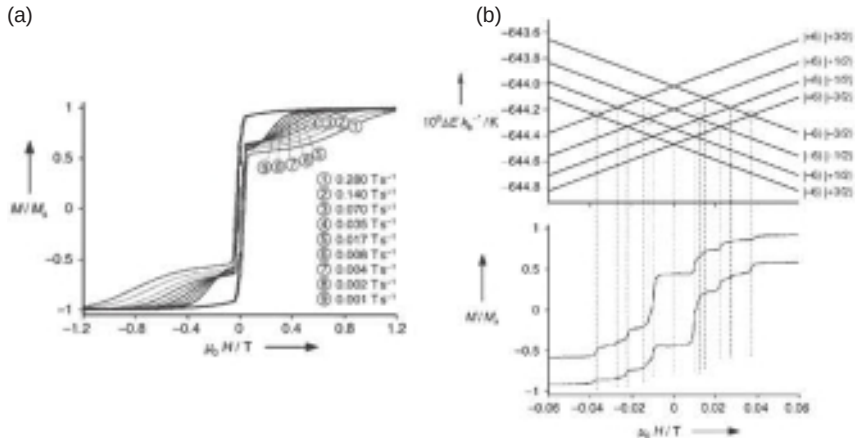

Figure 5.31 (a) $M(H)$ hysteresis loops for a single crystal of 2% Tb-doped $(Bu_4N)[Y(Pc)_2]$ at 0.04 K and with applied field (various sweep rates) along the easy axis. (b, lower) Expansion of low field area. (b, upper) Zeeman diagram for the $M_J = \pm 6$ doublet of Tb^{3+} including nuclear hyperfine and quadrupole interaction with the $I = 3/2$ ^{159}Tb nucleus. The states are labelled by their M_J, M_I quantum numbers and correspondence between level anti-crossings and QTM steps are shown. Reprinted with permission from Ishikawa *et al.*, 2005 [89]. Copyright (2005) Wiley-VCH

states given the huge energy gap to $M_J = \pm 5$, but can be explained by interactions with the ^{159}Tb (100% natural abundance), $I = 3/2$ nuclear spin. The hyperfine interaction splits each M_J into four sub-levels and the steps are due to anti-crossings between the combined M_J, M_I states. (The irregularity of the step spacing is due to the nuclear quadrupole interaction, essentially a ZFS effect for the nuclear spin.) This was the first direct observation of nuclear-spin driven QTM in SMMs. Similar effects were found for the Ho^{3+} complex.[86]

A second family of monometallic SMMs has since been prepared. These are also lanthanide sandwich compounds: $Na_9[LnW_{10}O_{36}]$ where Ln^{3+} is coordinated to two $\{W_5O_{18}\}^{6-}$ polyoxotungstate ligands.[90] Interestingly, SMM behaviour is found for Er^{3+} ($^4I_{15/2}$ ground state) but not Tb^{3+} or Dy^{3+}. In the phthalocyanine system the square-antiprismatic geometry at Er^{3+} is axially compressed while in the polyoxotungstate system it is elongated. This is found to lead to $M_J = \pm 1/2$ lowest lying sublevels for the former and $M_J = \pm 15/2$ for the latter, hence easy axis and easy plane type magnetic anisotropies.

5.5.2 Molecular Spintronics

Molecular electronics is concerned with the electrical transport properties of single molecules, the key point being that this is governed by the discrete electronic energy levels of the molecules. Spintronics is a growing technology based on the differences in transport properties of spin-up and spin-down electrons through a magnetic material – most famously the basis for the giant magnetoresistance effect exploited in hard drive read heads. Molecular spintronics is the marriage of these two fields, seeking to exploit the quantum magnetic properties of individual molecules in electronic devices. SMMs are obviously exciting materials in this context and there is a considerable literature growing in this area; an excellent review has been written by Wernsdorfer.[91]

The transport properties of $\{Mn_{12}\}$ derivatives have been measured by two groups,[92,93] in a 'molecular spin transistor' type arrangement. A molecule is grafted between two nonmagnetic metallic electrodes, called the 'source' and 'drain', which are lithographed on a conducting substrate called the 'gate' electrode. In Heersche *et al.* [92] this is achieved using a thioacetyl-derivatised carboxylate in $[Mn_{12}O_{12}(O_2C\text{-}C_6H_4\text{-}SCOMe)_{16}(H_2O)_4]$ and gold source and drain electrodes on an Al/Al_2O_3 gate (Figure 5.32a). The organic spacers between the magnetic

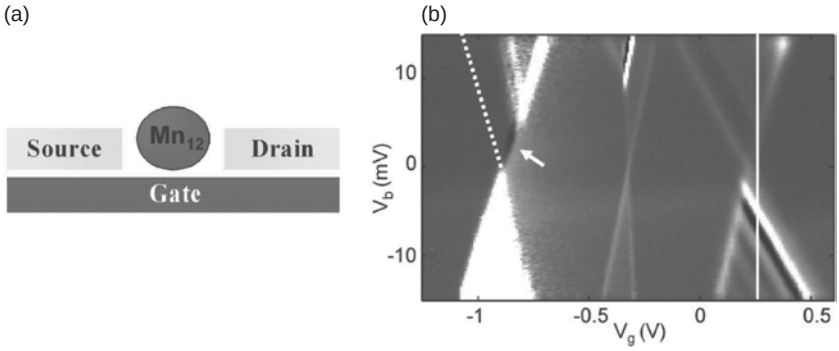

Figure 5.32 (a) Schematic of molecular spin transistor device. The source and drain are gold electrodes to which a single molecule of a derivatised $\{Mn_{12}\}$ is grafted. The gate electrode is an Al/Al_2O_3 surface. (b) Differential conductance plot [$T = 3$ K; gray scale from $dI/dV_b = -0.8$ (black) to $+1.4$ nS (white)]. Reprinted with permission from Heersche *et al.*, 2006 [92]. Copyright (2006) American Physical Society

core of the molecule and the gold surfaces ensure that the molecules are only weakly coupled to the electrodes, that is, that the molecular states are only weakly perturbed. The source–drain current (I) is monitored as a function of the bias voltage (V_b, between source and drain) for different gate voltages (V_g). In order for current to flow the electrons must tunnel through the potential barrier between electrode and molecule. At low temperature this is blocked (known as a 'Coulomb blockade' effect) unless the molecular states have the same energy as the Fermi energy (E_F) of the electrodes. This can be achieved by varying V_b to bring E_F to match the molecular levels, or by modulating the molecular levels *via* V_g to match E_F. The data are typically presented as maps of the differential conductance (dI/dV_b) *vs* V_b and V_g (Figure 5.32b).

For a given V_g, the current is suppressed up to a certain threshold V_b (positive or negative) the value of which varies linearly with V_g (bright lines in Figure 5.32b). This gives rise to 'Coulomb diamonds' with lines intersecting at $V_b = 0$; the presence of several such regions relates to different charge states depending on V_g, for example $\{Mn_{12}\}^{+/0/-}$, whose levels match in energy at the intersections.[92,93] Increasing V_b further leads to steps in I as excited states of the molecule come into resonance (striped features in Figure 5.32b).[3] Further interesting features were observed, including areas of complete current suppression (above the missing diamond edge shown by the dashed line in Figure 5.32b) and areas of negative differential conductance (solid line on the right-hand side of Figure 5.32b). Modelling showed that such features

could be reproduced qualitatively taking into account the magnetic levels of the multiple charge states and the smaller ZFS in $\{Mn_{12}\}^{+/-}$ *cf.* $\{Mn_{12}\}$.[2,3]

The effect of an applied magnetic field was also studied and found to be consistent with all charge states being magnetic.[93] However, one important feature was missing from these latter studies: no hysteresis effects were observed despite the experiments being performed at 300 mK. A possible reason for this is some degradation of the $\{Mn_{12}\}$ molecule when sorbed onto gold:[94] separate surface studies have shown evidence for reduction and have also failed to observe magnetic hysteresis.[95] However, a recent breakthrough has been made with another family of SMMs, $[Fe_4L_2(dpm)_6]$, grafted to a gold surface *via* thioacetyl groups from H_3L = 11-(acetylthio)-2,2-bis(hydroxymethyl)undecan-1-ol, where hysteresis in the magnetisation *vs* applied field response has been detected *via* X-ray magnetic circular dichorism.[66]

If the electronic coupling between molecule and gate electrodes is strong, then their wave functions are mixed and further important quantum phenomena are predicted. If the molecule is in a paramagnetic state then there is an exchange interaction between the (localised) unpaired electrons of the molecule and the delocalised conduction electrons of the electrodes, allowing tunnelling of electrons between molecule and electrodes and inducing spin-flips of the localised electron. This generates a new state for the system (molecule plus electrodes) with the same energy as E_F and, hence, an enhancement of the conductance at zero V_b. This is known as the Kondo effect,[96] and has been observed for magnetic molecules.[97] The multiple redox centres in magnetic clusters can be exploited to switch the Kondo effect on/off, as has been demonstrated in $[\{(Me_3tacn)(CN)_2V\}_2(\mu\text{-}C_4N_4)]^{0/+}$.[98] In the $S = 1/2$, $\{V^{IV}V^{V}\}$ state, the Kondo resonance is observed as a bright horizontal line at $V_b = 0$ in the appropriate Coulomb diamond (Figure 5.33, left). In the $\{V^{IV}V^{IV}\}$ state strong antiferromagnetic coupling gives an $S = 0$ ground state, the molecule is diamagnetic at low temperature and there is no Kondo peak (Figure 5.33, right). It has also been shown that the Kondo effect can be controlled in 'two-electron' molecular systems by tuning the singlet–triplet gap *via* the gate voltage.[99] Although important Kondo effects have been predicted for SMMs[100] they have yet to be observed. This is probably simply because their surface chemistry is not well enough developed for many of them to have been studied in this fashion.

Several molecular spintronic devices have been proposed, including molecular spin valves (where a spin-polarised current from a magnetic

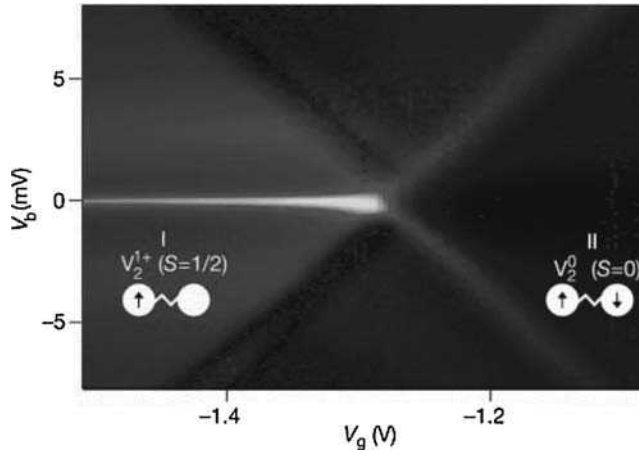

Figure 5.33 Differential conductance of $[\{(Me_3tacn)(CN)_2V\}_2(\mu\text{-}C_4N_4)]^{0/+}$ as a function of bias (V_b) and gate (V_g) voltage [T = 300 mK; colour scale from $dI/dV_b = 0$ (dark) to +50 μS (bright)]. Reprinted by permission from Liang *et al.*, 2002 [98]. Copyright (2002) Macmillan Publishers Ltd

electrode is blocked or transmitted *via* a magnetic molecule depending on relative orientation of magnetisation) and 'double dot' devices (where magnetic molecules are weakly coupled to a nonmagnetic conductor, *e.g.* a carbon nanotube,[101] which is itself bound to the electrodes) which could in principle allow coherent manipulation and read-out of spin information.[91]

5.5.3 Quantum Information Processing

The idea that the quantum behaviour of MNMs could be used in information processing was first proposed by Loss and Leuenberger[102] and this has been developed further by Loss and his co-workers,[103] and by others.[104] Quantum information processing (QIP) is itself controversial, with some unconvinced that such technology could ever be realised. The proposal to use MNMs in this context is also controversial, and one difficulty is that different groups describe identical phenomena in very different language; this makes the current literature on the subject difficult to disentangle.

Three immediate issues face any chemist attempting to design molecules for QIP: understanding QIP at an appropriate level, designing

individual units (qubits) to be used in QIP and thinking of methods for linking the qubits into structures where they can interact. Beyond these issues are questions concerning building devices so that individual qubits or arrays of qubits can be addressed; these issues require collaborations with electronic engineers and/or physicists and are beyond what is discussed here.

Conventional computing works by storing information in a two-state system, which can be either '0' or '1', or 'on/off'. Computation then involves processes where the information stored in individual bits is combined to produce a result. Combining the information involves two-bit logic gates (*e.g.* an AND gate where the output is 1 if both inputs are 1). To write the integers from zero to seven would require three bits, which would have the values, |0 0 0>, |0 0 1>, |0 1 0>, |0 1 1>, |1 0 1>, |1, 1, 0>, |1, 1, 1>.

A quantum computer involves storing information in microstates |0> and |1> and allowing for quantum superposition of the two microstates. The first result of this change is that much more information could be stored in a 'qubit', because the superposition creates the possibility of storing much more information than just 0 or 1 in a single unit. Thus, all the integers from 0 to 7 (and many more) could be written in a single qubit. The second change comes about when considering processing: any logical operation on one qubit will be performed on a quantum superposition of states and, therefore, will lead to an increase in speed of operation similar to a massive parallel computer.

There are several cases where algorithms have been developed that demonstrate that QIP would be much faster than conventional computing. The first is the Grover search algorithm,[105] which involves finding information in an unsorted database of information. An example would be finding the name corresponding to a telephone number in a telephone directory. For a classical computer the average length of time this search would take increases linearly with the size of the database (it is probably obvious that *on average* half the database has to be searched to find the correct answer). The parallel nature of a quantum computer means that the time taken is much less and scales as the square root of the number of entries.

The second algorithm is the Shor algorithm,[106] which demonstrates that a quantum computer could factorise very large numbers into primes much more quickly than a classical computer. This immediately becomes important because modern cryptography is dependent on the fact that classical computers are very good at multiplying many primes together to

generate a large number, but hopeless at factorising the large number back into the primes.

Identifying suitable physical systems to act as qubits is an active area. The proposal that MNMs could act as qubits was first made in 2001, where the proposal was made that $\{Mn_{12}\}$ could be used to implement the Grover algorithm, using the large number of M_S states within the $S = 10$ ground spin manifold. The idea proposed[102] is that one could choose to populate selectively the various different M_S levels of one of the two energy wells; the fact that the levels are not equally spaced is important. The method proposed to populate the different levels involves pulses of electromagnetic radiation with multi-photon absorptions needed. This proposal presents significant technical challenges.

More recent proposals have involved MNMs which have $S = 1/2$ ground states, with the two microstates $|+1/2\rangle$ and $|-1/2\rangle$ acting as the '0' and '1' that will undergo quantum superposition. Most work has been published on $\{Cr_7Ni\}$ rings,[107–109] with other work on $\{V_{15}\}$ polyoxometallates (POMs)[110] and on a mixed valence polyoxometallate $[PMo_{12}O_{40}(VO)_2]^{4-}$;[111] this last case contains two $S = 1/2$ centres on the vanadyl units. To be useful qubits the MNMs have to have a well-isolated $S = 1/2$ state, with no interference from higher lying energy levels that are not involved in the computation.

One major difficulty in using MNMs in quantum computing could be that the information stored in the MNM could be lost to the surroundings more quickly than it is possible to perform computations. The length of time the information can be stored is called the 'coherence time' or, confusingly, the 'decoherence time'. These times can be related to the transverse spin relaxation time, T_2, of the system. Rather surprisingly, despite the proposal that MNMs could be used in QIP being made in 2001,[102] no-one had reported coherence times in MNMs until Ardavan *et al.* did so in 2007.[108] This group used pulsed EPR spectroscopy, which is a technique that requires a significant coherence time otherwise the signal is not observed. Pulsed EPR spectroscopy has since been used in other MNMs, including for the first time in an SMM.[112] These are necessary experiments, yet at one level not new as pulsed EPR has been used previously to obtain spin relaxation times in multi-metallic enzymes, and pulsed EPR had been used to show that *endo*-fullerenes, also proposed for uses in QIP, have much longer coherence times.[113] However, the key observation is that even in complicated metal-organic molecules coherence times could be achieved of *ca* 3 μs, which is long enough to allow manipulation of spins.

If MNMs can be used as qubits – and the physical studies of individual molecules suggest that they can – the next problem is to link the individual qubits to produce multiple qubit arrays. The first significant work in this area is the linking of two {Mn_4} SMMs, reported by Christou and co-workers.[54,114] The chemical link between the two {Mn_4} units is extremely weak – a C–H. . .Cl hydrogen bond – but enough for the spin states on one SMM to interact with the other within a single crystal. The individual {Mn_4} cages have $S = 9/2$ ground states, and EPR studies of isolated {Mn_4} units show typical EPR transitions, for example $M_S = -9/2 \rightarrow -7/2$.[14] In the dimers the M_S states on the individual {Mn_4} units are involved in a quantum superposition, so that symmetric and antisymmetric superpositions of the individual spin states result, for example:

$$|M_1,M_2>_{\text{Symm}} = (|M_1,M_2> + |M_1,M_2>) \text{ and}$$
$$|M_1,M_2>_{\text{Antisymm}} = (|M_1,M_2> - |M_1,M_2>)$$

This leads to a splitting of some of the EPR transitions in the dimer, which is clear evidence for the superposition. As a physical demonstration of the principle this is extremely beautiful work; however, switching the superposition on and off requires recrystallisation of the {Mn_4} cages to achieve a different crystal packing.

More recently, Lehmann *et al.*[111] proposed a scheme where electrical gating could be used to switch on/off the interaction between two $S = 1/2$ units in a single polyoxometallate – $[PMo_{12}O_{40}(VO)_2]^{4-/5-}$. In one oxidation state the molybdenum section of the POM is diamagnetic, and the two $S = 1/2$ vanadyl fragments are isolated. Reduction of the POM places a single unpaired electron on the molybdenum section, and switches on the interaction. This is an interesting scheme, and should be feasible using current technology, for example the single electron could be injected or removed using STM.

Controlled interaction of $S = 1/2$ units has also been achieved by linking {Cr_7Ni} rings.[109] This can be done by functionalising the rings to introduce a donor group onto the exterior of the {Cr_7Ni} rings; two such rings are then bound to another metal complex, which can be paramagnetic or diamagnetic. Where the linking metal complex is paramagnetic the qubits interact, while when it is diamagnetic no interaction is observed. As with the {Mn_4} case, the switching on/off of the interaction currently requires a chemical reaction; however, design of suitable groups (*e.g.* photo- or redox-active units) to act as linkers should be possible in this system.

5.5.4 Antiferromagnetic (AF) Rings and Chains

AF rings have been mentioned above in the context of QIP. However, studies of these MNMs have also been used to examine spin dynamics in one-dimensional materials. The original AF ring examined was $[Fe_{10}(OMe)_{20}(O_2CCH_2Cl)_{10}]$ – the 'ferric wheel' made in Lippard's group.[115] There are a large number of homometallic AF rings, and almost without exception these are even-numbered. The result is that there are equal numbers of spins aligned 'up' and 'down'', and the spin ground state of these systems is zero. Much of the original interest was looking at behaviour in these antiferromagnetic systems at level crossings. As the magnetic field increases, the Zeeman splitting of the first excited state ($S = 1$) leads to the $M_S = -1$ sublevel falling in energy so that it crosses the $S = 0$ state and becomes the ground state at some magnetic field (as in Figure 5.8). The studies of the ferric wheel showed steps in magnetisation at these level crossings.

Many further Fe^{III} rings have been synthesised, with work from the Saalfrank group showing that the size of the rings can be controlled by choice of templates.[116] Further studies of other Fe^{III} AF rings showed that the energy spectrum of the spin levels could be described as a rotational band; there is a parabolic behaviour for the lowest lying energy level for each value of S.[117] This observation allows an estimate of the magnetic susceptibility behaviour of many large polymetallic cages, including the extraordinary icosidodecahedra discussed in Section 5.5.6.

More controversially, there have been proposals that the AF rings can be used to study the tunnelling of the Néel vector.[118] The classical description of the ground state of an AF ring is a Néel state, which can be regarded as spins on the odd-sites of the ring aligned in one direction (say 'up') with the spins on the even-sites aligned 'down'. Tunnelling of the Néel vector would then involve going from odd-up, even-down to the odd-down, even-up state of the ring. While these two descriptions of the $S = 0$ ground state have the same energy, getting from one to the other involves an energy barrier. The proposal is that INS studies have allowed this tunnelling of the Néel vector to be observed, but this interpretation is not universally accepted.

The introduction of a heteroatom into the AF rings has increased the range of available materials.[119] Building on the work of Saalfrank, it is possible to choose the size of these rings by choice of template. This has allowed the first synthesis of a large odd-numbered AF ring, a $\{Cr_8Ni\}$ ring.[120] In principle, odd-numbered AF rings should show

spin frustration leading to degenerate ground states. However, $\{Cr_8Ni\}$ is an even-electron system and the ground state is a singly degenerate $S = 0$ state. The work on heterometallic AF rings has produced eight-, nine-, ten-, twelve-, thirteen- and fourteen- membered rings, and also some heterometallic chains, such as the $\{Cr_{12}Ni_3\}$ chain[119] shown in Figure 5.34.

These heterometallic rings allow further studies of fundamental ideas in the physics of magnetism. A series of studies has looked in detail at what happens at level crossings when the symmetry of the system leads to mixing of the states that are due to cross, and hence changes crossings into avoided crossings. This contrasts with the work on iron(III) rings where the high symmetry of the molecules mean that the crossings are real, and there is a sharp step in magnetisation.[115] In the heterometallic AF rings the presence of a heterometal lowers the symmetry, and this leads to all magnetic states belonging to the same irreducible representation. In turn, this means that these states can mix, with the mixing increasing as the states approach each other in energy as a result of increasing magnetic field.

Figure 5.34 The structure of a $Cr_{12}Ni_3$ chain in the crystal. Key: Cr (large lighter spheres), Ni (large dark), C (small black), F (small light), O (small dark)

In {Cr_7Ni} this mixing of spin states has been studied by low temperature single crystal INS.[121] This work required a 3 g single crystal of the MNM, and the measurements took place in a variable magnetic field, reaching 11 T, and at 55 mK. However, the experiments allow direct measurement of the avoided crossing gap – giving a value of 0.12 meV (around 1 cm^{-1}). This illustrates one major advantage of molecular magnetism over solid state materials – the degree of control possible is huge and allows testing of theory without making allowances for impurities or polydispersity in the size of nanoparticles.

5.5.5 Magnetocaloric Effect

The magnetocaloric effect (MCE) is intrinsic to any paramagnet and describes its temperature change on changing applied magnetic field. This occurs because on magnetisation (demagnetisation) phonons are emitted to (absorbed from) the lattice, hence the temperature increases (decreases). This can be described by magnetic entropy–temperature curves (Figure 5.35). The $2S+1$ degeneracy of a spin S gives it a 'magnetic entropy' of $S_m = R\ln(2S+1)$ (the spin is disordered over the $2S+1$ M_S states; R is the gas constant). On application of a field the spin system orders and hence S_m decreases (to nil on saturation). Similarly,

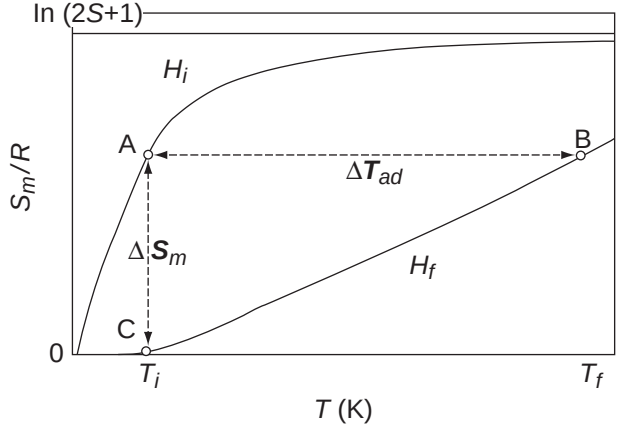

Figure 5.35 Entropy–temperature curves showing iso-field lines ($H_i < H_f$) for a paramagnet of spin S, showing possible isothermal magnetisation ($A \rightarrow C$) and adiabatic magnetisation ($A \rightarrow B$) processes. Reprinted with permission from Evangelisti *et al.*, 2006 [19]. Copyright (2006) Royal Society of Chemistry

S_m decreases when the temperature is decreased at constant field. These effects can be exploited in a process known as adiabatic demagnetisation. If a sample is magnetised by application of a field (from H_i to H_f) whilst in thermal equilibrium with its surroundings (*i.e.* its temperature is maintained constant) there is a magnetic entropy change ΔS_m (Figure 5.35, A $\rightarrow$ C). If the sample is thermally isolated and the field removed slowly (H_f to H_i) then an adiabatic demagnetisation can be performed. This means that the total entropy of the system is constant, hence the increase in S_m on randomising the spin system must be matched by a decrease in the entropy of the lattice. In other words, when thermally isolated the only energy available to randomise the spins is from the lattice phonon system. This results in a decrease in its temperature (B $\rightarrow$ A).

A bigger spin will give rise to a bigger entropy change. Because of their high spin ground states, SMMs were considered as magnetic refrigerants at low temperature (below say 20 K), where the large magnetisation, and hence entropy changes, are accessible,[122,123] with advantages over magnetic nanoparticles that there is no size distribution that tends to smear out the MCE response.[19] However, their magnetic anisotropy breaks the $2S+1$ degeneracy in zero field and below their blocking temperatures the spin system tends to lose thermal contact with the lattice (spin lattice relaxation is very slow). This results in lower MCE.[19] Hence, MNMs with large spin ground states but zero or very small magnetic anisotropy are promising. This is the case with $[Fe_{14}(bta)_6O_6Cl_6(OMe)_{18}]$ (Hbta = benzotriazole).[124] This molecule has an $S = 25$ ground state, resulting from competing antiferromagnetic interactions between the Fe(III) ions, with negligible anisotropy. The magnetic entropy can be determined from integration of specific heat data as a function of temperature for different applied fields. The S_m *vs* T curves can be constructed and ΔS_m and ΔT_{ad} determined as a function of initial temperature (Figure 5.36). For $\{Fe_{14}\}$, the MCE effect (ΔS_m and ΔT_{ad}) is at a maximum at *ca* 6 K. The value for ΔS_m is 5.0 R or 17.6 J kg^{-1} K^{-1} at 6 K for a field change of 0–7 T, corresponding to $\Delta T_{ad} = 5.8$ K. Hence, $\{Fe_{14}\}$ can be cooled by conventional means to 6 K and then, *via* an isothermal magnetisation–adiabatic demagnetisation cycle, achieve temperatures of the order 10^{-1} K. In fact, this ΔS_m is larger than that accessible from an isolated spin $S = 25$ [$\ln(2S+1) = 3.9$ R] and this is due to population of low-lying excited states, also of large spin, at zero field providing an additional source of magnetic entropy.

Hence, MNMs are promising materials for low temperature refrigeration applications. Derivatives of $\{Fe_{14}\}$[125] and ferromagnetically

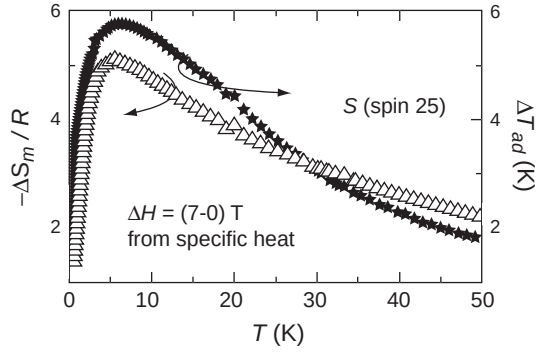

Figure 5.36 Magnetic entropy change and adiabatic temperature change, derived from specific heat data, for $[Fe_{14}(bta)_6O_6Cl_6(OMe)_{18}]$ on an applied field change of 7 to 0 T. Solid line is the entropy for an $S = 25$ paramagnet. Reprinted with permission from Evangelisti *et al.*, 2006 [19]. Copyright (2006) Royal Society of Chemistry

coupled $\{Mn^{III}_6Mn^{II}_4\}$ clusters[126] have been reported with larger MCE effects, and there are almost certainly molecules in the literature with greater performance still that have not as yet been studied in this context. An excellent review has been published by Evangelisti *et al.*[19]

5.5.6 High Symmetry Polyhedra and Spin Frustration

A simple antiferromagnetically coupled equilateral triangle of spins is a surprisingly interesting situation. This is because it is the simplest example of geometric 'spin frustration'. This can easily be visualised from Figure 5.37: if the two spins on the lower edge of the triangle are coupled 'up' and 'down', then the third spin cannot simultaneously satisfy both AF interactions. For a half-integer spin system where the interactions are all equal strength (*i.e.* an equilateral triangle) this results in a degenerate ground state of two different $S = 1/2$ states.[127] For an integer spin the ground state is nondegenerate, a single $S = 0$ state, and despite the fact that it is not possible to write a trivial 'spin up–spin down' picture it is not frustrated. However, for corner-sharing equilateral triangles the ground state is degenerate for both integer and half-integer spins and again there is spin frustration.[128] When such effects are extrapolated to infinite 2D and 3D lattices they can lead to many unusual magnetic phenomena and have been the object of much research in solid state physics.[129]

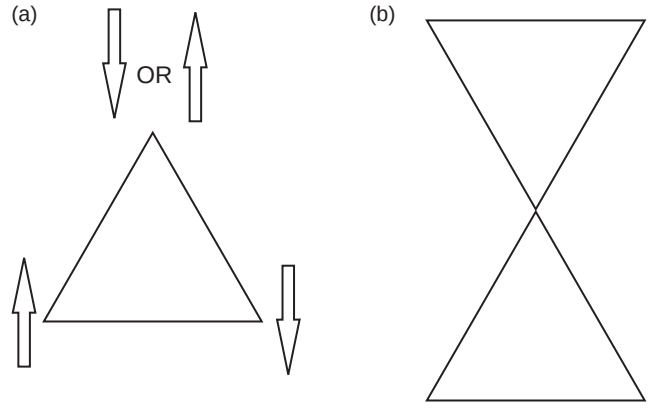

Figure 5.37 (a) An AF coupled equilateral triangle of spins. The AF interactions cannot all be satisfied simultaneously. (b) Vertex-sharing equilateral triangles

AF coupled MNMs based on high symmetry polyhedra of paramagnetic metal ions have proved fascinating materials in which to investigate frustration effects in large but finite spin systems. The most spectacular example to date is in Müller's so-called 'Keplerates', polyoxomolybdate species $\{Mo^{VI}_{72}M_{30}\}$ that contain 30 paramagnetic ions, $M = Fe^{III}$, Cr^{III} or $(VO)^{2+}$ (Mo^{VI} is diamagnetic), arranged on the vertices of an icosidodecahedron (I_h symmetry).[130,131] This Archimedian solid consists of 20 vertex-sharing triangles arranged round 12 pentagons (Figure 5.38); each vertex has identical (four-)connectivity and all interactions are AF. This can be considered as a 2D frustrated topology wrapped around a sphere, and low temperature magnetic effects that had been predicted for special types of frustrated 2D lattices, for example discontinuities in the susceptibility (dM/dH) at a specific fraction of the saturation magnetic field, were first observed in this molecule.[133] Similar effects have been predicted for other polyhedra.[133]

Calculating the full spin state structure exactly for such enormous spin systems (6^{30} for $Mo_{72}Fe_{30}$) is impossible, and these species have also been important in testing different approximate models. One method is to use 'classical' spins, that is the spins are treated as simple vectors and allowed to point in any orientation in space. In this case the lowest energy (*i.e.* 0 K) configuration for the AF equilateral triangle in Figure 5.37 has the three spins in the plane and oriented 120° from each other. As a field is applied the spins will tend to align with it continuously but maintain their 120° relative orientations until saturation when they align fully with the field.[134] In $\{Mo_{72}Fe_{30}\}$ the 30 spin vectors can be grouped into

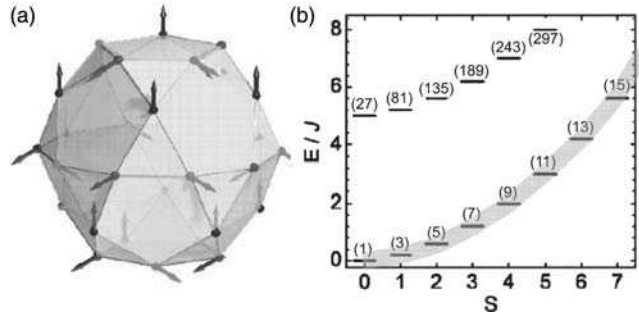

Figure 5.38 (a) The icosidodecahedron. In the $\{Mo_{72}M_{30}\}$ 'Keplerate' molecules the 30 paramagnetic M ions are at the vertices of this solid. The arrows represent the minimum energy classical spin orientation and the shading highlights the three different sub-lattices where each spin is oriented 120° from its nearest neighbours. (b) Lowest energy total spin states plotted as a function of S, from a rotational band model with the lowest band highlighted. The number of states of each S is in parentheses. Reprinted with permission from Garlea *et al.*, 2006 [132]. Copyright (2006) American Physical Society

three sub-lattices where all 10 spins in each sub-lattice are always co-parallel (Figure 5.38a) and each spin is oriented at 120° from its nearest neighbours, as in the isolated triangle. Remarkably, a classical model reproduces magnetisation data down to temperatures as low as 0.1 K,[135] where normally it would be expected to see quantum effects, such as steps in $M(H)$ due to level crossing between different total S states (as in Figure 5.8). The classical spin approximation becomes poorer as the spin gets smaller and the development of the $M = Fe^{III}$ ($S = 5/2$), $M = Cr^{III}$ ($S = 3/2$) and $(VO)^{2+}$ ($S = 1/2$) Keplerates should allow fascinating insight to the transition between classical and quantum spin models.[131] Approximate quantum models have also been developed (also based on coupling of sub-lattices). One model that appears to be quite general for spin topologies with 'homogeneous' AF coupling (including rings, tetrahedra, octahedra and icosahedra)[136] is the 'rotational band' model. The key feature is that the energy of the lowest energy state(s) for each possible value of the total spin S is, to a good approximation, proportional to $JS(S+1)$ giving a 'band' as highlighted in Figure 5.38b. There is a first excited band consisting of the next lowest energy states for each value of total spin, and so on. Excited rotational bands, in this and other molecules such as AF rings,[137] have been related to spin-waves – collective spin excitations in classical spin theory of

antiferromagnets – thus providing another link between quantum and classical magnetic behaviour.

Further fascinating properties, such as hysteresis (despite lack of anisotropy), and large high-field MCE effects (due to massive degeneracies of many *S* states at specific values of field before achievement of saturation) resulting from spin frustration in related but as yet unmade high symmetry topologies, such as icosahedra, have also been predicted,[138] providing an on-going challenge for synthetic chemists.

Another class of molecules with high degeneracy is the $\{Ni_{10}\}$ family,[139] where ten Ni^{II} ions ($S = 1$) lie on the vertices and edges of a tetrahedron (Figure 5.39a). There is strong antiferromagnetic coupling (J) between the edge ions across a central μ_6 oxide, and the four vertex metal ions are only weakly coupled to each other. This gives an unusual spin state structure of dense bands, the lowest having a degeneracy of $3^4 = 81$, separated by gaps of order J (Figure 5.39b). These molecules show slow magnetisation relaxation up to *ca* 17 K (the intrinsic nature of which is demonstrated by NMR),[140] and it has been proposed that this is a result of phonons becoming 'trapped' in the ground band (due to its high degeneracy), that is when a phonon is emitted by a molecule it has a higher probability of being reabsorbed by a neighbour than being dissipated to the lattice, thus drastically slowing relaxation.

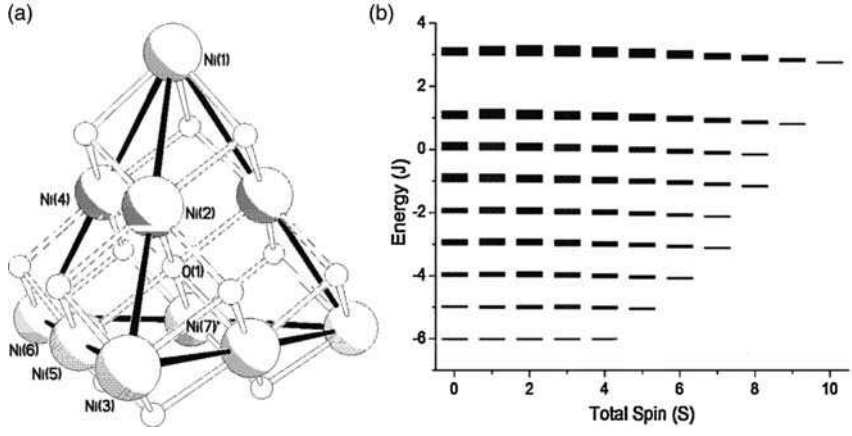

Figure 5.39 (a) Structure of the core of $[Ni_{10}(O)(thme)_4(dbm)_4(O_2CPh)_2(EtOH)_6]$ ($thme^{3-}$ is a tripodal alkoxide; dbm^- is a β-diketonate), highlighting the Ni_{10} tetrahedron. (b) Plot of energy *vs* total spin. Reprinted with permission from Shaw *et al.*, 2004 [141]. Copyright (2004) Royal Society of Chemistry

5.5.7 Single Chain Magnets

This chapter finishes with a short description of 'single chain magnets' (SCMs),[142] a growing class of 1D materials which, like SMMs, show magnetic hysteresis and Arrhenius-type dependence of relaxation time on temperature. While these materials are clearly not molecular their physics is related to those of SMMs, and SCMs can even be built from SMMs. The first example discovered was $[Co(hfac)_2(NITPhOMe)]_\infty$ ($hfac^-$ is a β-diketonate), in which the Co(II) ions are bridged by nitronyl nitroxides (NITPhOMe) in a 1D chain.[143] Slow relaxation is observed by AC susceptibility methods, with out-of-phase peaks reaching temperatures as high as 15 K ($\omega = 95$ kHz) and Arrhenius fitting gives an energy barrier to magnetisation reversal of 154 K (107 cm^{-1}), more than double that of $\{Mn_{12}\}$. Hysteresis in $M(H)$ is observed on single crystals below 4 K when H is applied along the chain axis.

This was the first observation of behaviour first proposed by Glauber in the 1960s for ferromagnetic 1D chains with Ising-type magnetic anisotropy.[144] 'Ising' means strong easy axis magnetic anisotropy, that is spins are restricted to 'up' and 'down' orientations (SMMs have Ising-type anisotropy at low temperature because of their $M_S = \pm S$ lowest substates). Glauber predicted that the magnetisation relaxation time τ should increase exponentially with decreasing temperature:

$$\tau = \tau_0 \exp\left(8JS^2/kT\right) \tag{5.4}$$

where S is the local spin. Note the energy barrier is proportional to the nearest-neighbour exchange interaction J, because the ferromagnetic interaction favours parallel alignment along the chain, and flipping any given spin in a saturated (fully aligned) chain requires overcoming two such interactions (Figure 5.40). Higher energy barriers are possible for SCMs than most SMMs because exchange interactions are typically larger than ZFS (the source of the barrier in SMMs). It is important that inter-chain interactions are vanishingly small in order to prevent 3D magnetic ordering (this is the reason it took about 40 years to observe Glauber dynamics in a real system).

Although $[Co(hfac)_2(NITPhOMe)]_\infty$ is not ferromagnetically coupled, a net magnetisation still results from antiferromagnetic coupling between the different spins of the radical ($S = 1/2$) and Co(II). Six-coordinate Co(II) has a $^4T_{1g}$ ground state; strong spin orbit coupling gives a well separated overall doublet ground state which can be treated at low temperature as an 'effective $S = 1/2$' with unusual and very anisotropic

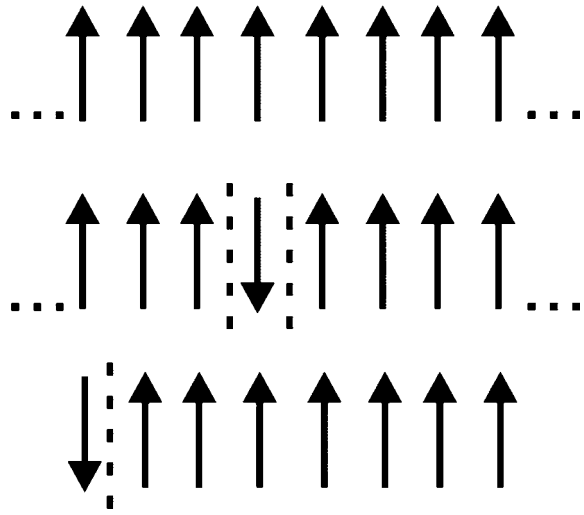

Figure 5.40 (Top) Fully aligned spins in an infinite ferromagnetic Ising chain on magnetic saturation. (Middle) Relaxation starts by flipping the orientation of one spin and requires overcoming two nearest-neighbour exchange interactions. (Bottom) In a *finite* chain reversal of the spin at chain termini only requires overcoming a single exchange interaction. Reprinted by permission of Gatteschi *et al.*, 2006 [9]. Copyright (2006) Oxford University Press

'effective g values'. These have been determined as ${g_z}^{\text{eff}} \approx 7.2$, ${g_{x,y}}^{\text{eff}} \approx 0.5$,[145] which means that there is an easy axis type anisotropy along z. For similar reasons lanthanide ions can be successfully incorporated into SCMs.[146]

Alternatively, the Ising type anisotropy can be from ZFS interactions of an $S > 1/2$ paramagnet. In fact, SCMs can be built from linking SMMs into chains. For example, $(NEt_4)[Mn^{III}{}_2(salmen)_2Fe^{III}(CN)_6]$ is an $S = 9/2$ ground state SMM with $U_{\text{eff}} = 14\,\text{K}$. By slight derivatisation of the ligand set at the peripheral metal ions these units can be linked into 1D chains in $\{(NEt_4)[Mn_2(5\text{-MeOsalen})_2Fe(CN)_6]\}_\infty$ (Figure 5.41a), with a ferromagnetic exchange interaction between the trimetallic units. This new material is an SCM with $U_{\text{eff}} = 31\,\text{K}$,[147] illustrating how the magnetic properties of SMMs can be enhanced by controlled linking. The energy barrier to relaxation now contains the exchange term and an additional contribution from the anisotropy barrier of the repeating unit, in this case the ZFS of the $S = 9/2$ ground state of the {MnFeMn} trimer:

$$\tau = \tau_0 \left[\exp\left(8JS^2 + DS^2\right)kT\right] \tag{5.5}$$

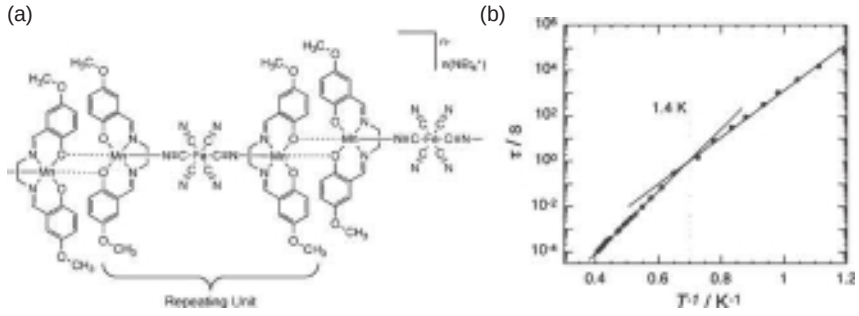

Figure 5.41 (a) $\{Mn^{III}Fe^{III}Mn^{III}\}$ SMM linked into a 1D chain that behaves as an SCM. (b) Arrhenius plots of relaxation time showing two different linear regimes. Reprinted with permission from Ferbinteanu *et al*., 2005 [147]. Copyright (2005) American Chemical Society

Several SCM examples have shown deviations from the Glauber behaviour at low temperatures; for example, below 1.4 K $\{(NEt_4)[Mn_2(5\text{-}MeOsalen)_2Fe(CN)_6]\}_\infty$ shows a second relaxation regime, with a reduced barrier of $U_{eff} = 25$ K (Figure 5.41b). This is due to the change in the correlation length (ξ) – the number of repeating units over which the spin is ordered – *versus* the actual length of the chain (n) limited by defects. As long as $\xi < n$ the Glauber dynamics hold. If $\xi > n$ then the barrier due to the exchange interaction is halved ($4JS^2$) because flipping the spins at the chain termini only requires overcoming one exchange interaction rather than two (Figure 5.40, bottom). Because ξ increases as the temperature decreases there will be a cross-over between these regimes at some temperature.

REFERENCES

[1] A. Caneschi, D. Gatteschi, J. Laugier, P. Rey, R. Sessoli and C. Zanchini, *J. Am. Chem. Soc*., **110**, 2795–2799 (1988).
[2] G. Christou, *Acc. Chem. Res*., **22**, 328–335 (1989).
[3] P. D. W. Boyd, Q. Li, J. B. Vincent, K. Folting, H. Chang, W. Streib, J. C. Huffman, G. Christou and D. N. Hendrickson, *J. Am. Chem. Soc*., **110**, 8537–8539 (1988).
[4] T. Lis, *Acta. Cryst. B*, **36**, 2042–2046 (1980).
[5] R. F. Weinland and G. Fischer, *Z. Anorg. Allg. Chem*., **120**, 161–180 (1921).
[6] R. Sessoli, D. Gatteschi, A. Caneschi and M. A. Novak, *Nature*, **365**, 141–143 (1993).

[7] R. Sessoli and D. Gatteschi, *Angew. Chem. Int. Ed.*, **42**, 268–297 (2003).
[8] R. E. P. Winpenny, (Ed.), *Struct. Bonding*, **122** (2006).
[9] D. Gatteschi, R. Sessoli and R. Villain, *Molecular Nanomagnets*, Oxford University Press, Oxford, 2006.
[10] G. Aromì and E. K. Brechin, *Struct. Bonding*, **122**, 1–67 (2006).
[11] R. Grinter, *The Quantum in Chemistry: An Experimentalist's View*, John Wiley & Sons Ltd, Chichester, 2005.
[12] J. A. Weil and J. R. Bolton, *Electron Paramagnetic Resonance: Elementary Theory and Practical Applications*, John Wiley & Sons Ltd, Chichester, 2007.
[13] O. Khan, *Molecular Magnetism*, Wiley-VCH Verlag GmbH, Weinheim, 1993.
[14] V. Marvaud, C. Decroix, A. Scuiller, C. Guyard-Duhayon, J. Vaissermann, F. Gonnet and M. Verdaguer, *Chem. Eur. J.*, **9**, 1677–1691 (2003).
[15] S. Maheswaran, G. Chastanet, S. J. Teat, T. Mallah, R. Sessoli, W. Wernsdorfer and R. E. P. Winpenny, *Angew. Chem. Int. Ed.*, **44**, 5044–5048 (2003).
[16] S. Piligkos, G. Rajaraman, M. Soler, N. Kirchner, J. van Slageren, R. Bircher, S. Parsons, H.-U. Güdel, J. Kortus, W. Wernsdorfer, G. Christou and E. K. Brechin, *J. Am. Chem. Soc.*, **127**, 5572–5580 (2005).
[17] W. Wernsdorfer, K. Hasselbach, A. Benoit, B. D. Mailly, J. Tuaillon, J. P. Perez, V. Dupuis, J. P. Dupin, G. Girauld and A. Perex, *J. Appl. Phys.*, **78**, 7192–7195 (1995).
[18] M. Affronte, J. C. Lasjaunias, A. Cornia and A. Caneschi, *Phys. Rev. B*, **60**, 1161–1166 (1999).
[19] M. Evangelisti, F. Luis, L. J. de Jongh and M. Affronte, *J. Mater. Chem.*, **16**, 2534–2549 (2006).
[20] J. van Slageren, R. Sessoli, D. Gatteschi, A. A. Smith, M. Helliwell, R. E. P. Winpenny, A. Cornia, A.-L. Barra, A. G. M. Jansen, E. Rentschler and G. A. Timco, *Chem. Eur. J.*, **8**, 277–285 (2002).
[21] A-L. Barra, D. Gatteschi, R. Sessoli and L. Sorace, *Magn. Reson. Chem.*, **43**, S183–S191 (2005).
[22] A. Bencini and D. Gatteschi, *EPR of Exchange Coupled Systems*, Springer-Verlag, Berlin, 1989.
[23] A.-L. Barra, L.-C. Brunel, D. Gatteschi, L. A. Pardi and R. Sessoli, *Acc. Chem. Res.*, **31**, 460–466 (1998).
[24] H. Andres, R. Basler, H. U. Güdel, G. Aromí, G. Christou, H. Buttner and B. Rufflé, *J. Am. Chem. Soc.*, **122**, 12469–12477 (2000).
[25] R. Basler, C. Boskovic, G. Chaboussant, H. U. Güdel, M. Murrie, S. T. Ochsenbein and A. Sieber, *Chem. Phys. Chem.*, **4**, 910–926 (2003).
[26] Y. Furukawa, K. Watanabe, K. Kumagai, Z. H. Jang, A. Lascialfari, F. Borsa and D. Gatteschi, *Phys. Rev. B*, **62** 14246_1–6 (2000).
[27] Y. Furukawa, K. Watanabe, K. Kumagai, F. Borsa and D. Gatteschi, *Phys. Rev. B*, **64** 104401_1–7 (2001).
[28] F. Borsa, A. Lascialfari and Y. Furukawa, *Lectr. Notes Phys.*, **684**, 297–349 (2006).
[29] F. Borsa, A. Lascialfari and Y. Furukawa, *Inorg. Chim. Acta*, **361**, 3777–3784 (2008).
[30] L. Thomas, F. Lionti, R. Ballou, D. Gatteschi, R. Sessoli and B. Barbara, *Nature*, **383**, 145–147 (1996).
[31] J. Friedman, M. P. Sarachik, J. Tejada, J. Maciejewski and R. Ziolo, *Phys. Rev. Lett.*, **76**, 3820–3833 (1996).

[32] W. Wernsdorfer and R. Sessoli, *Science*, **284**, 133–135 (1999).
[33] A. Caneschi, D. Gatteschi and R. Sessoli, *J. Am. Chem. Soc.*, **113**, 5873–5874 (1991).
[34] G. Chaboussant, A. Sieber, S. Ochsenbein, H. U. Güdel, M. Murrie, A. Honecker, N. Fukushima and B. Normand, *Phys. Rev. B*, **70**, 104422_1–16 (2004).
[35] A. L. Barra, D. Gatteschi and R. Sessoli, *Phys. Rev. B*, **56**, 8192–8198 (1997).
[36] I. Mirebeau, M. Hennion, H. Casalta, H. U. Güdel, A. V. Irodova and A. Caneschi, *Phys. Rev. Lett.*, **83**, 628–631 (1999).
[37] A. A. Mukhin, V. D. Travkin, A. K. Zvezdin, S. P. Lebedev, A. Caneschi and D. Gatteschi, *Europhys. Lett.*, **44**, 778–782 (1998).
[38] J. A. A. J. Perenboom, J. S. Brooks, S. Hill, T. Hathaway and N. S. Dalal, *Phys. Rev. B*, **58**, 330–338 (1999).
[39] Z. H. Jang, A. Lascialfari, F. Borsa and D. Gatteschi, *Phys. Rev. Lett.*, **84**, 2977–2980 (2000).
[40] T. Goto, T. Kubo, T. Koshiba, Y. Fujii, A. Oyamada, J. Arai, K. Takeda and K. Awaga, *Physica B*, **284–288**, 1227–1228 (2000).
[41] F. Fominaya, J. Villain, P. Gandit, J. Chaussy and A. Caneschi, *Phys. Rev. Lett.*, **79**, 1126–1129 (1997).
[42] L. Bokacheva, A. D. Kent and M. A. Walters, *Phys. Rev. Lett.*, **85**, 4803–4806 (2000).
[43] W. Wernsdorfer, M. Murugesu and G. Christou, *Phys. Rev. Lett.*, **96**, 057208_1–4 (2006).
[44] A. L. Barra, A. Caneschi, A. Cornia, A. Cornia, D. Gatteschi, L. Gorini, L. P. Heiniger, R. Sessoli and L. Sorace, *J. Am. Chem. Soc.*, **129**, 10754–10762 (2007).
[45] S. Hill, R. S. Edwards, S. I. Jones, N. S. Dalal and J. M. North, *Phys. Rev. Lett.*, **90**, 217204_1–4 (2003).
[46] R. Bircher, G. Chaboussant, A. Sieber, H. U. Güdel and H. Mutka, *Phys. Rev. B*, **70**, 212413_1–4 (2004).
[47] A. Cornia, R. Sessoli, L. Sorace, D. Gatteschi, A. L. Barra and C. Daiguebonne, *Phys. Rev. Lett.*, **89**, 257201_1–4 (2002).
[48] S. Takahashi, R. S. Edwards, S. I. Jones, D. S. Dalal and J. M. North, *Phys. Rev. B*, **70**, 094429_1–12 (2004).
[49] N. E. Chakov, S. C. Lee, A. G. Harter, P. L. Kuhns, A. P. Reyes, S. O. Hill, N. S. Dalal, W. Wernsdorfer, K. A. Abboud and G. Christou, *J. Am. Chem. Soc.*, **128**, 6975–6989 (2006).
[50] F. Luis, J. Bartolomé and J. F. Fernández, *Phys. Rev. B*, **57**, 505–513 (1998).
[51] A. L. Barra, D. Gatteschi and R. Sessoli, *Chem. Eur. J.*, **6** 1608–1614 (2000).
[52] C. Sangregorio, T. Ohm, C. Paulsen, R. Sessoli and D. Gatteschi, *Phys. Rev. Lett.*, **78**, 4645–4648 (1997).
[53] W. Wernsdorfer, N. E. Chakov and G. Christou, *Phys. Rev. Lett.*, **95** 037203_1–4 (2005).
[54] W. Wernsdorfer, N. Aliaga-Alcalde, D. N. Hendrickson and G. Christou, *Nature*, **416**, 406–409 (2002).
[55] L. Sorace, W. Wernsdorfer, C. Thirion, A. L. Barra, M. Pacchioni, D. Mailly and B. Barbara, *Phys. Rev. B*, **68**, 220407_1–4 (2003).
[56] M. Murugesu, M. Halbrych, W. Wernsdorfer, K. A. Abboud and G. Christou, *J. Am. Chem. Soc.*, **126**, 4766–4767 (2004).

[57] C. J. Milios, R. Inglis, A. Vinslava, R. Bagai, W. Wernsdorfer, S. Parsons, S. P. Perlepes, G. Christou and E. K. Brechin, *J. Am. Chem. Soc.*, **129**, 12505–12511 (2007).
[58] A. J. Tasiopoulous, W. Wernsdorfer, K. A. Abboud and G. Christou, *Angew. Chem. Int. Ed.*, **43**, 6338–6342 (2004).
[59] P. King, W. Wernsdorfer, K. A. Abboud and G. Christou, *Inorg. Chem.*, **43**, 7315–7323, (2004).
[60] A. T. Tasiopoulos, A. Vinslava, W. Wernsdorfer, K. A. Abboud and G. Christou, *Angew. Chem. Int. Ed.*, **43**, 2117–2121 (2004).
[61] E. K. Brechin, *Chem. Commun.*, 5141–5153 (2005).
[62] K. Wieghardt, K. Pohl, I. Jibril and G. Huttner, *Angew. Chem. Int. Ed. Engl.*, **23**, 77–78 (1984).
[63] J. C. Goodwin, R. Sessoli, D. Gatteschi, W. Wernsdorfer, A. L. Powell and S. L. Heath, *Dalton Trans.*, 1835–1840 (2000).
[64] W. Wernsdorfer, A. Caneschi, R. Sessoli, D. Gatteschi, A. Cornia, V. Villar and C. Paulsen, *Phys. Rev. Lett.*, **84**, 2965–2968 (2000).
[65] A. L. Barra, A. Caneschi, A. Cornia, A. Cornia, F. F. DeBiani, D. Gatteschi, C. Sangregorio, R. Sessoli and L. Sorace, *J. Am. Chem. Soc.*, **121**, 5302–5310 (1999).
[66] M. Mannini, F. Pineider, P. Sainctavit, C. Danieli, E. Otero, C. Sciancalepore, A. M. Talarico, M.-A. Arrio, A. Cornia, D. Gatteschi and R. Sessoli, *Nature Mater.*, **8**, 194–197 (2009).
[67] Z. M. Sun, C. M. Grant, S. L. Castro, D. N. Hendrickson and G. Christou, *Chem. Commun.*, 721–722 (1998).
[68] R. S. Edwards, S. Maccagnano, E. C. Yang, S. Hill, W. Wernsdorfer, D. Hendrickson and G. Christou, *J. Appl. Phys.*, **93**, 7807–7809 (2003).
[69] H. Andres, R. Basler, A. J. Blake, E. K. Brechin, C. Cadiou, G. Chaboussant, C. M. Grant, H.-U. Güdel, S. G. Harris, M. Murrie, S. Parsons, C. Paulsen, F. Semadini, V. Villar, W. Wernsdorfer and R. E. P. Winpenny, *Chem. Eur. J.*, **8**, 4867–4876 (2002).
[70] M. A. Halcrow, J.-S. Sun, J. C. Huffman and G. Christou, *Inorg. Chem.*, **34**, 4167–4177 (1995).
[71] M. Murrie, H. Stöeckli-Evans and H. U. Güdel, *Angew. Chem. Int. Ed.*, **40**, 1957–1960 (2001).
[72] For example: M. Murrie, S. J. Teat, H. Stoeckli-Evans and H. U. Güdel, *Angew. Chem. Int. Ed.*, **42**, 4653–4655 (2003); B. Moubaraki, K. S. Murray, T. A. Hudson and R. Robson, *Eur. J. Inorg. Chem.*, 4525–4529 (2008).
[73] E. C. Yang, D. N. Hendrickson, W. Wernsdorfer, M. Nakano, L. N. Zakharov, R. D. Sommer, A. L. Rheingold, M. Ledezma-Gairand and G. Christou, *J. Appl. Phys.*, **91**, 7382–7384 (2002).
[74] H. Oshio, N. Hoshino and T. Ito, *J. Am. Chem. Soc.*, **126**, 8805–8806 (2004).
[75] A. K. Boudalis, Y. Sanakis, J. M. Clemente-Juan, B. Donnadieu, V. Nastopoulos, A. Mari, Y. Coppel, J.-P. Tuchagues and S. P. Perlepes, *Chem. Eur. J.*, **14**, 2514–2526 (2008).
[76] J. J. Sokol, A. G. Hee and J. R. Long, *J. Am. Chem. Soc.*, **124**, 7656–7657 (2002).
[77] D. E. Freedman, D. M. Jenkins, A. T. Iavarone and J. R. Long, *J. Am. Chem. Soc.*, **130**, 2884–2885 (2008).

[78] A. J. Tasiopolous, W. Wernsdorfer, B. Moulton, M. J. Zawarotko and G. Christou, *J. Am. Chem. Soc.*, **125**, 15274–15275 (2003).
[79] For example: V. Mereacre, A. M. Ako, R. Clérac, W. Wernsdorfer, I. J. Hewitt, C. E. Anson and A. K. Powell, *Chem. Eur. J.*, **14**, 3577–3584 (2008).
[80] For example: C. Aronica, G. Pilet, G. Chastanet, W. Wernsdorfer, J.-F. Jacquot and D. Luneau, *Angew. Chem. Int. Ed.*, **45**, 4659–4662 (2006).
[81] C. Benelli and D. Gatteschi, *Chem. Rev.*, **102**, 2369–2388 (2002).
[82] J. N. Rebilly, G. Charron, E. Rivière, R. Guillot, A. L. Barra, M. D. Serrano, J. van Slageren and T. Mallah, *Chem. Eur. J.*, **14**, 1169–1177 (2008).
[83] T. Glaser, M. Heidemeier, T. Weyhermüller, R.-D. Hoffmann, H. Rupp and Paul Müller, *Angew. Chem. Int. Ed.*, **45**, 6033–6037 (2006).
[84] N. Ishikawa, M. Sugita, T. Ishikawa, S. Koshihara and Y. Kaizu, *J. Am. Chem. Soc.*, **125**, 8694–8695 (2003).
[85] N. Ishikawa, M. Sugita, T. Ishikawa, S. Koshihara and Y. Kaizu, *J. Phys. Chem. B*, **108**, 11265–11271 (2004).
[86] N. Ishikawa, M. Sugita and W. Wernsdorfer, *J. Am. Chem. Soc.*, **127**, 3650–3651 (2005).
[87] N. Ishikawa, M. Sugita, T. Okubo, T. Iino and Y. Kaizu, *Inorg. Chem.*, **42**, 2440–2446 (2003).
[88] S. Takamatsu, T. Ishikawa, S. Koshihara and N. Ishikawa, *Inorg. Chem.*, **46**, 7250–7252 (2007); N. Ishikawam, Y. Mizuno, S. Takamatsu, T. Ishikawa and S. Y. Koshihara, *Inorg. Chem.*, **47**, 10217–10219 (2008).
[89] N. Ishikawa, M. Sugita and W. Wernsdorfer, *Angew. Chem. Int. Ed.*, **44**, 2931–2935 (2005).
[90] M. A. AlDamen, J. M. Clemente-Juan, E. Coronado, C. Martí-Gastaldo and A. Gaita-Ariño, *J. Am. Chem. Soc.*, **130**, 8874–8875 (2008).
[91] W. Wernsdorfer, *Nature Mater.*, **7**, 179–186 (2008).
[92] H. B. Heersche, Z. de Groot, J. A. Folk, vander Zant, A H.S.J., C. Romeike, M. R. Wegewijs, L. Zobbi, D. Barreca, E. Tondello and A. Cornia, *Phys. Rev. Lett.*, **96**, 206801_1–4 (2006).
[93] M-H. Jo, J. E. Grose, K. Baheti, M. M. Deshmukh, J. J. Sokol, E. M. Rumberger, D. N. Hendrickson, J. R. Long, H. Park and D. C. Ralph, *Nano Lett.*, **6**, 2014–2020 (2006).
[94] For a recent review of the surface chemistry of SMMs, see: A. Cornia, A. F. Constantino, L. Zobbi, A. Caneschi, D. Gatteschi, M. Mannini and R. Sessoli, *Struct. Bonding*, **122**, 133–161 (2006).
[95] M. Mannini, P. Sainctavit, R. Sessoli, C. C. dit Moulin, F. Pineider, M. A. Arrio, A. Cornia and D. Gatteachi, *Chem. Eur. J.*, **14**, 7530–7535 (2008).
[96] For a simple review, see: L. Kouwenhoven and L. Glazman, *Physics World*, **14**, 33–38 (2001).
[97] J. Park, A. N. Pasupathy, J. I. Goldsmith, C. Chang, Y. Yaish, J. R. Petta, M. Rinkowski, J. P. Sethna, H. D. Abruña, P. L. McEuen and D. C. Ralph, *Nature*, **417**, 722–725 (2002).
[98] W. Liang, M. P. Shores, M. Bockrath, J. R. Long and H. Park, *Nature*, **417**, 725–729 (2002).
[99] N. Roch, S. Florens, V. Bouchiat, W. Wernsdorfer and F. Balestro, *Nature*, **453**, 633–638 (2008).

[100] C. Romeike, M. R. Wegewijs, W. Hoftstetter and H. Schoeller, *Phys. Rev. Lett.*, **97**, 206601_1–4 (2006).
[101] J. P. Cleuziou, W. Wernsdorfer, V. Bouchiat, T. Ondarçuhu and M. Monthioux, *Nat. Nanotech.*, **1**, 53–59 (2006).
[102] M. N. Leuenberger and D. Loss, *Nature*, **410**, 789–793 (2001).
[103] F. Meier, J. Levy and D. Loss, *Phys. Rev. Lett.*, **90**, 047901–047904 (2003).
[104] For example: F. Troiani, M. Affronte, S. Carretta, P. Santini and G. Amoretti, *Phys. Rev. Lett.* 94, 190501_1–4 (2005); E. Stamp and P. C. A. Gaita-Ariño, *J. Mater. Chem.*, **19**, 1718–1730 (2009).
[105] L. K. Grover, *Phys. Rev. Lett.*, **79**, 4709–4712 (1997).
[106] P. Shor, *Proceedings of the 35th Annual Symposium on Foundations of Computer Science* (ed. S. Goldwasser), IEEE Computer Society, 1994.
[107] F. Troiani, A. Ghirri, M. Affronte, S. Carretta, P. Santini, G. Amoretti, S. Piligkos, G. Timco and R. E. P. Winpenny, *Phys. Rev. Lett.*, **94**, 207208_1–4 (2005).
[108] A. Ardavan, O. Rival, J. J. L. Morton, S. J. Blundell, A. M. Tyryshkin, G. A. Timco and R. E. P. Winpenny, *Phys. Rev. Lett.*, **98**, 057201_1–4 (2007).
[109] G. A. Timco, S. Carretta, F. Troiani, R. J. Pritchard, E. J. L. McInnes, A. Ghirri, A. Candini, P. Santini, G. Amoretti, M. Affronte and R. E. P. Winpenny, *Nature Nanotech.*, **4**, 173–178 (2009).
[110] S. Bertaina, S. Gambarelli, T. Mitra, B. Tsukerblat, A. Müller and B. Barbara, *Nature*, **453**, 203–207 (2008).
[111] J. Lehmann, A. Gaita-Arino, E. Coronado and D. Loss, *Nature Nanotech.*, **2**, 312–317 (2007).
[112] C. Schlegel, J. van Slageren, M. Manoli, E. K. Brechin and M. Dressel, *Phys. Rev. Lett.*, **101**, 147203_1–4 (2008).
[113] J. J. L. Morton, A. M. Tyryshkin, A. Ardavan, K. Porfyrakis, S. A. Lyon and G. A. D. Briggs, *Phys. Rev. Lett.*, **95**, 200501_1–4 (2005).
[114] S. Hill, R. S. Edwards, N. Aliaga-Alcalde and G. Christou, *Science*, **302**, 1015–1018 (2003).
[115] K. L. Taft, C. D. Delfs, G. C. Papaethymiu, S. Foner, D. Gatteschi and S. J. Lippard, *J. Am. Chem. Soc.*, **116**, 823–832 (1994).
[116] O. Waldmann, R. Koch, S. Schromm, J. Schülein, P. Müller, I. Bernt, R. W. Saalfrank, F. Hampel and E. Balthes, *Inorg. Chem.*, **40**, 2986–2995 (2001) and references therein.
[117] J. Schnack and M. Luban, *Phys. Rev. B.*, **63**, 014418_1–7 (2000).
[118] O. Waldmann, C. Dobe, H. Mutka, A. Furrer and H. U. Gudel, *Phys. Rev. Lett.*, **95**, 057202_1–4 (2005).
[119] M. Affronte, S. Carretta, G. A. Timco and R. E. P. Winpenny, *Chem. Commun.*, 1789–1797 (2007).
[120] S. L. Heath, R. H. Laye, C. A. Muryn, N. Lima, R. Sessoli, R. Shaw, S. J. Teat, G. A. Timco and R. E. P. Winpenny, *Angew. Chem. Int. Ed.*, **43**, 6132–6135 (2004).
[121] S. Carretta, P. Santini, G. Amoretti, T. Guidi, J. R. D. Copley, Y. Qiu, R. Caciuffo, G. Timco and R. E. P. Winpenny, *Phys. Rev. Lett.*, **98**, 167401_1–4 (2007).
[122] F. Torres, J. M. Hernández, X. Bohigas and J. Tejada, *Appl. Phys. Lett.*, **77**, 3248–3250 (2000).
[123] Y. Spichkin, A. K. Zvedin, S. P. Gudin, A. S. Mischenko and A. M. Tishin, *J. Phys. D: Appl. Phys.*, **34**, 1162–1166 (2001).

[124] M. Evangelisti, A. Candini, A. Ghirri, M. Affronte, E. K. Brechin and E. J. L. McInnes, *Appl. Phys. Lett.*, **87**, 072504_1–3 (2006).
[125] R. Shaw, R. H. Laye, L. F. Jones, D. M. Low, C. Talbot-Eeckelaers, Q. Wei, C. J. Milios, S. Teat, M. Helliwell, J. Raftery, M. Evangelisti, M. Affronte, D. Collison, E. K. Brechin and E. J. L. McInnes, *Inorg. Chem.*, **46**, 4968–4978 (2007).
[126] M. Manoli, A. Collins, S. Parsons, A. Candini, M. Evangelisti and E. K. Brechin, *J. Am. Chem. Soc.*, **130**, 11129–11139 (2008).
[127] O. Khan, *Chem. Phys. Lett.*, **265**, 109–114 (1997).
[128] D. Dai and M. H. Whangbo, *J. Chem. Phys.*, **121**, 672–680 (2004).
[129] E. Greeden, *J. Mater. Chem.*, **11**, 37–53 (2001).
[130] A. Müller, S. Sarkar, S. Q. N. Shah, H. Bögge, M. Schmidtmann, Sh. Sharkar, P. Kögerler, B. Hauptfleisch, A. X. Trautwein and V. Schünemann, *Angew. Chem. Int. Ed.*, **38**, 3238–3241 (1999).
[131] A. Müller, A. M. Todea, J. van Slageren, M. Dressel, H. Bögge, M. Schmidtmann, M. Luban, L. Engelhardt and M. Rusu, *Angew. Chem. Int. Ed.*, **44**, 3857–3861 (2005).
[132] V. O. Garlea, S. E. Nagler, J. L. Zaretsky, C. Stassis, D. Vaknin, P. Kögerler, D. F. McMorrow, C. Niedermayer, D. A. Tennant, B. Lake, Y. Qiu, M. Exler, J. Schnack and M. Luban, *Phys. Rev. B*, **73**, 024414_ 1–5(2006).
[133] C. Schröder, H. Nojiri, J. Schnack, P. Hage, M. Luban and P. Kögerler, *Phys. Rev. Lett.*, **94**, 017205_1–4 (2005).
[134] For beautiful animations of classical spin calculations on large polyhedra see the 'Spinhenge' website at: http://spin.fh-bielefeld.de/
[135] A. Müller, M. Luban, C. Schröder, R. Modler, P. Kögerler, M. Axenovich, J. Schnack, P. Canfield, S. Bud'ko and N. Harrison, *Chem. Phys. Chem.*, **2**, 517–521 (2001).
[136] J. Schnack and M. Luban, *Phys. Rev. B*, **63**, 014418_1–7 (2000).
[137] O. Waldmann, *Coord. Chem. Rev.*, **249**, 2550–2566 (2005).
[138] J. Schnack, *C. R. Chemie*, **10**, 15–20 (2007).
[139] S. Carretta, P. Santini, G. Amoretti, M. Affronte, A. Candini, A. Ghirri, I. S. Tidmarsh, R. H. Laye, R. Shaw and E. J. L. McInnes, *Phys. Rev. Lett.*, **97**, 207201_1–4 (2006).
[140] M. Belesi, E. Micotti, M. Mariani, F. Borsa, A. Lascialfari, S. Carretta, P. Santini, G. Amoretti, E. J. L. McInnes, I. S. Tidmarsh and J. R. Hawkett, *Phys. Rev. Lett.*, **102**, 177201_1–4 (2009).
[141] R. Shaw, I. S. Tidmarsh, R. H. Laye, B. Breeze, M. Helliwell, E. K. Brechin, S. L. Heath, M. Murrie, S. Ochsenbein, H. U. Güdel and E. J. L. McInnes, *Chem. Commun.*, 1418–1419 (2004).
[142] For a thorough recent review, see: C. Coulon, H. Miyasaka and R. Clérac, *Struct. Bonding*, **122**, 163–206 (2006)
[143] A. Caneschi, D. Gatteschi, N. Lalioti, C. Sangregorio, R. Sessoli, G. Venturi, A. Vindigni, A. Rettori, M. G. Pini and M. A. Novak, *Angew. Chem. Int. Ed.*, **40**, 1760–1763 (2001).
[144] R. J. Glauber, *J. Math. Phys.*, **4**, 294–307 (1963).
[145] A. Caneschi, D. Gatteschi, N. Lalioti, R. Sessoli, L. Sorace, V. Tangoulis and A. Vindigni, *Chem. Eur. J.*, **8**, 286–292 (2002).
[146] K. Bernot, L. Bogani, A. Caneschi, D. Gatteschi and R. Sessoli, *J. Am. Chem. Soc.*, **128**, 7947–7956 (2006).
[147] M. Ferbinteanu, H. Miyasaka, W. Wernsodrfer, K. Nataka, K. Suguira, M. Yamashita, C. Coulon and R. Clerac, *J. Am. Chem. Soc.*, **127**, 3090–3099 (2005).

Index

Molecular Materials Edited by Duncan W. Bruce, Dermot O'Hare and Richard I. Walton